

MULTIDISCIPLINARY AND APPLIED OPTICS

Optics of the Human Eye

Second Edition

**David A. Atchison
and George Smith**



CRC Press
Taylor & Francis Group

Optics of the Human Eye

This book describes the optical structure and optical properties of the human eye. For ease of reference, the most commonly useful topics are at the beginning and topics with narrower appeal are placed towards the end. The book is divided into five sections, covering:

- Basic optical structure of the eye, including the refracting components, the pupil, axes, and simple models of the eye
- Image formation and refraction of the eye, including refractive errors, measurement, and correction
- Interactions between light and the eye, considering transmission, reflection, and scatter in the media and at the fundus
- Aberrations and retinal image quality
- Depth-of-field and age-related changes in the optics of the eye

The book concludes with five appendices; these cover mathematics relating to paraxial optics, aberration theory, image quality criteria and refraction across the pupil, and they provide construction data and optical parameters of several schematic eyes.

There have been many developments in the field of visual optics since the first edition was published in 2000. There have been advances in instrumentation for imagery, biometry, and aberrations of the eye. The refraction anomaly of myopia has increased in prevalence throughout the world, and is getting increasing attention because of its association with ocular pathology in the middle and later years of life. Ocular aberrations are now considered in terms of Zernike polynomials rather than Taylor polynomials. Aberrations can be manipulated to better understand their effects on visual performance to improve imagery of the retina for the betterment of diagnosis of various ocular conditions, and to treat the progression of myopia in children. To deal with these developments, the section on aberrations and retinal image quality has undergone considerable revision.

This book will be an invaluable purchase for all those with an interest in vision, such as optometrists, ophthalmologists, vision scientists, optical physics, and students of visual optics. An understanding of the optics of the human eye is particularly important to designers of ophthalmic diagnostic equipment and visual optical systems, such as telescopes.

Multidisciplinary and Applied Optics

Series Editor:

*Vasudevan Lakshminarayanan, University of Waterloo, Ontario,
Canada*

*Quantum Mechanics of Charged Particle Beam Optics: Understanding Devices from
Electron Microscopes to Particle Accelerators: Understanding Devices from Electron
Microscopes to Particle Accelerators*

Ramaswamy Jagannathan,
Sameen Ahmed Khan

Understanding Optics with Python

Vasudevan Lakshminarayanan, Hassen Ghalila, Ahmed Ammar,

L. Srinivasa Varadharajan

Hassen Ghalila, University Tunis El Manar, Tunisia

Ahmed Ammar, University Tunis El Manar, Tunisia

L. Srinivasa Varadharajan, University of Waterloo, Ontario, Canada

Contemporary Holography

C. S. Narayananamurthy

Fourier Theory in Optics and Optical Information Processing

Toyohiko Yatagai

Optics of the Human Eye, Second Edition

David A. Atchison and George Smith

For more information about this series, please visit: [https://www.crcpress.com/
Multidisciplinary-and-Applied-Optics/book-series/CRCMULAPPOPT](https://www.crcpress.com/Multidisciplinary-and-Applied-Optics/book-series/CRCMULAPPOPT)

Optics of the Human Eye

Second Edition

David A. Atchison and George Smith



CRC Press

Taylor & Francis Group

Boca Raton London New York

CRC Press is an imprint of the
Taylor & Francis Group, an **informa** business

Designed cover image: © Shutterstock

Second edition published 2023

by CRC Press

6000 Broken Sound Parkway NW, Suite 300, Boca Raton, FL 33487-2742

and by CRC Press

4 Park Square, Milton Park, Abingdon, Oxon, OX14 4RN

CRC Press is an imprint of Taylor & Francis Group, LLC

© 2023 Taylor & Francis Group, LLC

First edition published by Elsevier 2000

Reasonable efforts have been made to publish reliable data and information, but the author and publisher cannot assume responsibility for the validity of all materials or the consequences of their use. The authors and publishers have attempted to trace the copyright holders of all material reproduced in this publication and apologize to copyright holders if permission to publish in this form has not been obtained. If any copyright material has not been acknowledged please write and let us know so we may rectify in any future reprint.

Except as permitted under U.S. Copyright Law, no part of this book may be reprinted, reproduced, transmitted, or utilized in any form by any electronic, mechanical, or other means, now known or hereafter invented, including photocopying, microfilming, and recording, or in any information storage or retrieval system, without written permission from the publishers.

For permission to photocopy or use material electronically from this work, access www.copyright.com or contact the Copyright Clearance Center, Inc. (CCC), 222 Rosewood Drive, Danvers, MA 01923, 978-750-8400. For works that are not available on CCC please contact mpkbookspermissions@tandf.co.uk

Trademark notice: Product or corporate names may be trademarks or registered trademarks and are used only for identification and explanation without intent to infringe.

ISBN: 978-0-367-64051-4 (hbk)

ISBN: 978-0-367-65253-1 (pbk)

ISBN: 978-1-003-12860-1 (ebk)

DOI: 10.1201/9781003128601

Typeset in Times

by Newgen Publishing UK

Contents

Acknowledgements	xi
About the Authors	xiii
Sign Convention and Symbols	xv
Introduction.....	xvii

SECTION I Basic Optical Structure of the Human Eye

Chapter 1 The Human Eye: An Overview	3
1.1 Introduction.....	3
1.2 Optical Structure and Image Formation.....	4
1.3 The Retina.....	5
1.4 The Cardinal Points.....	8
1.5 The Equivalent Power and Focal Lengths.....	9
1.6 Axes of the Eye.....	10
1.7 Center-of-Rotation	10
1.8 Field-of-Vision	10
1.9 Binocular Vision and Binocular Overlap	11
1.10 Typical Dimensions.....	12
Chapter 2 Refracting Components: Cornea and Lens.....	15
2.1 Introduction.....	15
2.2 The Cornea.....	15
2.3 The Lens and its Parameters in the Unaccommodated State.....	25
2.4 Accommodation.....	31
Chapter 3 The Pupil	43
3.1 Introduction – the Iris.....	43
3.2 Entrance and Exit Pupils	43
3.3 Pupil Centration	46
3.4 Pupil Size	46
3.5 Pupil Aberration and Shape of the Obliquely Viewed Pupil.....	49
3.6 Significance of Pupil Size	53
3.7 Measurement of Pupil Size (Pupilometry).....	54
3.8 Artificial Pupils	54

Chapter 4	Axes of the Eye	57
4.1	Introduction.....	57
4.2	Definitions and Significance	57
4.3	Locating Some Axes	62
4.4	Angles between Axes	63
Chapter 5	Paraxial Schematic Eyes	69
5.1	Introduction.....	69
5.2	Development of Paraxial Schematic Eyes	70
5.3	Gaussian Properties and Cardinal Points	71
5.4	“Exact” Schematic Eyes	76
5.5	Simplified Schematic Eyes	77
5.6	Reduced Schematic Eyes	78
5.7	Variable Accommodating Eyes	79
<i>SECTION II Image Formation and Refraction</i>		
Chapter 6	Image Formation: The Focused Paraxial Image.....	85
6.1	Introduction.....	85
6.2	The General Case	85
6.3	Eye Focused at Infinity	88
6.4	Binocular Vision.....	89
Chapter 7	Refractive Anomalies	93
7.1	Introduction.....	93
7.2	Spherical Refractive Anomalies.....	94
7.3	Astigmatic Refractive Errors	97
7.4	Anisometropia.....	98
7.5	Distribution of Refractive Errors and Ocular Components	98
7.6	The Power of the Correcting Lens	102
7.7	Effect of Parameter Changes on Refractive Errors	108
Chapter 8	Measuring Refractive Errors	115
8.1	Introduction.....	115
8.2	Subjective Refraction Techniques.....	115
8.3	Subjective/Objective Refraction Techniques	121
8.4	Objective Refraction Techniques	123
8.5	Accuracy and Reliability of Refraction	131
8.6	Factors Affecting Refraction	133

Chapter 9	Image Formation: The Defocused Paraxial Image	139
9.1	Introduction.....	139
9.2	Retinal Image Size	140
9.3	Size of the Defocus Blur Disc.....	143
9.4	Other Effects of Defocus.....	148
Chapter 10	Some Optical Effects of Ophthalmic Lenses	153
10.1	Introduction.....	153
10.2	Spectacle Magnification.....	153
10.3	Pupil Position and Magnification.....	156
10.4	Relative Spectacle Magnification.....	158
10.5	Effects on Far and Near Points and Accommodative Demand.....	160
10.6	Rotation Magnification, Field-of-View, and Field-of-Vision	163
10.7	Spectacle Lens Design	164
10.8	Contact Lens Optics.....	168
10.9	Intraocular Lens Optics.....	173
SECTION III Light and the Eye		
Chapter 11	Light and the Eye: Introduction.....	183
11.1	Introduction.....	183
11.2	Radiation and the Electromagnetic Spectrum.....	183
11.3	Light.....	183
11.4	Photometric Quantities, Units, and Example Levels	187
11.5	Some Useful Relationships	189
11.6	Which Photometric Quantity to Use	190
11.7	Colorimetry	191
Chapter 12	Passage of Light into the Eye	195
12.1	Introduction.....	195
12.2	Specular Reflection	196
12.3	Transmittance	198
12.4	Scatter	203
12.5	Fluorescence	206
12.6	Birefringence.....	207
Chapter 13	Light Level at the Retina	213
13.1	Introduction.....	213
13.2	Retinal Illuminance: Directly Transmitted Light.....	213

13.3	Retinal Illuminance: Scattered Light	219
13.4	Photon Density Levels	222
13.5	Maxwellian View	224
Chapter 14	Light Interaction with the Fundus	229
14.1	Introduction.....	229
14.2	Fundus Reflectance	230
14.3	Absorption.....	232
14.4	Birefringence.....	234
14.5	The Stiles–Crawford Effect and Retinal Directionality	234
SECTION IV <i>Aberrations and Retinal Image Quality</i>		
Chapter 15	Monochromatic Aberrations.....	251
15.1	Introduction.....	251
15.2	Representation of Monochromatic Aberrations	251
15.3	Specification of Monochromatic Aberrations – Taylor Series	253
15.4	Specification of Monochromatic Aberrations – Zernike Aberration System	254
15.5	Techniques	273
15.6	Magnitudes of Aberrations.....	274
15.7	Influence of Monochromatic Aberrations on Visual Performance and Consequences of Correcting Them.....	283
Chapter 16	Monochromatic Aberrations of Optical Model Eyes	295
16.1	Introduction.....	295
16.2	Aberrations of Paraxial Schematic Eyes.....	295
16.3	Modeling Surface Shapes	298
16.4	Modeling the Lenticular Refractive Index Distribution.....	302
16.5	Modeling the Retina.....	306
16.6	Survey of Finite Schematic Eyes	306
16.7	Performance of Finite Schematic Eyes	309
16.8	Other Optical Model Eyes, Including Customized Models	316
16.9	Which Eye Model to Use.....	316
Chapter 17	Chromatic Aberrations	321
17.1	Introduction.....	321
17.2	Longitudinal Chromatic Aberration	321
17.3	Transverse Chromatic Aberration	322

17.4	Measurement of Longitudinal Chromatic Aberration	325
17.5	Measurement of Transverse Chromatic Aberration	329
17.6	Effects of Chromatic Aberrations on Vision	331
17.7	Aberration Compensation and Correction	334
17.8	Modeling Chromatic Aberrations	336
17.9	Estimating Lengths in Eyes	342
Chapter 18	Retinal Image Quality	349
18.1	Introduction.....	349
18.2	The Point and Line Spread Functions.....	350
18.3	The Optical Transfer Function	354
18.4	Retinal Image Quality	361
18.5	More Image Quality Criteria – Metrics	371
SECTION V <i>Miscellaneous</i>		
Chapter 19	Depth-of-Field.....	379
19.1	Introduction.....	379
19.2	Criteria for Determining Depth-of-Field	381
19.3	Modeling Depth-of-Field	386
19.4	Methods for Increasing Depth-of-Field	390
Chapter 20	The Aging Eye.....	395
20.1	Introduction.....	395
20.2	Cornea.....	395
20.3	Anterior Chamber	396
20.4	Pupil Diameter	396
20.5	Lens.....	397
20.6	Vitreous Chamber	401
20.7	Refractive Errors and Axial Length	401
20.8	Accommodation and Presbyopia	402
20.9	Aberrations.....	407
20.10	Photometry	407
20.11	Schematic Eyes	409
Appendices		
Appendix 1	Paraxial Optics	421
A1.1	Introduction.....	421
A1.2	The Paraxial Approximations and Paraxial Rays.....	422
A1.3	A Paraxial Raytracing Scheme	424

A1.4 The Optical Invariant	425
A1.5 Cardinal Points and Equivalent Power.....	426
A1.6 The Lens Equation	426
A1.7 Gaussian Optics	427
Appendix 2 Seidel Aberration Theory	429
A2.1 Quantification of Aberrations.....	429
A2.2 The Wave Aberration Function	431
A2.3 Seidel Aberrations.....	433
Appendix 3 Schematic Eyes.....	441
A3.1 Introduction.....	441
A3.2 Paraxial Schematic Eyes	441
A3.3 Finite Schematic Eyes.....	448
Appendix 4 Refraction Powers across the Pupil	455
Appendix 5 Calculation of PSF and OTF from Aberrations of an Optical System	465
A5.1 The Point Spread Function (PSF)	465
A5.2 The Optical Transfer Function (OTF).....	468
Index.....	471

Acknowledgements

Several colleagues commented on drafts or provided references and advice: David Alonso-Caneiro, Arthur Bradley, Juan Bueno, Charles Campbell, Neil Charman, Stephen Dain, Andreas Hartwig, Mo Jalie, Matt Jaskulski, Linda Lundström, Ankit Mathur, Vinay Nilagiri, Sotiris Plainis, Scott Read, Jos Rozema, Tom Salmon, Katrina Schmid, Michael Simpson, Lawrence Stark, Marwan Suheimat, Larry Thibos, Christopher Tyler, Tom van den Berg, and Stephen Vincent. In particular, we thank Larry Thibos for the derivations of refractive power across the pupil in Appendix 4.

We are grateful to Pablo Artal, Shrikant Bharadwaj, Linda Lundström, Jos Rozema, Tom Salmon, Larry Thibos, and Barry Winn for providing data for some figures; these are also acknowledged at relevant figure captions.



Taylor & Francis
Taylor & Francis Group
<http://taylorandfrancis.com>

About the Authors

David A. Atchison is Professor in the School of Optometry and Vision Sciences at Queensland University of Optometry in Brisbane, Australia, where he researches and teaches ophthalmic optics and visual optics. He is a Fellow of the Optical Society and of the American Academy Optometry, and is a board member of the journals *Clinical & Experimental Optometry* and *Ophthalmic & Physiological Optics*. Awards include the Garland W. Clay Award of the American Academy of Optometry (together with George Smith), the H.B. Collin Research medal of Optometry Australia, and the Glenn A. Fry award of the American Academy of Optometry.

George Smith was Associate Professor in the Department of Optometry at the University of Melbourne in Melbourne, Australia, where he researched optics and taught in the optometry program. Interests included lighting, visual ergonomics, and design of visual optics instruments. He ran a radiometry and photometric laboratory, was an expert assessor for National Association of Testing Authorities in Australia, and served on several committees of Standards Australia. As well as this book, he was the first author of *The Eye and Visual Optical Instruments*.



Taylor & Francis
Taylor & Francis Group
<http://taylorandfrancis.com>

Sign Convention and Symbols

When we examine image formation and raytracing, we need a sign convention. Although the choice of a sign convention is arbitrary, it must be consistent. In this book, distances to the left of a surface or other reference position or below the optical axis are negative, and those to the right or above are positive. Angles due to anticlockwise rotations of the ray from the optical axis are positive, and those due to clockwise rotations are negative. The sign convention is given in more detail on page 422.

DISTANCE NOTATION AND SIGN

Points are denoted by Roman letters in bold. Distances are denoted by either a single lower-case letter such as l , or by two upper-case letters such as \mathbf{PF} . In this example, \mathbf{P} and \mathbf{F} are both points and \mathbf{PF} denotes the distance from \mathbf{P} to \mathbf{F} . If \mathbf{F} is to the right of \mathbf{P} , this distance is positive, and if \mathbf{F} is to the left of \mathbf{P} , this distance is negative.

GREEK ALPHABET

Greek letters are used extensively throughout the book.

α A	alpha	β B	beta	γ Γ	gamma
δ Δ	delta	ε E	epsilon	ζ Z	zeta
η H	eta	θ Θ	theta	ι I	iota
κ K	kappa	λ Λ	lambda	μ M	mu
ν N	nu	ξ Ξ	xi	\circ O	omicron
π Π	pi	ρ P	rho	σ Σ	sigma
τ T	tau	υ Y	upsilon	ϕ Φ	phi
χ X	chi	ψ Ψ	psi	ω Ω	omega

UNITS AND THEIR ABBREVIATIONS

SI units are indicated by an asterisk

meter*	m
centimeter	cm
millimeter	mm
micrometer	μ m
nanometer	nm
diopter	D
prism diopter	Δ
Joule	J
Watt	W
candela*	cd
lumen	lm

steradian	st
second*	s
Hertz	Hz
Kelvin*	K
radian	rad
degree	°, deg
minutes of arc	min.arc
mole*	mol

Introduction

The purpose of this book is to describe the optical structure and optical properties of the human eye. It will be useful to those who have an interest in vision, such as optometrists, ophthalmologists, vision scientists, optical physicists, and students of visual optics. An understanding of the optics of the human eye is particularly important to designers of ophthalmic diagnostic equipment and visual optical systems, such as telescopes.

Many animals have some sort of eye structure or sophisticated light sense. Like humans, some rely heavily on vision, including predatory birds and insects such as honeybees and dragonflies. However, many animals rely much more on other senses, particularly hearing and smell, than on vision. The visual sense is very complex and can process huge amounts of information very rapidly. How this is done is not fully understood; it requires greater knowledge of how the neural components of vision (retina, visual cortex, and other brain centers) process the retinal image. However, the first stage in this complex process is the formation of the retinal image. In this text, we investigate how the image is formed and discuss factors that affect its quality.

Most animal eyes can be divided into two groups: compound eyes (as possessed by most insects), and vertebrate eyes (such as the human eye). Compared with vertebrate eyes, there is considerable variation in the compound eyes. Compound eyes contain many optical elements (ommatidia), each with its own aperture to the external world. Vertebrate eyes have a single aperture to the external world, which is used by all the detectors. Several other animals have simple eyes, which can be described as less developed versions of the vertebrate eye. All eyes, of whatever type, involve compromises between the need for detection (sensitivity), particularly at low light levels, and spatial resolving capability in terms of the direction or form of an object.

Although this book is about the optics of the human eye, we do not wish to consider the optics in complete isolation from the neural components, as otherwise we cannot appreciate what influence changes in the retinal image will have on vision performance. As an example, altering the optics has considerable influence on resolution of objects for central vision but not for peripheral vision. This is because the retina's neural structure is fine enough at its center, but not in the periphery, for large changes in optical quality to be of importance (Chapter 18). Thus, the neural components of the visual system, particularly the retinal detector, rate some mention in the book. The neural structures of the retina themselves produce optical effects. As an example, the photoreceptors exhibit waveguide properties that make light arriving from some directions more efficient at stimulating vision than light arriving from other directions. Another example is that the regular arrangement of the nerve fiber layers produces polarization effects.

While image formation in the eye is similar to that in man-made optical systems, such as cameras and must obey the conventional optical laws, there are some interesting differences because of the eye's biological basis. Perhaps the greatest difference is that, as a living organ, the eye responds to its environment, often to give the best image under different circumstances. Also, it grows, ages, and suffers

disease. Unlike most man-made optical systems, the eye is not rotationally symmetrical about a single axis, and different axes must be used to define image formation.

There are many interesting and important optical effects associated with ocular diseases such as keratoconus (conical cornea) and cataract. Furthermore, the balance between optical and neural contributions to overall vision performance changes with diseases of the retina and beyond. Although there are some passing references to cataract, we have concentrated on the healthy human eye. We give some prominence to age-related changes in the optics of the eye throughout the book, and devote Chapter 20 to this topic.

To make the book easy to read it is divided into several chapters, with each chapter dedicated to a single theme. The most commonly useful topics are at the beginning, and topics with narrower appeal (such as ocular aberrations) are placed towards the end. Section I covers the basic optical structure of the human eye, including the refracting components, the pupil, axes, and simple models of the eye. Section II is about image formation and refraction of the eye. This includes the refractive errors of the eye, their measurement and correction, and paraxial treatments of focused and defocused image sizes and positions. Section III deals with the interactions between light and the eye, considering transmission, reflection, and scatter in the media of the eye and at the fundus. Section IV deals with aberrations and retinal image quality. As well as considering these for real eyes, it covers the modeling of eyes and the performance of a range of schematic eyes of different levels of sophistication. Section V considers the topics of depth-of-field and age-related changes in the optics of the eye. While depth-of-field effects could possibly have been placed earlier in the book, understanding them well requires some knowledge about aberration and diffraction. The book concludes with five appendices, four of which (Appendices 1, 2, 4, and 5) cover some mathematics relating to paraxial optics, aberrations theory, image quality criteria, and refraction across the pupil. Appendix 3 lists construction data, optical parameters, and the Seidel aberrations of several schematic eyes.

There have been many developments in the field of visual optics since 2000 when the first edition was published. There have been advances in instrumentation for imagery, biometry, and aberrations of the eye. The refraction anomaly of myopia has increased in prevalence throughout the world, particularly in many Asian countries, and is getting increasing attention because of its association with ocular pathology in the middle and later years of life. The way that people think about ocular aberrations was changing about the time the book was first published in 2000, with the swapping from a system of Taylor aberration terms to Zernike polynomials; at the time of the first edition, the measurement of aberrations was the preserve of a few research laboratories whereas now aberrations for the eye and the cornea can be obtained by a practitioner at the touch of a button. Furthermore, aberrations can be manipulated to better understand their effects on visual performance, to improve imagery of the retina for the betterment of diagnosis of various ocular conditions, and to treat the progression of myopia in children. To deal with these developments, Section IV on aberrations and image quality has undergone considerable revision.

The important visual function accommodation, whose loss we rue when we get into our forties, has no dedicated chapter. We did not see a need as it features in all but three chapters and is prominent in Chapters 2 and 20.

The previous edition made extensive use of Seidel aberration theory. Although this is not accurate for large pupils and large field angles, this has the useful property of showing surface contributions to aberrations, including that of asphericity. Contributions of gradient index can also be determined. Seidel theory and aberrations are not used within the text, but for continuity with the previous edition they are covered in Appendices 2 and 3.



Taylor & Francis
Taylor & Francis Group
<http://taylorandfrancis.com>

Section I

*Basic Optical Structure of the
Human Eye*



Taylor & Francis
Taylor & Francis Group
<http://taylorandfrancis.com>

1 The Human Eye

An Overview

1.1 INTRODUCTION

This chapter is a short overview of the optical structure and function of the human eye. It mentions briefly some important aspects such as the cornea, the lens, and ocular axes, which are covered in more detail in later chapters. Other important topics, such as the passage of light, aberrations, and retinal image quality, are also discussed in later chapters.

The structure of the human eye is shown in Figure 1.1. The outer layer is in two parts: the anterior *cornea* and the posterior *sclera*. The cornea is transparent and approximately spherical with a radius of curvature of about 8 mm. Its diameter is approximately 11.5 mm horizontally and 10.5 mm vertically. The sclera is a dense, white, opaque, fibrous tissue that is mainly protective in function and is approximately spherical with a diameter of about 24 mm. The centers of curvature of the sclera and cornea are separated by about 5 mm. More accurate measures of shapes are given in subsequent chapters.

The middle layer of the eye is the uveal tract. It is composed of the *iris* anteriorly, the *choroid* posteriorly, and the intermediate *ciliary body*. The iris plays an important optical function through the size of its aperture, the ciliary body is important to the process of *accommodation*, and both the ciliary body and choroid support important vegetative processes.

The inner layer of the eye is the *retina*, which is an extension of the central nervous system and is connected to the brain by the optic nerve.

The inside of the posterior segment is called the *fundus*. This generally refers to the back of the eye that is visible in internal examination, such as in retinoscopy. The fundus includes the retina along with the optic disc and aspects of the choroid and possibly the sclera.

The inside of the eye is divided into three compartments:

1. The *anterior chamber*, between the cornea and iris, which contains the aqueous fluid.
2. The *posterior chamber*, between the iris, the ciliary body, and the lens, which contains the aqueous fluid.
3. The *vitreous chamber*, between the lens and the retina, which contains a transparent colorless and gelatinous mass called the vitreous humor or vitreous body.

The lens of the eye is immediately behind the iris, and is connected to the ciliary body via suspensory fibers called *zonules*.

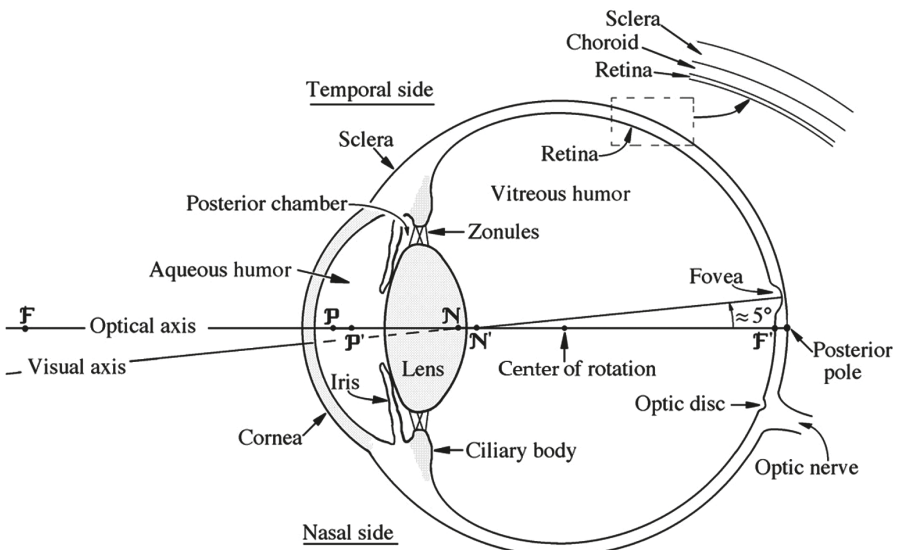


FIGURE 1.1 The horizontal section of the right eye as seen from above. The pupil is the opening in the iris. The cardinal points (F , F' , P , P' , N , and N') are for the relaxed eye.

The internal pressure of the eye must be higher than that of the atmosphere in order to maintain the shape of the cornea, and must be maintained at an approximately constant level in order to maintain the transparency of the ocular media. The pressure is controlled by the production of aqueous fluid in the ciliary body and by drainage of this aqueous fluid from the eye. This drainage is through the angle of the anterior chamber (between the cornea and the iris) to the canal of Schlemm (not shown in Figure 1.1) and, finally, to the venous drainage of the eye.

The eye rotates in its socket by the action of six extra-ocular muscles.

More detailed anatomical descriptions of the human eye can be found in books, such as those by Hogan et al. (1971), Snell and Lemp (1998), Bron et al. (2001), Remington (2012), and Freddo and Chaum (2018).

1.2 OPTICAL STRUCTURE AND IMAGE FORMATION

The principles of image formation by the eye are the same as for man-made optical systems, such as the camera lens. Image-forming light enters the eye through the cornea, and is refracted by the cornea and the lens to be focused at the retina. Of the two refracting elements, the cornea has the greater power. However, whereas the corneal power is constant, the power of the lens can change when the eye needs to focus at different distances. This process is called *accommodation*, and occurs because of an alteration in the lens shape. It is discussed further in Chapters 2 and 20, although its consequences for the ocular optics are mentioned in several other chapters. The diameter of the incoming beam of light is controlled by the iris, which forms the *aperture stop* of the eye. The opening in the iris is generally called the *pupil*. As with

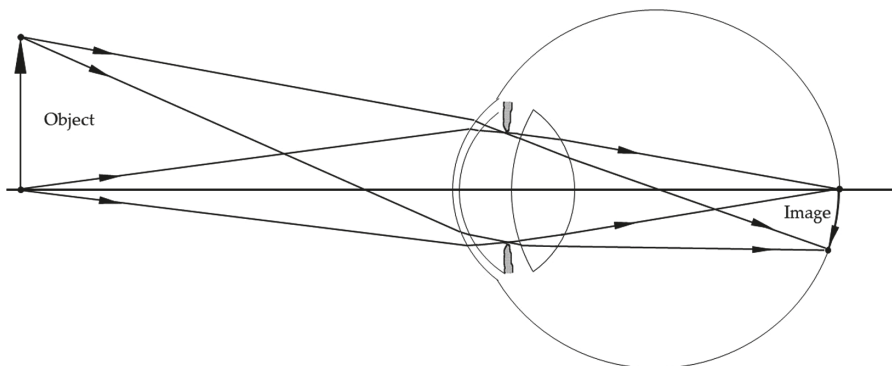


FIGURE 1.2 Image formation of the human eye.

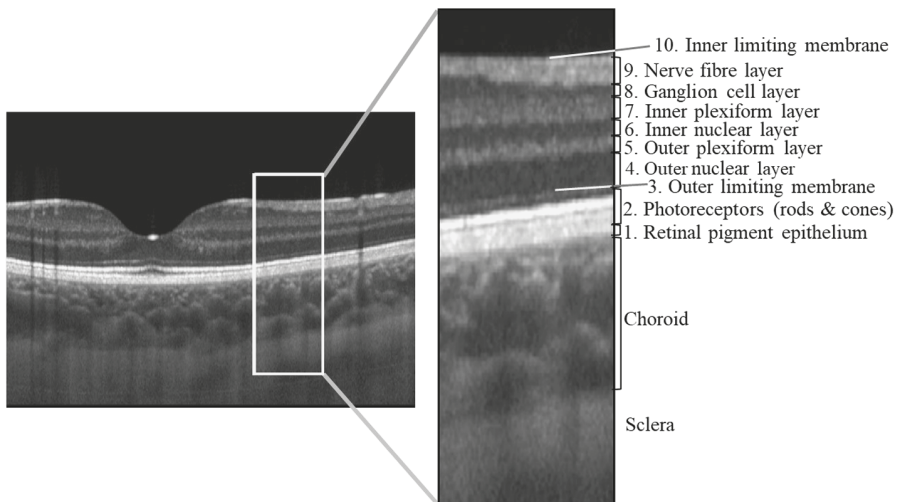


FIGURE 1.3 The layers of the retina. This figure was kindly provided by Scott Read and Stephen Vincent.

all optical systems, the aperture stop is a very important component of a system, affecting a wide range of optical processes, and it is discussed in detail in Chapter 3.

Figure 1.2 shows two light beams from object points forming images on the retina. The image is inverted, as it is for a camera. We discuss this image formation in more detail in Chapter 6.

1.3 THE RETINA

The light-sensitive tissue of the eye is the *retina* (Figure 1.3). It consists of a number of cellular and pigmented layers and a nerve fiber layer. These layers have varying degrees of optical significance, with the amount of incoming light being reflected

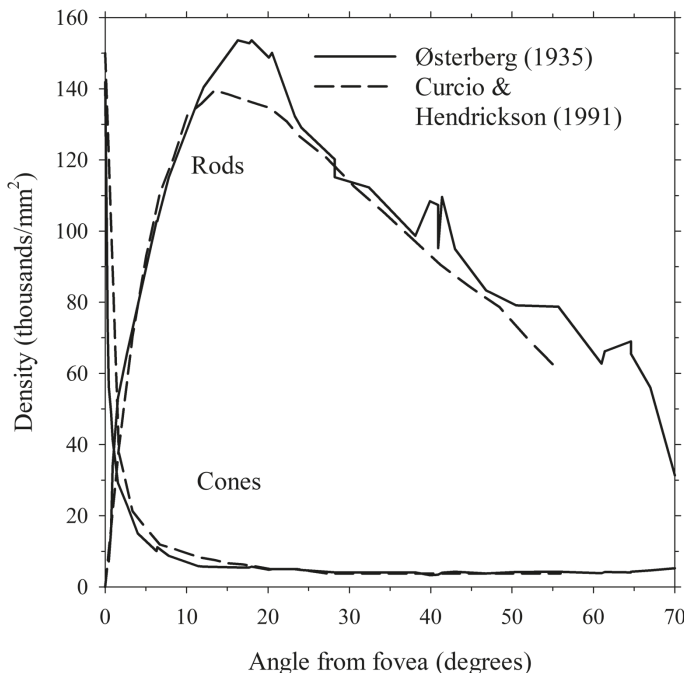


FIGURE 1.4 The density of cones and rods across the retina in the temporal direction from Østerberg (1935) and from Curcio and Hendrickson (1991). The data from Curcio and Hendrickson have been converted from distances along the retina to angles relative to the back nodal point of the eye, assuming a spherical retina of diameter 12 mm and a distance between the back nodal point and retina of 17.054 mm.

specularly and scattered by each layer being of particular importance. This aspect is discussed in greater depth in Chapter 14. The thickness of the retina varies from about 220 μm (0.22 mm) at the foveal center (Gong et al. 2016; Read et al. 2015) to about 350 μm about 1 mm from the center (Read et al. 2015) and then decreases to about 110 μm at its limits (Hogan et al. 1971).

There is a layer of light-sensitive cells at the back of the retina, and the light must pass through the other layers to reach these cells. These receptor cells are of two types, known as *rods* and *cones*. The names refer to their shapes, but considerable variations in shape occur with location, and it is not always possible to distinguish between the two types on this basis. Figure 1.4 shows their distribution along the horizontal temporal section of the retina. There are about 100 million rods in the retina, and they reach their maximum density at about 20° from the fovea. There are approximately 5 million cones in the retina.

In general, rods are longer and narrower than cones. Rods are sometimes described as highly sensitive low-level light detectors. However, much of this is due to the neural wiring that occurs rather than differences between the receptors. The retinal neural network of rods is such that the output of about 100 rods can combine on the way to the brain, so that the rod system has very high sensitivity to light but poor

spatial resolution. In contrast, the output of fewer cones is combined, so the cone system functions at higher light levels and is capable of higher spatial resolution. Cones recover from exposure to light more quickly than rods. The first stage in color vision is the existence of three types of cones, each with different wavelength sensitive properties: L (long), M (medium), and S (short) cones.

The cones predominate in the *fovea*, which is 1.5 mm or approximately 5° wide as subtended at the back nodal point N' of the eye. The fovea is free of rods in its central 1° field. At high light levels the best resolution is attained by the cones in the fovea, which occupies only about 1/1000th of the total retinal area. Despite the predominance of cones at the fovea, it contains only about 50,000 cones, or 1 % of the total, and an even smaller proportion (0.05 %) is found in the high-resolution *foveola* (Tyler 2015, 1996). Therefore, most cones are distributed throughout the peripheral retina. At low light levels the cones at the fovea do not operate; thus, the center of the fovea is “night blind”, and it is necessary to look eccentrically to see objects using the rods. At very low light levels, maximum visual acuity and detection ability occur about 10–15° away from the fovea.

The location of the fovea is shown in Figure 1.1. When the eye fixates on an object of interest, the center of its image is formed on the foveal center, which is inclined at about 5° from the “best fit” optical axis. At the fovea, the layers overlying the receptor cells are thinner than elsewhere in the retina (Figure 1.3) and, as a result, the fovea has a pit-like structure. The bottom of this pit is about 1° wide and corresponds to the rod-free region. The foveola is the approximately 0.5°-wide avascular center of the foveal pit and is the region of highest resolution.

The diameters and packing of the foveal cones affect visual acuity, and we examine this relationship briefly in section 18.4. Curcio et al.’s (1990) estimates of the diameters of foveal cones are given in Table 1.1.

The off-axis position of the fovea is most intriguing since aberration theory predicts that the best image of an optical system is usually formed on the optical axis. Therefore, the retinal image quality at the fovea should be worse than at the posterior pole. The off-axis position of the fovea has some interesting visual effects, which we discuss in Chapter 17.

TABLE 1.1
Diameters of Foveal Cones

μm	Min. arc	Position
2.2	0.45	central fovea
3.9	0.79	0.125 mm out
5.0	1.01	0.52 mm out
5.6	1.12	0.66 mm out
7.2	1.46	1.35 mm out

Source: Data from Curcio et al. (1990).

Note: The angular values are calculated assuming the distance between the back nodal point and the fovea is 17 mm.



FIGURE 1.5 Demonstration of the blind spot. Look steadily at the cross with your right eye (left eye closed) from about 20 cm. Vary this distance until you find a position for which the spot disappears.

The fovea is the central part of the *macula*, whose peripheral limits are where the cells of the outer nuclear layer are reduced to a single row (Hogan et al. 1971). The macular diameter is 5.5 mm (19°).

The photoreceptor cells synapse with bipolar cells, which in turn synapse with ganglion cells whose axons combine to form the optic disc. There are several types of ganglion cells, including intrinsically photosensitive retinal ganglion cells that are themselves photoceptors (Do 2019); these have a role in steady state pupil responses and circadian rhythms. They are several other cell types in the retina, some of which, such as the horizontal and amacrine cells, form synapses with the main retinal cells in the visual pathway.

1.3.1 THE OPTIC DISC AND BLIND SPOT

The vascular supply to the outer layers of the retina is carried in the choroid, which lies between the retina and the sclera. The vascular supply to the inner retina enters the eye at the optic disc, whose location is shown in Figure 1.1. There are no cones or rods here, and hence this region is blind. The name given to the corresponding region in the *visual field* is the *blind spot*. The optic disc is approximately 5° wide horizontally and 7° vertically, and its center is approximately 15° nasally and 1.5° upwards relative to the fovea. Correspondingly, the blind spot is 15° temporally and 1.5° downwards relative to the point of fixation. Figure 1.5 provides a demonstration of the blind spot.

1.4 THE CARDINAL POINTS

Every centered optical system that has some equivalent power (i.e., is not afocal) has six cardinal points that lie on the optical axis. These are in three pairs. Two are focal points, which we denote by the symbols \mathbf{F} and \mathbf{F}' , two are principal points denoted by the symbols \mathbf{P} and \mathbf{P}' , and two are nodal points denoted by the symbols \mathbf{N} and \mathbf{N}' . The positions of these cardinal points in an eye depend upon its structure and the level of accommodation. For an eye focused at infinity, the approximate positions of these cardinal points are shown in Figure 1.1. More precise positions are given in Chapter 5, where we discuss schematic eyes and their properties. These cardinal points are as follows (Figure 1.6):

1. *Focal points (\mathbf{F} and \mathbf{F}')*. Light leaving the front (also first and anterior) focal point \mathbf{F} passes into the eye, and would be imaged at infinity after final

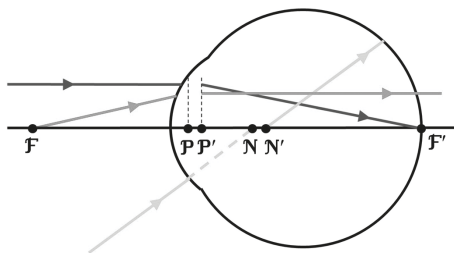


FIGURE 1.6 The cardinal points of the eye.

refraction by the lens if the retina was not in the way. Light parallel to the axis and coming into the eye from an infinite distance is imaged at the back (also second and posterior) focal point F' . Thus, for the eye focused at infinity, the retina coincides with the back focal point.

2. *Principal points* (P and P'). These are images of (or conjugate to) each other, such that their transverse magnification is +1. That is, if an object were placed at one of these points, an erect image of the same size would be formed at the other point. For raytracing purposes, object positions can be referenced to the front principal plane and image positions can be referenced to the back principal plane.
3. *Nodal points* (N and N'). These are also images or conjugates of each other, but have a special property such that a ray from an off-axis point passing towards N appears to pass through N' on the image side of the system, while inclined at the same angle to the axis on each side of the system. Such a ray is called the *nodal ray*, and when the off-axis point is the point of fixation, the ray is called the *visual axis*.

We make use of these cardinal points frequently in the following chapters.

1.5 THE EQUIVALENT POWER AND FOCAL LENGTHS

One of the important properties of any optical system is its *equivalent power*. This is a measure of the ability of the system to bend or deviate rays of light. The higher the power, the greater is the ability to deviate rays. We denote the equivalent power of an optical system by the symbol F . The equivalent power of the eye is related to the distances between the focal and principal points by the equation

$$F = -1/PF = n'/P'F' \quad (1.1)$$

where n' is the refractive index in the vitreous chamber. The average power of the eye for adults is about 60 m^{-1} , but the value varies greatly from eye to eye. Using this power and the commonly accepted refractive index n' of the vitreous chamber (1.336), the focal lengths of the eye are

$$PF = -16.7\text{ mm} \text{ and } P'F' = +22.3\text{ mm} \quad (1.2)$$

Note that power is usually specified as being in diopters, rather than m^{-1} , with the abbreviation “D”.

While the equivalent power of the eye is a very important property of the eye, it is not easy to measure directly. Its value is usually inferred from the other measurable quantities, such as surface radii of curvature, surface separations and eye length, and assumed refractive indices of the ocular media.

However, more important than equivalent power is *refractive error*. The refractive error can be regarded as an error in the equivalent power due to a mismatch between the equivalent power and the eye length. For example, if the equivalent power is too high for a certain eye length, the image is formed in front of the retina and this results in a *myopic* refractive error. If the power is too low, the image is formed behind the retina and results in a *hyperopic* refractive error. Refractive errors are discussed in Chapter 7.

1.6 AXES OF THE EYE

The eye has several axes. Figure 1.1 shows two of these: the *optical axis* and the *visual axis*. The optical axis is usually defined as the line joining the centers of curvatures of the refracting surfaces. However, the eye is not perfectly rotationally symmetric, and therefore even if the four refracting surfaces were each perfectly rotationally symmetric, the four centers of curvatures would not be co-linear. Thus, in the case of the eye, we define the optical axis as the line of best fit through these non-co-linear points. The visual axis is defined as the line joining the object of interest and the fovea, and which passes through the nodal points. These and the other axes are discussed in greater detail in Chapter 4.

1.7 CENTER-OF-ROTATION

The eye rotates in its socket under the action of the six extra-ocular muscles. Because of the way these muscles are positioned and operate, there is no unique center-of-rotation; however, we can nominate a mean position for this point. Fry and Hill (1962) found that the mean center-of-rotation was about 15 mm behind the cornea in horizontal gaze. Ohlendorf et al. (2022) obtained a similar result of 15.3 ± 1.5 mm, but a much smaller result of 12.5 ± 1.4 mm in vertical gaze.

1.8 FIELD-OF-VISION

Examination of the pupil from different angles shows that the pupil can still be seen at angles greater than 90° in the temporal field. Light can enter the pupil from about 105° to the temporal side, as shown in Figure 1.7. While this suggests that the radius of the field-of-vision may be as great as 105° , the real extent of the field-of-vision depends upon the extent of retina in the extreme directions. On the nasal side, vision is cut-off at about 60° because of the combination of the nose and the limited extent of the temporal retina.

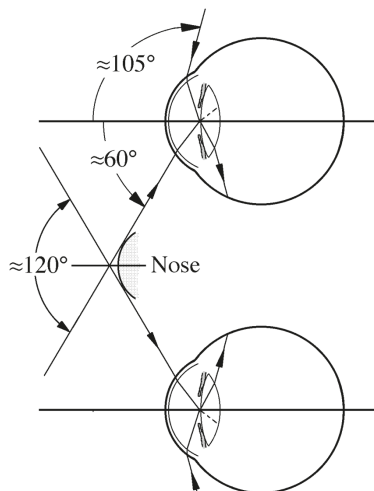


FIGURE 1.7 The horizontal field-of-vision in monocular and binocular vision.

1.9 BINOCULAR VISION AND BINOCULAR OVERLAP

The use of two eyes provides better perception of the external world than one eye alone. Binocular vision improves contrast sensitivity and visual acuity over those obtained with monocular vision (Campbell and Green 1965; Home 1978; Ardit et al. 1981; Legge 1984; Pardhan 1996; Legge and Rubin 1981; Meese et al. 2006), particularly under defocused conditions (Plainis et al. 2011). Two laterally displaced eyes give the potential for a three-dimensional view of the world, which includes the perception of depth known as *stereopsis*. The degree of stereopsis depends partly upon the distance between the two eyes, which is called the *interpupillary distance*. Stereopsis can be improved considerably by optical devices such as rangefinders, which increase the effective interpupillary distance.

1.9.1 INTERPUPILLARY DISTANCE

The interpupillary distance, or *PD*, is usually measured by the distance between the centers of the two pupils of the eyes. The *distance PD* is measured for the eyes looking straight ahead; that is, the visual axes are parallel. When the eyes focus on nearby objects, the eyes rotate inwards and hence there is a corresponding decrease in interpupillary distance. The *near PD* can then be measured or determined from the distance *PD* using simple trigonometry.

Yildirim et al. (2015) reported distance *PDs* in an adult Turkish population. Males and females had mean values of 63.9 ± 3.7 mm and 61.4 ± 3.7 mm, respectively. *PDs* increased until the eighth decade of life, and then decreased. The gender difference for adults across studies is 2–3 mm (Fesharaki et al. 2012; Osuobeni and Al-Musa 1993; Murphy and Laskin 1990; Pointer 2012).

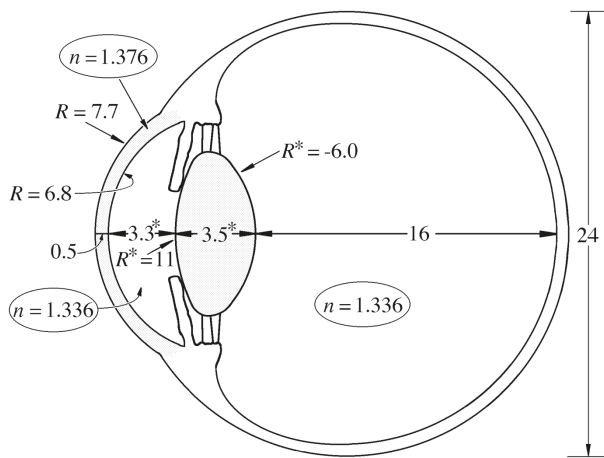


FIGURE 1.8 Representative dimensions (millimeters) and refractive indices of the (relaxed) eye. The starred values depend upon accommodation.

1.9.2 BINOCULAR OVERLAP

As shown in Figure 1.7, the total field-of-vision in the horizontal plane is about 210° with a 120° binocular overlap.

1.10 TYPICAL DIMENSIONS

All dimensions of the eye vary greatly between individuals. Some depend upon accommodation and age. Representative data are shown in Figure 1.8. Average values have been used to construct representative or schematic eyes, which we discuss in Chapter 5. More detailed data are presented in later chapters.

SUMMARY OF MAIN SYMBOLS

F	equivalent power of the eye
n'	refractive index of vitreous humor (usually taken as 1.336)
R	radius of curvature in millimeters
\mathbf{F}, \mathbf{F}'	front and back focal points
\mathbf{N}, \mathbf{N}'	front and back nodal points
\mathbf{P}, \mathbf{P}'	front and back principal points
PD	interpupillary distance

REFERENCES

- Arditi, A. R., P. A. Anderson, and J. A. Movshon. 1981. "Monocular and binocular detection of moving sinusoidal gratings." *Vision Res* 21 (3):329–36. doi: 10.1016/0042-6989(81)90160-7.

- Bron, A. J., R. C. Tripathi, and B. J. Tripathi. 2001. *Wolff's Anatomy of the Eye and Orbit*. 8th ed. London: Arnold.
- Campbell, F. W., and D. G. Green. 1965. "Monocular versus binocular visual acuity." *Nature* 208 (5006):191–2. doi: 10.1038/208191a0.
- Curcio, C. A., and A. E. Hendrickson. 1991. "Chapter 5. Organization and development of the primate photoreceptor mosaic." In *Progress in Retinal Research*, edited by N. N. Osborne and G. J. Chader, 89–120. Pergamon Press.
- Curcio, C. A., K. R. Sloan, R. E. Kalina, and A. E. Hendrickson. 1990. "Human photoreceptor topography." *J Comp Neurol* 292 (4):497–523. doi: 10.1002/cne.902920402.
- Do, M. T. H. 2019. "Melanopsin and the intrinsically photosensitive retinal ganglion cells: biophysics to behavior." *Neuron* 104 (2):205–26. doi: 10.1016/j.neuron.2019.07.016.
- Fesharaki, H., L. Rezaei, F. Farrahi, T. Banihashem, and A. Jahanbakhshi. 2012. "Normal interpupillary distance values in an Iranian population." *J Ophthalmic Vis Res* 7 (3):231–4.
- Freddo, T. F., and E. Chaum. 2018. *Anatomy of the Eye and Orbit: The Clinical Essentials*. Lippincott Williams & Wilkins.
- Fry, G. A., and W. W. Hill. 1962. "The center of rotation of the eye." *Am J Optom Arch Am Acad Optom* 39 (11):581–95. doi: 10.1097/00006324-196211000-00001.
- Gong, D., X. Zou, X. Zhang, W. Yu, et al. 2016. "The influence of age and central foveal thickness on foveal zone size in healthy people." *Ophthalmic Surg Lasers Imaging Retina* 47 (2):142–8. doi: 10.3928/23258160-20160126-07.
- Hogan, M. J., J. A. Alvarado, and J. E. Weddell. 1971. *Histology of the Human Eye*: W. B. Saunders and Co.
- Home, R. 1978. "Binocular summation: a study of contrast sensitivity, visual acuity and recognition." *Vision Res* 18 (5):579–85. doi: 10.1016/0042-6989(78)90206-7.
- Legge, G. E. 1984. "Binocular contrast summation—I. Detection and discrimination." *Vision Res* 24 (4):373–83. doi: 10.1016/0042-6989(84)90063-4.
- Legge, G. E., and G. S. Rubin. 1981. "Binocular interactions in suprathreshold contrast perception." *Percept Psychophys* 30 (1):49–61. doi: 10.3758/bf03206136.
- Meese, T. S., M. A. Georgeson, and D. H. Baker. 2006. "Binocular contrast vision at and above threshold." *J Vis* 6 (11):1224–43. doi: 10.1167/6.11.7.
- Murphy, W. K., and D. M. Laskin. 1990. "Intercanthal and interpupillary distance in the black population." *Oral Surg Oral Med Oral Pathol* 69 (6):676–80. doi: 10.1016/0030-4220(90)90346-t.
- Ohlendorf, A., F. Schaeffel, and S. Wahl. 2022. "Positions of the horizontal and vertical centre of rotation in eyes with different refractive errors." *Ophthalmic Physiol Opt* 42 (2):376–83. doi: 10.1111/opo.12940.
- Østerberg, G. 1935. "Topography of the layers of rods and cones in the human retina." *Acta Ophthalmol.(Suppl.)* 6:1–103.
- Osuobeni, E. P., and K. A. Al-Musa. 1993. "Gender differences in interpupillary distance among Arabs." *Optom. Vis. Sci* 70 (12):1027–30. doi: 10.1097/00006324-199312000-00006.
- Pardhan, S. 1996. "A comparison of binocular summation in young and older patients." *Curr Eye Res* 15 (3):315–9. doi: 10.3109/02713689609007626.
- Plainis, S., D. Petratou, T. Giannakopoulou, D. A. Atchison, and M. K. Tsilimbaris. 2011. "Binocular summation improves performance to defocus-induced blur." *Invest Ophthalmol Vis Sci* 52 (5):2784–9. doi: 10.1167/ivs.10-6545.
- Pointer, J. S. 2012. "The interpupillary distance in adult Caucasian subjects, with reference to 'readymade' reading spectacle centration." *Ophthalmic Physiol Opt* 32 (4):324–31. doi: 10.1111/j.1475-1313.2012.00910.x.

- Read, S. A., M. J. Collins, S. J. Vincent, and D. Alonso-Caneiro. 2015. "Macular retinal layer thickness in childhood." *Retina* 35 (6):1223–33. doi: 10.1097/IAE.0000000000000464.
- Remington, L. A. 2012. *Clinical Anatomy and Physiology of the Visual System*. 3rd ed: Butterworth-Heinemann.
- Snell, R. S., and M. A. Lemp. 1998. *Clinical Anatomy of the Eye*. 2nd ed. Oxford: Blackwell Science.
- Tyler, C. W. 1996. "Analysis of human receptor density." In *Applications of Vision Science, The Professor Jay M. Enoch Festschrift Volume*, edited by V. Lakshminayanan, 63–71. Kluger Academic Publishers.
- Tyler, C. W. 2015. "Peripheral color demo." *Iperception* 6 (6):2041669515613671. doi: 10.1177/2041669515613671.
- Yildirim, Y., I. Sahbaz, T. Kar, G. Kagan, et al. 2015. "Evaluation of interpupillary distance in the Turkish population." *Clin Ophthalmol* 9:1413–6. doi: 10.2147/OPTH.S85584.

2 Refracting Components Cornea and Lens

2.1 INTRODUCTION

The refracting elements of the eye are the cornea and the lens. To provide a good quality retinal image, these elements must be transparent and have appropriate curvatures and refractive indices. Refraction takes place at four surfaces, the anterior and posterior interfaces of the cornea and the lens, and there is also continuous refraction within the lens.

In this chapter we describe the optical structure of the normal cornea and lens, but we must be aware that in many eyes there are significant departures from these norms. Some of these are due to serious ocular defects or irregularities, which can have major impacts on vision. There are also changes with age, and any descriptions given in this section relate only to mean adult values. Detail on age dependencies is given in Chapter 20.

2.2 THE CORNEA

Most of the refracting power is provided by the *cornea*, the clear, curved “window” at the front of the eye. It has about two-thirds of the total power for the relaxed eye, but this fraction decreases as the lens increases in power during accommodation.

2.2.1 ANATOMICAL STRUCTURE

A schematic cross-sectional structure of the cornea is shown in Figure 2.1. It has a tear film at its front surface, and several distinct parts. These are, in order from the outer surface of the eye, the epithelium, Bowman’s membrane, the stroma, Descemet’s membrane and the endothelium. Approximate thicknesses of these components are given in Table 2.1.

The *tear film* is 4-7 µm thick (Tomlinson 1992). It is composed of oily, aqueous, and mucous layers, with 98 per cent of the thickness being provided by the aqueous layer. The tear film is essential for clear vision because it moistens the cornea and smooths out the “roughness” of the surface epithelial cells. The tear film does not contribute significant refractive power itself, since it is very thin and consists effectively of two very closely spaced surfaces of almost equal radii of curvature. However, the importance of this tear film is realized if it dries out. If this occurs, the transparency of the cornea decreases significantly.

The *epithelium* protects the rest of the cornea by providing a barrier against water, larger molecules, and toxic substances. It consists of approximately six layers of

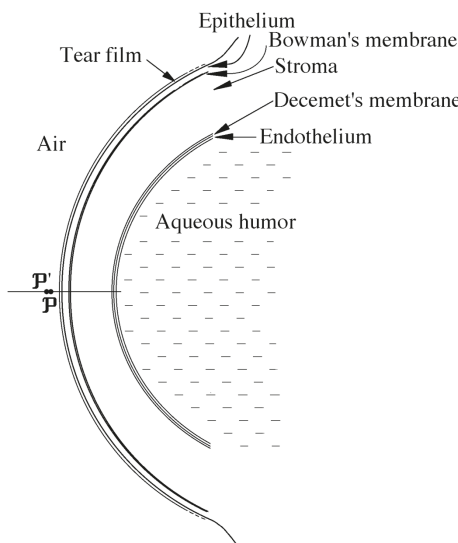


FIGURE 2.1 The structure of the cornea and the approximate positions of its principal points.

TABLE 2.1
Thicknesses (μm) of Corneal Layers (Hogan et al. 1971)

Tear Film	4–7
Epithelium	50
Bowman's Membrane	8–14
Stroma	500 (thickens by at least 150 μm from center to edge)
Descemet's Membrane	10–25
Endothelium	5
Total	\sim 580

cells, and only the innermost layer of these cells can divide. After cells are formed, they move gradually towards the surface as the superficial cells are shed.

Bowman's membrane is 8–14 μm thick and consists mainly of randomly arranged collagen fibrils.

The *stroma* comprises 90 per cent of the corneal thickness, and consists mainly of 200 or more collagen lamellae, which may extend across the extent of the cornea. The collagen fibrils within each lamella run parallel to each other, and the successive lamellae run across the cornea at angles to each other. This arrangement maintains an ordered transparent structure while enhancing mechanical strength. Transparency of the cornea (and of the lens) is discussed in Chapter 12. An additional part called Dua's layer has been claimed to be present between the stroma and Descemet's membrane (Dua et al. 2013).

Descemet's membrane is the basement membrane of the endothelial cells.

The *endothelium* consists of a single layer of cells, which are hexagonal and fit together like a honeycomb. Unlike the case for the inner epithelium, the cells lack the capacity to regenerate. The endothelium regulates the fluid balance of the cornea to maintain the stroma at about 78 per cent hydration and thus retain transparency.

2.2.2 REFRACTIVE INDEX

The refractive index of the cornea varies considerably, with estimates of 1.401–1.433 for the epithelium and 1.357–1.380 for the stroma (Lai and Tang 2014; Patel et al. 1995). There may be a slight reduction in index from the anterior to the posterior stroma (Patel and Alio 2012; Patel et al. 1995), which Barbero (2006) has shown would have some influence on spherical aberration. Since the stroma is by far the thickest layer, its refractive index dominates. The mean value of refractive index is usually taken as 1.376, or similar, and is adopted as the index of the whole cornea. However, this has been challenged by Patel and Tutchenko (2019), who claim the mean is of the order of 1.43. Values like 1.376 are used in much of this book, but revision of these values must be considered.

2.2.3 RADII OF CURVATURE, VERTEX POWERS, AND TOTAL CORNEAL POWER

Several studies have measured the anterior radius of curvature, but there have been far fewer investigations of the posterior surface. Experimental distributions of the vertex radii of curvature are given in Table 2.2. Similar results have been obtained by various investigators for the anterior cornea, but clearly there is a reasonable degree of variation between people, and females have slightly steeper anterior corneal surfaces than males (Atchison 2006; Atchison et al. 2008; Eysteinsson et al. 2005; Shufelt et al. 2005; Wickremasinghe et al. 2004; Dunne et al. 1992). There is a high linear correlation between the anterior and posterior radii of curvature (Dunne et al. 1992; Lowe and Clark 1973; Patel et al. 1993) and a reasonable fit of this relationship is

$$R_2 = 0.81R_1 \quad (2.1)$$

From these radii of curvature, we can calculate the surface powers (F) using the equation

$$F = (n' - n)/R \quad (2.2)$$

where n and n' are the refractive indices on the incident and refracted sides, respectively. At the anterior surface

$$n = 1 \text{ and } n' = 1.376$$

and at the posterior surface

$$n = 1.376 \text{ and } n' = 1.336$$

TABLE 2.2

Some Population Distributions of Corneal Vertex Radii of Curvature R and Corresponding Powers Calculated from Equations (2.2) and (2.3), assuming Corneal Refractive Index 1.376, Aqueous Refractive Index 1.336, and a Corneal Thickness 0.5 mm. Where Results Were Provided for More than One Meridian, Mean Values Have Been Used

Study	P/N	Anterior		Posterior		Total
		R (mm)	F (D)	R (mm)	F (D)	
Donders (1864)	38/-	7.80	48.2			
Females	79/-	7.86	47.9			
Males						
Stenström 1948	-/1000	7.86 ± 0.26	47.8			
Sorsby et al. 1957	-/194	7.82 ± 0.29	48.1			
Lowe and Clark 1973	46/92	7.65 ± 0.27	49.2	6.46 ± 0.26	-6.2	43.1
Kiely et al. 1983	88/176	7.72 ± 0.27	48.7			
Edmund and Sjøntoft 1985	40/80	7.76 ± 0.25	48.5			
Guillon et al. 1986	110/220	7.78 ± 0.25	48.3			
Koretz et al. 1989						
Females	68/-	7.69 ± 0.23	48.9			
Males	32/-	7.78 ± 0.24	48.3			
Dunne et al. 1992						
Females	40/40	7.93 ± 0.20	48.0	6.53 ± 0.20	-6.1	41.4
Males	40/40	8.08 ± 0.16	47.1	6.65 ± 0.16	-6.0	40.6
Patel et al. 1993	20/20	7.68 ± 0.40	49.0	5.81 ± 0.41	-6.9	42.2
Atchison et al. 2008						
Females	47/47	7.72 ± 0.25	48.7	6.47 ± 0.28	-6.2	42.6
Males	50/50	7.87 ± 0.20	47.8	6.53 ± 0.22	-6.1	41.8
Navarro et al. 2013b	211/407	7.62 ± 0.26	49.3	6.10 ± 0.27	-6.6	42.9
Mean (unweighted)		7.79	48.3	6.36	-6.3	42.1

Note: P = number of participants; N = number of eyes; - = number not provided.

Surface power values, using this equation and these refractive indices, are given in Table 2.2. The total power F of the cornea can be calculated from the “thick lens” equation:

$$F = F_1 + F_2 - F_1 F_2 d / \mu \quad (2.3)$$

where F_1 is the anterior surface power, F_2 is the posterior surface power, d is the vertex corneal thickness and μ is the refractive index of the cornea (usually taken as 1.376). The power of the cornea can be estimated from the sum of the surface powers

$$F \approx F_1 + F_2 \quad (2.3a)$$

This value is different from the exact value by $F_1 F_2 d/\mu$. Using the data given by Patel et al. (1993) in Table 2.2, a corneal thickness of 0.5 mm and a refractive index of 1.376, the exact equation (2.3) gives a corneal power of 42.2 diopters (D) and the approximate equation (2.3a) gives a slightly lower value of 42.1 D.

The above surface power values apply to the vertices of the cornea and would apply to other parts of the corneal surfaces only if they were spherical. However, surfaces have toricity and asphericity. Therefore, the radii of curvature do not fully describe the shape of the cornea and its refracting properties, e.g., Navarro et al. (2013a).

2.2.4 ANTERIOR SURFACE SHAPE

2.2.4.1 Toricity

Frequently the anterior corneal surface exhibits toricity, which produces power differences between meridians called *astigmatism*. This is the most obvious corneal imperfection in normal eyes. Prevalence of astigmatism in the anterior cornea varies considerably between studies, because of different demographics and definitions. A large European-based study found about three-quarters of the population had 0.5 D or more astigmatism (Hoffmann and Hütz 2010), with less than 3% of the group having 3 D or higher astigmatism.

Anterior corneal astigmatism can be classified according to the orientation of the principal meridians (Figure 2.2). “With-the-rule” astigmatism of a surface occurs where the radius of curvature is greatest in a meridian close to the horizontal meridian, or alternatively curvature is greatest near the vertical meridian. “Against-the-rule” astigmatism occurs where the radius of curvature is greatest in a meridian close to the vertical meridian. “Oblique” astigmatism occurs where the principal meridians are oblique, e.g., between 30° and 60° from the horizontal and vertical meridians. This terminology is used also for astigmatism as a refractive error of the eye (see section 7.3). Many young eyes have with-the-rule astigmatism, which changes to against-the-rule astigmatism in older eyes, with oblique astigmatism being less common (Huynh et al. 2006; Liu et al. 2011; Li et al. 2019; Leung et al. 2012; Hoffmann and Hütz 2010; Fledelius and Stubgaard 1986). Read et al. (2017) indicated that mirror symmetry of anterior corneal astigmatism axis is common between fellow eyes in most people, e.g., right eye axis 20° and left eye axis 160°.

2.2.4.2 Asphericity

In general, the radius of curvature increases with distance from the surface vertex, so that the surface flattens away from the vertex. Surfaces that are non-spherical in this sense are often described as *aspheric*.

The shape of the anterior corneal surface has been extensively studied, especially over the central 8 mm of its approximately 12 mm diameter. This central “optical” zone is the maximum zone of the cornea through which light passes to form the foveal image. To investigate the shape over this zone, corneal surfaces are often represented by conicoids in three dimensions or by conics in two dimensions. A conicoid can be expressed in the form

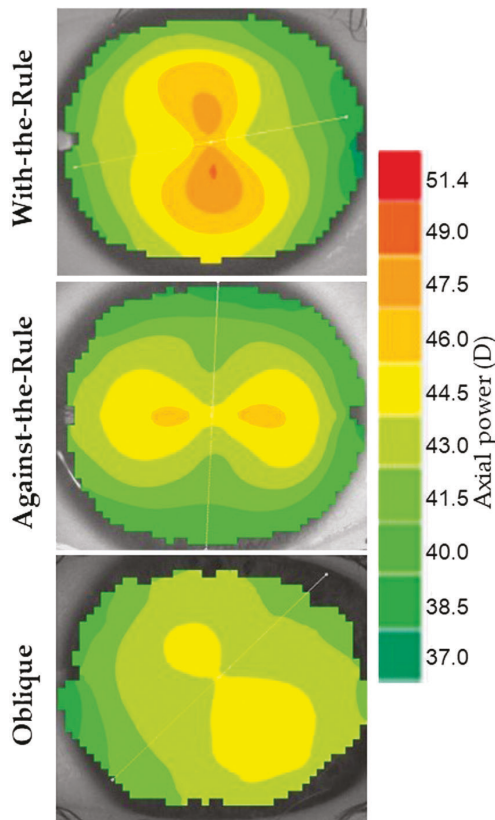


FIGURE 2.2 Axial power topography maps showing “with-the-rule”, “against-the-rule”, and oblique astigmatism of the anterior corneal surface. This figure was kindly provided by Scott Read and Stephen Vincent.

$$h^2 + (1 + Q)Z^2 - 2ZR = 0 \quad (2.4)$$

where

the Z -axis is the optical axis

$$h^2 = X^2 + Y^2$$

R is the vertex radius of curvature and

Q is the surface asphericity, where

$Q < -1$ specifies a hyperboloid

$Q = -1$ specifies a paraboloid

$-1 < Q < 0$ specifies an ellipsoid, with the Z -axis being the major axis

$Q = 0$ specifies a sphere

$Q > 0$ specifies an ellipsoid with the major axis in the $X-Y$ plane.

The effects of the value and sign of Q on the shape are shown in Figure 2.3. Sometimes asphericity is expressed in terms of a quantity p , which is related to Q by the equation

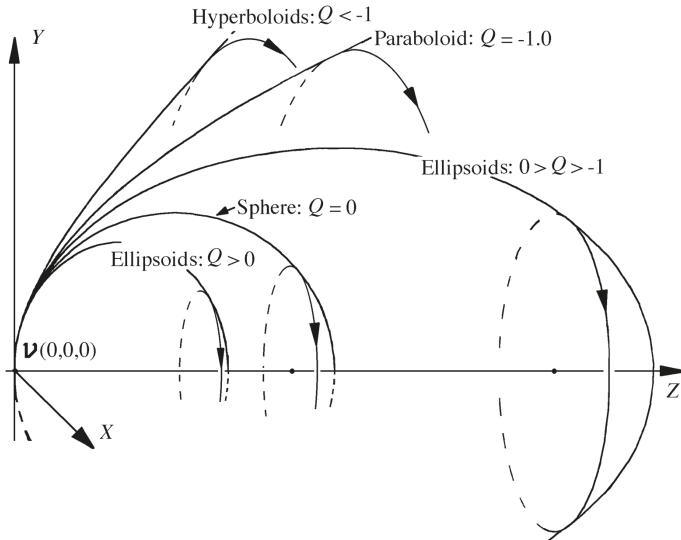


FIGURE 2.3 The effect of asphericity on the shape of a conicoid. All the curves have the same vertex radius of curvature.

$$p = 1 + Q \quad (2.5)$$

The conicoid form described by equation (2.4) is not the only mathematical representation used in the literature to describe conic(oid)s. Many investigators have measured surface shapes separately in different sections, and fitted the data to ellipses, which can be described by the equation

$$\frac{(Z-a)^2}{a^2} + \frac{y^2}{b^2} = 1 \quad (2.6)$$

where a and b are ellipse axes' semi-lengths. The shape of such ellipses is often described by the eccentricity e , which is related to a and b by the equation

$$e^2 = 1 - b^2/a^2 \quad (2.7)$$

provided that the Z-axis is the major axis.

Equation (2.6) can be transformed easily into the form of equation (2.4). If we do this, we find that the vertex radius of curvature R is related to a and b by the equation

$$R = + b^2/a \quad (2.8)$$

and that the asphericity Q is given by the equation

$$Q = b^2/a^2 - 1 \quad (2.9)$$

It follows from equations (2.7) and (2.9), that the quantities e and Q are related by the equation

$$Q = -e^2 \quad (2.10)$$

Specifying asphericity using e is not completely satisfactory because e^2 may be negative, in which case e cannot have a value.

Other forms of representing corneal shape are described in section 16.3. More complex forms are important to describe the shape of the cornea accurately, especially outside the optical zone.

Measured values of the anterior corneal asphericity are given in Table 2.3. The values of Q are usually negative, indicating that the cornea flattens away from the vertex. Figure 2.4 shows the profiles of corneal surfaces, all with a vertex radius of curvature of 7.8 mm but with different Q values.

There has been considerable speculation as to why the cornea flattens away from the center. It has been argued that the cornea flattens to reduce spherical aberration, and certainly the flattening does lead to a lower spherical aberration, but the amount of asphericity in the average cornea is not sufficient to eliminate it. The value of Q required to eliminate spherical aberration at the anterior surface is $-1/n^2$, where n is the corneal refractive index, and is -0.528 for an index of 1.376. Perhaps an important reason for the flattening is the need for the cornea to make a smooth join with the main globe of the eye.

For a spherical surface, the radius of curvature at any point and in any meridian is the same. However, for a conicoid surface, the radius of curvature at off-axis points depends not only upon the distance from the vertex, but also on the meridian at that

TABLE 2.3
Summary of Asphericity Data for the Anterior and Posterior Surfaces of the Cornea

Study	No. of Subjects/Eyes	Anterior Q	Posterior Q
Mandell and St Helen 1971	8/8	-0.23	
Kiely et al. 1982	88/176	-0.26 ± 0.18	
Edmund and Sjøntoft 1985	40/80	-0.28 ± 0.13	
Guillon et al. 1986*	110/220	-0.18 ± 0.15	
Patel et al. 1993	20/20	-0.01 ± 0.25	-0.42 ± 0.34
Lam and Douthwaite 1997	60/60	-0.30 ± 0.13	-0.66 ± 0.38
Douthwaite et al. 1999**	98/187	-0.21 ± 0.13	
Cheung et al. 2000	83/83	-0.18 ± 0.18	-0.38 ± 0.27
Dubbelman et al. 2006	114/114	-0.13 ± 0.11	-0.23 ± 0.17
Atchison 2006	101/101	-0.15 ± 0.11	
Atchison et al. 2008	101/101	-0.13 ± 0.14	
Navarro et al. 2013b*	211/407	-0.40 ± 0.13	-0.56 ± 0.14
Mean (unweighted)		-0.21	-0.45

Note: * Mean of the steepest and shallowest meridians; ** mean of horizontal and vertical meridians.

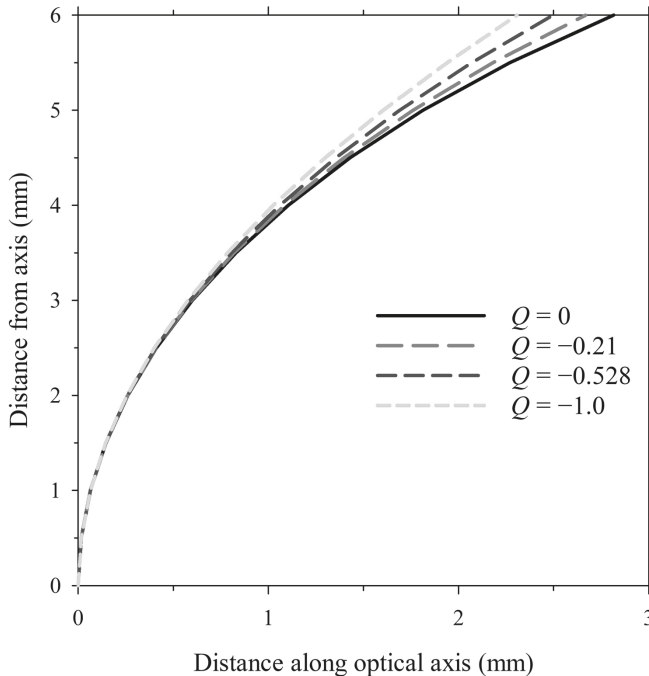


FIGURE 2.4 The effect of asphericity Q on the shape of a conicoid. All the curves have 7.8 mm vertex radius of curvature. $Q = 0$ specifies a sphere, $Q = -0.21$ is the mean asphericity of the studies of the anterior cornea surface in Table 2.3, $Q = -0.528$ is the asphericity for which the anterior corneal surface has no spherical aberration, and $Q = -1.0$ specifies a paraboloid.

point. There are two principal meridians: the tangential meridian, which lies along the radius line from the vertex, and the sagittal meridian, which is perpendicular to the tangential meridian. For conicoids, the corresponding equations for the sagittal radius of curvature (R_s) and the tangential radius of curvature (R_t) are

$$R_s = [R^2 - QY^2]^{1/2} \quad (2.11a)$$

and

$$R_t = [R^2 - QY^2]^{3/2}/R^2 = R_s^3/R^2 \quad (2.11b)$$

Figure 2.5 shows changes in R_t and R_s with distance Y from the anterior corneal vertex for an asphericity Q value of -0.18 (Guillon et al. 1986) and a vertex radius of curvature of 7.8 mm.

An alternative name for the tangential radius of curvature is the *instantaneous radius of curvature*, while the sagittal radius of curvature is also called the *axial radius of curvature*. Unfortunately, this last term may be readily confused with the vertex radius of curvature. These terms are used considerably in corneal topographers, including when rotational symmetry is lacking.

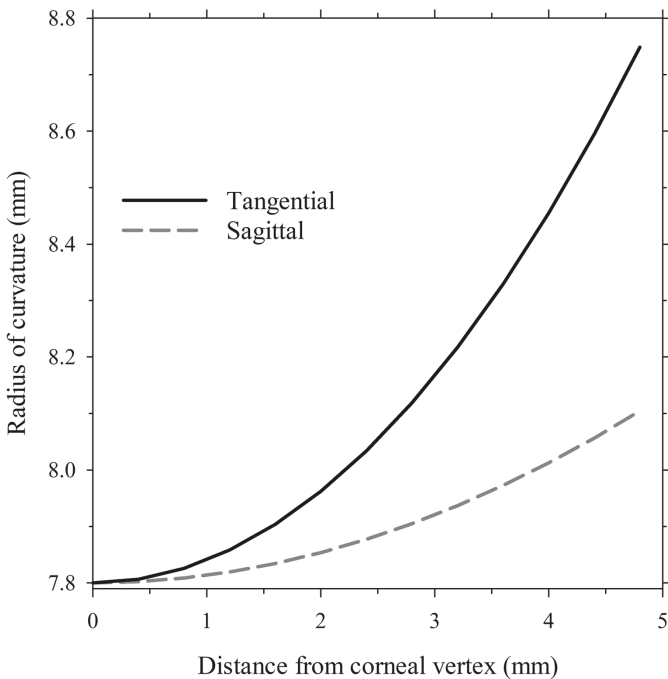


FIGURE 2.5 The radii of curvature in the sagittal and tangential directions of an anterior corneal surface with vertex radius of curvature 7.8 mm and asphericity $Q = -0.21$.

2.2.5 CENTRAL THICKNESS

Doughty and Zaman (2000) surveyed the literature and reported a mean center thickness of 0.536 ± 0.031 mm.

2.2.6 POSTERIOR SURFACE SHAPE

Astigmatism occurs at the posterior surface of the cornea as well as at the anterior surface. While in curvature terms the posterior surface usually has higher toricity than the anterior surface (Dubbelman et al. 2006), the astigmatism of the former is usually smaller because of the lower refractive index change across the corneal-aqueous boundary than across the air-corneal boundary. If the toricities are in the same direction, such as if both surfaces have their greatest radii of curvature horizontally, the astigmatism of the anterior surface will be partly compensated by the astigmatism of the posterior surface (Rozema et al. 2019; Atchison et al. 2016). The posterior cornea is predominantly flattest near the horizontal meridian across a wide age range (Koch et al. 2012; Rozema et al. 2019). A consequence of this is that the proportions of with-the-rule and against-the-rule astigmatism for the total cornea will be less and greater, respectively, than those of the anterior corneal surface.

Measured values of the posterior corneal surface asphericity are given in Table 2.3. As for the anterior surface, the values of Q are usually negative.

2.2.7 SHORT-TERM CHANGES IN THE CORNEA

Read et al. (2017) summarized the short-term changes in the cornea. These include diurnal (over the course of a day) changes in thickness, anterior surface curvature and some higher-order aberrations; the largest changes occur upon awakening. Although there have been reports of changes in the anterior surface with accommodation, these are probably artefacts of cyclotorsional eye movements (section 4.2.5). However, changes occur during near work associated with eyelid pressure and there are small changes with adductuve eye movements (Niyazmand et al. 2021).

2.2.8 POSITIONS OF THE PRINCIPAL POINTS

The positions of the principal points of the cornea depend upon the radii of curvatures of the anterior and posterior surfaces, the corneal thickness, and the refractive indices. Representative positions are shown in Figure 2.1. Note that both principal points are in front of the cornea and that P' is in front of P .

2.3 THE LENS AND ITS PARAMETERS IN THE UNACCOMMODATED STATE

Figure 2.6 shows a schematic cross-section of the lens. The lens bulk is a mass of cellular tissue of non-uniform gradient index, contained within an acellular elastic *capsule*. We do not have yet an accurate measure of this index distribution. There is a layer of epithelial cells, extending from the anterior pole of the lens to near the equator. The lens grows continually throughout life, with new epithelial cells forming at the equator. These cells elongate as fibers that wrap around the periphery of the lens, under the capsule and epithelium, to meet at sutures. The older fibers lose their nuclei and other intracellular organelles. Because of the continual growth of the lens throughout life, lenticular parameters are highly age-dependent; this is discussed in Chapter 20.

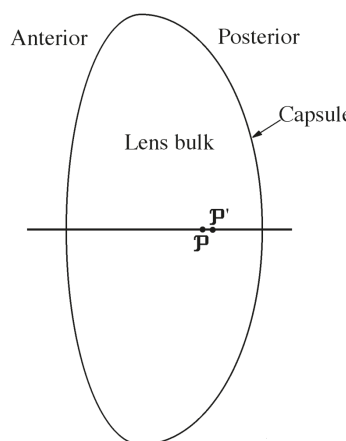


FIGURE 2.6 Cross-section of the lens showing the approximate positions of its principal points.

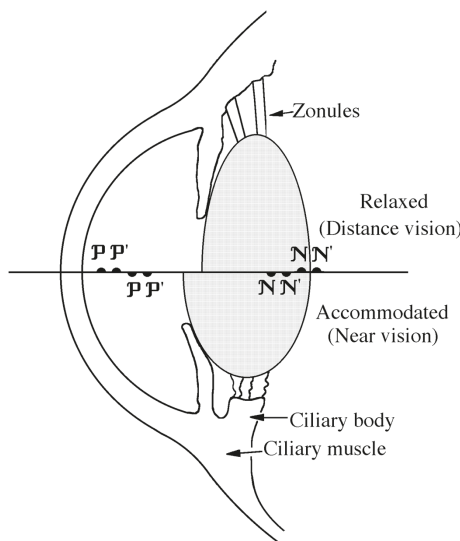


FIGURE 2.7 The effect of accommodation on the lens shape and lens position, and on the principal and nodal points of the eye.

The lens capsule plays an important role in the accommodation process. It is attached to the ciliary body via the zonules, as shown in a simplified fashion in Figure 2.7. Contraction of the ciliary muscle within the ciliary body leads to changes in zonular tension, which alter lens shape. This process causes a change in the equivalent power of the lens and hence in the ocular equivalent power and allows the eye to focus on objects at different distances. Note that contraction of the ciliary muscle *decreases* tension on the zonules and this allows the lens to take up a more curved form, appropriate for near vision.

The lens is classified into two regions, the nucleus, which is present at birth, and the cortex, which forms outside the nucleus after birth. The nucleus and cortex can be subdivided into zones according to the reflectivity observed with the biomicroscope.

In vivo measurements of the lens shape and size can be obtained by optical methods, such as Scheimpflug imaging, phakometry (sizes of images formed by reflection in the lens), and optical coherence tomography, by ultrasound and by magnetic resonance imaging. Optical methods are limited to the region inside the iris, and must be corrected for distortions caused by the cornea in the case of the anterior lens surface and by the cornea and preceding optical elements in the case of the posterior lens surface; this is a particular problem with the posterior surface because of the accumulated uncertainties of preceding surfaces and of the refractive index distribution in any lens. A variety of methods is available for *in vitro* measurements. It is assumed that the unrestrained lens shape will correspond to the fully accommodated lens within the eye, and various states of accommodation are simulated by stretching the lens. Manns et al. (2017) described *in vivo* and *in vitro* methods and their limitations.

Table 2.4 shows results from some studies of unaccommodated eyes. Where possible, these results are for young adult eyes. The values may be affected in some

TABLE 2.4
Lens Parameters (Mean \pm Standard Deviation) for Unaccommodated Eyes from *In Vivo* Studies

Ocular Parameter	Study	Method	Age Range (Years), No. Eyes	Mean \pm SD, Range
Anterior radius of curvature (mm)	Lowe 1972	Slit-lamp photography	23–77, 92	10.3 \pm 1.8
	Brown 1974	Scheimpflug photography	3–82, 100	12.4 \pm 2.6
	Garner and Smith 1997	Purkinje imaging	18–28, 11	11.5 \pm 1.3
	Hermans et al. 2009	MRI	18–35, 5	11.5 \pm 1.7
	Sheppard et al. 2011	MRI	19–30, 19	11.9 \pm 2.8
	Pérez-Merino et al. 2015	Anterior segment OCT	31 \pm 3, 9	13.1 \pm 1.3
	Martinez-Enriquez et al. 2017	Anterior segment OCT	29 \pm 4, 19	11.7 \pm 1.2
	Xiang et al. 2021	Anterior segment OCT	30–40, 22	11.0 \pm 1.7
Posterior radius of curvature (mm)	Brown 1974			8.1 \pm 1.6
	Garner and Smith 1997			6.7 \pm 1.0
	Kasthurirangan et al. 2011	MRI	19–29, 15	5.7 \pm 1.0
	Sheppard et al. 2011			6.1 \pm 0.8
	Pérez-Merino et al. 2015			6.5 \pm 0.5
	Martinez-Enriquez et al. 2017			6.3 \pm 0.5
	Xiang et al. 2021			6.0 \pm 0.6
	Dubbelman and Van der Heijde 2001	Scheimpflug photography	16–65, 102	-5 \pm 5
Anterior surface asphericity (Q)	Martinez-Enriquez et al. 2017			-4.4 \pm 3.2
	Dubbelman and Van der Heijde 2001			-4 \pm 4
	Kasthurirangan et al. 2011			-0.8 \pm 0.6
	Martinez-Enriquez et al. 2017			-2.3 \pm 1.3
Posterior surface asphericity (Q)	Hermans et al. 2009			3.66 \pm 0.14
	Kasthurirangan et al. 2011			3.69 \pm 0.25

(continued)

TABLE 2.4 (Continued)

Lens Parameters (Mean \pm Standard Deviation) for Unaccommodated Eyes from *In Vivo* Studies

Ocular Parameter	Study	Method	Age Range (Years), No. Eyes	Mean \pm SD, Range
Lens diameter (mm)	Sheppard et al. 2011			3.75 \pm 0.35
	Pérez-Merino et al. 2015			3.88 \pm 0.19
	Martinez-Enriquez et al. 2017			3.72 \pm 0.20
	Khan et al. 2018	MRI	18–29, 38	3.55 \pm 0.21
	Xiang et al. 2021			3.85 \pm 0.20
	Hermans et al. 2009			9.6 \pm 0.3
	Kasturirangan et al. 2011			9.0 \pm 0.3
	Sheppard et al. 2011			9.5 \pm 0.5
	Martinez-Enriquez et al. 2017			8.9 \pm 0.3
	Khan et al. 2018			9.3 \pm 0.3
Lens power (D)	Jongenelen et al. 2015	Bennett's method	20–24, 81	26.2 \pm 2.1
Equivalent refractive index	Garner and Smith 1997			1.428 \pm 0.001
	Dubbelman and Van der Heijde 2001			1.433 \pm 0.006
	Hermans et al. 2008	Scheimpflug photography	18–35, 5	1.435 \pm 0.008

Note: Several studies appear more than once; for second and subsequent appearances the method and age details are omitted. Note that both anterior and posterior surfaces have been assigned positive radii of curvature.

studies by residual accommodation. The dependence of lens parameters upon accommodation and age are discussed in sections 2.4 and 20.5, respectively.

2.3.1 SURFACE RADII OF CURVATURE AND SHAPES

The anterior surface is considerably flatter than the posterior surface (Table 2.4). There is a wide range of surface asphericities, due in part to difficulties in determining this quantity, particularly for the posterior surface. The few studies of lens toricity indicate that the anterior surface contributes with-the-rule astigmatism (flatter horizontally than vertically) while the posterior surface contributes against-the-rule astigmatism (flatter vertically than horizontally), with a slight excess of the latter over the

former (Dunne et al. 1996; Mutti et al. 2004; Ortiz et al. 2012). Rozema et al. (2019) determined that the corneal and internal (i.e., lenticular based) astigmatisms cancel partially in young adults, but this balance is lost in older adults.

2.3.2 THICKNESS

The lens central thickness is often taken to be about 3.6 mm in the unaccommodated state for the young eye, but increases upon accommodation (section 2.4) and aging (section 20.5).

2.3.3 REFRACTIVE INDEX DISTRIBUTION

The refractive index within the lens is not constant, being greatest in the center and least in the periphery, e.g., Kasturirangan et al. (2011); Pierscionek and Chan (1989); Khan et al. (2018). In the nucleus, the index magnitude is almost constant, with the greatest variations occurring in the cortex (periphery). This variation in index produces a progressive and continuous refraction of rays, and may improve the quality of the retinal image by reducing spherical aberration (Smith and Atchison 2001).

Gullstrand (1909a) gave an equation for the refractive index distribution within the lens. An equivalent form of his equation is

$$\begin{aligned} n(Y,Z) = & 1.406 - 0.0062685(Z - Z_0)^2 + 0.0003834(Z - Z_0)^3 \\ & - [0.00052375 + 0.00005735(Z - Z_0) + 0.00027875(Z - Z_0)^2] Y^2 \\ & - 0.000066717Y^4 \end{aligned} \quad (2.12)$$

This gives a maximum index of 1.406 at the nominal center of the lens, which occurs at $Z = Z_0$, and an index of 1.386 at the edge of the lens. Gullstrand gave a value for Z_0 of 1.7 mm, and the total lens thickness as 3.6 mm.

Another equation that has been used by a number of authors is a power function

$$n(r) = n_0 + (n_s - n_0)r^{2p} \quad (2.13)$$

where $n(r)$ is the relative distance in any direction, from the point of highest refractive index n_0 on the optical axis to n_s on the lens surface, and the coefficient p determines the steepness of the gradient (Jones et al. 2005; Kasturirangan et al. 2008; Khan et al. 2018; Bahrami and Goncharov 2014; Birkenfeld et al. 2013; Smith et al. 1991; Navarro et al. 2007). Figure 2.8 shows the effect of varying p on the refractive index profile. The higher the value of p , the wider is the plateau of constant index in the lens center and the greater is the rate of change of index near the lens edge; this also reduces the power of the gradient index (Smith et al. 1991).

The lens refractive index has been determined in different ways, such as with the Abbe refractometer, by determining relationships between protein concentrations and refractive indices, by laser raytracing, by Talbot X-ray imaging, and by fiber optic reflectometry. *In vivo* determinations have been made with magnetic resonance imaging in which spin-spin relaxation time is related to protein concentrations and then to refractive index. Manns et al. (2017) provided a fuller account of these methods.

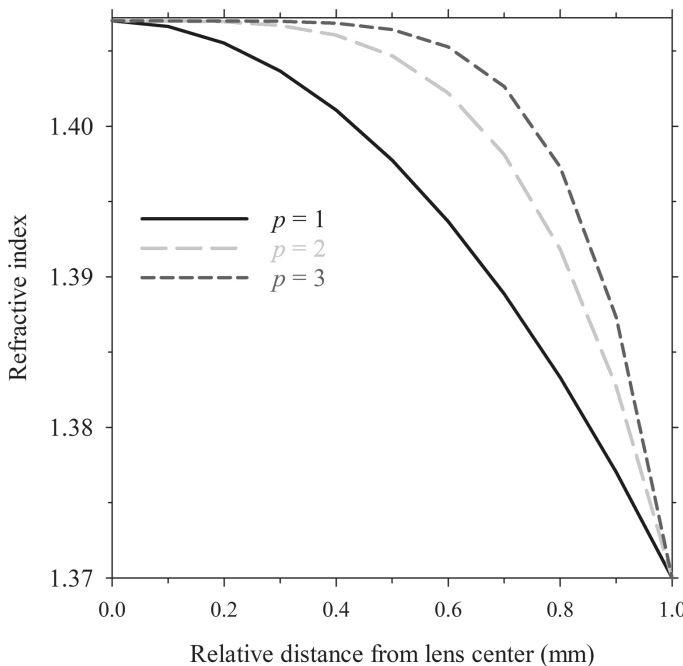


FIGURE 2.8 Refractive index profile corresponding to equation (2.13) for different p values, with $n_0 = 1.406$ and $n_c = 1.370$.

2.3.4 EQUIVALENT REFRACTIVE INDEX

If the real lens with its gradient index is replaced by one with the same thickness, same radii of curvature and a uniform refractive index, obtaining the same lens power requires this index must be made higher than the maximum index. The *equivalent refractive index* is often taken as 1.42, compared with the maximum value of about 1.41.

2.3.5 EQUATORIAL DIAMETER

Estimates of diameters for the unaccommodated state in healthy adult eyes are 8.6–9.9 mm; the mean across the studies in Table 2.4 is 9.3 mm.

2.3.6 LENS POWER

To determine *in vivo* lens power, Purkinje imaging (phakometry) can be used in which the sizes of the Purkinje images are combined with other data in the eye. This gives also determinations of radii of curvature and equivalent lens index, e.g., see Atchison et al. (2008). The method depends on ocular refraction, intraocular distances and corneal parameters having been determined and some refractive indices being assumed. An easy to implement method is that of Bennett (1988), which does not require the reflection measurements, but uses the other information. The principal points are determined by assuming that the ratio of surface radii of curvature is constant, such

as that for the Gullstrand-Emsley schematic eye (Chapter 5). Raytracing to the first principal point of the lens is done to provide an object reduced vergence L , while an image reduced vergence L' is obtained by dividing the refractive index of the vitreous by the distance between the second principal point of the lens and the retina. The lens power F is given by $F = L' - L$.

Most *in vitro* determinations are variants of laser raytracing, e.g., Glasser and Campbell (1999); Borja et al. (2008); Birkenfeld et al. (2014); Maceo Heilman et al. (2018); Jones et al. (2005). Manns et al. (2017) described methods in more detail.

Most model eyes have lens powers of 19–22 D, but the mean adult lens power is higher at about 25 D (Atchison et al. 2008; Jongenelen et al. 2015).

2.3.7 POSITIONS OF PRINCIPAL POINTS

The positions of the principal points of the lens depend upon the radii of curvature of the anterior and posterior surfaces, the center thickness, refractive index distribution, and the refractive indices of the surrounding media. Figure 2.6 shows representative positions.

2.4 ACCOMMODATION

Accommodation is the ability of the eye to change its power to bring objects of interest at different distances into focus. As such, it makes an essential contribution to visual performance. Our understanding of its mechanism is based on Helmholtz's 1855 theory (Helmholtz 1855, 1909; Gullstrand 1909b). In the unaccommodated form, with the focus of the eye at its far point, the suspensory ligaments (zonules) connecting the lens and ciliary body pull on the lens and flatten it. When changing focus from far to near vision, the ciliary body moves forwards and inwards upon contraction of its ciliary muscle, thus reducing the tension on the zonules. Because of the elastic properties of the capsule of the lens, the lens becomes rounder in shape with increases in surface curvatures, increase in lens thickness and decrease in equatorial diameter. The anterior surface moves forward. These changes, shown in Figure 2.7, result in an increase in the equivalent power of the lens and of the eye. When the eye must change focus from close to more distant objects, the reverse process occurs. See Glasser (2011) for an extensive cover of the process of accommodation and of the related anatomy.

The stimulus-response mechanism in accommodation is not fully understood. For example, we do not understand how the brain knows which way to change the lens power, although there are some indications that chromatic aberration, as well as blur due to defocus, plays a role (see Chapter 17).

In relaxed model eyes focused for infinity, the equivalent power of the lens is generally in the range 19–22 D. In an eye accommodating to a point 10 cm from the anterior cornea, the lens power is approximately 13 D higher.

While we measure the level of accommodation as the vergence of the “in focus” object, this vergence should not be mistaken as the power of the eye. For the relaxed eye, the accommodation level is zero, but the power of the eye is about 60 D. Although the accommodation level and increase in lens power are not the same, they are closely related.

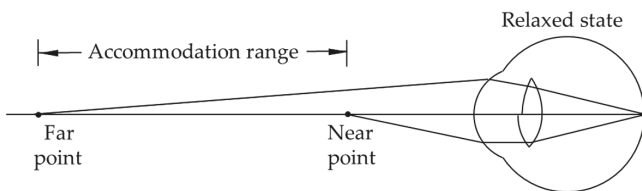


FIGURE 2.9 The near and far points of the eye. This is a myopic eye because the far point is in front of it. For a hyperopic eye the far point would be behind the eye, and for the emmetropic eye the far point would be at infinity.

There are physical limits to the range of lens shapes, and hence restrictions to changes in lens power and the range of clear vision. The furthest and closest object points along this range are called the *far point* and *near point*, respectively, and are shown schematically in Figure 2.9. When the ciliary muscle is completely relaxed the eye is focused on the far point, which is conjugate to the retina. When the ciliary muscle is maximally contracted or the lens maximally relaxed, the eye has its greatest equivalent power and the near point is conjugate to the retina.

The distance between the far and near points is called the range of accommodation – for example, from infinity to 20 cm. The difference between the vergences of the far and near points is called the *amplitude of accommodation*.

Example 2.1: Calculate the amplitude of accommodation of an eye with a far point of 1.25 m in front of the eye and a near point of 10 cm in front of the eye.

Solution: Taking distances in front of the eye as being negative, the vergence of the far point is $-1/1.25 = -0.8 \text{ m}^{-1}$ or -0.8 D , and the vergence of the near point is $-1/0.10 = -10.0 \text{ m}^{-1}$ or -10.0 D .

The difference is $-0.8 - -10.0 = 9.2 \text{ D}$.

Note that the subtraction is done in this order so that the amplitude is positive.

The amplitude of accommodation is affected by age. It probably reaches a peak early in the second decade of life, and then gradually declines to become zero in the mid-fifties. This and other effects of age are discussed in Chapter 20.

As the two eyes accommodate to focus clearly on a close object, they also must rotate inwards to fixate on the object. This inward rotation is called convergence. Accommodation and convergence are controlled to some extent by the same nervous pathway from the brain, and there is an interaction between accommodation and convergence called a *synkinesis*. A stimulus to either accommodation or convergence can cause both to change. An example is that of placing an occluder in front of one eye and placing a negative-powered lens in front of the other eye. As well as the negative lens stimulating accommodation, the occluded eye turns inwards.

As the accommodation level increases, all the cardinal points of the eye move towards the anterior surface of the lens (section 5.3.6).

Table 2.5 shows results of studies of the rate of change in various ocular parameters per diopter of accommodation. When considering changes in parameters with

TABLE 2.5
Changes in Lens Parameters (Mean \pm Standard Deviation) with Accommodation from *In Vivo* Studies

Ocular Parameter	Study	Change Unit per D Accomm*	Method, Stimulus/ Response Measure, Comment
Anterior radius of curvature (mm)	Garner and Smith 1997	-0.62	Purkinje imaging, stimulus
	Koretz et al. 2002	-0.47	Scheimpflug, stimulus
	Dubbelman et al. 2005	-0.61 \pm 0.15	Scheimpflug, stimulus
	Rosales et al. 2006	-0.6	Scheimpflug and Purkinje imaging, stimulus
	Hermans et al. 2009	-0.6	Scheimpflug and Purkinje imaging, response, average
	Sheppard et al. 2011	-0.63 \pm 0.50	MRI, response
	Pérez-Merino et al. 2015	-0.78 \pm 0.18	Anterior segment OCT, stimulus
	Martinez-Enriquez et al. 2017	-0.60	OCT, response
	Xiang et al. 2021	-0.44	Anterior segment OCT, stimulus
Posterior radius of curvature (mm)	Garner and Smith 1997	-0.17	
	Dubbelman et al. 2005	-0.13 \pm 0.06	
	Rosales et al. 2006	-0.3	
	Hermans et al. 2009	-0.15	
	Kasthurirangan et al. 2011	-0.10	MRI, stimulus
	Sheppard et al. 2011	-0.15 \pm 0.18	
	Pérez-Merino et al. 2015	-0.13 \pm 0.07	
	Martinez-Enriquez et al. 2017	-0.22	
	Xiang et al. 2021	-0.09	
Anterior surface asphericity (Q)	Martinez-Enriquez et al. 2017	-0.36	
Posterior surface asphericity (Q)	Martinez-Enriquez et al. 2017	+0.30	
Axial thickness (mm)	Kasthurirangan et al. 2011	ns	
	Garner and Smith 1997	+0.035	
	Strenk et al. 1999	+0.05 \pm 0.03	MRI, stimulus
	Dubbelman et al. 2005	+0.05 \pm 0.01	
	Ostrin et al. 2006	+0.07 \pm 0.01	Ultrasound, response
	Tsorbatzoglou et al. 2007	+0.04 \pm 0.02	Partial coherence interferometry, < 30 years, stimulus
	Jones et al. 2007	+0.05 \pm 0.02	MRI, stimulus
	Hermans et al. 2009	+0.05	

(continued)

TABLE 2.5 (Continued)
Changes in Lens Parameters (Mean \pm Standard Deviation) with Accommodation from *In Vivo* Studies

Ocular Parameter	Study	Change Unit per D Accomm*	Method, Stimulus/ Response Measure, Comment
Equivalent refractive index	Kasturirangan et al. 2011	+0.05 \pm 0.01	
	Sheppard et al. 2011	+0.08 \pm 0.04	
	Ni et al. 2011	+0.04 \pm 0.01	Scheimpflug stimulus
	Doyle et al. 2013	+0.05	Anterior segment OCT, 18–29 y group, up to 4 D, response
	Richdale et al. 2013	+0.06	MRI, response
	Richdale et al. 2016	+0.06	MRI, response
	Richdale et al. 2008	+0.05 \pm 0.02	Anterior segment OCT, response
	Ramasubramanian and Glasser 2015	+0.07	Ultrasound, stimulus
	Pérez-Merino et al. 2015	+0.04 \pm 0.01	
	Martinez-Enriquez et al. 2017	+0.07	
	Khan et al. 2018	+0.07 \pm 0.05	MRI, stimulus
	Xiang et al. 2021	+0.03	
Lens diameter (mm)	Garner and Smith 1997	ns	
	Dubbelman et al. 2005	+0.0013 \pm 0.0009	
	Jones et al. 2007	ns	
	Hermans et al. 2008	ns	Scheimpflug imaging, response
	Strenk et al. 1999	-0.08 \pm 0.02	
	Jones et al. 2007	-0.07 \pm 0.03	
	Hermans et al. 2009	-0.07 \pm 0.01	
	Kasturirangan et al. 2011	-0.05 \pm 0.01	
	Sheppard et al. 2011	-0.09 \pm 0.07	
	Richdale et al. 2013	-0.08	
	Richdale et al. 2016	-0.08	
	Martinez-Enriquez et al. 2017	-0.14	
	Khan et al. 2018	-0.08 \pm 0.04	

Note: * Standard deviations were not available for all studies. Note that both anterior and posterior surfaces have been assigned positive radii of curvature, and steepening results in negative changes for both. Several studies appear more than once; for second and subsequent appearances the method details are omitted. ns = no significant change.

accommodation, it must be borne in mind that some studies have used the stimulus to accommodation, but other studies have used the actual response. As the response is often less than the stimulus, it is to be expected that studies using response will demonstrate greater changes to parameter per unit change in accommodation.

To elaborate on the lens changes occurring with accommodation as given early in this section, both surfaces steepen with accommodation, with the anterior surface increasing at approximately twice the rate of the posterior surface. Martinez-Enriquez et al. (2017) determined changes in surface asphericity. Central thickness increases at approximately 0.06 mm per diopter, with the changes confined to the nucleus (Dubbelman et al. 2003). As well as the lens moving forward during accommodation, some studies (Bolz et al. 2007; Drexler et al. 1997; Dubbelman et al. 2005; Ostrin et al. 2006) but not others (Kasthurirangan et al. 2011; Koepll et al. 2005) have found a small backwards movement. Lens diameter reduces with accommodation at a rate of approximately 0.08 mm/diopter; using this value, a lens could have diameters of 9.0 mm and 8.5 mm in unaccommodated and 6 D accommodated states, respectively.

Gullstrand (1909a) attributed part of the increase in lens power with accommodation to the change in refractive index distribution, which he referred to as the intracapsular mechanism of accommodation, but finding supporting evidence has been difficult. Dubbelman et al. (2005) found a small effect of 0.0013 per diopter of accommodation, but Hermans et al. (2008) found that, if the accommodation response was used in determinations rather than the accommodation stimulus, there was no change. Kasthurirangan et al. (2008) found that the edge and central refractive indices in equation (2.13) did not change with accommodation, but there were small, significant decreases in the power coefficient along the axial and equatorial directions, which is consistent with Gullstrand's intracapsular mechanism of accommodation.

SUMMARY OF MAIN SYMBOLS

e	eccentricity of an aspheric surface
n, n'	refractive indices on incident and refraction sides of a surface
Q	surface asphericity ($= -e^2$)
p	surface asphericity ($= 1 + Q$)
R	radius of curvature
Z	optical axis
F	equivalent power
X, Y	distances perpendicular to optical axis
n_o	refractive index at center of lens with gradient index distribution
n_s	refractive index at surface of lens with gradient index distribution
r	relative distance from center of lens to surface
p	coefficient with r in gradient index formula

REFERENCES

- Atchison, D. A. 2006. "Optical models for human myopic eyes." *Vision Res* 46 (14):2236–50.
doi: 10.1016/j.visres.2006.01.004.

- Atchison, D. A., E. L. Markwell, S. Kasthurirangan, J. M. Pope, et al. 2008. "Age-related changes in optical and biometric characteristics of emmetropic eyes." *J Vis* 8 (4):29 1–0. doi: 10.1167/8.4.29.
- Atchison, D. A., M. Suheimat, A. Mathur, L. J. Lister, and J. Rozema. 2016. "Anterior corneal, posterior corneal, and lenticular contributions to ocular aberrations." *Invest Ophthalmol Vis Sci* 57 (13):5263–70. doi: 10.1167/iovs.16-20067.
- Bahrami, M., and A. V. Goncharov. 2014. "Geometry-invariant GRIN lens: finite ray tracing." *Opt Express* 22 (23):27797–2810. doi: 10.1364/OE.22.027797.
- Barbero, S. 2006. "Refractive power of a multilayer rotationally symmetric model of the human cornea and tear film." *J Opt Soc Am A* 23 (7):1578–85. doi: 10.1364/josaa.23.001578.
- Bennett, A. G. 1988. "A method of determining the equivalent powers of the eye and its crystalline lens without resorting to phakometry." *Ophthalmic Physiol Opt* 8 (1):53–9. doi: 10.1016/0275-5408(88)90089-0.
- Birkenfeld, J., A. de Castro, and S. Marcos. 2014. "Contribution of shape and gradient refractive index to the spherical aberration of isolated human lenses." *Invest Ophthalmol Vis Sci* 55 (4):2599–607. doi: 10.1167/iovs.14-14201.
- Birkenfeld, J., A. de Castro, S. Ortiz, D. Pascual, and S. Marcos. 2013. "Contribution of the gradient refractive index and shape to the crystalline lens spherical aberration and astigmatism." *Vision Res* 86:27–34. doi: 10.1016/j.visres.2013.04.004.
- Bolz, M., A. Prinz, W. Drexler, and O. Findl. 2007. "Linear relationship of refractive and biometric lenticular changes during accommodation in emmetropic and myopic eyes." *Brit J Ophthalmol* 91 (3):360–5. doi: 10.1364/josa.70.000220.
- Borja, D., F. Manns, A. Ho, N. Ziebarth, et al. 2008. "Optical power of the isolated human crystalline lens." *Invest Ophthalmol Vis Sci* 49 (6):2541–8. doi: 10.1167/iovs.07-1385.
- Brown, N.P. 1974. "The change in lens curvature with age." *Exp Eye Res* 19 (2):175–83. doi: 10.1016/0014-4835(74)90034-7.
- Cheung, S. W., P. Cho, and W. Douthwaite. 2000. "Corneal shape of Hong Kong-Chinese." *Ophthalmic Physiol Opt* 20 (2):119–25.
- Doughty, M. J., and M. L. Zaman. 2000. "Human corneal thickness and its impact on intraocular pressure measures: a review and meta-analysis approach." *Surv Ophthalmol* 44 (5):367–408. doi: 10.1016/s0039-6257(00)00110-7.
- Douthwaite, W. A., T. Hough, K. Edwards, and H. Notay. 1999. "The EyeSys videokeratoscopic assessment of apical radius and p-value in the normal human cornea." *Ophthalmic Physiol Opt* 19 (6):467–74. doi: 10.1046/j.1475-1313.1999.00462.x.
- Doyle, L., J. A. Little, and K. J. Saunders. 2013. "Repeatability of OCT lens thickness measures with age and accommodation." *Optom Vis Sci* 90 (12):1396–405. doi: 10.1097/OPX.0000000000000080.
- Drexler, W., A. Baumgartner, O. Findl, C. K. Hitzenberger, and A. F. Fercher. 1997. "Biometric investigation of changes in the anterior eye segment during accommodation." *Vision Res* 37 (19):2789–800. doi: 10.1016/s0042-6989(97)00066-7.
- Dua, H. S., L. A. Faraj, D. G. Said, T. Gray, and J. Lowe. 2013. "Human corneal anatomy redefined: a novel pre-Descemet's layer (Dua's layer)." *Ophthalmol* 120 (9):1778–85. doi: 10.1016/j.ophtha.2013.01.018.
- Dubbelman, M., V. A. Sicam, and G. L. Van der Heijde. 2006. "The shape of the anterior and posterior surface of the aging human cornea." *Vision Res* 46 (6-7):993–1001. doi: 10.1016/j.visres.2005.09.021.
- Dubbelman, M., and G. L. Van der Heijde. 2001. "The shape of the aging human lens: curvature, equivalent refractive index and the lens paradox." *Vision Res* 41 (14):1867–77. doi: 10.1016/s0042-6989(01)00057-8.

- Dubbelman, M., G. L. Van der Heijde, and H. A. Weeber. 2005. "Change in shape of the aging human crystalline lens with accommodation." *Vision Res* 45 (1):117–32. doi: 10.1016/j.visres.2004.07.032.
- Dubbelman, M., G. L. Van der Heijde, H. A. Weeber, and G. F. Vrensen. 2003. "Changes in the internal structure of the human crystalline lens with age and accommodation." *Vision Res* 43 (22):2363–75. doi: 10.1016/s0042-6989(03)00428-0.
- Dunne, M. C., M. E. Elawad, and D. A. Barnes. 1996. "Measurement of astigmatism arising from the internal ocular surfaces." *Acta Ophthalmol Scand* 74 (1):14–20. doi: 10.1111/j.1600-0420.1996.tb00674.x.
- Dunne, M.C.M., J.M. Royston, and D.A. Barnes. 1992. "Normal variations of the posterior corneal surface." *Acta Ophthalmol (Copenh)* 70 (2):255–61. doi: 10.1111/j.1755-3768.1992.tb04133.x.
- Edmund, C., and E. Sjøntoft. 1985. "The central-peripheral radius of the normal corneal curvature." *Acta Ophthalmologica* 63 (6):670–7. doi: 10.1111/j.1755-3768.1985.tb01579.x.
- Eysteinsson, T., F. Jonasson, A. Arnarsson, H. Sasaki, and K. Sasaki. 2005. "Relationships between ocular dimensions and adult stature among participants in the Reykjavik Eye Study." *Acta Ophthalmol Scand* 83 (6):734–8. doi: 10.1111/j.1600-0420.2005.00540.x.
- Fledelius, H. C., and M. Stubgaard. 1986. "Changes in refraction and corneal curvature during growth and adult life. A cross-sectional study." *Acta Ophthalmol (Copenh)* 64 (5):487–91. doi: 10.1111/j.1755-3768.1986.tb06959.x.
- Garner, L.F., and G. Smith. 1997. "Changes in equivalent and gradient refractive index of the crystalline lens with accommodation." *Optom Vis Sci* 74 (2):114–9. doi: 10.1097/00006324-199702000-00024.
- Glasser, A. 2011. "Chapter 3. Accommodation." In *Adler's Physiology of the Eye*, edited by P. L. Kaufman and A. Alm, 41–70. Elsevier.
- Glasser, A., and M. C. Campbell. 1999. "Biometric, optical and physical changes in the isolated human crystalline lens with age in relation to presbyopia." *Vision Res* 39 (11):1991–2015. doi: 10.1016/s0042-6989(98)00283-1.
- Guillon, M., D. P. Lydon, and C. Wilson. 1986. "Corneal topography: a clinical model." *Ophthalmic Physiol Opt* 6 (1):47–56.
- Gullstrand, A. 1909a. "Appendix II: Procedure of rays in the eye. Imagery - laws of the first order." In *Helmholtz's Handbuch der Physiologischen Optik*, vol. 1, 3rd edn (English translation edited by J. P. Southall, Optical Society of America, 1924), pp. 301–358.
- Gullstrand, A. 1909b. "Appendix IV: The mechanism of accommodation." In *Helmholtz's Handbuch der Physiologischen Optik*, vol. 1, 3rd edn (English translation edited by J. P. Southall, Optical Society of America, 1924), pp. 382–415.
- Helmholtz, H. 1855. "Ueber die Accommodation des Auges." *Archiv für Ophthalmologie* 1:1–74.
- Helmholtz, H. 1909. *Handbuch der Physiologischen Optik*, vol. 1, 3rd ed (English translation edited by J. P. Southall, Optical Society of America, 1924), pp. 143–172.
- Hermans, E. A., M. Dubbelman, R. Van der Heijde, and R. M. Heethaar. 2008. "Equivalent refractive index of the human lens upon accommodative response." *Optom Vis Sci* 85 (12):1179–84. doi: 10.1097/OPX.0b013e31818e8d57.
- Hermans, E. A., M. Dubbelman, R. Van der Heijde, and R. M. Heethaar. 2009. "Constant volume of the human lens and decrease in surface area of the capsular bag during accommodation: an MRI and Scheimpflug study." *Invest Ophthalmol Vis Sci* 50 (1):281–9.
- Hoffmann, P. C., and W. W. Hütz. 2010. "Analysis of biometry and prevalence data for corneal astigmatism in 23,239 eyes." *J Cataract Refract Surg* 36 (9):1479–85. doi: 10.1016/j.jcrs.2010.02.025.

- Hogan, M. J., J. A. Alvarado, and J. E. Weddell. 1971. *Histology of the Human Eye*: W. B. Saunders and Co.
- Huynh, S. C., A. Kifley, K. A. Rose, I. Morgan, et al. 2006. "Astigmatism and its components in 6-year-old children." *Invest Ophthalmol Vis Sci* 47 (1):55–64. doi: 10.1167/iovs.05-0182.
- Jones, C. E., D. A. Atchison, R. Meder, and J. M. Pope. 2005. "Refractive index distribution and optical properties of the isolated human lens measured using magnetic resonance imaging (MRI)." *Vision Res* 45 (18):2352–66. doi: 10.1016/j.visres.2005.03.008.
- Jones, C. E., D. A. Atchison, and J. M. Pope. 2007. "Changes in lens dimensions and refractive index with age and accommodation." *Optom Vis Sci* 84 (10):990–5. doi: 10.1097/OPX.0b013e318157c6b5.
- Jongenelen, S., J. J. Rozema, M. J. Tassignon, Evicr.net, and Group Project Gullstrand Study. 2015. "Distribution of the crystalline lens power in vivo as a function of age." *Invest Ophthalmol Vis Sci* 56 (12):7029–35. doi: 10.1167/iovs.15-18047.
- Kasthurirangan, S., E. L. Markwell, D. A. Atchison, and J. M. Pope. 2008. "In vivo study of changes in refractive index distribution in the human crystalline lens with age and accommodation." *Invest Ophthalmol Vis Sci* 49 (6):2531–40. doi: 10.1167/iovs.07-1443.
- Kasthurirangan, S., E. L. Markwell, D. A. Atchison, and J. M. Pope. 2011. "MRI study of the changes in crystalline lens shape with accommodation and aging in humans." *J Vis* 11 (3). doi: 10.1167/11.3.19.
- Khan, A., J. M. Pope, P. K. Verkiculara, M. Suheimat, and D. A. Atchison. 2018. "Change in human lens dimensions, lens refractive index distribution and ciliary body ring diameter with accommodation." *Biomed Opt Express* 9 (3):1272–82. doi: 10.1364/BOE.9.001272.
- Kiely, P.M., G. Smith, and L.G. Carney. 1982. "The mean shape of the human cornea." *Optica Acta (London)* 29 (8):1027–40. doi: 10.1080/713820960.
- Koch, D. D., S. F. Ali, M. P. Weikert, M. Shirayama, et al. 2012. "Contribution of posterior corneal astigmatism to total corneal astigmatism." *J Cataract Refract Surg* 38 (12):2080–7. doi: 10.1016/j.jcrs.2012.08.036.
- Koepll, C., O. Findl, K. Kriechbaum, and W. Drexler. 2005. "Comparison of pilocarpine-induced and stimulus-driven accommodation in phakic eyes." *Exp Eye Res* 80 (7):795–800. doi: 10.1080/713820960.
- Koretz, J. F., C. A. Cook, and P. L. Kaufman. 2002. "Aging of the human lens: changes in lens shape upon accommodation and with accommodative loss." *J Opt Soc Am A* 19 (1):144–51. doi: 10.1364/josaa.19.000144.
- Koretz, J.F., P.L. Kaufman, M.W. Neider, and P.A. Goeckner. 1989. "Accommodation and presbyopia in the human eye — aging of the anterior segment." *Vision Res* 29 (12):1685–92. doi: 10.1016/0042-6989(89)90150-8.
- Lai, T., and S. Tang. 2014. "Cornea characterization using a combined multiphoton microscopy and optical coherence tomography system." *Biomed Opt Express* 5 (5):1494–511. doi: 10.1364/BOE.5.001494.
- Lam, A. K. C., and W. A. Douthwaite. 1997. "Measurement of posterior corneal asphericity on Hong Kong Chinese: a pilot study." *Ophthalmic Physiol Opt* 17 (1):348–56. doi: 10.1111/j.1475-1313.1997.tb00066.x.
- Leung, T. W., A. K. Lam, L. Deng, and C. S. Kee. 2012. "Characteristics of astigmatism as a function of age in a Hong Kong clinical population." *Optom Vis Sci* 89 (7):984–92. doi: 10.1097/OPX.0b013e31825da156.
- Li, H., S. M. Li, L. R. Liu, Y. Z. Ji, et al. 2019. "Astigmatism and its components in 12-year-old Chinese children: the Anyang Childhood Eye Study." *Br J Ophthalmol* 103 (6):768–74. doi: 10.1136/bjophthalmol-2018-312114.

- Liu, Y. C., P. Chou, R. Wojciechowski, P. Y. Lin, et al. 2011. "Power vector analysis of refractive, corneal, and internal astigmatism in an elderly Chinese population: the Shihpai Eye Study." *Invest Ophthalmol Vis Sci* 52 (13):9651–7.
- Lowe, R. F. 1972. "Anterior lens curvature." *Brit J Ophthalmol* 56 (5):409–13. doi: 10.1136/bjo.56.5.409.
- Lowe, R. F., and B. A. J. Clark. 1973. "Posterior corneal curvature." *Br J Ophthalmol* 57 (7):464–70. doi: 10.1136/bjo.57.7.464.
- Maceo Heilman, B., F. Manns, M. Ruggeri, A. Ho, et al. 2018. "Peripheral defocus of the monkey crystalline lens with accommodation in a lens stretcher." *Invest Ophthalmol Vis Sci* 59 (5):2177–86. doi: 10.1167/iovs.17-23273.
- Mandell, R.B., and R. St. Helen. 1971. "Mathematical model of the corneal contour." *Br J Physiol Opt* 26 (2):183–97.
- Manns, F., A. Ho, and J.-M. Parel. 2017. "Chapter 15. The lens." In *Handbook of Visual Optics: Fundamentals and Eye Optics, Volume I* edited by P. Artal, 211–33. London: CRC Press.
- Martinez-Enriquez, E., P. Pérez-Merino, M. Velasco-Ocana, and S. Marcos. 2017. "OCT-based full crystalline lens shape change during accommodation in vivo." *Biomed Opt Express* 8 (2):918–33. doi: 10.1364/BOE.8.000918.
- Mutti, D. O., G. L. Mitchell, L. A. Jones, N. E. Friedman, et al. 2004. "Refractive astigmatism and the toricity of ocular components in human infants." *Optom Vis Sci* 81 (10):753–61. doi: 10.1097/00006324-200410000-00007.
- Navarro, R., F. Palos, and L. Gonzalez. 2007. "Adaptive model of the gradient index of the human lens. I. Formulation and model of aging ex vivo lenses." *J Opt Soc Am A* 24 (8):2175–85. doi: 10.1364/josaa.24.002175.
- Navarro, R., J. J. Rozema, and M. J. Tassignon. 2013a. "Orientation changes of the main corneal axes as a function of age." *Optom Vis Sci* 90 (1):23–30. doi: 10.1097/OPX.0b013e3182780f88.
- Navarro, R., J. J. Rozema, and M. J. Tassignon. 2013b. "Optical changes of the human cornea as a function of age." *Optom Vis Sci* 90 (6):587–98. doi: 10.1097/OPX.0b013e3182928bc6.
- Ni, Y., X.-L. Liu, M.-X. Wu, Y. Lin, et al. 2011. "Objective evaluation of the changes in the crystalline lens during accommodation in young and presbyopic populations using Pentacam HR system." *Int J Ophthalmol* 4 (6):611–5. doi: 10.3980/j.issn.2222-3959.2011.06.07.
- Niyazmand, H., S. A. Read, D. A. Atchison, and M. J. Collins. 2021. "Anterior scleral thickness and shape changes with different levels of convergence." *Exp Eye Res* 203:101361. doi: 10.1016/j.exer.2020.108435.
- Ortiz, S., P. Pérez-Merino, E. Gambra, A. de Castro, and S. Marcos. 2012. "In vivo human crystalline lens topography." *Biomed Opt Express* 3 (10):2471–88. doi: 10.1364/BOE.3.002471.
- Ostrin, L., S. Kasthurirangan, D. Win-Hall, and A. Glasser. 2006. "Simultaneous measurements of refraction and A-scan biometry during accommodation in humans." *Optom Vis Sci* 83 (9):657–65. doi: 10.1097/01.opx.0000232810.61191.02.
- Patel, S., and J. L. Alio. 2012. "Corneal refractive index-hydration relationship by objective refractometry." *Optom Vis Sci* 89 (11):1641–6. doi: 10.1097/OPX.0b013e31826c5dde.
- Patel, S., J. Marshall, and F. W. Fitzke. 1995. "Refractive index of the human corneal epithelium and stroma." *J Refract Surg* 11 (2):100–5. doi: 10.3928/1081-597X-19950301-09.
- Patel, S., J. Marshall, and F.W. Fitzke. 1993. "Shape and radius of posterior corneal surface." *Ref Corn Surg* 9 (3):173–81.
- Patel, S., and L. Tutchenko. 2019. "The refractive index of the human cornea: A review." *Cont Lens Ant Eye* 42 (5):575–80. doi: 10.1016/j.clae.2019.04.018.

- Pérez-Merino, P., M. Velasco-Ocana, E. Martinez-Enriquez, and S. Marcos. 2015. "OCT-based crystalline lens topography in accommodating eyes." *Biomed Opt Express* 6 (12):5039–54. doi: 10.1364/BOE.6.0005039.
- Pierscionek, B.K., and D.Y.C. Chan. 1989. "Refractive index gradient of human lenses." *Optom Vis Sci* 66 (12):822–9. doi: 10.1097/00006324-198912000-00004.
- Ramasubramanian, V., and A. Glasser. 2015. "Objective measurement of accommodative biometric changes using ultrasound biomicroscopy." *J Cataract Refract Surg* 41 (3):511–26. doi: 10.1016/j.jcrs.2014.08.033.
- Read, S. A., S. J. Vincent, and M. J. Collins. 2017. "Chapter 14. The cornea." In *Handbook of Visual Optics: Fundamentals and Eye Optics, Volume I* edited by P. Artal, 190–210. London: CRC Press.
- Richdale, K., M. A. Bullimore, L. T Sinnott, and K. Zadnik. 2016. "The effect of age, accommodation and refractive error on the adult human eye." *Optom Vis Sci* 93 (1):3–11. doi: 10.1097/OPX.0000000000000757.
- Richdale, K., M. A. Bullimore, and K. Zadnik. 2008. "Lens thickness with age and accommodation by optical coherence tomography." *Ophthalmic Physiol Opt* 28 (5):441–7. doi: 10.1111/j.1475-1313.2008.00594.x.
- Richdale, K., L. T. Sinnott, M. A. Bullimore, P. A. Wassenaar, et al. 2013. "Quantification of age-related and per diopter accommodative changes of the lens and ciliary muscle in the emmetropic human eye." *Invest Ophthalmol Vis Sci* 54 (2):1095–105.
- Rosales, P., M. Dubbelman, S. Marcos, and R. van der Heijde. 2006. "Crystalline lens radii of curvature from Purkinje and Scheimpflug imaging." *J Vis* 6 (10):1057–67.
- Rozema, J. J., S. Hershko, M. J. Tassignon, and Project Gullstrand Study Group for Evicr.net. 2019. "The components of adult astigmatism and their age-related changes." *Ophthalmic Physiol Opt* 39 (3):183–93. doi: 10.1111/opo.12616.
- Sheppard, A. L., C. J. Evans, K. D. Singh, J. S. Wolffsohn, et al. 2011. "Three-dimensional magnetic resonance imaging of the phakic crystalline lens during accommodation." *Invest Ophthalmol Vis Sci* 52 (6):3689–97. doi: 10.1167/iovs.10-6805.
- Shufelt, C., S. Fraser-Bell, M. Ying-Lai, M. Torres, et al. 2005. "Refractive error, ocular biometry, and lens opalescence in an adult population: the Los Angeles Latino Eye Study." *Invest Ophthalmol Vis Sci* 46 (12):4450–60. doi: 10.1167/iovs.05-0435.
- Smith, G., and D. A. Atchison. 2001. "The gradient index and spherical aberration of the lens of the human eye." *Ophthalmic Physiol Opt* 21 (4):317–26. doi: 10.1046/j.1475-1313.2001.00591.x.
- Smith, G., B. K. Pierscionek, and D. A. Atchison. 1991. "The optical modelling of the human lens." *Ophthalmic Physiol Opt* 11 (4):359–69. doi: 10.1016/0275-5408(91)90053-L.
- Sorsby, A., B. Benjamin, J. B. Davey, M. Sheridan, and J. M. Tanner. 1957. *Emmetropia and its Aberrations*. edited by Medical Research Council Special Report Series number 293. HMSO.
- Stenström, S. 1948. "Investigation of the variation and the correlation of the optical elements of human eyes. Part III - Chapter III. Translated by D. Woolf." *Am J Optom Arch Am Acad Optom* 25 (7):340–50.
- Strenk, S. A., J. L Semmlow, L. M Strenk, P. Munoz, et al. 1999. "Age-related changes in human ciliary muscle and lens: a magnetic resonance imaging study." *Invest Ophthalmol Vis Sci* 40 (6):1162–9.
- Tomlinson, A. 1992. "Tear film changes with contact lens wear." In *Complications of Contact Lens Wear*, edited by D.K. Marshall and J. Tryboski, 159–60. St. Louis: Mosby-Year Book Incorporated.

- Tsorbatzoglou, A., G. Nemeth, N. Szell, Z. Biro, and A. Berta. 2007. "Anterior segment changes with age and during accommodation measured with partial coherence interferometry." *J Cataract Refract Surg* 33 (9):1597–601. doi: 10.1016/j.jcrs.2007.05.021.
- Wickremasinghe, S., P. J. Foster, D. Uranchimeg, P. S. Lee, et al. 2004. "Ocular biometry and refraction in Mongolian adults." *Invest Ophthalmol Vis Sci* 45 (3):776–83. doi: 10.1167/ iovs.03-0456.
- Xiang, Y., T. Fu, Q. Xu, W. Chen, et al. 2021. "Quantitative analysis of internal components of the human crystalline lens during accommodation in adults." *Sci Rep* 11 (1):6688. doi: 10.1038/s41598-021-86007-6.



Taylor & Francis
Taylor & Francis Group
<http://taylorandfrancis.com>

3 The Pupil

3.1 INTRODUCTION – THE IRIS

The iris forms the *aperture stop* of the eye. Its aperture or opening is generally known as the *pupil*. The pupil size is determined by two antagonistic muscles, which are under autonomic (reflex) control:

1. The sphincter pupillae is a smooth muscle forming a ring around the pupillary margin of the iris. When it contracts, the pupil constricts. It is innervated by the parasympathetic fibers from the oculomotor (third cranial) nerve by the way of the ciliary ganglion and the short ciliary nerves.
2. The dilator pupillae consists of myo-epithelial cells that extend radially from the sphincter into the ciliary body. It dilates the pupil and is innervated by sympathetic nerve fibers, which synapse in the superior cervical ganglion and enter the eye by way of the short and long ciliary nerves.

Iris color varies markedly between different people and depends upon the amount of pigmentation within the stroma and anterior limiting layer. Lightly pigmented irises appear blue, and the more pigment there is in the iris, the browner the eye appears.

In this chapter, we discuss the properties of the aperture stop/pupils, factors that affect pupil size and centration, and the effect of pupil size on the retinal image.

3.2 ENTRANCE AND EXIT PUPILS

In general optical systems, the opening in the aperture stop is not referred to as the pupil. The word “pupil” is used for the images of the aperture stop. The image of the stop formed by the optical elements in front of it is the *entrance pupil* – in other words, the entrance pupil of an optical system is the image of the aperture stop formed in object space. The image of the aperture stop formed by the elements behind it is the *exit pupil*. Alternatively, we can say that the exit pupil is the image of the aperture stop formed in image space.

With respect to the eye, and depending on the context, the term “pupil” is generally used to refer to either the aperture stop opening – the “real” or “actual” pupil – or to the entrance pupil that we see. Compared with the entrance pupil, the exit pupil of the eye has little practical significance. In the rest of the chapter, when we refer to pupil size we are referring to the entrance pupil size.

Given the ocular parameters of an eye (for example, the schematic eyes in Appendix 3), paraxial optics can determine the size and positions of the entrance and exit pupils.

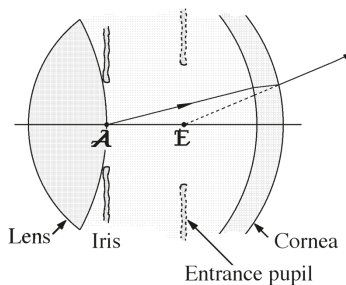


FIGURE 3.1 The formation of the entrance pupil.

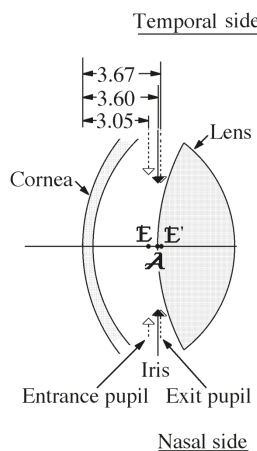


FIGURE 3.2 The iris and the entrance and exit pupils of the Gullstrand number 1 relaxed schematic eye (unit is mm).

To determine the entrance pupil position and size, we need to trace a ray from the center of the iris out of the eye. For the exit pupil, we trace a ray from the same point towards the retina. We show how this is done in Chapter 5. In such calculations, we usually assume that the actual pupil lies in the front vertex plane of the lens.

Figure 3.1 shows, in schematic form, a ray traced from the iris at A through the cornea and out of the eye. This ray appears to cross the axis at the point E, which locates the entrance pupil. This figure is not to scale but shows correctly that the entrance pupil is forward of and larger than the aperture. In one schematic eye, the Gullstrand number 1 relaxed schematic eye, the aperture is 3.6 mm from the corneal vertex and the entrance pupil is 3.05 mm from the corneal vertex. The entrance pupil is 13.3 per cent larger than the aperture. The exit pupil is 0.07 mm behind the aperture and 3.1 per cent larger. Figure 3.2 shows the positions and sizes of the aperture and entrance and exit pupils of this schematic eye.

3.2.1 EFFECT OF ABBERRATIONS

The above calculations are based upon paraxial optics, which ignore aberration effects. The predictions are valid only for small pupils observed along or close to the optical axis. Aberrations of the cornea have some effect for wide pupils and for oblique viewing. Effect of aberrations on pupil magnification as discussed in section 3.5.

3.2.2 ACCOMMODATION

Upon accommodation, the anterior surface of the lens moves forward. Gullstrand's number 1 schematic eye has a highly accommodated version in which this movement and that of the aperture stop is 0.4 mm. The entrance and exit pupils move forward by similar amounts.

3.2.3 THE PARAXIAL MARGINAL RAY AND PARAXIAL PUPIL RAY

If we wish to analyze the optical properties of the eye, two useful and special rays are the *paraxial marginal ray* and the *paraxial pupil ray* (also *paraxial chief ray*). These are defined as follows:

- The paraxial marginal ray is the paraxial ray from an on-axis object point, which passes through the edges of the pupils and the aperture stop and to the image point (which also must be on axis).
- The paraxial pupil ray is the paraxial ray from an object point, at the edge of a nominated field-of-view, which passes through the centers of the pupils and the aperture stop.

Figures 3.3a and 3.3b show the nominal paths of these two rays, and paraxial raytracing gives the actual paths for schematic eyes (Appendix 1). These two rays are useful in various ways. For example, the path of the paraxial marginal ray and the angle α' inside the eye are useful in determining retinal light level (Chapter 13). The paraxial pupil ray is useful in calculating the position of off-axis retinal images (see Chapters 6, 9, and 10), and both rays are useful in estimating the aberrations of the eye.

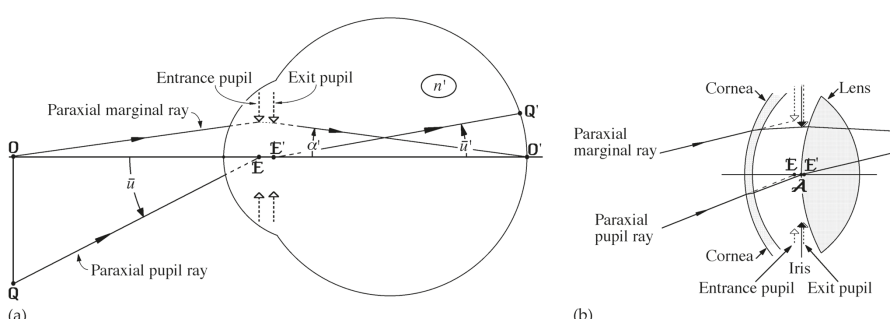


FIGURE 3.3 The entrance and exit pupils of the eye and the paraxial marginal and pupil rays.

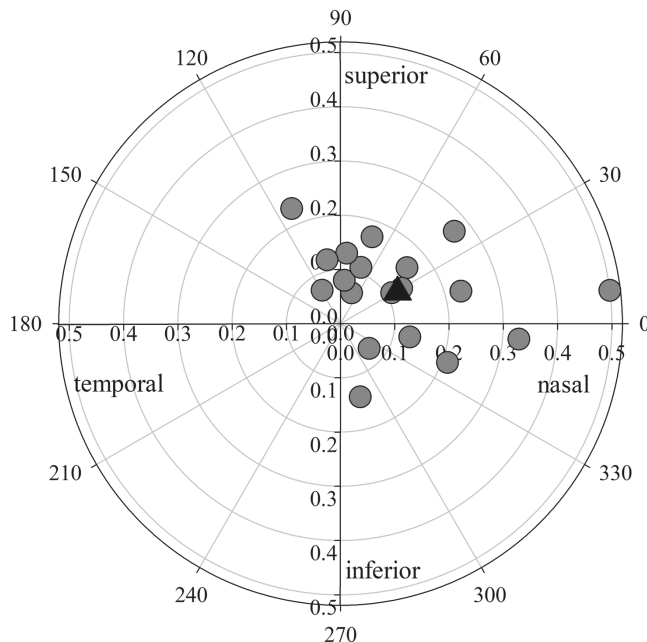


FIGURE 3.4 Pupil center shifts from a 0.01 cd/m^2 , 0 D luminance-accommodation stimulus combination to a 6100 cd/m^2 –6 D combination, for a group of 19 18–25-year-olds. The black triangle shows the mean shift ($\approx 0.11 \text{ mm}$ nasal) and the other symbols represent individual participants. Data are from Figure 4 of Mathur et al. (2014).

3.3 PUPIL CENTRATION

In any rotationally symmetric optical system, the pupils are centered. However, the pupils of real eyes are usually decentred. The position of the (entrance) pupil controls the direction of the path of a beam passing into the eye, and therefore affects the amount and type of aberrations and hence retinal image quality.

The pupil center moves with change in pupil diameter. For pupil dilation caused naturally by reduction in luminance, the pupil center moves by up to 0.4 mm and generally in the temporal direction (Walsh 1988; Wilson et al. 1992; Wyatt 1995; Yang et al. 2002; Donnenfield 2004; Wildenmann and Schaeffel 2013; Mathur et al. 2014) (Figure 3.4). In drug-induced dilation, the degree of movement can be of this order, but does not always follow the same direction and can include a substantial vertical component (Hoang et al. 2016). Accommodation has no significant effect upon pupil centration (Mathur et al. 2014).

3.4 PUPIL SIZE

Some of the factors controlling or affecting pupil size are discussed briefly here. Loewenfeld (1993) gave a comprehensive cover of these factors.

3.4.1 LEVEL OF ILLUMINATION

This is the most important factor affecting pupil size. The diameter of the pupil may vary from about 2 mm at high illumination to about 8 mm in darkness, corresponding to approximately 16 times variation in area. At normal levels of photopic illumination, the pupil fluctuates in size at a temporal frequency of approximate 1.4 Hz, exaggerated cases of which are referred to as *hippus*.

The pupil responds to an increase in illumination by a decrease in size. When the light intensity is low, there is a latency of 0.5 s before constriction begins. As the stimulating light intensity increases, this latency reduces to 0.2-0.3 s. The extent of the response also depends on the distribution of light in the field-of-view. There is less response as a light source moves from the central visual field into the peripheral field, e.g., Crawford (1936). Pupil response to changes in light level is mediated by rod and cone receptors, together with the intrinsically photoreceptive retinal ganglion cells.

The response to an increase in light level is usually complete within a few seconds, whereas the response to the withdrawal of light may take up to a minute to be completed (Reeves 1920; Crawford 1936).

Reeves (1918) and Crawford (1936) investigated the effect of a large source ($\approx 55^\circ$ diameter subtense) on pupil diameter (Figure 3.5). There was considerable variation between subjects, as can be seen from the large standard deviations in the figure. Moon and Spencer (1944) reviewed the results of several studies, and proposed an equation, which, using the unit of cd/m^2 instead of millilamberts for luminance, is

$$D = 4.90 - 3.00 \tanh\{0.400[\log_{10}(L) + 1.0]\} \quad (3.1a)$$

where D is pupil diameter (mm) and L is field luminance (cd/m^2). Using all available data, de Groot and Gebhard (1952) proposed an equation, which, again using the unit of cd/m^2 instead of millilamberts for luminance, is

$$\log_{10}(D) = 0.8558 - 4.01 \times 10^{-4}[\log_{10}(L) + 8.6]^3 \quad (3.1b)$$

These two equations are shown in Figure 3.5. The curve fits should be treated with caution because of the wide differences between subjects, and because pupil sizes tend to reduce and become less responsive to changes in light level with increasing age (see Chapter 20).

Watson and Yellott (2012) provided formulae of pupil diameter given by, or derived from, several studies.

3.4.2 FIELD SIZE

There is an interaction between luminance and field size (Crawford 1936; Stanley and Davies 1995; Atchison et al. 2011), in which pupil size is dependent approximately on the product of the two. Stanley and Davies (1995) appear to have been the first to combine these parameters into an equation, which based on their data was

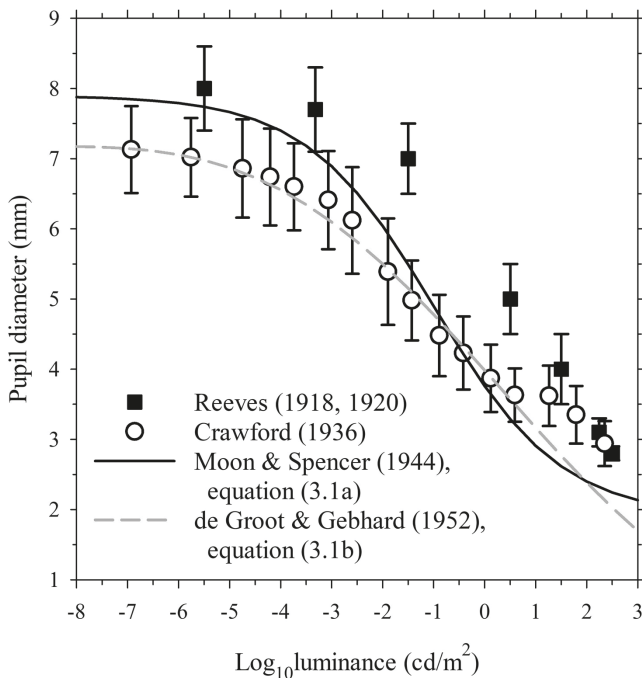


FIGURE 3.5 Pupil diameter as a function of light level for a uniformly extended field. Experimental data are from Reeves (1918 and 1920) and Crawford (1936), and mathematical “mean” curves are from Moon and Spencer (1944) and de Groot and Gebhard (1952).

$$D = 7.75 - \frac{\left(\frac{F}{846}\right)^{0.41}}{\left(\frac{F}{846}\right)^{0.41} + 2} \quad (3.1c)$$

where D is again pupil diameter, and F is the corneal flux density which is the product of field area in deg² and luminance in cd/m².

3.4.3 INFLUENCES OF BINOCULAR VISION AND ACCOMMODATION

The constriction of the pupil due to direct light stimulation is referred to as the *direct light reflex*. In a healthy visual system, there is also a *consensual light reflex*, in which the pupils of both eyes respond equally to stimulation of only one eye. Pupil reactions are more extensive when both eyes of a person are stimulated than when only one eye is stimulated. The pupil decreases in diameter when the eyes converge or accommodate. This is referred to as the *near reflex*. The initial pupil constriction upon increase in accommodation and/or convergence is not maintained, but there is a sustained effect.

Pupil size is smaller under binocular than under monocular viewing conditions (Reeves 1918; Blanchard 1918; ten Doesschate and Alpern 1967). Watson and Yellott (2012) found that this could be modeled well as an attenuation effect of 0.1.

Accommodation has an influence on pupil diameter under steady-state conditions, but this is much small than the effect of luminance (Mathur et al. 2014). Kasthurirangan and Glasser (2005) described pupil size changes in response to stepped changes in accommodation stimulus.

3.4.4 AGE

With increase in age, pupil size decreases and pupils react less to changes in light level. This is considered further in Chapter 20.

3.4.5 DRUGS

Drugs that cause pupil dilation are called *mydriatics*. These can act by stimulating the sympathetic division of the autonomic nervous system (*sympathomimetics*) or by blocking its parasympathetic division (*parasympatholytics*). Drugs that cause pupil constriction are called *miotics* and can act by stimulating the parasympathetic division (*parasympathomimetics*) or by blocking the sympathetic division (*sympatholytics*). Some drugs influence pupil size through their effects on the central nervous system.

Many drugs that affect pupil size also affect accommodation.

3.4.6 PSYCHOLOGICAL FACTORS

Emotional states such as fear, joy, and surprise cause the pupil to dilate. Hess (1965) found that pupil size was affected by mental activities. For example, pleasant, arousal-causing mental images increased pupil size, while unpleasant mental images decreased pupil size.

3.4.7 COMBINING FACTORS

Watson and Yellott (2012) reviewed studies of pupil sizes, and developed a “unified” formula of pupil size incorporating effects of illumination, field size, age, and number of eyes adapted (one or both). As they acknowledged, this did not consider dynamic changes nor individual differences and assumed that the illuminated field is centered about the fixation point. They have made available a useful tool for implementing this formula.

3.5 PUPIL ABERRATION AND SHAPE OF THE OBLIQUELY VIEWED PUPIL

The aberration called *distortion* increases with object size by at least the square of the object size, and affects the size of the entrance pupil. As the stop becomes larger, negative pupil distortion leads to a smaller magnification than the 13 per cent predicted from Gaussian optics for most schematic eyes (see Appendix 3).

Alexandridis and Baumann (1967) examined the effect of stop size on the entrance pupil diameter using excised corneas. For large sizes, pupil magnification was less than the expected 1.13. We predicted the magnification using a Gullstrand number 1 relaxed schematic eye (see Chapter 5) with the anterior corneal surface aspherized with a Q value of -0.2 , which is close to the means of the studies in Table 2.3. Figure 3.6 compares experimental and theoretical results. They show similar values.

So far, we have assumed that the pupil is circular, and we continue to make this assumption even though this is not true for some people.

If we observe the pupil from increasingly oblique angles, the pupil becomes narrower in the direction of view (the *tangential section*) but remains approximately the same in the perpendicular section (the *sagittal section*), as shown in Figure 3.7. Thus, the apparent area of the pupil decreases as the oblique viewing angle increases. The decrease in tangential diameter with viewing angle has important implications for (a) the oblique aberrations and hence retinal image quality, and (b) the amount of light entering the eye from oblique angles, and hence the brightness of a peripheral retinal image (Sloan 1950; Bedell and Katz 1982).

We can estimate the apparent tangential diameter and area from simple geometry, as follows. In the simple geometrical model, a circle appears to be elliptical when

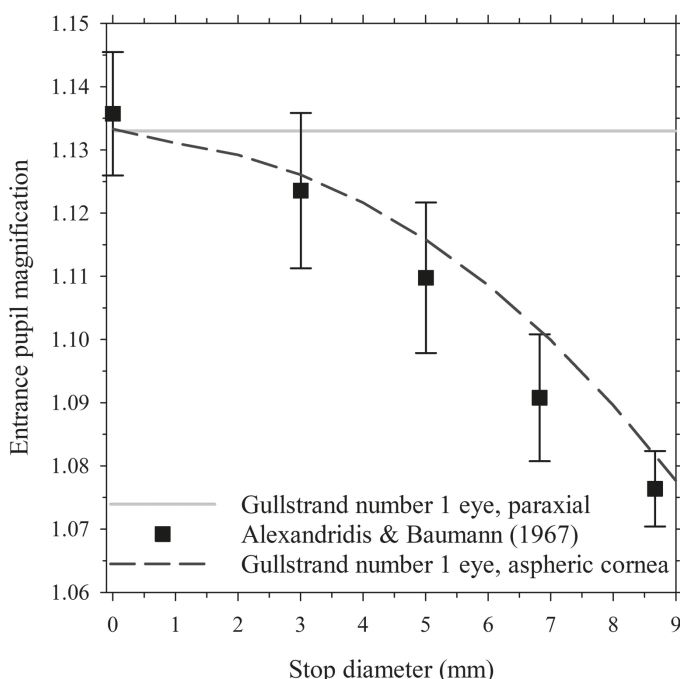


FIGURE 3.6 Entrance pupil magnification from measurements of Alexandridis and Baumann (1967), paraxial prediction of the Gullstrand number 1 eye, and theoretical results using Gullstrand's number 1 schematic eye with an anterior corneal surface of asphericity $Q = -0.2$. The experimental measurements are the means and standard deviations from seven excised corneas positioned approximately 3.6 mm in front of a grid.

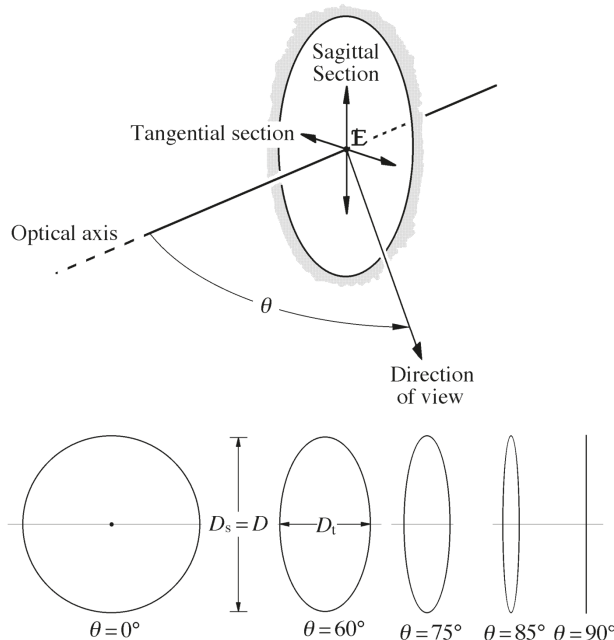


FIGURE 3.7 The shape of the pupil from an oblique direction.

viewed obliquely. Thus, if we view an entrance pupil of diameter D from an oblique angle θ in any direction, the sagittal diameter D_s does not vary with the eccentricity, but the tangential diameter D_t is given by the equation

$$D_t = D \cos(\theta) \quad (3.2)$$

as shown in Figure 3.7. The projected or apparent area $A_p(\theta)$ is the area of an ellipse, and is given by the equation

$$A_p(\theta) = \pi D_s D_t / 4 \quad (3.3)$$

Alternatively, this area can be expressed in the form

$$A_p(\theta) = A(0)_p \cos(\theta) \quad (3.4)$$

where

$$A(0)_p = \pi D^2 / 4 \quad (3.4a)$$

Thus the apparent area decreases with $\cos(\theta)$, and the ratio of the apparent area at an angle θ to that for axial viewing is also $\cos(\theta)$.

This model assumes that the aperture stop (not the entrance pupil) is plane and does not suffer any aberration when imaged by the cornea. It assumes also that the iris rim has minimal thickness. Using complex raytracing with a model eye, Fedtke et al.

(2010) found that with the increasing angle, the entrance pupil may be considered to move forward, tilt, and move out of a single plane, and undergo asymmetric changes in shape with the center no longer coinciding with the on-axis center.

Dimensions of obliquely viewed pupils when the direction of view is horizontal have been determined by Spring and Stiles (1948a, 1948b), Sloan (1950), Jay (1961), Haines (1969), and Jennings and Charman (1978), but facial features restricted measurements from the nasal direction. Mathur et al. (2013) measured across the whole horizontal visual field. In all studies, the sagittal (vertical) diameter varied little with eccentricity. Figure 3.8 shows the mean ratios of tangential to sagittal pupil diameter from some of the studies. These decrease at slower rates than predicted by equation (3.2). Mathur et al. fitted their data to the equation

$$D_t/D_s = 0.99\cos[(\theta + 5.3)/1.121] \quad (3.5a)$$

where they took the visual field angle to be positive for the nasal field. This shows a maximum in the temporal visual field at about 5° and a cosine function that is flatter by 12% than equation (3.2). Atchison et al. (2014) referred to this maximum as the pupillary circular axis. Taking D_s as the same as D and rounding the 0.99 in equation (3.5a) to 1.0, the apparent pupil area is

$$A(\theta)_p = A(0)_p \cos[(\theta + 5.3)/1.121] \quad (3.5b)$$

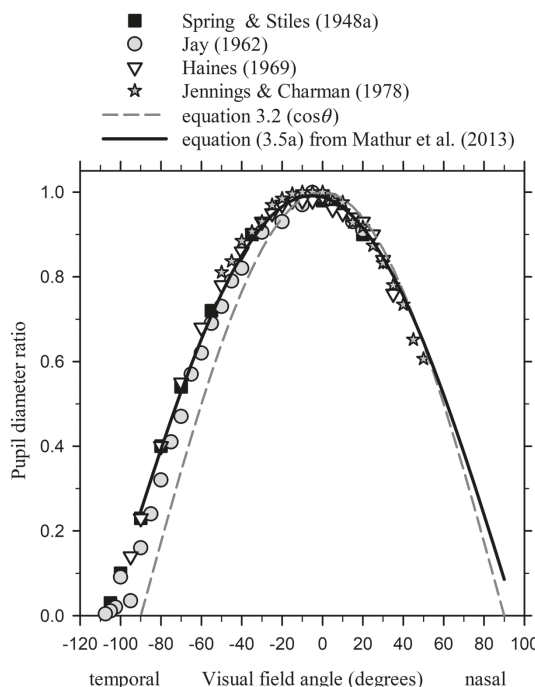


FIGURE 3.8 Pupil diameter ratio as a function of visual field angle from some studies using pupil dilation. The dotted line, equation (3.2), is the ratio expected from a simple geometric model. The solid line, equation (3.5a), is the data fit from Mathur et al. (2013).

Atchison et al. (2014) developed a procedure for determining the vertical component of the pupillary circular axis based on horizontal visual field data. For 30 adults, they obtained a horizontal component range of $(-)1^\circ$ to $(-)9^\circ$ temporal with mean and standard deviation $(-5\pm2^\circ)$, and a vertical component range of $(-)7^\circ$ to $(-)0^\circ$ inferior with mean and standard deviation $(-3\pm2^\circ)$.

3.6 SIGNIFICANCE OF PUPIL SIZE

Pupil size has a number of effects on vision.

3.6.1 DEPTH-OF-FIELD

As with conventional optical systems, the diameter of the pupil affects the depth-of-field. The larger the pupil, the narrower is the depth-of-field. This is discussed in detail in Chapter 19.

3.6.2 RETINAL LIGHT LEVEL

Obviously, pupil diameter affects retinal light level. A detailed analysis of the dependency is included in Chapter 13.

3.6.3 RETINAL IMAGE QUALITY AND VISUAL PERFORMANCE

For large pupil diameters, aberrations cause deterioration in retinal image quality. For small pupil diameters, diffraction limits image quality. There is an optimum pupil diameter range of 2-3 mm that gives the best balance between these two effects for the corrected eye. The effect of pupil diameter on retinal image quality is discussed in greater detail in Chapter 18.

Campbell and Gregory (1960) and Woodhouse (1975) found that the artificial pupil size that gives the optimum (corrected) visual acuity is close to the natural pupil size at various background lighting levels. The visual acuity of a defocused eye is strongly dependent upon pupil diameter. This is discussed further in Chapter 9.

3.6.4 PURPOSE OF THE PUPILLARY LIGHT RESPONSE

We may expect that pupil size varies to maintain a constant light level on the retina, but this is not so. The variation of pupil size with light level is not sufficient to ensure a constant retinal illuminance, because if the pupil size changes from 2 to 8 mm in diameter, the amount of light entering the pupil changes by a factor of only 16. By contrast, we operate comfortably over a 10^5 times luminance range, from full moon-light ($\sim 0.01 \text{ cd/m}^2$) to bright daylight ($\sim 1000 \text{ cd/m}^2$).

The work of Campbell and Gregory (1960) and Woodhouse (1975) suggests that pupil size variations optimize visual acuity for various light levels. This is only applicable for corrected eyes; uncorrected eyes require much smaller pupil sizes. Woodhouse and Campbell (1975) suggested that the purpose of pupil size changes with changes in light level is to reduce retinal illumination and thus help adaptation if there is a return to darkness.

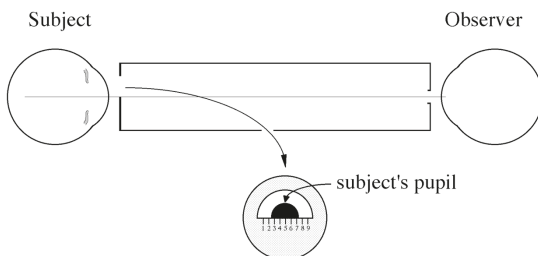


FIGURE 3.9 A simple pupillometer.

3.7 MEASUREMENT OF PUPIL SIZE (PUPILLOMETRY)

There are several experimental and clinical methods for measuring pupil diameter. These vary both in the level of intrusion to the subject and in accuracy. A simple clinical device has the construction shown in Figure 3.9. The inside surface of the end nearest the patient's eye contains a millimeter scale. Parallax is a source of error.

More accurate and less intrusive methods involve photography, either using standard photography or a video camera. A distinct advantage of a photographic method is that it can be done with infrared radiation in complete darkness, and therefore does not affect pupil size. The use of a video camera offers the further advantage that rapid changes in pupil diameter can be recorded and monitored.

Loewenfeld (1993) gave a comprehensive review of pupillometry.

3.8 ARTIFICIAL PUPILS

Artificial pupils are often used to control the effective pupil size of the eye in visual experiments. The pupil of the eye must be dilated first. Artificial pupils can simply be apertures placed immediately in front of the eye, or they can be projected onto the plane of the actual pupil by a relay system. The artificial pupils may be annular, slit, or circular pupils, and may be decentered relative to the actual pupil by a controlled amount. Because of aberrations, retinal image quality varies according to the position of artificial pupils, and careful centration is important (Walsh and Charman 1988).

Artificial pupils are often used in clinical practice as aids in refraction. When corrected visual acuity does not reach normal levels, placing a small pupil (e.g., 1 mm diameter) in front of the eye may improve visual acuity markedly if the refraction is not accurate, but a lack of improvement suggests a pathological basis for the poor vision. Medium-sized artificial pupils (e.g., 3-4 mm) may be used when the pupil has been previously dilated by drugs; the pupils reduce the influence of aberrations, which may make refraction difficult or inaccurate.

SUMMARY OF MAIN SYMBOLS

$A(\theta)_p$	projected or apparent pupil area in the direction θ
D	(entrance) pupil diameter
D_s	pupil diameter in the sagittal section

D_t	pupil diameter in the tangential section
F	corneal flex density ($\deg^2 \cdot cd/m^2$)
L	scene luminance (cd/m^2)
θ	oblique angle

REFERENCES

- Alexandridis, E., and C. Baumann. 1967. "Wirkliche und scheinbare Pupillenweiten des menschlichen Auges." *Optica Acta* 14 (3):311–6.
- Atchison, D. A., C. C. Giregnti, G. M. Campbell, J. P. Dodds, et al. 2011. "Influence of field size on pupil diameter under photopic and mesopic light levels." *Clin Exp Optom* 94 (6):545–8. doi: 10.1111/j.1444-0938.2011.00636.x.
- Atchison, D. A., A. Mathur, M. Suheimat, and W. N. Charman. 2014. "Visual field coordinates of pupillary circular axis and optical axis." *Optom Vis Sci* 91 (5):582–7. doi: 10.1097/OPX.0000000000000228.
- Bedell, H. E., and L. M. Katz. 1982. "On the necessity of correcting peripheral target luminance for pupillary area." *Am J Optom Physiol Opt* 59 (10):767–9. doi: 10.1097/00006324-198210000-00001.
- Blanchard, J. 1918. "The brightness sensibility of the retina." *The Physical Review* 11:81–99.
- Campbell, F. W., and A. H. Gregory. 1960. "Effect of size of pupil on visual acuity." *Nature* 187:1121–3. doi: 10.1038/1871121c0.
- Crawford, B. H. 1936. "The dependence of pupil size upon external light stimulus under static and variable conditions." *Proc R Soc B* 121:376–95.
- de Groot, S. G., and J. W. Gebhard. 1952. "Pupil size as determined by adapting luminance." *J Opt Soc Am A* 42 (7):492–5.
- Donnenfield, E. 2004. "The pupil is a moving target: centration, repeatability, and registration." *J Refract Surg* 20:593–6.
- Fedtke, C., F. Manns, and A. Ho. 2010. "The entrance pupil of the human eye: a three-dimensional model as a function of viewing angle." *Opt Express* 18 (21):22364–76. doi: 10.1364/OE.18.022364.
- Haines, R. F. 1969. "Dimensions of the apparent pupil when viewed at oblique angles." *Am J Ophthalmol* 68 (4):649–56. doi: 10.1016/0002-9394(69)91247-1.
- Hess, E. H. 1965. "Attitude and pupil size." *Sci Am* 212 (4):46–54.
- Hoang, T. A., J. E. Macdonnell, M. C. Mangan, C. S. Monsour, et al. 2016. "Time course of pupil center location after ocular drug application." *Optom Vis Sci* 93 (6):594–9. doi: 10.1097/OPX.0000000000000837.
- Jay, B. S. 1961. "The effective pupillary area at varying perimetric angles." *Vision Res* 1 (5–6):418–24.
- Jennings, J. A. M., and W. N. Charman. 1978. "Optical image quality in the peripheral retina." *Am J Optom Physiol Opt* 55 (8):582–90. doi: 10.1097/00006324-197808000-00008.
- Kasthurirangan, S., and A. Glasser. 2005. "Characteristics of pupil responses during far-to-near and near-to-far accommodation." *Ophthalmic Physiol Opt* 25 (4):328–39. doi: 10.1111/j.1475-1313.2005.00293.x.
- Loewenfeld, I. E. 1993. *The Pupil. Anatomy, Physiology, and Clinical Applications, Vols. 1 and 2*: Iowa State University Press.
- Mathur, A., J. Gehrmann, and D. A. Atchison. 2013. "Pupil shape as viewed along the horizontal visual field." *J Vis* 13(6):3, 1–8. doi: 10.1167/13.6.3.
- Mathur, A., J. Gehrmann, and D. A. Atchison. 2014. "Influences of luminance and accommodation stimuli on pupil size and pupil center location." *Invest Ophthalmol Vis Sci* 55 (4):2166–72. doi: 10.1167/iovs.13-13492.

- Moon, P., and D .E. Spencer. 1944. "On the Stiles-Crawford effect." *J Opt Soc Am* 34 (6):319–29.
- Reeves, P. 1918. "Rate of pupillary dilation and contraction." *Psychol Rev* 25 (2):330–40.
- Reeves, P. 1920. "The response of the average pupil to various intensities of light." *J Opt Soc Am* 4 (2):35–43.
- Sloan, L. L. 1950. "The threshold gradients of the rods and cones: In the dark-adapted and in the partially light-adapted eye." *Am J Ophthalmol* 33 (7):1077–89.
- Spring, K. H., and W. S. Stiles. 1948a. "Apparent shape and size of pupil viewed obliquely." *Brit J Ophthalmol* 32 (6):347–54.
- Spring, K. H., and W. S. Stiles. 1948b. "Variation of pupil size with change in the angle at which the light stimulus strikes the retina." *Brit J Ophthalmol* 32 (6):340–6.
- Stanley, P. A., and A. K. Davies. 1995. "The effect of field of view size on steady-state pupil diameter." *Ophthalmic Physiol Opt* 15 (6):601–3.
- ten Doeschate, J., and M. Alpren. 1967. "Effect of photoexcitation of the two retinas on pupil size." *J Neurophysiol* 30 (3):562–76.
- Walsh, G. 1988. "The effect of mydriasis on the pupillary centration of the human eye." *Ophthalmic Physiol Opt* 8 (2):178–82. doi: 10.1111/j.1475-1313.1988.tb01034.x.
- Walsh, G., and W. N. Charman. 1988. "The effect of pupil centration and diameter on ocular performance." *Vision Res* 28 (5):659–65. doi: 10.1016/0042-6989(88)90114-9.
- Watson, A. B., and J. I. Yellott. 2012. "A unified formula for light-adapted pupil size." *J Vis* 12 (10):12.
- Wildenmann, U., and F. Schaeffel. 2013. "Variations of pupil centration and their effects on video eye tracking." *Ophthalmic Physiol Opt* 33 (6):634–41. doi: 10.1111/opo.12086.
- Wilson, M. A., M. C. W. Campbell, and P. Simonet. 1992. "Change of pupil centration with change of illumination and pupil size." *Optom Vis Sci* 69 (2):129–36. doi: 10.1097/00006324-199202000-00006.
- Woodhouse, J. M. 1975. "The effect of pupil size on grating detection at various contrast levels." *Vision Res* 15 (6):645–8. doi: 10.1016/0042-6989(75)90278-3.
- Woodhouse, J. M., and F. W. Campbell. 1975. "The role of the pupil light reflex in aiding adaptation to the dark." *Vision Res* 15 (6):649–53. doi: 10.1016/0042-6989(75)90279-5.
- Wyatt, H. J. 1995. "The form of the human pupil." *Vision Res* 35 (14):2021–36. doi: 10.1016/0042-6989(94)00268-q.
- Yang, Y., K. Thompson, and S. A. Burns. 2002. "Pupil location under mesopic, photopic, and pharmacologically dilated conditions." *Invest Ophthalmol Vis Sci* 43 (7):2508–12.

4 Axes of the Eye

4.1 INTRODUCTION

Most man-made optical systems are rotationally symmetric about one line, the optical axis. If the reflecting and refracting surfaces are spherical, this is the line joining the centers of curvatures of these surfaces. Some systems contain astigmatic or toroidal components and have two planes of symmetry; the line of intersection of these two planes is the optical axis.

By contrast, to fully describe the optical properties of the eye, we need to introduce several axes. This is because of the lack of symmetry of the eye and because the fixation point and fovea are not along a best-fit axis of symmetry. The optical and visual axes were mentioned in Chapter 1. In this chapter we describe these and other axes, their significance, their applications, and how they may be determined.

The validity of some of these axes is dependent upon some idealized properties of the eye. For example, the visual axis requires the existence of the nodal points, which exist only if the eye is rotationally symmetric. A second example is the fixation axis, which requires the existence of a unique center-of-rotation of the eye.

Some of the methods for determining the axes depend upon observing the images of a small light source formed by specular reflections from the refracting surfaces of the eye. These Purkinje images are discussed in greater depth in section 12.2.

These axes are meaningless without a means of determining their directions and where they enter the eye. The directions are defined relative to each other, and we often refer to the angles between the axes. Table 4.1 lists some axes, and the symbols used to denote the angles between them. Three of the axes pass through the center of the pupil and, since the pupil center can change with change in diameter (see section 3.3), their directions depend upon pupil size.

4.2 DEFINITIONS AND SIGNIFICANCE

Martin (1942) gave an early account of the angles and axes, which highlighted the confusing array of terms that have been used in this area. The definitions of optical axis, line of sight, visual axis, pupillary axis, and fixation axis given below are similar to those provided in dictionaries of visual science (Cline et al. 1997; Millodot 2009).

4.2.1 OPTICAL AXIS

This is the line passing through the centers of curvatures of the refracting and reflecting surfaces of a centered system. The optical axis is not of particular importance by itself, but it is a useful reference for some of the other axes of the eye.

TABLE 4.1

Some Different Axes Used for the Eye and the Symbols Used to Denote the Angles between Them

	Optical Axis	Visual Axis	Line of Sight	Achromatic Axis
Visual Axis	α	—	—	ψ
Pupillary Axis	—	κ	λ	—
Fixation Axis	γ	—	—	—

In a conventional centered optical system, the centers of curvatures of each refracting or reflecting surface lie on one line (i.e., they are co-linear). This line is the optical axis. The eye is not a centered system and does not contain a true optical axis. The concept of optical axis can be applied to the eye by defining the optical axis as the line of “best fit” through the centers of curvature of the “best-fit” spheres to each surface.

4.2.2 LINE OF SIGHT

This is the line joining the fixation point and the center of the entrance pupil.

The line of sight is the most important axis from the point of view of visual function, including refraction procedures, as it defines the center of the beam of light entering the eye. As mentioned in the previous section, it is unfortunately not fixed because the pupil center may alter with fluctuations in pupil size.

The fovea is usually on the temporal side of the optical axis (Chapter 1). Therefore, the point in object space conjugate to the fovea is also off axis, but on the nasal side of the optical axis. The line of sight is the central ray of the beam from the fixation point T as shown in Figure 4.1. In paraxial optics, the line of sight is called the paraxial pupil ray, which was defined in section 3.2. The position at which it intercepts the cornea is called the *corneal sighting center* (Mandell 1995) or *visual center of the cornea* (Cline et al. 1997).

4.2.3 VISUAL AXIS

This is the line joining the fixation point and the foveal image by way of the nodal points.

The visual axis is a convenient reference axis for visual functions, particularly as it does not depend on pupil size. It is usually close to the line of sight at the cornea and entrance pupil (see section 4.3).

The visual axis is the line segments TN and $N'T'$ shown in Figure 4.1. This is not a single straight line since the nodal points are not coincident. Allowing for the exaggeration in Figure 4.1, this shows the proximity of the visual axis to the line of sight.

The *foveal achromatic axis* is closely related to the visual axis, and can be defined as the path from the fixation point to the fovea such that the ray does

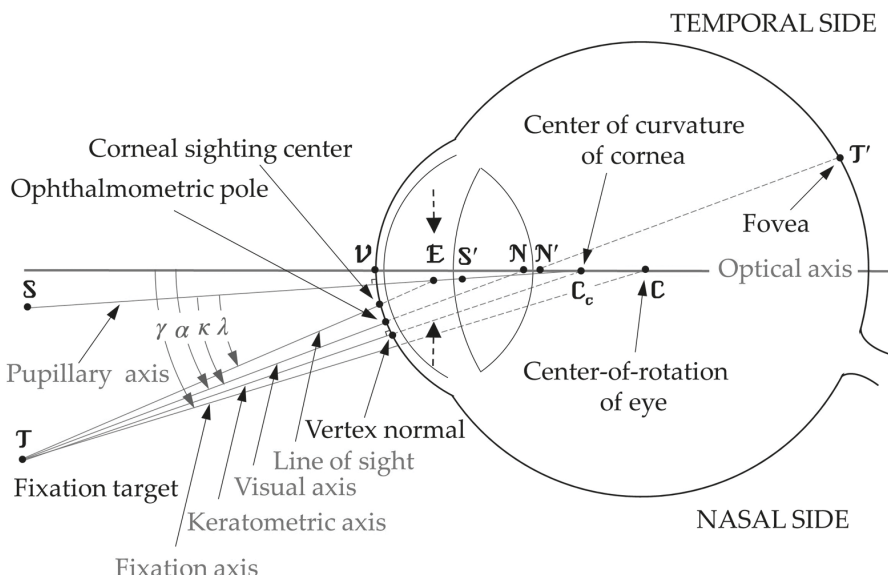


FIGURE 4.1 Most of the axes and angles referred to in this chapter. The object has been shown extremely close to the eye, thus exaggerating angular differences between visual axis, line of sight and fixation axis.

not suffer from any transverse chromatic aberration. Ignoring the small change in the nodal points that occurs with change in wavelength, this axis is the same as the visual axis and its definition can be used as a basis for locating the visual axis. Ivanoff (1953) referred to this axis as simply the *achromatic axis*. However, Thibos et al. (1990) redefined this term to refer to the *pupil nodal ray*, which is the ray passing through the center of the pupil and which has no transverse chromatic aberration. It is like the optical axis but, unlike the optical axis, it is dependent on pupil position. Where Ivanoff used the term achromatic axis, we use the term foveal achromatic axis, and we have adopted Thibos and co-workers' use of achromatic axis (Figure 4.2).

Rabbatts (2007) criticized the use of the term “visual axis” for the ray passing through the nodal points, on the grounds that such a ray is not representative of the beam passing into the eye from a fixation target. He preferred to call it the “nodal axis” and reserved the term “visual axis” for the axis we have defined as the line of sight.

Le Grand and El Hage (1980) referred to the intersection of the visual axis with the cornea as the *ophthalmometric pole* (Figure 4.1).

4.2.4 PUPILLARY AXIS

This is the line passing through the center of the entrance pupil, and which is normal to the cornea.

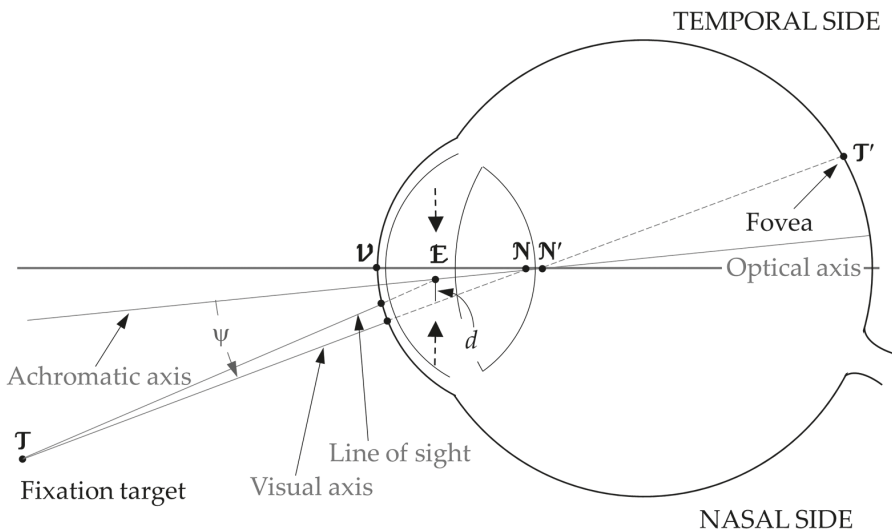


FIGURE 4.2 Ocular axes: the optical axis, line of sight, visual axis, and achromatic axis; the angle Ψ between the visual axis and the achromatic axis; the distance d between the visual axis and line of sight at the entrance pupil.

The pupillary axis is used as an objective measure to judge the amount of *eccentric fixation*, the condition in which a retinal point other than the center of the fovea is used for fixation. Eccentric fixation is an adaptation to *heterotropia* (squint or turned eye). We discuss the measurement of eccentric fixation and heterophoria further in section 4.4.2.

If the eye was a centered system and the pupil was also centered, the pupillary axis would lie along the optical axis. However, the pupil is often not centered relative to the cornea and, furthermore, the cornea may not be a regular shape. Both these factors cause the pupil axis to lie in some other direction, and in general it does not pass through the fixation point **T** as shown in Figure 4.1.

4.2.5 FIXATION AXIS

This is the line passing through the fixation point and the center-of-rotation of the eye.

The fixation axis is the reference for measuring eye movements.

This axis is shown in Figure 4.1. There is no unique center-of-rotation, and estimates of it depend on the direction of rotation of the eye (see section 1.7). Accordingly, the idea of a fixation axis is just an approximation and estimates of it depend also upon the direction of rotation.

As a complication, in vertical gaze there is cyclotorsion of the eyes up to a few degrees. Typically with upwards gaze the superior eye rotates towards the nose (in-cyclorotation) and with downwards gaze there is ex-cyclorotation (Enright 1980).

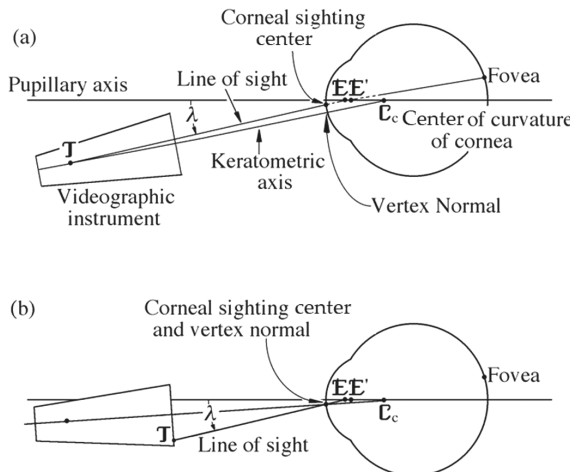


FIGURE 4.3 The keratometric axis and the line of sight of a corneal topographer. (a) Standard operation: the line of sight and the keratometric axis intersect at the fixation point. (b) The alignment has been altered so that the line of sight and the keratometric axis intersect at the cornea (corneal sighting center). (Based on Mandell et al. 1995.)

4.2.6 KERATOMETRIC AXIS

This is the axis of a keratometer or automated corneal topographer, and it contains the center of curvature of the anterior cornea.

This axis is used for alignment in corneal topography measurements. In the standard operation of a corneal topographic instrument, the axis intercepts the line of sight at the fixation target (Figure 4.3a), although the fixation target may be moved deliberately so that this is not the case (Figure 4.3b). According to Mandell (1994), in standard use a small but negligible variation occurs in this axis between different instruments, because of differences in the distance of the fixation point.

When a corneal topographer is used in standard operation, the keratometric axis is neither the line of sight nor does it pass through the apex of the cornea (the point with the smallest radius of curvature (Mandell and St. Helen 1969)). The point at which the axis intercepts the cornea is sometimes called the *vertex normal* (Maloney 1990), and is the center of keratogram images. If the vertex normal is sufficiently decentered from the corneal apex, the topographer gives a false representation of the surface curvature across the cornea (Mandell and Horner 1995).

4.2.7 PUPILLARY CIRCULAR AXIS

As described in section 3.5, the pupil appears approximately circular as viewed along the line of sight, but appears elliptical when viewed at considerable angles from the line of sight. The visual field position at which the pupil appears most circular, the peak in Figure 3.7, can be referred to as the *pupillary circular axis*. As there is

considerable information in section 3.5 about how this is determined and its values, it is not referred to further in this chapter.

4.3 LOCATING SOME AXES

4.3.1 THE LINE OF SIGHT

Many automated instruments have a display showing the front of the eye. To achieve alignment while a patient is fixating a reference target, either the patient or the instrument is moved vertically and horizontally until the pupil is correctly centered. Thus, the line of sight is made to coincide with the optical axis of the instrument. Sometimes this is aided by imaging a centered annulus as well as the eye.

4.3.2 THE VISUAL AXIS

The intercept of the visual axis at the cornea (ophthalmometric pole) can be determined by having the subject view a vernier target involving blue and red colors. Two possible targets are shown in Figure 4.4. The subject views the target through a small artificial pupil, say 1 mm diameter. For the target in Figure 4.4a, if the artificial pupil is not centered on the visual axis, there is a break in the alignment of the black lines as they cross between the blue and red parts of the target. For the target in Figure 4.4b, if the artificial pupil is not centered on the visual axis, there is a break in the alignment of the blue and red parts of the target. The position of the subject's eye is adjusted until alignment is obtained both horizontally and vertically. The reliability of the method should improve as the wavelength bands of the target are narrowed.

Thibos et al. (1990) indicated a simple way of estimating the separation of the visual axis from the line of sight at the entrance pupil (the distance d in Figure 4.2). The small artificial pupil, referred to in the previous paragraph, can be scanned across the eye both vertically and horizontally to find the real pupil limits at which the vernier target disappears. The mean of these positions corresponds to the corneal sighting

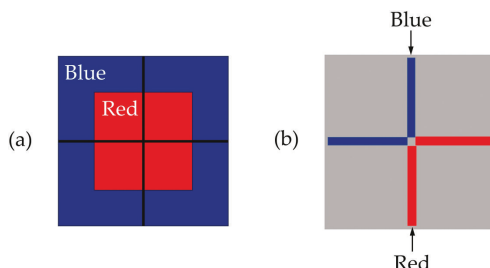


FIGURE 4.4 Two vernier targets for locating the visual axis. (a) Black cross placed on a central red area and a blue surround. (b) Red and blue bracket shaped verniers on a neutral background.

center (on the line of sight). This position is then compared with the ophthalmometric pole (visual axis intercept at the cornea). Thibos and co-workers measured five subjects with drug-induced pupil dilation, considering only the horizontal meridian. They obtained values of d between -0.1 mm and $+0.4$ mm, with a mean of $+0.14$ mm (a positive sign indicating that the visual axis is nasal to the line of sight in object space).

Simonet and Campbell (1990) used a videomonitor to determine the difference in horizontal position of the visual axis (which they referred to as the achromatic axis) and the line of sight. For natural (although generally large) pupils, the differences for eight eyes of five subjects were between -0.08 mm and $+0.51$ mm, with a mean of $+0.11$ mm.

4.3.3 KERATOMETRIC AXIS

Mandell et al. (1995) described methods of determining the location of the keratometric axis relative to the corneal sighting center and the corneal apex. Using a corneal topographer in its standard operation and 20 normal subjects, they found a mean difference between the keratometric axis and the corneal sighting center of 0.4 ± 0.1 mm, with most subjects having the keratometric axis below and nasal to the corneal sighting center. The mean difference between the keratometric axis and the corneal apex was 0.6 ± 0.2 mm, with the majority of subjects having the keratometric axis above the corneal apex. Applegate et al. (2009) determined the keratometric axis to be 0.15 ± 0.14 mm nasal and 0.04 ± 0.12 mm inferior to the corneal sighting center. As the natural pupil moves temporally with dilation, the horizontal component of the difference is affected by pupil size.

4.4 ANGLES BETWEEN AXES

Here we define some of the angles between various axes. In some cases, methods for determining these and measurements are given. The angles alpha, lambda, and kappa have been used differently by different authors. In Table 4.2 we indicate some of the variations from those used here. These variations involve either the line of sight or the visual axis.

TABLE 4.2
Different Terms used for Angles

Term used here	Millodot (2009)	Le Grand and El Hage (1980)	Cline et al. (1997)
α	α	α	α
λ	κ^*	λ	λ
κ	λ	κ	κ

Note: * Between the line of sight and optical axis.

4.4.1 VISUAL AXIS AND OPTICAL AXIS: THE ANGLE ALPHA (α)

Most authors use the term “angle alpha” to refer to the angle between the optical and visual axes (Le Grand and El Hage 1980; Cline et al. 1997; Millodot 2009). We have retained this use but, as the technique of measuring this angle involves the subject fixating on a target, it may be considered that the line of sight (i.e., center of entrance pupil) is involved rather than the visual axis (i.e., nodal points). The distinction is of no practical importance.

In optical laboratories, a frequent need is to locate the optical axis of an optical system. One method of locating this axis is to shine a distant point source into the system and observe the images of this source of light reflected from each surface inside the system. In a centered optical system, if the source of light falls on the optical axis, it and the reflected images are co-linear.

Since the eye has four reflecting surfaces, there are four main reflected (Purkinje) images. However, as the eye is not a centered system, there is no position or direction of the light source that enables the Purkinje images to be aligned. All that can be done is to minimize the spread of these images, and the corresponding direction of the source identifies the direction of the optical axis.

Clinically, the angle α is determined with the ophthalmophakometer (Figure 4.5). This instrument contains a graduated arc, with an observing telescope mounted centrally in the arc. The patient's eye is at the center of curvature of the arc. Two small light sources are placed on the arc near the telescope, with one slightly above and one slightly below it. This gives pairs of Purkinje images. A small fixation object T is moved along the arc until the observer looking through the telescope judges that the Purkinje images are in the best possible alignment. At this point, the optical axis of the eye corresponds with the axis of the instrument. The angle α is given by the scale reading at the position of the fixation target. The instrument can be rotated through 90 degrees to obtain a value in the vertical direction. The distance between the eye and the arc is relatively large (typically 86 cm) so that discrepancies between the front nodal point and the center of curvature of the arc are not critical.

The angle between the visual axis and the optical axis is considered to be positive if the visual axis is on the nasal side of the optical axis in object space. The mean value of angle α is taken often to be about $+5^\circ$ horizontally, but is usually in the range $+3$ to $+5^\circ$, and is rarely negative. The visual axis is also upwards relative to the optical axis by $2\text{--}3^\circ$ (Tscherning 1900).

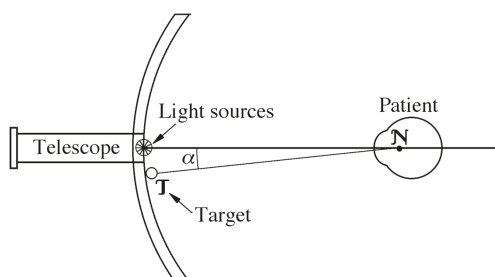


FIGURE 4.5 The ophthalmophakometer.

4.4.2 PUPILLARY AXIS AND LINE OF SIGHT: ANGLE LAMBDA (λ)

This angle is one of the easiest to determine. It can be determined using the ophthalmophakometer just described, but it is determined easily with simpler equipment (Figure 4.1). The subject fixates on some suitable target **T**, and an observer watches the anterior corneal reflection (Purkinje image **P**₁) of a small source of light **S** close to the observer's eye. The position of the light is changed, and the observer's eye is maintained next to the light source, until the reflected image **S'** is seen in the center of the pupil **E** (Figure 4.1). The observation axis is now the pupillary axis. The angle between the line of sight and the pupillary axis at the eye is the angle λ .

For most people, the pupillary axis is temporal to the line of sight in object space. Artal (2014) obtained horizontal and vertical components of $+3.9 \pm 2.2^\circ$ and $+0.2 \pm 1.7^\circ$, respectively, with positive signs indicating temporal and superior displacements of the pupillary axis from the line of sight (Figure 4.6).

The angle λ is important for diagnosis of eccentric fixation and heterotropia. In testing for the presence of eccentric fixation, angle λ is determined monocularly (with the other eye occluded). A large angle indicates the likely presence of eccentric fixation. The line of sight as we have defined it is not being used, because the patient has rotated the eye to align a retinal point eccentric to the fovea with the fixation point. Angle λ is estimated binocularly (with both eyes open) to test for direction and amount of heterotropia in the *Hirschberg test*. In the presence of heterotropia, a large angle λ is observed because one eye rotates so that its fovea is not being used to align the fixation target. Either the fovea is being suppressed or another retinal point

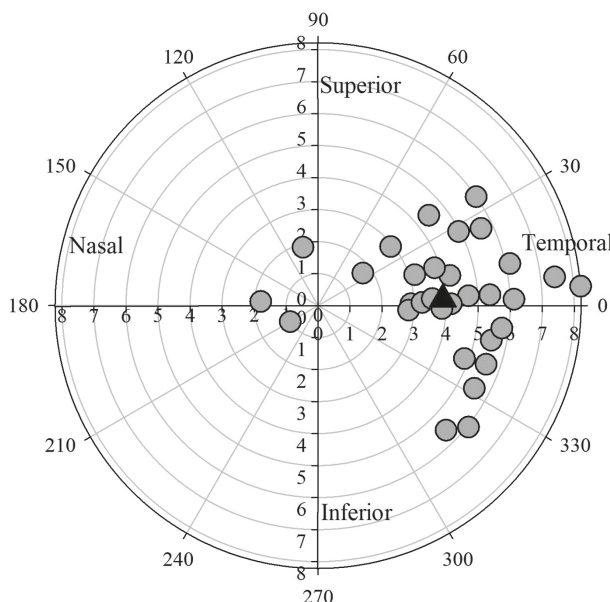


FIGURE 4.6 Angle λ in a group of normal adults. The black triangle shows the mean angle ($\approx 4^\circ$ temporal). Based on Figure 6 of Artal (2014), with data kindly provided by Pablo Artal and with permission from The Optical Society.

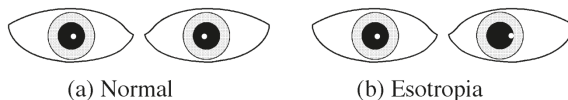


FIGURE 4.7 The Hirschberg test for measuring the angle of heterotropia. (a) Appearance of corneal reflexes for no heterotropia. (b) Appearance of reflexes for left esotropia (left eye turned in).

is being used for fixation (anomalous correspondence), or both are occurring. Again, we are not strictly measuring angle λ because of the change in reference axis away from the line of sight.

The usual application of these tests involves the clinician shining a penlight at the patient's eye or eyes. The penlight is just in front of the clinician's face, and the patient is instructed to look at it. The clinician observes the position of the corneal reflection (or reflex) in the pupil (Figure 4.7). Usually, the reflex is about half a millimeter nasal to the center of the pupil (Figure 4.7a). Each millimeter change in reflex position away from this corresponds to approximately 22 prism diopters (13°) of eye rotation (Grosvenor 2007). Care must be taken in the monocular test, as some patients may have normal fixation but unusual angles. Results from the two eyes should be compared. Similarly, in the Hirschberg test it is important to compare the difference in reflex positions between the two eyes.

4.4.3 PUPILLARY AXIS AND THE VISUAL AXIS: ANGLE K

In practical terms, this is the same as angle λ . It is shown in Figure 4.1.

4.4.4 VISUAL AXIS AND ACHROMATIC AXIS: ANGLE PSI (Ψ)

Thibos et al. (1990) estimated this angle from the equation

$$\sin(\Psi) = d/\mathbf{E}\mathbf{N} \quad (4.1)$$

where d is the distance between the visual axis and line of sight at the entrance pupil and **EN** is the estimate of the distance between the entrance pupil and the nodal point (Figure 4.2). Based on either the Gullstrand number 1 or number 2 eyes, the distance **EN** is 4.0 mm. An approximate, but sufficiently accurate, method for determining d is given in section 4.3.2. Using five subjects, Thibos and co-workers determined a range of angles from -1.2° to $+5.3^\circ$, with a mean of $+2.1^\circ$ (positive angles indicate the visual axis is inclined nasally to the achromatic axis in object space).

4.4.5 FIXATION AXIS AND OPTICAL AXIS: ANGLE GAMMA (γ)

Figure 4.8 shows the relationship between angles γ and α . In this figure, y is the distance between the optical axis and the fixation target **T**. **N** is the front nodal point, **C** is

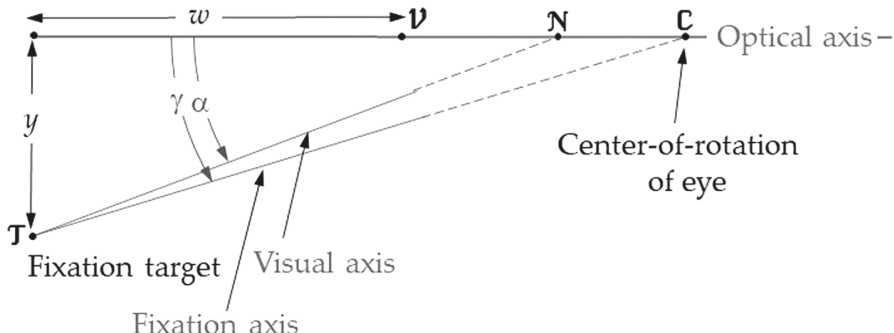


FIGURE 4.8 Determination of the angle γ .

the center-of-rotation of the eye, and w is the distance from the projection of \mathbf{T} , onto the optical axis, to the cornea at \mathbf{V} . We have the equations

$$\tan(\alpha) = y/(w + \mathbf{VN}) \quad (4.2)$$

and

$$\tan(\gamma) = y/(w + \mathbf{VC}) \quad (4.3)$$

which, combined, give

$$\tan(\gamma) = \tan(\alpha)(w + \mathbf{VN})/(w + \mathbf{VC}) \quad (4.4)$$

Angle γ is within 1 per cent of angle α for object distances greater than 50 cm.

SUMMARY OF MAIN SYMBOLS

C	center-of-rotation of the eye
C_c	center of curvature of the anterior corneal surface
\mathbf{E}, \mathbf{E}'	centers of entrance and exit pupils
\mathbf{N}, \mathbf{N}'	front and back nodal points
\mathbf{T}	fixation target
\mathbf{T}'	conjugate of \mathbf{T} on the retina, i.e., the fovea
\mathbf{S}, \mathbf{S}'	source of light and its image, used to find the pupillary axis
\mathbf{V}	intersection of the optical axis with the cornea
d	distance between visual axis and line of sight at the entrance pupil
α	angle between visual axis and optical axis
γ	angle between fixation axis and optical axis
κ	angle between pupillary axis and visual axis
λ	angle between pupillary axis and line of sight
ψ	angle between visual axis and achromatic axis

REFERENCES

- Applegate, R. A., L. N. Thibos, M. D. Twa, and E. J. Sarver. 2009. "Importance of fixation, pupil center, and reference axis in ocular wavefront sensing, videokeratography, and retinal image quality." *J Cataract Refract Surg* 35 (1):139–52. doi: 10.1016/j.jcrs.2008.09.014.
- Artal, P. 2014. "Optics of the eye and its impact on vision: a tutorial." *Advances in Optics and Photonics* 6:340–67. doi: 10.1364/AOP.6.000340.
- Cline, D., H. W. Hofstetter, and J. R. Griffin. 1997. *Dictionary of Visual Science*. Boston: Butterworth-Heinemann.
- Enright, J. T. 1980. "Ocular translation and cyclotorsion due to changes in fixation distance." *Vision Res* 20 (7):596–601. doi: 10.1364/josa.63.000205.
- Grosvenor, T. P. 2007. "Chapter 7. The preliminary examination." In *Primary Care Optometry*, 112–36. St Louis, Missouri, USA: Butterworth-Heinemann.
- Ivanoff, A. 1953. *Les aberrations de l'œil. Leur rôle dans l'accommodation*. Paris: Éditions de la Revue d'Optique Théorique et Instrumentale. Masson and Cie.
- Le Grand, Y., and S. G. El Hage. 1980. In *Physiological Optics. Translation and update of Le Grand, Y. (1968). La dioptrique de l'œil et sa correction*, vol. 1 of *Optique physiologique*, 65–7. Springer-Verlag.
- Maloney, R. K. 1990. "Corneal topography and optical zone location in photorefractive keratectomy." *Refract Corneal Surg* 6 (5):363–71.
- Mandell, R. B. 1994. "Apparent pupil displacement in videokeratography." *CLAO J* 20 (2):123–7.
- Mandell, R. B. 1995. "Locating the corneal sighting center from videokeratography." *J Refract Surg* 11 (4):253–9. doi: 10.3928/1081-597X-19950701-09.
- Mandell, R. B., C. S. Chiang, and S. A. Klein. 1995. "Location of the major corneal reference points." *Optom Vis Sci* 72 (11):776–84. doi: 10.1097/00006324-199511000-00002.
- Mandell, R. B., and R. St Helen. 1969. "Position and curvature of the corneal apex." *Am J Optom Arch Am Acad Optom* 46:25–9. doi: 10.1097/00006324-196901000-00005.
- Mandell, R. B., and D. Horner. 1995. "Alignment of videokeratographs." In *Corneal Topography: The State of the Art*, 17–23. New Jersey: SLACK Incorporated.
- Martin, F. E. 1942. "The importance and measurement of angle alpha." *Br J Physiol Opt* 3 (1):27–45.
- Millodot, M. 2009. In *Dictionary of Optometry*. Oxford: Butterworth-Heinemann.
- Rabbatts, R. B. 2007. "Chapter 12. Schematic eyes." In *Bennett and Rabbatts' Clinical Visual Optics*, 4th ed., 221–43. Butterworth-Heinemann.
- Simonet, P., and M. C. W. Campbell. 1990. "The optical transverse chromatic aberration on the fovea of the human eye." *Vision Res* 30 (2):187–206. doi: 10.1016/0042-6989(90)90035-j.
- Thibos, L.N., A. Bradley, D. L. Still, X. Zhang, and P. A. Howarth. 1990. "Theory and measurement of ocular chromatic aberration." *Vision Res* 30 (1):33–49. doi: 10.1016/0042-6989(90)90126-6.
- Tscherning, M. 1900. *Physiologic Optics*. Translated by C. Weiland. 1st edn ed. Philadelphia: The Keystone.

5 Paraxial Schematic Eyes

5.1 INTRODUCTION

We can construct model eyes using population mean values for relevant ocular parameters. This can be done at different levels of sophistication. If we assume that the refractive surfaces are spherical and centered on a common optical axis, and that the refractive indices are constant within each medium, this gives a simple family of models referred to as *paraxial* schematic eyes.

Paraxial schematic eyes are accurate only within the paraxial region. They do not accurately predict aberrations and retinal image formation for large pupils or for angles at more than a few degrees from the optical axis. The paraxial region is defined in geometrical optics as the region in which the replacement of sines of angles by the angles leads to no appreciable error. If we limit the errors to less than 0.01 per cent, this limits object field angles to less than 2° and the entrance pupil diameter to less than 0.5 mm.

Paraxial schematic eyes serve as a framework for examining a range of optical properties. The location of the paraxial image plane or calculation of the paraxial image height has many useful applications. Information can be obtained from schematic eyes concerning magnification, retinal illumination, surface reflections, such as the Purkinje images, entrance and exit pupils, and effects of refractive errors. A study of cardinal points of the systems can also have practical applications, such as the observation that the second nodal point moves little on accommodation and therefore that angular resolution is expected to change little with accommodation. Further applications to retinal image formation are discussed in Chapters 6 and 9.

For accurate determinations of quantities such as large retinal image sizes and image quality due to aberrations, we need more realistic models than the paraxial schematic eyes. These are referred to as *finite* or *wide-angle* schematic eyes. These include one or more of the following features: non-spherical refractive surfaces, a lack of surface alignment along a common axis, and a lens gradient refractive index.

Historically, paraxial schematic eyes have had uniform refractive indices, and it might be considered that schematic eyes with gradient indices must be finite eyes because the gradient index influences aberrations. However, replacing a uniform refractive index by a gradient index affects the paths of paraxial rays and hence paraxial properties, and thus gradient indices may be included in paraxial model eyes.

This chapter considers paraxial schematic eyes only. A discussion of finite model eyes is given in Chapter 16, following a review of the monochromatic aberrations of real eyes in Chapter 15.

5.2 DEVELOPMENT OF PARAXIAL SCHEMATIC EYES

The historical development of the understanding of the optical system of the human eye has been described in detail by Polyak (1957). The lens was believed to be the receptive element of the eye for 13 centuries following the work of Galen in 200 AD. Leonardo DaVinci (c. 1500 AD) proposed that the lens is only one element of the refractive system, which forms a real image on the retina. In 1604, Kepler realized that the image is inverted; this was verified by Scheiner 15 years later. The first clear, accurate description of the eye's optical system was given by Descartes in 1637 in his *La Dioptrique*, which also included the first publication of what has become known as Snell's law of refraction.

The first physical model of the eye was probably that of Christian Huygens (1629–95). Smith (1738) described Huygens's eye as consisting of two hemispheres representing the cornea and retina, respectively, with the retinal hemisphere having a radius of curvature three times that of the corneal hemisphere. The two hemispheres were filled with water and a diaphragm was placed between them.

Young (1801) discussed the optics of the eye and presented data, some of which are close to present day values. He gave the anterior corneal radius of curvature as 7.9 mm, and the anterior and posterior lenticular radii of curvature as 7.6 mm and 5.6 mm, respectively. The anterior chamber depth was given as 3.0 mm. His refractive index for the aqueous and vitreous media was 1.333 (water), and that for the lens was 1.436.

According to Le Grand and El Hage (1980), Moser in 1844 was the first to construct a schematic eye, but this was hyperopic because it had a very low value for the refractive index of the lens. The first "accurate" schematic eye has been attributed to Listing. In 1851, he described a three refracting surfaces schematic eye with a single surface cornea and a homogeneous lens, with an aperture stop 0.5 mm in front of the lens. Helmholtz (1909) modified Listing's schematic eye by changing the positions of the lenticular surfaces. He also gave this model in a form accommodated to 130.1 mm in front of the corneal vertex. He described also a much simpler schematic eye designed by Listing. This contains only one refracting surface (the cornea) and is referred to as a *reduced eye*.

Tscherning (1900) published a four refracting surfaces schematic eye containing a posterior corneal surface, which he claimed to be the first to measure.

Gullstrand (1909a, b) used a comprehensive analysis of ocular data to construct a six refracting surfaces schematic eye that used a four surfaces lens with the lenticular complexity aimed at accounting for refractive index variation within the lens. This schematic eye is referred to as Gullstrand's number 1 (exact) eye. Gullstrand presented this eye at two levels of accommodation. Gullstrand also presented a simplified version referred to as Gullstrand's number 2 (simplified) eye, also at two levels of accommodation. This simplified eye contains three refracting surfaces, with only one corneal surface and a zero lens thickness.

Emsley (1952) presented a modified version of Gullstrand's simplified eye. Emsley gave the lens the thickness that it has in Gullstrand's exact eye, and changed the aqueous, vitreous, and lens refractive indices. This modified eye is sometimes called the Gullstrand–Emsley eye. Emsley also presented a reduced schematic eye.

As well as the Gullstrand exact eye, the Gullstrand–Emsley eye and Emsley's reduced eye, another popular schematic eye is Le Grand's 1945 four refracting surfaces eye, which is referred to as Le Grand's full theoretical eye (Le Grand and El Hage 1980). Le Grand presented also a simplified three refracting surfaces model with a single corneal surface and a lens of zero thickness. The lack of lens thickness limits the usefulness of this model.

Bennett and Rabbets (1989) presented a modification of the Gullstrand–Emsley eye, which they justified on the grounds that the data used to construct the earlier eye was from a restricted number of eyes and that the mean power is closer to 60 D than previously thought. They used the data from the study of Sorsby et al. (1957), which was based upon 341 eyes (mostly pairs of left and right eyes) with mean equivalent power of 60.1 ± 2.2 D.

Other schematic eyes have been proposed from time to time. For example, Swaine (1921) gave details of several eyes referred to as Matthiessen B, D, and G eyes, and Laurance I and II eyes.

Blaker (1980) described an adaptive schematic eye. It is a modified Gullstrand number 1 paraxial schematic eye, in which the lens has been reduced to two surfaces but is given a gradient refractive index. The lens gradient index, lens surface curvatures, lens thickness, and the anterior chamber depth vary as linear functions of accommodation. Blaker (1991) revised his model to include aging effects, with the lens curvatures, lens thickness, and anterior chamber depth altering in the unaccommodated state as a function of age. Other adaptive schematic eyes have been developed for accommodation (Navarro et al. 1985; Rabbets 1998), refractive errors (Atchison 2006), and aging (Smith et al. 1992; Rabbets 1998; Goncharov and Dainty 2007; Atchison 2009).

Some of the above-mentioned eyes are discussed in greater detail later in this chapter, and constructional details of some eyes are given in Appendix 3.

For a more extensive treatment of the history of schematic eyes, see Atchison and Thibos (2016).

5.3 GAUSSIAN PROPERTIES AND CARDINAL POINTS

One of the main applications of paraxial schematic eyes is predicting the Gaussian properties of real eyes. Of these, probably the most important are the equivalent power F , positions of the six cardinal points (\mathbf{F} , \mathbf{F}' , \mathbf{P} , \mathbf{P}' , \mathbf{N} , and \mathbf{N}') and the positions and magnifications of the pupils. We can use the paraxial optics theory described in Appendix 1 to determine these properties. The Gaussian properties are given for specific schematic eyes in Appendix 3, and Table 5.1 shows a limited amount of data.

5.3.1 EQUIVALENT POWER AND CARDINAL POINTS

The cardinal points are defined in section 1.4. Figure 1.3 shows nominal positions of these in the emmetropic relaxed eye.

There are useful equations connecting the cardinal points, including

$$F = -n/\mathbf{PF} = n'/\mathbf{P}'\mathbf{F}' \quad (5.1)$$

TABLE 5.1
Summary of Gaussian Data

General	Length					
Relaxed Eyes	F	VE	VN	E'F' = E'R'	N'F' = N'R'	\bar{m}
Gullstrand number 1	24.385					
Le Grand (full theoretical)	24.197					
Le Grand (simplified)	24.192					
Gullstrand–Emsley	23.896					
Bennett and Rabbetts (simplified)	24.086					
Emsley (reduced)	22.222					
Gullstrand number 1	58.636	3.047	7.078	20.720	17.054	0.8231
Le Grand (full theoretical)	59.940	3.038	7.200	20.515	16.683	0.8132
Gullstrand–Emsley	60.483	3.052	7.062	20.209	16.534	0.8181
Bennett and Rabbetts (simplified)	60.000	3.048	7.111	20.387	16.667	0.8175
Emsley (reduced)	60.000	0.0	50/9	22.222	16.667	0.7500
Accommodated Eyes	F	Accom.	VE	VN	E'R'	N'R'
Gullstrand number 1	70.576	10.870	2.668	6.533	21.173	17.539
Le Grand (full theoretical)	67.677	7.053	2.660	7.156	20.942	17.041
Gullstrand–Emsley	69.721	8.599	2.674	6.562	20.647	16.987
Bennett and Rabbetts (10 D)	71.120	10.192	2.680	6.598	21.140	17.135

Note: Distances are in millimeters and powers are in diopters.

$$PN = P'N' = (n' - n)/F \quad (5.2)$$

$$FN = P'F' \quad (5.3a)$$

$$N'F' = FP \quad (5.3b)$$

where n and n' are the refractive indices of object space (air) and image space (the vitreous), respectively.

Since the mean equivalent power of the eye is close to 60 D and the values of n and n' are 1.0 and 1.336, respectively, we can calculate expected approximate mean values of the above quantities. These are

$$F = 60 \text{ D}$$

$$\mathbf{FP} = \mathbf{N'F'} = 16.67 \text{ mm}$$

$$\mathbf{P'F'} = \mathbf{FN} = 22.27 \text{ mm}$$

$$\mathbf{PN} = \mathbf{P'N'} = 5.6 \text{ mm.}$$

5.3.2 THE APERTURE STOP AND ENTRANCE AND EXIT PUPILS

After the equivalent power and positions of the cardinal points, probably the next most important Gaussian properties of an eye are the aperture stop and pupil formation. The aperture stop of an eye is the opening in the iris. Reduced eyes do not have an iris, but we can place an aperture stop in the plane of the cornea or at some other suitable position. The image of the aperture stop formed in object space by the cornea is called the entrance pupil. The image of the aperture formed in image space by the lens is called the exit pupil. These concepts are discussed fully in Chapter 3.

5.3.3 POSITION AND MAGNIFICATION OF ENTRANCE PUPIL

For schematic eyes with a single surface cornea, the calculations are simple. In this case, we can use the lens equation A1.21 given in Appendix 1:

$$n'/l' - n/l = F \quad (5.4)$$

Figure 5.1 shows the path of a paraxial ray that can be used to locate the image of the aperture stop. l is the anterior chamber depth, l' is the apparent anterior chamber depth, n is the refractive index of the aqueous, and n' is the refractive index of air ($= 1.0$). Solving for l' in equation (5.4) gives

$$l' = n'l/(n + lF) \quad (5.5)$$

and the pupil magnification \bar{M}_{EA} , defined as the ratio of the entrance pupil diameter to that of the stop, is given by

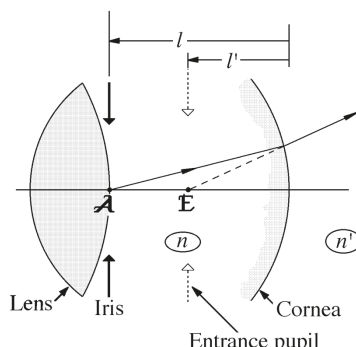


FIGURE 5.1 The formation of the entrance pupil of the eye and its relationship to the iris in a schematic eye with a single surface cornea.

$$\bar{M}_{EA} = nl' / n'l \quad (5.6)$$

The standard sign convention was used in the development of these equations, with distances to the left of the refracting surface being negative and distances to the right being positive. Distances l and l' are negative, although usually we express the final answers in a positive form.

Example 5.1: Calculate the position and magnification of the entrance pupil of the Gullstrand–Emsley simplified relaxed eye.

Solution: From the Gullstrand–Emsley schematic eye data given in Appendix 3, we have

$$n = 4/3$$

$$n' = 1$$

$$l = -3.6 \text{ mm and}$$

$$F = 42.735 \text{ D}$$

Substituting these data into equations (5.5) and (5.6) gives

$$l' = \frac{1 \times (-3.6)}{\frac{4}{3} + (-3.6) \times 42.735 / 100} = (-)3.052 \text{ mm}$$

$$\bar{M}_{EA} = \frac{\frac{4}{3} \times (-3.052)}{1 \times (-3.6)} = 1.1304$$

Thus, the entrance pupil is 3.05 mm inside the eye, compared with 3.6 mm for the aperture stop. The entrance pupil is also 13 per cent larger than the actual pupil. The pupil position is shown in Table 5.1, along with the values for other schematic eyes.

5.3.4 PARAXIAL MARGINAL RAY AND PARAXIAL PUPIL RAY

These are the two special paraxial rays that were introduced and defined in section 3.2.3. As can be seen from Figure 3.3, the paths of these rays depend upon the position of the object/image conjugates, field size and the position of the aperture stop and its diameter. The details of these rays (angles and heights) are given in Appendix 3 for each schematic eye with an entrance pupil diameter of 8 mm and a field-of-view of angular radius 5°. Here, as a rule, we denote the marginal ray angles and heights by the respective symbols u and h and the paraxial pupil ray angles and heights by the respective symbols \bar{u} and \bar{h} .

5.3.5 PARAXIAL PUPIL RAY ANGLE RATIO \bar{m}

A quantity that is useful in the calculation of retinal image sizes is the ratio \bar{m} of the paraxial pupil ray angles

$$\bar{m} = \bar{u}' / \bar{u} \quad (5.7)$$

The angles \bar{u} and \bar{u}' are the angles of the paraxial pupil ray in object and image space respectively, as shown in Figure 5.2. They are related by the paraxial refraction equation A1.4 in Appendix 1:

$$n' \bar{u}' - n \bar{u} = -\bar{h}F \quad (5.8)$$

where F is the equivalent power of the eye and \bar{h} is the ray height at the principal planes. Equation (5.8) can be rearranged to give

$$\bar{m} = [n - (\bar{h} / \bar{u})F] / n' \quad (5.9)$$

where n has a value of 1 for air.

From Figure 5.2, within the paraxial approximation we have

$$h / \bar{u} = -\mathbf{PE} = -\bar{l} \quad (5.10)$$

Substituting the right-hand side for the left-hand side of this equation in equation (5.9), we have

$$\bar{m} = [n + \bar{l}F] / n' \quad (5.11)$$

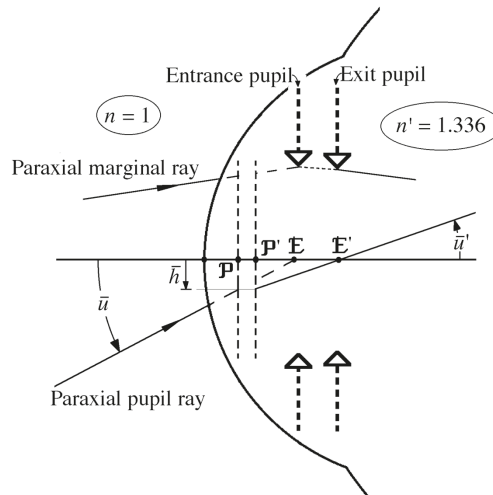


FIGURE 5.2 The paraxial pupil ray and its use in calculation of \bar{m} .

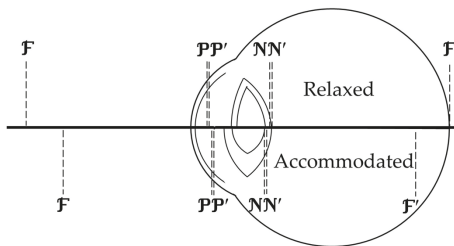


FIGURE 5.3 The Gullstrand number 1 exact schematic eye.

which shows that the value of \bar{m} depends upon the refractive index of the vitreous, which is fixed, the distance of the entrance pupil \bar{l} from the front principal point and the equivalent power F . The values of both \bar{l} and F depend upon accommodation level. For a typical schematic eye, $\bar{l} \approx 1.5$ mm, $F \approx 60$ D, and $n' = 1.336$, giving $\bar{m} \approx 0.82$. Precise values for schematic eyes and at different levels of accommodation are given in Table 5.1. Equation (5.11) can be manipulated into the following form

$$\bar{m} = \frac{n}{n' \bar{M}_{E'E}} \quad (5.11a)$$

where $\bar{M}_{E'E}$ is the pupil magnification = exit pupil diameter/entrance pupil diameter.

5.3.6 EFFECT OF ACCOMMODATION

The cardinal point positions of the relaxed (zero accommodation) and accommodated versions of schematic eyes can be compared in Figures 5.3, 5.4, and 5.5. Upon accommodation, the principal points move away from the cornea, the nodal points move towards the cornea, and the focal points move towards the cornea.

5.4 “EXACT” SCHEMATIC EYES

In the “exact” schematic eyes, an attempt is made to model the optical structure of real eyes as closely as possible while using spherical surfaces. The minimum requirement of an “exact” eye is that it must have at least four refracting surfaces, two for the cornea and two for the lens.

5.4.1 GULLSTRAND NUMBER 1 (EXACT) EYE

This schematic eye considers the variation of refractive index within the lens (Figure 5.3). It is presented in both relaxed and accommodated versions. It consists of six refracting surfaces: two for the cornea and four for the lens. The lens contains a central nucleus (core) of high refractive index surrounded by a cortex of lower refractive index. The lens can be regarded as a combination of three lenses. The anterior and posterior lenses are thinner in the center than at the edge, and may be considered

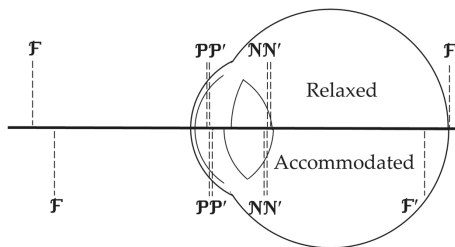


FIGURE 5.4 The Le Grand full theoretical schematic eye.

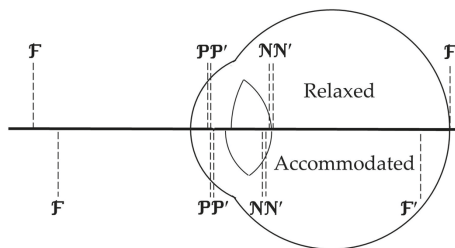


FIGURE 5.5 The Gullstrand–Emsley schematic eye.

erroneously to have negative power. However, they have positive power because the refractive index of the core lens is higher than that of the cortex.

Gullstrand placed the retina 0.39 mm short of the back focal point F' because he thought that the positive spherical aberration would lead to the best image plane being slightly in front of the paraxial image. However, this is arbitrary, because the level of spherical aberration depends upon pupil diameter, with primary wave spherical aberration depending upon the fourth power of this diameter. Furthermore, the role of spherical aberration may have been exaggerated since real eyes have much less spherical aberration than schematic eyes. We adopt the usual practice of increasing the length of the eye so that the retina coincides with F' .

5.4.2 LE GRAND FULL THEORETICAL EYE

The lens of this eye has a constant refractive index, and thus has only two refracting surfaces (Figure 5.4). The eye is presented in both relaxed and accommodated forms.

5.5 SIMPLIFIED SCHEMATIC EYES

For paraxial calculations, the Gullstrand number 1 eye and the Le Grand full theoretical eye are more complex than is required for many optical calculations, such as measurement of retinal image sizes. Simpler eyes are now considered to be adequate. This is because errors that arise in using these simpler models are usually less than the expected variations between real eyes.

In simplified schematic eyes, the cornea is reduced to a single refracting surface and the lens has two surfaces with a uniform refractive index.

5.5.1 GULLSTRAND NUMBER 2 (SIMPLIFIED) EYE AS MODIFIED BY EMSLEY – THE GULLSTRAND–EMSLEY EYE

Emsley (1952) modified Gullstrand's number 2 eye to simplify computation (Figure 5.5). The modifications included altering the aqueous and vitreous refractive indices to 4/3, altering the lens refractive index to 1.416 for both relaxed and accommodated eyes, thickening the lens and changing the accommodated lens surface radii of curvature to ± 5.00 mm.

5.5.2 LE GRAND SIMPLIFIED EYE

Most of the parameters of this eye are different from those of Le Grand's full schematic eye. The lens is given a zero thickness. The eye has both relaxed and accommodated forms.

5.5.3 BENNETT AND RABBETTS' SIMPLIFIED EYE

Bennett and Rabbetts (1988, 1989) modified the relaxed version of the Gullstrand–Emsley eye (see Appendix 3). Rabbetts (1998) included forms for accommodation levels of 2.5, 5.0, 7.5, and 10 D. He introduced an “elderly” version of the eye, which has a lower lens refractive index than do the other forms and has a refractive error of 1 D hyperopia (see Chapter 7).

5.6 REDUCED SCHEMATIC EYES

Further simplifications are possible which may give models accurate enough for some calculations estimates of retinal image size.

Reduced eyes contain only one refracting surface, which is the cornea. In the exact and simplified eyes already presented, the two principal points and the two nodal points are each separated by values in the range 0.12–0.37 mm. In reduced eyes, the use of a single refracting surface means that its vertex must be at the principal points $P(P')$ and its center of curvature must be at the nodal points $N(N')$. To keep powers similar to those of the more sophisticated eyes, reduced eyes must have shorter axial lengths. As the cornea has absorbed the power of the lens, the radii of curvature are much smaller than real values. Since reduced eyes do not have a lens, they cannot be used to examine the optical consequences of accommodation.

5.6.1 EMSLEY'S REDUCED EYE (1952)

This eye has a corneal radius of curvature of 50/9 mm, a refractive index of 4/3, and a power of 60 D (Figure 5.6).

5.6.2 BENNETT AND RABBETTS (1989)

This eye has a corneal radius of curvature of 5.6 mm, a refractive index of 1.336 and a power of 60 D.

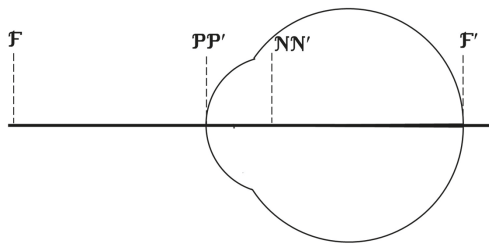


FIGURE 5.6 The Emsley reduced schematic eye.

5.7 VARIABLE ACCOMMODATING EYES

While most of the above models have fixed accommodated forms, none has a variable level of accommodation. As mentioned previously, Blaker (1980) presented a variable accommodating paraxial eye, which was later modified to consider aging effects (Blaker 1991). Navarro et al. (1985) presented a finite accommodating schematic eye, which is suitable for easy paraxial calculations because the refractive index of the lens remains uniform, but we leave discussion of this eye until Chapter 16.

We present here a variable version of Gullstrand's number 1 schematic eye. The eye was specified at two levels of accommodation (zero and 10.870 D), but we can modify this eye to have a variable accommodation by assuming that the following individual parameters of this eye vary with accommodation:

- anterior chamber depth
- lens thicknesses
- lens cortex anterior curvature
- lens core anterior curvature
- lens core posterior curvature
- lens cortex anterior curvature

To simplify the model, we relate the accommodation level A , measured at the corneal vertex, to a parameter x , where

$$x = 1.052A - 0.00531A^2 + 0.000048564A^3 \quad (5.12)$$

and the variable parameters of the eye are related to x by the equations

$$\text{anterior chamber depth} = 3.1 - (3.1 - 2.7)x/A_0$$

$$\text{anterior cortical thickness} = 0.546 - (0.546 - 0.6725)x/A_0$$

$$\text{core thickness} = 2.419 - (2.419 - 2.655)x/A_0$$

$$\text{posterior cortical thickness} = 0.635 - (0.635 - 0.6725)x/A_0$$

$$\text{anterior lens curvature} = 1/10 - (1/10 - 1/5.333)x/A_0$$

$$\text{lens core anterior curvature} = 1/7.911 - (1/7.911 - 1/2.655)x/A_0$$

$$\text{lens core posterior curvature} = -1/5.760 - [-1/5.760 - 1/(-2.655)]x/A_0$$

$$\text{lens posterior curvature} = -1/6 - [-1/6 - 1/(-5.333)]x/A_0$$

where the distance unit is millimeters and A_0 is the level of the Gullstrand accommodated eye in diopters, i.e., 10.870 D.

5.7.1 EQUIVALENT POWER AND POSITIONS OF CARDINAL POINTS

We can now assemble a schematic eye at any level of accommodation and, by paraxial ray tracing, calculate various quantities. For example,

$$F_a(A) = 58.636 + 11.940A/A_0 \text{ D}$$

$$N'R'(A) = 17.054 - 0.485A/A_0 \text{ mm} = 1/F_R - 0.485A/A_0 \text{ mm}$$

where F_R is the equivalent power of the relaxed eye. The values of \bar{m} and the distances of the entrance pupil and the front nodal point from the anterior corneal vertex (**VE** and **VN**) are plotted as a function of accommodation in Figure 5.7.

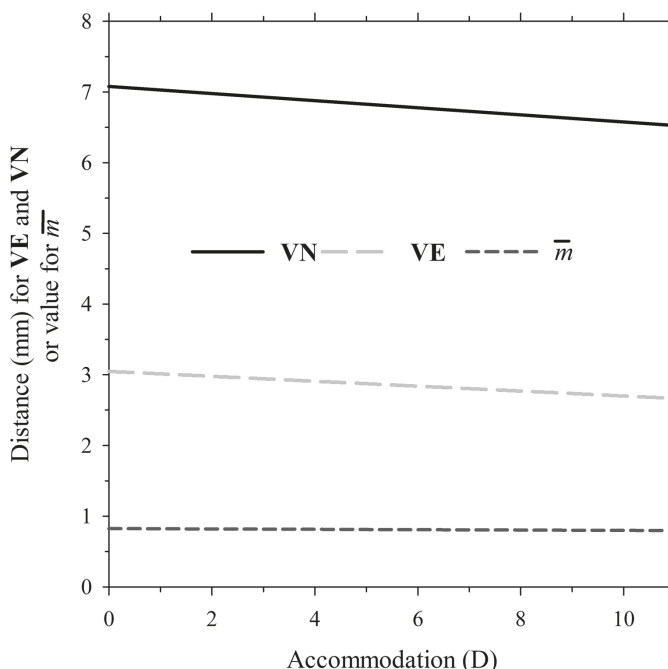


FIGURE 5.7 The effect of accommodation on \bar{m} , **VE**, and **VN** of a variable accommodating version of the Gullstrand number 1 schematic eye.

SUMMARY OF MAIN SYMBOLS

A	accommodation level at corneal vertex in diopters
d	surface separations
F	equivalent power of the eye
\bar{m}	ratio \bar{u}'/\bar{u} of paraxial pupil ray angles – this value is a constant for any particular eye at any particular level of accommodation
\bar{M}_{EA}	pupil magnification, the ratio of entrance pupil diameter to stop diameter
$\bar{M}_{E'E}$	pupil magnification, the ratio of exit pupil diameter to entrance pupil diameter
n, n'	refractive indices (usually of object and image space, respectively)
r	radius of curvature
\bar{u}	paraxial pupil ray angle in object space (air)
\bar{u}'	paraxial pupil ray angle in image space (in the vitreous)
E, E'	positions of entrance and exit pupils
F, F'	front and back focal points
N, N'	front and back nodal points
O, O'	general object and corresponding image point
P, P'	front and back principal points
R', R	axial retinal point and corresponding conjugate in object space

REFERENCES

- Atchison, D. A. 2006. "Optical models for human myopic eyes." *Vision Res* 46 (14):2236–50. doi: 10.1016/j.visres.2006.01.004.
- Atchison, D. A. 2009. "Age-related paraxial schematic emmetropic eyes." *Ophthal. Physiol. Opt.* 29 (1):58–64. doi: 10.1111/j.1475-1313.2008.00598.x.
- Atchison, D. A., and L. N. Thibos. 2016. "Optical models of the human eye." *Clin Exp Optom* 99 (2):99–106. doi: 10.1111/cxo.12352.
- Bennett, A. G., and R. B. Rabbets. 1988. "Schematic eyes—time for a change?" *Optician* 196 (5169):14–5.
- Bennett, A. G., and R. B. Rabbets. 1989. "Letter to the editor. Proposals for new reduced and schematic eyes." *Ophthalmic Physiol Opt* 9 (2):228–30. doi: 10.1111/j.1475-1313.1989.tb00851.x.
- Blaker, J. W. 1980. "Toward an adaptive model of the human eye." *J Opt Soc Am* 70 (2):220–3. doi: 10.1364/josa.70.000220.
- Blaker, J. W. 1991. "A comprehensive optical model of the aging, accommodating adult eye." In *Technical Digest on Ophthalmic and Visual Optics*, 28–31. Optical Society of America.
- Emsley, H. H. 1952. *Visual Optics*. 5th ed. Vol. 1: Butterworths.
- Goncharov, A. V., and C. Dainty. 2007. "Wide-field schematic eye models with gradient-index lens." *J Opt Soc Am A* 24 (8):2157–74. doi: 10.1364/ao.46.006076.
- Gullstrand, A. 1909a. "Appendix II: Procedure of rays in the eye. Imagery - laws of the first order." In *Helmholtz's Handbuch der Physiologischen Optik*, vol. 1, 3rd edn (English translation edited by J. P. Southall, Optical Society of America, 1924), 301–358.
- Gullstrand, A. 1909b. "Appendix IV: The mechanism of accommodation." In *Helmholtz's Handbuch der Physiologischen Optik*, vol. 1, 3rd edn (English translation edited by J. P. Southall, Optical Society of America, 1924), 382–415.

- Helmholtz, H. von. 1909. *Handbuch der Physiologischen Optik*, vol. 1, 3rd ed (English translation edited by J. P. Southall, Optical Society of America, 1924), 95–96, 152.
- Le Grand, Y., and S. G. El Hage. 1980. *Physiological Optics. Translation and update of Le Grand, Y. (1968). La dioptrique de l'œil et sa correction*, vol. 1 of *Optique physiologique*, 65–7. Springer-Verlag.
- Navarro, R., J. Santamaría, and J. Bescós. 1985. "Accommodation-dependent model of the human eye." *J Opt Soc Am* 2 (8):1273–81. doi: 10.1364/josaa.2.001273.
- Polyak, S. L. 1957. "Chapter I. History of the investigation of the structure and development of the optical sciences." In *The Vertebrate Visual System*, 9–72. Chicago, Illinois: The University of Chicago Press.
- Rabbetts, R. B. 1998. "Chapter 12. Schematic eyes." In *Bennett and Rabbetts' Clinical Visual Optics*, 3rd ed, 221–43. Butterworth-Heinemann.
- Smith, G., D. A. Atchison, and B. K. Pierscionek. 1992. "Modeling the power of the aging human eye." *J Opt Soc Am A* 9 (12):2111–7. doi: 10.1364/JOSAA.9.002111.
- Smith, R. A. 1738. *A Compleat System of Opticks*: Cornelius Crownfield.
- Sorsby, A., B. Benjamin, J. B. Davey, M. Sheridan, and J. M. Tanner. 1957. Emmetropia and its Aberrations. edited by Medical Research Council Special Report Series number 293. HMSO.
- Swaine, W. 1921. "Geometrical and ophthalmic optics - VII: paraxial schematic and reduced eyes." *Optician Sci Instr Maker* 62:133–6.
- Tscherning, M. 1900. *Physiologic Optics*. Translated by C. Weiland. 1st edn ed. Philadelphia: The Keystone.
- Young, T. 1801. "The Bakerian Lecture. On the mechanism of the eye." *Phil Trans R Soc Lond* 91 (1):23–88 + plates.

Section II

Image Formation and Refraction



Taylor & Francis
Taylor & Francis Group
<http://taylorandfrancis.com>

6 Image Formation

The Focused Paraxial Image

6.1 INTRODUCTION

In this chapter, we consider in-focus image formation assuming the image-forming rays behave as paraxial rays. The treatment is applicable to small angles only as it ignores aberrations and the curvature of the retina.

The ability to predict retinal image size, given an object of known size, has many applications. For example, if the two eyes of a person with different levels of refractive error are corrected with ophthalmic lenses, the retinal image sizes of the two eyes may be different and this difference can lead to binocular vision problems (see section 10.4). A second example is the calculation of risks from radiation damage where, in the case of thermal damage (due to wavelengths longer than approximately 500 nm), the retinal image size affects the level of risk.

6.2 THE GENERAL CASE

Figure 6.1 shows an axial point at \mathbf{O} and an off-axis point at \mathbf{Q} on the perpendicular plane through \mathbf{O} . Beams of rays from each of these points pass into the eye through the cornea, iris, and lens, and are imaged at \mathbf{O}' and \mathbf{Q}' respectively on the retina at \mathbf{R}' . All the rays in each beam are concurrent (i.e., focus) at the appropriate points \mathbf{O}' or \mathbf{Q}' . According to the rules of paraxial optics, the point \mathbf{Q}' lies on the plane passing through \mathbf{O}' and perpendicular to the optical axis.

The points \mathbf{O} and \mathbf{Q} are at the edges of an object, and \mathbf{O}' and \mathbf{Q}' are at the edges of the corresponding image. By noting the relative orientations of the object and image, we can deduce that the image is inverted. Extending this to two dimensions, we would note that the image is inverted in both horizontal and vertical directions (equivalent to a 180° rotation). The inversion is opposite to our perception because a further inversion process occurs in the brain.

We cannot readily consider the image formation in a particular eye unless we know its construction details; in particular, surface radii of curvature, surface separations, and refractive indices. These data are not easy to determine. In many situations, all we need are reasonable estimates from a schematic eye. We can determine the image formation in the schematic eye either by tracing suitable paraxial rays or by using known positions of the cardinal points and pupils. Since these are readily available for the standard schematic eyes, we take this approach in the following discussion. The reader should be familiar with the properties of cardinal points and pupils as discussed in earlier chapters.

Figure 6.2 shows a beam of rays from an off-axis point \mathbf{Q} being imaged to a point \mathbf{Q}' on the retina of an eye with some level of accommodation. We have drawn two

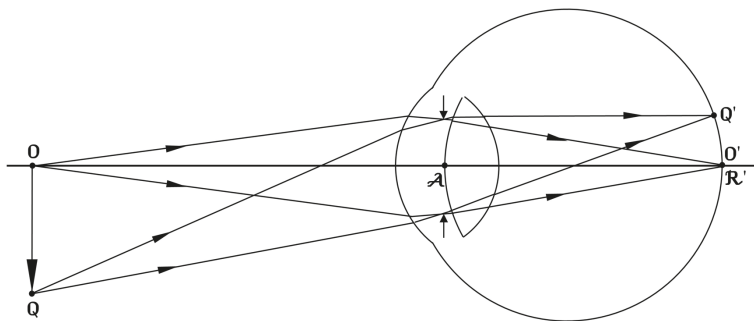


FIGURE 6.1 The general case of formation of the retinal image and image-forming beams.

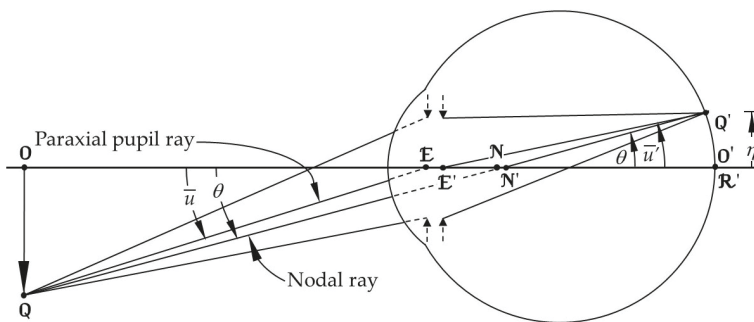


FIGURE 6.2 The formation of an off-axis image point, the paraxial pupil ray, and the nodal ray for an arbitrary level of accommodation.

special paraxial rays, the *nodal ray* and the *paraxial pupil ray* (also *paraxial chief ray*). The nodal ray was introduced in Chapter 1. It is the ray from an off-axis object which is inclined at the same angle to the optical axis in both object and image spaces. In object space it is directed towards the first nodal point \mathbf{N} , and in image space it is directed from the second nodal point \mathbf{N}' . The paraxial pupil ray was introduced in Chapter 3. It is the ray that, in object space, is directed towards the center of the entrance pupil \mathbf{E} , and in image space is directed from the central of the exit pupil \mathbf{E}' . Both rays can help us to determine the size of the retinal image.

We can use the nodal ray to find the size of the retinal image, using Figure 6.2. Within the limits of paraxial optics, the retinal image size η' is given by the equation

$$\eta' = \theta \mathbf{N}' \mathbf{R}' \quad (6.1)$$

where

$$\theta = -\eta / \mathbf{O} \mathbf{N} \quad (6.2)$$

The minus sign is present because, in the figure, η is negative and θ and the distance $\mathbf{O} \mathbf{N}$ are positive. Combining these two equations gives

$$\eta' = -\eta \mathbf{N}' \mathbf{R}' / \mathbf{O} \mathbf{N} \quad (6.3)$$

To find the image size in a particular case, we need the object size η and distances $\mathbf{O} \mathbf{N}$ and $\mathbf{N}' \mathbf{R}'$. The positions of the nodal points depend upon the level of accommodation of the eye, and estimates are available only for a limited range of accommodation for schematic eyes. If the positions are known, the use of the nodal rays to find the size or magnification of the image is straightforward.

An alternative method uses the paraxial pupil ray. One advantage of this ray is that it always (by definition) lies in the center of the image-forming beam. From Figure 6.2, it follows that

$$\eta' = \bar{u}' \mathbf{E}' \mathbf{R}' \quad (6.4)$$

We can express the image size η' in terms of the angle \bar{u} the pupil ray is inclined to the axis in object space. The angles \bar{u}' and \bar{u} are connected by the paraxial pupil ray ratio given by equation (5.7), i.e.,

$$\bar{u}' / \bar{u} = \text{a constant} = \bar{m} \quad (6.5)$$

with the value of the constant \bar{m} depending upon the schematic eye used and level of accommodation. Combining these equations gives

$$\eta' = \bar{u} \bar{m} \mathbf{E}' \mathbf{R}' \quad (6.6)$$

where

$$\bar{u} = -\eta / \mathbf{O} \mathbf{E} \quad (6.7)$$

Therefore, we can finally express the image size η' by the equation

$$\eta' = -\eta \bar{m} \mathbf{E}' \mathbf{R}' / \mathbf{O} \mathbf{E} \quad (6.8)$$

Values for \bar{m} and the positions of the cardinal points for different schematic eyes are given in Table 5.1.

Example 6.1: Calculate the retinal image size of a letter of height 1 mm, seen at the near point of the accommodated Gullstrand number 1 schematic eye.

Solution: From Table 5.1 we have the following data:

$$\mathbf{N}' \mathbf{R}' = 17.539 \text{ mm}$$

$$\mathbf{O} \mathbf{N} = 1000 / 10.870 + \mathbf{V} \mathbf{N} = 91.996 + 6.533 = 98.529 \text{ mm}$$

$$\bar{m} = 0.7959$$

$$\mathbf{E}' \mathbf{R}' = 21.173 \text{ mm}$$

$$\mathbf{O} \mathbf{E} = 91.996 + \mathbf{V} \mathbf{E} = 91.996 + 2.668 = 94.664 \text{ mm.}$$

Choosing a value of $\eta' = -1$ mm, which is negative because the object is below the optical axis, and using equation (6.3) we have

$$\eta' = 1 \times 17.539/98.529 \text{ mm} = 0.1780 \text{ mm}$$

Alternatively, using equation (6.8) we have

$$\eta' = 1 \times 0.7959 \times 21.173/94.664 \text{ mm} = 0.1780 \text{ mm.}$$

Note that the two solutions should be, and are, the same.

6.2.1 RETINAL IMAGE SIZE AND PERCEIVED ANGULAR SIZE IN OBJECT SPACE

In analyzing visual images, we can specify the image size in two ways; one is the image size on the retina, and the other is a perceived angular size in object space. These two quantities are related. Let us consider the situation in Figure 6.2, where an eye is looking at an object at \mathbf{O} and this is imaged at \mathbf{O}' on the retina at \mathbf{R}' . The nodal points \mathbf{N} and \mathbf{N}' and the nodal ray are shown. The angle of inclination of this ray with the axis is the same in both object and image spaces. If the object subtends an angle θ at the front nodal point \mathbf{N} , then the retinal image subtends the same angle at the back nodal point \mathbf{N}' . For typical working distances, the distance to the object is large in comparison with the dimensions of the eye. Therefore, in determining the angular size of the object, we can take the reference point as the corneal vertex, the entrance pupil position, or the front nodal point. In summary, we can conclude that the angular size of the perceived image is that angle subtended by the retinal image at the back nodal point. This conclusion is useful in some discussions on image sizes.

6.3 EYE FOCUSED AT INFINITY

If the eye is focused at infinity, we can simplify the above equations. For an object at infinity (or very distant), its size can only be expressed as an angular measure, say θ . For the eye focused at infinity, the retinal point \mathbf{R}' coincides with the back focal point \mathbf{F}' and thus

$$\mathbf{N}'\mathbf{R}' = \mathbf{N}'\mathbf{F}' \tag{6.9}$$

Combining equations (5.1) and (5.3b) with $n = 1$ gives

$$\mathbf{N}'\mathbf{F}' = 1/F \tag{6.10}$$

where F is the equivalent power of the eye. Combining equations (6.1), (6.9), and (6.10) gives

$$\eta' = \theta/F \tag{6.11}$$

The values of F for different schematic eyes are given in Table 5.1.

Alternatively, we can use the pupil ray equation (6.8). Because the object is at infinity, its angular size is independent of the point from which this angle is measured. Therefore, we can write

$$\theta = -\eta/\text{OE} \quad (6.12)$$

Thus equation (6.8) reduces to

$$\eta' = \theta \bar{m} \mathbf{E}' \mathbf{F}' \quad (6.13)$$

We now use equations (6.11) and (6.13) in a numerical example.

Example 6.2: Calculate the retinal image size of the moon (angular diameter of 0.5°) using the Gullstrand number 1 relaxed schematic eye.

Solution: For the Gullstrand number 1 relaxed schematic eye, the relevant data are given in Table 5.1; in particular,

$$F = 58.636 \text{ D}$$

$$\mathbf{E}' \mathbf{F}' = 20.720 \text{ mm and}$$

$$\bar{m} = 0.8231$$

Substituting the relevant values and $\theta = 0.5^\circ = 0.00872665$ radians into equation (6.11) gives

$$\eta' = 0.00872665/58.636 \text{ m} = 0.1488 \text{ mm}$$

Substituting the relevant values into equation (6.13) gives

$$\eta' = 0.00872665 \times 0.8231 \times 20.720 = 0.1488 \text{ mm}$$

Note that these two solutions should be, and are, the same.

If we take an approximate value of the mean power of the eye of 60 D, then we can write equation (6.11) in the form

$$\eta' \approx 0.00485\theta \text{ mm} \quad (6.14)$$

where θ is in minutes of arc. This equation is a useful rule of thumb equation for working out expected retinal image sizes and indicates that 1 min. arc is approximately equivalent to 0.005 mm on the retina, and 1 mm on the retina is approximately equivalent to 200 min. arc.

6.4 BINOCULAR VISION

6.4.1 STEREOPSIS

The use of two eyes provides the potential for seeing depth in a scene. This perception of depth is called *stereoscopic vision* or *stereopsis*. The retinal images of that

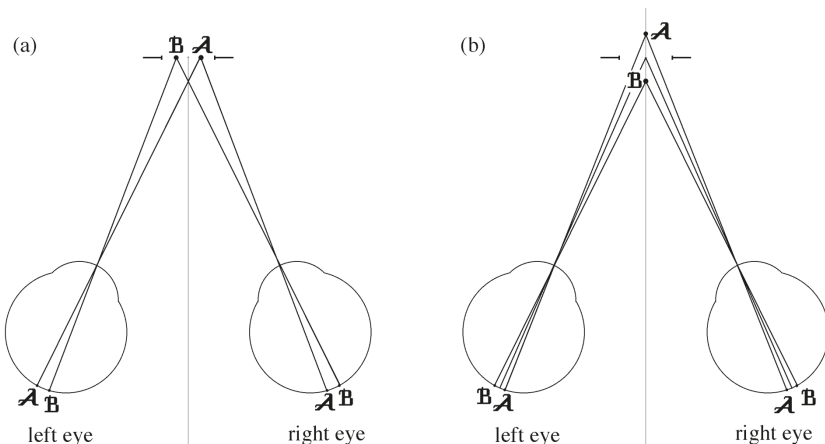


FIGURE 6.3 Binocular vision and the relative positions of the retinal images for two point objects. (a) Objects side by side. (b) One object behind the other.

world, while flat two-dimensional images, are slightly different. This is explained with the help of Figure 6.3. Figure 6.3a shows, from above, the two eyes of a person who is looking at two points **A** and **B** in a horizontal plane. From an observer's point of view, **A** is imaged to the left of **B** by both eyes, and no perception of depth occurs. Figure 6.3b shows the person looking at **A** and **B**, which are now in line but at different distances. From the observer's point of view, **A** is imaged to the right of **B** for the left eye, but **A** is imaged to the left of **B** for the right eye – i.e., the two retinal images of **A** are closer together than are the two retinal images of **B**. This difference in relative position of the retinal images of **A** and **B** leads to the perception of depth.

6.4.2 ANISEIKONIA

Aniseikonia is usually defined as a relative difference in size and/or shape of the two retinal images, e.g., Cline et al. (1997). However, this is a simplification, as it is the brain that ultimately “sees”, rather than the eyes. A person can have different retinal image sizes and not have any problems, so we would like to replace the word “retinal” by “cortical” in the above definition. Most clinically significant cases of aniseikonia result from correcting anisometropia, which is where the two eyes have different refractive errors. Anisometropia is discussed at greater length in Chapter 10.

The symptoms of aniseikonia are usually indistinguishable from those caused by other binocular vision problems and by uncorrected refractive errors. The classical symptom is a distortion of spatial perception when both eyes are being used, but this occurs in relatively few patients (Bannon and Triller 1944). Binocular vision must be well developed for aniseikonia to be a problem, and usually the clinician should consider other possible causes of symptoms before attempting to correct aniseikonia.

Clinical treatments of aniseikonia, in order of increasing complexity, include the following:

1. Altering the prescription to reduce the amount of aniseikonia, for example, reducing high cylindrical corrections, omitting low cylindrical corrections, and reducing the difference in spherical powers.
2. Prescribing contact lenses rather than spectacles, because the former have much smaller effects on retinal image size.
3. Prescribing a pair of spectacle lenses called *isogonal lenses*, which have similar magnifications to each other.
4. Prescribing a pair of aniseikonic correcting lenses called *iseikonic (size) lenses*, according to results of the *eikonometer*, an instrument which measures aniseikonia.

Further information on aniseikonia is found in texts such as Benjamin (2006) and Rabbetts (2007).

SUMMARY OF MAIN SYMBOLS

\bar{m}	ratio \bar{u}'/\bar{u} of the angles of inclination of the paraxial pupil ray with the axis in image and object space, respectively. This ratio is a constant for any particular schematic eye at a particular level of accommodation
η, η'	object and image sizes
θ	angular size of object. This angle is assumed to be small so it can be regarded as a paraxial angle
E, E'	positions of entrance and exit pupils
N, N'	positions of front and back nodal points
O, O'	general object point and corresponding image point
R', R	axial retinal point and corresponding conjugate in object space

REFERENCES

- Bannon, R. E., and T. Triller. 1944. "Aniseikonia - a clinical report covering a 10-year period." *Am J Optom Arch Am Acad Optom* 21 (2):171–82.
- Benjamin, W. J. 2006. *Borish's Clinical Refraction, Chapters 18, 19*. 2nd ed: W. B. Saunders.
- Cline, D., H. W. Hofstetter, and J. R. Griffin. 1997. *Dictionary of Visual Science*. Boston: Butterworth-Heinemann.
- Rabbetts, R. B. 2007. *Bennett and Rabbetts' Clinical Visual Optics, Chapters 6, 17 and 18*. 4th ed: Butterworth-Heinemann.



Taylor & Francis
Taylor & Francis Group
<http://taylorandfrancis.com>

7 Refractive Anomalies

7.1 INTRODUCTION

Ideally, when the eye fixates an object of interest, the image is focused sharply on the fovea. In paraxial optical terms, the object and fovea are conjugate. However, the object can only be focused sharply if it is within the accommodation range of the eye. If the accommodation range is inappropriate or too small, objects of interest cannot be focused sharply on the fovea. In these cases, the retinal image is out-of-focus or blurred, and visual functions such as visual acuity are reduced. The effects of these focus errors on the retinal image are discussed in Chapter 9 and in Chapter 18.

An appropriate range of accommodation includes all reasonable object distances of interest. This includes distant objects, effectively at infinity, down to objects as close as a few centimeters.

An eye with a far point of distinct vision at infinity is called an *emmetropic* eye. The emmetropic eye is regarded as the “normal” eye, if it has an appropriate range of accommodation. A refractive anomaly occurs if the far point is not at infinity. An eye whose far point is not at infinity is called an *ametropic* eye. The departure from emmetropia is often considered to be an error of refraction, and ametropias are also referred to as *refractive errors*. Emmetropia and ametropia may be regarded as opposites, but an alternative and more appropriate view is that emmetropia is part of the distribution of ametropias.

Another refractive anomaly occurs when the range of accommodation is reduced so that near objects of interest cannot be seen clearly. This is called *presbyopia* and is usually age-related.

Defocused retinal images may occur because the far point is closer to the eye than infinity or is beyond infinity. By beyond infinity, we mean that it is located behind a person’s head. Defocused retinal images occur also when the refractive power of the eye varies with meridian. This is commonly due to one or more refractive surfaces in the eye being toroidal, transversely displaced, or tilted. There are now two far points, one corresponding to each of the two principal meridians. These errors are referred to as *astigmatic* or *cylindrical* refractive errors, in contrast to *spherical* refractive errors, which are present when the refractive error is the same in all meridians.

Refractive errors may occur because of surgery. The most obvious example of this is *aphakia*. In the aphakic eye, the lens has been removed, usually because of cataracts (semi-transparent and translucent formations in the lens) which absorb, reflect, and scatter the image-forming light.

Whatever the cause of the refractive error, it can be corrected with appropriate *ophthalmic* lenses, which include spectacle, contact, and intra-ocular lenses. When an ametropic eye is corrected by an ophthalmic lens, the equivalent power of the eye – ophthalmic lens system is different from that of the uncorrected ametropic eye

and hence there are shifts in the cardinal points. This causes changes in retinal image sizes, and hence produces magnification effects, which are discussed in Chapter 10.

Most ophthalmic practitioners do not make a distinction between the terms refractive error, *refraction*, and *refractive correction*, a practice that we shall follow in this book, although from a purist perspective the second and the third should be opposites of the first. Hence, we may refer to a myopic eye having a -2 D refractive error whereas, strictly speaking, we should say either that the myope is corrected by a -2 D lens or requires a -2 D refraction.

Some confusion can arise when different degrees of myopia are compared, as high myopia is associated with more negative corrections than low myopia. Using the International Myopia Institute definitions of low and high myopia, the former has values $\leq -0.50\text{ D}$ and $> -6.00\text{ D}$ and the latter has values $\leq -6.00\text{ D}$ (Flitcroft et al. 2019).

Refractive errors are often considered only for foveal viewing. Nevertheless, the peripheral retina also experiences refractive errors that often differ dramatically from the foveal refractive error. Peripheral refraction is considered separately in Chapters 15 and 16.

7.2 SPHERICAL REFRACTIVE ANOMALIES

Spherical refractive anomalies are categorized according to the position of the far point (the spherical refractive errors) or of the near point (presbyopia).

7.2.1 SPHERICAL REFRACTIVE ERRORS

7.2.1.1 Emmetropia (Normal Sight)

We wrote in the previous section that the far point of the emmetropic eye is at infinity. This is a paraxial concept and is upset a little in practice by the natural monochromatic and chromatic aberrations of the eye. In addition, this is not a practical definition in terms of deciding whether an eye is emmetropic because there are few eyes for which the definition is exactly met. Instead, an emmetropic range may be considered to include refractive errors smaller than the smallest measurement interval, which is usually 0.25 D – i.e., the far point is greater than 4 m away. For research purposes, a wider range may be used; for example, -0.25 D to $+0.75\text{ D}$.

7.2.1.2 Myopia (Short Sight)

If the far point is at a finite distance in front of the eye, as shown in Figure 7.1a, the eye is *myopic* or is said to suffer from *myopia*. This means also that the back focal point F' of the eye is in front of the retina as shown in the figure. An object at infinity is focused in the back focal plane at F' and is out-of-focus on the retina. This situation can be regarded as due to a mismatch between the length of the eye and its power – the eye can be regarded as being too powerful for its length, or as being too long for its power. The eye is not able to reduce its power to focus distant objects on the retina.

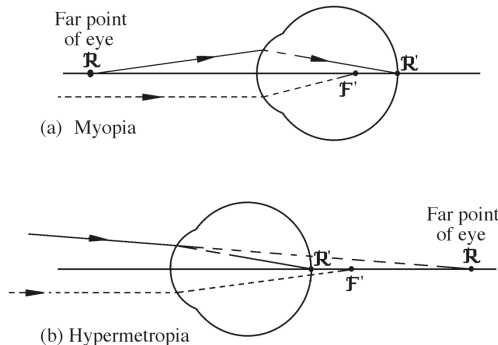


FIGURE 7.1 The (a) myopic and (b) hyperopic eyes and their far points.

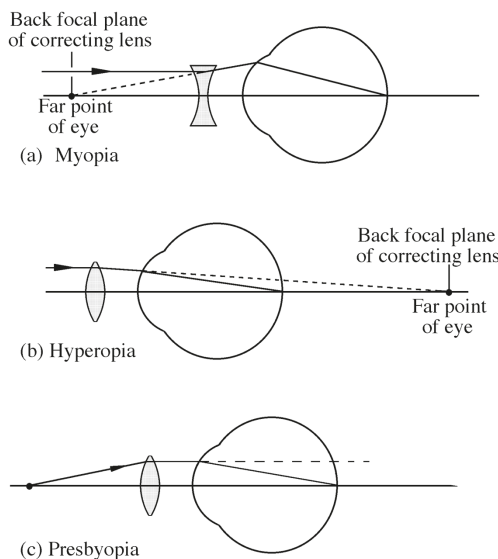


FIGURE 7.2 The spectacle correction of (a) myopia, (b) hyperopia, and (c) presbyopia.

This eye can focus clearly on distant objects with relaxed accommodation by viewing through a negative powered ophthalmic lens of appropriate power, as shown in Figure 7.2a. This lens forms a distant and virtual image at its back focal plane, which coincides with the far point of the eye.

Myopia can be classified in many ways (Flitcroft et al. 2019). These include presumed etiology (e.g., axial, corneal), age at onset (e.g., juvenile), progression pattern (e.g., stable, progressing), magnitude (e.g., low, moderate, high), and structural complications (e.g., degenerative).

Uncorrected myopes tend to complain of blurred distance vision, which is more noticeable at night. Depending on the degree of myopia, they may notice that close objects appear blurred as well.

7.2.1.3 Hyperopia (Hypermetropia)

The terms hyperopia and hypermetropia refer to the same optical state of the eye. Usage depends on the country and has changed over time (Charman et al. 2015). We will use the former term throughout this book. In a hyperopic eye, the far point lies behind the eye and the back focal point F' is behind the retina, as shown in Figure 7.1b. An object at infinity is focused in this back focal plane but, once again, the retinal image is defocused. This eye can bring the image into sharp focus if there is sufficient amplitude of accommodation. Once again, this situation can be regarded as due to a mismatch between the length of the eye and its power - the eye can be regarded as being too weak for its length, or as being too short for its power.

This eye can focus clearly on distant objects with relaxed accommodation by viewing through a positive powered lens of appropriate power, as shown in Figure 7.2b. This lens forms a distant and real image on its back focal plane, which coincides with the far point of the eye.

Many young hyperopes have difficulty relaxing their accommodation completely. A residual tonus in the ciliary muscle produces a degree of latent hyperopia, which cannot be determined by subjective refraction without the use of cycloplegic drugs. *Total hyperopia* can then be regarded as consisting of *manifest* and *latent* components. The part of the manifest hyperopia that can be overcome by accommodative effort is referred to as *facultative* hyperopia. Any deficit remaining is referred to as *absolute* hyperopia. With increase in age and loss in amplitude of accommodation, the manifest component of total hyperopia increases at the expense of the latent component. Similarly, the absolute component of manifest hyperopia increases at the expense of the facultative component.

Uncorrected hyperopes tend to complain of sore eyes and headaches associated with close visual tasks. These symptoms may be referred to as asthenopia or visual discomfort. Symptoms are experienced because they must make more accommodative effort than emmetropes and myopes to view close objects. In addition, the degree of convergence they use is inappropriate for the level of accommodation demanded. They may also complain of blurred near and distance vision, depending on the level of hyperopia and the amplitude of accommodation. The blurring is greater at near than at distance, because of the greater accommodative demand at near.

As hyperopes may not be able to see distant objects clearly, the term *long sight* to describe hyperopia should be discouraged.

7.2.2 PRESBYOPIA

Presbyopia is the difficulty people have in performing close tasks because of the age-related decrease in amplitude of accommodation. The nearest point of distinct vision, or simply the *near point*, recedes from the eye so that it is close to or beyond the position at which a near task is performed. The onset of presbyopia is related to the degree of refractive errors, with uncorrected hyperopes likely to have problems earlier in life than uncorrected myopes. Depending on the degree of myopia and the near task, the latter may not suffer from presbyopia. To compensate for presbyopia, ophthalmic lenses are required that are more positively powered or less negatively

powered than the distance correction (Figure 7.2c). We discuss presbyopia further in section 20.8.

Not surprisingly, uncorrected presbyopes usually complain of difficulty performing close tasks.

7.3 ASTIGMATIC REFRACTIVE ERRORS

In many eyes, the refractive error is dependent upon meridian. This type of refractive error is known as an *astigmatic* refractive error (Figure 7.3). This is usually due to one or more refracting surfaces, most commonly the anterior cornea, having a toroidal shape. However, it may also be due to one or more surfaces being transversely displaced or tilted.

There are different types of astigmatism, which may be related to the associated spherical refractive errors as follows:

1. *Myopic astigmatism*: the eye is too powerful for its length in one principal meridian for *simple myopic astigmatism*, and in both principal meridians for *compound myopic astigmatism* as shown in Figure 7.3.
2. *Hyperopic astigmatism*: the eye is too weak for its length in one principal meridian for *simple hyperopic astigmatism*, and in both principal meridians for *compound hyperopic astigmatism*.
3. *Mixed astigmatism*: the eye is too powerful for its length in one principal meridian (*myopic astigmatism*), and too weak for its length in the other principal meridian (*hyperopic astigmatism*).

Astigmatism may also be classified by the axis direction. This was discussed for the cornea (section 2.2). *With-the-rule* astigmatism of the eye occurs when the eye has greater positive power along the vertical than along the horizontal meridian. The eye requires a correcting lens whose negative cylinder axis is within $\pm 30^\circ$ of the horizontal meridian. Conversely, *against-the-rule* astigmatism occurs when the eye has greater positive power along the horizontal than along the vertical meridian. The eye requires a correcting lens whose negative cylinder axis is within $\pm 30^\circ$ of the

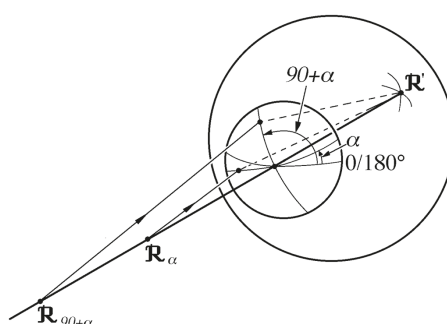


FIGURE 7.3 An astigmatic eye. The far points R_α and $R_{90+\alpha}$ are imaged at the retinal point R' .

vertical meridian. Astigmatism with axes more than 30° from the horizontal and vertical meridians is referred to as *oblique astigmatism*.

One further classification of astigmatism is related to its *regularity*. Astigmatism is usually *regular*, which means that the principal (maximum and minimum power) meridians are perpendicular to each other, and the astigmatism is correctable with conventional spherocylindrical lenses (see section 7.6). *Irregular astigmatism* occurs when the principal meridians are not perpendicular to each other; it is accompanied by considerable higher-order aberrations (Chapter 15). It may occur in corneal conditions such as keratoconus.

Astigmatism is corrected with an astigmatic ophthalmic lens. Usually this has one spherical surface and one toroidal surface, the latter generally being the back surface. Astigmatic lenses are often referred to as *spherocylindrical* lenses for the historical reason that at one stage most astigmatic lenses had one spherical surface and one cylindrical surface. If rigid contact lenses are used for correction, a tear fluid film forms between the lens and anterior corneal surface that neutralizes most of the astigmatism if this is caused, as is often the case, by toricity of the anterior cornea (see section 10.8).

To make analysis of large-scale population data relatively easy when astigmatism is present, an *equivalent sphere* (also called the *mean sphere*) is used, which is the average refractive error of the two principal meridians.

People with astigmatism have blurred vision at all distances, although this may be worse at distance or near depending on the type of astigmatism. They may complain of sore eyes and headaches associated with demanding visual tasks.

7.4 ANISOMETROPIA

This is the condition in which the refractive errors of the two eyes of a person are different. Sub-classifications include *anisomyopia*, in which both eyes are myopic, *anisohyperopia*, in which both eyes are hyperopic, and *anisometropia*, in which one eye is myopic and one eye is hyperopic.

Spectacle lens correction of anisometropia may result in different retinal image sizes and different prismatic effects when looking through lens peripheries. These effects may compromise comfortable binocular vision. Some discussion of these side effects is provided in Chapter 10.

7.5 DISTRIBUTION OF REFRACTIVE ERRORS AND OCULAR COMPONENTS

7.5.1 DISTRIBUTION

The distribution of refractive errors is strongly age-dependent, particular in childhood (Wolffsohn, Flitcroft et al. 2019). Neonates have a normal distribution of refractive errors. From birth to maturity (about 11–13 years) the ocular components are growing, and the relationships among them must be coordinated so that emmetropia can be achieved and maintained. The term *emmetropization* is given to this fine-tuning of refraction, and it is thought that the process is visually regulated. Several

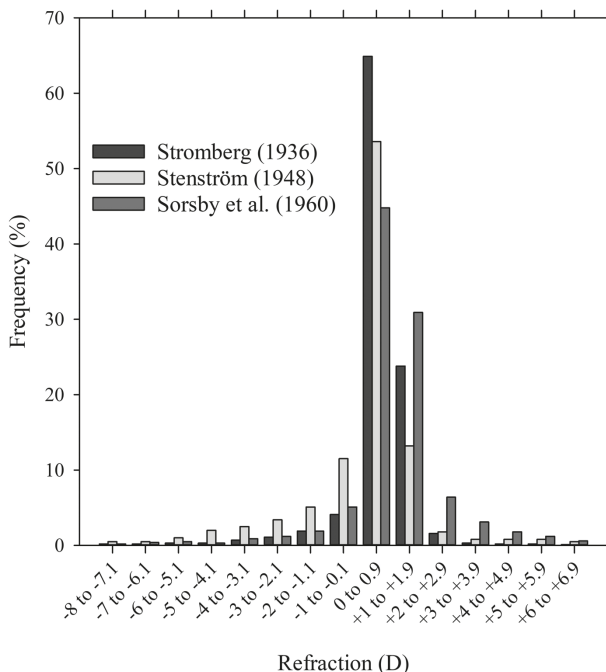


FIGURE 7.4 Population distribution of refractive errors. Data of Strömberg (1936), Stenström (1948), and Sorsby et al. (1960). Strömberg's data were obtained from Stenström (1948).

studies have been carried out on the distribution of ametropia in the adult population. Results of early studies of Strömberg (1936), Stenström (1948), and Sorsby et al. (1960) are shown in Figure 7.4. The mean refractive error is usually slightly hyperopic, and the distributions are *leptokurtotic*. This means that in comparison to the normal distribution there are more individuals at the center and tails of the distribution and fewer in the shoulders of the distribution. In addition, the distributions have more pronounced tails in the myopic direction than in the hyperopic direction (negative skewness). The distribution of refractive errors is fairly stable between the ages of 20 and 40 years, after which the distribution becomes less leptokurtic (Grosvenor 1991).

An idea that can be applied to the increasing prevalence of myopia in recent decades is that the general population can be divided into two subgroups: those with an optimal and those with a non-optimal refractive development (Flitcroft 2013; Rozema et al. 2014). Each group forms a Gaussian distribution of refraction, and together these distributions form a bi-Gaussian distribution giving the leptokurtic appearance. In countries with considerable myopia, a “dysregulated” component of the bi-Gaussian distribution becomes dominant in urban areas while an “emmetropized” component of the bi-Gaussian distribution is dominant in rural areas (Figure 7.5).

Stenström (1948) found that the corneal power and radii of curvature were normally distributed, as were the depth of the anterior chamber, lens power, and total

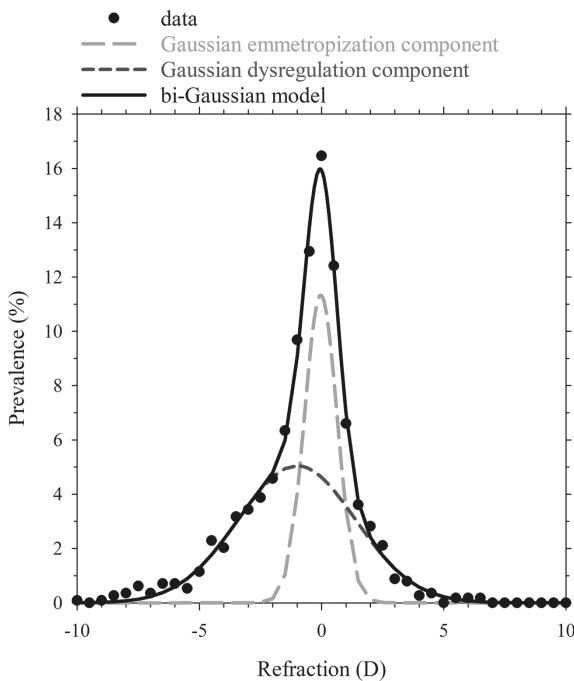


FIGURE 7.5 Distribution of refraction, showing original data, a Gaussian emmetropization component, a Gaussian dysregulation component, and a bi-Gaussian model (the combination of emmetropization and dysregulation components). Data are from Figures 4 and 5B of Rozema et al. (2014), kindly provided by Jos Rozema.

power. He found that axial length was not normally distributed, but Sorsby et al. (1957) claimed that all components including axial length were normally distributed. Rozema et al. (2014) found anterior corneal curvature, anterior chamber depth, and lens power to have normal distributions, but axial length had a leptokurtic distribution that could be modeled as a bi-Gaussian distribution.

Sorsby et al. (1960) carried out an extensive study of the relationship between the various ocular parameters, and came to the following conclusions:

1. In emmetropic eyes, wide ranges of corneal power (39–48 D), lens power (16–24 D), and axial length (22–26 mm) occur.
2. In ametropic eyes with refractive errors in the range -4 D to +6 D, the same range of parameters occurred as for emmetropic eyes, but these were combined inadequately. Such eyes were referred to as *correlation ametropic eyes*.
3. For refractive errors outside the range of -4 D to +6 D, the axial length seemed to be the cause of the ametropia. It was too long for myopia and too short for hyperopia. These eyes were referred to as *component ametropic eyes*.

Component ametropia can be divided into *axial* and *refractive* categories by comparing dimensions of an eye with the range of values in the emmetropic population

or with those of a schematic eye such as Gullstrand's number 1 eye. The refractive error is regarded as refractive in nature if the axial length is within an "emmetropic" range, but the power of the eye or one of its components is outside the emmetropic range. The refractive error is regarded as axial in nature if the axial length is outside the emmetropic range, but the power of the eye and its components are within emmetropic ranges. Aphakia, in which the lens has been removed, is an obvious case of refractive ametropia. Most astigmatisms, including those caused by corneal conditions, such as keratoconus, can be regarded as cases of refractive ametropia.

The ocular component most highly correlated with refractive error is axial length. Longitudinal studies indicate that axial elongation is the mechanism for much of myopia and its progression (Kaphle et al. 2020). This suggests that most of the myopes that Sorsby et al. (1962) classified as correlation ametropes were actually axial component myopes.

If an eye is deprived of suitable visual stimuli early in its development, it grows to be unusually long, leading to myopia. This growth is controlled by local factors within the retina (Troilo et al. 2019). This indicates that a change in axial length is the main cause of emmetropization, with the eye increasing its length until emmetropia is achieved.

Myopia receives a little more attention in this section. It is a public health issue because its prevalence has been increasing in recent decades, particularly in some Asian countries, and higher levels of myopia are associated with ocular pathologies such as glaucoma, maculopathy, retinal detachment, and cataract. One report estimated that about half the world's population will be affected by myopia by the year 2050 (Holden et al. 2016). A number of reports have been prepared by the International Myopia Institute on myopia, including definitions (Flitcroft et al. 2019), animal studies (Troilo et al. 2019), genetic inheritance (Tedja et al. 2019), treatment interventions and instrumentation (Wildsoet et al. 2019; Wolffsohn, Kollbaum et al. 2019), risk factors (Gifford et al. 2019), and accommodation and binocular vision (Logan et al. 2021).

The definition of myopia adopted by the International Myopia Institute is like the description given in section 7.2.1 and brings in the component issue: "A refractive error in which rays of light entering the eye parallel to the optic axis are brought to a focus in front of the retina when ocular accommodation is relaxed. This results from the eyeball being too long from front to back, but can be caused by an overly curved cornea and/or lens with increased power. It is also called nearsightedness" (Flitcroft et al. 2019).

Increased vitreous length is the main biometric change in most cases of myopia so that myopic eyes are larger globally than emmetropic eyes (Atchison et al. 2004; Singh et al. 2006; Pope et al. 2017). Other biometric changes including increased corneal curvature (Goss et al. 1997; Atchison 2006), and choroid thinning (Read et al. 2019; Kaphle et al. 2023). In the unaccommodated state, myopes have a thinner anterior component of the ciliary muscle (Pucker et al. 2013; Kuchem et al. 2013; Wagner et al. 2019) and a thicker posterior component of the ciliary muscle (Oliveira et al. 2005; Bailey et al. 2008; Schultz et al. 2009; Richdale et al. 2012; Lewis et al. 2012; Buckhurst et al. 2013; Pucker et al. 2013; Kuchem et al. 2013; Wagner et al. 2018) than emmetropes. From time to time, it has been suggested that myopes have

bigger pupils than emmetropes, but this does not seem to be the case (Jones 1990; Winn et al. 1994; Subbaram and Bullimore 2002).

7.5.2 ASTIGMATISM

As with spherical refractive errors (or spherical equivalents), the distribution of astigmatism changes with age. Considerable astigmatism, usually against-the-rule, exists in the first year of life and decreases quickly during early infancy. Most clinically measurable astigmatism is thereafter with-the-rule up to the age of 40 years, after which the prevalence of against-the-rule astigmatism increases (Lyle 1991; Leung et al. 2012). Read et al. (2014) gave a review of age-related prevalence of the different orientations of astigmatism and the contributions of the intraocular components.

7.6 THE POWER OF THE CORRECTING LENS

This section explores the power of lenses required to correct a refractive error, starting with the thin lens case. While this approximation leads to some errors, it is satisfactory for examining trends. A thick lens treatment and its implications are supplied in a number of ophthalmic texts, e.g., Jalie (2021). The section applies to lenses placed in front of the eye; contact lenses are considered in section 10.8.

In ophthalmic practice, the power of the correcting lens is determined by subjective techniques (using trial case lenses or refractor heads), or by objective techniques such as retinoscopy (described briefly in Chapter 8) or autorefraction. In none of these cases is the far point found directly, but mathematical analysis of the required lens power is made easier by reference to the far point distance. Consider a hyperopic eye, as shown in Figure 7.6, in which the far point is a distance d behind the corneal vertex. The value of d must be given a sign. In our sign convention, d is positive if the far point is to the right of the corneal vertex and negative if it is to the left of the corneal vertex. Therefore, in the myopic eye d is negative, and in the hyperopic eye d is positive. If a lens is now placed a distance h in front of the corneal vertex, the power $F_s(h)$ of the correcting lens, also called the *spectacle refraction*, is a function of vertex distance h , and is given by the equation

$$F_s(h) = 1/f_s = 1/(h + d) \quad (7.1)$$

where the distance h is always regarded as positive. We can express equation (7.1) in the form

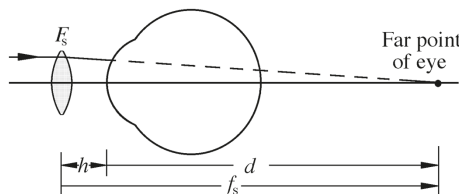


FIGURE 7.6 The power of the correcting lens (example of hyperopia).

$$F_s(h) = R_e / (1 + hR_e) \quad (7.2)$$

where

$$R_e = 1/d \quad (7.3)$$

is the refractive error (or refractive correction) of the eye at the corneal plane. This is also referred to as the *ocular refraction*.

Example 7.1: Calculate the spectacle lens power, if the far point is 45 cm in front of the eye (i.e., a myopic error) and the spectacle lens vertex distance is to be 15 mm.

Solution: Here we have $h = 15$ mm and $d = -45$ cm. Substituting these values in equation (7.1) gives

$$F_s(15 \text{ mm}) = -2.30 \text{ D}$$

The sensitivity of the power to changes in distance h can be investigated by differentiating equation (7.2) with respect to h . If we do this, we have

$$\frac{\delta F_s(h)}{\delta h} = -\frac{R_e^2}{(1+hR_e)^2} = -F_s^2(h) \quad (7.4)$$

It follows that a small change δh in h leads to a change δF_s in F_s , given by the approximate equation

$$\delta F_s \approx -F_s^2(h)\delta h \quad (7.5)$$

The above change in power δF_s is equivalent to a change in refractive error δR_e . Thus, we have

$$\delta R_e \approx -F_s^2(h)\delta h \quad (7.5a)$$

Example 7.2: Consider an eye requiring a +12 D spectacle lens placed at a vertex distance of $h = 12$ mm. If the lens is placed at 13 mm, estimate the induced refractive error.

Solution: In this problem, the change δh in h is $\delta h = +1$ mm, and substituting $F_s = +12$ D and $h = 12$ mm into equation (7.5a) gives the approximate induced refractive error

$$\delta R_e = -0.144 \text{ D}$$

In clinical practice it is common to determine the refractive error at one distance (say h_1) and prescribe for another (say h_2). A typical example is in the

prescription of contact lenses. Knowing $F(h_1)$, it can be shown using equation (7.1) that $F(h_2)$ is given by the equation

$$F(h_2) = \frac{F(h_1)}{(h_2 - h_1)F(h_1) + 1} \quad (7.6)$$

Example 7.3: Consider the +12 D lens in Example 7.2. If the eye is to be corrected with a contact lens, calculate the power of that lens.

Solution: In this problem, h_1 is 12 mm, h_2 is 0 mm, and $F_s = +12$ D. Substituting these values into equation (7.6) gives

$$F(0 \text{ mm}) = +14.0 \text{ D}$$

If the vertex distance of a spectacle lens is increased (e.g., change of frame), then the myopic eye needs more negative lens power, and the hyperopic eye needs less positive power. If changing from spectacle to contact lens correction, the myopic eye requires less negative power in its contact lens and the hyperopic eye requires greater positive power. The effects of typically encountered changes in vertex distances (i.e., $h_2 - h_1$) are small for correcting lenses in the range ± 4 D.

7.6.1 ASTIGMATIC CORRECTIVE POWERS

In the simplest mathematical model describing a spherocylindrical error in the eye, the power can be thought of as varying with azimuth angle θ in the pupil according to the equation

$$F(\theta) = F_{sp} + F_{cy} \sin^2(\theta - \alpha) \quad (7.7)$$

According to this equation, the correction is composed of a spherical component of power F_{sp} and a cylindrical component of power F_{cy} with the cylindrical axis along the direction α . The clinical representation of astigmatic corrections is often written as

$$F_{sp}/F_{cy} \times \alpha$$

noting that this is not an arithmetic expression requiring division and multiplication. The standard axis notation specifies the axis by the anticlockwise angle that it makes with the horizontal meridian. This is taken from the viewpoint of an observer looking at both lenses as worn in front of the two eyes of a patient. The axis varies between 0° and 180°. A horizontal axis can be either 0° or 180°, but is usually taken as the latter.

7.6.2 ALTERNATIVE SYSTEM OF SPECIFYING REFRACTIVE ERRORS AND CORRECTING LENS POWERS

A disadvantage of the standard notation of sphere, cylinder, and axis is that it is not amenable to basic arithmetic and cannot be used in statistical analyses. For example,

a simple average of two axes usually yields an incorrect answer because axis is a circular variable rather than a linear variable, and two cylinders may combine to yield a sphere with no cylindrical component. Various matrix and vector representations of spherocylindrical power have been developed that allow valid mathematical calculations (Long 1976; Keating 1981; Harris 2000; Thibos et al. 1997).

We start from the conventional spherocylinder notation $F_{\text{sp}}/F_{\text{cy}} \times \alpha$ included in equation (7.7) and shown in Figure 7.7. This can be represented as

$$F(\theta) = F_{\text{sp}} + F_{\text{cy}} \cos^2(\theta - \alpha + 90)$$

Using the trigonometric identity $\cos^2\gamma = [1 + \cos(2\gamma)]/2$, this becomes

$$\begin{aligned} F(\theta) &= F_{\text{sp}} + F_{\text{cy}} \{1 + \cos[2(\theta - \alpha + 90)]\}/2 \\ &= F_{\text{sp}} + F_{\text{cy}}/2 - (F_{\text{cy}}/2)\cos[2(\theta - \alpha)] \\ &= F_{\text{sp}} + F_{\text{cy}}/2 - (F_{\text{cy}}/2)[\cos(2\theta)\cos(2\alpha) + \sin(2\theta)\sin(2\alpha)] \quad (7.8) \end{aligned}$$

This can be represented by a constant term M , by a 180-degree component J_{180} , which is the coefficient of $\cos(2\theta)$, and by a 45-degree component J_{45} , which is the coefficient of $\sin(2\theta)$:

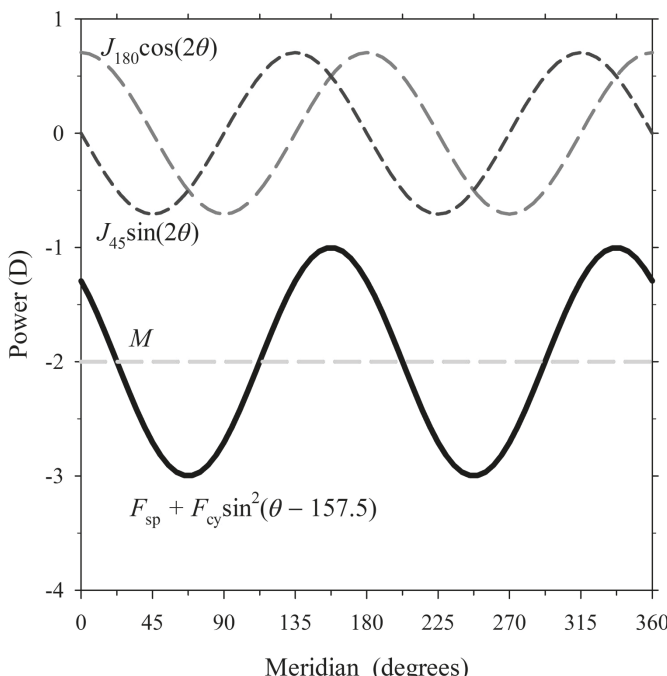


FIGURE 7.7 Representation of spherocylinder power varying with azimuth angle θ in the pupil. The spherocylinder power $-1.00/-2.00 \times 157.5$ is represented by $M = -2.0$ D, $J_{180} = +0.71$ D, and $J_{45} = -0.71$ D.

$$M = F_{\text{sp}} + F_{\text{cy}}/2 \quad (7.9)$$

$$J_{180} = -(F_{\text{cy}}/2)\cos(2\alpha) \quad (7.10)$$

$$J_{45} = -(F_{\text{cy}}/2)\sin(2\alpha) \quad (7.11)$$

Here M is an abbreviation of *mean sphere* and J_{180} and J_{45} are *Jackson crossed cylinders*. These three variables may also be treated as the members of a vector $[M J_{180} J_{45}]$ for plotting in three-dimensional dioptric space.

The reverse set of equations, using a negative power for the cylinder, is given by

$$F_{\text{cy}} = -2\sqrt{(J_{180}^2 + J_{45}^2)} \quad (7.12)$$

$$F_{\text{sp}} = M - F_{\text{cy}}/2 \quad (7.13)$$

$$\alpha = [\tan^{-1}(J_{45}/J_{180})]/2 \quad (7.14)$$

It is easiest to calculate α with a four-quadrant inverse tangent function. If this is not available, then the following steps should be followed. If J_{180} is 0, there will be an indeterminate result. In this case, if $J_{45} < 0$, $\alpha = 135^\circ$, and if $J_{45} \geq 0$, $\alpha = 45^\circ$. To keep α within the clinical conventional range of 0 – 180° , the following equations must be applied for a calculator giving results between -90° and 90° :

If $J_{180} < 0$

$$\alpha = \alpha + 90^\circ \quad (7.14a)$$

If $J_{180} \geq 0$ and $J_{45} \leq 0$

$$\alpha = \alpha + 180^\circ \quad (7.14b)$$

There have been different systems for putting spherocylinders into such components, but the one proposed above by Thibos et al. (1997) enjoys considerable popularity. They used the symbol J_0 rather than J_{180} but the latter has been used here to match the clinical practice of specifying the horizontal axis as 180° rather than 0° .

An advantage of these components is that it simplifies the process of combining or averaging spherocylinder powers when the cylinders are not parallel or orthogonal. Spherocylinders can be converted from $F_{\text{sp}}/F_{\text{cy}}/\alpha$ format to the vector $[M J_{180} J_{45}]$, and back again after the process. Spherocylinder powers $F_{\text{sp}} - F_{\text{cy}1}$, $F_{\text{sp}} - F_{\text{cy}2}$ etc., are added as

$$M = (F_{\text{sp}1} + F_{\text{cy}1}/2) + (F_{\text{sp}2} + F_{\text{cy}2}/2) + \dots$$

or

$$M = M_1 + M_2 + \dots \quad (7.15)$$

$$J_{180} = -(F_{\text{cy}1}/2)\cos(2\alpha_1) - (F_{\text{cy}2}/2)\cos(2\alpha_2) - \dots$$

or

$$J_{180} = (J_{180})_1 + (J_{180})_2 + \dots \quad (7.16)$$

$$J_{45} = -(F_{cy11}/2)\sin(2\alpha_1) - (F_{cy12}/2)\sin(2\alpha_2) - \dots$$

or

$$J_{45} = (J_{45})_1 + (J_{45})_2 + \dots \quad (7.17)$$

Example 7.4: Add the spherocylinders +2.00 DS/−3.00 DC × 20 and +2.00 DS/+2.00 DC × 140

Solution: The two spherocylinders are denoted by $k = 1$ and $k = 2$, and the equations used are denoted by (7.9), (7.10), etc.

	F_{sp}	F_{cy}	α	M (7.9)	J_{180} (7.10)	J_{45} (7.11)
$k = 1$	+2.00	−3.00	20	+0.50	+1.15	+0.965
$k = 2$	+2.00	+2.00	140	+3.00	−0.175	+0.985
Totals:				+3.50	(7.15) +0.975 (7.16) +1.949 (7.17)	

$$F_{cy} = -2\sqrt{[0.975^2 + 1.949^2]} = -4.36 \text{ D} \quad (7.12)$$

$$F_{sp} = +3.50 + 4.36/2 = +5.68 \text{ D} \quad (7.13)$$

$$\alpha = [\tan^{-1}(1.949/0.975)]/2 = 31.7^\circ \quad (7.14)$$

As $J_{180} \geq 0$ and $J_{45} > 0$, equations (7.14a) and (7.14b) are not required.

If the spherocylinder form with a positive cylinder is required, the new sphere is the sum of the sphere and cylinder, the cylinder changes sign, and the axis is changed by 90° so that it stays within the 0° – 180° range:

$$F_{sp} = +5.68 + -4.36 = +1.32 \text{ D}, F_{cy} = +4.36 \text{ D}, \alpha = 31.7 + 90 = 121.7^\circ$$

Answer: $+5.68/-4.36 \times 32$ or $+1.32/+4.36 \times 122$

7.6.3 THICK LENSES AND THE EFFECT OF THICKNESS

Correcting lenses have some thickness, and therefore the above theory requires some modification in the case of real lenses. In ophthalmic optics, it is conventional to measure the distance of the lens from the eye by the *vertex distance*, which is the distance from the back vertex of the lens (the vertex closest to the eye) to the corneal vertex. When this is done, the focal length f_s in Figure 7.6 and in the preceding equations becomes the back vertex focal length f'_v , and thus the power F_s in these equations becomes the back vertex power F'_v . Therefore, equations (7.1) to (7.6)

still apply, providing the distance h is the back vertex distance and the power F_s is replaced by the back vertex power F'_{v_s} .

However, when specifying the retinal image sizes in eyes corrected with ophthalmic lenses, it is the equivalent power rather than the back vertex power that sets the image size. When we go from thin to thick lenses, we cannot take all the equations and simply replace the equivalent power by back vertex power. For image size calculations the situation becomes more complex, and we look at this problem in Chapter 10.

7.7 EFFECT OF PARAMETER CHANGES ON REFRACTIVE ERRORS

7.7.1 REFRACTIVE ERROR AND AXIAL LENGTH

As already mentioned, spherical refractive errors are due to a mismatch between the refractive power of the eye and its axial length. In some cases, it is important to know how a change in axial length can affect the level of ametropia. This can be investigated using a schematic eye.

The lens equation for the eye can be written as

$$n'/l' - L = F \quad (7.18)$$

where n' is the refractive index of the vitreous, F is the equivalent power of the eye and $L (= 1/l)$ is the vergence of the object, conjugate to the fovea of the eye, relative to the first principal plane.

Suppose that the axial length changes by an amount $\delta l'$, as shown in Figure 7.8. This change $\delta l'$ leads to a change δL in the object vergence, given by differentiating equation (7.18) and using small changes to get

$$-\frac{n'\delta l'}{l'^2} - \delta L = 0$$

Therefore,

$$\delta l' = -l'^2 \delta L / n' \quad (7.19)$$

If the eye is initially emmetropic with relaxed accommodation, then $l = \infty$ and so

$$l' = n'/F$$

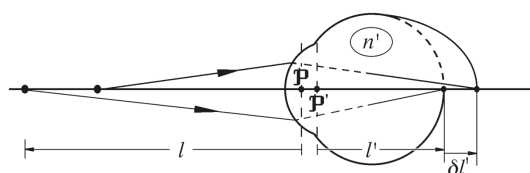


FIGURE 7.8 The change of axial length and corresponding change in refractive error.

Therefore, equation (7.19) can be written as

$$\delta l' = -n' \delta L / F^2$$

or

$$\delta L = -\delta l' F^2 / n' \quad (7.19a)$$

This change in object vergence can be equated to the refractive error R_e . Thus

$$R_e = -\delta l' F^2 / n' \quad (7.20)$$

which shows that the relationship between changes or error in axial length and refractive error depends upon the equivalent power of the eye.

If we take an equivalent power for the eye of 60 D and a vitreous humor refractive index of 1.336, we have

$$R_e = -2694.6 \delta l' \text{ D}$$

Expressing $\delta l'$ in millimeters rather than meters, we have

$$R_e = -2.69 \delta l' \text{ D} \quad (7.21a)$$

or

$$\delta l' = -0.371 R_e \text{ mm} \quad (7.21b)$$

These two equations are useful as a guide in relating changes in axial length to changes in refractive error. They assume a value of 60 D for the equivalent power of the eye. If a more accurate value is available in a particular case, it can be substituted into equation (7.20).

7.7.2 CHANGE IN CORNEAL CURVATURE

The power F_c of the anterior surface of the cornea is given by the equation

$$F_c = (n - 1)/r \quad (7.22)$$

where r is the radius of curvature of the surface and n is the refractive index of the cornea. A small change δr in radius of curvature r leads to a change δF_c in corneal power F_c given by the equation

$$\delta F_c \approx -(n - 1) \delta r / r^2 \quad (7.23)$$

where r is the original corneal radius of curvature. This equation can also be expressed in the form

$$\delta F_c \approx -F_c^2 \delta r / (n - 1) \quad (7.24)$$

If we measure the refractive error from the principal planes, the change in equivalent power is the refractive error. We need to relate the change in anterior corneal power to the equivalent power.

The equivalent power of the eye is due to the power of the cornea and lens. The above power of the cornea is only the anterior surface power. To relate this change in anterior corneal power to a change in equivalent power of the eye is not simple, and initially we will take a short cut and neglect the interaction of the posterior corneal power and the lens power.

With these approximations, the above change in corneal power is the same as the corresponding change in equivalent power, which in turn is the negative value of the induced refractive error δR_e . Therefore, we have

$$\delta R_e \approx F_c^2 \delta r / (n - 1) \quad (7.25)$$

Example 7.5: Using the Gullstrand number 1 eye, calculate the induced refractive error caused by an increase in corneal radius of 1 per cent.

Solution: For this eye, from data given in Appendix 3, $r = 7.7$ mm, $n = 1.376$, and the power of the anterior corneal surface F_c is

$$F_c \approx (n - 1)/r = 0.376/7.7 = 0.04883 \text{ mm}^{-1}$$

Also

$$\delta r = 0.01 \times 7.7 = 0.077 \text{ mm}$$

Substituting the values for F_c , δr , and n into equation (7.25) gives

$$\delta R_e \approx 0.04883^2 \times 0.077/0.376 \approx 0.000488 \text{ mm}^{-1} \approx 0.488 \text{ D}$$

which, being positive, indicates that the induced refractive error is a hyperopic error.

7.7.3 OTHER PARAMETER CHANGES

Using paraxial mathematical modeling and paraxial raytracing, we can investigate the effect of changes in any optical parameter on the refractive state of an eye. Table 7.1 shows the results of some calculations based upon the Gullstrand number 1 relaxed eye. The refractive error induced by a change of +1 per cent in anterior corneal radius is +0.483 D, which is only about 1 per cent different from the value given in Example 7.5. The major source of the difference is neglecting the effects of the lens and the posterior corneal surface in equation (7.25).

TABLE 7.1
**Effects of Small Parameter Changes on Change in
 Refractive Error Using the Gullstrand Number 1
 Relaxed Schematic Eye with Paraxial Raytracing**

	$\delta R_e(D)$
Refractive index +1% increase	
cornea	+0.173
aqueous	-0.814
lens	-2.398
vitreous	+1.689
Radius of curvature +1% increase	
cornea anterior	+0.483
cornea posterior	-0.056
lens anterior	+0.039
lens posterior	+0.047
Distance +0.1 mm increase	
corneal thickness	-0.173
anterior chamber depth	-0.138
lens thickness (core)	-0.177
vitreous length	-0.256

Note: Negative values indicate myopic refractive errors and positive values indicate hyperopic refractive errors.

SUMMARY OF MAIN SYMBOLS

- d distance of far point from the corneal vertex. This distance is negative for myopic eyes and positive for hyperopic eyes
 F equivalent power of the eye
 F_c power of anterior surface of the cornea
 F_s power of a correcting spherical lens. Also called the spectacle refraction
 h vertex distance, i.e., the distance from the correcting lens to corneal vertex (always positive)
 F_{sp} power of the spherical component of a spherocylinder lens
 F_{cy} power of a cylindrical component of an astigmatic or spherocylinder lens
 α orientation of a cylindrical lens (usually the direction of the cylindrical axis)
 θ azimuth angle for a spherocylinder lens
 $F(\theta)$ power along θ
 M mean sphere component of spherocylinder lens
 J_{180} $0^\circ\text{--}90^\circ$ Jackson cross-cylinder component of spherocylinder lens
 J_{45} $45^\circ\text{--}135^\circ$ Jackson cross-cylinder component of spherocylinder lens
 l, l' object and image distances (from principal planes of refracting component)

L	corresponding reduced vergence ($= n/l$) of l . It is also the vergence if $n = 1$.
n, n'	refractive indices (usually of object and image space)
r	radius of curvature of cornea (anterior corneal surface)
R_e	refractive error measured at the corneal plane. Also called the ocular refraction

REFERENCES

- Atchison, D. A. 2006. "Optical models for human myopic eyes." *Vision Res* 46 (14):2236–50. doi: 10.1016/j.visres.2006.01.004.
- Atchison, D. A., C. E. Jones, K. L. Schmid, N. Pritchard, et al. 2004. "Eye shape in emmetropia and myopia." *Invest Ophthalmol Vis Sci* 45 (10):3380–6. doi: 10.1167/iovs.04-0292.
- Bailey, M. D., L. T. Sinnott, and D. O. Mutti. 2008. "Ciliary body thickness and refractive error in children." *Invest Ophthalmol Vis Sci* 49 (10):4353–60. doi: 10.1167/iovs.08-2008.
- Buckhurst, H., B. Gilmartin, R. P. Cubbage, M. Nagra, and N. S. Logan. 2013. "Ocular biometric correlates of ciliary muscle thickness in human myopia." *Ophthalmic Physiol Opt* 33 (3):294–304. doi: 10.1111/opo.12039.
- Charman, W. N., S. Plainis, J. Rozema, and D. A. Atchison. 2015. "Hypermetropia or hyperopia?" *Ophthalmic Physiol Optics* 35 (1):2–7.
- Flitcroft, D. I. 2013. "Is myopia a failure of homeostasis?" *Exp Eye Res* 114 (1):16–24. doi: 10.1016/j.exer.2013.02.008.
- Flitcroft, D. I., M. He, J. B. Jonas, M. Jong, et al. 2019. "IMI - Defining and classifying myopia: A proposed set of standards for clinical and epidemiologic studies." *Invest Ophthalmol Vis Sci* 60 (3):M20–M30. doi: 10.1167/iovs.18-25957.
- Gifford, K. L., K. Richdale, P. Kang, T. A. Aller, et al. 2019. "IMI - Clinical management guidelines report." *Invest Ophthalmol Vis Sci* 60 (3):M184–M203. doi: 10.1167/iovs.18-25977.
- Goss, D. A., H. G. Van Veen, B. B. Rainey, and B. Feng. 1997. "Ocular components measured by keratometry, phakometry, and ultrasonography in emmetropic and myopic optometry students." *Optom Vis Sci* 74 (7):489–95. doi: 10.1097/00006324-199707000-00015.
- Grosvenor, T. 1991. "Changes in spherical refraction during the adult years." In *Refractive Anomalies. Research and Clinical Applications*, edited by T. Grosvenor and M. C. Flom, 131–45. Butterworth-Heinemann.
- Harris, W. F. 2000. "Astigmatism." *Ophthalmic Physiol Opt* 20 (1):11–30.
- Holden, B. A., T. R. Fricke, D. A. Wilson, M. Jong, et al. 2016. "Global prevalence of myopia and high myopia and temporal trends from 2000 through 2050." *Ophthalmology* 123 (5):1036–42. doi: 10.1016/j.ophtha.2016.01.006.
- Jalie, M. 2021. *The Principles of Ophthalmic Lenses*. 6th ed. London: Association of Dispensing Opticians.
- Jones, R. 1990. "Do women and myopes have larger pupils?" *Invest Ophthalmol Vis Sci* 31 (7):1413–5.
- Kaphle, D., D. A. Atchison, and K. L. Schmid. 2020. "Multifocal spectacles in childhood myopia: Are treatment effects maintained? A systematic review and meta-analysis." *Surv Ophthalmol* 65 (2):239–49. doi: 10.1016/j.survophthal.2019.10.001.
- Kaphle, D., K. L. Schmid, M. Suheimat, S. A. Read, and D. A. Atchison. 2023. "Peripheral axial length and choroidal thickness changes during accommodation." *Ophthalmic Physiol Opt* 43. doi: 10.1111/opo.13084.
- Keating, M. P. 1981. "Lens effectivity in terms of dioptric power matrices." *Am J Optom Physiol Opt* 58 (12):1154–60. doi: 10.1097/00006324-198112000-00016.

- Kuchem, M. K., L. T. Sinnott, C. Y. Kao, and M. D. Bailey. 2013. "Ciliary muscle thickness in anisometropia." *Optom Vis Sci* 90 (11):1312–20. doi: 10.1097/OPX.0000000000000070.
- Leung, T. W., A. K. Lam, L. Deng, and C. S. Kee. 2012. "Characteristics of astigmatism as a function of age in a Hong Kong clinical population." *Optom Vis Sci* 89 (7):984–92. doi: 10.1097/OPX.0b013e31825da156.
- Lewis, H. A., C. Y. Kao, L. T. Sinnott, and M. D. Bailey. 2012. "Changes in ciliary muscle thickness during accommodation in children." *Optom Vis Sci* 89(5):727–37. doi: 10.1097/OPX.0b013e318253de7e.
- Logan, N. S., H. Radhakrishnan, F. E. Cruickshank, P. M. Allen, et al. 2021. "IMI Accommodation and binocular vision in myopia development and progression." *Invest Ophthalmol Vis Sci* 62 (5):4. doi: 10.1167/iovs.62.5.4.
- Long, W. F. 1976. "A matrix formalism for decentration problems." *Am J Optom Physiol Opt* 53 (1):27–33. doi: 10.1097/00006324-197601000-00005.
- Lyle, W. M. 1991. "Astigmatism." In *Refractive Anomalies. Research and Clinical Applications*, edited by T. Grosvenor and M. C. Flom, 146–73. Butterworth-Heinemann.
- Oliveira, C., C. Tello, J. M. Liebmann, and R. Ritch. 2005. "Ciliary body thickness increases with increasing axial myopia." *Am J Ophthalmol* 140 (2):324–5. doi: 10.1016/j.ajo.2005.01.047.
- Pope, J. M., P. K. Verkiculara, F. Sepehrband, M. Suheimat, et al. 2017. "Three-dimensional MRI study of the relationship between eye dimensions, retinal shape and myopia." *Biomed Opt Express* 8 (5):2386–95. doi: 10.1364/BOE.8.002386.
- Pucker, A. D., L. T. Sinnott, C. Y. Kao, and M. D. Bailey. 2013. "Region-specific relationships between refractive error and ciliary muscle thickness in children." *Invest Ophthalmol Vis Sci* 54 (7):4710–6. doi: 10.1167/iovs.13-11658.
- Read, S. A., J. A. Fuss, S. J. Vincent, M. J. Collins, and D. Alonso-Caneiro. 2019. "Choroidal changes in human myopia: insights from optical coherence tomography imaging." *Clin Exp Optom* 102 (3):270–85. doi: 10.1111/cxo.12862.
- Read, S. A., S. J. Vincent, and M. J. Collins. 2014. "The visual and functional impacts of astigmatism and its clinical management." *Ophthalmic Physiol Opt* 34 (3):267–94. doi: 10.1111/opo.12128.
- Richdale, K., M. D. Bailey, L. T. Sinnott, C. Y. Kao, et al. 2012. "The effect of phenylephrine on the ciliary muscle and accommodation." *Optom Vis Sci* 89 (10):1507–11. doi: 10.1097/OPX.0b013e318269c8d0.
- Rozema, J. J., M. J. Tassignon, and Project Gullstrand Study Group. 2014. "The bigaussian nature of ocular biometry." *Optom Vis Sci* 91 (7):713–22. doi: 10.1097/OPX.0000000000000296.
- Schultz, K. E., L. T. Sinnott, D. O. Mutti, and M. D. Bailey. 2009. "Accommodative fluctuations, lens tension, and ciliary body thickness in children." *Optom Vis Sci* 86 (6):677–84. doi: 10.1097/OPX.0b013e3181a7b3ce.
- Singh, K. D., N. S. Logan, and B. Gilmartin. 2006. "Three-dimensional modeling of the human eye based on magnetic resonance imaging." *Invest Ophthalmol Vis Sci* 47 (6):2272–9. doi: 10.1167/iovs.05-0856.
- Sorsby, A., B. Benjamin, J. B. Davey, and et al. 1957. Emmetropia and its Aberrations. In *Medical Research Council Special Report Series number 293. HMSO*.
- Sorsby, A., G. A. Leary, and M. J. Richards. 1962. "Correlation ametropia and component ametropia." *Vision Res* 2 (9-10):309–13.
- Sorsby, A., M. Sheridan, G. Leary, and B. Benjamin. 1960. "Vision, visual acuity, and ocular refraction of young men." *British Medical Journal* i:1394–8.

- Stenström, S. 1948. "Investigation of the variation and the correlation of the optical elements of human eyes. Parts I and III. Translated by D. Woolf." *Am J Optom Arch Am Acad Optom* 25 (5, 7):218–32, 340–50.
- Strömborg, E. 1936. "Über Refraktion und Achsenlänge des menschlichen Auges." *Acta Ophthalmologica* 14:281–93.
- Subbaram, M. V., and M. A. Bullimore. 2002. "Visual acuity and the accuracy of the accommodative response." *Ophthalmic Physiol Opt* 22 (4):312–8. doi: 10.1046/j.1475-1313.2002.00037.x.
- Tedja, M. S., A. E. G. Haarman, M. A. Meester-Smoor, J. Kaprio, et al. 2019. "IMI - Myopia genetics report." *Invest Ophthalmol Vis Sci* 60 (3):M89–M105. doi: 10.1167/iovs.18-25965.
- Thibos, L. N., W. Wheeler, and D. Horner. 1997. "Power vectors: an application of Fourier analysis to the description and statistical analysis of refractive error." *Optom Vis Sci* 74 (6):367–75. doi: 10.1097/00006324-199706000-00019.
- Troilo, D., E. L. Smith, 3rd, D. L. Nickla, R. Ashby, et al. 2019. "IMI - Report on experimental models of emmetropization and myopia." *Invest Ophthalmol Vis Sci* 60 (3):M31–M88. doi: 10.1167/iovs.18-25967.
- Wagner, S., F. Schaeffel, E. Zrenner, and T. Strasser. 2019. "Prolonged nearwork affects the ciliary muscle morphology." *Exp Eye Res* 186:107741. doi: 10.1016/j.exer.2019.107741.
- Wagner, S., E. Zrenner, and T. Strasser. 2018. "Ciliary muscle thickness profiles derived from optical coherence tomography images." *Biomed Opt Express* 9 (10):5100–14. doi: 10.1364/BOE.9.005100.
- Wildsoet, C. F., A. Chia, P. Cho, J. A. Guggenheim, et al. 2019. "IMI - Interventions for controlling myopia onset and progression report." *Invest Ophthalmol Vis Sci* 60 (3):M106–M31. doi: 10.1167/iovs.18-25958.
- Winn, B., D. Whitaker, D. B. Elliott, and N. J. Phillips. 1994. "Factors affecting light-adapted pupil size in normal human subjects." *Invest Ophthalmol Vis Sci* 35 (3):1132–7.
- Wolffsohn, J. S., D. I. Flitcroft, K. L. Gifford, M. Jong, et al. 2019. "IMI - Myopia control reports overview and introduction." *Invest Ophthalmol Vis Sci* 60 (3):M1–M19. doi: 10.1167/iovs.18-25980.
- Wolffsohn, J. S., P. S. Kollbaum, D. A. Berntsen, D. A. Atchison, et al. 2019. "IMI - Clinical myopia control trials and instrumentation report." *Invest Ophthalmol Vis Sci* 60 (3):M132–M60.

8 Measuring Refractive Errors

8.1 INTRODUCTION

This chapter is concerned with techniques for measuring refractive error. This is an area that has received wide coverage in ophthalmic texts, particularly regarding the subjective techniques. The emphasis here is on principles rather than on a detailed investigation of techniques or instruments. For descriptions of particular commercial instruments, readers can refer to texts such as Benjamin (2006), Rabbets (2007), and Rosenfield and Logan (2009).

The techniques for determining refractive error can be classified in three groups: those that are subjective, those that may be subjective or objective, and those that can be only objective. Some of the objective methods may be automated.

In subjective techniques, the patient makes a judgement of the correct focus. In the objective methods, the clinician or an instrument makes a judgement of the correct focus. The clinician makes the judgement in the case of manual or visual instruments, but with automatic optometers the clinician's role is limited to ensuring the correct alignment of the instrument. Automated instruments, which have largely replaced manual instruments, use infrared sources in the wavelength range 800–1000 nm, and the clinician is replaced by an electronic focus detector. These instruments have separate fixation targets, which are designed to encourage relaxation of accommodation.

Objective optometers rely upon the fact that some of the light incident upon the patient's fundus (including the retina, choroid, and sclera) is reflected diffusely. Refractive error is determined either by measuring the vergence of light leaving the eye after fundus reflection, or by adjusting the vergence of light entering the eye so that a focused image of a target is formed on the fundus. With respect to objective refraction, we refer to the fundus image rather than the retinal image.

The measurement of refractive error has a few inherent problems and potential sources of error. These are discussed in section 8.6.

8.2 SUBJECTIVE REFRACTION TECHNIQUES

8.2.1 SIMPLE PERCEPTION OF BLUR

Most refraction techniques are based on asking the patient to observe a suitable target, such as part of a letter chart, and make judgements about the best focus.

8.2.1.1 Conventional Subjective Refraction Techniques

Conventional subjective refraction usually involves the patient reporting which of two views, seen through two slightly different combinations of lenses, gives a

“better” view of the target. The lens combinations may be placed as trial lenses into a trial frame, or as lenses in a refractor head (phoropter). These techniques include “fogging” (also “fan and block”), the cross-cylinder technique, and binocular balancing. As these techniques are covered in considerable detail by texts, such as those by Grosvenor (2007), Benjamin (2006), Rabbets (2007), and Rosenfield and Logan (2009), they are not discussed further here.

8.2.1.2 Optometers

Most of the below comments concerning optometers are applicable to objective tests. An optometer contains a target moving in front of a suitable optical system, which is placed close to the eye. A simple optometer consists of a target T and a single positive lens. The vergence of the image in the lens depends upon the target position. Under the clinician’s instruction, the patient moves the target towards the optometer lens from a position at which it is blurred to a position at which it first appears sharp. This point is taken as the measure of refraction. If the patient is emmetropic with relaxed accommodation, this point is at the front focal point F of the lens (Figure 8.1). For a hyperope, the point is farther away from the lens than F . For a myope, it is closer. In the case of astigmatism, the refraction can be found by using a rotatable line target or a target consisting of a “fan” of lines. For the former the patient must identify the two positions at which the line is in focus, and for the latter the patients must identify the positions at which two of the lines are in focus.

For the optometer shown in Figure 8.1a, l is the required target distance, F is the power of the optometer lens, and d is the distance between the lens and the eye. The vergence of the image in the lens, measured at the eye, is also the refractive error R_e . This is given by

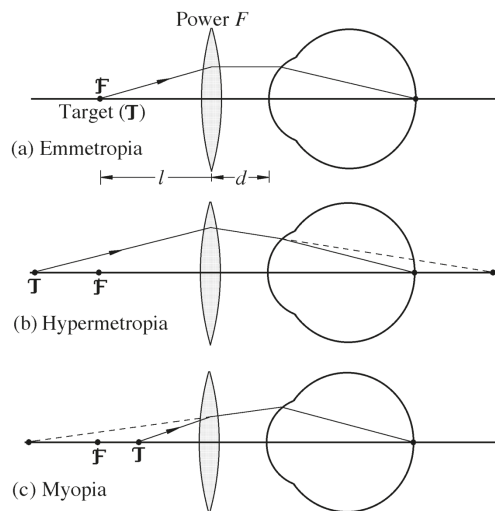


FIGURE 8.1 Use of simple optometer in emmetropia, myopia, and hyperopia.

$$R_e = \frac{1+LF}{l(1-dF)-d} \quad (8.1)$$

Such a design has several weaknesses. The ideal optometer should have the following properties:

1. The refractive error should be linearly related to the target displacement l from the lens, which allows easy and accurate calibration. Equation (8.1) shows that R_e is not linearly related to l for the arrangement shown in Figure 8.1.
2. The apparent size of the target should be independent of its position so that there is no size variation to stimulate accommodation.
3. The refractive error measuring range should be adequate.
4. The eye clearance (the distance from the back surface of the optometer to the eye) should be as large as possible so that the optometer's proximity to the eye does not stimulate accommodation.

The first two of these requirements are satisfied by the Badal optometer (Badal 1876), which is shown in Figure 8.2. It is essentially the same as the optometer shown in Figure 8.1, but with the restriction that the eye must be placed at the back focal point F' of the lens. We can then substitute $1/F$ for d into equation (8.1) to obtain

$$R_e = -(1 + LF)F \quad (8.1a)$$

An alternative version of this equation is

$$R_e = -xF^2 \quad (8.1b)$$

where x is the target displacement from the front focal point F of the lens. An often convenient value for F is 10 D, which means that each 1 cm of target movement is equivalent to 1 D of refractive error. Unfortunately, this has led to the misunderstanding by many students that a Badal lens has 10 D power rather than being a positive power lens placed at its focal distance from the eye.

The apparent angular size θ of a target of physical size η is given by the equation

$$\theta = \eta F \quad (8.2)$$

which is independent of target position.

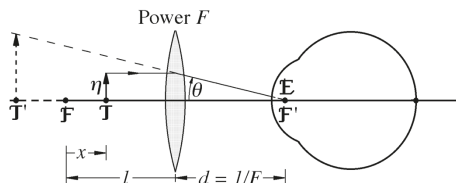


FIGURE 8.2 The simple Badal optometer.

There are different opinions of the appropriate ocular reference position for a Badal optometer, with candidates including the front focal point of the eye, its front nodal point, and the entrance pupil. The authors favor the entrance pupil, because the consistency of angular size occurs not only when the target is in focus but also when it is blurred.

A single lens Badal optometer may not satisfy requirements of range and eye clearance. While there is no theoretical upper limit to the hyperopic range of the single lens Badal optometer, the maximum level of myopia occurs when the target is at the optometer lens. Putting $l = 0$ into equation (8.1a) or $x = -1/F$ into (8.1b) shows that the maximum myopic error measurable is $-F$, the negative of the power of the Badal lens. If we increase this power to improve the range of the instrument, there is a corresponding decrease in eye clearance ($1/F$), which is clearly undesirable.

The negative range of the Badal optometer can be extended by various modifications. One simple example is by the addition of a moveable auxiliary system consisting of the target and a positive lens, which may provide a virtual target for the Badal lens (Atchison et al. 1995) (Figure 8.3a). Another alternative is to use a multilens Badal system. One such solution is the inverse telephoto design suggested by Gallagher and Citek (1995). The Badal optometer is combined with a lens of equal and opposite power, with the second lens placed in front of the Badal lens – the lenses being separated by the focal length of the Badal lens (Figure 8.3b). As the equivalent power of a system of two lenses of power F_1 and F_2 , separated by distance t in air, is given by

$$F_1 + F_2 - tF_1F_2 \quad (8.3)$$

the equivalent power for this arrangement with the Badal lens of power F is

$$F + F - (1/F)(-F)F = F$$

– that is, the same as the power of the Badal lens. The back principal plane of the system through \mathbf{P}' is at a distance $1/F$ from the Badal lens. To place the Badal lens at the back focal point of the eye, this point must be a distance $2/F$ from the Badal lens. The advantage of such a system is that it increases the distance between the eye and the Badal lens (Gallagher and Citek 1995). The two lenses do not give a negative vergence range because the front focal point \mathbf{F} coincides with the negative lens, but this can be overcome in turn by using a moveable auxiliary system as shown in Figure 8.3b. One other solution to increasing the negative power range that avoids the use of the auxiliary system is to use a symmetric system, in which the principal points are outside the system, as shown in Figure 8.3c.

In the Badal system and its modifications described above, the target would usually be placed close to the system. This requires the target to be small. The development of computer-generated displays, with the limited resolution that this entails, requires a modification that allows a much larger target. This can be achieved by using a fixed, distant target and a moveable auxiliary lens (Figure 8.3d). The scale in diopters is linear with movement of the lens (Atchison et al. 1995).

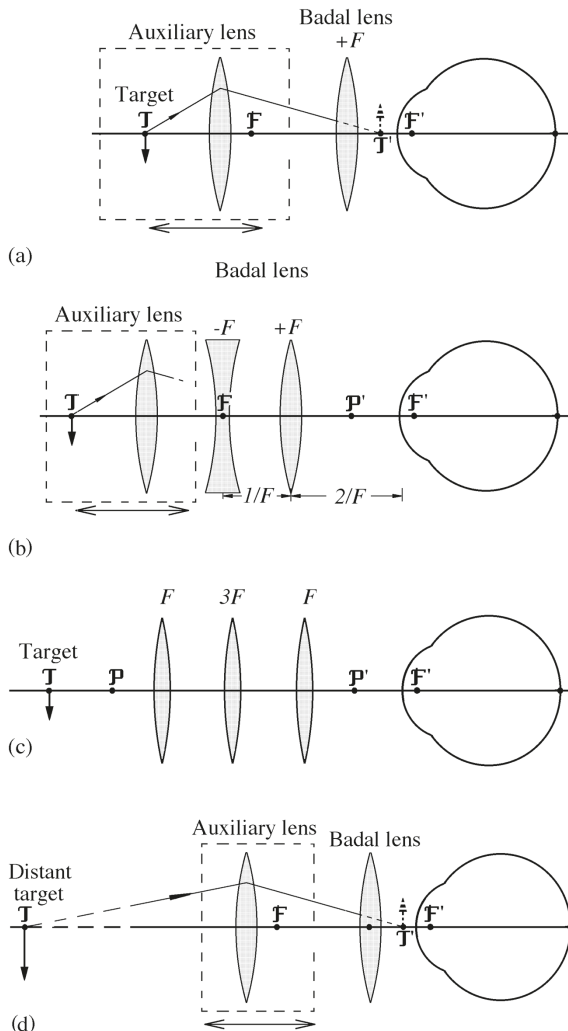


FIGURE 8.3 Variations of the Badal optometer. (a) Badal optometer with an auxiliary system to increase the negative power range. (b) Badal optometer with a second lens of equal and opposite power to the Badal lens to increase the distance between the Badal lens and the eye. The auxiliary system is needed to provide a negative vergence range. (c) Badal lens system with external principal points to increase the range of the optometer. (d) Badal optometer with a distance target and a movable auxiliary lens to overcome the problem of poor resolution with computer-generated displays. The auxiliary lens power and sign can be selected according to the refractive error range required.

Another variation of the use of the perception of blur to estimate refractive error is in some telescopic arrangements. Von Graefe used a Galilean telescope, varying the separation between the objective and eye lens to alter the vergence of the emergent light (Rabbetts 2007). Moving the eye lens away from the eye produces a

more convergent beam, while moving the eyepiece towards the objective produces a more divergent beam. The former movement can be used to measure hyperopia, and the latter movement to measure myopia. The telescopic tube can be graduated to show the effective power as the eyepiece is moved. Unfortunately the scale is not linear, and the angular subtense of the image at the eye varies with the position of the eyepiece. Dudrigne (1951) described a telescope optometer in which a +20 D lens, placed at its focal distance from the eye, was combined with a moveable -20 D lens. This is the same as the Badal optometer variation described above and in Figure 8.3d.

8.2.2 LONGITUDINAL CHROMATIC ABERRATION OF THE EYE

The eye has approximately 2 D of longitudinal chromatic aberration between the wavelengths of 400 nm and 700 nm (section 17.4.2). If a small white light is viewed through a piece of cobalt glass, only red and blue light are transmitted, with the blue light focused in front of the red light inside the eye (Figure 8.4). If the light is a long distance away, an emmetrope sees a purple disc, because the red and blue images are approximately equal in size. A myope of moderate degree (say 2 D) sees a red central spot surrounded by a blue annulus. Conversely, a hyperope sees a blue central spot surrounded by a red annulus. The strongest positive or weakest negative lens placed close to the eye that reduces the colored fringes to a single purple disc gives the refractive correction. With appropriate modification in technique, astigmatic refractive errors can be corrected.

The cobalt filter is rarely used, but the eye's chromatic aberration is often used in the *duochrome test*, in which the patient compares the sharpness of letters presented on red and green backgrounds. This technique is used often as at the end of a refraction. Refraction is adjusted until the letters on the two backgrounds appear equally clear, or until the letters on one of the backgrounds are slightly clearer. By putting a prism in front of one eye to provide separate duochrome images to the two eyes, a binocular balance refinement to refraction can be provided.

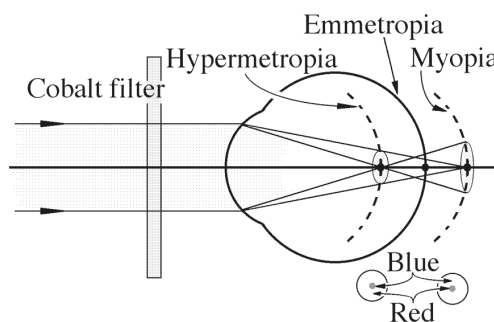


FIGURE 8.4 Chromatic optometer, showing the appearance of a distant spot viewed by emmetropes, myopes, and hyperopes.

8.3 SUBJECTIVE/OBJECTIVE REFRACTION TECHNIQUES

8.3.1 REMOTE REFRACTION AND RELAY SYSTEMS

Positioning equipment close to the face means that the clinician is not able to see the patient's face. The patient may also feel uncomfortable. The proximity of the equipment may induce "instrument" myopia in some susceptible individuals. To overcome these problems, some instruments use an auxiliary lens or mirror system to image a remote correcting lens at the eye. The auxiliary system is thus a relay system.

Figure 8.5a shows a correcting lens of power F , which is imaged by an auxiliary lens of power F_a to the eye. The target at T for the correcting lens may be the real object, or it may be the image of the real target, in which case it may be referred to as the "intermediate" target. A concave mirror may replace the auxiliary lens (Humphrey 1976; Bennett 1977; Alvarez 1978).

Another system that might be considered to be remote refraction uses a $-1\times$ telescope consisting of two lenses of equal power separated by twice their focal lengths. The correcting lens is placed at the first focal point of the first telescope element, and the eye is placed at the second focal plane of the second telescope element (Figure 8.5b).

A full description of the imaging properties of these relay systems is beyond the scope of this book.

8.3.2 SPLIT IMAGE AND VERNIER ACUITY (COINCIDENCE METHOD)

The target using this method has at least one straight edge, which is split into two. Defocusing moves one part of this edge sideways relative to the other part, so that

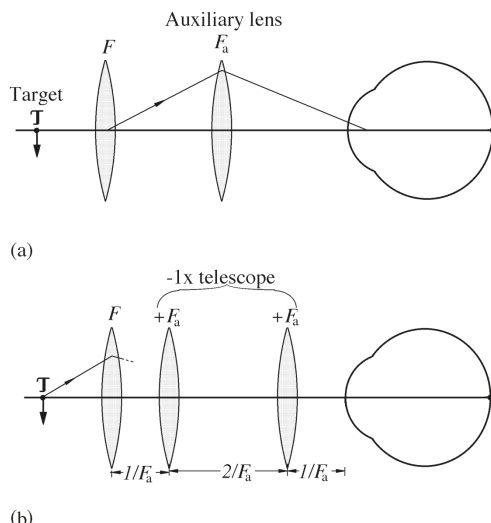


FIGURE 8.5 Remote refraction systems. (a) Remote refraction with an auxiliary lens. (b) Remote refraction with a $-1\times$ telescope system.

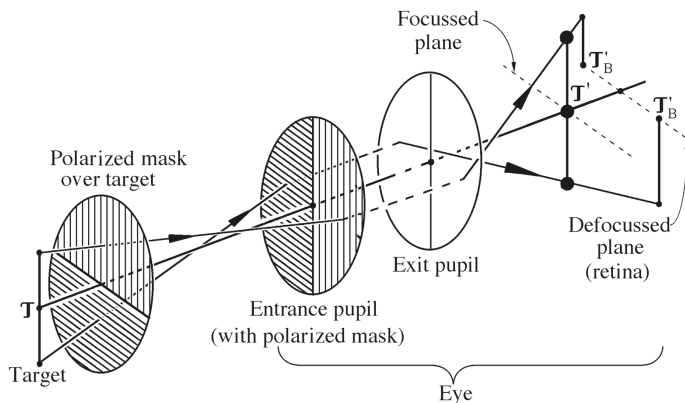


FIGURE 8.6 Coincidence method of focusing using polarized filters.

the patient (or clinician) sees the straight edge separated into two. When the system is correctly focused, the two parts are aligned (that is, in coincidence). Usually, this coincidence principle is combined with the Scheiner principle (see below), which ensures that radiation from the two halves of the target pass into the eye through different pupil regions. The coincidence principle works well because the patient (for subjective instruments) or the clinician (viewing light reflected from the fundus for objective instruments) is very sensitive to vernier misalignment.

A subjective instrument using the coincidence principle is the polarizing optometer (Simonelli 1980). A pair of crossed polarized filters is placed over the target, and another pair is placed over the pupil of the eye. The second pair is cut at right angles to the first pair – for example, if the first pair join along the horizontal meridian, then the second pair join along the vertical meridian (Figure 8.6). The beam from half of the target enters only half the pupil, and the beam from the other half of the target enters the other half of the pupil. The target is moved until its two halves appeared aligned.

8.3.3 SCHEINER PRINCIPLE

When an unaccommodating, emmetropic patient views a target through a disc with two holes in it, the target appears doubled if it is beyond the focal point of the lens (Figure 8.7a). If the pinholes are aligned vertically, the upper hole corresponds to the spot appearing higher up (lower retinal projection). When the target is placed closer than the focal point of the lens, the target again appears doubled, with the upper hole corresponding to the spot appearing lower down (Figure 8.7b). When the target is placed at the focal point of the lens, the target appears single (Figure 8.7c).

A simple optometer incorporating this doubling or Scheiner principle consists of a moveable target, which is usually a small light spot, and a Scheiner disc, which is an opaque disc with two pinhole apertures about 2 mm apart. The patient moves the target towards the optometer lens from a position at which the target appears double to a position at which it appears single. This position is the measure of the refraction.

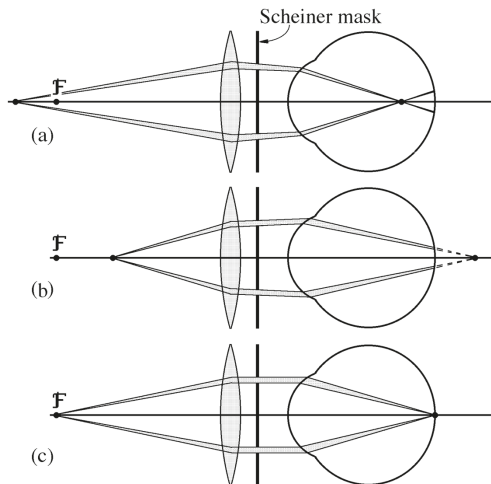


FIGURE 8.7 Imagery of a point source for an unaccommodating emmetrope using a Scheiner disc optometer. (a) Target beyond far point of lens. (b) Target closer than focal point of lens. (c) Target at focal point of lens.

For astigmatism, the axis of the two image points coincides with that of the pinholes only when the pinhole axis coincides with one of the principal meridians.

The Scheiner principle has been incorporated into several automated optometers. In one configuration, two infrared sources replace the two pinholes and are imaged in the plane of the patient's pupil. The target is a moveable diaphragm. Two blurred images of the diaphragm are produced at the fundus at different positions, one from each of the two infrared sources, except when the diaphragm is conjugate with the fundus. Radiation from the fundus passes out of the eye to a detector unit, which senses this difference in position and controls the movement of the target so that only one fundus image is formed.

8.4 OBJECTIVE REFRACTION TECHNIQUES

Table 8.1 lists some principles upon which optometers are based, and their associated features. More than one principle is applied in many optometers. Some optometers are called “into-the-eye” instruments as the quality or position of the fundus image is important, such as for the laser raytracing technique. Other optometers are called “out of the eye” instruments as the fundus acts merely as a secondary radiation source, such as for Hartmann–Shack aberrometers. Some optometers are called “sequential” as measurements are required in succession, such as when refraction is measured in one principal meridian before the other principal meridian or when a range of pupil positions is used in succession. Other optometers are called “simultaneous” because all measurements are taken at the same time. Some instruments are called “nulling” as active optical elements respond to signals from detectors to make the fundus conjugate with the detector or at some other suitable position; with the absence of these features other instruments are called “non-nulling” or “open-loop”. Instruments that

TABLE 8.1
Optometer Principles and Associated Features

Principle	Manual/ Automated	Into/Out-of- the Eye	Sequential/ Simultaneous	Nulling/ Non-Nulling
Parallax*	manual	into	sequential	nulling
Split image*	manual	into	sequential	nulling
Scheiner*	automated	into	sequential	nulling
Retinoscopy	automated	out	sequential	can be either
Best focus	automated	into	can be either	nulling
Image-size principle	automated	both	simultaneous	non-nulling
Ray deflection				
Hartmann-Shack	automated	out	simultaneous	partial nulling
Laser raytracing	automated	into	sequential	non-nulling
Photorefraction	automated	out	both	non-nulling

Note: * Described under subjective/objective refraction techniques.

measure higher-order aberrations as well as perform basic refraction are referred to as “aberrometers”, such as the Hartmann–Shack aberrometer and laser raytracing aberrometers.

8.4.1 RETINOSCOPY

Retinoscopy is probably the most common method of measuring refractive error. In this technique, the fundus of the eye acts as a screen over which a spot or streak of light is moved by tilting an instrument called a retinoscope back and forth. The clinician watches the shape and movement of the patch of reflected light within the patient’s pupil. The patch is known as the “reflex”. By placing trial lenses in front of the patient’s eye, the speed of movement of the reflex is modified until it moves infinitely fast (or as close to this as can be judged). This condition is known as “reversal”. At this position, the fundus of the patient’s eye is conjugate with the sight hole of the retinoscope, so that there is an almost instantaneous cut-off of the return beam entering the examiner’s eye as the light patch moves over the patient’s fundus. As this is a well-known clinical technique, we refer readers to book chapters such as those by Campbell et al. (2006), Rabbets (2007), and Atchison (2009).

Retinoscopy falls into a category called “knife-edge” techniques. Retinoscopy has been modified for use in some automated optometers, with a detector system with two photodetectors replacing the sight hole and the clinician. Refractive error is determined by the phase shift between the signals reaching the two detectors from the fundus.

8.4.2 PARALLAX MOVEMENT BETWEEN OBJECT AND IMAGE

The instrument used for this technique is a modification of the single lens indirect ophthalmoscope (Figure 8.8). The image S_2' of the intermediate (off-axis) source S_1' is formed near the edge of the patient’s pupil. A test object T on the common optical

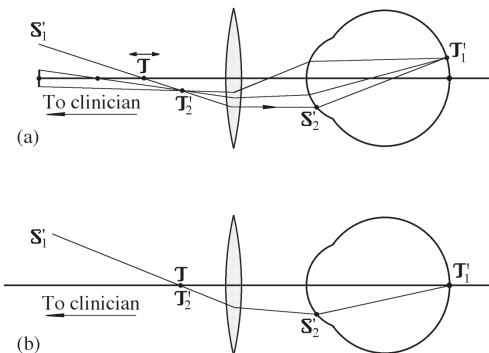


FIGURE 8.8 The parallax optometer. (a) Target T is not conjugate with its fundus image at T_1' . The clinician sees T_2' displaced laterally relative to T . (b) Target T has been moved so that it is now conjugate with fundus image T_1' . The clinician sees T_2' aligned with T .

axis of the patient's eye and the optometer occludes the illuminating beam along the ray path $TS_2'T_1'S_1'$.

Viewing at an angle to the axis of illumination, the clinician sees both the original test object T and its aerial image T' displaced laterally. Moving T along the axis of the instrument alters S_2' and the angle of incidence of the ray through T , causing T_1' to move across the fundus. At the same time, image T_2' moves laterally. When T is focused on the fundus, T_1' is on the axis of the system, and T_2' coincides with T . Thus T_2' appears to move in parallax as T is moved back and forth.

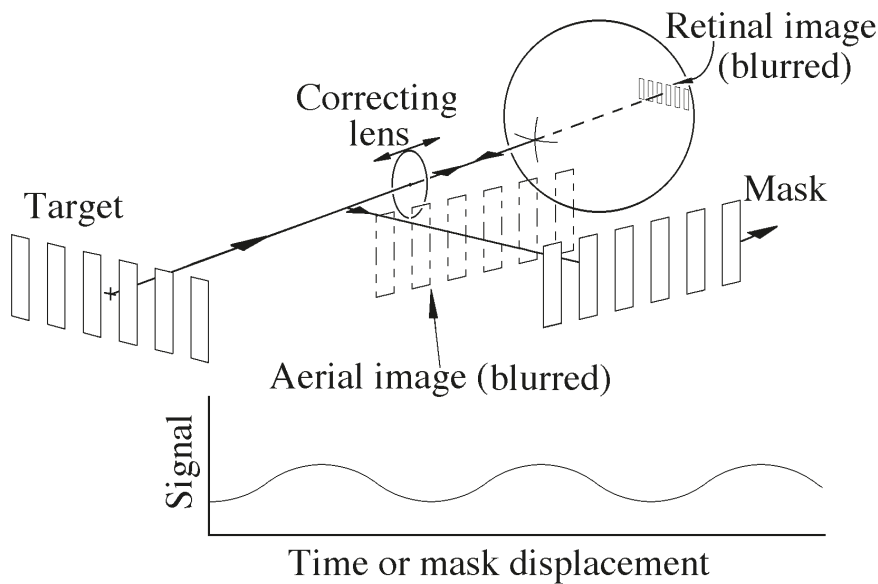
We are not aware that the parallax technique is being used currently.

8.4.3 GRATING FOCUS

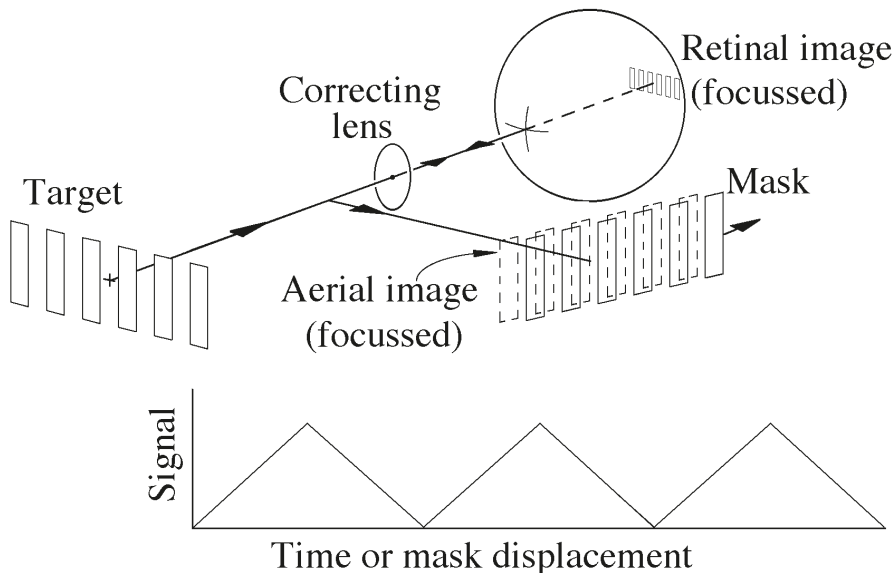
The grating focus principle is like the perception of blur, but here an automated optometer analyses the intensity of a signal to determine refractive error. The object is a square wave infrared intensity pattern (grating) (Figure 8.9). This is imaged into the eye. Radiation reflected by the fundus is imaged on a photodetector through a square wave grating mask. Either the mask or the target moves transversely, with the former situation being shown in Figure 8.9. The spatial frequency of the mask and the aerial image are matched. The signal from the photodetector modulates with the mask (or target) movement. The maximum modulation occurs when the aerial image is focused at the mask – this corresponds to the object being focused at the fundus (Figure 8.9b). The signal modulation is monitored as an optometer lens moves along the optical axis. An estimate of the refraction is given by the optometer lens position corresponding to the maximum modulation. To obtain the full refractive state of the eye, measures are made in a few meridians.

8.4.4 IMAGE-SIZE PRINCIPLE

A pair of masks ensures that radiation passes into the eye through a narrow region, typically in the form of an annulus. If the radiation is diverging before reaching the



(a) Out of focus



(b) In focus

FIGURE 8.9 The grating focus principle. See text for details.

eye, it would come to a focus well behind the retina, and if it is converging it will focus in front of the retina. The retinal image is reimaged, passing through a small aperture conjugated to the cornea, and to a detector plane where the image size is measured. The refraction R_e was given as Campbell et al. (2022) as

$$R_e = \pm(\alpha + \theta)/h_1$$

where θ is the angle of the ingoing beam just before it gets to the eye, α is the angle of the beam after exiting the eye, and h_1 is the height of the ingoing beam at the eye (usually an image of one of the masks). A positive sign is used outside the bracket if the beam is *converging* at the eye, and a negative sign is used outside the bracket if the beam is *diverging* at the eye. The former occurs for the Grand–Seiko/Shin–Nippon group of autorefractors, which also provide an open-field to makes them suitable for measuring peripheral refraction, and a theoretical study indicated that they were suitable for this purpose (Atchison et al. 2022).

The signs in the above equation depend upon the particular sign convention that was adopted for angles. Avoiding this, the previous equation becomes

$$R_e = \pm(|\alpha| - |\theta|)/|h_1| \quad (8.4)$$

with the positive sign used outside the bracket if the beam is *diverging* as it enters the eye, and the negative sign used outside the bracket if the beam is *converging* as it enters the eye. Figure 8.10 shows the latter situation for hyperopia and myopia.

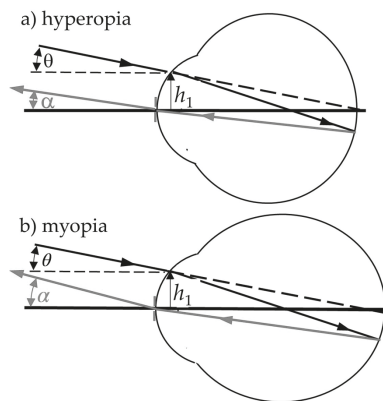


FIGURE 8.10 Image-size principle for the situation when the radiation is converging when reaching the eye. h_1 is the height of the ingoing beam at the eye, θ is the angle of the ingoing beam just before it gets to the eye, and α is the angle of the beam after exiting the eye. In (a), for a hyperopic eye the absolute value of α is smaller than that of θ , and the refraction is positive. In (b), for a myopic eye the absolute value of α is greater than that of θ , and the refraction is negative.

8.4.5 HARTMANN-SHACK ABERROMETER

Hartmann-Shack aberrometers, along with laser raytracing aberrometers (see section 8.4.6) and some other instruments, uses the ray detection principle. The basis of this is that the angle of a ray is compared with its ideal angle, with the difference referred to as the angle of deflection. With knowledge about the positions of rays in the pupil, angles of deflection can be converted into refraction. When many positions are examined, higher-order aberrations can be determined also (Chapter 15).

Hartmann-Shack aberrometers (Liang et al. 1994; Liang and Williams 1997) are currently the most popular commercial aberrometers. A narrow beam from a point radiation source passes into an eye, and the light reflected from the fundus travels through an optical system to the sensor consisting of an array of micro-lenses and a CCD camera (Figure 8.11). The micro-lens array is conjugate with the eye pupil, and the micro-lens array's focal plane is at the camera image plane. Each micro-lens isolates a beam passing through a small region of the pupil. Depending on the setup of pupil size, magnification between the pupil and the array sampling density, several hundred pupil positions may be sampled. For an ideal eye, the wavefront arriving at the sensor is a plane and there is a corresponding ideal position on the image plane. For an eye with aberrations, the transverse ray aberration (slope of the wavefront) associated with each micro-lens can be determined from the departure of its corresponding image from the ideal position. Wave aberration functions are derived from the collection of transverse aberrations, and refractions can then be determined (see section 15.4.3).

Usually, only a few milliseconds are required to capture an image. Fluctuations in aberrations over the order of seconds can be followed and the Hartmann-Shack

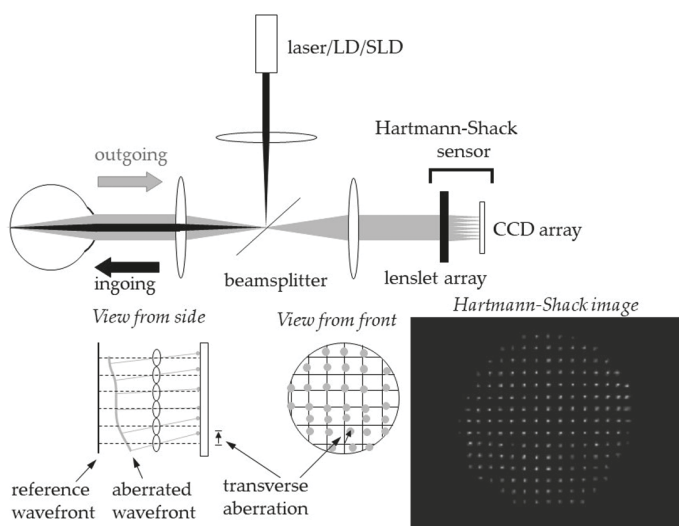


FIGURE 8.11 Hartmann-Shack aberrometer. The top part shows the basic setup, the bottom-left part shows transverse aberrations, and the bottom-right part shows an image of an eye. Based on Figure 3 of Atchison (2005).

aberrometer can be included in an adaptive optics system to correct ocular aberrations. Even if pupil centration is not precise, software algorithms can determine pupil center accurately. Because of the simultaneous measurement at all pupil locations, images may overlap when there are high levels of defocus or higher-order aberrations. This means that the technique has a limited dynamic range, depending on the focal length and sampling density of the sensor and software algorithms. Auxiliary moving optics are usually added in the imaging path to improve the dynamic range by correcting most of defocus, which is the reason for describing the technique as “partially nulling” (Table 8.1).

8.4.6 LASER RAYTRACING ABERROMETER

Laser raytracing can be described as into-the-eye and sequential (Navarro and Losada 1997). A narrow laser beam is deflected by two scanning mirrors to pass through a sequence of several pupil positions in the eye (Figure 8.12). For each pupil position, the fundus image becomes a secondary source to pass light back through the whole pupil and onto the CCD array of a camera. In the presence of aberrations, the fundus images corresponding to different pupil positions will be at different positions, as will occur for the final images on the camera. However, all should be similar in appearance. Image centroids are compared with that of the reference image, corresponding to the pupil center, to give transverse aberrations. As for the Hartmann–Shack aberrometer, wave aberrations and refractions can be determined.

Many measurements can be taken within a second. Considerable computing is required and potentially eye movements affect results. The technique has a large dynamic range, being able to measure wide ranges of refractive errors and aberrations. Unlike “simultaneous” aberration techniques, it does not suffer from the possibility that centroids corresponding to different pupil locations can be confused, but an oddly shaped retina can affect results.

8.4.7 PHOTOGRAPHY

The use of photography for determining the refraction of the eye is termed photorefraction (Howland and Howland 1974). Its main application is screening of

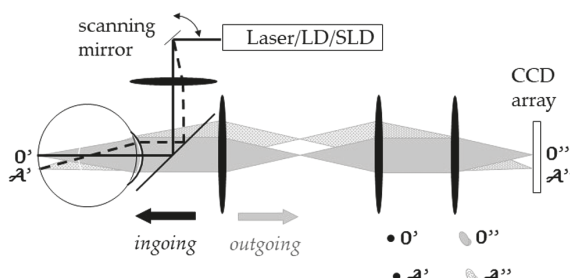


FIGURE 8.12 Laser raytracing. Details are given in the text. Based on Figure 13.26 of Atchison (2009).

infants and young children. A flash photograph is taken of the eyes, with the flash source near the plane of the camera. The size and location of the pupil reflex recorded by the camera indicates the degree and direction of refractive error. Variations of the technique include *orthogonal*, *isotropic*, and *eccentric* photorefraction.

In its simplest form, known as isotropic photorefraction (Howland et al. 1983), a small flash source of light is mounted in front of a camera with a lens system such that one or both eyes are imaged with the pupil large enough to allow analysis (Figure 8.13). The source is imaged on the fundus of each eye. If the eye is focused at the source, the light leaving the eye returns to the source and is occluded from the camera lens. Thus, the pupil appears dark. When the eye is not focused at the source, a blur circle (in spherical errors) or an ellipse (in astigmatism) is formed at the fundus. In turn, this produces an illuminated zone around the source, so that light enters the camera. The pupil appears illuminated, with the size of the film image depending upon the refractive error relative to the plane of the source. The sign of the refractive error cannot be determined by this basic technique, so Howland and co-workers took photographs with the camera focused both in front of and behind the patient's pupil plane. Using simple geometrical optics, the refractive error can be determined from the film image sizes, the pupil size and other dimensions of the camera setup.

The refractive error range that can be measured by the isotropic method is limited (Howland et al. 1983). Larger errors can be measured with eccentric photorefraction (Howland 1985), which is similar to retinoscopy and is sometimes called photoretinoscopy. In this method, an eccentric point source of light is used. Some of the light reflected from the fundus is vignetted by the camera, and this produces an image shaped like the profile of a biconvex lens. In hyperopia relative to the light source, the image is on the side of the pupil opposite to the flash; myopia relative to the light source produces an image on the same side of the pupil as the source (Figure 8.14). From the placement of the camera, flash, and patient, the refractive error can be determined.

The photoretinoscopic technique has developed into video-retinoscopy, in which there are rows of infrared LEDs within the mask. The slope of luminous intensity in the image at right angles to the edge of the mask is determined, with the slope being linearly related to refraction for a considerable refraction range. There can be several sets of LEDs at different orientations to give refraction in a range of meridians. Accommodation, pupil size, and gaze direction can be monitored across time, which

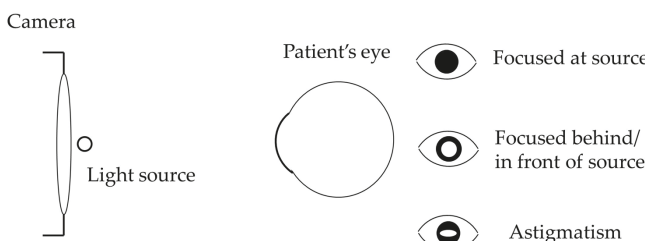


FIGURE 8.13 Isotropic photorefraction, showing camera images in spherical ametropia and when astigmatism is present.

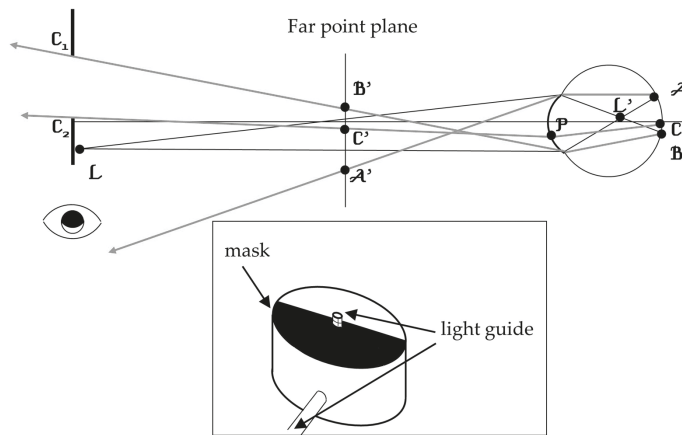


FIGURE 8.14 Eccentric photorefraction for a myopic eye. The bottom part of pupil (which is on same side as light source) is illuminated. L is the eccentric light source, L' is the image of image source in eye, C_1 and C_2 are edges of the camera aperture, ACB is the blurred image on retina, $A'C'B'$ is the image of fundus reflex, and the path $CPC'C_2$ is the ray path corresponding to the top edge of the illuminated crescent in the pupil. The bottom half of the figure shows the appearance of a photoretinoscope placed on a camera. Based on Figures 18.50 and 18.52 of Campbell et al. (2006).

makes such devices useful in research applications, e.g., Kasthurirangan et al. (2003). Limitations of the techniques associated with its calibration were explored by Wu et al. (2018).

8.4.8 VISUAL EVOKED RESPONSE

The visual evoked response is the response of the visual cortex to visual stimulation, primarily reflecting activity at the central retinal area. An active electrode is placed on the occipital scalp region, and an inactive electrode is placed in another part of the scalp. Pre-amplifiers, recorders, and a computer averaging technique are used to obtain electrical responses. With appropriate targets, the amplitude of the VER depends upon the refractive status of the eye. It is a useful, but not precise, method for patients who cannot be assessed by more conventional methods.

8.5 ACCURACY AND RELIABILITY OF REFRACTION

It is not possible to know absolute accuracy, or validity, for any refraction technique. What is usually done is to compare results with those obtained using a subjective refraction as the gold standard.

Reliability, which is the ability of an instrument or technique to give repeatable results, is easier to determine. This can be given as intra-examiner or inter-examiner repeatability. It can be expressed as 95% limits of agreement or as the percentage agreement for a particular refraction. Reliability can be applied to describing the

difference in refractions between two or more instruments. As an example, for a single clinician, the percentage of times in which two measures of spherical equivalent refraction might agree to within 0.25 D is 50%, together with 95 % limits of agreement (within two standard deviations of the mean difference) being 0.70 D.

Some studies of accuracy and reliability have considered sphere S , cylinder C , and axis α of refraction separately. As these are interdependent quantities, it is better to consider mean sphere M and the two Jackson cross-cylindrical components J_{180} and J_{45} (section 7.6.2). A useful overall measurement to compare two measures is the difference in dioptric strengths ΔS given by

$$\Delta S = \sqrt{(\Delta M^2 + \Delta J_{180}^2 + \Delta J_{45}^2)} \quad (8.5)$$

where ΔM , ΔJ_{180} , and ΔJ_{45} are the component differences of the two measures.

Accuracy or reliability can be plotted using Bland–Altman diagrams (Bland and Altman 1986) in which differences between two measures are plotted against means of the two measures. These diagrams readily show differences between the two measures, together with any trends in the differences as a function of refraction (Figure 8.15).

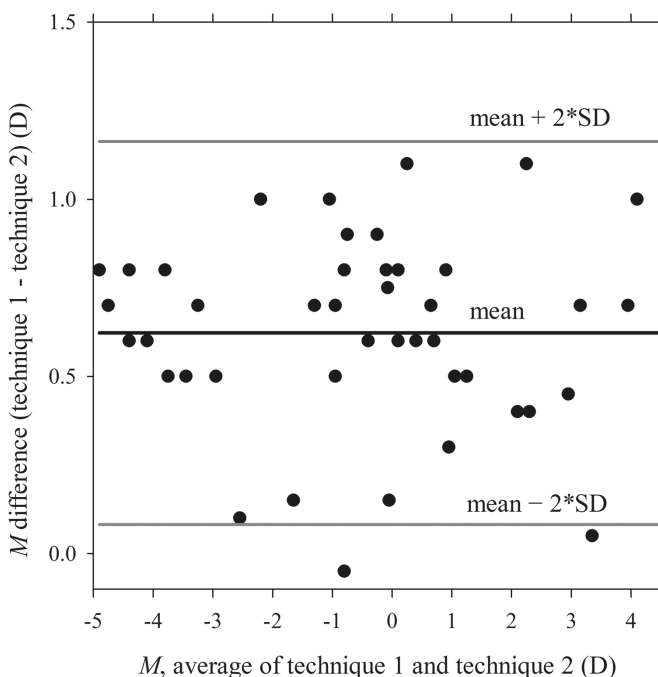


FIGURE 8.15 Bland–Altman plot comparing two refraction techniques. For a group of patients, differences between mean spheres are compared with the averages of the mean spheres. The lines show mean difference and 95% limits of agreement between the techniques. There is a systematic difference between the two techniques, with technique 1 giving more positive/less negative measurements than technique 2, although without any trends in the difference as a function of refraction.

Goss and Grosvenor (1996) summarized non-cycloplegic refraction studies of reliability up to the mid-1990s, and found that objective autorefractors and subjective refraction had similar reliability. They found also that some autorefractors had a positive bias compared with subjective refraction, while others had a negative bias. Accuracy and repeatability will be affected by patient population characteristics, such as refraction range, contact lens wear, media clarity, refractive surgery, and age (Strang et al. 1998), and by various target, optical, and neural factors (see section 8.6).

8.6 FACTORS AFFECTING REFRACTION

Several factors affecting refraction are described below. Several headings are used, but some factors described are common to two or more headings, e.g., wavelength of radiation source is an optical factor and influences the site of fundus reflection and accommodation.

8.6.1 TARGET FACTORS

Different refraction methods may give systematically different results because of the different conditions under which the refractions are determined – for example, different luminances, spatial frequency distributions, and spectral distributions. These interact with ocular factors, such as aberrations and pupil size.

8.6.2 OPTICAL FACTORS

Subjective depth-of-field decreases, or subjective reliability increases, with increase in pupil diameters up to approximately 5 mm, and then changes little. This is discussed further in Chapter 19.

Many automated optometers have a minimum pupil size requirement; the pupil needs to be a certain size to pass the radiation from the stimulus into and out of the eye, and the electronic signals provided by the detectors need to have sufficient strength to be distinguished from background noise.

Monochromatic aberrations, particularly spherical aberration, may affect refraction through their interaction with pupil size and target factors. With large pupils, spherical aberration may cause the refraction to be dependent upon target spatial distribution, with positive spherical aberration causing the refraction to move in the myopic direction for targets having considerable low spatial frequency components. Large monochromatic aberrations can decrease the reliability of refraction techniques through their influence on depth-of-field.

Aberrometers sample over the whole pupil or a large proportion of a large pupil. Various methods can be used to determine the refraction from these aberrations. These include calculations directly from the wave aberration functions and aberration-based image quality metrics such as the Strehl intensity ratio. These are discussed in Chapters 15 and 18.

8.6.3 ECCENTRIC VIEWING

Retinoscopy is usually performed at a small angle to the visual axis. Provided this angle is within 3°, the peripheral power errors introduced should be less than 0.25 D (see Chapter 15). When there is eccentric fixation or heterotropia, the clinician may need to direct the patient's gaze to the most appropriate axis.

8.6.4 REFERENCE PLANE

Objective refractors are usually referenced to the corneal plane, but most optometers allow the examiner to select from a range of vertex distances.

8.6.5 SITE OF FUNDUS REFLECTANCE IN OBJECTIVE REFRACTION

This is affected by the spectral distribution and by any polarization of the radiation source. The longer the wavelength, the deeper into the retina and choroid are the main reflecting layers (see also section 8.6.8).

8.6.6 ACCOMMODATION

It is important for the eye's accommodation to be relaxed during refraction. This may be attempted by the following methods:

1. Placing positive lenses in front of the non-tested eye so that accommodation blurs the image.
2. Ensuring that the axes of both right and left eye channels are parallel in instruments so that convergence cannot stimulate accommodation.
3. Using a blue fixation target, which provides a reduced stimulus to accommodation because the eye has greater power for blue light than for other visible wavelengths.
4. Using cycloplegic drugs.

8.6.7 MAXIMUM POTENTIAL VISUAL ACUITY

Attenuation of high spatial frequency contrast by defocus is generally greater than that of low spatial frequencies (section 18.4.1). Thus, high visual acuities may give a greater reliability of subjective refraction than lower visual acuities.

8.6.8 DISCREPANCIES BETWEEN SUBJECTIVE AND OBJECTIVE REFRACTION

A major problem with manual optometers is that there is not sufficient control over the patient's accommodation. The targets are visible to the patient, and the stimulus to accommodation is altered as vergence from the target is altered.

Optometers may give more myopic (or less hyperopic) refractions than subjective refractions because of instrument or proximal myopia, the awareness that a target is

close. This is a particular problem with manual optometers as the patient can clearly see the target and there is no inducement to relax accommodation. In automated optometers using near infrared radiation, an auxiliary fixation target is required. Attempts are made to relax accommodation by keeping this target “fogged” during refraction.

Automated instruments use near-infrared radiation in the approximate range 800–900 nm so as provide high reflectance from the retina. Although the source is visible to the patient because of the high intensities, it is understood that these wavelengths provide little stimulus to accommodation. Other advantages include pupil dilation not usually required because pupillary responses are not sensitive to infrared, and fundus reflectance is much higher than in visible radiation. The disadvantage of near-infrared radiation is considerable choroidal scattering of the radiation because the retinal pigment epithelium is fairly transparent at these wavelengths. This gives the reflection site increased depth and size. Because of the longitudinal chromatic aberration of the eye, the eye is more hyperopic for the near-infrared wavelengths than for visible wavelengths. This is counteracted to some extent because the infrared wavelengths penetrate further than visible wavelengths into the retinal and choroidal layers, although some researchers consider that the waveguide properties of photoreceptors ensure that the effective site of most of the fundus reflection is the outer limiting membrane of the retina (Williams et al. 1994; López-Gil and Artal 1997). A calibration correction must be made to results so that the refraction is relevant to visible wavelengths and hence relevant to vision, amounting to approximately –0.75 D.

SUMMARY OF MAIN SYMBOLS

R_e	refractive error
l	distance from lens to object
d	distance from lens to eye
F	power of lens
F_a	power of auxiliary lens
x	distance from front focal point of lens to object
θ	angular subtense of image of target at eye
t	distance between lenses
η	object size
F, F'	front and back focal points of lens or optical system
P, P'	front and back principal planes of lens or optical system
$S, S_1' S_2'$	positions of source and its conjugates using the parallax principle
T, T_1', T_2'	positions of target and its images using the parallax principle
θ, α	angles of ingoing and outgoing beams for instruments using the image-size principle
h_1	height of the ingoing beam at the eye for instruments using the image-size principle.
$\Delta M, \Delta J_{180}, \Delta J_{45}$	component differences of two refraction measures
ΔS	difference in dioptic strengths of two refraction measures

REFERENCES

- Alvarez, L. W. 1978. "Development of variable-focus lenses and a new refractor." *J Am Optom Assoc* 49 (1):24–9.
- Atchison, D. A. 2005. "Recent advances in measurement of monochromatic aberrations of human eyes." *Clin Exp Optom* 88 (1):5–27. doi: 10.1111/j.1444-0938.2005.tb06659.x.
- Atchison, D. A. 2009. "Chapter 13. Objective refraction." In *Optometry: Science Techniques and Clinical Management*, edited by M. Rosenfield and N. Logan, 186–208. Oxford: Butterworth-Heinemann.
- Atchison, D. A., A Bradley, L. Thibos, and G. Smith. 1995. "Useful variations of the Badal optometer." *Optom Vis Sci* 72 (4):279–84. doi: 10.1097/00006324-199504000-00010.
- Atchison, D. A., M. Suheimat, S. Zacharovas, and C. E. Campbell. 2022. "The use of autorefractors using the image-size principle in determining on-axis and off-axis refraction. Part 2: Theoretical study of peripheral refraction with the Grand Seiko AutoRef/Keratometer WAM-5500." *Ophthalmic Physiol Opt* 42 (2):293–300. doi: 10.1111/opo.12936.
- Badal, J. 1876. "Optomètre métrique international. Pour la mesure simultanée de la réfraction et de l'acuité visuelle même chez les illettrés." *Annales d'Oculistique* 75 (May/April):101–17.
- Benjamin, W. J. 2006. *Borish's Clinical Refraction, Chapters 18, 19*. 2nd ed: W. B. Saunders.
- Bennett, A. G. 1977. "Some novel optical features of the Humphrey Vision Analyzer." *Optician* 173(4481):7–16.
- Bland, J. M., and D. G. Altman. 1986. "Statistical method for assessing agreement between two methods of clinical measurement." *Lancet* 1 (8476):307–10. doi: 10.1016/s0140-6736(86)90837-8.
- Campbell, C. E., W. J. Benjamin, and H. C. Howland. 2006. "Chapter 18. Objective refraction: retinoscopy, autorefraction, and photorefraction." In *Borish's Clinical Refraction* 2nd ed, edited by W. J. Benjamin, 682–764. W. B. Saunders.
- Campbell, C. E., M. Suheimat, S. Zacharovas, and D. A. Atchison. 2022. "The use of autorefractors using the image-size principle in determining on-axis and off-axis refraction. Part 1: Analysis of optical principles of autorefractors." *Ophthalmic Physiol Opt* 42 (2):283–92. doi: 10.1111/opo.12933.
- Dudrigne, R.A. 1951. "Optomètre à variation continue de puissance." In *International Optical Congress 1951*, 286–98. London: British Optical Association.
- Gallagher, J.T., and K. Citek. 1995. "A Badal optical stimulator for the Canon Autoref R-1 optometer." *Optom Vis Sci* 72 (4):276–8.
- Goss, D. A., and T. Grosvenor. 1996. "Reliability of refraction: a literature review." *J Am Optom Assoc* 67 (10):619–30.
- Grosvenor, T. P. 2007. *Chapter 10. Subjective refraction*. 5th ed, *Primary Care Optometry*. St Louis, Mo.: Butterworth-Heinemann/Elsevier.
- Howland, H. C. 1985. "Optics of photoretinoscopy: results from ray tracing." *Am J Optom Physiol Opt* 62 (9):621–5.
- Howland, H. C., O. Braddick, J. Atkinson, and B. Howland. 1983. "Optics of photorefraction: orthogonal and isotropic methods." *J Opt Soc Am* 73 (12):1701–8. doi: 10.1364/josa.73.001701.
- Howland, H. C., and B. Howland. 1974. "Photorefraction: a technique for study of refractive state at a distance." *J Opt Soc Am* 64 (2):240–9. doi: 10.1364/josa.64.000240.
- Humphrey, W. E. 1976. "A remote subjective refractor employing continuously variable sphere-cylinder corrections." *Opt Engr* 15 (4):286–91. doi: <https://doi.org/10.1117/12.7971977>.

- Kasturirangan, S., A. S. Vilupuru, and A. Glasser. 2003. "Amplitude dependent accommodative dynamics in humans." *Vision Res* 43 (27):2945–56. doi: 10.1016/j.visres.2003.08.004.
- Liang, J., B Grimm, S. Goelz, and J. F. Bille. 1994. "Objective measurement of wave aberrations of the human eye with the use of a Hartmann-Shack wave-front sensor." *J Opt Soc Am A* 11 (7):1949–57. doi: 10.1364/josaa.11.001949.
- Liang, J., and D. R. Williams. 1997. "Aberrations and retinal image quality of the normal human eye." *J Opt Soc Am A* 14 (11):2873–83. doi: 10.1364/josaa.14.002873.
- López-Gil, N., and P. Artal. 1997. "Comparison of double-pass estimates of the retinal-image quality obtained with green and near-infrared light." *J Opt Soc Am A* 14 (5):961–71. doi: 10.1364/josaa.14.000961.
- Navarro, R., and M. A. Losada. 1997. "Aberrations and relative efficiency of light pencils in the living human eye." *Optom Vis Sci* 74 (7):540–7. doi: 10.1097/00006324-199707000-00023.
- Rabbets, R. B. 2007. *Bennett and Rabbets' Clinical Visual Optics, Chapters 6, 17 and 18*. 4th ed: Butterworth-Heinemann.
- Rosenfield, M., and N. Logan. 2009. *Optometry: Science Techniques and Clinical Management, Chapters 13, 14*. Oxford: Butterworth-Heinemann.
- Simonelli, N. M. 1980. "Polarized vernier optometer." *Behav Res Meth Inst* 12 (3):293–6. doi: 10.3758/BF03201668.
- Strang, N. C., L. S. Gray, B. Winn, and Pugh J. R. 1998. "Clinical evaluation of patient tolerance to autorefractor prescriptions." *Clin Exp Optom* 81 (3):112–8. doi: 10.1111/j.1444-0938.1998.tb06729.x.
- Williams, D. R., D. H. Brainard, M. J. McMahon, and R. Navarro. 1994. "Double-pass and interferometric measures of the optical quality of the eye." *J Opt Soc Am A* 11 (12):3123–35. doi: 10.1364/josaa.11.003123.
- Wu, Y., L. N. Thibos, and T. R. Candy. 2018. "Two-dimensional simulation of eccentric photorefraction images for ametropes: factors influencing the measurement." *Ophthalmic Physiol Opt* 38 (4):432–46. doi: 10.1111/opo.12563.



Taylor & Francis
Taylor & Francis Group
<http://taylorandfrancis.com>

9 Image Formation

The Defocused Paraxial Image

9.1 INTRODUCTION

In Chapter 6 we examined image formation for the focused eye. However, often the eye is not focused on the object of interest. This may be because of an uncorrected refractive error. Also, when there is a poor stimulus – such as a bright empty field or at low luminance – the accommodation system tends to settle towards an intermediate resting state or tonic accommodation level (Rosenfield et al. 1993). This corresponds to about 1.5 D of accommodation for habitually corrected young people.

The effect of such focus errors on vision is important. A focus error affects the quality of the retinal image, and hence visual performance, e.g., Pascal (1952); Westheimer and McKee (1980); Simpson et al. (1986). Of particular clinical importance is the effect of defocus on visual acuity (Prince and Fry 1956; Atchison et al. 1979; Simpson et al. 1986; Smith 1991, 1996) and on image size (Pascal 1952; Marsh and Temme 1990; Smith et al. 1992). To fully understand the effect of defocus in these situations, the optics of defocused vision must be understood, and this is developed in this chapter.

Let us consider the situation shown in Figure 9.1, which shows the eye focused to the plane at **R**, but observing an object point **Q** in the perpendicular plane at **O**. Following a beam of rays from **Q** through the pupils, this beam focuses at the point **Q'** on the perpendicular plane at **O'** in front of the retina but continues to the retina. Thus, the retinal image **Q'** of this object is out-of-focus. If we ignore the effects of aberrations and diffraction, the light distribution of **Q'** on the retina is uniform and the area illuminated is the projection of the exit pupil at **E'**, through **Q'** onto the retina at **Q_b'**. Therefore, the beam cross-section on the retina has the same shape as the pupils. It is assumed that the normal pupil of the eye is circular, and therefore the light distribution at **Q_b'** is called the defocus blur disc for the object point **Q'**. Similarly, the circle centered on **R'** is the *defocus blur disc* for the object point **O**.

The center of the defocus blur disc is at **Q_b'**, and this is the intersection of the paraxial pupil ray (the *line of sight*) with the retina. We can see from Figure 9.1 that the retinal image of the object **OQ** is blurred or defocused, and it is a different size from the focused image **O'Q'** formed in front of the retina. In this chapter, we explore the effect of such a defocus on the apparent size of the blurred retinal image and the size of the defocus blur disc. We start with the retinal image size of the object **OQ**.

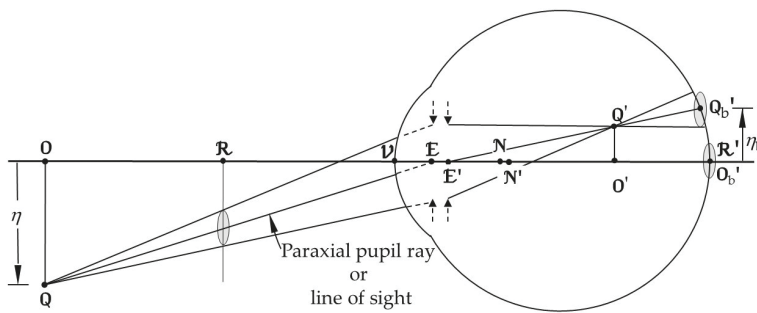


FIGURE 9.1 The formation of the blurred image of a distant point by an eye focused at some finite distance.

9.2 RETINAL IMAGE SIZE

Consider the points **O** and **Q** shown in Figure 9.1 as the ends of a line object. Each point on this line is imaged as a defocus blur disc (assuming a circular pupil), but only the blur discs for the points **O** and **Q** are shown. We could define the size of the blurred image of **OQ** as being measured from the bottom of the blur disc centered on **O_b'** to the top of the blur disc centered on **Q_b'**. However, with this definition the defocused image size depends upon pupil size, and it is preferable to have a definition that is independent of pupil size. A definition that satisfies this criterion is the image size measured from the centers of the defocused blur discs at **O'** and **Q'**, that is, the distance η'_b where the pupil rays from **O** and **Q** meet the retina.

In this case of a defocused retinal image, we should not use the nodal ray to determine the image size, as we did in Chapter 6 for focused images. The nodal ray is not the central ray of the beam and may not be part of the image-forming beam. It can be seen in Figure 9.1 that, if the pupil diameter is small enough, the rays through the nodal points are blocked and do not reach the retina. The likelihood of this happening increases as **Q** moves further away from the axis. When we investigate the size of a defocused image, we should use pupil rays only. We can find equations for this image size and its magnification relative to the focused image.

9.2.1 THE SIZE OF THE DEFOCUSSED IMAGE

Figure 9.2 shows the eye focused on the point **O₂** but observing the scene at the plane at **O₁**. From this figure, the size η'_b of the defocused image is

$$\eta'_b = \bar{u}'_2 \mathbf{E}_2' \mathbf{R}' \quad (9.1)$$

Now the angles \bar{u}'_2 and \bar{u}_2 shown in Figure 9.2 are connected by equation (5.7). Therefore,

$$\bar{u}'_2 = \bar{m}_2 \bar{u}_2 \quad (9.2)$$

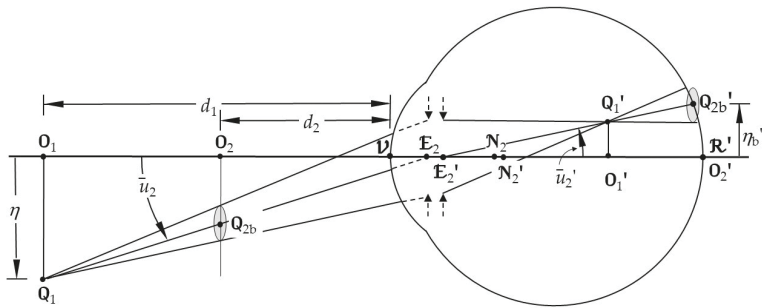


FIGURE 9.2 The retinal image and perceived angular sizes of defocused images.

with the value of the constant \bar{m}_2 depending upon the actual schematic eye used, in particular the equivalent power and positions of the pupils and principal planes. Combining the above two equations gives

$$\eta'_b = \bar{m}_2 \bar{u}_2 \mathbf{E}'_2 \mathbf{R}' \quad (9.3)$$

where

$$\bar{u}_2 = \eta / \mathbf{O}_1 \mathbf{E}_2 \quad (9.4)$$

is the angular size of the object, measured at the entrance pupil. Equation (9.3) shows that the retinal image size (whether focused or not) is proportional to the angular size of the object measured at the entrance pupil at \mathbf{E}_2 .

More meaningful than the defocused image size η'_b is its size relative to the size η' of the image if it were in focus. This ratio is the magnification M

$$M = \eta'_b / \eta' \quad (9.5)$$

The size of focused images was discussed in Chapter 6, and equation (6.6) is relevant. Here we have

$$\eta' = \bar{m}_1 \bar{u}_1 \mathbf{E}'_1 \mathbf{R}' \quad (9.6)$$

where the subscript “1” refers to the quantities measured for the eye focused on the point \mathbf{O}_1 instead of \mathbf{O}_2 . Equation (9.5) can now be written as

$$M = \frac{\bar{m}_2 \bar{u}_2 \mathbf{E}'_2 \mathbf{R}'}{\bar{m}_1 \bar{u}_1 \mathbf{E}'_1 \mathbf{R}'} \quad (9.7a)$$

Using equation (9.4), we can express this equation in terms of the distance d_1 and d_2 of the focused planes from the corneal vertex as

$$M = \frac{\bar{m}_2(d_1 + \mathbf{VE}_1)\mathbf{E}'_2\mathbf{R}'}{\bar{m}_1(d_2 + \mathbf{VE}_2)\mathbf{E}'_1\mathbf{R}'} \quad (9.7b)$$

As the eye changes its refractive state, there is a change in entrance and exit pupil positions. This in turn leads to changes in most of the above quantities.

9.2.2 AN EYE FOCUSED AT A FINITE DISTANCE, LOOKING AT AN OBJECT AT INFINITY

Before deriving an equation for the expected change in the image size, we will examine the optics of this process. As the eye accommodates, the equivalent power increases and, according to equation (6.11), the in-focus image size must decrease. However, because the object is at infinity, this focused image is formed in front of the retina as shown in Figure 9.3. Therefore, we may expect that the perceived image also decreases in size. However, in Figure 9.3, the height of the retinal image is set by the position where the pupil ray intersects the retina, and this position is higher than the image point \mathbf{Q}' .

To determine whether the observed image decreases or increases with accommodation, it is possible to derive a suitable equation directly from first principles using Figure 9.3. Equation (9.3) still applies, and for the focused image we can use equation (6.11), with the angle θ replaced by the angle \bar{u}_1 and the power here written as F_e . Thus

$$\eta' = \bar{u}_1 / F_e \quad (9.8)$$

Since the object is at infinity, $\bar{u}_1 = \bar{u}_2$, and if we now substitute for η_b' from equation (9.3) and for η' from the equation (9.8), equation (9.5) becomes

$$M = \bar{m}_2 \mathbf{E}'_2 \mathbf{R}' F_e \quad (9.9)$$

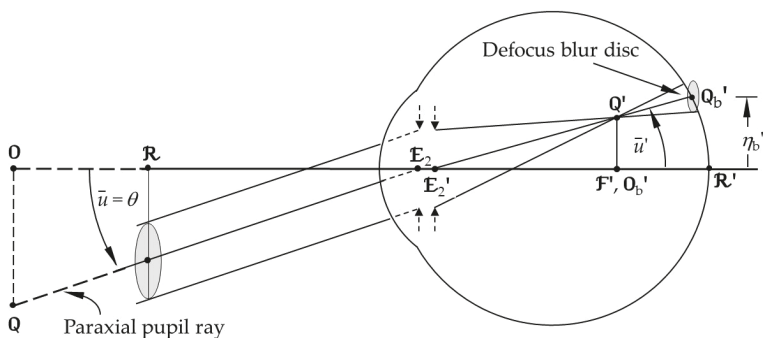


FIGURE 9.3 The retinal image and perceived angular sizes of defocused images (as in Figure 9.2), but with the object at infinity.

Example 9.1: Compare the retinal image sizes of the moon for the two extreme states of accommodation of the Gullstrand number 1 eye.

Solution: Equation (9.9) is used, with the following data from Table 5.1,

For the relaxed eye: $F_e = 58.636 \text{ D}$

For the accommodated eye: $\bar{m}_2 = 0.7959$ and $E_2' R' = 21.173 \text{ mm}$

Substituting these values into equation (9.9) gives

$$M = 0.7959 \times 0.058636 \times 21.173 = 0.9881$$

The value of 0.9881 corresponds to a 1.2 % decrease in image size.

Thus, if the eye accommodated by 10 D while looking at the moon, the moon's image would decrease by only 1.2 %, showing that the retinal image size is remarkably stable with focus error.

9.2.3 THE USE OF ARTIFICIAL PUPILS

The results of this section 9.2 show that the effect of a focus error on retinal image size depends upon the position of the entrance pupil of the eye. In some experimental situations, the eye's natural pupil is dilated, and artificial pupils are placed close to the spectacle plane about 12–15 mm in front of the eye. The artificial pupil becomes the effective aperture stop and the entrance pupil of the eye, and its position and size affect the size of defocused images.

9.3 SIZE OF THE DEFOCUS BLUR DISC

9.3.1 THE GEOMETRICAL ABERRATION-FREE DEFOCUS BLUR DISC

Calculations of the diameter of the defocus blur disc, whether by physical or geometric optics, have traditionally used schematic eye models, e.g., Charman and Jennings (1976); Obstfeld (1982); van Meeteren (1974). These calculations use a schematic eye with a given refractive power and a specific pupil diameter. Appropriate rays are traced to the retina to determine the diameter of the defocus blur circle on the retina. The expected or perceived angular diameter of this blur disc is then found by calculating the angular diameter of the retinal image subtended at the back nodal point. This method has the disadvantage that schematic eyes are only specified in the relaxed or in a greatly accommodated state, usually about 10 D, and thus defocus calculations at other levels of accommodation are not readily found.

If the retinal image diameter is not required, the expected perceived angular diameter can be found by a very simple equation, which, although approximate, may be accurate enough for many circumstances. Smith (1982) showed two derivations of this equation, the second and simpler of which is presented here.

In Figure 9.4, an eye with its front principal plane at \mathbf{P} is focused on a plane at \mathbf{R} a distance l_R from \mathbf{P} . If the eye views a point \mathbf{O} at distance l while still focused on \mathbf{R} ,

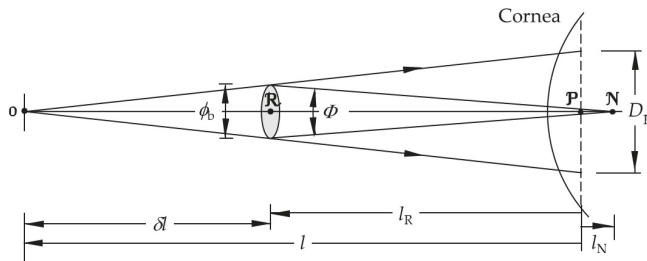


FIGURE 9.4 The formation of the perceived diameter of the defocus blur disc.

the point **O** appears as a blur circle or disc superimposed on the plane at **R**. The longitudinal focus error δl is

$$\delta l = l - l_R \quad (9.10)$$

and the physical linear diameter ϕ_b of the blur circle using similar triangles can be shown to be

$$\phi_b = D_p \delta l / l = D_p (l - l_R) / l \quad (9.11)$$

where D_p is the diameter of the beam at the principal planes. The expected perceived or visual angular diameter Φ of this disc must be measured at the front nodal point **N**, as shown in the figure. Thus,

$$\Phi = \phi_b / (l_N - l_R)$$

that is

$$\Phi = \frac{D_p (l_R - l)}{l (l_N - l_R)} \quad (9.12)$$

In terms of vergences, this equation can be written

$$\Phi = \frac{D_p (L - L_R)}{(1 - l_N L_R)} \quad (9.13)$$

There is a sign change here, but it is not important since the angle Φ corresponds to a diameter.

The beam diameter D_p is not in general the diameter D of the entrance pupil. The relation between these two quantities can be found by referring to Figure 9.5. From this figure, the two quantities are related by the equation

$$D = D_p (l - \bar{l}) / l$$

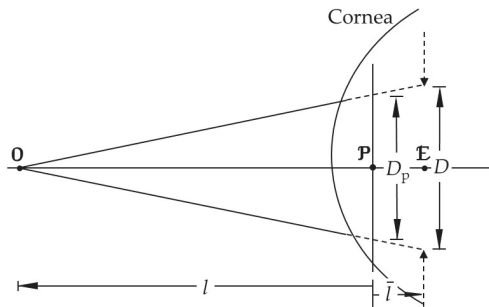


FIGURE 9.5 The difference between beam diameter at the front principal plane and the entrance pupil.

that is,

$$D_p = D / (1 - \bar{l}l) \quad (9.14)$$

where \bar{l} is the distance between the front principal plane and the entrance pupil. This distance depends upon the level of accommodation, and is 1.7 mm in the relaxed Gullstrand number 1 eye and 0.9 mm in the accommodated version. If D_p in equation (9.13) is replaced by D using equation (9.14), then

$$\Phi = \frac{D(L - L_R)}{(1 - \bar{l}l)(1 - l_N L_R)} \quad (9.15)$$

For low to medium levels of refractive error, we can make some useful approximations as follows:

1. If \bar{l} is neglected the fractional error is \bar{l}/l , and its value depends upon the level of accommodation and the distance l of the out-of-focus object. However, if this distance is infinite, the error is zero.
2. The quantity l_N can be neglected if the quantity $l_N L_R \ll 1$. While l_N depends upon the equivalent power of the eye and hence accommodation level, its value is about 5 mm. For a value of L_R of 10 D, the error induced in neglecting this term is about 5%, but for $L_R = 0$, the error is zero.

If we accept these two approximations, equation (9.15) reduces to

$$\Phi = (L_R - L)D \quad (9.16)$$

If $(L_R - L)$ is replaced by the focus error ΔL , the above equation can be re-expressed as

$$\Phi = \Delta L D \text{ radian} \quad (9.17)$$

which expresses the visual angular subtense Φ of the defocus blur disc in terms of the dioptric level of defocus ΔL and the pupil diameter D . Thus, within the limits of the approximations made in deriving this equation, the angular diameter of the defocus blur disc is independent of the constructional parameters of the schematic eye and the accommodation level.

If we express the pupil diameter in millimeters and defocus in diopters and Φ in minutes of arc, we have

$$\Phi = 3.483 \Delta L D_{\text{mm}} \text{ min. arc} \quad (9.17a)$$

Example 9.2: Calculate the defocus blur disc size for an object at infinity viewed by a 1 D uncorrected myopic eye with a 4 mm diameter pupil.

Solution: We substitute $\Delta L = 1$ and $D_{\text{mm}} = 4$ into equation (9.17a), to give

$$\Phi = 3.483 \times 1 \times 4 = 13.8 \text{ min. arc}$$

9.3.2 EXPERIMENTALLY DETERMINED ANGULAR DIAMETER OF THE BLUR DISCS

The accuracy of equation (9.17) relative to the more accurate equation (9.15) is shown in Figure 9.6, where we have plotted the values for a 4.2 mm diameter pupil and an eye focused at different distances but viewing a scene at infinity, i.e., $L = 0$. The values of \bar{l} and l_N are taken from the Gullstrand relaxed number 1 eye data in Appendix 3. The approximate equation gives values that are too high, but by only a few per cent.

Smith (1982) suggested that the perceived angular diameters of the blur discs can be measured using two small light sources, such as illuminated optical fibers, whose separation is adjustable. When these sources are defocused, they are seen as blur discs. The separation between the sources is varied until the two blur discs appear to just touch, and the angular diameter of one blur disc is then equivalent to the angular separation of the sources. At low defocus levels the blur disc takes on an irregular star-shaped pattern, which is due to ocular aberrations, making it difficult to locate the edge of the blur discs. At high levels of defocus, where the defocus dominates over the ocular aberrations, the defocus blur discs are more regular.

Chan et al. (1985) used this technique to test the accuracy of equation (9.17). Six observers were used, and since the differences between observers were small, the mean data are shown in Figure 9.6. The spectacle plane lens power was converted to an equivalent power at the front principal plane of the eye. There is good agreement between theory and measurements at intermediate levels of refractive error (3–9 D). However, at lower refractive errors the theoretical values are too low, while at higher refractive errors the theoretical values are too high. At the lower levels of refractive error, the discrepancy is because of the effects of ocular aberrations and diffraction, which give a wider spread of light than expected by aberration-free geometrical optics. At the higher levels of refractive error, the deviations can be explained by equation (9.17) being only approximate. The more accurate equation (9.15) agrees well with the measured values at these levels.

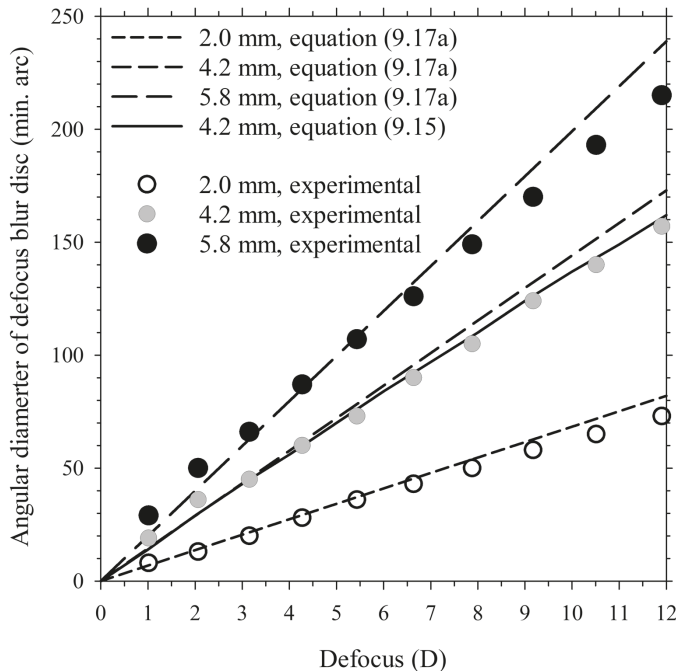


FIGURE 9.6 The diameter ϕ of defocused blur discs measured by Chan et al. (1985), corresponding values (full lines) predicted by the approximate equation (9.17a), and values for a 4.2 mm diameter pupil using the exact equation (9.15), with $L = 0$.

9.3.3 DEFOCUS RATIO

The level of defocus can be quantified by the diameter ϕ'_b of the defocus blur disc in the image and the diameter ϕ_b of the defocus blur disc in object space, or its corresponding angular size Φ . Alternatively, if we want to study the effect of a defocus on the visibility of an object of a certain size η , a more appropriate quantity is the defocus ratio, which we define by the equation

$$\text{Defocus ratio} = \phi'_b / \eta' = \phi_b / \eta \quad (9.18)$$

In angular terms in object or visual space we have

$$\text{Defocus ratio} = \Phi / \theta \quad (9.19)$$

where θ is the angular size of the object.

Example 9.3: Calculate the defocus blur ratio for the situation given in Example 9.2, if the eye is observing a 6/6 letter, i.e., one that subtends 5 min. arc.

Solution: Substitute $\Phi = 13.8$ min. arc and $\theta = 5$ min. arc into equation (9.19) to give

$$\text{Defocus ratio} = 13.8/5 = 2.76$$

9.4 OTHER EFFECTS OF DEFOCUS

9.4.1 ALIGNMENT OF TWO TARGETS AT DIFFERENT DISTANCES

In some visual experiments, the eye is aligned by asking the subject to subjectively align two targets at different distances. Figure 9.7 shows points Q_1 and Q_2 aligned along the visual axis (the line joining the fixation point and the foveal image by way of the nodal points). If these points are so aligned, do they appear superimposed in the visual field? In other words, are their retinal images superimposed? By analyzing the situation shown in Figure 9.7, we can deduce that the targets do not appear to be aligned. This shows the point Q_2 imaged, in focus, at Q_2' on the retina. The other point Q_1 is imaged in front of the retina at Q_1' and is therefore defocused at the retina. The retinal image of Q_1 is the defocus blur disc centered on the point Q_{1b}' , which is laterally displaced with respect to the in-focus image Q_2' . Therefore, while the two points are aligned along the visual axis, their retinal images are transversely displaced.

If the points are to appear superimposed, the two targets must lie along the paraxial pupil ray (i.e., the line of sight) rather than the visual axis.

9.4.2 EFFECT ON VISUAL ACUITY

Defocus reduces the quality of the retinal image and hence various aspects of visual performance. Uncorrected visual acuity correlates with refractive error. However, the correlation is not perfect, even after pupil size is taken into account (Atchison et al. 1979). The relationship has been quantified from time to time by various investigators fitting regression equations to clinical data. Perhaps the most common equation used is of the form

$$\log(A) = a + b \log(\Delta L) \quad (9.20)$$

where A is the (uncorrected) visual acuity as the minimum angle of resolution (angle specified in min. arc), ΔL is the refractive error (say in diopters), and a and b are

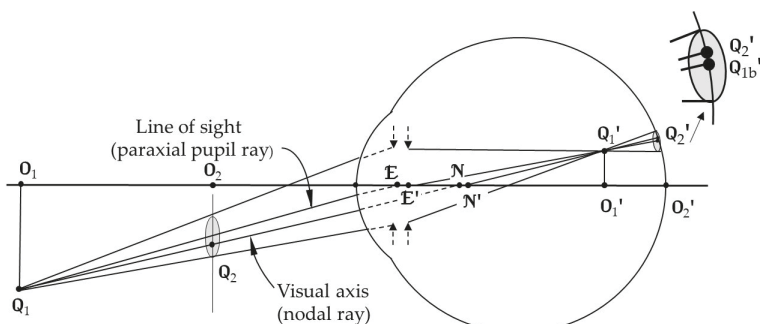


FIGURE 9.7 The alignment of two targets along the visual axis. Their retinal images are not superimposed, and hence they do not appear to be aligned.

constants. This equation is not based upon any theoretical optics justification. In contrast, an argument based upon the defocus blur circle model described in the preceding section suggests that the minimum angle of resolution should be linearly related to refractive error, except for low levels of refractive errors. Smith (1991) used the defocused blur disc concept and the optical transfer function to show that, for typical pupil diameters and for refractive errors greater than about 1 D, the expected relationship is a simple one of the form

$$A = kD\Delta L \quad (9.21)$$

where D is the pupil diameter and k is a constant whose value depends on the structure of the acuity target and the recognition rate, e.g., 50 per cent, 75 per cent, etc. For letters of the alphabet and a 50 per cent recognition rate, the value of k is approximately 650 for A in minutes of arc, D in meters, and ΔL in diopters (Smith 1996).

For low levels of defocus, aberrations and diffraction dominate the quality of the retinal image, but these factors are beyond the scope of the paraxial optics discussion of this chapter. The influence of these factors is considered in Chapter 18.

9.4.2.1 The Value of k and the Corresponding Defocus Ratio

From the above value of k , we can estimate the defocus ratio of alphabetical characters at the 50 per cent threshold of visibility.

The letter size is regarded as five times the minimum angle or detail in the letter. Using this value, transforming equation (9.21) to the threshold letter size H in radians gives

$$H = 5A = 5 \times 650 \times D\Delta L \times \pi / (180 \times 60) = 0.945 D\Delta L \text{ radians}$$

and since

$$\Phi = D\Delta L,$$

from equation (9.17) it follows that

$$\text{Defocus ratio} = \Phi/H = 1.06 \quad (9.22)$$

which indicates that a letter may be recognized at a 50 per cent success level when the defocus blur disc is about the same diameter as the letter height.

SUMMARY OF MAIN SYMBOLS

A	visual acuity in minutes of arc
D	entrance pupil diameter
D_p	equivalent beam diameter at the principal planes
F_e	equivalent power of eye focused on infinity
F_a	the power of the same eye at some level of accommodation
\bar{m}	ratio \bar{u}'/\bar{u} of angles that paraxial pupil ray subtends at axis in image and object space, respectively

l, l'	object and image distances from front and back principal planes, respectively
L	corresponding vergence of the distance l
ΔL	refractive error
l_{N}	distance of nodal point from principal plane
l_{R}	distance of object, conjugate with the retina, from principal plane
L_{R}	vergence corresponding to l_{R}
\bar{l}	distance of entrance pupil from front principal plane
η_{b}'	defocused image size at retina
η, η'	object and image sizes
θ	angular size of object
$\phi_{\text{b}}', \phi_{\text{b}}$	diameter of defocus blur disc on retina and its conjugate in object space
Φ	corresponding perceived angular diameter of defocus blur disc, measured at the nodal points (always positive)
E, E'	positions of entrance and exit pupils
N, N'	positions of front and back nodal points
O, O'	general object point and corresponding image point
P, P'	positions of front and back principal points
R, R'	axial retinal point and corresponding conjugate in object space

REFERENCES

- Atchison, D. A., G. Smith, and N. Efron. 1979. "The effect of pupil size on visual acuity in uncorrected and corrected myopia." *Am J Optom Physiol Opt* 56 (5):315–23. doi: 10.1097/00006324-197905000-00006.
- Chan, C., G. Smith, and R. J. Jacobs. 1985. "Simulating refractive errors: source and observer methods." *Am J Optom Physiol Opt* 62 (3):207–16.
- Charman, W. N., and J. A. Jennings. 1976. "The optical quality of the monochromatic retinal image as a function of focus." *Br J Physiol Opt* 31 (3):119–34.
- Marsh, J. S., and L. A. Temme. 1990. "Optical factors in judgments of size through an aperture." *Hum Factors* 32 (1):109–18.
- Obstfeld, H. 1982. *Optics in Vision*. 2nd ed. London: Butterworths.
- Pascal, J. I. 1952. "Effect of accommodation on the retinal image." *Br J Ophthalmol* 36 (12):676–8.
- Prince, J. H., and G. A. Fry. 1956. "The effect of errors of refraction on visual acuity." *Am J Optom Arch Am Acad Optom* 33 (7):353–73.
- Rosenfield, M., K. J. Ciuffreda, G. K. Hung, and B. Gilmartin. 1993. "Tonic accommodation: a review. I. Basic aspects." *Ophthalmic Physiol Opt* 13 (3):266–84. doi: 10.1111/j.1475-1313.1993.tb00469.x.
- Simpson, T. L., R. Barbeito, and H. E. Bedell. 1986. "The effect of optical blur on visual acuity for targets of different luminances." *Ophthalmic Physiol Opt* 6 (3):279–81. doi: 10.1016/0275-5408(86)90086-4.
- Smith, G. 1982. "Angular diameter of defocus blur discs." *Am J Optom Physiol Opt* 59 (11):885–9. doi: 10.1097/00006324-198211000-00006.
- Smith, G. 1991. "Relation between spherical refractive error and visual acuity." *Optom Vis Sci* 68 (8):591–8. doi: 10.1097/00006324-199108000-00004.
- Smith, G. 1996. "Visual acuity and refractive error. Is there a mathematical relationship?" *Optometry Today* 36(17):22–7.

- Smith, G., J. W. Meehan, and R. H. Day. 1992. "The effect of accommodation on retinal image size." *Hum Factors* 34 (3):289–301. doi: 10.1177/001872089203400304.
- van Meeteren, A. 1974. "Calculations on the optical modulation transfer function of the human eye for white light." *Optica Acta* 21 (5):395–412.
- Westheimer, G., and S. P. McKee. 1980. "Stereoscopic acuity with defocused and spatially filtered retinal images." *J Opt Soc Am* 70 (7):772–8. doi: 10.1364/JOSA.70.000772.



Taylor & Francis
Taylor & Francis Group
<http://taylorandfrancis.com>

10 Some Optical Effects of Ophthalmic Lenses

10.1 INTRODUCTION

When an eye is corrected by an ophthalmic lens as a spectacle or contact lens, aspects of the retinal image are changed as well as the image being focused. Most noticeably, the lens affects the size of the retinal image. This change in image size can be measured in two different ways. One of these is the *spectacle magnification*, which is the ratio of the image sizes after and before correction. The second, which is of limited use, is called *relative spectacle magnification*. This is the corrected or focused retinal image size compared with that of a “standard” eye. These magnifications are associated with other effects. For example, a positive power lens produces a magnified image and a blank part of the visual field called a *scotoma*. Image magnification of spectacle lenses is associated with prismatic effects and changes in the required eye rotation to look at an object, which is not on the lens optical axis. There are also effects on binocular vision. In anisometropia the two eyes are corrected by different lens powers, and differential effects between eyes, such as different amounts of eye rotations may produce eyestrain.

In this chapter we investigate some of these effects, but consider only thin lenses. While this leads to some approximation and inaccuracies, the equations are simple and readily show trends. We refer readers who want a full thick lens treatment to texts such as Jalie (2021).

Most of the equations in this chapter apply to both spectacle and contact lenses. Exceptions are the equations dealing with rotational magnification and field-of-view in section 10.5. The equations assume a rotating eye behind a fixed lens, which is not applicable for contact lenses, which rotate with the eye. Most of the effects described have much smaller magnitudes for contact lenses than for spectacle lenses, because of the small distance between contact lenses and relevant ocular reference positions, such as the entrance pupil.

The emphasis in the chapter is on spectacle lenses. Short descriptions of the optics of contact lenses and intraocular lenses are given in sections 10.8 and 10.9, respectively.

10.2 SPECTACLE MAGNIFICATION

Spectacle magnification SM is defined as

$$SM = \frac{\text{retinal image size after correction}}{\text{retinal image size before correction}} \quad (10.1)$$

An equivalent definition is

$$SM = \frac{\text{angular subtense of image in correcting lens at eye}}{\text{angular subtense of object at eye before correction}} \quad (10.1a)$$

In both cases, the pupil ray is used as the reference ray because it determines the center of the defocused image (neglecting aberrations).

The following equation is derived for spectacle magnification using Figure 10.1. An object of height η is at a distance q from the entrance pupil of the eye at E (Figure 10.1a). It subtends an angle ω at the entrance pupil of the eye, given by

$$\omega = \eta/q \quad (10.2)$$

In Figure 10.1b, a correcting lens of power F_s has been placed in front of the eye. The object is a distance l from the lens, and the eye's entrance pupil is a distance h_e from the lens. The object subtends an angle ϕ at the lens, given by

$$\phi = \eta/l \quad (10.3)$$

The image of the object in the lens has height η' and is a distance l' from the lens. From the figure, η' is given by

$$\eta' = \phi l' \quad (10.4)$$

Substituting the right-hand side of equation (10.3) for ϕ into equation (10.4) gives

$$\eta' = \eta l'/l \quad (10.5)$$

The angle ω' subtended by the image at the entrance pupil E is given by

$$\omega' = \eta'/(l' - h_e) \quad (10.6)$$

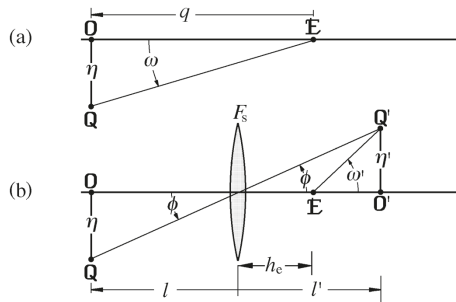


FIGURE 10.1 The optics of spectacle magnification and the angular size of the images. (a) The uncorrected eye looking at an object. (b) The eye looking at the object through a correcting spectacle lens.

Substituting the right-hand side of equation (10.5) for η' into equation (10.6) gives

$$\omega' = \eta l' / [l(l' - h_e)] \quad (10.7)$$

From the definition in equation (10.1a), SM is given by

$$SM = \omega'/\omega \quad (10.8)$$

Substituting the right-hand sides of equations (10.2) and (10.7) for ω and ω' , respectively, into equation (10.8) gives

$$SM = ql' / [l(l' - h_e)] \quad (10.8a)$$

If we replace l and l' by their corresponding vergences L ($= 1/l$) and L' ($= 1/l'$), we obtain

$$SM = qL / (1 - h_e L') \quad (10.8b)$$

Given that L is known, L' is found simply by the refraction equation $L' = L + F_s$. For the object at infinity, it can easily be shown that

$$SM = 1 / (1 - h_e F_s) \quad (10.8c)$$

Equations (10.8b) and (10.8c) can be extended to the thick lens case, with F now the equivalent power of the lens and L and L' determined relative to the front and back principal planes, respectively, of the lens.

Examination of equation (10.8c) shows the following:

1. For positive lens powers, spectacle magnification is greater than 1, i.e., the observed object is enlarged. For negative power lenses, spectacle magnification is less than 1.
2. The departure of spectacle magnification from a value of 1 is increased with increase in distance between the lens and the eye.

In ophthalmic optics, it is more convenient to measure the back vertex power rather than the equivalent power of a lens. For the object at infinity, it can be shown (see, for example, Jalie (2021)) that

$$SM = \frac{1}{1 - tF_1/n} \cdot \frac{1}{1 - h_{ve} F'_v} \quad (10.9)$$

where t is lens thickness, n is lens refractive index, h_{ve} is the distance between the lens back vertex and the eye's entrance pupil, F_1 is the front surface power of the lens, and F'_v is the back vertex power of the lens. This equation shows how SM is dependent on the parameters of the lens. The expressions $(1 - tF_1/n)^{-1}$ and $(1 - h_{ve} F'_v)^{-1}$ on the right-hand side of the equation are referred to as the shape factor and power factor, respectively.

Example 10.1: An object is 30 cm in front of the corneal vertex of the eye. A correcting thin lens of power -5 D is placed 12 mm in front of the eye. What is the spectacle magnification?

Solution: Refer the positions of the lens and the object to the entrance pupil of the eye. As this is approximately 3 mm inside the eye (3.05 mm for the Gullstrand number 1 relaxed eye),

$$q = -(0.3 + 0.003) = -0.303 \text{ m}$$

and

$$h_e = 0.012 + 0.003 = 0.015 \text{ m}$$

From Figure 10.1,

$$l = q + h_e = -0.303 + 0.015 = -0.288 \text{ m}$$

L is given by

$$L = 1/l = -1/0.288 = -3.472 \text{ D}$$

From the lens equation $L' = L + F$

$$L' = -3.472 - 5 = -8.472$$

Substituting the values obtained for q , h_e , L , and L' into equation (10.8b) gives

$$SM = (-0.303 \times -3.472)/[1 - (0.015 \times -8.472)] = 0.933$$

The object is perceived to be minified by 0.067 or 6.7 per cent by the spectacle lens.

Note: q and l (or L) are always negative if the object is not at infinity, and h_e is always positive.

Example 10.2: If the object in the previous example is now at infinity, what is SM ?

Solution: Using $h_e = 0.015$ and $F_s = -5 \text{ D}$, in equation (10.8c)

$$SM = 1/[1 - (0.015 \times -5)] = 0.930$$

The object is seen to be minified by 0.003 or 0.3 per cent relative to the previous example.

10.3 PUPIL POSITION AND MAGNIFICATION

Figure 10.2 shows the effect of the correcting ophthalmic lens on the position of the entrance pupil of the eye. The ray from the center of the actual entrance pupil is refracted by the lens, and the image of this entrance pupil (the new effective entrance pupil of the lens/eye system) is displaced from the original pupil and is also different

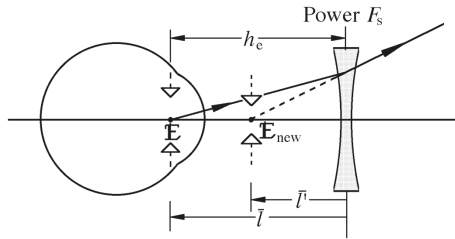


FIGURE 10.2 The effect of the correcting spectacle lens on pupil position and size.

in size. Application of the lens equation allows us to determine the new pupil position and the magnification.

The lens equation applied to the ray shown in Figure 10.2 is

$$\frac{1}{l'} - \frac{1}{l} = F_s \quad (10.10)$$

and solving for \bar{l}' gives

$$\bar{l}' = \bar{l} / (1 + \bar{l} F_s) \quad (10.11)$$

The magnification \bar{M} of the pupil defined as

$$\bar{M} = \frac{\text{new pupil diameter}}{\text{old pupil diameter}} \quad (10.12)$$

is given by the lens equation

$$\bar{M} = \bar{l}' / \bar{l}$$

and therefore

$$\bar{M} = 1 / (1 + \bar{l} F_s) \quad (10.13)$$

However,

$$\bar{l} = -h_e$$

with the negative sign present because h_e is always positive and \bar{l} is negative in the figure. It follows that

$$\bar{M} = 1 / (1 - h_e F_s) \quad (10.14)$$

The right-hand side expression is the same as that of the spectacle magnification given by equation (10.8c). Thus, pupil magnification is the same as spectacle magnification of a distant object.

10.3.1 RETINAL IMAGE ILLUMINANCE

The above equations show that, for positive power lenses, the effective entrance pupil is enlarged, and this allows an increase in the amount of luminous flux entering a system. The amount of luminous flux entering is proportional to the area of the pupil, and is thus proportional to the square of the pupil diameter – or, in this case, the increase is proportional to the square of the pupil magnification. However, this does not lead to a change in image brightness, because the image has the same magnification as the pupil, and the area of the retinal image changes by the same amount. Thus, the effects of spectacle magnification and pupil magnification on retinal illuminance cancel each other out. However, there is some light loss due to surface reflections of lenses without antireflection coatings (approximately 8 per cent for a lens with a refractive index of 1.5).

10.4 RELATIVE SPECTACLE MAGNIFICATION

Spectacle magnification does not tell this about the relative retinal image size of different eyes. This is covered by relative spectacle magnification RSM , which is the ratio of retinal image sizes for a correcting eye compared with that of a standard emmetropic eye. Setting this as an equation,

$$RSM = \frac{\text{retinal image size in the corrected ametropic eye}}{\text{retinal image size in a standard emmetropic eye}} \quad (10.15)$$

with both images in focus and when viewing the same object at the same distance. In this section, for simplification, it is assumed that the object is at infinity.

The in-focus image size η' of a distant object of angular subtense ω is given by equation (6.11), i.e.,

$$\eta' = \omega/F \quad (10.16)$$

where F is the power of the eye. Therefore,

$$RSM = F_e/F_t \quad (10.17)$$

where F_e is the equivalent power of the emmetropic eye, and F_t is the equivalent power of the combined system of the ophthalmic lens and ametropic eye. For the corrected ametropes,

$$F_t = F_a + F_s - h_p F_a F_s \quad (10.18)$$

where F_a is the equivalent power of the uncorrected eye, h_p is the distance between the back principal point of the ophthalmic lens and the front principal point of the ametropic eye, and F_s is the equivalent power of the correcting ophthalmic lens (Figure 10.3). Thus

$$RSM = \frac{F_e}{F_a + F_s - h_p F_a F_s} \quad (10.19)$$

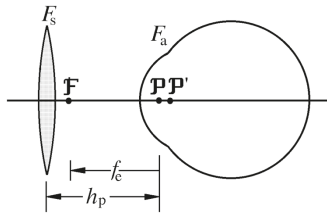


FIGURE 10.3 Parameters for calculation of relative spectacle magnification.

10.4.1 AXIAL AMETROPIA

If the difference between an uncorrected ametropic eye and the standard eye is the axial length only, they have the same powers. Substituting F_e for F_a in equation (10.19) gives

$$RSM = \frac{F_e}{F_a + F_s - h_p F_a F_a} = \frac{1}{1 - (h_p + f_e) F_s} \quad (10.20)$$

where f_e is the anterior focal length ($-1/F_e$) of the eye. Typical values of h_p are 15–20 mm, while $f_e = -16.67$ mm for an eye of power +60 D. If h_p is equal and opposite to f_e , the previous equation reduces to

$$RSM = 1 \quad (10.21)$$

This is *Knapp's law*, which states that an axially ametropic eye, with a correcting spectacle lens placed at its anterior focal point, has the same retinal image size as that of a standard emmetropic eye.

10.4.2 REFRACTIVE AMETROPIA

If the length of an uncorrected ametropic eye is the same as that of the standard eye, their powers must be different. The effective power of the ophthalmic lens at the eye, together with the power of the ametropic eye, is the same as that of the standard eye, that is

$$F_e = F_s / (1 - h_p F_s) + F_a = (F_a + F_s - h_p F_a F_s) / (1 - h_p F_s) \quad (10.22)$$

Substituting the right-hand side of this equation for F_e into equation (10.19) gives, after some simplification

$$RSM = 1 / (1 - h_p F_s) \quad (10.23)$$

RSM is now similar to the spectacle magnification given by equation (10.8c), except that the distance between the lens and the entrance pupil of the eye has been replaced by the distance between the lens and the front principal plane of the eye. The difference in positions of the entrance pupil and the front principal plane is approximately

1.5 mm (1.70 mm for the Gullstrand number 1 relaxed eye). There is an error with the equation because the principal points of the refractive ametropic eye are not exactly the same as those of the standard eye, but this is small enough to disregard.

10.4.3 FURTHER COMMENTS

Relative spectacle magnification may be applied to a comparison of fellow eyes, neither of which need be a “standard emmetropic eye”.

The concept of relative spectacle magnification has limited use for three reasons:

1. It is not always known whether the ametropia is axial or refractive. The distinction is useful for anisometropia known to be caused by differences in a single parameter, for example axial length.
2. The concept of a standard emmetropic eye power is of limited value. The power of an emmetropic eye can vary over a wide range (Sorsby et al. 1957). This is unimportant in cases of anisometropia, where the ratio of the relative spectacle magnifications of the two eyes does not even require a definition of a standard eye.
3. The relative spectacle magnification difference in anisometropia is not necessarily a good indicator of the likelihood of magnification problems. A good example of this is axial anisometropia – spectacles may provide equal retinal image sizes according to Knapp’s law, but this does not mean that the brain’s cortical images are the same sizes. A stretching of the retina that may accompany elongation of the eye in myopia may move the retina’s receptors further apart. Alternatively, there may be “rewiring” occurring between the retina and the brain. Some evidence for these possibilities was provided by Winn et al. (1988), who measured *aniseikonia*, which is a measure of differences in cortical image sizes (section 6.4.2), in myopic axial anisometropes. They found smaller aniseikonia with contact lenses, for which $RSM > 1$, than for spectacle lenses, which would be expected to have RSM values close to 1 as in equations (10.20) and (10.21).

Atchison (1996) developed further equations that give relative retinal image sizes of a pair of corrected eyes. These are useful in calculations involving anisometropia and/or refractive surgery.

10.5 EFFECTS ON FAR AND NEAR POINTS AND ACCOMMODATIVE DEMAND

The farthest and closest distances of clear vision are called the far point and near point, respectively. These positions are different for the eye–ophthalmic lens system than for the uncorrected eye alone. The accommodative demand, that is, the amount of accommodation required to focus clearly to an object, is also affected by a correcting ophthalmic lens.

For correcting distance vision, the far point of the eye–ophthalmic lens system is placed at infinity. Consider what happens to the near point. Figure 10.4 shows

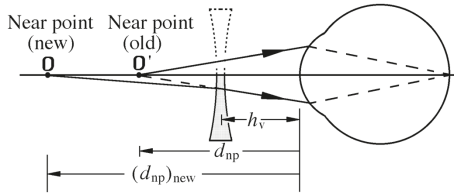


FIGURE 10.4 The effect of the correcting lens on the near point.

a spectacle lens imaging a point \mathbf{O} to \mathbf{O}' . Take the point \mathbf{O} to be the near point of the uncorrected eye. The object and image distances can be related using the lens equation. For the situation shown in Figure 10.4, the lens equation is

$$\frac{1}{d_{np} + h_v} - \frac{1}{(d_{np})_{\text{new}} + h_v} = F_s \quad (10.24)$$

where d_{np} and $(d_{np})_{\text{new}}$ are the near point distances in uncorrected and corrected vision respectively, F_s is the lens power and is assumed to be a function of position, and h_v is the distance from the lens to the corneal vertex. Solving for $(d_{np})_{\text{new}}$,

$$(d_{np})_{\text{new}} = \frac{d_{np} + h_v}{1 - (d_{np} + h_v)F_s} - h_v \quad (10.25)$$

This equation (and Figure 10.4) shows that negative ophthalmic lenses push the effective near point of myopes away from the eye. For positive power lens and hyperopes, the near point comes closer to the eye.

10.5.1 ACCOMMODATION THROUGH A CORRECTING LENS

The presence of an ophthalmic lens in front of the eye changes the apparent position of the object and therefore changes the accommodative demand. In equation (10.25), we replace d_{np} and $(d_{np})_{\text{new}}$ by general distances ω and ω' respectively. If we then replace these distances by their corresponding vergences W and W' , we can obtain

$$W' = \frac{(1 + h_v W) + w}{1 - h_v F_s - h_v^2 h_v F_s W} \quad (10.26)$$

Now the effective spectacle refraction at the corneal vertex F_{so} is given by

$$F_{so} = \frac{F_s}{1 - h_v F_s} \quad (10.27)$$

The *ocular accommodative demand* $A(W)$, referenced to the corneal vertex, is simply

given by

$$A(W) = F_{\text{so}} - W \quad (10.28a)$$

which can be shown to be

$$A(W) = \frac{-W}{(1 - h_v F_s)(1 - h_v F_s - h_v^2 F_s W)} \quad (10.28b)$$

Sometimes the accommodative demand is referred to the spectacle lens plane. In this case, we can set h_v to zero and replace W in the above equation by L , which is the vergence of the object relative to the spectacle plane. We then have the spectacle accommodative demand $A(L)$, which is

$$A(L) = -L \quad (10.28c)$$

Hence, the *spectacle accommodative demand* is simply the absolute value of the inverse of the distance of the object from the lens.

Example 10.3: An eye looks at an object 30 cm away through a distance correction of -5 D placed 12 mm in front of the cornea. What are the ocular and spectacle accommodative demands?

Solution: We can make the following substitutions into equation (10.28b):

$$W = -1/0.3 = -3.333 \text{ D}, h_v = 0.012 \text{ m}, \text{ and } F_s = -5 \text{ D}$$

to give the ocular accommodative demand as

$$A(W) = \frac{3.333}{[1 - 0.012(-5)][1 - 0.012(-5) - 0.012^2(-5) \times (-3.333)]} = 2.97 \text{ D}$$

The object is a distance $-(0.3 - 0.012) = -0.288 \text{ m}$ away from the lens, which makes the object vergence relative to the lens

$$L = -1/0.288 = -3.47 \text{ D}$$

from which, using equation (10.28c), the spectacle accommodative demand is

$$A(L) = 3.47 \text{ D}$$

If we repeat the above exercise for a $+5 \text{ D}$ lens, we obtain an ocular accommodative demand of 3.76 D . This tells us that corrected hyperopes have greater ocular accommodative demands than corrected myopes. Thus, all other things being equal, corrected hyperopes experience presbyopia earlier in life than corrected myopes.

10.6 ROTATION MAGNIFICATION, FIELD-OF-VIEW, AND FIELD-OF-VISION

10.6.1 ROTATIONAL MAGNIFICATION

The magnification effect of ophthalmic lenses influences the eye's rotation to look at off-axis objects of regard. We quantify this by the *rotational magnification*, which we define as

$$R_o M = \frac{\text{angle of rotation of eye looking through the lens } (\theta')}{\text{angle of rotation of eye without lens } (\theta)} \quad (10.29a)$$

This is like determining spectacle magnification (SM) at the beginning of this chapter, except that the ocular reference point is the center-of-rotation rather than the entrance pupil. In line with equation (10.8b), $R_o M$ is given by

$$R_o M = q_c L / (1 - h_c L') \quad (10.29b)$$

where q_c is the distance from the object to the center-of-rotation of the eye, and h_c is the distance from the spectacle lens to the center-of-rotation. Because h_c is approximately twice the value of h_e in equation (10.8b), values of $R_o M$ are much further from 1 than are values of SM . For the object at infinity, it can easily be shown that

$$R_o M = 1 / (1 - h_c F_c) \quad (10.29c)$$

10.6.2 FIELD-OF-VIEW

Apparent and *real fields-of-view* are shown for positive and negative power lenses in Figure 10.5. The apparent field-of-view is the maximum ocular rotation θ'_{\max} of the eye, about its center-of-rotation C , for which the eye can look through a lens at an object of regard. The real field-of-view is given by the angle θ_{\max} . From Figure 10.5, the apparent field-of-view is

$$\theta'_{\max} = D_s / (2h_c) \quad (10.30)$$

Combining equations (10.29) and (10.29a), but using θ_{\max} and θ'_{\max} instead of θ' and θ , gives the equation

$$\theta_{\max} = \theta'_{\max} (1 - h_c L') / (q_c L) \quad (10.31a)$$

Substituting the right-hand side of equation (10.30) for θ'_{\max} into equation (10.31a) gives

$$\theta_{\max} = D_s (1 - h_c L') / (2h_c q_c L) \quad (10.31b)$$

For a distant object, this equation reduces to

$$\theta_{\max} = D_s (1 - h_c F_s) / (2h_c) \quad (10.31c)$$

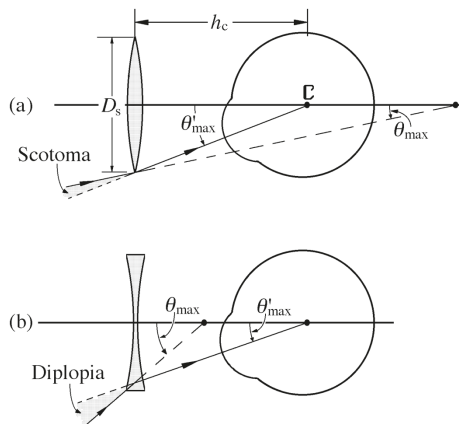


FIGURE 10.5 Real and apparent fields-of-view. (a) Hyperopia corrected with a positive powered lens. (b) Myopia corrected with a negative powered lens.

Comparing the last equation with equation (10.30) shows clearly that the real field-of-view is less than the apparent field-of-view for positive lens powers (corrected hyperopia). This gives a scotoma (blind area) of magnitude ($\theta'_{\max} - \theta_{\max}$) in the field-of-vision (Figure 10.5a). This can be a considerable problem for moderate and high power hyperopes.

The real field-of-view is greater than the apparent field-of-view for negative lens powers (corrected myopia). This gives a region of diplopia (double vision) of magnitude ($\theta_{\max} - \theta'_{\max}$) in the field-of-vision (Figure 10.5b), but this does not seem to inconvenience corrected myopes.

As these are first order equations, which ignore the influence of the aberration distortion on the real field-of-view, we caution their use with large angles.

10.6.3 FIELD-OF-VISION

This is like field-of-view, except that the eye is stationary and looking through the center of the lens. Limits correspond to the field seen by the periphery of the eye through the lens. A similar set of equations to equations (10.30)–(10.31c) apply, except that we revert to using the distances q and h_e , that were used for the spectacle magnification calculations in section 10.2, instead of q_c and h_c .

10.7 SPECTACLE LENS DESIGN

The following is an overview of the design of spectacle lenses and does not consider multifocal and progressive lenses for the correction of presbyopia. Jalie (2021) has provided an extensive and advanced treatment.

When an eye rotates behind a spectacle lens to look at objects of interest off the lens optical axis, considerable aberrations can be produced. These arise because of the oblique incidence of light at the lens surfaces and take the form of unwanted

power errors and transverse chromatic aberration. These aberrations are affected by the shape of the lenses (i.e., the relative curvatures of front and back surface powers and the asphericities of the surfaces), the refractive index and chromatic dispersion of lens materials, and the fitting characteristics of the lenses in front of the eye. Because we are always concerned with foveal vision and higher-order aberrations such as coma and spherical aberration produced by the lenses are negligible, we can largely leave the eye out of consideration.

Figure 10.6 shows a simple setup for a positive powered lens in front of a hyperopic eye. The eye's center-of-rotation is necessary and is often taken about 13.5 mm behind the cornea. The far point of the eye rotates about this point in all meridians to form a *far point sphere* (for a near object there would be a corresponding near sphere). Thin beams of rays, called pencils, are traced from an off-axis position of interest to pass through the center-of-rotation. Ideally the light would be focused on the far point sphere, but this is not possible and errors must instead be minimized. A pencil is refracted differently in different meridians. The light refracted in the tangential section (Figure 10.7), containing the optical axis and the chief ray, which passes through the center-of-rotation, comes to a different focus than light that is refracted in the sagittal section at right angles to it. At the front surface of the lens, the "Coddington" refraction equations are

$$\frac{n \cos^2 I'_1}{t'_1} - \frac{\cos^2 I_1}{t_1} = (n \cos I'_1 - \cos I_1) c_1 \quad (10.32a)$$

$$\frac{n_1}{s'_1} - \frac{1}{s_1} = (n \cos I'_1 - \cos I_1) c_1 \quad (10.32b)$$

where t_1 and t'_1 are the distances along the chief ray of the object and image conjugates relative to the first surface for the tangential equation, s_1 and s'_1 are corresponding quantities for the sagittal equation, 1 and n are object (air) and image (lens medium) refractive indices of the surface, c_1 is surface curvature, and I_1 and I'_1 are the angles of incidence and refraction of the chief ray at the surface. After

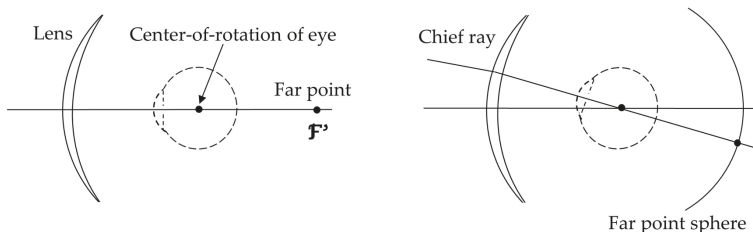


FIGURE 10.6 Basis of conventional spectacle lens design (not to scale). The left part shows a hyperopic eye in its primary position looking through the lens center; the far point of the eye is at \mathbf{F}' . The right side shows the far point rotating about the eye's center-of-rotation to form the far point sphere.

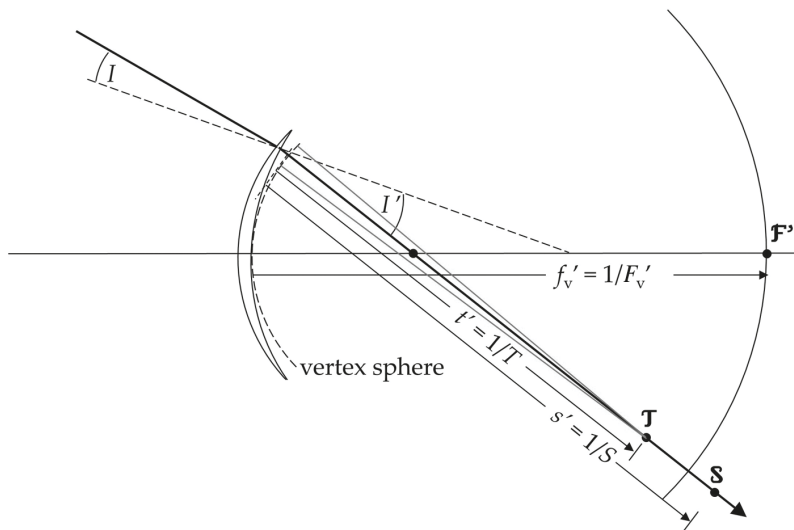


FIGURE 10.7 Tangential section showing convergence of beam towards the tangential focus at \mathbf{T} . The position of the \mathbf{S} focus is also shown. I and I' are the angles of incidence and refraction at the back surface of the lens.

refraction at the front surface, there is a transfer to the back surface, and the refraction equations there are

$$\frac{\cos^2 I'_2}{t'_2} - \frac{n \cos^2 I_1}{t_2} = (\cos I'_2 - n \cos I_2) c_2 \quad (10.33a)$$

$$\frac{1}{s'_2} - \frac{n}{s_2} = (\cos I'_2 - n \cos I_2) c_2 \quad (10.33b)$$

The same symbols are used as for the front surface, except that the subscript “2” is used for the back surface. There is then a transfer to the vertex sphere, which intersects the back vertex of the lens and is centered at the center-of-rotation. The inverses of t' and s' , given as T and S , are obtained and their magnitudes are compared with the back vertex power F'_v of the lens. Tangential and sagittal power errors are

$$\Delta T = T - F'_v \quad (10.34)$$

$$\Delta S = S - F'_v \quad (10.35)$$

Different combinations of these power errors can be obtained, such as eliminating their difference, which is referred to as eliminating *oblique astigmatism OA*:

$$OA = \Delta T - \Delta S = T - S = 0 \quad (10.36)$$

Another combination is to make the average of power errors the same as the back vertex power, which is referred to as eliminating *mean oblique error MOE*:

$$MOE = (T + S)/2 - F_v' = (\Delta T + \Delta S)/2 = 0 \quad (10.37)$$

Solutions provide meniscus shaped lenses with the concave surface facing the eye. Solutions for oblique astigmatism are more curved (bent) than those for mean oblique error. When the transverse chromatic aberration is considered in lens design, the tangential power error tends to be well corrected.

The major design variable for spherical spectacle lenses is the relative powers of the two surfaces, and these are selected to give the best compromise over variables that include vertex distance, object distances, off-axis angles, and pantoscopic tilt (usual tilt of lenses in the vertical meridian). Lenses designed according to such principles are described as *corrected curve* or *best form* lenses.

By using approximate raytracing with “third-order” theory and for which lenses are assumed to be thin, the tangential and sagittal power errors (and their derivations) become quadratic functions of either of the surface powers. While this approach is not used for designing actual lenses, it is useful for showing approximate solutions, such as to eliminate oblique astigmatism. For any lens power, there are either two solutions of surface power, no solutions, or two equal solutions. When lens power is plotted against surface power, these solutions lie on oblique ellipses called *Tscherning ellipses* (Figure 10.8).

The above treatments have considered only spherical powered lenses, but can be expanded to consider the principal meridians of spherocylindrical lenses.

The lack of design variables means that the designer is restricted in what can be achieved. For examples, good optical results are not possible for high positive powers (Figure 10.8) or good optical results may be accompanied by poor cosmetic forms. To overcome this, one or both surfaces can be aspherized, such as into conicoids (section 2.2.4.2). Using conicoids for one surface means that approximate power errors become cubic functions of lens shape, which means at any lens power there is always at least one solution of the back surface power, and up to three, to eliminate the error (Smith and Atchison 1983; Atchison 2021). In the Coddington equations (10.32) and (10.33), the surface curvature c would be replaced by off-axis tangential and sagittal curvatures c_t and c_s , respectively. Before the widespread use of intraocular lenses, this was applicable to high powered positive spectacle lenses used after cataract removal, as without surface aspherizing these had high off-axis powers. Aspherizing can also be applied to lower lens powers to allow flatter, more cosmetically appealing forms without sacrificing good quality peripheral optics.

As mentioned at the start of this section, the lens design discussed here is relevant to foveal vision. Lenses can also be designed to correct (or otherwise modify) peripheral vision in which the eye is assumed to be stationary and fixating along the lens optical axis (Atchison 2006, 2011). Hence the stop of the system becomes the entrance pupil of the eye rather than the center-of-rotation of the eye. The peripheral refractive errors of the eye (see Chapter 15) should be considered in such designs.

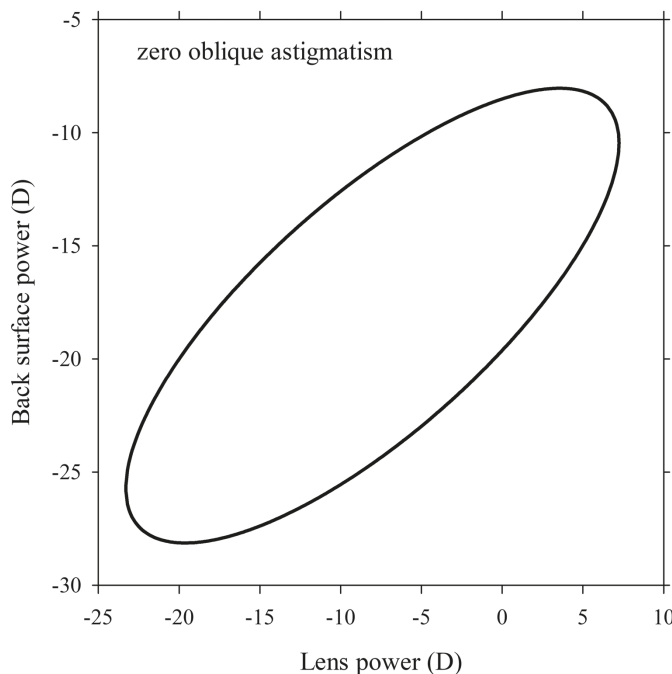


FIGURE 10.8 Tscherning ellipse for zero oblique astigmatism (parameters: distance object, refractive index 1.5, distance from vertex sphere to center-of-rotation 27 mm). The top, flatter Ostwalt form is the basis for lens shapes rather than the bottom, steeper Wollaston form. Lens power limits for solutions are -23.3 D and +7.2 D.

10.8 CONTACT LENS OPTICS

The following is a brief introduction to the optics of contact lenses. Fuller details can be found in texts such as Douthwaite (2006). As for the spectacle lenses in the previous section, no account is given of presbyopic corrections. A contact lens sits on the eye rather than in front of it as do spectacle lenses. This produces several changes to the optics, including

- magnification and prismatic effects are minimal;
- large field-of-view;
- different powers may be required because the vertex distance is minimal and because of the effect of the tear film under the contact lens (known also as the fluid lens);
- the lenses move with the eyes so the off-axis aberrations of spectacle lens associated with foveal vision (section 10.7) are unimportant for contact lenses; and
- because of the highly curved surfaces, higher-order aberrations can be considerable, even at low powers.

There are two broad classes of contact lenses – soft (flexible) and hard (rigid). Most lenses are soft lenses. The back surface of a soft contact lens conforms to some degree to the underlying anterior cornea, with corresponding changes occurring at the anterior surface. Thus the lens is considered to wrap to the cornea, although to what extent this occurs is not fully understood, particularly in highly aspheric lenses designed to correct presbyopia or to treat myopia progression (Jaisankar et al. 2020). Hydration variations and non-uniformities in the fluid under the lens can affect effective lens power (Charman 2018). To correct astigmatism, a toric lens needs some stabilization, such as with prism-ballast.

The fluid lens associated with hard contact lenses has an important contribution to the eye correction; accordingly the emphasis in this section is on the hard contact lenses.

The effective power of a hard contact lens on the eye may be very different from its power in air. The effective power is a combination of front surface power, back surface power, and fluid lens power. Lens thicknesses that might be ignored for spectacle lenses cannot be ignored for contact lenses because of the high powers of contact lens surfaces.

In what follows, a three-surface model is used consisting of the two contact lens surfaces and the back surface of the fluid lens, which has the same shape as the front surface of the cornea (Figure 10.9). Air is placed after the tear film to make it separate from the eye. In some treatments, a thin air layer is placed between the lens and the fluid lens as well as between the fluid lens and the cornea, and enables determination of the fluid lens power. The refractive index of the tear film and cornea are assumed to be 1.336 and 1.376, respectively. Like the case for spectacle lens design, the contact lens optics can be considered largely in isolation from the eye, at least in the simple treatments described here.

Example 10.4: What is the back vertex power of a contact lens in air and what is its effective power on the eye? Lens anterior and posterior radii of curvature are 8.1 mm and 7.9 mm, respectively, the anterior corneal power is 48 D, lens

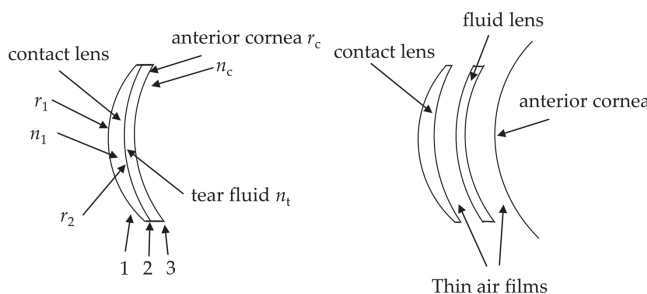


FIGURE 10.9 The modeling used for a hard contact lens on the eye. A three-surface model is shown on the left, consisting of front and back surfaces of the contact lens and the back surface of the tear film (whose curvature matches that of the anterior cornea). The right side shows a variation of this model to determine the fluid lens power by itself.

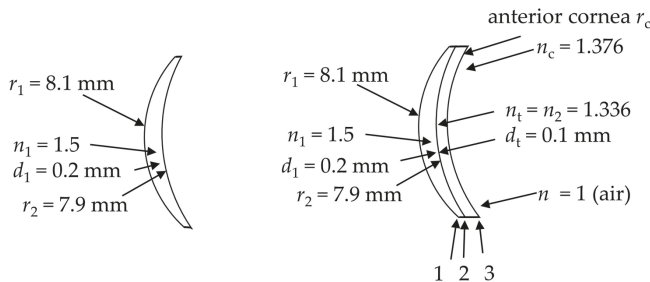


FIGURE 10.10 The setup for Example 10.4. (left) lens in air, (right) lens with tear film.

thickness is 0.2 mm, tear film thickness is 0.1 mm, and refractive indices are 1.5 (lens), 1.336 (tear film), and 1.376 (cornea). [See Figure 10.10.]

Solution: For the lens in air, the power of the front surface is

$$F_1 = (n_1 - 1)/r_1 = (1.5 - 1.0)/0.0081 = +61.7284 \text{ D}$$

The power of the back surface is

$$F_2 = (1 - n_1)/r_2 = (1.0 - 1.5)/0.0079 = -63.2911 \text{ D}$$

The effective power of the front surface at the back surface is

$$L_2 = F_1/(1 - d_1 F_1/n_1) = 61.7284/(1 - 0.0002 \times 61.7284/1.5) = +62.2407 \text{ D}$$

Back vertex power is

$$F_v' = L_2 + F_2 = +62.2407 - 63.2911 = -1.0504 \text{ D}$$

For the effective power of the lens on the eye, the power of the front surface is

$$F_1 = (n_1 - 1)/r_1 = (1.5 - 1.0)/0.0081 = +61.7284 \text{ D} \text{ (as above)}$$

The power of the back surface is

$$F_2 = (n_2 - n_1)/r_2 = (1.336 - 1.5)/0.0079 = -20.7595 \text{ D}$$

At this point we need the anterior radius of curvature of the cornea. This is given by

$$R_c = (n_c - 1)/48 = (1.376 - 1.0)/48 = +0.007833 \text{ m}$$

The surface power at the back of the tear film is

$$F_3 = (1.0 - n_2)/r_c = (1.0 - 1.336)/0.007833 = -42.895 \text{ D}$$

To work out the effective power of the contact lens, some simple raytracing is required.

$$L_2 = +62.2407 \text{ D} \text{ (as for the lens in air)}$$

$$L_2' = L_2 + F_2 = +62.2407 + -20.7595 = +41.4812 \text{ D}$$

$$L_3 = L_2'/(1 - d_1 L_2'/n_2) = +41.4812/(1 - 0.0001 \times 41.4812/1.336) = +41.6104 \text{ D}$$

$$F_v' = L_3' = L_3 + F_3 = +41.6104 + -42.895 = -1.28 \text{ D}$$

For this example, F_v' in air is -1.05 D, while its effective power on the eye is -1.28 D. The 0.23 D difference is a consequence of the difference between the radii of curvature of the posterior contact lens surface and the anterior cornea. Note that because of the importance of the fluid lens, it is possible to have a contact lens with zero power in air, which has considerable effective power on the eye.

As contact lens surfaces usually have optical components outside of which the surface curvature may change to enhance the fitting, the terms front optic zone radius (FOZR) and back optic zone radius (BOZR) are often used clinically rather than front and back surface radii of curvature.

10.8.1 OVER-REFRACTION

In clinical practice for hard contact lenses, trial contact lenses are put on the eye. When a good fit is obtained (back surface of the contact lens is a good match to the eye), the over-refraction is determined and a lens with the appropriate front surface is ordered.

Example 10.5: A trial lens contact lens of plano (zero) power in air is fitted to the eye. If its front surface radius of curvature is 7.7 mm, refractive index is 1.5 , lens thickness is 0.2 mm, and the over-refraction is -3.00 D at a 14 mm vertex distance, what should be the front surface radius of curvature of the prescribed contact lens in the same thickness? [See Figure 10.11.]

Solution: The front surface power of the trial contact lens is

$$F_1 = (n_1 - 1)/r_1 = (1.5 - 1.0)/0.0077 = +64.9351 \text{ D}$$

The effective power of the over-correction at the front surface of the contact lens is, correcting the vertex distance for the thickness of the lens,

$$-3/[1 - 0.0138 \times (-3)/1.0] = -2.8807 \text{ D}$$

Refraction at the front surface of the contact lens gives

$$L_1' = L_1 + F_1 = -2.8807 + 64.9351 = +62.0544 \text{ D}$$

This is the new front surface power that is wanted for the prescribed contact lens. The front surface radius of curvature is given by

$$r_1 = (n_1 - 1)/F_1 = (1.5 - 1)/62.0544 = +0.008057 \text{ m (or } +8.06 \text{ mm)}$$

In Example 10.5, little raytracing has been required. The situation becomes more complicated if the lens to be ordered has a different back surface radius of curvature than the trial lens.

10.8.2 FLUID LENS

The fluid lens neutralizes most of the corneal toricity. Provided that most of the astigmatism of the eye is due to the anterior cornea, which is common, it can be corrected

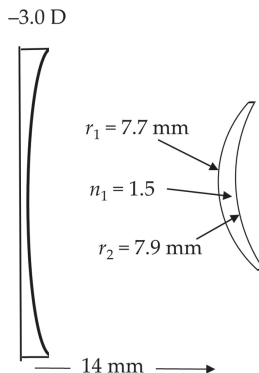


FIGURE 10.11 The setup for Example 10.5 showing an over-refraction lens of power -3.00 D combined with a trial lens of zero power in air.

for astigmatism within about 2 D without requiring a toric shape as is necessary for soft contact lenses. Denoting the principal meridians of the cornea as having radii of curvature r_{c1} and r_{c2} , the cornea has astigmatism of

$$(1.376 - 1.0)/r_{c1} - (1.376 - 1.0)/r_{c2}$$

and the fluid lens back surface has astigmatism of

$$(1.0 - 1.336)/r_{c1} - (1 - 1.336)/r_{c2}$$

Thus, the percentage of astigmatism neutralised by the tear film is

$$(1.336 - 1)/(1.376 - 1) \times 100 = 89 \%$$

Example 10.6: A cornea has radii of curvature of 7.8 mm along 180 and 8.0 mm along 90. How much of the corneal astigmatism is neutralized by the tear film under a contact lens?

Solution: The astigmatism of the cornea is given by

$$(1.376 - 1)/0.0078 - (1.376 - 1)/0.0080 = 48.3051 - 47.000 = 1.2051 \text{ D}$$

so the amount that is neutralized is

$$1.2051 \times 0.336/0.376 = 1.0769 \text{ D} = 1.08 \text{ D}$$

Example 10.7: In example 10.6, if the fluid lens thickness is 0.2 mm and the back surface of a correcting contact lens has radius of curvature 8.0 mm, what is the power of the fluid lens? [See Figure 10.12.]

Solution: In this situation we consider a thin layer of air to be between the contact lens and the fluid lens as well as between the fluid lens and the eye (Figure 10.9, right).

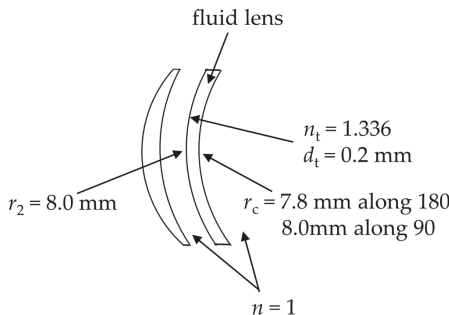


FIGURE 10.12 The setup for Example 10.7.

The front surface power of the tear film is

$$(n_t - 1)/r_2 = 0.336/0.008 = +42.000 \text{ D}$$

and its back surface powers are

$$\begin{aligned} (1 - n)/r_c &= -0.336/0.0078 \text{ along } 180, -0.336/0.008 \text{ along } 90 \\ &= -43.078 \text{ D along } 180, -42.000 \text{ D along } 90 \end{aligned}$$

Back vertex power is

$$\begin{aligned} F_v' &= F_1/(1 - d_t F_1/n_t) + F_2 \\ &= 42.2657 + -43.078 = -0.8123 \text{ D along } 180, \\ &\quad 42.2657 + -42.000 = +0.2657 \text{ D along } 90 \\ &= -0.81 \times 90/+0.27 \text{ D } \times 180 \end{aligned}$$

10.8.3 SPECTACLE MAGNIFICATION

As mentioned at the start of section 10.8, spectacle magnification with contact lenses is small. Considering equation (10.9), it can be seen that this occurs because of the small, approximately 3 mm distance h_{ve} between contact lenses and the entrance pupil of the eye, and the small thickness, about 0.2 mm maximum, of contact lenses. Figure 10.13 contrasts the spectacle magnification differences between the contact lenses and spectacles.

10.9 INTRAOCULAR LENS OPTICS

Intraocular lenses (IOLs) date back to the early 1950s (Ridley 1952). An intraocular lens (IOL) is a lens implanted in the eye as part of treating cataracts, high myopia, or hyperopia (Alshamrani and Alharbi 2019). The first is the most common type and is discussed in this section. In high myopia and in hyperopia, IOLs are placed next to the existing natural lens.

The optics associated with IOLs are very different from those of spectacle lenses and contact lenses because they are located within the eye. Thus, any treatment of the optics of IOLs must always consider the optics of the rest of the eye, including internal distances, refractive indices, and corneal surface powers. Unlike spectacle lenses, but in common with contact lenses, they move with the eye. Like contact

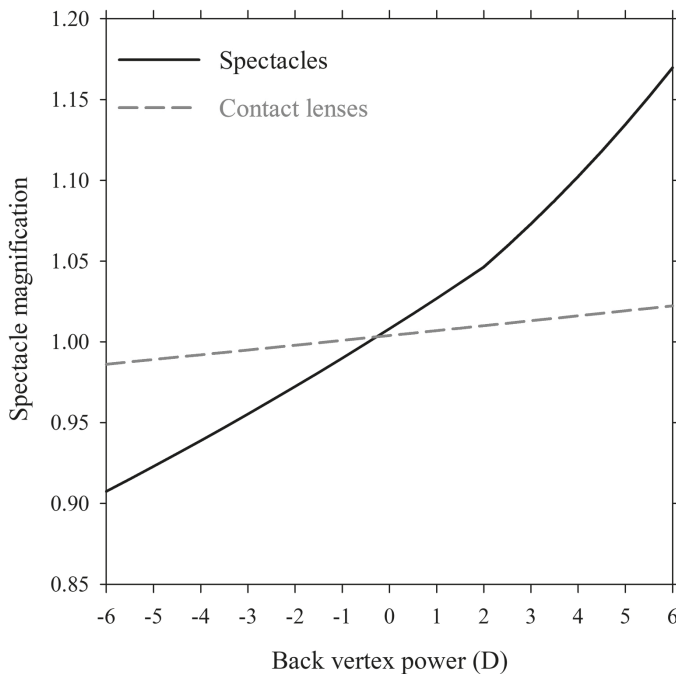


FIGURE 10.13 Spectacle magnification of contact lenses and spectacle lenses. For contact lenses, $n = 1.43$, $t = 0.10$ mm, $F_1 = 55.13$ D, $h_{ve} = 3.0$ mm, and tear film is ignored. For spectacle lenses, $n = 1.5$, $h_{ve} = 17$ mm. $t = 2.0$ mm if $F'_v < +2$ D, t in mm for other positive lenses is the same as F'_v in diopters, $F_1 = F'_v + 6$ D. Symbols are those used in equation (10.9).

(lenses, IOLs overcome many of the problems produced by high positive powered spectacle lenses worn following the removal of the natural lens because of cataract: weight, poor cosmesis, high spectacle magnification, high off-axis power errors, and restricted visual field through the lenses accompanied by scotomas that move with eye rotation.

Much effort with IOLs and the associated surgery has gone into improving the prediction of power so that the need for spectacles to correct residual refractive errors is reduced. Nowadays, most lenses are made of soft, foldable materials that can be placed (often injected) through small holes near the edge of the cornea and spring open in the intact capsule to be held in place by struts called haptics. As surgery has improved, the interference with the eye has diminished (apart from obviously the replacement of one lens by another).

Early on in IOL history, most lenses had the same power, such as 18 D for anterior chamber placement, with the assumption of retaining the refractive error before cataract development. This was followed by a correction for refractive error such as in the equation

$$F = 18 + 1.25R_e \quad (10.38)$$

where R_e is the pre-existing refractive correction, referenced to the corneal plane.

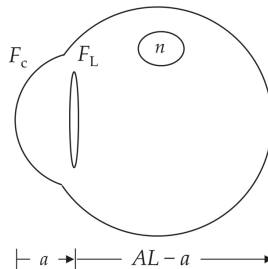


FIGURE 10.14 Simple theoretical method for determining IOL power.

There are two main approaches to predicting the IOL power. One may be considered the theoretical, or modeling, approach, which is based on biometric measurements such as corneal power and distances within the eye prior to surgery. The problem with this approach is that surgery will affect measurements of distances and power made before surgery, and the cataractous lens will affect determinations of distance within the eye according to how the cataract affects refractive index (Cooke et al. 2021). A simplistic formula for the power F_L of the lens to produce emmetropia after surgery is (Figure 10.14)

$$F_L = n/(AL - a) - F_c/[1 - (a/n)F_c] \quad (10.39)$$

Here n is the refractive index of the aqueous and vitreous, AL is the axial length, F_c is corneal power, and a is assumed anterior chamber depth following surgery. The first term on the right-hand side of the equation is the incident reduced vergence at the lens, and the second term on the right-hand side is the reduced vergence leaving the lens. This formula assumes a thin lens and a single surface cornea. More sophisticated formulae include allowance for thick components (e.g., distances could be determined relative to the appropriate principal planes of the lens) and retinal thickness.

The other main approach to predicting lens power is empirical. Following the collection of considerable data of ocular parameters, powers of lenses inserted and the residual refractions, regression equations are determined to predict the appropriate power. The first of these was the SRK formula (Sanders et al. 1980), which reduced the prediction to three factors:

$$F_L = A - 2.5AL - 0.9F_c \quad (10.40)$$

Here AL is the axial length (in mm), F_c is the corneal power (D), and A is a factor that is specific to a particular lens and can be manipulated to suit a particular surgeon. The original SRK formula has undergone various transformations, sometimes specific to a particular group of patients, such as those with long eyes. Biometric instruments will often provide a range of prediction formulae.

The approaches described above can be modified if the goal is not emmetropia, such as in *monovision* where one eye becomes emmetropic and the fellow eye becomes myopic for the purpose of presbyopia compensation. Hoffer (1998) provides a personalized account of the history of IOL power calculations.

Intraocular lenses are available in spherical and toric forms, with care required during insertion of the latter to ensure that the benefit of full astigmatic correction is not canceled by faulty orientation. Bifocal, trifocal, and “extended depth of focus” types are available to give acceptable ranges of clear vision, using both refractive and diffractive optics.

On the assumption that the accommodative apparatus remains largely functional during most of life, there has been considerable interest in developing “accommodating” intraocular lenses. Many types have been made, or are under development, in an attempt to restore “youthful vision”, although success to date has been extremely limited. These types include the following (Pepose et al. 2017):

Single-Optics IOLs, with a hinge arrangement, so that the lens moves forwards in the capsule under the influence of ciliary contraction. Modeling indicates small potential effects of 1 D to 2 D, depending on the length of the eye, per 1 mm movement;

Dual Optic IOLs in which two lenses can be moved by a spring action, either longitudinally or transversely, relative to each other to change the effective power of the combination;

Shape-changing IOLs in which the lens changes shape on being forced through an aperture, fluid is exchanged between the optic and the haptic, or the capsular bag is filled with fluid;

Refractive index modulating lenses containing two liquids of different refractive indices, with different angles of gaze determining the relative mixture affecting effective refractive index and hence power;

Electro-active IOLs involving liquid-crystals that can alter power after sensing light changes induced by accommodative effort.

Any lens that can accurately restore at least 3 D accommodation would be a boon to presbyopes, but Schor (2012) suggested that at least 5 D accommodation is needed for comfortable performance of near tasks. Schor discussed the limitations of various types, as well as binocular vision adaptation issues.

Magnification effects in anisometropia, already described for spectacle lenses and contact lenses, apply also to eyes wearing IOLs. Atchison and Rozema (2021) conducted a treatment for retinal image sizes termed relative magnification (*RM*). It was determined when IOL power was the same as that of a reference eye and spectacle correction was required, and also when the IOL power was altered from that of the reference power, to compensate for axial ametropia or for refractive ametropia (change in corneal power or IOL position). When a full IOL correction was used and in axial ametropia,

$$RM = (l'_1 + \Delta l') / l'_1 \quad (10.42)$$

where l'_1 is the vitreous length of the standard eye and $\Delta l'$ is the change in vitreous length. For refractive ametropic eyes, varying only in corneal power,

$$RM = \frac{n - a_1 F_{Cl}}{n - a_1 (F_{Cl} + \Delta F_c)} \quad (10.43)$$

where n is the refractive index of the aqueous and vitreous, a_1 is anterior chamber depth, F_{C1} is the corneal power of the reference eye, and ΔF_C is the change in corneal power. For refractive ametropic eyes, varying in the position of the IOL (but without change in axial length),

$$RM = \frac{\left[1 - \left(\frac{a_1}{n}\right)F_C\right](l'_1 - \Delta a)}{\left[1 - \left(\frac{a_1 + \Delta a}{n}\right)F_C\right]l'_1} \quad (10.44)$$

where anterior chamber depth changes by Δa .

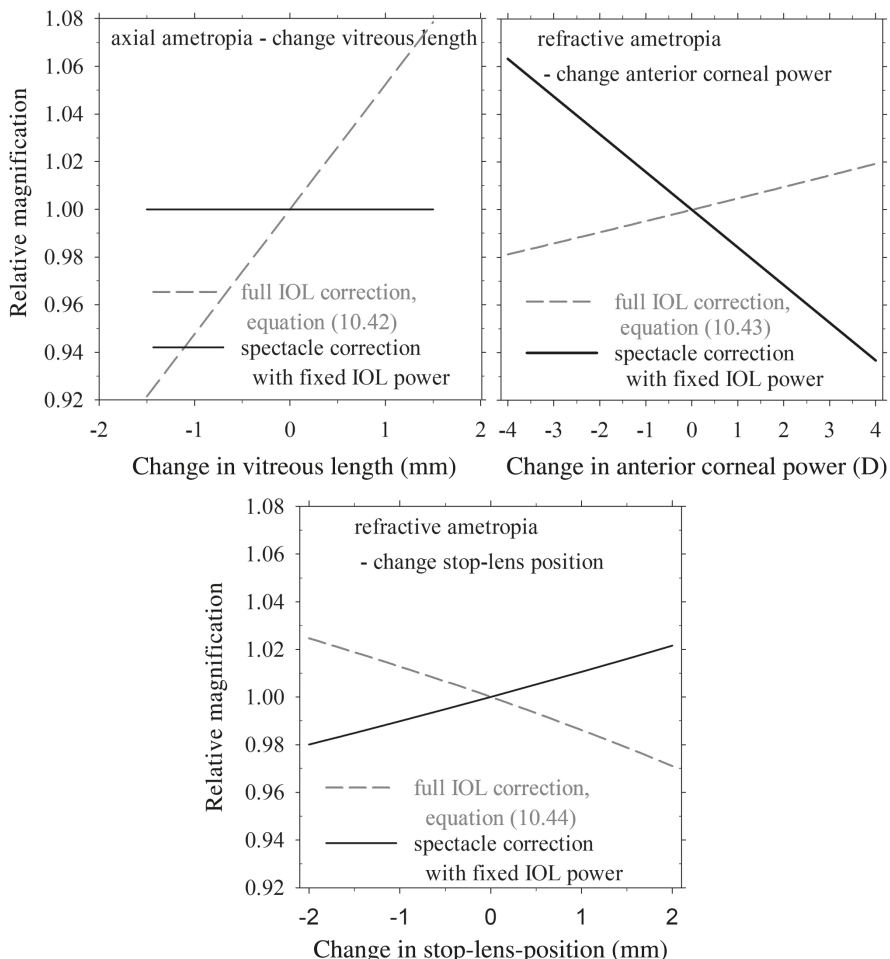


FIGURE 10.15 Relative magnifications for fellow model eyes with IOLs, which differ by vitreous length, anterior corneal power, and stop-lens position. The dotted lines for full IOL correction are from equations (10.42)–(10.44). The solid lines are determined for a fixed IOL power and spectacle correction according to raytracing. Data of Atchison and Rozema (2021).

In these equations, the anterior chamber depth is from the second principal point of the cornea to the first principal point of the lens, the vitreous length is from the second principal point of the lens to the retina, but changes in these positions due to changes in cornea and IOL power are ignored. Even with substituting thin corneas and thin IOLs into an eye model, the equations work well.

Figure 10.15 shows relative magnifications for fellow schematic eyes modified to include intraocular lenses, using an eye with a “standard” intraocular lens as the reference. For full IOL corrections (dotted lines), there is a considerable effect of vitreous length of +5.2%/mm, while effects of corneal power and anterior chamber depth are +0.4%/D and -1.4 %/mm, respectively. When the same IOL power is used in both eyes, supplemented by spectacle corrections (solid lines), these effects become 0%/D (vitreous depth), -1.6%/D (corneal power), and +1.0%/mm (IOL position).

SUMMARY OF MAIN SYMBOLS

h_e	distance from ophthalmic lens to the entrance pupil of eye (always positive)
h_c	distance from ophthalmic lens to the center-of-rotation of eye (always positive)
h_p	distance from ophthalmic lens to the front principal point of eye (always positive)
h_v	distance from ophthalmic lens to the corneal vertex (always positive)
n	refractive index of a spectacle lens
D_s	diameter of spectacle lens
l	distance from ophthalmic lens to object (always negative)
l'	distance from ophthalmic lens to image
L, L'	reduced vergences corresponding to l and l' . These are also the vergences when the corresponding refractive index is 1.
q	distance between entrance pupil of eye and the object (always negative)
q_c	distance between center-of-rotation of eye and the object (always negative)
d_{np}	distance from corneal vertex to near point of uncorrected eye
$(d_{np})_{\text{new}}$	distance from corneal vertex to near point of corrected eye
F_s	equivalent power of ophthalmic lens
F'_v	back vertex power
F_a	equivalent power of the ametropic eye
F_e	equivalent power of the emmetropic eye
F_t	equivalent power of ophthalmic lens and ametropic eye
$A(W)$	ocular accommodative demand
ω	angular diameter of the object
θ_{\max}	real field-of-view through a spectacle lens
θ'_{\max}	apparent field-of-view through a spectacle lens
SM	spectacle magnification
\bar{M}	pupil magnification
RSM	relative spectacle magnification
$R_o M$	rotational magnification

Spectacle lens design

I, n	air and lens medium refractive indices
t, t'	distances from surface along the chief ray to the object and image tangential conjugates
s, s'	distances from a surface along the chief ray to the object and image sagittal conjugates
I, I'	angles of incidence and refraction of a chief ray at a surface
T, S	off-axis tangential and sagittal powers of spectacle lens
$\Delta T, \Delta S$	off-axis tangential and sagittal power errors of a spectacle lens
OA	oblique astigmatism
MOE	mean oblique error

Contact lenses

r_1, r_2, r_c	radii of curvature of anterior lens surface, posterior lens surface of lens, and anterior corneal surface
F_1, F_2, F_3	surface powers corresponding to radii of curvature
d_t	lens center thickness
n_1, n_t	contact lens and tear film refractive indices
r_{c1}, r_{c2}	radii of curvature of principal meridians of corneal surface
FOZR	front optic zone radius (of curvature)
BOZR	back optic zone radius (of curvature)

Intraocular lenses

IOL	intraocular lens
RM	relative magnification
F	equivalent power of an eye with an IOL
F_v'	back vertex power of eye
F_c	corneal power
F_L	IOL power
n	refractive index of aqueous and cornea
a	anterior chamber depth
l'	vitreous chamber depth
$l'_1, \Delta l'$	vitreous length of a reference eye and change from it to another eye
$F_{c1}, \Delta F_c$	corneal power of a reference eye and change from it to another eye
$a_1, \Delta a_1$	anterior chamber depth of reference eye and change from it to another eye

REFERENCES

- Alshamrani, A. A., and S. S. Alharbi. 2019. "Phakic intraocular lens implantation for the correction of hyperopia." *J Cat Refract Surg* 45 (10):1503–11. doi: 10.1016/j.jcrs.2019.05.051.
- Atchison, D. A., and J. J. Rozema. 2021. "Retinal image size in pseudophakia." *Ophthalmic Physiol Opt* 41 (6):1222–30. doi: 10.1111/opo.12874.
- Atchison, D. A. 1996. "Calculating relative retinal image sizes of eyes." *Ophthalmic Physiol Opt* 16 (6):532–8. doi: 10.1111/opo.12771.
- Atchison, D. A. 2006. "Optical models for human myopic eyes." *Vision Res* 46 (14):2236–50. doi: 10.1016/j.visres.2006.01.004.

- Atchison, D. A. 2011. "Third-order theory of spectacle lenses applied to correction of peripheral refractive errors." *Optom Vis Sci* 88 (2):E227–33. doi: 10.1097/OPX.0b013e31820847d2.
- Atchison, D. A. 2021. "Modified forms of Tscherning ellipses." *Ophthalmic Physiol Opt* 41 (2):401–8.
- Charman, W. N. 2018. "Chapter 6. Soft lens optics." In *Contact Lens Practice*, edited by N. Efron. Edinburgh: Elsevier.
- Cooke, D. L., T. L. Cooke, and D. A. Atchison. 2021. "Effect of cataract-induced refractive change on intraocular lens power formula predictions." *Biomed Opt Express* 12 (5):2550–6. doi: 10.1364/BOE.422190.
- Douthwaite, W. A. 2006. *Contact Lens Optics and Lens Design*. 3rd ed. Oxford: Elsevier Butterworth-Heinemann.
- Hoffer, K. J. 1998. "The history of IOL power calculation in North America." In *The History of Modern Cataract Surgery*, edited by M. L. Kwitko and C. D. Kelman, 193–208. The Hague: Klugher Publications.
- Jaisankar, D., Y. Liu, P. Kollbaum, M. Jaskulski, et al. 2020. "Nasal-temporal asymmetry in peripheral refraction with an aspheric myopia control contact lens." *Biomed Opt Express* 11 (12):7376–94. doi: 10.1364/BOE.406101.
- Jalie, M. 2021. *The Principles of Ophthalmic Lenses*. 6th ed. London: Association of Dispensing Opticians.
- Pepose, J. S., J. Burke, and M. Qazi. 2017. "Accommodating intraocular lenses." *Asia Pac J Ophthalmol (Phila)* 6 (4):350–7. doi: 10.22608/APO.2017198.
- Ridley, H. 1952. "Intra-ocular acrylic lenses. A recent development in the surgery of cataract." *Brit J Ophthalmol* 36 (3):113–22. doi: 10.1136/bjo.36.3.113.
- Sanders, D., J. Retzlaff, and M. Kraff. 1980. "Improvement of intraocular lens power calculation using empirical data." *Am Intra-Ocular Implant Soc J* 6 (3):263–7. doi: 10.1016/s0146-2776(80)80075-9.
- Schor, C. M. 2012. "Chapter 19. Accommodating intraocular lenses." In *Presbyopia. Origins, Effects and Treatments*, edited by I. G. Pallikaris, S. Plainis and W. N. Charman, 167–73. Thorofare, N.J.: Slack.
- Smith, G., and D. A. Atchison. 1983. "Effect of conicoid asphericity on the Tscherning ellipses of ophthalmic spectacle lenses." *J Opt Soc Am* 73 (4):441–5. doi: 10.1364/josa.73.000441.
- Sorsby, A., B. Benjamin, J. B. Davey, and et al. 1957. Emmetropia and its Aberrations. In *Medical Research Council Special Report Series number 293. HMSO*.
- Winn, B., R. G. Ackerley, C. A. Brown, F. K. Murray, et al. 1988. "Reduced aniseikonia in axial anisometropia with contact lens correction." *Ophthalmic Physiol Opt* 8 (3):341–4. doi: 10.1111/j.1475-1313.1988.tb01064.x.

Section III

Light and the Eye



Taylor & Francis
Taylor & Francis Group
<http://taylorandfrancis.com>

11 Light and the Eye

Introduction

11.1 INTRODUCTION

Since the eye is the organ of light sense, how the eye interacts with light is of great importance in understanding the visual process and the limits to vision. In this chapter we discuss the nature of light, how it is quantified, and the different aspects of it that affect vision. The measurement of light is referred to as *photometry*. As we see in the next few chapters, not all the light entering the eye forms the intended image on the retina. Some light is reflected, scattered, and absorbed, with a small part of the absorbed light being re-emitted in the form of fluorescence.

11.2 RADIATION AND THE ELECTROMAGNETIC SPECTRUM

Light is a small part of the electromagnetic spectrum. The complete electromagnetic spectrum is shown schematically in Figure 11.1. The range of wavelengths that cover the ultraviolet, visible, and infrared ranges is called *optical radiation*. The limits of the three optical radiation bands overlap since at the junction the radiation may have the properties of more than one type. For instance, radiation in the vicinity of 380 nm is both damaging (in sufficient quantities) and visible. Ultraviolet radiation is defined as being from 100 to 400 nm, visible radiation from 360 nm to 830 nm, and infra-red radiation from 780 nm to 1 mm (CIE 2011).

If a beam of electromagnetic energy has a spectral radiant flux denoted by $F_R(\lambda)$, the amount of radiant power or flux Φ_e in the beam is given by the integral

$$\Phi_e = \int_0^{\infty} \Phi_e(\lambda) \cdot d\lambda \text{ watt} \quad (11.1)$$

where $\Phi_e(\lambda)$ has the unit of watt/unit of wavelength. The measurement of radiation is referred to as *radiometry*.

11.3 LIGHT

The Commision Internationale de L'Éclairage (CIE 2011) defined light as

1. characteristic of all sensations and perceptions that is specific to vision;
2. radiation that is considered from the point of view of its ability to excite the human visual system.

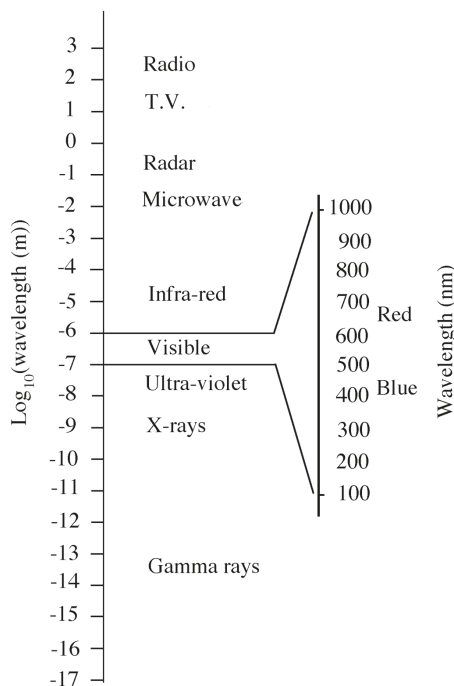


FIGURE 11.1 The electromagnetic spectrum.

While these are correct, agencies other than the narrow band of the electromagnetic spectrum that we normally call light can produce a visual sensation. Our sense of light arises usually from stimulation of the cones and rods in the retina and by signals being transmitted from them to the visual centers of the brain through a number of different types of nerve cells and pathways. If any of these cells or centers are stimulated by other means, a visual sensation still occurs. For example, these cells may be activated by chemicals, X-rays, and pressure from a knock on the head.

Light can be defined simply as that band of the electromagnetic spectrum that produces a visual response. This band is defined as 360–830 nm for daytime vision although the human eye can see up to at least 850 nm with sufficient energy. For most purposes, the limits of 380–780 nm are used. The eye is not equally responsive to all wavelengths in this band. The spectral visual response curve is approximately “bell”-shaped, with its shape and position depending upon the light level. Two extreme forms of the spectral response curve are identified: one for moderate to high light levels, and one for low light levels. For moderate to high light levels, the cones dominate vision, we see color, and the spectral response is referred to as the *photopic* response. For low light levels, the rods dominate vision, we are unable to distinguish color, and the spectral response is referred to as the *scotopic* response. The range of light levels intermediate between these two extremes, where both cones and rods operate, is called the **mesopic** range. Throughout this book, the photopic case is assumed unless stated otherwise.

11.3.1 PHOTOPIC VISION

The amount of light Φ (luminous flux) in an electromagnetic beam of radiation is given by the equation

$$\Phi = K_m \int_0^{\infty} \Phi_e(\lambda) \cdot V(\lambda) \cdot d\lambda \text{ lumen} \quad (11.2)$$

where the constant K_m is known as the *maximum spectral luminous efficacy of radiation for photopic vision*. It has a value of 683.002 lm/W (CIE 1983). $V(\lambda)$ is known as the *spectral luminous efficiency function for photopic vision*. It was determined from the average response of many subjects across a small number of studies and was defined by the Commission Internationale de l'Éclairage (CIE) in 1924. $V(\lambda)$ has a maximum value of 1 at 555 nm. Figure 11.2 shows the $V(\lambda)$ function. In some contexts, luminous values are given the subscript v, e.g., Φ_v to distinguish from Φ_e . Either is accepted by the CIE (CIE 2011).

The $V(\lambda)$ function is too low below about 450 nm because of shortcomings in the studies from which it was developed, but the advantages to be gained from correcting it are considered to be outweighed by the practical inconvenience. Nevertheless, the CIE (CIE 1990) defined an improved, supplementary function called $V'_M(\lambda)$. The CIE

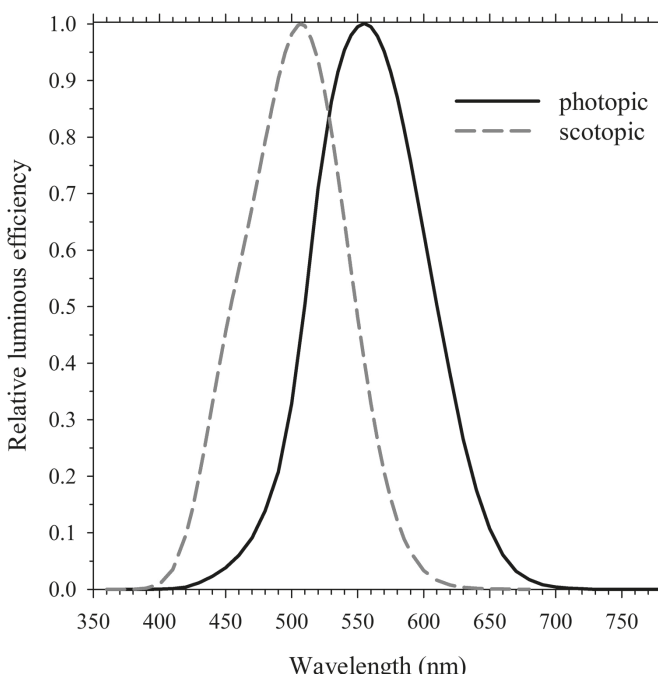


FIGURE 11.2 The relative luminous efficiency functions $V(\lambda)$ – photopic and $V'(\lambda)$ – scotopic. The peaks of these functions are at 555 nm and 507 nm, respectively.

(CIE 2005) has also defined a $V_{10}(\lambda)$ function for larger fields-of-view. It should be appreciated that individuals' photopic relative sensitivities differ for a number of reasons, including the following:

1. Luminous efficiency is the combined effect of the three types of cones (containing short, medium, and long wavelength sensitive photopigments), so that while the spectral sensitivity of the cones may be the same for each individual, the relative number of cones may vary. In addition, color deficient people have a missing cone type (dichromasy) or a cone type whose photopigment has an altered spectral sensitivity (anomalous trichromats).
2. Variations in spectral transmittance by the ocular media and variations in the density of a yellow pigment (xanthophyll) in the macula of the retina. In particular, as we age our sensitivity to blue light decreases because our lenses absorb more blue light and there are neural changes associated with the short wavelength-sensitive cones (Werner et al. 1990).

11.3.2 MESOPIC VISION

As the light level decreases from photopic towards scotopic levels, there is a change in relative spectral sensitivity accompanying the transition from cone to rod vision. This transition region is called the mesopic region and the shift in relative spectral sensitivity is called the *Purkinje shift*. The CIE has published spectral luminance efficiency functions for mesopic vision (CIE 2010).

11.3.3 SCOTOPIC VISION

The CIE defined the spectral luminous efficiency function for scotopic vision $V'(\lambda)$ in 1951. This function has a maximum value of 1 at 507 nm. It is shown, along with $V(\lambda)$, in Figure 11.2. If we convert radiant energy into light using $V'(\lambda)$, we use equation (11.2) with $V'(\lambda)$ replacing $V(\lambda)$ and K'_m , the *maximum spectral luminous efficacy of radiation for scotopic vision*, replacing K_m . The value of K'_m is 1700.06 lm/W (CIE 1983), which is derived from the definition that 1 photopic lumen = 1 scotopic lumen for a monochromatic source with a frequency of 540×10^{12} Hz. The ratio of the two K_m values is the ratio of the $V(\lambda)$ and $V'(\lambda)$ values at a wavelength of 555.016 nm in air with a refractive index of 1.00028.

Since there is only one class of cells (the rods) operating at scotopic light levels, we would expect less variability between individuals for scotopic relative sensitivity than for photopic relative sensitivity.

11.3.4 PHOTOPIC, MESOPIC, AND SCOTOPIC LIMITS

There is no sharp division between the boundaries of these three ranges. The lower luminance limit of photopic vision is approximately 3 cd/m^2 , with mesopic vision extending from this level to 0.03 cd/m^2 , below which scotopic vision starts (see next section for unit of luminance).

11.4 PHOTOMETRIC QUANTITIES, UNITS, AND EXAMPLE LEVELS

There are four fundamental photometric quantities: luminous flux, luminous intensity, luminance, and illuminance. These are related to radiometric quantities of radiant flux, radiant intensity, irradiance, and radiance through the sensitivity of the eye to radiation.

11.4.1 LUMINOUS FLUX (F)

Luminous flux is the measure of the total amount of light in a beam, and has the unit of lumen (CIE 2011).

If we think of a light source as emitting so many watts of electromagnetic radiation, it emits a certain number of lumens of light. The ratio of lumens to watts of a particular light source is known as its luminous efficacy. For example, there are about 10 lumens for each watt of a tungsten filament light source (about 600 lumens for a 60 W incandescent light bulb), about 16 lumens/watt for a quartz halide incandescent light bulb, about 40 lumens per watt for a fluorescent tube, about 120 lumens per watt for a white light emitting diode, and about 95 lumens per watt for sunlight (Littlefair 1985).

11.4.2 LUMINOUS INTENSITY (I)

Luminous intensity is a measure of the amount of light emitted per unit solid angle by a point source of light, and has the unit of candela (CIE 2011). It is a measure of luminous flux density. The luminous intensity in a given direction is the ratio of the luminous flux ($\delta\Phi$), contained in an infinitesimally narrow cone in the given direction, to the solid angle ($\delta\Omega$) of the cone (Figure 11.3). That is,

$$I = \delta\Phi/\delta\Omega \text{ lumen/steradian or candela (CIE 2011)} \quad (11.3)$$

Here $\delta\Omega$ is the ratio of the area on a spherical surface, with its center of curvature at the origin of the cone, to the square of the radius of curvature of the sphere. In the above example of the 60 W light bulb, the 600 lumens are not emitted nor distributed evenly in all directions in space. For many light sources, it is more important to know the luminous intensity emitted in a given direction rather than the total luminous flux emitted. In practice, luminous intensity is used only for sources of small angular subtense.

The luminous intensity of a common wax candle is about 1 cd, and this is the origin of the word “candela”. Traffic signal lights have axial luminous intensities of about 200–600 cd, or even higher. The axial luminous intensity of a car headlight on

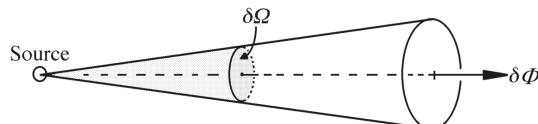


FIGURE 11.3 Luminous intensity $I = \delta\Phi/\delta\Omega$.

full beam can be about 20,000 cd. Marine lighthouses have intensities of millions of candelas.

11.4.3 LUMINANCE (L)

Luminance is the objective measure of the “brightness” of an extended source, and has the unit of candela per square meter (cd/m^2).

For a small element of an extended source, luminance can be related to the luminous intensity of the element and a direction. Referring to Figure 11.4, if the source is a small plane element of area δA with luminance $L(\theta)$ in a direction θ , the luminous intensity $I(\theta)$ in that direction is given by the equation

$$I(\theta) = L(\theta) \cdot \cos(\theta) \cdot \delta A$$

That is

$$L(\theta) = \frac{I(\theta)}{\delta A \cdot \cos(\theta)} \text{cd/m}^2 \quad (11.4)$$

Some sources have the same “brightness” or luminance in all directions, i.e., luminance is independent of θ . These sources are referred to as *Lambertian*.

Many sources of light, such as the sky, are effective sources because they scatter incident light. A perfectly diffusing surface scatters incident light equally in all directions, which means that the surface luminance is the same for all directions, and it acts as a Lambertian source. Magnesium oxide, soot, barium sulphate, and roughened chalk (calcium carbonate) come close to being perfect diffusers. For a Lambertian source or surface

$$L(\theta) = \text{constant} = L \quad (11.5)$$

and the luminous intensity is given by

$$I(\theta) = L \cdot \delta A \cdot \cos(\theta) \quad (11.6a)$$

For normal viewing, $\theta = 0^\circ$ and

$$I = L \cdot \delta A \quad (11.6b)$$

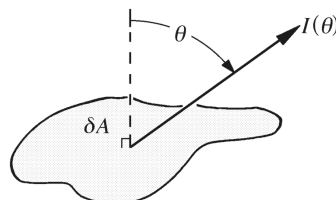


FIGURE 11.4 Relationship between luminance L and luminous intensity I .

For a perfect *specular surface*, which is the opposite of a perfect diffusing surface, all the incident light is reflected according to Snell's law. All surfaces have both specular and diffusing properties, thus lying somewhere between the two extremes.

The luminance of the sun depends upon its elevation above the horizon and the scattering, reflection and absorption by water vapor, dust, and other substances in the atmosphere. The scatter and absorption by atmospheric molecules is wavelength-dependent, thus producing the blue sky and the reddish sun at sunset. Under clear atmospheric conditions, the luminance of the sun at high elevations is about 1.6×10^9 cd/m² and the luminance of the moon is about 2500 cd/m² (Sliney and Worlbarsht 1980).

11.4.4 ILLUMINANCE (E)

Illuminance is a measure of the luminous flux density incident on a surface, and has the unit of lumens per square meter (lm/m² or lux).

Since illuminance can vary over a surface, it is best defined in terms of small elements of area δA . Thus

$$E = \delta\Phi/\delta A \text{ lux} \quad (11.7)$$

On a clear day with the sun high in the sky, the illuminance at the Earth's surface can be as high as 100,000 lux. The illuminance at a desk in a well-lit office is about 200–1000 lux.

11.5 SOME USEFUL RELATIONSHIPS

The four basic photometric units are connected within the preceding definitions, but there are other relationships that are useful in a number of different situations. We discuss two of these in this section.

11.5.1 LUMINOUS INTENSITY AND ILLUMINANCE: THE INVERSE SQUARE LAW

The illuminance E on a surface at a distance d from a small source of light, described by its luminous intensity I , is given by the inverse square law equation

$$E = (I/d^2)\cos(\theta) \quad (11.8)$$

where θ is the angle of inclination of the surface normal to the direction of the source.

This equation assumes that the source is a point source. Since all sources have some size, this equation is only an approximation. If the angular subtense of the longest dimension of the source is less than 5° at the distance d , the error in this equation is less than 1 per cent. For sources of angles less than 1 min. arc, the source is effectively a point, and the illuminance is referred to as *point brilliance*.

11.5.2 LUMINANCE AND ILLUMINANCE

Visual performance in any task is related to light level, and it is the stimulus luminance that is the important measure of light level. For many stimuli that reflect light,

such as a visual acuity chart, the luminance depends upon the illuminance in the plane of the stimulus. The relationship between the two quantities depends on the scattering properties of the stimulus material. If the stimulus is perfectly diffusing and reflects a fraction ρ of the incident light, luminance L is related to illuminance E by the simple equation

$$L = \rho \cdot E / \pi \quad (11.9)$$

11.6 WHICH PHOTOMETRIC QUANTITY TO USE

Since visual performance is dependent upon light level, we may need to specify light levels for particular tasks. We need to know which of the four photometric quantities of luminous flux, luminous intensity, illuminance, and luminance is most relevant to each task.

11.6.1 THRESHOLD DETECTION

The threshold light level for detection of a light stimulus with a small angular subtense depends upon the total amount of light collected by the retina – that is, the luminous flux. This is because the light from this stimulus falls on a few photoreceptors, which pool their input. This is known as spatial summation. Since this pooled amount of light is the product of local illuminance and the area, the amount of light collected is the luminous flux. Under such circumstances, *Ricco's law* states that

$$\text{luminance} \times \text{area} = \text{constant}$$

but more strictly speaking this should be

$$\text{local illuminance} \times \text{area} = \text{luminous flux} = \text{constant}$$

For a large source, whose retinal image is much larger than the region of spatial summation, detection thresholds depend upon the stimulus luminance (or retinal illuminance) and not on stimulus size. The detection threshold depends upon the luminance contrast of the stimulus relative to its background.

In between the extremes of size, thresholds vary approximately with the square root of the product of luminance and area (*Piper's law*).

11.6.2 SUPRA-THRESHOLD VISIBILITY OF SOURCES WITH A SMALL ANGULAR SUBTENSE

For light levels well above threshold, the visibility of a small “point” source is related to its luminous intensity. For example, the performances of signal and warning lamps such as traffic signal lamps are specified by their luminous intensities.

11.6.3 SUPRA-THRESHOLD VISIBILITY OF SOURCES WITH A LARGE ANGULAR SUBTENSE

The visibility of a source with a large angular subtense is usually correlated with its luminance. For example, the performances of pedestrian road crossing signals are specified by their luminances.

11.6.4 MEASUREMENT OF AMBIENT LIGHT LEVEL

In general, visual performance improves with increase in light level. Most realistic scenes contain many objects of various sizes, luminances, and luminous intensities. We need a consistent, repeatable method of measuring the ambient light level of such scenes. The obvious approach is to measure the amount of light entering an observer's eye, i.e., the luminous flux. However, this requires knowing the pupil size of the observer. This problem can be avoided by using the illuminance at the pupil plane of the observer.

11.6.5 OTHER COMMENTS

While thresholds and levels of visibility depend upon the light level reaching the retina, we can measure accurately only the photometric properties of the source itself and corresponding light levels (e.g., illuminance) at any distance from the source. However, the light level reaching the retina is dependent upon pupil size, and therefore threshold and supra-threshold levels depend upon pupil diameter. We discuss how pupil size affects retinal light level in Chapter 13.

11.7 COLORIMETRY

Colorimetry is concerned with the measurement and specification of color. It is based on experiments in which colors were matched with a combination of three primary colors. With transformations, the original functions were converted into color-matching functions $\bar{x}(\lambda), \bar{y}(\lambda), \bar{z}(\lambda)$, such that $\bar{y}(\lambda) = V(\lambda)$. These functions are shown in Figure 11.5, defined in ISO 11664.1 (International Standardization Organization 2007) and given in a number of publications, e.g., Wyszecki and Stiles (1982). Light stimuli of any spectral power distribution $\phi_\lambda(\lambda)$ can be specified by tristimulus values X, Y, Z where

$$X = k \int_{\lambda} P_{\lambda} \cdot \bar{x}(\lambda) \cdot d\lambda, Y = k \int_{\lambda} P_{\lambda} \cdot \bar{y}(\lambda) \cdot d\lambda, Z = k \int_{\lambda} P_{\lambda} \cdot \bar{z}(\lambda) \cdot d\lambda \quad (11.10)$$

with P_{λ} referring to a radiometry quantity (such as spectral flux, radiance or irradiance) and k is a normalizing constant. In turn, the tristimulus values can be converted into chromaticity co-ordinates x, y, z where

$$x = \frac{X}{X+Y+Z}, y = \frac{Y}{X+Y+Z}, z = \frac{Z}{X+Y+Z} \quad (11.11)$$

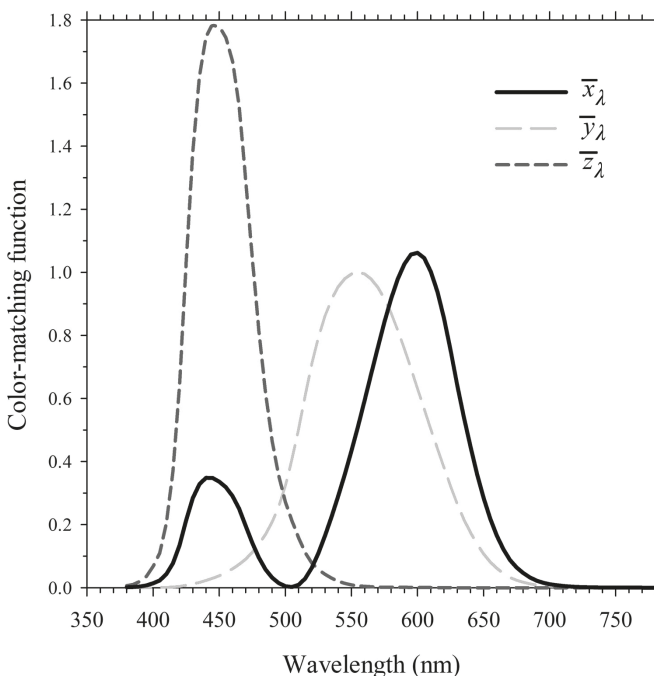


FIGURE 11.5 Color-matching functions.

These are shown two-dimensionally on the CIE (x , y) chromaticity diagram (Figure 11.6), for which the boundaries consist of the monochromatic radiations and increasingly desaturated colors are towards the center. Two white light sources, CIE standard illuminants A and D65 (International Standardization Organization 2008), are indicated. The former is typical for an incandescent lamp and the latter represents the color of a phase of daylight. The CIE (x , y) diagram is widely used for communicating the color of objects but is non-uniform in terms of color differences, color appearance, and things like tolerances of acceptable color or the ease with which colors are discriminated from one another are not accurately represented. Other transformations of the tristimulus values have been developed, such as the CIE 1976 u' , v' co-ordinate system (or CIE 1976 Luv) used widely in the lighting and color reproduction industries, and the CIE 1976 L^*a^*b system (or CIE 1976 Lab) used in the textile industry (CIE 2018).

The curve in Figure 11.6 is the Planckian locus (see section 13.4.1), which represents chromaticity co-ordinates of blackbody radiation at a range of temperatures; such sources can be specified as *color temperatures*. A source whose chromaticity lies close to the Planckian locus can be specified in terms of *correlated color temperature* by finding the temperature of the blackbody whose chromaticity is closest to that of the source when plotted in a modified u' , v' chromaticity system. All sources with the same correlated color temperature will look the same regardless of their spectral distribution. However, the differing spectral distributions will mean that colors illuminated by sources of the same correlated color temperature

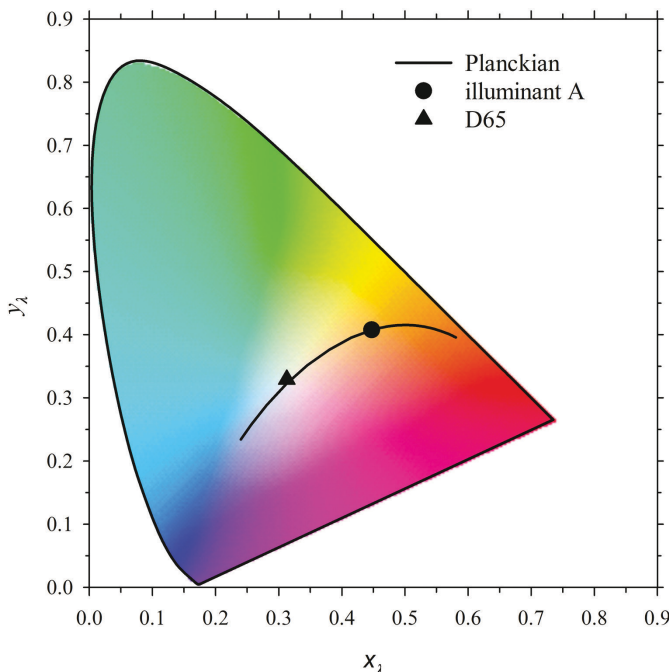


FIGURE 11.6 The CIE (x , y) chromaticity diagram. The curve is the Planckian locus. The symbols show the locations of illuminant A and illuminant D65.

may look very different. In this case, there is the measure of CIE color rendering index (CRI or R_a). In this measure, the chromaticities of eight colors under a test source are compared with the chromaticities under the Planckian radiator or phase of daylight of the same or similar color. If the color rendering is perfect, $R_a = 100$. A CRI of at least 80 is required for work that involves color and of at least 90 is required for critical color work such as color matching and color vision examination (CIE 1995). Another method has been proposed for light emitting diode sources (CIE 2007).

This is a brief introduction to colorimetry, and more details are provided in texts such as Schanda (2007), Oleari (2016), and (CIE 2018).

SUMMARY OF MAIN SYMBOLS

λ	wavelength
(λ)	used after a symbol, to indicate that it is a spectral value
$F_R(\lambda)$	spectral radiant flux
Φ_e	radiant power (integrated over all wavelengths)
P	is used in equations that might be used with radiant flux, radiant intensity, radiance or irradiance
$V(\lambda)$, $V'(\lambda)$	spectral luminous efficiency functions for photopic and scotopic vision

K_m, K'_m	maximum spectral luminous efficacies of radiation for photopic and scotopic vision
Φ	luminous flux
I	luminous intensity
L	luminance
E	illuminance
Ω	solid angle
A	area
d	distance
θ	direction relative to the normal of a surface
ρ	proportion of radiation reflected
$\bar{x}(\lambda), \bar{y}(\lambda), \bar{z}(\lambda)$	color-matching functions
X, Y, Z	tristimulus values
x, y, z	chromaticity co-ordinates

REFERENCES

- CIE. 1983. The Basis of Physical Photometry. CIE publication No. 18.2 (TC-1.2). Commission Internationale de L'Éclairage.
- CIE. 1990. CIE 1988 2° Spectral Luminance Efficiency Function for Photopic Vision. Vienna, Austria: Commission Internationale de L'Éclairage.
- CIE. 1995. CIE 13.3. Method of Measuring and Specifying Colour Rendering Properties of Light Sources In Vienna, Austria: Commission Internationale de l'Éclairage.
- CIE. 2005. CIE 10 degree Photopic Photometric Observer. Vienna, Austria: Commission Internationale de L'Éclairage.
- CIE. 2007. CIE 177. Colour Rendering of White LED Sources. Vienna, Austria: Commission Internationale de L'Éclairage.
- CIE. 2010. Recommended System for Mesopic Photometry based on Visual Performance. Vienna, Austria: Commission Internationale de L'Éclairage.
- CIE. 2011. CIE publication S 017:2011. ILV: International Lighting vocabulary. Vienna, Austria: Commission Internationale de L'Éclairage.
- CIE. 2018. Colorimetry (4th Edition). Geneva: Commission Internationale de L'Éclairage.
- International Standardization Organization. 2007. 11664-1 CIE S 014-1. Colorimetry - Part 1: CIE standard observers. Geneva, Switzerland.
- International Standardization Organization. 2008. ISO 11664-2 CIE S 014-2. Colorimetry - Part 2: CIE standard illuminants. Geneva, Switzerland.
- Littlefair, P. J. 1985. "The luminous efficacy of daylight: a review." *Light Res Tech* 17 (4):162–82.
- Oleari, C. 2016. *Standard Colorimetry*. Edited by Society of Dyers and Colorists. Chichester, United Kingdom: Wiley.
- Schanda, J. 2007. *Understanding the CIE system*. Edited by Society of Dyers and Colorists. Hoboken, New Jersey: Wiley.
- Sliney, D., and M. Worlbarsh. 1980. *Safety with Lasers and other Optical Sources*. New York: Plenum Press.
- Werner, J.S., D.H. Peterzell, and A.J. Scheetz. 1990. "Light, vision and aging." *Optom Vis Sci* 67 (3):214–29. doi: 10.1097/00006324-199003000-00013.
- Wyszecki, G., and W. S. Stiles. 1982. *Color Science: Concepts and Methods, Quantitative Data and Formulae*. 2nd ed. New York: Wiley.

12 Passage of Light into the Eye

12.1 INTRODUCTION

Not all the light entering the eye forms the retinal image. A significant amount is lost by the following processes:

1. Some light is specularly reflected at the four major refracting surfaces.
2. Some light is elastically scattered (no change in wavelength) by the ocular media. In some other chapters we refer to diffusely reflected light, e.g., Chapter 8, but in this chapter we refer to the light which is diffusely reflected as back-scattered light, to distinguish it from forward-scattered light.
3. Some light is absorbed and is then either
 - a. re-emitted at other (longer) wavelengths, which is known as inelastic scattering or as fluorescence, or
 - b. converted to other forms of energy.

Both 2 and 3a above are causes of veiling glare (also *straylight*). Veiling glare from elastically scattered light is not usually uniform and has an angular distribution, which we discuss further in Chapter 13. By contrast, fluorescence produces a uniformly distributed veiling glare, and we discuss the source of this fluorescence later in this chapter.

Of the above three causes of light loss, specular reflection by the refracting surfaces makes up only a small proportion. Most of this occurs at the anterior cornea, and this is useful in determining the radius of curvature of this surface. However, this may be annoying because it produces veiling glare for the clinician during direct ophthalmoscopy. Light scattered by the ocular media plays a similar dual role. Light that is specularly reflected or back-scattered out of the eye helps clinicians to delineate the different components of the eye during internal eye examination with the slit-lamp, particularly in examination of the lens and the cornea. However, any forward-scattered light produces a veiling glare at the retina and reduces scene contrast. This is a problem particularly when bright lights are present in otherwise dark fields and in low contrast fields, and increases with age. While the loss of light due to absorption reduces the amount of light reaching the retina, it protects the retina from light of shorter wavelengths which may be damaging to ocular structures.

Light is able to reach the retina after passage through the iris and sclera. van den Berg et al. (1991) determined that, for eyes with light irises, the effective transmission is between 0.2 per cent and 1 per cent, and that the eye wall around the iris transmits a significant amount of light. This light contributes to veiling glare at large angles, a

contribution that would be much greater if not for the ameliorating influence of the Stiles–Crawford effect (section 14.5).

12.2 SPECULAR REFLECTION

Some light is reflected at each interface in the eye. If the surfaces are smooth, the specularly reflected light is image forming. The fractions of reflected and transmitted light depend on the refractive indices on each side of the surface, and these fractions are given by the Fresnel equations. If the indices are n and n' on the incident and refracted sides respectively, for normal incidence the reflectance (i.e., fraction of light reflected) R and the transmittance (i.e., the fraction of light transmitted) T are given by the equations

$$R = [(n' - n)/(n' + n)]^2 \text{ and } T = 4nn'/(n' + n)^2 \quad (12.1)$$

We may note that from these equations

$$R + T = 1 \quad (12.2)$$

implying that there is no absorption of light at the surface. However, there is some absorption by the bulk tissue. Since the eye contains four main reflecting surfaces, there are four main reflected images. These are called Purkinje-Sanson or Purkinje images, and are often denoted by the symbols P_I , P_{II} , P_{III} , and P_{IV} .

The above equations apply strictly only to a simple smooth surface between two homogeneous media with well-defined refractive indices n and n' . In biological systems, this ideal situation does not exist. For example, in the case of the anterior corneal surface, the boundary consists of a few layers (see section 2.2) of different refractive indices. The outermost layer (the tear film) has an index of approximately 1.336, compared with a value of 1.376 for the bulk of the cornea. The lens surfaces are also complicated by the presence of the capsule, and are not as smooth as the cornea, and this makes their Purkinje images more diffuse than those of the cornea. A rigorous analysis of the reflectance of surfaces would have to consider the fine structure of the cellular matrix.

The positions, sizes, and brightnesses of the Purkinje images depend upon the position of the light source and the optical structure of the eye. Table 12.1 has these

TABLE 12.1
The Purkinje Images of the Le Grand Full Theoretical Schematic Eye for a Distant Light Source

Purkinje Image	Relative Size	Distance from Corneal Pole (mm)	Relative Brightness
P_I (anterior cornea)	1.000	3.90	1.000
P_{II} (posterior cornea)	0.82	3.61	0.008
P_{III} (anterior lens)	1.95	10.73	0.034
P_{IV} (posterior lens)	-0.76	4.34	0.035

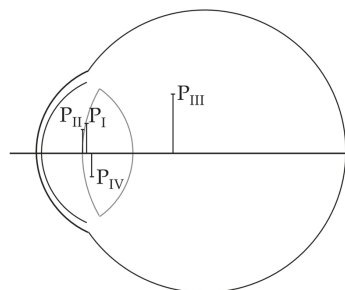


FIGURE 12.1 The positions and relative sizes of the Purkinje images for the Le Grand full theoretical schematic eye, for the light source at infinity.

details for the Le Grand full theoretical schematic eye schematic eye and an axial, distant light source. Figure 12.1 shows the positions and sizes of the images of this schematic eye.

These images can be used to determine the positions and curvatures of the intra-ocular surfaces and, in particular, those of the lens. Measuring Purkinje image sizes allows us to monitor lens changes due to accommodation and aging in the lens.

The Purkinje images are useful also in locating the different axes of the eye (see section 4.4) and for monitoring eye movements. The brightnesses of Purkinje images have also been used to determine the spectral transmission of the lens (Said and Weale 1959; Johnson et al. 1993).

Specular reflections may occur that are not Purkinje images. For example, the lenticular cortex shows a small steady increase in back-scatter with age, which may be because of the specular reflections from the ever increasing zones of discontinuity in the cortex (Weale 1986).

12.2.1 IMAGES FORMED BY MULTIPLE REFLECTIONS

The Purkinje images discussed above are formed from single reflections. Some light suffers more than one reflection, but the amount of light in a multireflected beam is rapidly attenuated as the number of reflections increases. If there is an odd number of reflections, the beam exits the eye. On the other hand, if the beam suffers an even number of reflections, it finally reaches the retina and forms an image somewhere along its path. There are six possible combinations of double reflection images, and the brightest are the three involving the anterior corneal surface. However, to see any of these double reflections, the image must be formed near the retina and must arise from a bright source in a dim or dark field.

The degree of focus at the retina of these higher-order Purkinje images depends upon the distance of the source, the structure of a particular eye, and the level of accommodation. If the source is about 25 cm in front of the cornea, the combined reflections from the posterior lens surface and the anterior corneal surface focus close to the retina and form an erect image.

12.3 TRANSMITTANCE

There have been several studies measuring the transmittance of the eye, particularly of the lens. These include psychophysical and physical methods. Physical methods include comparing the relative intensities of the third and fourth Purkinje images, and *in vitro* measurements of individual parts of the eye or the whole of the eye.

12.3.1 SPECTRAL TRANSMITTANCE OF THE WHOLE EYE

Figure 12.2 shows spectral transmittances of the whole eye (which includes the cornea, aqueous, lens, and vitreous) from the work of Ludvigh and McCarthy (1938), Boettner and Wolter (1962), and Geeraets and Berry (1968). The mean age of the four eyes of Ludvigh and McCarthy was 62 years, but they adjusted the transmittances as if the eyes contained lenses of a mean age of 21.5 years. Boettner and Wolter (1962) investigated nine eyes ranging from 4 weeks to 75 years of age. Geeraets and Berry (1968) measured seven eyes, whose ages were not given.

Since the ocular components scatter light, the measured transmittance depends upon the amount of scattered light that is collected by the instrument. Boettner and Wolter (1962) measured the transmittance under two conditions: first, light collected only within a 1° cone centered on the transmitted beam, and second, light collected within a 170° cone. The first condition simulated directly transmitted light plus a small amount of scattered light, and the second condition included most of the

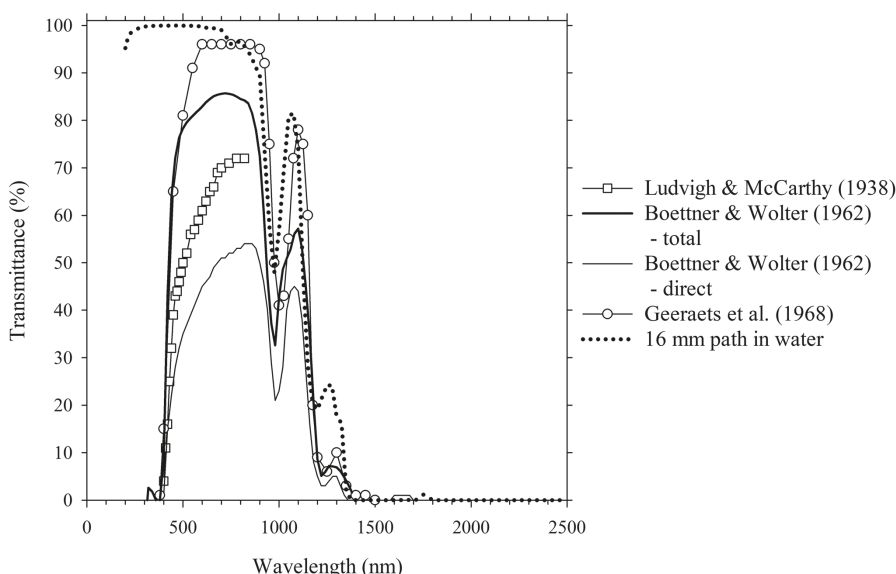


FIGURE 12.2 The spectral transmittance of the whole eye from Ludvigh and McCarthy (1938), Boettner and Wolter (1962), Geeraets and Berry (1968), and 16 mm of water. The data of Boettner are for a young child/young adult, except for wavelengths less than 380 nm, where they are those for a young child.

forward-scattered light and measured total transmittance. Boettner and Wolters' results show a strong dependency on age. Ludvigh and McCarthy (1938) and Geeraets and Berry (1968) did not state their collecting angles.

The transmittance of the whole eye can be found by removing the sclera, choroid, and retina in the region of the fovea. However, Boettner and Wolter calculated their whole eye values from the transmittances of individual components. Their individual component transmittances, as well as data from other sources, are discussed below.

12.3.2 SPECTRAL TRANSMITTANCE OF EACH OCULAR COMPONENT

12.3.2.1 The Cornea

Figure 12.3a shows the spectral transmittances of the cornea (Boettner and Wolter 1962; Beems and van Best 1990; van den Berg and Tan 1994). Boettner and Wolter stated that the total transmittance (scattered plus direct light) was representative of six eyes with no age effect, and that the direct (scattered light excluded) transmittance for the 53-year-old eye was close to the mean of eight eyes. They found that the direct transmittance is age-dependent, but Beems and van Best (1990) and van den Berg and Tan (1994) did not find an age dependency.

12.3.2.2 The Aqueous

Figure 12.3b shows the mean spectral transmittance of the aqueous of several eyes from Boettner and Wolter (1962). They found no differences in transmission due to age. They found no difference between total and direct transmittance, indicating that there is no significant scattering in the aqueous.

12.3.2.3 The Lens

Figure 12.3c shows spectral transmittance of the lens (Said and Weale 1959; Boettner and Wolter 1962; Mellerio 1971). The data for Said and Weale and for Mellerio are estimated means of their results, which show a strong age-dependence. Boettner and Wolter (1962) found that both the total and direct transmittances decrease with age, particularly at the short wavelengths. This decreased transmittance at shorter wavelength produces the yellowing of the lens with age.

12.3.2.4 The Vitreous

Figure 12.3d shows the total and direct spectral transmittances of the vitreous (Boettner and Wolter 1962). There is a measurable amount of scattering in the vitreous, which does not seem to be dependent upon wavelength. No differences in transmittance due to age were found.

12.3.3 PROGRESSIVE LOSS OF LIGHT AS IT PASSES THROUGH THE EYE

Figure 12.4 shows the decrease in direct transmittance as light passes through the eye (Boettner and Wolter 1962). The data shows the spectral transmittance at the posterior surface of each ocular component.

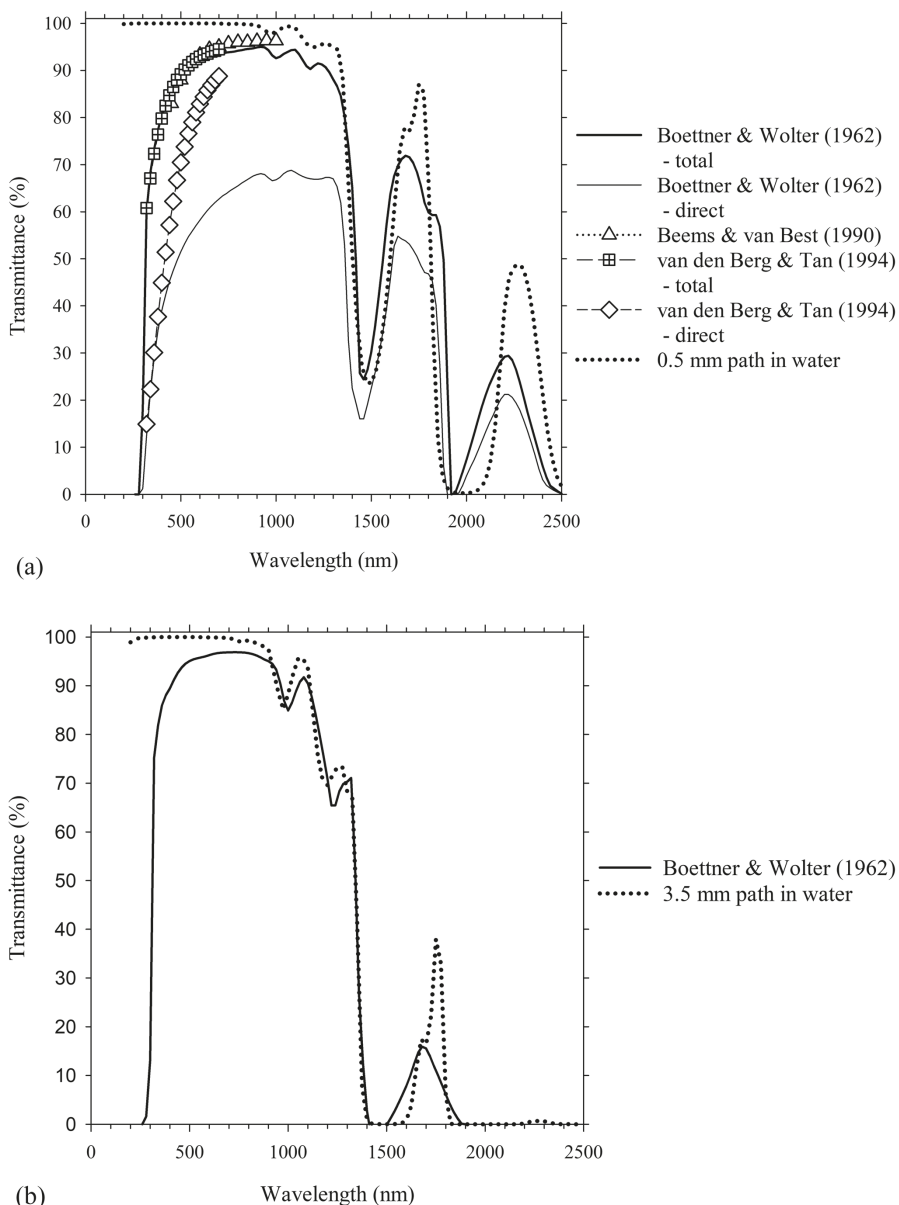
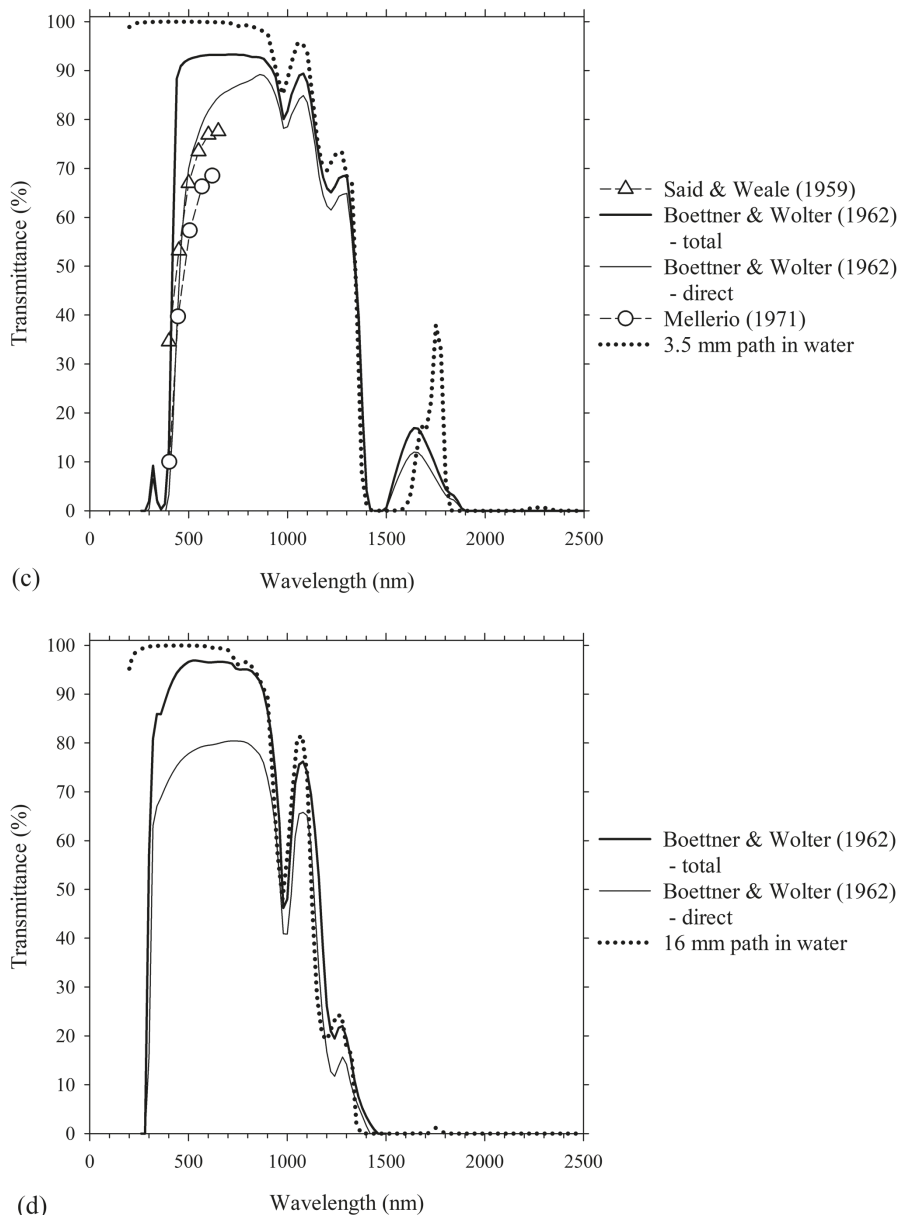


FIGURE 12.3 The spectral transmittances of the ocular components from various sources. (a) The cornea, from Boettner and Wolter (1962) for a 53-year-old subject, Beems and van Best (1990) mean data for groups of 22–43 years and 67–87 years, and van den Berg and Tan (1994) from their equation (1). (b) The aqueous, from Boettner and Wolter (1962), both direct and total. (c) The lens, from Said and Weale's (1959) mean of ages 21–45 years, Boettner and Wolter (1962) for a young child, and Mellerio's (1971) estimated mean of groups 19–32 years and 46–66 years. (d) The vitreous, from Boettner and Wolter (1962).

**FIGURE 12.3** (Continued)

12.3.4 CAUSES OF ABSORPTION BANDS

Since the major component of the eye is water, we may expect that the spectral absorption of the ocular media is strongly influenced by the absorption properties of water. Spectral absorption data for water have been given by Hulbert (1945), Curcio

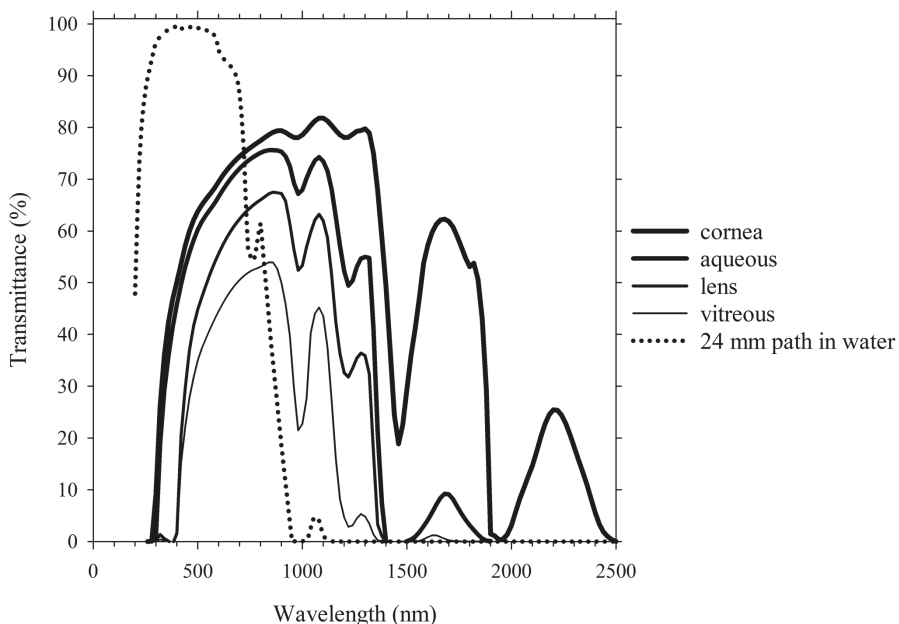


FIGURE 12.4 The cumulative spectral transmittances at the posterior surfaces of the ocular components, from Boettner and Wolter (1962). These data are for direct transmittance and for a young child/young adult, except for wavelengths less than 380 nm, where they are those for a young child.

and Petty (1951), and Smith and Baker (1981). These data have been used to calculate the spectral transmittances of different thicknesses of water samples, and appropriate curves are plotted on Figures 12.2 and 12.1a–d. Since the eye is not made totally of water, we would expect that, for any component, the best match occurs for a length of water shorter than the eye component thickness. We would expect a good match for the aqueous, which has the highest concentration of water, and the worst match for the cornea and lens. For the eye as a whole, it appears that a 16 mm thickness of water matches the whole eye well.

Examination of the transmittance curves for water in Figures 12.2 and 12.3a–d shows that the spectral absorption of the eye is dominated by water for wavelengths greater than about 600 nm. Absorption of energy by water at these wavelengths leads to heating of the water and surrounding tissue, and this may pose a risk of thermal damage.

For shorter wavelengths, the ocular tissue is far more absorbing than a similar path length of water, indicating that the absorption properties of proteins and other cellular components are dominating the absorption process. Since these materials dominate the absorption, there is a risk that they will be damaged by the radiation.

Figures 12.2–12.4 show that there is strong absorption for wavelengths less than about 400 nm. The cornea absorbs all radiation below 290 nm. Wavelengths less than 300 nm are potentially damaging to the cornea, and it is most sensitive to damage at

a wavelength of about 270 nm, where the threshold for observable damage is about 50 J/m². The lens absorbs radiation strongly between 300 nm and 400 nm, with the shortest wavelength reaching the retina being approximately 380 nm.

12.3.5 LUMINOUS TRANSMITTANCE

The above data describe the spectral transmittance of the ocular media. Of equal importance is the transmittance for a given light source. This can be calculated, given the spectral transmittance and the spectral output of the particular light source, as

$$\text{Luminous transmittance} = \frac{\int S(\lambda)T(\lambda)V(\lambda)d(\lambda)}{\int S(\lambda)V(\lambda)d(\lambda)} \quad (12.3)$$

where $S(\lambda)$ is the spectral output of the light source, $T(\lambda)$ is the spectral transmittance of the eye, $V(\lambda)$ is the photopic relative luminous efficiency value, λ is wavelength and the region of integration is over the visible spectrum, typically 380–780 nm.

12.4 SCATTER

Scatter is due to spatial variations in the refractive index within a medium, usually on a microscopic scale. Scatter is due to a combination of diffraction, refraction, and reflection. For example, light incident on a transparent object embedded in a medium of a different refractive index is scattered. Some of this light reflects from the incident surface, some passes through the surface and is refracted in a forward direction, and some is reflected inside the object several times and is finally refracted, either backwards or forwards. Finally, light outside the object but near its edge is diffracted in a forward direction.

The angular distribution of this scatter depends upon a few factors; in particular, the size and shape of the scattering particles, the refractive index mismatch, the scale of the inhomogeneities relative to the wavelength, and whether the inhomogeneities have any regularity. Thus, the angular distribution of scattered light may be complex. The complexity increases if the light is scattered more than once. In biological media, the angular distribution can be so complex that it is not usually possible to predict the amount of forward-scatter from measures of back-scatter. This is particularly important in visual optics, because it is easy to measure back-scattered light objectively but impossible to measure forward-scatter objectively in the living eye. Forward-scattered light is usually measured subjectively using psychophysical measures (see Chapter 13).

Since the cornea and lens consist of cells and connective tissue, which contain inhomogeneities on the scale of the order of the wavelength of light, it is surprising that they have a high transparency. By contrast, other cells (such as those in the skin) scatter light strongly. We need to understand why the normal cornea and lens have such a high transparency. The aqueous and vitreous humors are much more homogeneous, and are therefore less likely to scatter light.

Even in healthy eyes, scatter within the eye is usually sufficient to cause a reduction in visual performance in the presence of bright light sources (veiling glare), but this is much worse if cataracts are present. Cataracts are due to an aggregation of lens proteins, which lead to an increase in inhomogeneity and anisotropy of the lens. The forward-scatter from cataracts produces a veiling glare, while back-scatter from them reduces the amount of light reaching the retina.

The effect of forward-scattered light is partly mitigated by the directional sensitivity of the receptors – the Stiles–Crawford effect, which is described in section 14.5.

12.4.1 SCATTERING THEORY

For particles whose dimensions are much smaller than the wavelengths under consideration, and for which the scattering particles are mutually incoherent and independent, Rayleigh theory may be used to describe the scattering process. This theory assumes that the scattering particles are polarizable. Incident radiation polarizes the electronic structure of each particle into the form of a dipole, in which the electrons are pushed towards one side of the particle, leaving a positive charge on the opposite side. These dipoles oscillate in time with the incident radiation. According to classical physics, oscillating dipoles must radiate energy; thus, they absorb energy from the incident field and re-radiate it. The re-radiated energy is maximally radiated in a direction perpendicular to the dipole axis, and zero energy is radiated along the axis of the dipole.

Rayleigh scattering predicts the following:

1. The radiation scattered at 90° to the directly transmitted beam is completely polarized.
2. The amount of scattered light is proportional to the inverse of the fourth power of the wavelength. Therefore, blue light of 400 nm is scattered 9.4 times more strongly than red light of 700 nm wavelength.
3. The amounts of forward- and backward-scattering are the same.

Rayleigh theory does not apply when the sizes of scattering particles are similar or greater than the wavelength under consideration, and in this case one must use more complex scattering models. The significance of particle size is as follows:

1. If the oscillating dipole is much longer than the wavelength, the calculation of the amount of radiation emitted in any direction must consider the radiation from each point of the dipole. Since these are now at different distances, and hence have different phases with respect to an observer or detector, interference from the different points on the dipole must be considered.
2. If a scattering particle is much longer than the wavelength along the direction of light travel, there are a number of oscillating dipoles in the particle, which interfere in a constructive manner in the forward direction, but tend to interfere destructively in the backwards direction. These trends become

more pronounced with increase in particle size. Therefore, as the particle size increases, forward-scatter increases at the expense of backward-scatter.

The prediction of the scattering properties of particles of arbitrary size and shape is very difficult, if not impossible, but solutions are available for simple shapes. Because the amount of scattered light is proportional to the amount of light incident on the particle, the greater the cross-sectional area of the particle, the greater the scatter. For example, Mie theory explains the scattering by spheres of any size and wavelength. For very large spheres, the scattering is independent of wavelength, and the amount of scattered light is twice that incident on the cross-section of the particle. For example, in liquid water aerosols the scattering is proportional to the total cross-sectional area of the droplets. This means that, for a given volume of water in droplet form, the scattering is inversely proportional to the droplet radius or proportional to $N^{1/3}$, where N is the number of droplets.

A third scattering theory is the Rayleigh–Gans theory, or Rayleigh–Deybe theory according to Kerker (1969). This theory applies when the refractive index of the scattering particles is close to that of the medium in which they are imbedded. Applied to spherical scattering particles, this theory predicts that, for spheres, forward-scatter increases and back-scatter decreases with increase in size.

More information about the scattering according to these theories is provided by van den Berg (2017). The theories can be readily applied when the scattering particles are independent of each other. This assumes that they are weakly scattering and randomly ordered.

The main sources of scatter within the eye that affect vision are those due to the cornea, the lens, the iris and anterior sclera, and reflection from the fundus of the eye. The last of these is covered in section 14.2.

12.4.2 CORNEA

The bulk of the cornea is the corneal stroma (section 2.2). The stroma contains 200–250 or more layers (lamellae) of long cylindrical collagen fibrils, with the thickness of each lamella being about 2.0 µm (Hogan et al. 1971). Fibrils within each lamella have diameters of 32–36 nm and are separated by 20–50 nm. The fibrils within a layer are parallel to each other, and uniform in size and spacing (Hogan et al. 1971). The fibrils within a layer are inclined at large angles to fibrils in adjacent lamellae. The refractive index of fibers is about 1.47, and the surrounding ground substance has a refractive index of about 1.354 (Maurice 1969).

Hart and Farrell (1969), using a theoretical model of scattering by arrays of cylindrical structures with the degree of regularity found in real corneas, argued that the transparency of the cornea is due to the regularity of the fibril separation. Their theoretical predictions for the rabbit cornea closely matched experimental measures of transparency. Their theory was based upon the diffraction/interference from regular arrays. According to their theory, for an infinite array of equally spaced point-scattering particles, with a separation that is negligible compared to wavelength, the scattered light destructively interferes in all directions for all wavelengths except in

the direction of the incident beam. However, because the fibrils have finite diameters, their array is not perfectly regular and infinite, and because the spacing is not negligible compared with the wavelength, there is some residual scattering that is wavelength dependent. It follows that, if this regularity is disrupted further, scattering increases.

McCalley and Farrell (1988) investigated the wavelength dependency of scatter within the cornea and concluded that the range of the ordering of the fibrils (e.g., short distance versus long distance order) would affect scatter. They argued that if the order is short range, the dependency is proportional to the inverse of the cube of the wavelength (i.e., λ^{-3}). This was supported experimentally for the rabbit cornea. This cubic dependency is in contrast with the Rayleigh fourth power, i.e., λ^{-4} dependency, which assumes no regularity of the scattering particles and that the particles have negligible dimensions compared with the wavelength.

12.4.3 LENS

The bulk of the lens consists of proteins called crystallines. They appear to be arranged in a highly ordered fashion to reduce their light scattering effect. However, this ordering is imperfect, resulting in residual scattering. Moreover, larger sized scattering particles are interspersed. Scatter increases with age, with the forward-scatter being greater than the back-scatter (Bettelheim and Paunovic 1979). From studying lenses *in vivo*, van den Berg and Spekreijse (1999) found that the Rayleigh scattering was prominent for angles $> 30^\circ$, indicating that the scatter is caused by small protein molecules. For smaller angles, there was less wavelength dependence, which could be due to larger protein aggregates.

12.4.4 IRIS AND SCLERA

The iris and the surrounding anterior sclera, are somewhat translucent, thus contributing scattered light in the eye. Using a psychophysical technique, van den Berg et al. (1991) determined that light-blue irises transmit about 1% and 0.2% of red and green light, respectively, while dark-brown irises may transmit only hundredths of these amounts.

12.5 FLUORESCENCE

Fluorescence is the absorption of radiation by a medium at one wavelength, and the immediate re-emission of radiation at longer wavelengths. The re-emission is isotropic and therefore, in the eye, tends to produce a uniform veiling glare on the retina.

Fluorescence occurs mostly in the lens, and increases with age and in people with cataract (Lerman and Borkman 1976; Siik et al. 1993; Bleeker et al. 1986). The lens contains at least three fluorescent compounds: one called tryptophan, with a maximum sensitivity at 290 nm, and at least two fluorogens, with maximum sensitivities at 370 nm and 430 nm. Figure 12.5 shows the spectral emission properties of these compounds, with emission maxima at 332 nm for tryptophan and at 440 nm and 500 nm for the fluorogens. Tryptophan is present at birth, and does not change

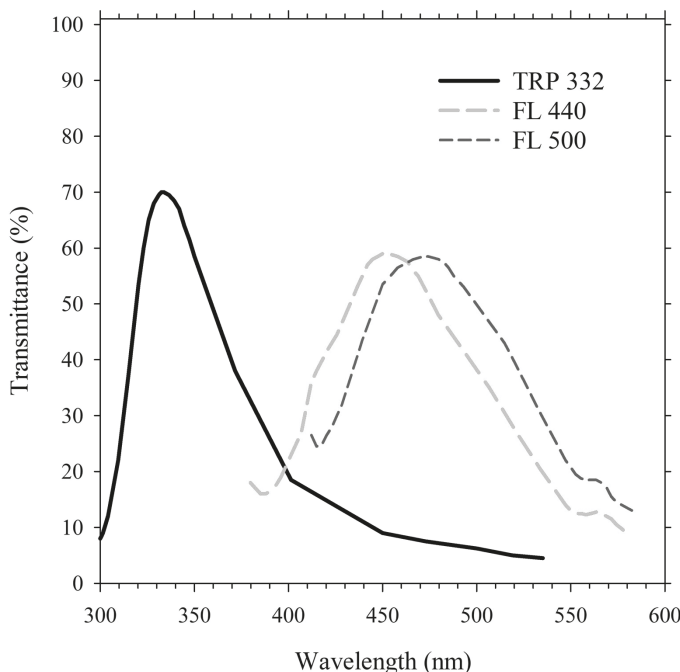


FIGURE 12.5 The fluorescent emission profiles of tryptophan and two fluorogens for a 78-year-old human lens (from Lerman and Borkman, 1978).

greatly with age, but the two fluorogens are not present at birth and accumulate throughout life.

The veiling glare produced by fluorescence can lead to a small loss in visual acuity of low contrast targets, an effect that increases with age (Elliott et al. 1993). The level of fluorescence depends upon the spectral sensitivity of the fluorescent compound and the spectral profile of the incident radiation, i.e., how much ultraviolet radiation and blue light is contained in the illuminating source. The contribution from tryptophan is minimized because the cornea absorbs much of the activating wavelengths.

12.6 BIREFRINGENCE

Optical materials such as water and glass are *isotropic*, which means that their physical properties are the same in all directions. This is because of the lack of atomic or molecular order. In contrast, many crystals have a well-defined atomic order. In some crystals, such as calcite, the physical properties (in particular the speed of light) depend upon direction of travel. This is referred to as *anisotropy*. Materials are called *birefringent* when the speed of light (or of refractive index) depends not only on direction of travel, but also on the orientation of the electric field. This can occur in glasses and plastics when they are placed under stress. This type of material presents two different refractive indices.

If a polarized light beam enters a birefringent material, a phenomenon called double refraction occurs. The beam splits into two parts (called ordinary and extra-ordinary) on entering the material, with the electric vectors at right angles to each other. These rays are now refracted differently according to Snell's law due to the two refractive indices, n_o for the ordinary ray and n_e for the extra-ordinary ray. The birefringence, Δn , is quantified by the difference ($n_e - n_o$) between these two refractive indices. This Δn produces a retardation between the two components of the light, which leads to a change in the polarization state of the outgoing beam. A material presenting this optical behavior is described as uniaxial. When the refractive effects are different for the three spatial directions, this is referred as biaxial.

Birefringence arising from crystal-like atomic order or a particular molecular arrangement is called *intrinsic birefringence*. The same effect can occur in glasses and plastics when they are placed under strain or are stretched (induced birefringence or *photoelasticity*). However, some tissue structural distributions might also generate birefringence. This is the case of elongated parallel structures with separation and thickness smaller than the wavelength of the incident light. This is known as *form birefringence*.

The eye exhibits both intrinsic and form birefringence. In this section, we look at birefringence in the cornea and lens. Birefringence of the retina is covered in section 14.4.

For a more extensive coverage of birefringence than given below, see Bueno (2017).

12.6.1 CORNEA

As mentioned in section 12.4, the bulk of the cornea consists of the approximately 200 lamellae of the stroma, in which the fibrils are cylindrical in shape and are usually regularly spaced. The fibrils in adjacent layers lie at large angles. According to Bour (1991), Wiener (1912) showed that an assembly of parallel rods immersed in a medium of lower index acts as a uniaxial crystal, with a positive birefringence with the optical axis in the direction of the rods. However, because of the large number of layers and their wide-ranging orientation, a light beam incident normally on the cornea would not encounter fibrils with any overall preferred orientation. Therefore, the cornea would not appear to be birefringent. On the other hand, a beam inclined to the corneal surface would undergo a slight birefringence. Bour and Lopez Cardozo (1981) estimated corneal birefringence to be +0.0020. Different authors have reported that the central cornea behaves as a *uniaxial crystal* (i.e., as a fixed retardation plate) with its slow axis along the nasally and downwards direction (in ophthalmic axis terms, between 90° and 180° for right eyes or between 0° and 90° for left eyes, lying in a plane (XY) perpendicular to the light propagation direction (Z axis) (Knighton and Huang 2002; Bueno 2011). This retardation increases from the central to the peripheral cornea (Sobczak et al. 2021).

In contrast with the uniaxial model of the cornea, van Blokland and Verhelst (1987) argued that the cornea acts as a *biaxial crystal* with two slow axes (and not just one as in a uniaxial structure). The axes changed from the nasal-downward direction at the central cornea to a tangential direction at the periphery. Although some

theoretical studies have been reported (Misson 2010), the issue of whether the cornea is better described as acting as an uniaxial or as a biaxial crystal is yet to be resolved (Bueno 2017).

12.6.2 LENS

The structure of the lens is different from that of the cornea. The lens consists of fibers (about 8 mm in diameter) that are laid down radially, rather than being parallel as in the cornea. Therefore, the same level of birefringence is not to be expected. The much greater thickness of the fibers (8 μm) than visible light will produce some form birefringence, to which will be added an intrinsic component due to cellular organelles (Bour 1991). Weale (1979) gave values varying between -0.5×10^{-6} and -3.5×10^{-6} . For *in vitro* measurements, Bueno and Campbell (2003) found small values varying from -4×10^{-6} in the center to -2×10^{-6} in the periphery of the lens. Klein Brink (1991) did not find differences in the total ocular retardation when measuring accommodated and non-accommodated living human eyes.

SUMMARY OF MAIN SYMBOLS

n, n'	refractive indices on the incident and refracted side of a surface
R	Fresnel reflectance at a surface
T	Fresnel transmittance at a surface
λ	wavelength
$S(\lambda)$	spectral output
$T(\lambda)$	spectral transmittance
$V(\lambda)$	photopic relative luminous efficiency

REFERENCES

- Beems, E.M., and J. van Best. 1990. "Light transmission of the cornea in whole human eyes." *Exp Eye Res* 50 (4):393–5. doi: 10.1016/0014-4835(90)90140-p.
- Bettelheim, F.A., and M. Paunovic. 1979. "Light scattering of normal human lens I. Application of random density and orientation fluctuation theory." *Biophys J* 26 (1):85–99. doi: 10.1016/S0006-3495(79)85237-6.
- Bleeker, J. C., J. A. van Best, and L. et al. Vrij. 1986. "Autofluorescence of the lens in diabetic and healthy subjects by fluorophotometry." *Invest Ophthalmol Vis Sci* 27 (5):791–4.
- Boettner, E.A., and J.R. Wolter. 1962. "Transmission of the ocular media." *Invest Ophthalmol* 1 (6):776–83.
- Bour, L.J. 1991. "Chapter 13. Polarized light and the eye." In *Visual Optics and Instrumentation, Vol. 1 in Cronly-Dillon, J. R. (series ed), Vision and Visual Dysfunction*, edited by W. N. Charman, 310–25. MacMillan Press.
- Bour, L.J., and N.J. Lopez Cardozo. 1981. "On the birefringence of the living human eye." *Vision Res* 21 (9):1413–21. doi: 10.1016/0042-6989(81)90248-0.
- Bueno, J. M. 2011. "Analysis of the central corneal birefringence with double-pass polarimetric images." *J Mod Opt* 58 (19–20):1664–870. doi: 10.1097/I.CO.0b013e3182000f94.
- Bueno, J. M. 2017. "Chapter 28. Polarization properties." In *Fundamentals and Eye Optics: Handbook of Visual Optics, Volume I* edited by P. Artal, 413–29. London: CRC Press.

- Bueno, J. M., and M. C. W. Campbell. 2003. "Polarization properties of the *in vitro* old human crystalline lens." *Ophthalmic Physiol Opt* 23 (2):109–18. doi: 10.1046/j.1475-1313.2003.00095.x.
- Curcio, J. A., and C. C. Petty. 1951. "The near infrared absorption spectrum of liquid water." *J Opt Soc Am* 41 (5):302–4. doi: 10.1016/0042-6989(93)90173-t.
- Elliott, D. B., K. C. H. Yang, K. Dumbleton, and A. P. Cullen. 1993. "Ultraviolet-induced lenticular fluorescence: intraocular straylight affecting visual function." *Vision Res* 33 (13):1827–33.
- Geeraets, W. J., and E. R. Berry. 1968. "Ocular spectral characteristics as related to hazards from lasers and other light sources." *Am J Ophthalmol* 66 (1):15–20.
- Hart, R. W., and R. A. Farrell. 1969. "Light scattering in the cornea." *J Opt Soc Am* 59 (6):766–74. doi: 10.1364/josa.59.000766.
- Hogan, M. J., J. A. Alvarado, and J. E. Weddell. 1971. *Histology of the Human Eye. An Atlas and Textbook*, 89. W. B. Saunders.
- Hulbert, E. O. 1945. "Optics of distilled and natural water." *J Opt Soc Am* 35 (11):698–705.
- Johnson, C. A., D. L. Howard, D. Marshall, and H. Shu. 1993. "A noninvasive video-based method of measuring lens transmission properties of the human eye." *Optom Vis Sci* 70 (11):944–55. doi: 10.1097/00006324-199311000-00012.
- Kerker, M. 1969. *The scattering of light and other electromagnetic radiation*. New York: Academic Press.
- klein Brink, H. B. 1991. "Birefringence of the human crystalline lens *in vivo*." *J Opt Soc Am A* 8 (11):1788–93. doi: 10.1364/josaa.8.001788.
- Knighton, R. W., and X.-R. Huang. 2002. "Linear birefringence of the central human cornea." *Invest Ophthalmol Vis Sci* 43 (2):82–6. doi: 10.1117/1.1463050.
- Lerman, S., and R. Borkman. 1976. "Spectroscopic evaluation and classification of the normal aging, and cataractous lens." *Ophthal Res* 8 (5):335–53. doi: 10.1159/000264841.
- Ludvigh, E., and E. F. McCarthy. 1938. "Absorption of visible light by the refractive media of the human eye." *Arch Ophthalmol* 20 (1):37–51.
- Maurice, D. M. 1969. "The cornea and sclera." In *Vol. 1, The Eye, 3rd ed*, edited by H. Davson, 486–600. London: Academic Press.
- McCally, R. L., and R. A. Farrell. 1988. "Interaction of light and the cornea: light scattering versus transparency." In *The Cornea. Transactions of the World Congress on the Cornea III*, edited by H. D. Cavanagh, 165–71. Raven Press.
- Mellerio, J. 1971. "Light absorption and scatter in the human lens." *Vision Res* 11 (2):129–41. doi: 10.1016/0042-6989(71)90229-x.
- Misson, G. P. 2010. "The theory and implications of the biaxial model of corneal birefringence." *Ophthalmic Physiol Opt* 30 (6):834–46. doi: 10.1111/j.1475-1313.2010.00782.x.
- Said, F. S., and R. A. Weale. 1959. "The variation with age of the spectral transmissivity of the living human crystalline lens." *Gerontologia* 3 (3):213–31. doi: 10.1159/000210900.
- Siik, S., P. J. Airaksinen, A. Tuulonen, and H. Nieminen. 1993. "Autofluorescence in cataractous human lens and its relationship to light scatter." *Acta Ophthalmol* 71 (3):388–92. doi: 10.1111/j.1755-3768.1993.tb07153.x.
- Smith, R. C., and K. S. Baker. 1981. "Optical properties of the clearest natural waters." *Appl Opt* 20 (2):177–84. doi: 10.1364/AO.20.000177.
- Sobczak, M., M. Owczarek, W. A. Woźniak, and P. Kurzynowski. 2021. "In vivo measurements of corneal birefringence properties using the one-way reflective Mueller polarimetry." *Biomed Opt Express* 29 (10):15356–65. doi: 10.1364/OE.421067.
- van Blokland, G. J., and S. C. Verhelst. 1987. "Corneal polarization in the living human eye explained with a biaxial model." *J Opt Soc Am* 4 (1):82–90. doi: 10.1364/josaa.4.000082.

- van den Berg, T. J. T. P. 2017. “Chapter 23. Scattering, straylight, and glare.” In *Handbook of Visual Optics: Fundamentals and Eye Optics, Volume I* edited by P. Artal, 349–62. London: CRC Press.
- van den Berg, T. J. T. P., and H. Spekreijse. 1999. “Light scattering model for donor lenses as a function of depth.” *Vision Res* 39 (8):1437–45. doi: 10.1016/s0042-6989(98)00220-x.
- van den Berg, T. J. T. P., and K. E. W. P. Tan. 1994. “Light transmittance of the human cornea from 320 to 700 nm for different ages.” *Vision Res* 34 (11):1453–6. doi: 10.1016/0042-6989(94)90146-5.
- van den Berg, T. J. T. P., J. K. IJsspeert, and P. W. T. De Waard. 1991. “Dependence of intraocular straylight on pigmentation and light transmission through the ocular wall.” *Vision Res* 31 (7/8):1361–7. doi: 10.1016/0042-6989(91)90057-c.
- Weale, R. A. 1979. “Sex, age and the birefringence of the human crystalline lens.” *J Exp Eye Res* 29 (4):449–61. doi: 10.1016/0014-4835(79)90062-9.
- Weale, R. A. 1986. “Real light scatter in the human crystalline lens.” *Graefe’s Arch Clin Exp Ophthalmol* 224 (5):463–6. doi: 10.1007/BF02173364.
- Wiener, O. 1912. “Allgemeine Sätze über die Dielektrizitätskonstanten der Mischkörper.” *Abh Sächs Ges Akad wiss Math-Phys Kl* 32:574 cited by Bour, L. J. (1991).



Taylor & Francis
Taylor & Francis Group
<http://taylorandfrancis.com>

13 Light Level at the Retina

13.1 INTRODUCTION

In the previous chapter, we considered the transmittance of the ocular media. Given the spectral transmittance data of the media, we can determine the amount of radiation and light reaching the retina from a source of known spectral output. The results shown in Figure 12.2 indicate that 50–90 per cent of the light entering the eye reaches the retina as image-forming light, although it is important to be aware that results from different studies vary considerably, and there is considerable age-dependence.

Ideally, the spectral and spatial light distributions in the retinal image should be proportional to those in the object. In reality this is not so, because of the effects of aberrations, absorption, diffraction, and scatter. Absorption and diffraction are wavelength-dependent, and aberrations, diffraction, and scatter affect the spatial distribution. In this chapter, we assess the spatial light distribution in the image.

13.2 RETINAL ILLUMINANCE: DIRECTLY TRANSMITTED LIGHT

In this section, we present equations that can be used to calculate the retinal light level or illuminance, given the brightness of the object (luminance of large area sources or luminous intensity for effectively point sources). We assume that the eye is correctly focused on that object, and therefore the equations are not strictly valid if the object is out of focus. If the level of defocus is small compared with the size of the object, the defocus has little effect on retinal illuminance except near the edge of the object. On the other hand, if the defocus is large compared with the size of the object, the equations give very misleading results. This is particularly so for point sources. Campbell (1994) presented a scheme for extended sources that can be used whether the eye is focused or not. Campbell's scheme is for calculating retinal irradiance, not retinal illuminance, but the equations apply equally to illuminance.

In this section, we consider only directly transmitted light, i.e., image-forming light. To determine the retinal illuminance of images formed from this directly transmitted light, it is most convenient to divide this section into two parts: one dealing with on-axis imagery, and the other dealing with off-axis imagery.

13.2.1 ON AXIS

13.2.1.1 Large Area Sources

For large area sources, small angle scatter, aberrations and diffraction can be neglected, and then the light distribution in the image has the same form as the object. When the eye is observing an object of large angular subtense, which has a luminance

L (cd/m^2), the corresponding retinal illuminance E' is given by the equation (Smith and Atchison 1997)

$$E' = \tau\pi L n'^2 \sin^2(\alpha') \text{ lux} \quad (13.1)$$

where τ is the transmittance of the ocular media (≈ 0.6 to 0.9) considering light losses due to reflection, absorption, and scatter, n' = the refractive index of the vitreous humour (usually taken as 1.336), and α' is the half angular subtense of the exit pupil measured at the retina. We can re-express this equation in terms of the (entrance) pupil diameter D rather than the angle α' as

$$E' = \tau\pi L D^2 F^2 / 4 \text{ lux} \quad (13.2a)$$

where F is the equivalent power of the eye and has a value of about 60 D.

We can also express the retinal illuminance in terms of area A of the (entrance) pupil, instead of its diameter D , as

$$E' = \tau L A F^2 \text{ lux} \quad (13.2b)$$

Since the power of the average eye is close to 60 D, and if we take D and A in millimeter units, the above two equations can be approximated by the equations

$$E' \approx 0.002830 \tau L D_{\text{mm}}^2 \text{ or } \approx 0.003600 \tau L A_{\text{mm}} \text{ lux} \quad (13.2c)$$

The Troland

The retinal illuminance is sometimes expressed in terms of trolands, which are the product of the object luminance L measured in cd/m^2 and the area A of the pupil measured in square millimeters. Thus, the retinal illuminance E'_T in trolands for a source of luminance L and viewed through a pupil of area A_{mm} in square millimeters is given by the equation

$$E'_T = L A_{\text{mm}} \text{ trolands} \quad (13.3a)$$

and since

$$A_{\text{mm}} = \pi D_{\text{mm}}^2 / 4$$

then

$$E'_T = \pi L D_{\text{mm}}^2 / 4 \text{ trolands} \quad (13.3b)$$

Relationship between Troland and Lux

We can relate retinal illuminance E' in lux with retinal illuminance E'_T in troland by equation (13.2a) and equation (13.3b). In relating these two equations, we must use the same units for pupil diameter, and if we replace the pupil diameter D in equation (13.2a) (which is in meters) with the diameter D_{mm} in millimeters, we have

$$E' = \tau F^2 E'_T / 10^6 \text{ lux} \quad (13.4a)$$

or

$$E'_T = 10^6 E' / (\tau F^2) \text{ troland} \quad (13.4b)$$

If we now use the approximation that the power is 60 D, we can write these equations as

$$E' = 0.0036 \tau E'_T \text{ lux} \quad (13.5a)$$

or

$$E'_T = (278/\tau) E' \text{ troland} \quad (13.5b)$$

As pointed out by Thibos et al. (2018), the troland is the same as 10^{-6} cd, i.e., it is really an intensity measure. They showed that the troland value of an extended source is the intensity in micro-candelas of an equivalent point source located at the eye's posterior nodal point that produces the same retinal illuminance as that produced by the extended source.

13.2.1.2 The Point Source – Diffraction Limited

The preceding equations do not apply for very small sources imaged without any aberration. The light distribution of the image of a point source is called the point spread function. In this case the geometrical optical image is smaller than the diffraction limited (i.e., aberration-free) point spread function, which has an angular radius

$$\theta = 1.22\lambda/D \quad (13.6)$$

In general, while the point spread function is affected by aberrations and diffraction, only the diffraction effect is easily predicted for any optical system.

The total luminous flux in the image of a point source, whether aberrated or not, is given by the equation (Smith and Atchison 1997)

$$\text{Flux} = \frac{\pi\tau ID^2}{4d^2} \quad (13.7)$$

where d is the distance of the source and I is the luminous intensity of the source.

For the diffraction limited image, the peak value of the illuminance is given by the equation (Smith and Atchison 1997)

$$E' = \tau ID^4 \left(\frac{\pi F}{4n'd\lambda} \right)^2 \quad (13.8)$$

The last two equations demonstrate two useful results:

1. The total luminous flux in a point spread function is proportional to the square of the pupil diameter (i.e., proportional to pupil area).
2. The peak illuminance is proportional to the fourth power of the pupil diameter or the square of the area.

13.2.1.3 The Point Source – Aberrated

The light distributions in real eyes and the effects of aberrations and diffraction are discussed in detail in Chapter 18.

13.2.2 OFF-AXIS OR PERIPHERAL SOURCES

The retinal illuminance of off-axis sources is more complicated than for on-axis sources. In conventional optical systems, such as a camera, the image plane illuminance decreases as the fourth power of the cosine of the peripheral angle, a result often known as the \cos^4 law. This is due to a combination of the following:

1. The reduction in apparent size of the peripheral pupil (proportional to $\cos(\text{angle})$).
2. The increase in distance from the exit pupil to the image on the image plane (the inverse square law, proportional to $\cos^2(\text{angle})$).
3. The inclination of the image plane to the direction of the incident beam (tilt, which is proportional to $\cos(\text{angle})$).

In the case of the eye, the \cos^4 law does not hold. While the effective pupil area decreases with distance off-axis, approximately as $\cos(\text{angle})$, the curved shape of the retina means that factors 2 and 3 above do not apply. The curved retina puts the image surface closer to the exit pupil, and tilts the normal to the surface in the direction of the exit pupil.

How the retinal light level depends upon peripheral angle is important in the measurement of visual fields and the calculation of the risk of the retina being damaged by hazardous radiation sources. Because of this importance, there have been a number of studies in the area (Drasdo and Fowler 1974; Bedell and Katz 1982; Kooijman 1983; Kooijman and Witmer 1986; Charman 1989).

Using Figure 13.1, we examine this situation with a simple model of the eye looking at a plane Lambertian source of infinite subtense and of luminance L . Let us consider an annular zone of this source as shown in Figure 13.1. The luminous flux entering the pupil of the eye is given by the equation

$$\text{Flux} = 2\pi L A(\theta_p) \sin\delta\theta \quad (13.9)$$

where $A(\theta_p)$ is the projected or apparent area of the circular pupil in the direction of the source. This equation shows that the luminous flux incident on the pupil depends only upon the solid angle of the annulus, and not on its distance and shape.

If we now assume that this annular light source is focused on the retina, it is imaged as an annular zone on the retina as shown in the figure. The area of this zone is given by the equation

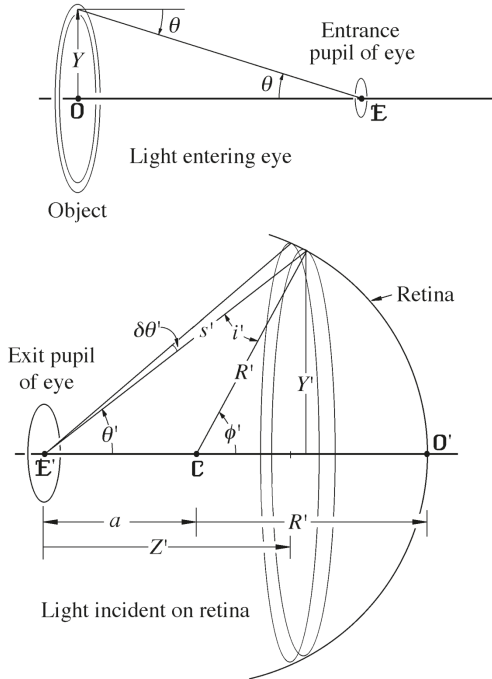


FIGURE 13.1 Geometry for calculating the retinal illuminance for peripheral large area sources. See text for details.

$$\text{Area} = s' \delta\theta' 2\pi Y' / \cos(i') \quad (13.10)$$

where the internal and external angles are connected by some function $\theta' = f(\theta)$. For small angles, paraxial theory predicts that

$$\tan(\theta') = \bar{m} \tan(\theta) \quad (13.11)$$

where \bar{m} has a value of about 0.82 (section 5.3.5). For larger angles, we should use a more accurate analysis (e.g., raytrace through a finite schematic eye) to determine the relationship, but we will leave this calculation for Chapter 16.

The retinal illuminance E' is the ratio of flux to illuminated area and thus is given by the equation

$$E' = \frac{LA(\theta)_p \sin(\theta) \cos(i')}{s' Y' (\delta\theta' / \delta\theta)} \quad (13.12)$$

To calculate values for this equation, we need to relate s' , Y' and i' to θ . We can do this as follows. First, from Figure 13.1 we have

$$Y' = Z' \tan(\theta') \quad (13.13a)$$

We can find the intersection (Y', Z') of this line with the retina, which we will assume to be circular in cross-section and described by the equation

$$Y'^2 + (Z' - a)^2 = R'^2 \quad (13.13b)$$

and then we have

$$s' = \sqrt{Y'^2 + Z'^2} \quad (13.13c)$$

$$\tan(\phi') = Y'/(Z' - a) \quad (13.13d)$$

and

$$i' = \phi' - \theta' \quad (13.13e)$$

and equation (13.11) gives

$$\delta\theta' / \delta\theta = \bar{m} \sec^2(\theta) \sec^2(\theta') \quad (13.14)$$

Figure 13.2 shows estimates of the relative retinal illuminance as a function of off-axis angle for a spherical retina ($R' = 12$ mm) and the distance $a = 8$ mm for a projected pupil area $A(\theta)_p$ falling off as $\cos(\theta')$. The relative retinal illuminance assuming the \cos^4 law is shown for comparison.

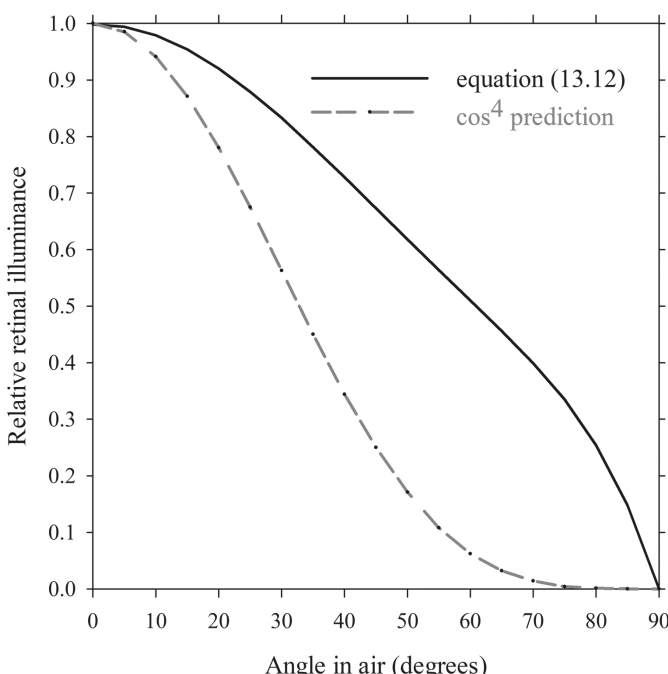


FIGURE 13.2 Variation of retinal illuminance with peripheral angle for a large area source, predicted from paraxial raytracing with a simple model eye.

Figure 13.2 predicts that, as an object moves off-axis, the retinal illuminance decreases, although not as rapidly as predicted by the \cos^4 law. The simple model neglects some important factors:

1. The retina is not spherical.
2. The effective pupil of the eye is slightly larger at peripheral angles than that predicted by the simple cosine reduction (section 3.5).
3. The exact relationship between the external angle θ and internal angle θ' . Equation (13.11) is accurate only for small angles. For larger angles, the aberrations affect the relationship between θ and θ' .
4. Variation of ocular transmittance with peripheral angle. We expect the transmittance to decrease as peripheral angle increases because of the increase in path length within the lens.
5. Aberrations of the eye increase with increase in peripheral angle, and this will affect the illuminance distribution for small sources.

Kooijman and Witmer (1986) found that the light level in excised eyes reduces more slowly with increase in peripheral angle than given by the above theoretical predictions (Figure 13.2). In Chapter 16 we use more realistic models of the eye, with more accurate estimates of apparent pupil area $A(\theta)_p$, and of the relationship between internal and external angles θ and θ' .

13.3 RETINAL ILLUMINANCE: SCATTERED LIGHT

As discussed in the previous chapter, a significant amount of light entering the eye is scattered forward, but out of the image-forming beam. In this section, we examine the light distribution due to scatter from a point source of light. This can be considered in terms of the retinal illuminance or an equivalent luminance of the image. Because we do not yet have accurate models of the complex nature of scatter, and because the light level on the retina is too low to be measured directly, the only determinations that can be made of the scattered light distribution are subjective measurements.

Several investigators have measured the light level at the retina due to scatter from a glare source in terms of the *equivalent veiling luminance*. In the presence of a glare source, the threshold luminance of a small patch of light was determined. The glare source was then turned off and the luminance L_v of a uniform background determined, which gave the same threshold for the small patch of light. This equivalent veiling luminance was fitted at the fovea $L_v(\theta)$ by equations of the form

$$L_v(\theta) = KE/\theta^n \quad (13.15)$$

where E is the illuminance in the plane of the eye of the glare source, θ is the off-axis angle in degrees of the glare source, and K and n are constants depending upon the particular investigation and the range of values of θ . Setting θ to 2, this equation is well known as the Stiles–Holladay relationship. Some specific equations are as follows:

$$L_v(\theta) = 9.2E/\theta^2 \quad 2.5^\circ \leq \theta \leq 25^\circ$$

$$\text{Holladay (1927)} \quad (13.16a)$$

$$L_v(\theta) = 4.16E/\theta^{1.5} \quad 1^\circ \leq \theta \leq 10^\circ \quad \text{Stiles (1929)} \quad (13.16b)$$

$$L_v(\theta) = 29E/\theta^{2.8} \quad 1^\circ < \theta < 8^\circ \quad \text{Vos and Bouman (1959)} \quad (13.16c)$$

$$L_v(\theta) = 29 E/(\theta + 0.13)^{2.8} \quad 0.15^\circ < \theta < 8^\circ \quad \text{Walraven (1973)} \quad (13.16d)$$

$$L_v(\theta) = sE/\theta^2 \quad \text{van den Berg (1995)} \quad (13.16e)$$

with $L_v(\theta)$ in cd/m², E in lux and θ in degrees. s is the *straylight parameter*, which may vary with factors such as age.

Vos (1984) showed that, in young subjects, the equivalent veiling luminance is produced in approximately equal proportions by the cornea, lens, and fundus. Scatter by the cornea and lens is discussed in section 12.4, and scatter by the fundus is discussed in Chapter 14.

Various attempts at modeling the equivalent veiling luminance have been made. For example, Fry (1954) used a reduced schematic eye with a refractive index n' (1.333) and axial length t (20 mm), and derived the theoretical equation

$$L_v(\theta) = (2/3)tRE[\cot(\theta/n') - \cos(\theta/n')]/n'^2 \quad (13.17)$$

where R is a constant. If E is given a value of 1 and R is given a value of 3.39, this equation gives the same value of $L_v(\theta)$ at 5° as equations (13.16a) and (13.16b).

The constant n in equations (13.15)–(13.16d) is a measure of the veiling light (or straylight). Other terms related to scatter are disability glare, which is much the same as straylight, and discomfort glare, which is much more difficult to define or measure (van den Berg 2017). van den Berg considered a three times increase in the straylight parameter of equation (13.16e) to provide a serious visual handicap.

13.3.1 EFFECT OF POSITION IN THE LENS OF A SCATTERING CENTER

It is often observed that the effect of a scattering center is strongly dependent upon its position. For example, posterior polar cataracts have more severe effects on vision than cataracts of similar size that are situated more anteriorly. This has often been explained by the proximity of the scattering center to the nodal points of the eye, but there is no optical reason why this should affect the scatter properties.

13.3.2 MEASUREMENT OF ANGULAR DISTRIBUTION OF SCATTERED LIGHT

The light distribution of the image of a point source, the point spread function, was introduced in section 13.2.1. The shape and width of the point spread function depend

upon the levels of diffraction, aberrations, and scatter, and upon the shape of the pupil. The effects of diffraction and aberration are discussed in Chapter 18, where it is shown that diffraction and aberrations produce a point spread function that has a half-width of a few minutes of arc. On the other hand, scatter causes light to be directed over much wider angles. Therefore, the light in the periphery of the point spread function is easily identified as scattered light. Close to the center of the point spread function, most of the light is from both diffraction and aberrations, and it is difficult to extract the scattered component. For this reason, investigators of scattered light usually consider only that component of light scattered through an angle greater than 1° (van den Berg 1995).

Various methods have been developed for measures of scattered light (van den Berg et al. 2013). Two subjective methods and one objective method are described below. Only the subjective methods can be considered to give a measure of the veiling glare.

13.3.2.1 Conventional Threshold Method

The essence of this method was given near the start of this section. The threshold luminance of a small patch of light is determined in the presence of a glare source. With the glare source turned off, the luminance of a uniform background is determined that produces the same threshold for the small patch of light. This luminance is the equivalent veiling luminance, and it is determined for a range of intensities of the glare source and of off-axis angles of the glare source. This approach can be modified by alternating the glare source and the background and varying one or the other until the perception of flicker is minimized.

13.3.2.2 Flicker Compensation Comparison Method

The modified approach mentioned above has been developed as a “compensation comparison” method. The straylight source is a peripheral annulus of flickering light (Figure 13.3, top). Some of this light is scattered by the eye into the right and left halves of a central test field. One half of the central test field (field “b”) is also presented with a compensation light, modulated at the same frequency but in counter-phase with the straylight (Figure 13.3, bottom). The other half (field “a”) receives the straylight and, in both phases, half the compensation light. This results in two different flickers in the central half fields, both of which modulate around half the sum of straylight and compensation light. Depending upon the level of compensation light, the field “b” either flickers stronger or weaker than the field “a”. The observer chooses the half that is perceived to have stronger flicker. The two flickers appear similar when the compensation light is twice the straylight. In the first of two stages, the intensity of the straylight source is varied, while that of the compensation light is kept constant. In the second stage, the intensity of the straylight source is kept constant, while that of the compensation light is varied. The first stage determines a coarse estimate of the straylight value while the final stage refines it. This has been developed in a commercial instrument called the C-Quant (Oculus Optikgeräte), which uses a maximum likelihood technique to obtain the straylight parameter s , defined in equation (13.6e), which is half the 50 per cent compensation point of a fitted psychometric curve (Franssen et al. 2006).

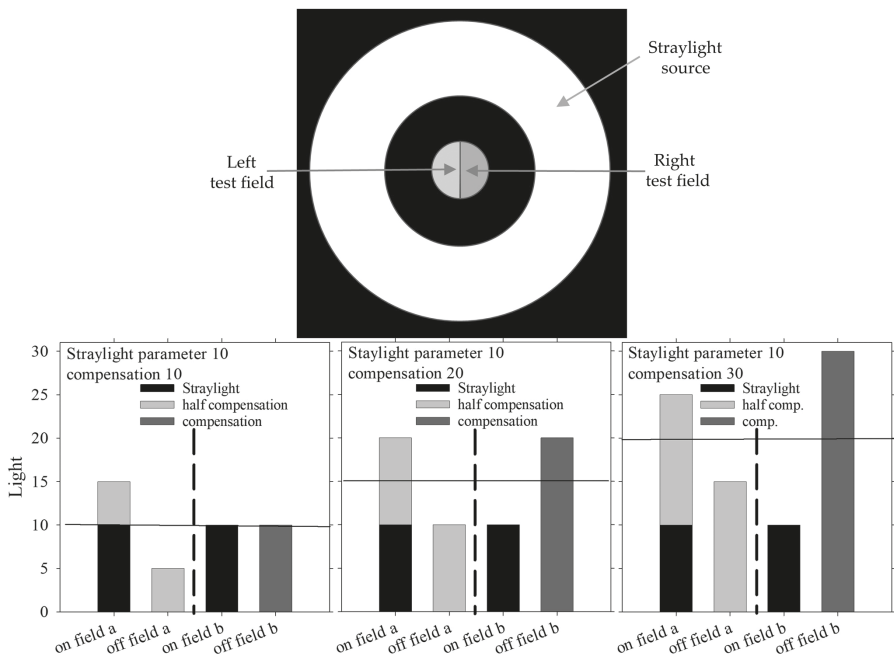


FIGURE 13.3 Retinal straylight measurement in C-Quant. Top: a flickering straylight source is presented in the peripheral ring field. The central test field is divided into two halves, each of which is perceived as flickering, due to the combination of flickering straylight and compensation light. The observer chooses the half that has stronger flicker. Bottom: in the on phase, field a has a light level equal to the straylight and half the compensation, while in the off phase it has half the compensation level. In the on phase, field b has a light level equal to the straylight, while in the off phase it has the compensation. In the figures, the scatter level is 10, and the compensation is set as follows: (left) 10 with the flicker greater in field a, (middle) 20 with the fields a and b having similar flicker, and (right) 30 so that the flicker is greater in field b. The horizontal lines indicate the light levels about which flicker occurs. Figure modified from Franssen, Coppens, and van den Berg (2006).

13.3.2.3 Hartmann-Shack Aberrometer

For the Hartmann–Shack aberrometer, described in section 8.4.5, displacements of the spots with respect to their ideal positions carry information about the aberrations. In addition, their spreads carry information about the scatter. The standard deviation for each lenslet across its image spot can be determined, and this can be averaged across all image spots (Donnelly et al. 2004). Such an analysis must be treated with caution as residual defocus and astigmatism will also cause spread of the image spots.

13.4 PHOTON DENSITY LEVELS

Sometimes there is a need to express the light level at the retina in terms of photon or quantal density (e.g., photons/m²/s), rather than in terms of lux or trolands. We can find an equation for this quantity by proceeding as follows.

Let us suppose that the spectral irradiance at the retina is $E'_r(\lambda)\Delta\lambda$ in the bandwidth $\Delta\lambda$. The corresponding number $N(\lambda)\Delta\lambda$ of photons/m²/s in the same bandwidth is given by the equation

$$N(\lambda)\Delta\lambda = \frac{E'_r(\lambda)\Delta\lambda}{hv} = \frac{E'_r(\lambda)\lambda\Delta\lambda}{hc} \quad (13.18)$$

where h is Planck's constant (6.62620×10^{-34} J/s), c is the speed of light (2.99792×10^8 m/s), and v is the frequency in Hertz. Weighting the photon density by a function $W(\lambda)$ over the entire spectrum, we have

$$N_{\text{tot}} = \int \frac{E'_r(\lambda)W(\lambda)\lambda}{hc} d\lambda \quad (13.19)$$

where $W(\lambda)$ may be the photopic or scotopic relative luminous efficiency functions, i.e., $V(\lambda)$ or $V'(\lambda)$. Now from equation (13.2a), for an extended source

$$E'_r = \tau\pi L_r(\lambda)D^2F^2/4 \quad (13.20)$$

where $L_r(\lambda)$ is the corresponding spectral radiance of the source in W/(st.m³). Equation (13.19) can now be written in the form

$$N_{\text{tot}} = \frac{\tau\pi D^2 F^2}{4hc} \int L_r(\lambda)W(\lambda)d\lambda \text{ photon /m}^2/\text{s} \quad (13.21)$$

13.4.1 BLACKBODY

The form of $L_r(\lambda)$ in the previous equation depends upon the nature of the source. One source of particular interest is an idealized opaque, non-reflective body called the *blackbody*. For a blackbody of known temperature T Kelvin, the spectral radiance $L_r(\lambda, T)$ from Planck's law is

$$L_r(\lambda, T) = \frac{c_1}{\pi\lambda^5 [e^{c_2/(\lambda T)} - 1]} \text{ W/(st.m}^3\text{)} \quad (13.22)$$

where

$$c_1 = 3.7418 \times 10^{-6} \text{ W.m}^2 \text{ and } c_2 = 1.4388 \times 10^{-2} \text{ m.K.}$$

13.4.2 REAL SOURCES

For real sources, the amount of radiation emitted is always less than that of the blackbody, and the ratio of the emittances is the emissivity ε . That is

$$\varepsilon = \frac{\text{output of real source}}{\text{output of the black body at the same temperature}} \quad (13.23)$$

This is usually a function of wavelength and temperature. However, for approximate calculations a constant value can be assumed, and values for various materials can be found in the Handbook of Chemistry and Physics (1975).

13.5 MAXWELLIAN VIEW

In many visual optical instruments, a small light source S provides a uniform field-of-view. If the entrance pupil of the eye coincides with the image S' of the source, the field-of-view has maximum width and maximum uniformity of luminance. This arrangement is called Maxwellian view (Figure 13.4). The exit pupil of the instrument at E' is uniformly illuminated and subtends an angular radius α' to the eye. The eye is focused approximately on this exit pupil. If S' is much smaller than the entrance pupil of the eye, pupil fluctuations and small eye movements do not affect retinal illuminance.

Illumination and viewing with Maxwellian view are optically very different from conventional viewing. For example, the fact that the effective pupil may be much smaller than the normal pupil places limits on expected visual acuity. The illumination may no longer be completely incoherent, so that conventional incoherent image quality criteria such as the point spread and modulation transfer functions may no longer be valid (Westheimer 1966). Here, only the light levels are considered.

13.5.1 EQUIVALENT LUMINANCE OF A LAMBERTIAN SOURCE

Based on equation (13.1), the light in the exit pupil of the instrument produces an illuminance E_1 at the plane of the entrance pupil of the eye, given by

$$E_1 = \pi L \sin^2(\alpha') \quad (13.24)$$

where L is the luminance of the instrument's exit pupil, and this exit pupil subtends an angular radius α' to the entrance pupil of the eye (Figure 13.4). If the image S' of the source S has an area A'_s , the luminous flux Flux_1 falling on the plane of the entrance pupil of the eye is given by

$$\text{Flux}_1 = E_1 A'_s = \pi L \sin^2(\alpha') A'_s \quad (13.25)$$

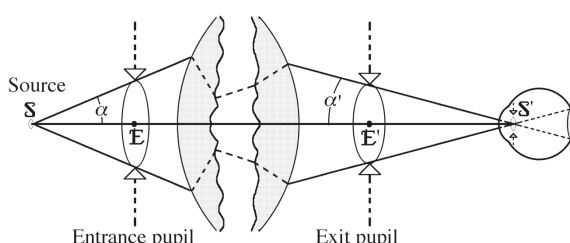


FIGURE 13.4 Maxwellian view.

If S' is smaller than the entrance pupil of the eye, all this flux falls on the retina, and the exit pupil appears to have a luminance L' .

If the observed bright field of the instrument exit pupil is replaced by a Lambertian source of the same luminance L' , the illuminance E_2 in the plane of the entrance pupil of the eye is

$$E_2 = \pi L' \sin^2(\alpha') \quad (13.26)$$

Since the new source is Lambertian, light from it fills the pupil of the eye completely. If the entrance pupil of the eye has area A_p , the luminous flux Flux_2 falling on the plane of the entrance pupil of the eye is given by

$$\text{Flux}_2 = E_2 A_p = \pi L' \sin^2(\alpha') A_p \quad (13.27)$$

The illuminated area of the retina is the same in the cases given by equations (13.25) and (13.27), and therefore the ratio of retinal illuminances and hence luminances is the ratio of the fluxes entering the eye. Since the two luminances are equal, the fluxes are equal, and

$$\pi L' \sin^2(\alpha') A_p = \pi L \sin^2(\alpha') A'_s$$

Therefore,

$$L' = L A'_s / A_p \quad (13.28)$$

As an example, if the area of the Maxwellian image is 2 mm^2 , the area of the entrance pupil of the eye is 10 mm^2 and the luminance at the instrument exit pupil is 100 cd/m^2 , the equivalent luminance of a Lambertian source is $100 \times 2/10 = 20 \text{ cd/m}^2$.

13.5.2 ADAPTING PUPIL SIZE

If the pupil is fully illuminated, pupil size affects retinal illuminance, which in turn controls pupil size. This feedback system cannot operate in Maxwellian view, where the source image is usually smaller than the smallest pupil size. Palmer (1966) found that, provided the source image in Maxwellian view is smaller than the natural pupil, the natural pupil is larger than in the case for the same light flux entering the eye in normal viewing.

SUMMARY OF MAIN SYMBOLS

General

A	area of the pupil in square meters
A_{mm}	area of the pupil in square millimeters
D	pupil diameter in meters
D_{mm}	pupil diameter in millimeters
E'	retinal illuminance in lux
F	equivalent power of the eye in diopters (i.e., m^{-1})

L luminance of an extended source in cd/m²

r ray height in pupil

τ mean luminous transmittance of ocular media of the eye

Retinal Illuminance: Directly Transmitted Light

E'_T retinal illuminance in trolands

I luminous intensity of a point source in cd

Retinal Illuminance: Scattered Light

E illuminance in plane of eye

$L_v(\theta)$ equivalent veiling luminance in a direction θ

Photon Density Levels

$N(\lambda)\Delta\lambda$ photon density in photons/m²/s

Maxwellian View

A_p area of pupil of eye

A'_s area of image of light source, imaged in the pupil plane of the eye

L' apparent luminance of field

REFERENCES

- Bedell, H. E., and L. M. Katz. 1982. "On the necessity of correcting peripheral target luminance for pupillary area." *Am J Optom Physiol Opt* 59 (10):767–9. doi: 10.1097/00006324-198210000-00001.
- Campbell, C. 1994. "Calculation method for retinal irradiance from extended sources." *Ophthalmic Physiol Opt* 14 (3):326–9. doi: 10.1111/j.1475-1313.1994.tb00021.x.
- Charman, W. N. 1989. "Light on the peripheral retina." *Ophthalmic Physiol Opt* 9 (1):91–2. doi: 10.1111/j.1475-1313.1989.tb00815.x.
- Donnelly, W. J., K. Pesudovs, J. D. Marsack, E. J. Sarver, and R. A. Applegate. 2004. "Quantifying scatter in Shack-Hartmann images to evaluate nuclear cataract." *J Refract Surg* 20 (5):S515–S22.
- Drasdo, N., and C. W. Fowler. 1974. "Non-linear projection of the retinal image in a wide-angle schematic eye." *Br J Ophthalmol* 58 (8):709–14. doi: 10.1136/bjo.58.8.709.
- Franssen, L., J. E. Coppens, and T. J. van den Berg. 2006. "Compensation comparison method for assessment of retinal straylight." *Invest Ophthalmol Vis Sci* 47 (2):768–76. doi: 10.1167/iovs.05-0690.
- Fry, G. A. 1954. "A re-evaluation of the scattering theory of blur." *Illum Eng* 49 (2):98–102.
- Handbook of Chemistry and Physics. 1975. 56th ed: CRC Press.
- Holladay, L. L. 1927. "Action of a light source in the field of view in lowering visibility." *J Opt Soc Am* 14 (1):1–15.
- Kooijman, A. C. 1983. "Light distribution on the retina of a wide-angle theoretical eye." *J Opt Soc Am* 73 (11):1544–50. doi: 10.1364/josa.73.001544.
- Kooijman, A. C., and F. K. Witmer. 1986. "Ganzfeld light distribution on the retina of human and rabbit eyes: calculations and in vitro measurements." *J Opt Soc Am A* 3 (12):2116–20. doi: 10.1364/josaa.3.002116.
- Palmer, D. A. 1966. "The size of the human pupil in viewing through optical instruments." *Vision Res* 6 (7):471–7. doi: 10.1016/0042-6989(66)90054-x.
- Smith, G., and D. A. Atchison. 1997. *The Eye and Visual Optical Instruments*, pp. 286, 308, 547. New York: Cambridge University Press.

- Stiles, W. S. 1929. "The effect of glare in the brightness difference threshold." *Proc Roy Soc B* 104 (731):322–51. doi: 10.1364/oe.16.021339.
- Thibos, L. N., N. Lopez-Gil, and A. Bradley. 2018. "What is a troland?" *J Opt Soc Am A* 35 (5):813–6. doi: 10.1364/JOSAA.35.000813.
- van den Berg, T. J. 1995. "Analysis of intraocular straylight, especially in relation to age." *Optom Vis Sci* 72 (2):52–9. doi: 10.1097/00006324-199502000-00003.
- van den Berg, T. J. T. P. 2017. "Chapter 23. Scattering, straylight, and glare." In *Handbook of Visual Optics: Fundamentals and Eye Optics, Volume I* edited by P. Artal, 349–62. London: CRC Press.
- van den Berg, T. J. T. P., L. Franssen, B. Kruijt, and J. E. Coppens. 2013. "History of ocular straylight measurement: A review." *Z Med Phys* 23 (1):6–20. doi: 10.1016/j.zemedi.2012.10.009.
- Vos, J. J. 1984. "Disability glare - a state of the art report." *CIE-J* 3 (2):39–53.
- Vos, J. J., and M. A. Bouman. 1959. "Disability glare: theory and practice." *Proc CIE, Brussels*:298–306.
- Walraven, J. 1973. "Spatial characteristics of chromatic induction; the segregation of lateral effects from straylight artefacts." *Vision Res* 13 (9):1739–53. doi: 10.1016/0042-6989(73)90091-6.
- Westheimer, G. 1966. "The Maxwellian view." *Vision Res* 6 (12):669–82. doi: 10.1016/0042-6989(66)90078-2.



Taylor & Francis
Taylor & Francis Group
<http://taylorandfrancis.com>

14 Light Interaction with the Fundus

14.1 INTRODUCTION

As well as the absorption of light by the retinal photoreceptors, which initiates the neural processes of vision, other interactions of light with the *fundus* (a term that generally includes the retina, choroid, and sclera) are important. Light from the fundus that passes out of the eye is essential for the diagnosis of ocular disease in ophthalmoscopy. Light from the fundus passing out of the eye is also important for determination of refractive error by retinoscopy and other objective techniques (Chapter 8). The spectral absorption by the fundus is important for understanding the processes of retinal damage by excessive light levels. In this chapter, we examine the specular reflection, scatter, and absorption of light at the fundus.

These properties are affected by the optical properties of the fundus layers (see Figure 1.3). Of particular importance are four absorbing pigments: macular pigment in the retina, visual pigments in the photoreceptors, melanin mainly in the pigment epithelium, and hemoglobin mainly in the choroid. There are individual and racial differences in the amount of the pigments, particularly melanin (Hunold and Malessa 1974). We will consider specular reflection, scatter, and absorption at the layers along a typical ray path.

14.1.1 INNER LIMITING MEMBRANE TO PHOTORECEPTORS (SIX LAYERS)

Light is first incident on the retina at the inner limiting membrane, and there will be some specular reflection at this boundary. The six layers between this boundary and the photoreceptors are highly transparent, but the regular array of the fibers in the nerve fiber layer has some effect on polarized light. There is a yellow pigment called xanthophyll in the macula (the macula pigment), and the amount of this pigment varies greatly between individuals (Ruddock 1963; Bone and Sparrock 1971; Hammond et al. 1997).

14.1.2 THE PHOTORECEPTORS

Some light is absorbed by the visual pigments in the photoreceptors. There are little data available on the proportion of light incident on the retina that is absorbed by the visual pigments and therefore contributes to visual perception, but the proportion will vary with state of light adaptation and retinal location. Rodieck (1998) made some estimations of the proportion of light that stimulates vision for a large pupil (≈ 7 mm diameter) when looking directly at a star. Ninety-two per cent of the light incident at the inner limiting membrane reaches the cones after absorption by the macular

pigment. Of this amount, 53% reaches the cone outer segments that contain the visual pigments. Of this amount, 38% is absorbed by visual pigment. Finally, 67% of this amount results in a photochemical reaction. Combining these proportions gives a retinal “efficiency” of 12%. Combining the 12% with the 54% of the light incident at the cornea which reaches the retina, approximately 7% of the light incident at the cornea is responsible for initiating the neural responses in the retina and beyond. Rodieck made estimates at 15° eccentricity to obtain a similar overall result for the rods of the dark-adapted retina.

14.1.3 THE PIGMENT EPITHELIUM

The remaining light passes into the pigment epithelium, where there is strong absorption and scatter by melanin granules. Some light passes through the pigment epithelium and enters the choroid.

14.1.4 THE CHOROID

The thin (350–450 mm) choroid is highly vascularized but contains some melanin. Thirty to sixty per cent of the choroid is blood (Delori and Pflibsen 1989). This contains hemoglobin, which is mainly oxygenated and strongly absorbs short wavelength light and back-scatters longer wavelengths. A small amount of light penetrates the choroid to reach the sclera.

14.1.5 THE SCLERA

This dense, whitish tissue back-scatters light strongly, so that most light reaching the sclera passes back through the retina.

14.2 FUNDUS REFLECTANCE

The term fundus reflectance refers to the light specularly reflected and scattered at the fundus and which eventually passes back out of the eye. Fundus reflectance can be measured by illuminating the fundus with a light source and analyzing the spectrum of light emerging from the eye. However, this is complicated by a number of factors:

1. *In vivo* spectral reflectance measurements involve the passage of light through the ocular media twice. We know from Chapter 12 that the ocular media absorb light, and that this absorption is not spectrally neutral. The effect of the spectral absorption of the ocular media is thus doubled.
2. *In vivo* results are contaminated by specular reflections from the refracting surfaces.
3. Reflectance measurements must use a reference baseline, which is often taken to be a white tile of high, diffuse reflectance, such as one based upon magnesium oxide.
4. Pigment absorption by the photoreceptors depends upon the level of bleaching and hence their immediate previous light exposure.

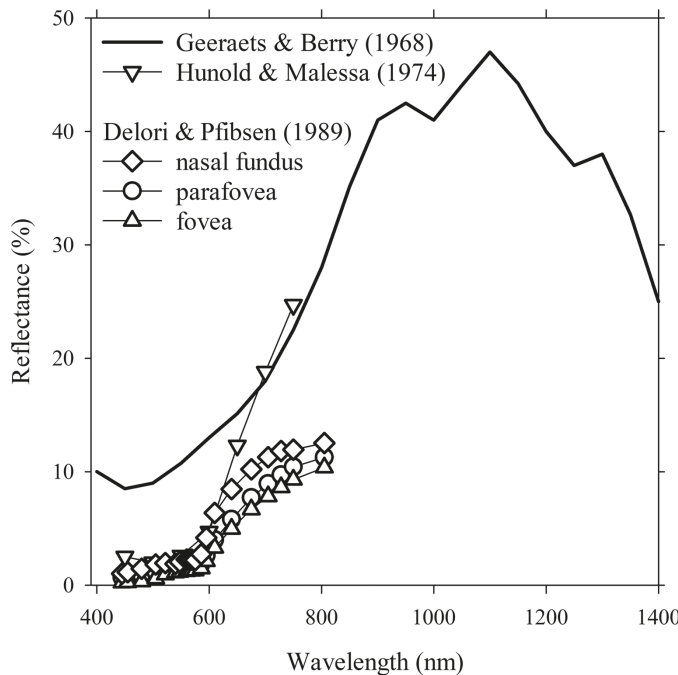


FIGURE 14.1 Spectral reflectance of the fundus from Geeraets and Berry (1968) – reflectance of pigment epithelium and choroid, Hunold and Malessa (1974) – derived from their extinction values, and Delori and Pflibsen (1989) – *in vivo* measurements on ten normal subjects at different retinal locations.

Measured values of fundus reflectance are shown in Figure 14.1. Reflectance is low at short wavelengths, and gradually increases with increase in wavelength. The high reflectance at the longer wavelengths is attributed to the blood in the choroid.

14.2.1 POLARIZED LIGHT

Some early workers in ocular polarization concluded that most polarized light incident upon the fundus is depolarized upon return out of the eye. This was because conversion of linear polarized light into elliptical polarized light was mistaken as depolarization (van Blokland 1985). More recent studies have found that most polarization is retained, although the orientation of polarization may change due to birefringence from the cornea and retina. van Blokland (1985) found about 90 per cent retention (fovea, 514 nm) and Dreher et al. (1992) found 50-80 per cent retention (close to the optic disc, 633 nm). van Blokland and van Norren (1986) found that the retained polarization at the fovea decreases with increase in wavelength (\approx 90 per cent at 488 nm and \approx 40 per cent at 647 nm).

Normal young eyes show low depolarization effects of \sim 10–20% (Bueno 2001). Whereas directional light coming from the photoreceptors is highly polarized,

depolarized light corresponds to the fraction that suffers scattering. This portion increases with age as the crystalline lens becomes cataractous (Bueno and Campbell 2003; Bueno et al. 2009) or after corneal refractive surgery (Bueno et al. 2006).

14.2.2 GUIDED AND UNGUIDED LIGHT

Some of the light incident on the retinal pigment epithelium is returned within the outer segments of photoreceptors, and can be considered to be guided or directed (van Blokland and van Norren 1986). The rest of the returned light may be considered to be unguided. Burns et al. (1995; 1997) developed and used an objective instrument for measuring cone photoreceptor alignment by measuring the distribution of light returning from the retina corresponding to different positions of a small light source at the pupil. The distribution was affected by the guiding of light along the photoreceptors. For bleached retinas, this produced functions with peak pupil positions that matched those obtained by psychophysical measurements of the Stiles–Crawford effect (see section 14.5).

14.2.3 LAYERS RESPONSIBLE FOR THE FUNDUS REFLECTANCE

On the basis that different components of reflectance (polarized versus unpolarized, and guided versus unguided) showed similar dependencies on wavelength, van Blokland and van Norren (1986) proposed a simple model in which one layer is mainly responsible. Because the wavelength dependence of the fundus reflectance was similar to that of the retinal pigment epithelium, they suggested that the retinal pigment epithelium is this layer. This argument was supported by the fact that the guided component increased with increased bleaching of retinal pigment, an effect that would not occur if the responsible layer was in front of the receptors. More sophisticated models have been developed since with van de Kraats et al. (1996) proposing that the outer aspects of the cones are responsible for the guided component of reflectance.

14.2.4 VEILING GLARE

Some of the light scattered by the fundus will contribute to veiling glare, because light that is scattered sideways (**halation**) and backwards can illuminate photoreceptors, some a long way from the original site of incidence. The Stiles–Crawford effect reduces the luminous efficiency of this scattered light (section 14.5). Veiling glare is reduced for people with dark irises compared to people with light irises, and this has been attributed largely to the level of fundus pigmentation (IJsspeert et al. 1990; van den Berg 1995).

14.3 ABSORPTION

Light that is not specularly reflected or scattered back out of the eye from the fundus is either absorbed or scattered in other directions within the eye. Since scattered light has the potential to excite photoreceptors in other parts of the eye,

one would expect the eye preferentially to absorb rather than scatter. The layers of the retina in front of the cones and rods are highly transparent. Absorption occurs mainly in the pigment epithelium, due to melanin, and in the choroid, due to hemoglobin.

Figure 14.2a shows spectral absorption of the pigment epithelium and choroid (Geeraets and Berry 1968), Figure 14.2b shows spectral absorption of oxygenated hemoglobin (van Assendelft 1970), and Figure 14.2c shows spectral absorption of the macular pigment (Wyszecki and Stiles 1982). Macular pigment consists of two pigments, zeaxanthin, which is found in dark green leafy vegetables such as broccoli and spinach, and lutein, which is found in sweetcorn and orange capsicum. It is thought that the macular pigment protects the retina by absorbing high-energy blue light and by scavenging free radicals, thus reducing the likelihood of degenerative macular disease (Lima et al. 2016).

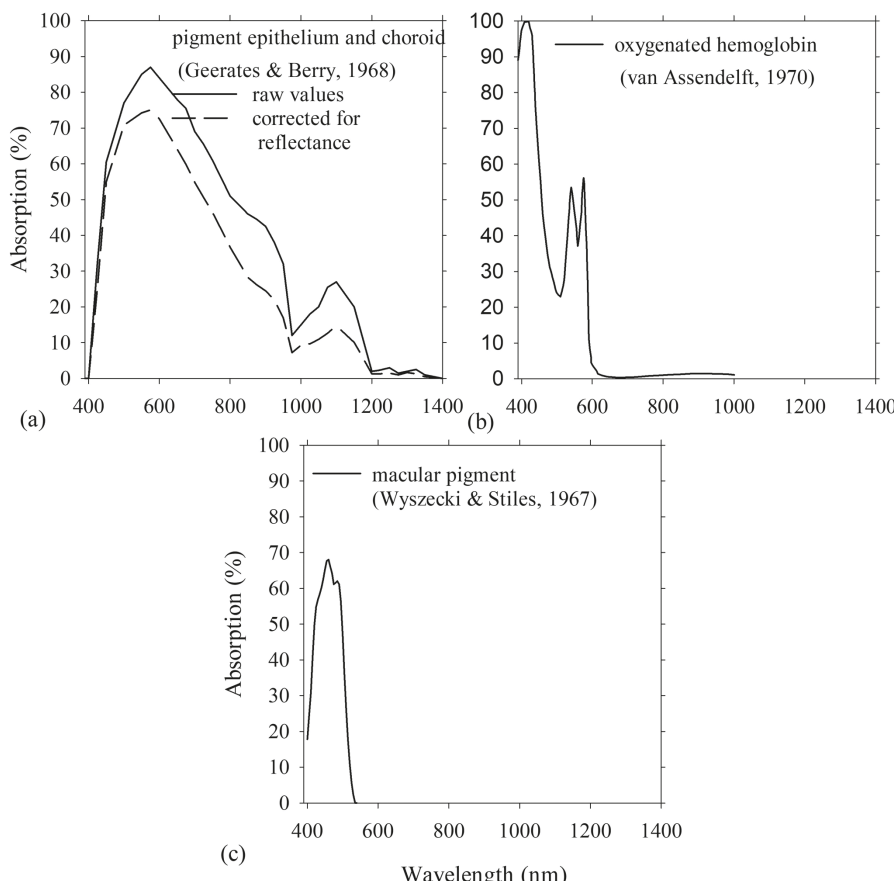


FIGURE 14.2 Absorption of the fundus. (a) Pigment epithelium and choroid (Geeraets and Berry 1968). (b) Oxygenated hemoglobin (van Assendelft 1970). This is for a concentration of 0.00233 mol/liter and 0.1 mm thickness. (c) Macular pigment (Wyszecki and Stiles 1967).

14.4 BIREFRINGENCE

Birefringence has been discussed in section 12.6 with regard to the cornea and lens. In birefringent materials, the incident light beam is affected by a different refractive index depending upon the direction of the electric vector. The retinal nerve fiber layer exhibits birefringence because of the structure of the nerve fibers, their size, and their regular arrangement (Dreher et al. 1992). The nerve fibers form a radial pattern centered on both the optic disc and the fovea with cylindrical fibers parallel to the retinal surface. Such an arrangement acts as a uniaxial crystal (i.e., form birefringence), with its optic axis being parallel to the axis of the cylinders and perpendicular to the incident light. The refractive index will be a minimum for the electric vector perpendicular to the nerve fiber direction and a maximum for the electric vector parallel to the nerve fibers. The arrangement of nerve fibers is similar to the fibril layers in the cornea (section 12.4), but whereas the corneal fibril diameters are smaller than the wavelength of light, the nerve fiber diameters in the retina are about the same size or larger than the incident wavelengths (0.6–2.0 μm , Hogan et al. (1971)).

There have been several *in vivo* studies of retinal birefringence, for example, van Blokland (1985), Dreher et al. (1992), and Twietmeyer et al. (2008). Measurements of retinal birefringence must take into account or eliminate any birefringence from the cornea (Zhou and Weinreb 2002).

Birefringence of the nerve fiber layer has an application in scanning laser polarimetry (Dreher et al. 1992; Weinreb et al. 1995), which estimates nerve fiber loss due to diseases, such as glaucoma. Red or near infrared light from a laser, initially linearly polarized, passes into the retina. It is scattered from the deeper retinal layers and the choroid to pass back out of the eye. The plane of polarization is changed by its passage (twice) through the nerve fiber layer. The change in the polarization state is used to estimate nerve fiber layer thickness, and the thickness is determined at the retinal area of interest.

As well as the nerve fiber layer, birefringence also occurs at the Henle fiber layer, which is the foveal component of the outer plexiform layer, consisting of bundles of photoreceptor axons. Retinal birefringence at the foveal area can be used as a tool to assess foveal fixation and detect amblyopia (Hunter et al. 2003).

14.5 THE STILES–CRAWFORD EFFECT AND RETINAL DIRECTIONALITY

Stiles and Crawford (1933) discovered that the luminous efficiency of a beam of light entering the eye and incident on the fovea depends upon the entry point in the pupil. This phenomenon is known as the Stiles–Crawford effect of the first kind, but more generally as the Stiles–Crawford effect (SCE). It is often called *retinal directionality*. Later, Stiles (1937) reported that varying the entry of the beam also altered the perceived saturation and hue of the light. This is called the Stiles–Crawford effect of the second kind. Vohnsen (2009) attempted a common explanation for the two effects. The latter is not discussed further here.

The Stiles–Crawford effect is relevant to visual photometry and retinal image quality. It can be considered both as a neural and as an optical phenomenon, as it is

retinal in origin but is often explained as photoreceptors acting like waveguide properties. It is a predominantly a cone phenomenon, and hence predominantly a photopic phenomenon. A good review of the Stiles–Crawford effect is given by Vohnsen (2017).

A number of different mathematical functions have been used to describe the Stiles–Crawford effect, with the most popular one being a Gaussian distribution as first used by Stiles (1937). This can be given as

$$\eta = \eta_{\max} e^{-\rho_e(x-x_{\max})^2} \quad (14.1)$$

where η is the brightness sensitivity at pupil entry position x (in millimeters) relative to a reference position near the pupil center, η_{\max} is the maximum brightness sensitivity at the pupil-entry position x_{\max} (peak location in the pupil or the photoreceptor alignment), and ρ_e is the parameter assumed to reflect the directionality of the photoreceptor population being tested. Sometimes, ρ_{10} is used instead of ρ_e in equation (14.1a), where ρ_{10} and ρ_e are related by $\rho_{10} = \rho_e / \log_e 10 = 0.434 \rho_e$:

$$\eta = \eta_{\max} 10^{-\rho_{10}(x-x_{\max})^2} \quad (14.1a)$$

Other equations to describe the Stiles–Crawford effect have been proposed (Moon and Spencer 1944; Enoch 1958; Safir et al. 1970; Rativa and Vohnsen 2011b). Rativa and Vohnsen used a super-Gaussian equation

$$\eta = \eta_{1\max} 10^{-\rho_{10-1}(x-x_{\max})^2} + \eta_{2\max} 10^{-\rho_{10-2}(x-x_{\max})^4} \quad (14.1b)$$

where $\eta_{1\max}$, $\eta_{2\max}$, $\eta_{1\max} \eta_{2\max} \rho_{10-1}$, ρ_{10-2} , and x_{\max} describe the multimode effects of a waveguide model. Using ρ_e 's rather than ρ_{10} 's, this equation becomes

$$\eta = \eta_{1\max} e^{-\rho_{e-1}(x-x_{\max})^2} + \eta_{2\max} e^{-\rho_{e-2}(x-x_{\max})^4} \quad (14.1c)$$

While the Gaussian function is usually a good fit to experimental data out to 3 mm from the peak of the function, and has the addition virtue of simplicity, the super-Gaussian equation produces flatter central responses, which can sometimes improve the accuracy of fits (Figure 14.3).

In what follows, we restrict ourselves to the Gaussian function given by equation (14.1). It may be extended to two dimensions, for example,

$$\eta = \eta_{\max} e^{-\rho_e [(x-x_{\max})^2 + (y-y_{\max})^2]} \quad (14.1d)$$

Measured ρ_e coefficient for the large scale study of Applegate and Lakshminarayanan (1993) are given in Table 14.1, and Figure 14.3 shows the Stiles–Crawford effect for different ρ_e coefficients. Combining the data across many studies gives a mean value of 0.12 mm^{-2} (Applegate and Lakshminarayanan 1993).

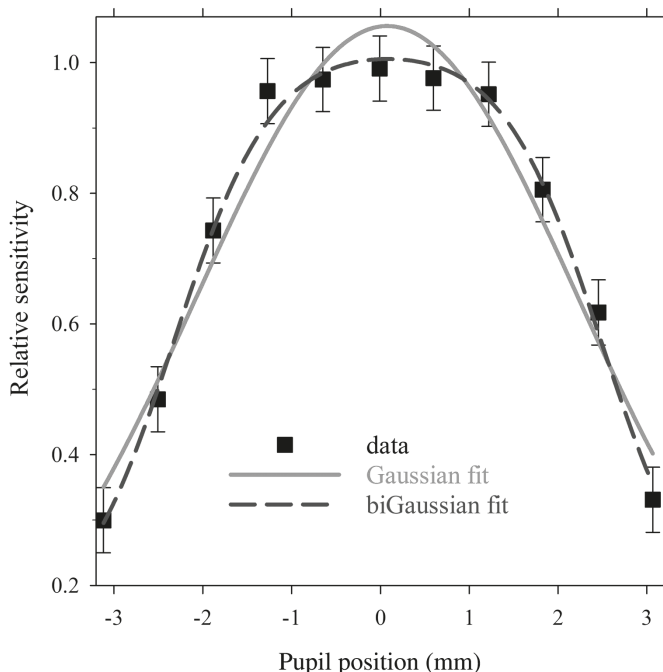


FIGURE 14.3 Example of Stiles–Crawford data and their Gaussian and super-Gaussian fits. For the Gaussian fit (equation (14.1)), $\eta_{\max} = 1.0560$, $\rho_e = 0.1081 \text{ mm}^{-2}$, and $x_{\max} = +0.0762 \text{ mm}$ (adjusted $R^2 = 0.95$). For the super-Gaussian fit (equation (14.1c)), $\eta_{1\max}$ and $\eta_{2\max}$ are each 0.503, $\rho_{e,1} = 0.0692 \text{ mm}^{-2}$, $\rho_{e,2} = 0.0224 \text{ mm}^{-4}$, and $x_{\max} = +0.0807 \text{ mm}$ (adjusted $R^2 = 0.99$). Data of Rativa and Vohnsen (2011b).

TABLE 14.1
Some Published Values of the Stiles–Crawford ρ_e Parameter and the Position of the Peak of the Stiles–Crawford Effect^a

Investigation	No. Participants/Eyes	$\rho_e \pm 1 \text{ sd} (\text{mm}^{-2})$	peak $\pm 1 \text{ sd} (\text{mm})$
Dunnewold 1964 ^b	29/47	–	$0.37 \pm 0.78 \text{ n}, 0.29 \pm 0.8 \text{ s}^c$
Applegate and Lakshminarayanan 1993 ^d	49/49	0.116 ± 0.029^e	$0.47 \pm 0.68 \text{ n}, 0.20 \pm 0.64 \text{ s}$

Note: n = nasal; s = superior. ^a ρ_{10} values have been converted to ρ_e values by multiplying by 2.303.

^b Relative to center of pupil. ^c Determined by Applegate and Lakshminarayanan (1993) from Figure 45 of Dunnewold (1964). ^d Relative to first Purkinje image. ^e Mean of horizontal and vertical values.

14.5.1 PEAK OF THE STILES–CRAWFORD EFFECT

The position of the peak does not usually correspond to the center of the pupil (which itself varies with pupil diameter – see section 3.3), and it also varies between individuals. Its position is considered to reflect the overall alignment in the pupil of the photoreceptor population being tested. Measured values of the peak from two large-scale studies are given in Table 14.1. Combining the data across many studies gives mean values of ≈ 0.4 mm nasal and ≈ 0.2 mm superior relative to the pupil reference, whether this be the pupil center or the pupillary axis (Applegate and Lakshminarayanan 1993).

14.5.2 INTEGRATING THE STILES–CRAWFORD EFFECT ACROSS THE PUPIL

The Stiles–Crawford effect can be integrated across the area of the pupil to determine a *photometric equivalent pupil*, by which is meant a pupil size in the absence of the effect that is photometrically equivalent to the pupil size with the effect. The ratio of the two sizes is the photometric efficiency E_p , or the effective visibility (Vohnsen et al. 2017). Following Atchison et al. (2000), an annulus in the pupil of radius R and width dR has an area of $2\pi R dR$ and is weighted by the Stiles–Crawford relative sensitivity $\eta(R)/\eta_{\max}$. Integrating across the pupil area, E_p for a pupil semi-diameter R_p is given by

$$E_p = \frac{\int_0^{R_p} 2\pi \frac{\eta(R)}{\eta_{\max}} R dR}{\pi R_p^2} \quad (14.3)$$

From equation (14.1), $\eta(R)/\eta_{\max}$ can be given as $e^{-\rho_e R_p^2}$, which substituted into equation (14.3) gives

$$E_p = \frac{1 - e^{-\rho_e R_p^2}}{\rho_e R_p^2} \quad (14.4)$$

In terms of the entrance pupil diameter D , E_p is

$$E_p = \frac{4 \left(1 - e^{-\frac{\rho_e D^2}{4}} \right)}{\rho_e D^2} \quad (14.5)$$

and the *photometric equivalent pupil diameter* D_e is given by

$$D_e = D \sqrt{E_p} \quad (14.6)$$

Equation (14.3) can be modified if the Stiles–Crawford effect is not centered on the pupil (Atchison et al. 2000).

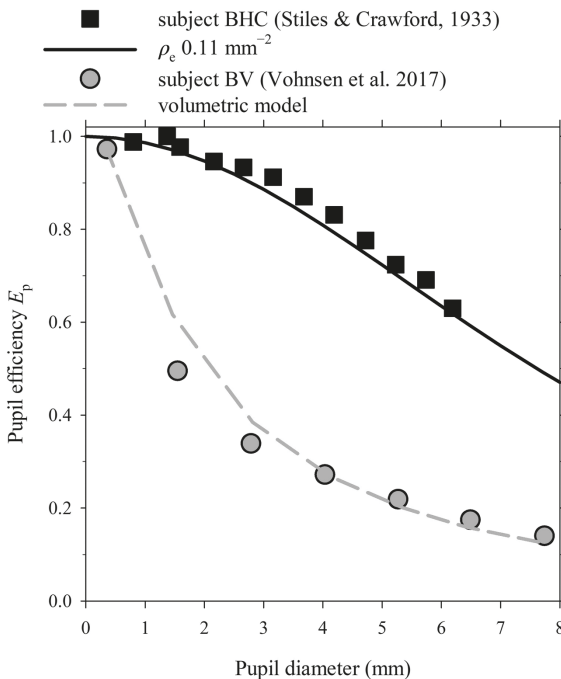


FIGURE 14.4 Photometric efficiency E_p as a function of pupil diameter. (a) Measurement and prediction for participant BHC, data of Stiles and Crawford (1933). (b) Measurement and predictions of participant BV. Squares indicate E_p predicted from $\rho_e = 0.11 \text{ mm}^{-2}$, and the dotted line indicates E_p predicted from a geometric optics absorption model. Data in (b) are from Figure 8 of Vohnsen et al. (2017).

The Stiles–Crawford effect is being treated here as an *apodization*, which means it is being treated as an optical filter of variable density placed at the pupil rather than an effect occurring at the retina. Furthermore, the directionality is being determined from measurements in Maxwellian view (source imaged at the pupil rather than at the retina). Nevertheless, Stiles and Crawford (1933) and Enoch (1958) found the above modeling and experimental determinations of E_p to be in good to reasonable agreement. However, Vohnsen et al. (2017) found reduction in experimental E_p with increase in pupil size was 3–4 times faster than the theoretical prediction, but results were in good agreement with their geometric optics absorption model (see section 14.5.4). Figure 14.4 shows some results of Stiles and Crawford and of Vohnsen et al. The reason for the discrepancies between the older and the newer experimental results is not known.

14.5.3 SOME FACTORS INFLUENCING THE STILES–CRAWFORD EFFECT

14.5.3.1 Wavelength

Directionality varies with wavelength with lower values at intermediate wavelengths than at shorter and longer wavelengths (Stiles 1937, 1939; Wijngaard and van

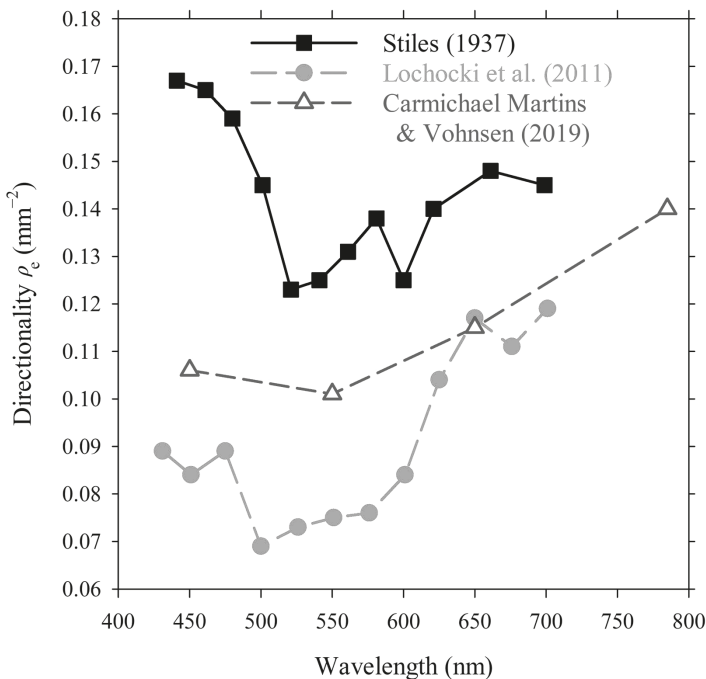


FIGURE 14.5 Directionality as a function of wavelength. Stiles' results are for one participant. Lochocki et al.'s results are the average of three participants' data, and Carmichael Martins and Vohnsen's results are the average of six participants.

Kruysbergen 1975; Lochocki et al. 2011; Carmichael Martins and Vohnsen 2019) (Figure 14.5). (Stiles 1937) attributed this to variation in the directional properties of the three cone types. At 5° from the fovea, Stiles (1939) found little difference for blue and green regions of the spectrum, and an increase at long wavelengths.

14.5.3.2 Eccentricity

Under photopic conditions, directionality increases with increasing retinal eccentricity to a few degrees from fixation (Figure 14.6). Choi et al. (2003) reported increasing directionality from the fovea out to 15° horizontally (Figure 7.2), but Bedell and Enoch (1979) reported similar directionality values at the fovea and at 35°. Carmichael Martins and Vohnsen (2019) measured directionality at parafoveal retinal eccentricities ranging from 5° temporal retina to the 7.5° nasal retina in 2.5° steps. The directionality increased at 2.5° from the fovea in both nasal and temporal directions and decreased thereafter.

Variation with eccentricity may be due to changing shape, length, and density of retinal receptors; cones in the central fovea are packed densely and are elongated and resemble rods, whereas cones in the parafovea are packed less densely and have cone-like shapes. Carmichael Martins and Vohnsen (2019) were able to explain their results by a volumetric absorption model (section 14.5.4).

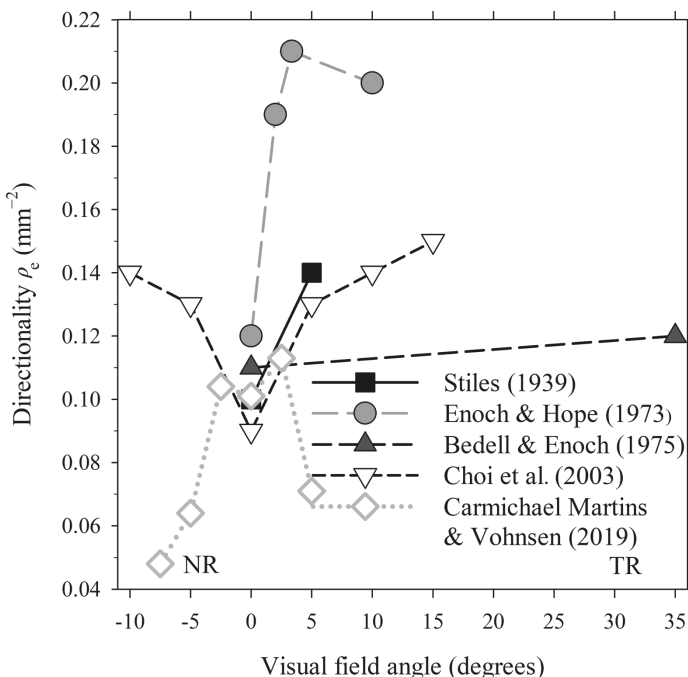


FIGURE 14.6 Directionality as a function of retinal eccentricity. TR indicates temporal retina and NR indicates nasal retina.

14.5.3.3 Luminance

Stiles–Crawford directionality is constant at the fovea, and is higher for photopic luminances than for scotopic luminances at the parafovea, indicating the involvement of the cone photoreceptors (Crawford 1937; Stiles 1939). Crawford (1937) examined the effect of luminance on directionality at the centre of the fovea and at 5° and 14° retinal eccentricities, and found that the SCE was the same at the fovea for high and almost zero luminance conditions (Figure 14.7a). However, the directionality at the parafoveal locations was similar to that of the fovea at high luminance (237 cd/m²) and changed little below 0.01 cd/m², with the directional sensitivity varying by four times between these levels (Figure 14.7b). This difference in the directional sensitivity at the parafovea and fovea is attributed to a transition from cone to rod directional sensitivity as brightness is lowered (Crawford 1937; Stiles 1939). Flamant and Stiles (1948) and Van Loo and Enoch (1975) showed low scotopic directional sensitivity at 5° parafovea. Carmichael Martins and Vohnsen (2019) examined the effect of luminance on the SCE at the fovea and 5° nasal parafovea. The directionality was lowest in the scotopic condition (0.03 cd/m²) and increased rapidly by 63% in a mesopic condition with a luminance of 1.3 cd/m², and the directionality did not change at higher luminance at either location.

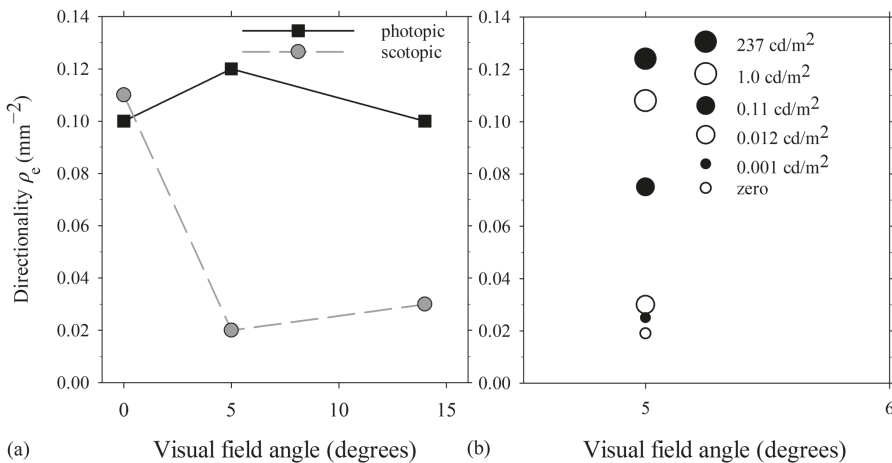


FIGURE 14.7 Directionality as a function of retinal eccentricity with different luminance conditions. (a) Directionality of participant B.H.C. with high and zero luminance conditions at the fovea and at 5° and 14° temporal retinal eccentricities. (b) Directionality at 5° retinal eccentricity with different luminance conditions for participant B.H.C. Directionalities were calculated from data of Figures 3, 5, and 6 in Crawford (1937). Equation (14.1) was used to fit the data to obtain directionality for each curve in the figure.

14.5.3.4 Field size

Under photopic conditions, Nilagiri, Suheimat, Lambert, Turpin et al. (2021) found directionality increased for central vision as field size increased from 0.5° to 4.7° diameter, although this was noted only for four mild myopes and not for two emmetropes. The change with field size was supported by a geometric optics absorption model (section 14.5.4).

14.5.3.5 Refractive Errors and Aberrations

Blur influences the Stiles–Crawford effect due to defocus and higher-order aberrations. Because of aberrations associated with the off-axis light entry, it would be expected that a blurred test field will have to be even brighter to match the reference field. For one myopic participant, Singh et al. (2009) showed increased directionality by 24% for myopic defocus (as would occur with positive power trial lenses) and decreased directionality by 14% for negative defocus. They suggested that the asymmetry in directionality between positive and negative defocus is due to the interaction of defocus with aberrations. Across six emmetropic participants, Carmichael Martins and Vohnsen (2018) showed decreasing directionality from 16% to 30% for every 3 D increase in induced myopia up to +9 D and increased directionality by 10% with -3 D induced hyperopia. The differences in the results of these studies could be due to differences in measurement methods and to the interaction of defocus and higher-order aberrations associated with the off-axis light entry in emmetropes and myopes.

14.5.3.6 Accommodation

Findings concerning accommodation have been mixed. Singh et al. (2009) found a modest increase in directionality of up to 15–25% at 6 D accommodation stimulus in a combined group of emmetropes and myopes. When groups were analyzed separately, there was a significant increase for emmetropes (ρ_e slope = 0.001 mm⁻²/D), but not for myopes. However, Nilagiri, Suheimat, Lambert and Atchison (2021) did not find changes in directionality in a group of emmetropes with an increase in accommodation stimulus up to 6 D.

Blank et al. (1975) reported that the peak of the Stiles–Crawford effect shifted between 0.4 mm and 1.0 mm nasally in three subjects with a 9 D increase in accommodative stimulus. They attributed this to retinal stretch during accommodation. Singh et al. found a significant temporal peak shift (x_{\max} slope = 0.054 mm/D) with increase in accommodation for their myopic group, while Nilagiri et al. found a mean 0.62 mm temporal shift for 6 D stimulus for their emmetropes. The latter group suggested that the direction of shift could change between 6 D and the very high level of 9 D.

14.5.3.7 Eye Disease

Several studies have shown influence of diseases on the Stiles–Crawford effect. The conditions include retinal detachment (Alpern et al. 1961), central serous retinopathy (Dunnewold 1964), central serous chorioidopathy (Smith et al. 1978), choroidal rupture (Campos et al. 1978), age-related macular changes (Smith et al. 1978; Fitzgerald et al. 1979), choroidal atrophy (Bedell et al. 1981), retinitis pigmentosa (Birch et al. 1982), iris coloboma (Bailey et al. 1994), and fundus ectasia (Lakshminarayanan et al. 1997). Enoch (1959) showed reduced directionality and disturbed peak sensitivity in people with amblyopia.

14.5.3.8 Phototropism

Some studies provide evidence of an active phototropism in receptor alignment. Dunnewold (1964) reported peak location at the center of the eccentric pupil, that was located downwards and nasal in a participant with congenital retinal coloboma. Bonds and MacLeod (1978) showed photoreceptor alignment at the center of a pupil displaced nearly 3 mm nasally as a result of injury, suggesting that the photoreceptors were trained towards the abnormally situated pupil. Applegate and Bonds (1981) demonstrated 0.8 mm change in the photoreceptor alignment in an eye with a displaced natural pupil, towards a new artificial pupil provided by a contact lens, over a period of 5 days. The photoreceptor alignment returned to its original position within 5 days after the removal of the contact lens. Enoch and Birch (1981) found that the peak location shifted towards the displaced aperture of a contact lens, with the peak location recovering to its original position in 3–5 days after contact lens removal. Smallman et al. (2001) showed photoreceptor alignment towards the temporal margins of the pupil corresponding to clear end regions in a participant with congenital bilateral cataracts. The photoreceptor alignment took 10 days to shift to the center of the pupil after the cataract surgery.

14.5.4 THEORY

Various theories have been developed to explain the Stiles–Crawford effect, with the waveguide theory of photoreceptor directionality being the most widely accepted (Wright and Nelson 1936; Di Francia 1949; Enoch 1961; Vohnsen et al. 2005; Rativa and Vohnsen 2011b). Here cones act like waveguides that guide light orientated near their axes better than the light at more oblique angles.

The waveguide theory does not account for the light that is not guided, but which may leak into adjacent receptors and affect vision (Vohnsen 2014; Meadoway and Sincich 2018). Vohnsen et al. (2017) proposed a geometric optics absorption model based on the fraction of overlap of light at the retina and the photoreceptor outer segments. The model accounts for density, dimensions, and spacing of cone outer segments. The model offers good support to experimental findings for foveal and parafoveal regions (Carmichael Martins and Vohnsen 2019) and increases in directionality as foveal field size increases (Nilagiri, Suheimat, Lambert, Turpin et al. 2021).

14.5.5 MEASUREMENT

The Stiles–Crawford effect has been measured by several subjective and objective techniques. The values of ρ_e and the peak position mentioned above are from subjective methods. Subjective techniques involve subjective assessment of brightness of test and reference fields in Maxwellian view illumination as the test entry position is varied across the pupil (Stiles and Crawford 1933; Singh et al. 2009; Lochocki and Vohnsen 2017; Carmichael Martins and Vohnsen 2018). Two typical ways are with a single channel, in which comparison of fields is simultaneous side by side or by sequential flickering, or with two channels in which the test field is seen superimposed upon the reference field and the luminance of the former is reduced until it disappears into the latter.

Most objective tests involve measuring illuminance of light back-scattered from the fundus as the position of light at the pupil is varied for light either travelling into or out of the eye (Burns et al. 1995; Gorrard and Delori 1995; Roorda and Williams 2002; Rativa and Vohnsen 2011a; Morris et al. 2015). The Stiles–Crawford effect determined by objective techniques is called the *optical SCE*. Directionalities obtained with these methods are usually higher than those reported using subjective measurements, partly because the light passes twice through the photoreceptors (Gorrard and Delori 1995; Delint et al. 1997; Gao et al. 2008; Morris et al. 2015). Subjective techniques are much slower than objective techniques, but are more applicable to how vision operates.

Other objective methods that have been tried include consensual pupillary response and the electroretinogram (Birch et al. 1982; McCulloch and Lakshminarayanan 2009).

14.5.6 ROLE OF THE STILES–CRAWFORD EFFECT

As mentioned at the start of section 14.5, the Stiles–Crawford effect is relevant to visual photometry and retinal image quality. Concerning visual photometry, it reduces

the effective retinal illuminance; as discussed earlier, and as given by equations (14.5) and (14.6), this is equivalent to having a smaller effective pupil size. It can be included in optical modeling of the eye as an apodization, and its influence in this respect and for visual performance, as discussed further in section 18.4.1, is small. However, work by Vohnsen (Vohnsen 2007; Vohnsen et al. 2017) suggests that the influence of the Stiles–Crawford effect is underestimated by this modeling.

As mentioned in section 12.1, light is able to reach the retina after passage through the iris and sclera. In addition, long wavelength light is backscattered from the choroid. The major contribution of the Stiles–Crawford effect to the visual system is probably a reduction in sensitivity to intraocular scattering of light and glare by dampening the influence of highly oblique incident light.

SUMMARY OF MAIN SYMBOLS

Stiles–Crawford Effect

η	brightness sensitivity for a ray entering pupil at distance x from the peak sensitivity position
η_{\max}	maximum brightness sensitivity
x_{\max}	pupil entry position at which maximum brightness sensitivity occurs
ρ_e	Stiles–Crawford directionality coefficient
ρ_{10}	Stiles–Crawford directionality coefficient (10 base)
E_p	photometric efficiency for pupil semi-diameter R_p or pupil diameter D .
D_e	photometric equivalent pupil diameter

REFERENCES

- Alpern, F., J. Enoch, and P. Cibis. 1961. “Receptor orientation in retinal pathology: a first study.” *Am J Ophthalmol* 52 (5):767–83.
- Applegate, R.A., and A.B. Bonds. 1981. “Induced movement of receptor alignment toward a new pupillary aperture.” *Invest Ophthalmol Vis Sci* 21 (6):869–72.
- Applegate, R.A., and V. Lakshminarayanan. 1993. “Parametric representation of Stiles–Crawford functions: normal variation of peak location and directionality.” *J Opt Soc Am A* 10 (7):1611–23. doi: 10.1364/josaa.10.001611.
- Atchison, D.A., D.H. Scott, and G. Smith. 2000. “Pupil photometric efficiency and effective centre.” *Ophthalmic Physiol Opt* 20 (6):501–3.
- Bailey, J. E., V. Lakshminarayanan, and J. M. Enoch. 1994. “Photoreceptor orientation in iris coloboma.” *Optom Vis Sci* 71 (2):120–4. doi: 10.1097/00006324-199402000-00012.
- Bedell, H. E., and J. E. Enoch. 1979. “A study of the Stiles-Crawford (SC) function at 35° in the temporal field and the stability of the foveal SC function peak over time.” *J Opt Soc Am* 69 (3):435–42. doi: 10.1364/josa.69.000435.
- Bedell, H. E., J. M. Enoch, and C. R. Fitzgerald. 1981. “Photoreceptor orientation: a graded disturbance bordering a region of choroidal atrophy.” *Arch Ophthalmol* 99 (10):1841–4. doi: 10.1001/archopht.1981.03930020715018.
- Birch, D. G., M. A. Sandberg, and E. L. Berson. 1982. “The Stiles-Crawford effect in retinitis pigmentosa.” *Invest Ophthalmol Vis Sci* 22 (2):157–64.
- Blank, K., R. R. Provine, and J. M. Enoch. 1975. “Shift in the peak of the photopic Stiles–Crawford function with marked accommodation.” *Vision Res* 15 (4):499–507. doi: 10.1016/0042-6989(75)90027-9.

- Bonds, A. B., and D. I. MacLeod. 1978. "Displaced Stiles-Crawford effect associated with an eccentric pupil." *Invest Ophthalmol Vis Sci* 17 (8):754–61.
- Bone, R. A., and J. M. Sparrock. 1971. "Comparison of macular pigment densities in human eyes." *Vision Res* 11 (10):1057–64. doi: 10.1016/0042-6989(71)90112-x.
- Bueno, J. M. 2001. "Depolarization effects in the human eye." *Vision Res* 41 (21):2687–96. doi: 10.1016/s0042-6989(01)00167-5.
- Bueno, J. M., E. Berrio, and P. Artal. 2006. "Corneal polarimetry after LASIK refractive surgery." *J Biomed Opt* 11:014001. doi: 10.1117/1.2154747.
- Bueno, J. M., and M. C. W. Campbell. 2003. "Polarization properties of the *in vitro* old human crystalline lens." *Ophthalmic Physiol Opt* 23 (2):109–18. doi: 10.1046/j.1475-1313.2003.00095.x.
- Bueno, J. M., C. J. Cookson, J. J. Hunter, M. L. Kisilak, and Campbell M. C. W. 2009. "Depolarization properties of the optic nerve head: the effect of age." *Ophthalmic Physiol Opt* 29 (3):247–55. doi: 10.1111/j.1475-1313.2009.00644.x.
- Burns, S. A., S. Wu, F. Delori, and A. E. Elsner. 1995. "Direct measurement of human-cone-photoreceptor alignment." *J Opt Soc Am A* 12 (10):2329–38. doi: 10.1364/josaa.12.002329.
- Burns, S. A., S. Wu, J. C. He, and A. E. Elsner. 1997. "Variations in photoreceptor directionality across the central retina." *J Opt Soc Am A* 14 (9):2033–40. doi: 10.1364/josaa.14.002033.
- Campos, E. C., H. E. Bedell, J. M. Enoch, and C. R. Fitzgerald. 1978. "Retinal receptive field-like properties and Stiles-Crawford effect in a patient with a traumatic choroidal rupture." *Doc Ophthalmol* 45 (2):381–95. doi: 10.1007/BF00161673.
- Carmichael Martins, A., and B. Vohnsen. 2019. "Directional light-capture efficiency of the foveal and parafoveal photoreceptors at different luminance levels: an experimental and analytical study." *Biomed Opt Express* 10 (8):3760–72. doi: 10.1364/BOE.10.003760.
- Carmichael Martins, A., and B. Vohnsen. 2018. "Analysing the impact of myopia on the Stiles-Crawford effect of the first kind using a digital micromirror device." *Ophthalmic Physiol Opt* 38 (3):273–80. doi: 10.1111/opo.12441.
- Choi, S. S., L. F. Garner, and J. M. Enoch. 2003. "The relationship between the Stiles-Crawford effect of the first kind (SCE-I) and myopia." *Ophthalmic Physiol Opt* 23 (5):465–72. doi: 10.1046/j.1475-1313.2003.00142.x.
- Crawford, B. H. 1937. "The luminous efficiency of light entering the eye pupil at different points and its relation to brightness threshold measurements." *Proc Roy Soc Lond B* 124 (834):81–96.
- Delint, P. J., T. T. J. M. Berendschot, and D. Van Norren. 1997. "Local photoreceptor alignment measured with a scanning laser ophthalmoscope." *Vision Res* 37 (2):243–8. doi: 10.1016/s0042-6989(96)00118-6.
- Delori, F. C., and K. P. Pflibsen. 1989. "Spectral reflectance of the human ocular fundus." *Appl Opt* 28 (6):1061–77. doi: 10.1364/AO.28.001061.
- Di Francia, T.G. 1949. "Retina cones as dielectric antennas." *J. Opt. Soc. Am.* 39 (4):324.
- Dreher, A. W., K. Reiter, and R. N. Weinreb. 1992. "Spatially resolved birefringence of the retinal nerve fiber layer assessed with a retinal laser ellipsometer." *Appl Opt* 31 (19):3730–5. doi: 10.1364/AO.31.003730.
- Dunnewold, C. J. W. 1964. *On the Campbell and Stiles-Crawford effects and their clinical importance*: Institute for Perception. The Netherlands National Defence Research Organisation RVOTNO.
- Enoch, J. M. 1958. "Summated response of the retina to light entering different parts of the pupil." *J Opt Soc Am* 48 (6):392–405.
- Enoch, J. M., and D. G. Birch. 1981. "Inferred positive phototropic activity in human photoreceptors." *Phil Trans Roy Soc B* 291 (1051):323–51. doi: 10.1098/rstb.1981.0002.

- Enoch, J. M. 1959. "Further studies on the relationship between amblyopia and the Stiles-Crawford effect." *Am J Optom Arch Am Acad Optom* 36 (3):111–28.
- Enoch, J. M. 1961. "Wave-guide modes in retinal receptors." *Science* 133 (3461):1353–4.
- Enoch, J. M., and G. M. Hope. 1973. "Directional sensitivity of the foveal and parafoveal retina." *Invest Ophthalmol Vis Sci* 12 (7):497–503.
- Fitzgerald, C. R., J. M. Enoch, E. C. Campos, and H. E. Bedell. 1979. "Comparison of visual function studies in two cases of senile macular degeneration." *Albrecht v Graefes Arch klin exp Ophthalmol* 210 (2):79–91. doi: 10.1007/BF00409994.
- Flamant, F., and W. S. Stiles. 1948. "The directionality and sensitivities of the retinal rods to adapting fields of different wave-lengths." *J. Physiol.* 107 (2):187–202.
- Gao, W., B. Cense, Y. Zhang, R.S. Jonnal, and D.T. Miller. 2008. "Measuring retinal contributions to the optical Stiles-Crawford effect with optical coherence tomography." *Opt Express* 16 (9):6486–501. doi: 10.1364/OE.16.006486.
- Geeraets, W. J., and E. R. Berry. 1968. "Ocular spectral characteristics as related to hazards from lasers and other light sources." *Am J Ophthalmol* 66 (1):15–20.
- Gorrand, J-M., and F. Delori. 1995. "A reflectometric technique for assessing photoreceptor alignment." *Vision Res* 35 (7):999–1010. doi: 10.1016/0042-6989(94)00203-x.
- Hammond, B. R., Jr., B. R. Wooten, and D. M. Snodderly. 1997. "Individual variations in the spatial profile of human macular pigment." *J Opt Soc Am A* 14 (6):1187–96. doi: 10.1364/josaa.14.001187.
- Hogan, M. J., J. A. Alvarado, and J. E. Weddell. 1971. *Histology of the Human Eye. An Atlas and Textbook*, 483. W. B. Saunders.
- Hunold, W., and P. Malessa. 1974. "Spectrophotometric determination of the melanin pigmentation of the human ocular fundus *in vivo*." *Ophthal Res* 6 (5-6):355–62.
- Hunter, D. G., A. S. Shah, S. Sau, D. Nassif, and D. L. Guyton. 2003. "Automated detection of ocular alignment with binocular retinal birefringence scanning." *Appl Opt.* 42 (16):3047–53. doi: 10.1364/ao.42.003047.
- IJsspeert, J. K., P. W. de Waard, T. J. van den Berg, and P. T. de Jong. 1990. "The intraocular straylight function in 129 healthy volunteers; dependence on angle, age and pigmentation." *Vision Res* 30 (5):699–707. doi: 10.1016/0042-6989(90)90096-4.
- Lakshminarayanan, V., J. E. Bailey, and J. M. Enoch. 1997. "Photoreceptor orientation and alignment in nasal fundus ectasia." *Optom Vis Sci* 74 (12):1011–8. doi: 10.1097/00006324-199712000-00022.
- Lima, V. C., R. B. Rosen, and M. Farah. 2016. "Macular pigment in retinal health and disease." *Int J Ret Vit* 2 19. doi: <https://doi.org/10.1186/s40942-016-0044-9>
- Lochichi, B., D. Rativa, and B. Vohsen. 2011. "Spatial and spectral characterisation of the first and second Stiles–Crawford effects using tuneable liquid-crystal filters." *J Mod Opt* 58 (19-20):1817–25. doi: 10.1080/09500340.2011.566638.
- Lochocki, B., and B. Vohnsen. 2017. "Uniaxial flicker analysis of the psychophysical Stiles–Crawford effects." *J Mod Opt* 64 (4):347–56. doi: 10.1080/09500340.2016.1237683.
- McCulloch, D. L., and V. Lakshminarayanan. 2009. "The Stiles-Crawford effect of the first kind and the full-field electroretinogram (ERG)." *J Mod Opt* 56 (20):2176–80. doi: 10.1080/09500340903374169.
- Meadway, A., and L. C. Sincich. 2018. "Light propagation and capture in cone photoreceptors." *Biomed. Opt. Express* 9 (11):5543–65. doi: 10.1364/BOE.9.005543.
- Moon, P., and D. E. Spencer. 1944. "On the Stiles-Crawford effect." *J Opt Soc Am* 34 (6):319–29.
- Morris, H. J., L. Blanco, J.L. Codona, S.L. Li, et al. 2015. "Directionality of individual cone photoreceptors in the parafoveal region." *Vision Res* 117:67–80. doi: 10.1016/j.visres.2015.10.008.

- Nilagiri, V. K., M. Suheimat, A. J. Lambert, and D. A. Atchison. 2021. "Subjective measurement of the Stiles-Crawford effect with accommodation." *Ophthalmic Physiol Opt* 41 (5):1010–8. doi: 10.1111/opo.12855.
- Nilagiri, V. K., M. Suheimat, A. J. Lambert, A. Turpin, et al. 2021. "Subjective measurement of the Stiles-Crawford effect with different field sizes." *Biomed Opt Express* 12 (8):4969–81. doi: 10.1364/BOE.427834.
- Rativa, D., and B. Vohnsen. 2011a. "Analysis of individual cone-photoreceptor directionality using scanning laser ophthalmoscopy." *Biomed Opt Express* 2 (6):1423–31. doi: 10.1364/BOE.2.001423.
- Rativa, D., and B. Vohnsen. 2011b. "Single-and multimode characteristics of the foveal cones: the super-Gaussian function." *J Mod Opt* 58 (19-20):1809–16. doi: 10.1080/09500340.2011.573879.
- Rodieck, R. W. 1998. *Chapter 4. The rain of photons onto cones; Chapter 6. The rain of photons onto rods, The First Steps in Seeing*: Sinauer.
- Roorda, A., and D. R. Williams. 2002. "Optical fiber properties of individual human cones." *J Vis* 2 (5):404–12. doi: 10.1167/2.5.4.
- Ruddock, K. H. 1963. "Evidence for macular pigmentation from colour matching data." *Vision Res* 61:417–29.
- Safir, A., L. Hyams, and J. Philpot. 1970. "Movement of the Stiles-Crawford effect." *Invest Ophthalmol* 9 (10):820–5.
- Singh, N., D. A. Atchison, S. Kasturirangan, and H. Guo. 2009. "Influences of accommodation and myopia on the foveal Stiles-Crawford effect." *J Mod Opt* 56 (20):2217–30. doi: 10.1080/09500340902721915.
- Smallman, H. S., D. I. MacLeod, and P. Doyle. 2001. "Vision. Realignment of cones after cataract removal." *Nature* 412 (6847):604–5. doi: 10.1038/35088126.
- Smith, V. C., J. Pokorny, and K. R. Diddie. 1978. "Color matching and Stiles-Crawford effect in central serous choroidopathy." *Mod Probl Ophthalmol* 19:284–95.
- Stiles, W. S. 1937. "The luminous efficiency of monochromatic rays entering the eye pupil at different points and a new colour effect." *Proc Roy Soc Lond B* 123 (830):90–118. doi: 10.1098/rspb.1937.0045.
- Stiles, W. S. 1939. "The directional sensitivity of the retina and the spectral sensitivities of the rods and cones." *Proc Roy Soc Lond B* 127 (846):64–105. doi: 10.1098/rspb.1939.0012.
- Stiles, W. S., and B. H. Crawford. 1933. "The luminous efficiency of rays entering the eye pupil at different points." *Proc Roy Soc Lond B* 112:428–50.
- Twietmeyer, K. M., R. A. Chipman, A. E. Elsner, Y. Zhao, and D. A. VanNasdale. 2008. "Mueller matrix retinal imager with optimized polarization conditions." *Opt. Express* 16 (26):21339–54. doi: 10.1364/oe.16.021339.
- van Assendelft, O. W. 1970. *Spectrophotometry of haemoglobin derivatives*. Assen: Royal VanGorcum.
- van Blokland, G. J. 1985. "Ellipsometry of the human retina in vivo: preservation of polarization." *J Opt Soc Am A* 2 (1):72–5. doi: 10.1364/josaa.2.000072.
- van Blokland, G. J., and D. van Norren. 1986. "Intensity and polarization of light scattered at small angles from the human fovea." *Vision Res* 26 (3):485–94. doi: 10.1016/0042-6989(86)90191-4.
- van de Kraats, J., T. T. Berendschot, and D. van Norren. 1996. "The pathways of light measured in fundus reflectometry." *Vision Res* 36 (15):2229–47. doi: 10.1016/0042-6989(96)00001-6.
- van den Berg, T. J. 1995. "Analysis of intraocular straylight, especially in relation to age." *Optom Vis Sci* 72 (2):52–9. doi: 10.1097/00006324-199502000-00003.

- Van Loo, J. A., and J. M. Enoch. 1975. "The scotopic Stiles-Crawford effect." *Vision Res* 15 (8-9):1005–9. doi: 10.1016/0042-6989(75)90243-6.
- Vohnsen, B. 2007. "Photoreceptor waveguides and effective retinal image quality." *J Opt Soc Am A* 24 (3):597–607. doi: 10.1364/josaa.24.000597.
- Vohnsen, B. 2009. "On the spectral relation between the first and second Stiles-Crawford effect." *J Mod Opt* 56:2261–71. doi: 10.1080/09500340902990049.
- Vohnsen, B. 2014. "Directional sensitivity of the retina: A layered scattering model of outer-segment photoreceptor pigments." *Biomed Opt Express* 5 (5):1569–87. doi: 10.1364/BOE.5.001569.
- Vohnsen, B. 2017. "Chapter 18. The retina and the Stiles-Crawford effects." In *Handbook of Visual Optics: Fundamentals and Eye Optics, Volume I*, edited by P. Artal, 257–76. London: CRC Press.
- Vohnsen, B., A. Carmichael, N. Sharmin, S. Qaysi, and D. Valente. 2017. "Volumetric integration model of the Stiles-Crawford effect of the first kind and its experimental verification." *J Vis* 17 (12):18, 1–1. doi: 10.1167/17.12.18.
- Vohnsen, B., I. Iglesias, and P. Artal. 2005. "Guided light and diffraction model of human-eye photoreceptors." *J Opt Soc Am A* 22 (11):2318–28. doi: 10.1364/josaa.22.002318.
- Weinreb, R. N., S. Shakiba, and L. Zangwill. 1995. "Scanning laser polarimetry to measure the nerve fiber layer of normal and glaucomatous eyes." *Am J Ophthalmol* 119 (5):627–36. doi: 10.1016/s0002-9394(14)70221-1.
- Wijngaard, W., and J. van Kruysbergen. 1975. "The function of the non-guided light in some explanations of the Stiles-Crawford effects in photoreceptor optics" In *Photoreceptor Optics*, edited by A. H. Snyder and R. Menzel, 175–83. Springer-Verlag.
- Wright, W. D., and J. H. Nelson. 1936. "The relation between the apparent intensity of a beam of light and the angle at which the beam strikes the retina." *Proc Phys Soc.* 48 (3):401–5.
- Wyszecki, G., and W. S. Stiles. 1982. *Color Science: Concepts and Methods, Quantitative Data and Formulae*. 2nd ed. New York: Wiley.
- Zhou, Q., and R. N. Weinreb. 2002. "Individualized compensation of anterior segment birefringence during scanning laser polarimetry." *Invest Ophthalmol Vis Sci* 43 (7):2221–8.

Section IV

*Aberrations and Retinal Image
Quality*



Taylor & Francis
Taylor & Francis Group
<http://taylorandfrancis.com>

15 Monochromatic Aberrations

15.1 INTRODUCTION

The term “monochromatic aberrations” refers to the aberrations of an optical system that are present at any wavelength, rather than because of chromatic dispersion, which is the variation in refractive index at different wavelengths. The chromatic aberrations are discussed in Chapter 17.

Aberrations reduce the image quality of optical systems such as the eye. Ignoring size and luminance differences, they contribute to an image not being a perfect replica of its object. Aberrations affect the visual performance of the eye. This may be measured spatially, such as the smallest detail, which can be resolved or the contrast between an object and its background for the object to be seen.

Once a firm distinction was drawn between the refractive anomalies covered in Chapter 7 and other aberrations. With the widespread use of the Zernike polynomial system to specify aberrations, the distinction is less useful. Also, several aberrations can contribute to determining the objective ophthalmic correction. This will become clear later in the chapter.

15.2 REPRESENTATION OF MONOCHROMATIC ABERRATIONS

The representation of aberrations in optical systems depends on what is most convenient in the particular circumstances. These representations include the following (Figure 15.1a):

1. Wave aberration. This is the departure of a wavefront from the ideal wavefront, multiplied by the refractive index in image space as measured at the exit pupil.

We start from an originating point object, and a spherical wavefront moving outwards from it. The aberrations of the system prevent the wavefront from remaining spherical while passing through to the image side. This aberrated wavefront can be compared with the ideal spherical wavefront, which has a center of curvature at the ideal image position corresponding to the pupil (also chief) ray. A convenient position to compare the wavefronts is at the exit pupil of the system, which as described in section 3.2 is the image of the limiting aperture (stop) as seen from the image side. The wave aberration for any point at the exit pupil is the departure of the aberrated wavefront from the ideal wavefront, multiplied by the refractive index in image space. If the aberrated wavefront is ahead of the ideal wavefront at this point, there is positive wave aberration. As wave aberrations are small quantities, it is convenient

to express them in micrometers (μm) or in wavelengths. For a light wavelength of 550 nm, 1.0 μm is equivalent to 1.8 wavelengths. In visual optics, micrometers are used.

- Transverse aberration. This is the departure of a ray from its ideal position at the image surface.

Rays describe the path of a particular point of the wavefront through the optical system. A transverse aberration can have both horizontal and vertical components. Transverse aberrations are often expressed in millimeters or in minutes of arc.

- Longitudinal aberration. This is the departure of the intersection, where this occurs, of a ray with chief ray from the ideal image position.

A longitudinal aberration may have different values in horizontal and vertical planes. It may be measured as a length (meters) or as a vergence (diopters).

Because we cannot easily measure the aberrations on the image side of the eye's optical system, the aberrations of the eye are usually measured in object space and are referenced to the entrance pupil rather than to the exit pupil (Figure 15.1b). Most methods of measuring aberrations of the eye work in this fashion. Provided that the aberration and defocus levels are not unduly high, these "object" aberrations are like "image" aberrations. When the aberrations are large, such as in the case of peripheral vision, this is no longer the case.

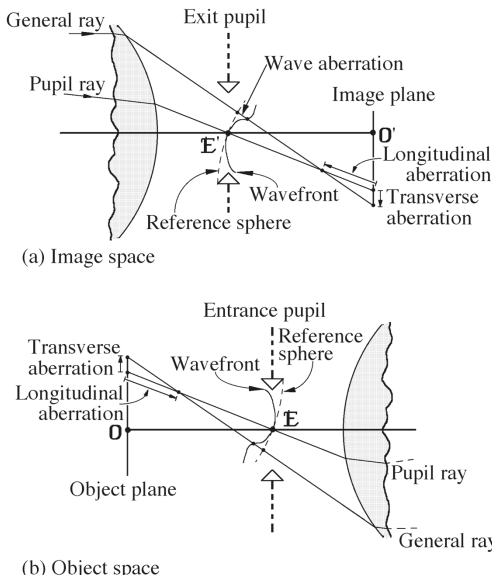


FIGURE 15.1 Wave, transverse, and longitudinal aberrations. (a) For a general optical system. (b) Aberrations determined in object space, as is done for the eye. Note that longitudinal aberration occurs for a ray only when it intersects the reference ray, i.e., the pupil ray.

15.3 SPECIFICATION OF MONOCHROMATIC ABERRATIONS – TAYLOR SERIES

The aberrations of an optical system with a point object can be represented by a wave aberration polynomial (or function) in the form of a Taylor series as

$$\begin{aligned} W(X,Y) = & W_0 + W_1 X + W_2 Y + W_3 X^2 + W_4 XY + W_5 Y^2 + W_6 X^3 + W_7 X^2 Y + W_8 XY^2 + \\ & W_9 Y^3 + W_{10} X^4 + W_{11} X^3 Y + W_{12} X^2 Y^2 + W_{13} XY^3 + W_{14} Y^4 + W_{15} X^5 + W_{16} X^4 Y \\ & + W_{17} X^3 Y^2 + W_{18} X^2 Y^3 + W_{19} XY^4 + W_{20} Y^5 + W_{21} X^6 + W_{22} X^5 Y + W_{23} X^4 Y^2 + \\ & W_{24} X^3 Y^3 + W_{25} X^2 Y^4 + W_{26} XY^5 + W_{27} Y^6 + \text{higher order terms} \end{aligned} \quad (15.1a)$$

where (X, Y) are pupil coordinates. The weightings, or coefficients, of the power terms can be described as follows: W_0 piston coefficient; W_1 and W_2 , tilt (prismatic or distortion) coefficients; W_3 , W_4 , and W_5 , defocus and astigmatism coefficients; W_6 , W_7 , W_8 , and W_9 , “coma-like” coefficients; W_{10} , W_{11} , W_{12} , W_{13} , and W_{14} , “spherical aberration-like” coefficients.

An alternative form to the above equation uses relative pupil coordinates (x, y) , that is,

$$\begin{aligned} W(x,y) = & W_0 + W_1 x + W_2 y + W_3 x^2 + W_4 xy + W_5 y^2 + W_6 x^3 + W_7 x^2 y + W_8 xy^2 + W_9 y^3 + \\ & W_{10} x^4 + W_{11} x^3 y + W_{12} x^2 y^2 + W_{13} xy^3 + W_{14} y^4 + W_{15} x^5 + W_{16} x^4 y + W_{17} x^3 y^2 + \\ & W_{18} x^2 y^3 + W_{19} xy^4 + W_{20} y^5 + W_{21} x^6 + W_{22} x^5 y + W_{23} x^4 y^2 + W_{24} x^3 y^3 + W_{25} x^2 y^4 + \\ & W_{26} xy^5 + W_{27} y^6 + \text{higher order terms} \end{aligned} \quad (15.1b)$$

From now on we will use these instead of unnormalized coordinates. In this case, coefficients must be recalculated whenever pupil size changes. Relative coordinates are used also for Zernike aberrations (section 15.4).

Coefficients depend upon the position of an object in the field. For a rotationally symmetrical system in which the object lies in the Y - Z section containing the optical axis and the Y -axis, the polynomial can be reduced to

$$\begin{aligned} W(X,Y) = & W_0 + W_2 y + W_3 x^2 + W_5 y^2 + W_7 x^2 y + W_9 y^3 + W_{10} x^4 + W_{12} x^2 y^2 + W_{14} y^4 + \\ & \text{higher order terms} \end{aligned} \quad (15.2)$$

where the terms still present retain the same meaning as previously. In this case,

$$W_7 = W_9 \text{ and } W_{10} = W_{14} = 0.5W_{12}$$

so we can now write

$$W(X,Y) = W_0 + W_2 y + W_3 x^2 + W_5 y^2 + W_7 y(x^2 + y^2) + W_{10}(x^2 + y^2)^2 + \text{higher order terms} \quad (15.3)$$

An alternative way of expressing the aberrations of a rotationally symmetrical optical system, which omits the terms in the zeroth and first orders, is

$$W(\eta; x, y) = {}_0 W_{2,0}(x^2 + y^2) + {}_0 W_{4,0}(x^2 + y^2)^2 + {}_1 W_{3,1}\eta(x^2 + y^2)y + {}_2 W_{2,0}\eta^2(x^2 + y^2) + \\ {}_2 W_{2,2}\eta^2y^2 + {}_3 W_{1,1}\eta^3y + \text{higher order terms} \quad (15.4)$$

where η indicates dependence on the position of the object in the field corresponding to the Y - Z plane. The first term in this expansion is a defocus term and the next five terms are known as monochromatic *primary aberrations* or *third-order aberrations*, and the coefficients are as follows: ${}_0 W_{4,0}$ spherical aberration coefficient, ${}_1 W_{3,1}$ coma coefficient, ${}_2 W_{2,0}$ field curvature coefficient, ${}_2 W_{2,2}$ astigmatism coefficient, ${}_3 W_{1,1}$ distortion coefficient. The significance of the term “primary” is explained in Appendix 2, where general aberration theory is discussed. Of these five monochromatic aberrations, only spherical aberration occurs on-axis. The other four occur off-axis and worsen with increase in distance off-axis. There are two other primary aberrations called chromatic aberrations, which become manifest when more than one wavelength is imaged by an optical system (see Chapter 17).

Eyes are not rotationally symmetric about an appropriate reference axis such as the line of sight or the visual axis. Consequently, ocular aberrations are not described well by equations such as equations (15.2), (15.3), and (15.4), but require the use of an equation such as equations (15.1a) and (15.1b). Contributors to this lack of rotational symmetry are the difference between the best-fit optical axis and the line of sight (because of component tilts and displacements and the fovea being inclined a few degrees to the optical axis), the lack of rotational symmetry of refracting surfaces, and possibly a lack of rotational symmetry of the lens refractive index.

15.4 SPECIFICATION OF MONOCHROMATIC ABERRATIONS – ZERNIKE ABERRATION SYSTEM

An issue with the Taylor series is that terms are not independent: as additional terms are added to the series, the lower-order terms are altered. One series in which the terms are independent is the Zernike polynomial function series. Zernike aberrations have several useful features as discussed below. The “OSA” Zernike system used in visual optics (International Organization for Standardization 2008) has the form

$$W(\rho, \theta) = \sum_{n=0}^k \sum_{m=2i-n}^n c_n^m Z_n^m(\rho, \theta) \quad (15.5)$$

where $W(\rho, \theta)$ is a polar representation of the wave aberration, Z_n^m is a particular Zernike polynomial, and c_n^m is the coefficient of the Zernike polynomial. ρ is the relative distance from the center of the pupil and thus ranges from 0 to 1. θ is the azimuth angle and ranges from 0 to 2π radians (or 0° to 360°); it is measured from the positive X -axis (to an observer’s right when looking at a person’s eye) with an anticlockwise angle just as in ophthalmic optics (Figure 15.2). i is counted from 0 to n . k is the maximum order of the polynomial series. For ease of typing, Z_n^m and c_n^m may be given as $Z(n, m)$ and $c(n, m)$.

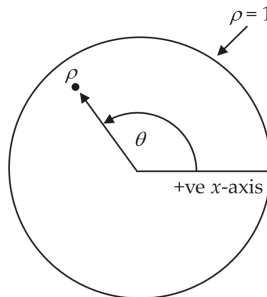


FIGURE 15.2 Polar coordinate system for Zernike aberrations.

The Zernike polynomial function $Z_n^m(\rho, \theta)$ in equation (15.5) is defined as

$$Z_n^m(\rho, \theta) = \begin{cases} N_n^m R_n^{|m|}(\rho) \cos(m\theta), & \text{for } m \geq 0 \\ N_n^m R_n^{|m|}(\rho) \sin(|m|\theta), & \text{for } m < 0 \end{cases} \quad (15.6)$$

$R_n^{|m|}(\rho)$ is a radial polynomial given by

$$R_n^{|m|}(\rho) = \sum_{s=0}^{0.5(n-|m|)} \frac{(-1)^s (n-s)!}{s! [0.5(n+|m|)-s]! [0.5(n-|m|)-s]!} \rho^{n-2s}$$

where index n is the highest power (or order) of the radial polynomial and index m describes the meridional frequency of the sinusoidal component of the Zernike polynomial. N_n^m is a normalization term given by

$$N_n^m = \sqrt{n+1} \quad (15.7a)$$

if $m = 0$, and

$$N_n^m = \sqrt{2(n+1)} \quad (15.7b)$$

if $m \neq 0$.

The normalization terms make the variance of each Zernike polynomial function equal to 1, which means that the square of the coefficient of the Zernike polynomial function represents the contribution of that function to the total variance of the wave aberration. Summing the squares of the coefficients for Zernike polynomial functions of a particular order gives the contribution of that order to the variance. Variance has the same meaning here as it does in statistics. When determining the total variance, both the piston coefficient, whose value is arbitrary, and the tilt (or prism) coefficients are ignored. Although the latter contribute to image position, they do not contribute to its quality (at least in monochromatic light). Many instruments

use the root-mean-square (*RMS*) of the wave aberration (the square root of the variance) as a measure of image quality. In mathematical terms

$$RMS = \sqrt{\sum_{n>1, all m} (c_n^m)^2} \quad (15.8)$$

Other measures of image quality are discussed in Chapter 18.

As the c_n^m coefficients are determined for one particular pupil size, they must change if pupil size changes. The change is not simple. There are different ways in which Zernike coefficients, determined at one pupil size, can be determined at a second pupil size. One way is to make measurements at the second pupil size, or in the case of a smaller pupil size isolate the measurements corresponding to it. Several mathematical transformations have been described (Schwiegerling 2002; Campbell 2003a; Bará et al. 2006; Shu et al. 2006; Dai 2006; Lundström and Unsbo 2007; Díaz et al. 2009; Lakshminarayanan and Fleck 2011). It is valid to interpolate from a larger to a smaller pupil size, but the reverse procedure is not advisable. Comparing aberration of different eyes, or the aberrations of a single eye at different times, is only valid if done at the same pupil size.

The double indexing scheme is a logical, easy system to use, but there is also a single index numbering scheme that can be used, for which

$$W(\rho, \theta) = \sum_{j=0}^{\infty} c_j Z_j \quad (15.9)$$

such that Z_j is the j th Zernike polynomial function and c_j is its coefficient. In the OSA Zernike system, j is related to n and m by

$$j = [n(n + 2) + m]/2 \quad (15.10)$$

The number j , order n , and frequency m of the Zernike polynomials are given in Table 15.1 up to the sixth order, and more extensive lists are available in other references.

Figure 15.3 shows the Zernike polynomial functions in the form of a pyramid in which order n changes vertically and frequency m changes horizontally. Plots are given as a function of position in the pupil for terms to the end of the fourth-order. The normalization terms have been ignored to improve clarity, which means that each term has values within the range -1 and $+1$.

The first row has order $n = 0$. The single function has a value of 1 and is called piston. This coefficient does not have significance to image quality, and the coefficient is usually manipulated so that the wave aberration is zero in the pupil center.

The second row has order $n = 1$, that is, it contains the first-order functions. These are tilts or prism, one in the (vertical) y -direction and one in the (horizontal) x -direction of the pupil. They are rotated functions of one another. This rotation nature continues down the pyramid, so that in any row a function with a positive value of the index m is a rotated form of the function with the same, but negative, value for m .

TABLE 15.1
Zernike Polynomials, up to the Sixth-Order, in Polar and Cartesian Representations

Number <i>j</i>	Radial order <i>n</i>	Frequency <i>m</i>	Polar Representation	Cartesian Representation
0	0	0	1	1
1	1	-1	$\sqrt{4\rho}\sin(\theta)$	$\sqrt{4}y$
2	1	1	$\sqrt{4\rho}\cos(\theta)$	$\sqrt{4}x$
3	2	-2	$\sqrt{6\rho^2}\sin(2\theta)$	$2\sqrt{6}xy$
4	2	0	$\sqrt{3}(2\rho^2-1)$	$\sqrt{3}(2x^2+2y^2-1)$
5	2	2	$\sqrt{6\rho^2}\cos(2\theta)$	$\sqrt{6}(x^2-y^2)$
6	3	-3	$\sqrt{8\rho^3}\sin(3\theta)$	$\sqrt{8}(3x^2y-y^3)$
7	3	-1	$\sqrt{8}(3\rho^3-2\rho)\sin(\theta)$	$\sqrt{8}(3x^2y+3y^3-2y)$
8	3	1	$\sqrt{8}(3\rho^3-2\rho)\cos(\theta)$	$\sqrt{8}(3x^3+3xy^2-2x)$
9	3	3	$\sqrt{8\rho^3}\cos(3\theta)$	$\sqrt{8}(x^3-3xy^2)$
10	4	-4	$\sqrt{10\rho^4}\sin(4\theta)$	$\sqrt{10}(4x^3y-4xy^3)$
11	4	-2	$\sqrt{10}(4\rho^4-3\rho^2)\sin(2\theta)$	$\sqrt{10}(8x^3y+8xy^3-6xy)$
12	4	0	$\sqrt{5}(6\rho^4-6\rho^2+1)$	$\sqrt{5}(6x^4+12x^2y^2+6y^4-6x^2-6y^2+1)$
13	4	2	$\sqrt{10}(4\rho^4-3\rho^2)\cos(2\theta)$	$\sqrt{10}(4x^4-3x^2-4y^4+3y^2)$
14	4	4	$\sqrt{10\rho^4}\cos(4\theta)$	$\sqrt{10}(x^4-6x^2y^2+y^4)$
15	5	-5	$\sqrt{12\rho^5}\sin(5\theta)$	$\sqrt{12}(5x^4y-10x^2y^3+y^5)$
16	5	-3	$\sqrt{12}(5\rho^5-4\rho^3)\sin(3\theta)$	$\sqrt{12}(15x^4y+10x^2y^3-12x^2y-5y^5+4y^3)$
17	5	-1	$\sqrt{12}(10\rho^5-12\rho^3+3\rho)\sin(\theta)$	$\sqrt{12}(10x^4y+20x^2y^3-12x^2y+10y^5-12y^3+3y)$
18	5	1	$\sqrt{12}(10\rho^5-12\rho^3+3\rho)\cos(\theta)$	$\sqrt{12}(10x^5+20x^3y^2+10xy^4-12x^3-12xy^2+3x)$
19	5	3	$\sqrt{12}(5\rho^5-4\rho^3)\cos(3\theta)$	$\sqrt{12}(5x^5-4x^3-10x^3y^2-15xy^4+12xy^2)$
20	5	5	$\sqrt{12\rho^5}\cos(5\theta)$	$\sqrt{12}(x^5-10x^3y^2+5xy^4)$
21	6	-6	$\sqrt{14\rho^6}\sin(6\theta)$	$\sqrt{14}(6x^5y-20x^3y^3+6xy^5)$
22	6	-4	$\sqrt{14}(6\rho^6-5\rho^4)\sin(4\theta)$	$\sqrt{14}(24x^5y-20x^3y-24xy^5+20xy^3)$
23	6	-2	$\sqrt{14}(15\rho^6-20\rho^4+6\rho^2)\sin(2\theta)$	$\sqrt{14}(30x^5y+60x^3y^3+30xy^5-40x^3y-40xy^3+12xy)$
24	6	0	$\sqrt{7}(20\rho^6-30\rho^4+12\rho^2-1)$	$\sqrt{7}(20x^6+60x^4y^2+60x^2y^4+20y^6-30x^4-60x^2y^2-30y^4+12x^2+12y^2-1)$
25	6	2	$\sqrt{14}(15\rho^6-20\rho^4+6\rho^2)\cos(2\theta)$	$\sqrt{14}(15x^6+15x^4y^2-20x^4+6x^2-15x^2y^4-15y^6+20y^4-6y^2)$
26	6	4	$\sqrt{14}(6\rho^6-5\rho^4)\cos(4\theta)$	$\sqrt{14}(6x^6-5x^4-30x^4y^2-30x^2y^4+30x^2y^6+6y^6-5y^4)$
27	6	6	$\sqrt{14}\rho^6\cos(6\theta)$	$\sqrt{14}(x^6-15x^4y^2+15x^2y^4-y^6)$

The third row has order *n* = 2, that is, it contains the second-order polynomial functions. These are important for determining refraction. The center term is rotationally symmetric, with an index *m* = 0, and is called “defocus”. It is bounded by the astigmatism functions. The polynomial function with *m* = -2 is called oblique astigmatism and has a maximum value of +1 along the 45° meridian and a minimum

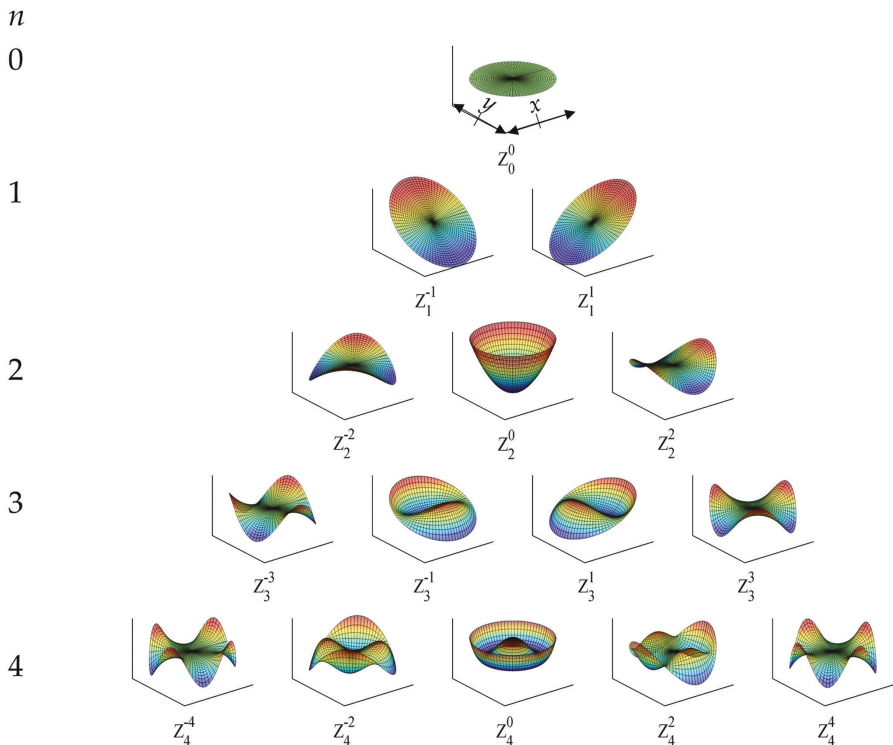


FIGURE 15.3 Three-dimensional representation of Zernike function pyramid up to the fourth-order. Adapted from Atchison (2004), copyright © Optometry Australia and with permission from Taylor and Francis Ltd.

value of -1 along the 135° meridian. The other polynomial function for which $m = +2$ is the same but is rotated by -45° to have a maximum value along the horizontal meridian of $+1$ and a minimum value along the vertical meridian of -1 . The defocus and astigmatism coefficients can be converted into a conventional refraction, with the defocus equivalent being called mean sphere or spherical equivalent (see section 15.4.3).

The fourth row has order $n = 3$, that is, it contains the third-order polynomial functions, which are the first of what are referred to as the higher-order polynomial functions. The middle functions are comas, with one vertical and one horizontal.

The fifth row has order $n = 4$, that is, it contains the fourth-order aberrations. The central, rotationally symmetric term is known as spherical aberration. If its coefficient is positive, we can consider the eye to be more myopic in the pupil periphery than in the pupil center.

Figure 15.3 shows only the first few rows of the Zernike pyramid. Moving down the pyramid and away from the center, the shapes of the terms become more complex. For example, the number of repetitions of the pattern increases around the pupil as m has higher values.

Each Zernike polynomial function can be given a Cartesian representation, obtained by converting it from a radial to a Cartesian (x, y) coordinate system, where

$$x = \rho\cos(\theta), y = \rho\sin(\theta) \quad (15.11)$$

Both polar and Cartesian representations of Zernike polynomial functions are given in Table 15.1. Most Zernike polynomial functions contain various orders of the Taylor series, e.g., the Cartesian representation of Zernike polynomial function Z_5^1 (secondary horizontal coma) is $\sqrt{12}(10x^5 + 20x^3y^2 + 10xy^4 - 12x^3 - 12xy^2 + 3x)$, which includes first-, third-, and fifth-order Taylor terms. Each Zernike polynomial function can be referred to as being balanced. This means that the highest-order Taylor term appearing in it is balanced by lower-order Taylor terms to minimize the variance of the Zernike polynomial function across the pupil.

When representing aberrations of an optical system, a decision must be made as to how many orders are required. For a Taylor series, as higher terms are added, fitting techniques will change the lower-order Taylor terms. Because of the independent nature of the Zernike polynomial series, at least theoretically adding additional polynomial functions will not change the coefficients of the lower-order functions.

Table 15.2 and Figure 15.4 show some of the points made above. The table shows the first 28 Zernike polynomial functions and their coefficients for a patient's eye at 4 mm and 6 mm diameter pupil sizes. Considerable differences between the magnitudes of the coefficients at the two pupil sizes are evident, with change in signs for some of the coefficients. The piston and tilt coefficients are ignored in the calculation of *RMS* as they do not affect image quality. The second-order aberrations are correctable with ophthalmic lenses, so as shown in the table sometimes an instrument might give both the total *RMS* (from second-order and higher-order coefficients) and the higher-order *RMS* (from third-order and above coefficients) as shown in the fifth-last and fourth-last rows, respectively, of the table.

Figure 15.4 shows a three-dimension map of the patient's aberrations, in which the height represents the magnitude of aberration as a function of position in the pupil. A projection (contour map) of the aberrations is shown as part of this figure. In the left-hand side, the tilt has been removed (or set to zero) and the piston manipulated so that the wave aberration is zero at the center of the pupil. In the right-hand side, the second-order aberrations have been also set to zero to show just the higher-order aberrations. Note the change of scale between the two parts of the figure.

15.4.1 COMPARING ZERNIKE AND TAYLOR ABERRATION SYSTEMS

Tables 15.3 and 15.4 show the conversions between coefficients of the Zernike and Taylor aberration systems, with the latter using relative pupil co-ordinates. These use up to the sixth order in each system. These are derived from a set, which included up to the tenth-order terms, but used a different numbering system for Taylor terms and did not include the Zernike normalization terms (Atchison et al. 2000).

Some Zernike aberration coefficients may be equated to Taylor coefficients found in a rotationally symmetrical system (equation (15.4)). Zernike spherical aberration is

TABLE 15.2
Zernike Aberration Coefficients of the Eye, Whose Wave Aberration Maps Are Shown in Figure 15.4, and Derived Quantities

Zernike Polynomial	Name	Coefficient 4 mm Pupil (μm)	Coefficient 6 mm Pupil (μm)
Z_0^0	Piston	0.427	1.733
Z_1^{-1}	Vertical tilt	0.707	1.214
Z_1^1	Horizontal tilt	0.859	1.404
Z_2^{-2}	Oblique astigmatism	-0.025	-0.034
Z_2^0	defocus	0.309	1.356
Z_2^2	With-/against-the-rule astigmatism	-0.272	-0.448
Z_3^{-3}	Oblique trefoil	0.114	0.218
Z_3^{-1}	Vertical coma	0.025	0.098
Z_3^1	Horizontal coma	0.015	0.046
Z_3^3	Horizontal trefoil	0.036	0.135
Z_4^{-4}	Oblique quatrefoil	0.007	0.006
Z_4^{-2}	Oblique secondary astigmatism	-0.009	-0.017
Z_4^0	Spherical aberration	0.045	0.357
Z_4^2	With-/against-the-rule secondary astigmatism	0.022	0.053
Z_4^4	Quatrefoil	0.004	0.009
Z_5^{-5}		-0.006	-0.007
Z_5^{-3}		-0.024	-0.025
Z_5^{-1}	Secondary vertical coma	-0.002	-0.015
Z_5^1	Secondary horizontal coma	-0.007	0.008
Z_5^3		0.007	-0.007
Z_5^5		-0.001	-0.027
Z_6^{-6}		0.010	0.015
Z_6^{-4}		0.009	-0.019
Z_6^{-2}		0.001	0.003
Z_6^0	Secondary spherical aberration	-0.002	0.069
Z_6^2		-0.001	-0.011
Z_6^4		-0.013	0.014
Z_6^6		0.011	-0.010
Total RMS		0.433	1.501
Higher-order RMS		0.132	0.458
Refraction, second-order (D)		$-0.21/-0.67 \times 3$	$-0.80/-0.49 \times 2$
Refraction, second- and fourth-orders (D)		$+0.20/-0.88 \times 179$	$+0.38/-0.71 \times 179$
Refraction, second-, fourth-, and sixth-orders (D)		$+0.27/-0.90 \times 179$	$-0.06/-0.82 \times 178$

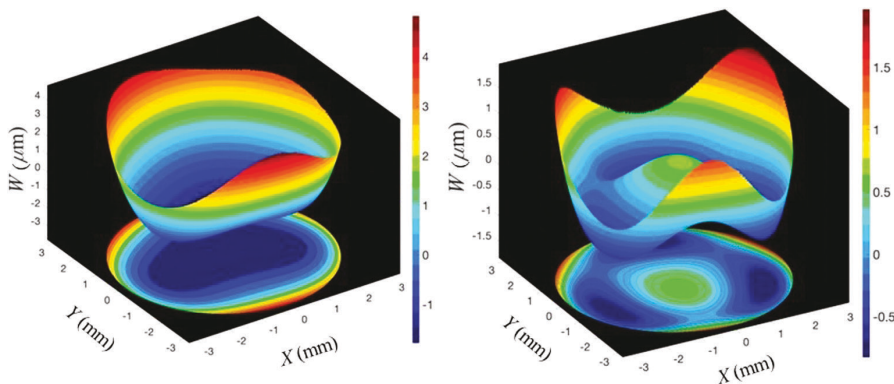


FIGURE 15.4 Three-dimensional wave aberration maps with a 6 mm pupil of a patient following refractive surgery. The left map includes aberrations of the second- and higher-orders, and the right map shows only the higher-order aberrations. This figure was kindly provided by Charles Campbell.

TABLE 15.3
Conversion from Zernike Aberration Coefficients to Taylor Aberration Coefficients

Taylor Aberration Coefficient	Equivalent Combination of Zernike Aberration Coefficients
W_0	$c_0^0 - \sqrt{3}c_2^0 + \sqrt{5}c_4^0 - \sqrt{7}c_6^0$
W_1	$\sqrt{4}c_1^1 - 2\sqrt{8}c_3^1 + 3\sqrt{12}c_5^1$
W_2	$\sqrt{4}c_1^{-1} - 2\sqrt{8}c_3^{-1} + 3\sqrt{12}c_5^{-3}$
W_3	$2\sqrt{3}c_2^0 + \sqrt{6}c_2^2 - 6\sqrt{5}c_4^0 - 3\sqrt{10}c_4^2 + 12\sqrt{7}c_6^0 + 6\sqrt{14}c_6^2$
W_4	$2\sqrt{6}c_2^{-2} - 6\sqrt{10}c_4^{-2} + 12\sqrt{14}c_6^{-2}$
W_5	$2\sqrt{3}c_2^0 - \sqrt{6}c_2^2 - 6\sqrt{10}c_4^0 + 3\sqrt{10}c_4^2 + 12\sqrt{7}c_6^0 - 6\sqrt{14}c_6^2$
W_6	$3\sqrt{8}c_3^1 + \sqrt{8}c_3^3 - 12\sqrt{12}c_5^{-1} - 4\sqrt{12}c_5^3$
W_7	$3\sqrt{8}c_3^{-3} + 3\sqrt{8}c_3^{-1} - 12\sqrt{12}c_5^{-3} - 12\sqrt{12}c_5^{-1}$
W_8	$3\sqrt{8}c_3^1 - 3\sqrt{8}c_3^3 - 12\sqrt{12}c_5^1 + 12\sqrt{12}c_5^3$
W_9	$-\sqrt{8}c_3^{-3} + 3\sqrt{8}c_3^{-1} + 4\sqrt{12}c_5^{-3} - 12\sqrt{12}c_5^{-1}$
W_{10}	$6\sqrt{5}c_4^0 + 4\sqrt{10}c_4^2 + \sqrt{10}c_4^4 - 30\sqrt{7}c_6^0 - 20\sqrt{14}c_6^2 - 5\sqrt{14}c_6^4$
W_{11}	$4\sqrt{10}c_4^{-4} + 8\sqrt{10}c_4^{-2} - 20\sqrt{14}c_6^{-4} - 40\sqrt{14}c_6^{-2}$
W_{12}	$12\sqrt{5}c_4^0 - 6\sqrt{10}c_4^4 - 60\sqrt{7}c_6^0 + 30\sqrt{14}c_6^4$
W_{13}	$-4\sqrt{10}c_4^{-4} + 8\sqrt{10}c_4^{-2} + 20\sqrt{14}c_6^{-4} - 40\sqrt{14}c_6^{-2}$
W_{14}	$6\sqrt{5}c_4^0 - 4\sqrt{10}c_4^2 + \sqrt{10}c_4^4 - 30\sqrt{7}c_6^0 + 20\sqrt{14}c_6^2 - 5\sqrt{14}c_6^4$
W_{15}	$10\sqrt{12}c_5^1 + 5\sqrt{12}c_5^3 + \sqrt{12}c_5^5$
W_{16}	$5\sqrt{12}c_5^{-5} + 15\sqrt{12}c_5^{-3} + 10\sqrt{12}c_5^{-1}$

(continued)

TABLE 15.3 (Continued)
Conversion from Zernike Aberration Coefficients to Taylor Aberration Coefficients

Taylor Aberration Coefficient	Equivalent Combination of Zernike Aberration Coefficients
W_{17}	$20\sqrt{12}c_5^1 - 10\sqrt{12}c_5^3 - 10\sqrt{12}c_5^5$
W_{18}	$-10\sqrt{12}c_5^{-5} + 10\sqrt{12}c_5^{-3} + 20\sqrt{12}c_5^{-1}$
W_{19}	$10\sqrt{12}c_5^1 - 15\sqrt{12}c_5^3 + 5\sqrt{12}c_5^5$
W_{20}	$\sqrt{12}c_5^{-5} - 5\sqrt{12}c_5^{-3} + 10\sqrt{12}c_5^{-1}$
W_{21}	$20\sqrt{7}c_6^0 + 15\sqrt{14}c_6^2 + 6\sqrt{14}c_6^4 + \sqrt{14}c_6^6$
W_{22}	$6\sqrt{14}c_6^{-6} + 24\sqrt{14}c_6^{-4} + 30\sqrt{14}c_6^{-2}$
W_{23}	$60\sqrt{7}c_6^0 + 15\sqrt{14}c_6^2 - 30\sqrt{14}c_6^4 - 15\sqrt{14}c_6^6$
W_{24}	$-20\sqrt{14}c_6^{-6} + 60\sqrt{14}c_6^{-2}$
W_{25}	$60\sqrt{7}c_6^0 - 15\sqrt{14}c_6^2 - 30\sqrt{14}c_6^4 + 15\sqrt{14}c_6^6$
W_{26}	$6\sqrt{14}c_6^{-6} - 24\sqrt{14}c_6^{-4} + 30\sqrt{14}c_6^{-2}$
W_{27}	$20\sqrt{7}c_6^0 - 15\sqrt{14}c_6^2 + 6\sqrt{14}c_6^4 - \sqrt{14}c_6^6$

TABLE 15.4
Conversion from Taylor Aberration Coefficients to Zernike Aberration Coefficients

Zernike Aberration Coefficient	Equivalent Combination of Taylor Aberration Coefficients
c_0^0	$W_0 + (W_3 + W_5) / 4 + (3W_{10} + W_{12} + 3W_{14}) / 24 + (5W_{21} + W_{23} + W_{25} + 5W_{27}) / 64$
c_1^{-1}	$[W_2 + (W_7 + 3W_9) / 6 + (W_{16} + W_{18} + 5W_{20}) / 16] / \sqrt{4}$
c_1^1	$[W_1 + (3W_7 + W_9) / 6 + (5W_{16} + W_{18} + 5W_{20}) / 16] / \sqrt{4}$
c_2^{-2}	$[W_4 / 2 + (3W_{11} + 3W_{13}) / 16 + (15W_{22} + 9W_{24} + 15W_{26}) / 160] / \sqrt{6}$
c_2^0	$[(W_3 + W_5) / 4 + (3W_{10} + W_{12} + 3W_{14}) / 16 + (45W_{21} + 9W_{23} + 9W_{25} + 45W_{27}) / 320] / \sqrt{3}$
c_2^2	$[(W_3 - W_5) / 2 + (3W_{10} - 3W_{14}) / 8 + (45W_{21} + 3W_{23} - 3W_{25} - 45W_{27}) / 160] / \sqrt{6}$
c_3^{-3}	$[(W_7 - W_9) / 4 + (3W_{16} + W_{18} - 5W_{20}) / 20] / \sqrt{8}$
c_3^{-1}	$[(W_7 + 3W_9) / 12 + (W_{16} + W_{18} + 5W_{20}) / 20] / \sqrt{8}$
c_3^1	$[(3W_6 + W_8) / 12 + (5W_{15} + W_{17} + W_{19}) / 20] / \sqrt{8}$
c_3^1	$[(W_6 - W_8) / 4 + (5W_{15} - W_{17} - 3W_{19}) / 20] / \sqrt{8}$
c_4^{-4}	$[(W_{11} - W_{13}) / 8 + (5W_{22} - 5W_{26}) / 48] / \sqrt{10}$
c_4^{-2}	$[(W_{11} + W_{13}) / 16 + (5W_{22} + 3W_{24} + 5W_{26}) / 96] / \sqrt{10}$
c_4^0	$[(3W_{10} + W_{12} + 3W_{14}) / 48 + (5W_{21} + W_{23} + W_{25} + 5W_{27}) / 64] / \sqrt{5}$
c_4^2	$[(W_{10} - 3W_{14}) / 8 + (15W_{21} + W_{23} - W_{25} - 15W_{27}) / 96] / \sqrt{10}$

TABLE 15.4 (Continued)**Conversion from Taylor Aberration Coefficients to Zernike Aberration Coefficients**

Zernike Aberration Coefficient	Equivalent Combination of Taylor Aberration Coefficients
c_4^4	$\left[(W_{10} - W_{12} + W_{14})/8 + (15W_{21} - 5W_{23} - 5W_{25} + 15W_{27})/96 \right] / \sqrt{10}$
c_5^{-5}	$\left[(W_{16} - W_{18} + W_{20})/16 \right] / \sqrt{12}$
c_5^{-3}	$\left[(3W_{16} + W_{18} - 5W_{20})/80 \right] / \sqrt{12}$
c_5^{-1}	$\left[(W_{16} + W_{18} + 5W_{20})/80 \right] / \sqrt{12}$
c_5^1	$\left[(5W_{15} + W_{17} + 5W_{19})/80 \right] / \sqrt{12}$
c_5^3	$\left[(5W_{15} - W_{17} - 3W_{19})/80 \right] / \sqrt{12}$
c_5^5	$\left[(W_{15} - W_{17} + W_{19})/16 \right] / \sqrt{12}$
c_6^{-6}	$\left[(W_{22} - W_{24} + W_{26})/32 \right] / \sqrt{14}$
c_6^{-4}	$\left[(W_{22} - W_{26})/48 \right] / \sqrt{14}$
c_6^{-2}	$\left[(5W_{22} + 3W_{24} + 5W_{26})/480 \right] / \sqrt{14}$
c_6^0	$\left[(5W_{21} + W_{23} + W_{25} + 5W_{27})/320 \right] / \sqrt{7}$
c_6^2	$\left[(15W_{21} + W_{23} - W_{25} - 15W_{27})/480 \right] / \sqrt{14}$
c_6^4	$\left[(3W_{21} - W_{23} - W_{25} + 3W_{27})/96 \right] / \sqrt{14}$
c_6^6	$\left[(W_{21} - W_{23} + W_{25} - W_{27})/32 \right] / \sqrt{14}$

$c_4^0 \sqrt{5}(6\rho^4 - 6\rho^2 + 1)$ and the Taylor spherical aberration is ${}_0 W_{4,0} \rho^4$. Ignoring the lower balancing terms in the Zernike polynomial, we get

$$c_4^0 \approx {}_0 W_{4,0} / (6\sqrt{5}) \quad (15.12)$$

Using the same approach for vertical coma gives

$$c_3^{-1} \approx {}_1 W_{3,1} / (3\sqrt{8}) \quad (15.13)$$

Zernike defocus and astigmatism coefficients can be equated to Taylor field curvature and astigmatism coefficient terms. The Taylor field curvature represents a shift in focus over all meridians to which there is astigmatism corresponding to the vertical meridian. The equations are

$$c_2^0 \approx (2 {}_2 W_{2,0} + {}_2 W_{2,2}) / (4\sqrt{3}) \quad (15.14)$$

$$c_2^2 \approx - {}_2 W_{2,2} / (2\sqrt{6}) \quad (15.15)$$

Zernike defocus can be equated to Taylor defocus as

$$c_2^0 \approx {}_0W_{2,0} / (2\sqrt{3}) \quad (15.16)$$

In Appendix 3, aberrations of some schematic eyes are given in wavelengths according to primary aberration (Seidel) theory. After multiplying by the wavelength, the Zernike equivalents can be determined using equations (15.12) to (15.15).

15.4.2 RIGHT AND LEFT EYES

The expected nasal-temporal asymmetry should be considered when right and left eyes are compared or if both right and left eye data are to be used in a pooled data set. Right eye and left eye data can be treated separately, or the signs of some of the Zernike coefficients can be altered for one eye. The ISO convention for the latter is to alter signs of left eye coefficients, for which the Zernike polynomial functions have negative and even m indices such as Z_2^{-2} , Z_4^{-4} , and Z_4^{-2} , or positive, odd m indices such as Z_1^1 , Z_3^1 , and Z_3^3 .

15.4.3 USING ZERNIKE ABBERRATIONS TO DETERMINE REFRACTION

Figure 15.5 shows the wave aberration $W(r)$ as a function of the distance r from pupil center, with r having values between 0 and R . The radial r axis is perpendicular to the optical Z -axis. The dashed line is tangent to the wave aberration at r , i.e., it is the slope of the wavefront error. The angle τ is formed both between the

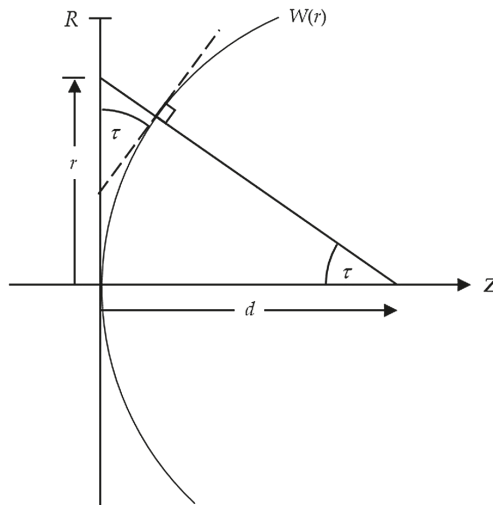


FIGURE 15.5 Relationship between the wavefront aberration $W(r)$, the angle τ , and the distance d along the Z -axis to the focus point.

r -axis and the dashed line and between the normal to the wavefront error and the Z-axis, and so

$$\tan(\tau) = \frac{dW}{dr} = \frac{r}{d}$$

from which

$$\frac{1}{d} = \frac{dW}{dr} / r$$

This equation gives the vergence of the wavefront at r . Using a negative sign to convert from an error to a refraction, the refraction ΔF_r is

$$\Delta F_r = -\frac{dW}{dr} / r \quad (15.17)$$

Using the polar representations of the Zernike polynomials in Table 15.1 after replacing ρ by r/R in equation (15.17), we have

$$\begin{aligned} \Delta F_r = & -\frac{1}{R^2} \left[2\sqrt{6}c_2^{-2} \sin(2\theta) + 4\sqrt{3}c_2^0 + 2\sqrt{6}c_2^2 \cos(2\theta) \right] \\ & -\frac{1}{R^2} \left[3\sqrt{8}c_3^{-3}r \sin(3\theta) + \sqrt{8}c_3^{-1} \left(9r - \frac{2R^2}{r} \right) \sin(\theta) \right. \\ & \quad \left. + \sqrt{8}c_3^1 \left(9r - \frac{2R^2}{r} \right) \cos(\theta) + 3\sqrt{8}c_3^3r \cos(3\theta) \right] \\ & -\frac{1}{R^4} \left[4\sqrt{10}c_4^{-4}r^2 \sin(4\theta) + \sqrt{10}c_4^{-2} (16r^2 - 6R^2) \sin(2\theta) \right. \\ & \quad \left. + 12\sqrt{5}c_4^0 (2r^2 - R^2) + \sqrt{10}c_4^2 (16r^2 - 6R^2) \cos(2\theta) \right. \\ & \quad \left. + 4\sqrt{10}c_4^4r^2 \cos(4\theta) \right] + \dots \end{aligned} \quad (15.18)$$

Equation (15.18) shows results only to the fourth-order. The higher-order Zernike polynomials contain lower-order terms that balance the higher-order terms, which minimizes the *RMS* value of individual polynomials and makes the different polynomials mutually orthogonal. A potentially confusing result arises when computing the refraction due to individual Zernike modes for those higher-order polynomials balanced by first-order tilt (prismatic) terms, such as the second and third terms divided by R^3 in this equation. The formula has division of the tilt slope by r , which means the refraction grows infinitely large as r approaches zero. This result clashes with the understanding that prisms do not contribute power. This contradiction is resolved by adopting the International Standards Organisation (2008) standard for specifying aberrations of eyes, which requires the Z-axis of the coordinate system used to specify a wavefront to coincide with the chief ray. This convention ensures that the wavefront slope is always zero at the pupil center, which implies the prismatic coefficients contained in a Zernike expansion do not contribute

to refraction. Thus, we are justified in disregarding the problematic prismatic terms in individual Zernike polynomials. This changes the coma terms so that equation (15.18) becomes

$$\begin{aligned}\Delta F_r = & -\frac{1}{R^2} \left[2\sqrt{6}c_2^{-2} \sin(2\theta) + 4\sqrt{3}c_2^0 + 2\sqrt{6}c_2^2 \cos(2\theta) \right] \\ & -\frac{1}{R^3} \left[3\sqrt{8}c_3^{-3}r \sin(3\theta) + 9\sqrt{8}c_3^{-1}r \sin(\theta) \right. \\ & \quad \left. + 9\sqrt{8}c_3^1r \cos(\theta) + 3\sqrt{8}c_3^3r \cos(3\theta) \right] \\ & -\frac{1}{R^4} \left[4\sqrt{10}c_4^{-4}r^2 \sin(4\theta) + \sqrt{10}c_4^{-2}(16r^2 - 6R^2) \sin(2\theta) \right. \\ & \quad \left. + 12\sqrt{5}c_4^0(2r^2 - R^2) + \sqrt{10}c_4^2(16r^2 - 6R^2) \cos(2\theta) \right. \\ & \quad \left. + 4\sqrt{10}c_4^4r^2 \cos(4\theta) \right] + \dots\end{aligned}\quad (15.19)$$

As r in equation (15.19) approaches zero, we get the central refraction as a combination of the mean sphere (spherical equivalent) M , a (Jackson) cross-cylinder that has powers of equal magnitude but opposite sign along the 180 and 90° meridians called J_{180} , and a cross-cylinder that has powers of equal magnitude but opposite sign along the 45 and 135° meridians called J_{45} . The equations for M , J_{180} , and J_{45} are

$$M = -\left(4\sqrt{3}c_2^0 - 12\sqrt{5}c_4^0 + 24\sqrt{7}c_6^0 - 40\sqrt{9}c_8^0 + 60\sqrt{11}c_{10}^0 - \dots\right)/R^2 \quad (15.20)$$

$$J_{180} = -\left(2\sqrt{6}c_2^2 - 6\sqrt{10}c_4^2 + 12\sqrt{14}c_6^2 - 20\sqrt{18}c_8^2 + 30\sqrt{22}c_{10}^2 - \dots\right)/R^2 \quad (15.21)$$

$$J_{45} = -\left(2\sqrt{6}c_2^{-2} - 6\sqrt{10}c_4^{-2} + 12\sqrt{14}c_6^{-2} - 20\sqrt{18}c_8^{-2} + 30\sqrt{22}c_{10}^{-2} - \dots\right)/R^2 \quad (15.22)$$

Conversion to conventional spherocylinder form S/C × α with a negative cylinder is given by equations (7.12)–(7.14b). If coefficients are in micrometers and pupil size is in millimeters, the corrections have the unit of m⁻¹ or diopter.

One criterion for refraction is to provide a correcting lens that minimizes the *RMS* of the wavefront. We can do this by considering only the second-order Zernike coefficients c_2^{-2} , c_2^0 , and c_2^2 in equations (15.20)–(15.22), and this is referred to as *Zernike refraction*. Zernike refraction is affected considerably by pupil size – see Table 15.2 for large changes in sphere and cylinder refraction components when the pupil size is changed from 4 mm to 6 mm for an eye with high levels of spherical aberration.

Another criterion is to correct the Taylor defocus and astigmatism terms appearing in equation (15.1b). This is a *paraxial refraction*, in which we are determining the refraction for the inner pupil. It is sometimes referred to as *Seidel refraction*. A similar refraction is provided by using a number of orders in the Zernike system, such as the second-, fourth-, and sixth-orders shown in equations (15.20)–(15.22). Table 15.2 shows reduced refraction changes, using second- to the sixth-orders rather than only the second-order, when pupil size is changed from 4 mm to 6 mm.

In theory, paraxial refraction will be determined more accurately as the number of orders used in the equations is increased. However, at some point the error of the fit associated with a coefficient will become as significant as the coefficient

itself; it is probably not necessary to go above the sixth-order for pupils up to 6 mm. Schwiegerling et al. (1996) showed an exception to this, where an early form of refractive surgery called radial keratotomy using eight regularly spaced radial cuts produced considerable eighth-order coefficients.

Refraction can be determined from various criteria or metrics. Some of these criteria are based on the Zernike aberration coefficients, and two such criteria are the Zernike and paraxial (Seidel) refractions described above. Other criteria are measures of retinal image quality derived from the aberration coefficients; optimizing these gives refractions. See Chapter 18 for a description of various criteria.

15.4.4 ZERNIKE ABERRATIONS PRESENTED IN MAGNITUDE/AXIS FORMAT

Campbell (Campbell 2003b; International Organization for Standardization 2008) suggested a way to reduce the number of Zernike polynomial functions by combining polynomial functions in a way similar to that given for the astigmatic refraction components in equations (7.12)–(7.14b). The polynomial functions to be combined are those of the same radial order, n , and having meridional indices, m , of the same magnitude but with opposite signs. This gives new polynomial functions:

$$Z_{mn}(\rho, \theta, \alpha_{nm}) = N_n^m R_n^{|m|}(\rho) \cos[m(\theta - \alpha_{nm})] \quad (15.23)$$

where m takes only positive values and $R_n^{|m|}(\rho)$ and N_n^m have been defined by equations (15.6) and (15.7), respectively. Coefficients and angular parameters are given by

$$c_{nm} = \sqrt{(c_n^{-m})^2 + (c_n^m)^2} \quad (15.24)$$

$$\text{and } \alpha_{nm} = \tan^{-1}\left(\frac{c_n^{-m}}{c_n^m}\right) / |m| \quad (15.25)$$

Common names of Zernike polynomial functions in the magnitude/axis form include the following: Z_{00} piston, Z_{11} tilt, Z_{20} defocus, Z_{22} astigmatism, Z_{31} coma, Z_{33} trefoil, Z_{40} spherical aberration, Z_{42} secondary astigmatism, and Z_{44} quatrefoil. The wave aberration across the pupil is now given by

$$W(\rho, \theta) = \sum_{\text{all } n \text{ and } m} c_{nm} Z_{nm}(\rho, \theta, \alpha_{nm}) \quad (15.26)$$

instead of equation (15.5). As an example of this system, if the coefficients c_3^{-3} and c_3^3 of the trefoil polynomial functions Z_3^{-3} and Z_3^3 are $+0.218 \mu\text{m}$ and $+0.135 \mu\text{m}$, respectively, as given in the last column of Table 15.2, the combined Zernike polynomial function $Z_{33}(\rho, \theta, \alpha_{33})$ is $\sqrt{8}\rho^3 \cos[3(\theta - 19.4^\circ)]$, and is accompanied by the coefficient $c_{33} = +0.256 \mu\text{m}$ (Figure 15.6). Although Campbell's system reduces the number of Zernike polynomial functions, it introduces an angle so there is no reduction in the amount of information needed.

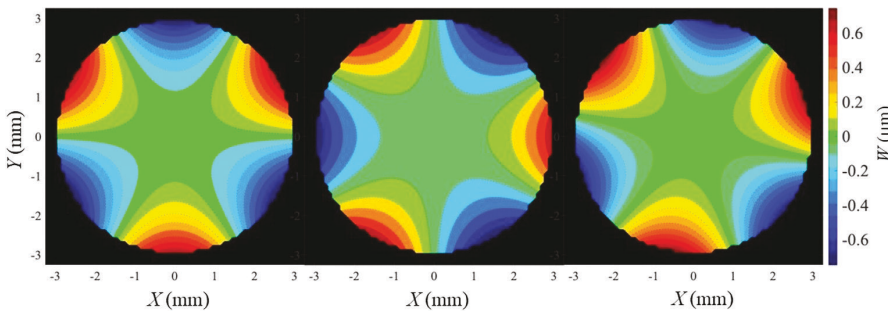


FIGURE 15.6 Two-dimensional wave aberration maps with a 6 mm pupil of a patient following refractive surgery. The left map shows the aberration with the polynomial function $Z(-3, 3)$, the middle map shows the aberration with the polynomial function $Z(3, 3)$ and the right map shows the combination of the two aberrations for Zernike polynomial function Z_{33} with a coefficient c_{33} . This figure was kindly provided by Charles Campbell.

15.4.5 POWER VARIATION ACROSS THE PUPIL

It is sometimes of interest to know how the refraction varies across the pupil, particularly in the case of spherical aberration. This variation in refraction ΔF_r is given by equation (15.19). For Zernike defocus $\sqrt{3}c_2^0(2\rho^2 - 1)$, in equation (15.19) we have

$$\Delta F_r = -4\sqrt{3}c_2^0 / R^2 \quad (15.27a)$$

which as expected is unaffected by position in the pupil. For Zernike spherical aberration $\sqrt{5}c_4^0(6\rho^4 - 6\rho^2 + 1)$, in equation (15.19) we have

$$\Delta F_r = -12\sqrt{5}c_4^0 \left(\frac{2r^2}{R^4} - \frac{1}{R^2} \right) \quad (15.27b)$$

This can be determined at the center of the pupil and at the edge, and the difference gives the longitudinal spherical aberration across the pupil as

$$LSA = 12\sqrt{5}c_4^0 \left[\left(\frac{2R^2}{R^4} - \frac{1}{R^2} \right) - \left(-\frac{1}{R^2} \right) \right] = 24\sqrt{5}c_4^0 / R^2 \quad (15.27c)$$

Figure 15.7 shows examples of variation in refraction across the pupil in the presence of defocus, spherical aberration, and horizontal coma.

For numerical work involving computer processing of slope data collected at discrete locations by a wavefront sensor/aberrometer, determining radial slopes requires the use of Cartesian co-ordinates. For the derivative $\frac{dW}{dr}$, we need the equation given by Nam et al. (2009)

$$\frac{dW}{dr} = \frac{dW}{dX} \cos(\theta) + \frac{dW}{dY} \sin(\theta) \quad (15.28)$$

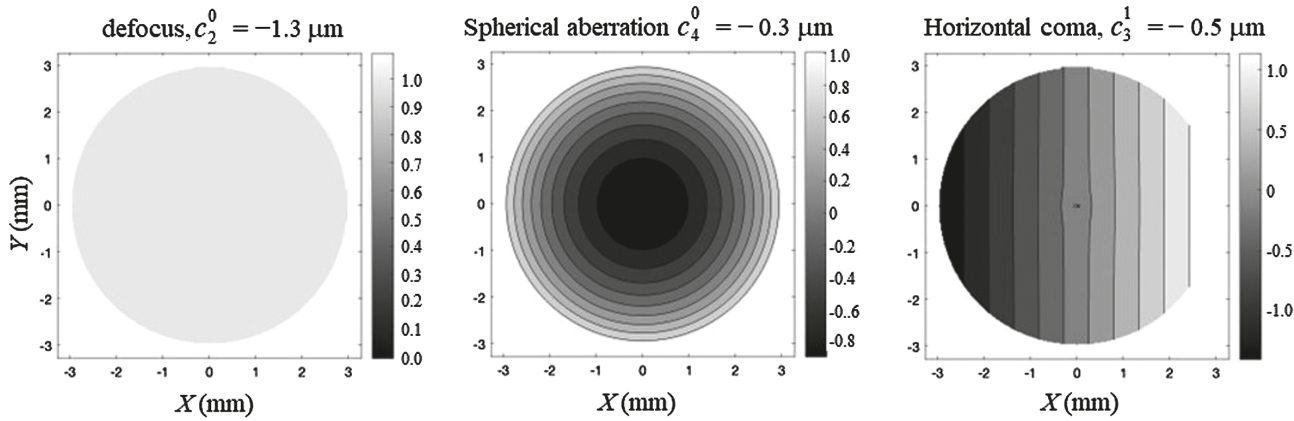


FIGURE 15.7 Refraction in diopters across a 6 mm diameter pupil ($R = 3 \text{ mm}$) in the presence of aberrations. The left map shows defocus with $c_2^0 = -1.3 \mu\text{m}$ (or constant refraction = +1 D), the middle map shows spherical aberration with $c_4^0 = -0.3 \mu\text{m}$, and the right map shows horizontal coma with $c_3^1 = -0.5 \mu\text{m}$. The prismatic term has been taken out of the refraction produced by coma. The figure was modified from figures kindly provided by Larry Thibos.

where

$$X = r \cos(\theta), Y = r \sin(\theta) \quad (15.28a)$$

Appendix 4 provides a development of different ways of expressing power across the pupil. The different ways include the radial power as given by equation (15.19), its horizontal and vertical components, and a tangential power that is perpendicular to the radial power.

15.4.6 OTHER ABERRATION SYSTEMS

Other polynomial systems have been investigated including Bhatia-Wolf polynomial functions (Iskander et al. 2002), but more polynomials are needed for a particular radial order n , and there is loss of the appreciation of the importance of individual terms.

A polynomial system is not the best way to describe the wavefront aberration if local abrupt irregularities are present. In such cases, the number of polynomial terms needed to adequately fit complex data becomes large, losing the obvious compression of the data set. Avoiding function fitting altogether, other approaches use the individual aberrometer measured wavefront local slopes to construct wavefront error by local integration (Southwell's "zonal" reconstruction). Also, the measured slopes can be used to assess the local refractive state (Nam et al. 2009) and generate detailed maps of refractive state across the pupil, which can be useful when assessing the refractive impact of complex multifocal optics such as post refractive surgery eyes, post orthokeratology eyes and lenses, e.g., Jaskulski et al. (2020).

15.4.7 REFERENCE AXIS

Based on the work of Applegate et al. (2000), the International Organization for Standardization (2008) recommended that the reference axis for on-axis vision should be the line of sight. This is defined it as "The line from the point of interest in object space to the center of the entrance pupil of the eye and continuing from the center of the exit pupil to the retinal point of fixation (generally the foveola)" and it is given more simply in section 4.2.2 as "the line joining the fixation point and the center of the entrance pupil". One problem with the line of sight is that the pupil center moves slightly with changes in pupil size caused by accommodation or illumination changes (section 3.3), and this is an issue when comparing aberrations at a range of pupil sizes. For peripheral vision, the reference axis should be that from the off-axis target to the center of the entrance pupil, i.e., the chief ray.

15.4.8 CORNEA AND LENTICULAR COMPONENTS OF ABERRATIONS

Determining the component contributions of the aberrations is of considerable interest. Some studies have determined anterior corneal aberrations from the corneal topography, with the difference between the aberrations of the eye and the anterior corneal component being the internal aberration component. The latter includes the influence of the posterior cornea and the lens. If information about the posterior cornea is

available, the lenticular component can be determined as the difference between the aberrations of the eye with the sum of the anterior and posterior corneal components.

For accurate determination of the components, two points need to be considered:

1. Appropriate object/image conjugates should be used. For example, it may be inappropriate to trace into the anterior cornea from infinity to determine anterior corneal aberrations if the eye has an appreciable refractive error, and the object for the posterior cornea should coincide with the image of the anterior cornea (Atchison et al. 2016). In the case of peripheral imagery, this may include appropriate curvatures of object or image surfaces (Mathur et al. 2012).
2. Where information about surface decentration and tilt is known, data should be re-referenced from the surface to the line of sight. For example, the corneal topographical data should be re-referenced from the keratometric axis, e.g., (Atchison et al. 2016; Jaisankar et al. 2020)

15.4.9 CHANGE OF WAVELENGTH

Most instruments use infrared wavelengths, and a correction in the defocus coefficient can be made for visible wavelengths. The Indiana Chromatic eye models the longitudinal chromatic aberration of human eyes well (section 17.8.2). The change in mean sphere correction ΔM for this eye, from the infrared to the visible, is given by the hyperbolic equation

$$\Delta M = 633.46[1/(\lambda_{\text{IR}} - 214.102) - 1/(\lambda_v - 214.102)] \quad (15.29)$$

where λ_{IR} is the infrared wavelength of an instrument and λ_v is a visible wavelength, both in nanometers. As an example, for the wavelengths 840 nm and 550 nm, ΔM is -0.87 D. From this equation and a truncated form of equation (15.20), the corresponding change in defocus wave aberration coefficient is

$$\Delta c_2^0 = -\Delta M \cdot R^2 / (4\sqrt{3}) \quad (15.30)$$

where R is the pupil semi-diameter.

15.4.10 PERIPHERAL ABERRATIONS

While the periphery of the eye has much poorer resolution than the central vision, peripheral vision is essential for many daily tasks, such as driving and mobility. Consequently, the quality of the peripheral optics is of considerable interest.

Aberrations in the visual field can be very high, even if small on-axis. The defocus and astigmatism aberrations dwarf the other aberrations under most circumstances, and the main emphasis in the periphery has been on refraction, particularly along the horizontal and vertical visual fields. Refraction components in the horizontal (H) and vertical meridians (V) of the pupil can be related to conventional sphere S , cylinder C and axis α by

$$H = S + C \sin^2(\alpha), V = S + C \cos^2(\alpha) \quad (15.31)$$

and to the (M, J_{180}, J_{45}) system by

$$H = M + J_{180}, V = M - J_{180} \quad (15.32a \text{ & } b)$$

or

$$M = (H + V)/2, J_{180} = (H - V)/2 \quad (15.33a \text{ & } b)$$

Sometimes we refer to tangential (T) and sagittal (S) refractions, where the T refraction is along the meridian of the visual field investigated and the S refraction is perpendicular to this. For refraction in the horizontal visual field, the tangential meridian corresponds to the horizontal meridian and the sagittal meridian corresponds to the vertical meridian. T and S are related to the (M, J_{180}, J_{45}) system by

$$M = (T + S)/2, J_{180} = (T - S)/2 \quad (15.34)$$

Sometimes *relative peripheral refraction (RPR)* is specified in which central M is subtracted from peripheral refraction M values.

The pupil is close to circular on-axis but becomes elliptical in shape when viewed off-axis (section 3.5). Alternatives to dealing with this using Zernike fitting include using an elliptical pupil shape stretched along its minor axis to become a circle, using a circular pupil whose diameter matches the larger elliptical dimension, and using a circular pupil whose diameter matches the smaller elliptical dimension. These approaches give different aberration estimates, but give similar refraction estimates with correct manipulation (Lundström et al. 2009). Although the stretching pupil approach has advantages, such as most accurately determining wave aberration coefficients and providing the most realistic comparison of aberrations between different visual field positions, the circular pupil approach based on diameters within the actual pupil is probably best because of ease of understanding, simplicity, and the possible departures of off-axis pupils from ellipticity (Charman et al. 2012; Lundström and Rosén 2017).

Charman et al. (2012) used the stretching method to determine wave aberration coefficients from Hartmann–Shack images. Assuming that the ellipticity is proportional to the cosine of the visual field angle, for off-axis vision along any meridian β and at any visual field angle ϕ , the wave aberration coefficients can be converted into refraction corrections using modified forms of equations (15.20) to (15.22):

$$M = \frac{-\left[\begin{array}{l} \left(2\sqrt{3}C_2^0 - 6\sqrt{5}C_4^0 + 12\sqrt{7}C_6^0\right)(1 + \cos^2 \phi) \\ + \left(\sqrt{6}C_2^{-2} - 3\sqrt{10}C_4^{-2} + 6\sqrt{14}C_6^{-2}\right)\sin 2\beta \sin^2 \phi \\ + \left(\sqrt{6}C_2^2 - 3\sqrt{10}C_4^2 + 6\sqrt{14}C_6^2\right)\cos 2\beta \sin^2 \phi \end{array} \right]}{R^2 \cos^2 \phi} \quad (15.35)$$

$$J_{180} = \frac{-\left[\begin{array}{l} (2\sqrt{3}C_2^0 - 6\sqrt{5}C_4^0 + 12\sqrt{7}C_6^0)\cos 2\beta \sin^2 \phi \\ + (\sqrt{6}C_2^{-2} - 3\sqrt{10}C_4^{-2} + 6\sqrt{14}C_6^{-2})\cos 2\beta \sin 2\beta \cos \phi (1 - \cos \phi)^2 \\ + (\sqrt{6}C_2^2 - 3\sqrt{10}C_4^2 + 6\sqrt{14}C_6^2)[2 \sin^2 2\beta \cos \phi + \cos^2 2\beta (1 + \cos^2 \phi)] \end{array} \right]}{R^2 \cos^2 \phi} \quad (15.36)$$

$$J_{45} = \frac{-\left[\begin{array}{l} (2\sqrt{3}C_2^0 - 6\sqrt{5}C_4^0 + 12\sqrt{7}C_6^0)\sin 2\beta \sin^2 \phi \\ + (\sqrt{6}C_2^{-2} - 3\sqrt{10}C_4^{-2} + 6\sqrt{14}C_6^{-2})[2 \cos^2 2\beta \cos \phi + \sin^2 2\beta (1 + \cos^2 \phi)] \\ + (\sqrt{6}C_2^2 - 3\sqrt{10}C_4^2 + 6\sqrt{14}C_6^2)\cos 2\beta \sin 2\beta (1 - \cos \phi)^2 \end{array} \right]}{R \cos^2 \phi} \quad (15.37)$$

Charman et al. (2012) argued that a visual field reference (such as the superior visual field) should be used rather than a retinal reference (such as the inferior retina) for describing peripheral refraction. This is because specified angles are in visual field space, while angles within the eye are unknown. Most peripheral refraction studies have used positive values for the nasal and superior visual fields (Lundström and Rosén 2017). If the ophthalmic optics convention of determining visual field meridian β in terms of an anticlockwise angle from the right side when viewing a patient's eye is used, eccentricity would not require a sign.

Concerning mirror symmetry of right and left eyes, in a pooled data set (such as when combining temporal visual data of right and left eyes and combining nasal visual data of right and left eyes), the correction needed is that used for positions in the pupil for on-axis aberrations as specified in the ISO standard for ophthalmic wave aberrations (section 15.4.2).

15.5 TECHNIQUES

Aberrations of the eye have been noted and measured since at least the time of Thomas Young (Young 1801). Several earlier methods, most applied only in a research setting, were described in the first edition of this book (Atchison and Smith 2000). Currently, the main techniques to measure aberrations are Hartmann–Shack sensing and laser raytracing tracing (section 8.4). Both of these measure transverse aberrations, which are converted to wave aberration polynomials through integration, and then to refractions to give equations (15.20)–(15.22). Refractors using an open-field of view are very popular for determining peripheral refraction (section 8.4.4). Lundström and Rosén (2017) described a range of methods that have been used for peripheral refraction, including Hartmann–Shack based methods for obtaining fast results (Jaeken and Artal 2012; Fedtke et al. 2014).

As far as possible, aberrations should be determined without the wearing of spectacle or trial lenses for Hartmann–Shack instruments. If these are worn and the

images of entrance pupils or corneas in the lens are used to specify aberrations, these images rather than the entrance pupil or cornea are imaged on the plane of the lenslet array. Because the real (or effective) entrance pupils are bigger than their images in corrected myopia, aberrations would be increasingly overestimated as myopia increased; the reverse is the case for hyperopia (Atchison, Schmid et al. 2006).

15.6 MAGNITUDES OF ABERRATIONS

15.6.1 CENTRAL FIELD

Figure 15.8 shows higher-order aberration coefficients from Salmon and van de Pol's (2006) study. This figure shows some of the important results concerning higher-order aberrations in populations that are listed below:

1. Most aberrations occur in the second-order, even in the case of well-corrected eyes (Thibos, Hong, et al. 2002; Castejón et al. 2002), and the magnitudes of coefficients decrease as the order becomes higher.
2. Higher-order aberrations vary considerably. Mean higher-order RMS is about $0.3 \mu\text{m}$ for a 6 mm pupil, e.g., Salmon and van de Pol (2006) obtained $0.27 \pm 0.22 \mu\text{m}$. As would be expected, the aberrations increase with increase in

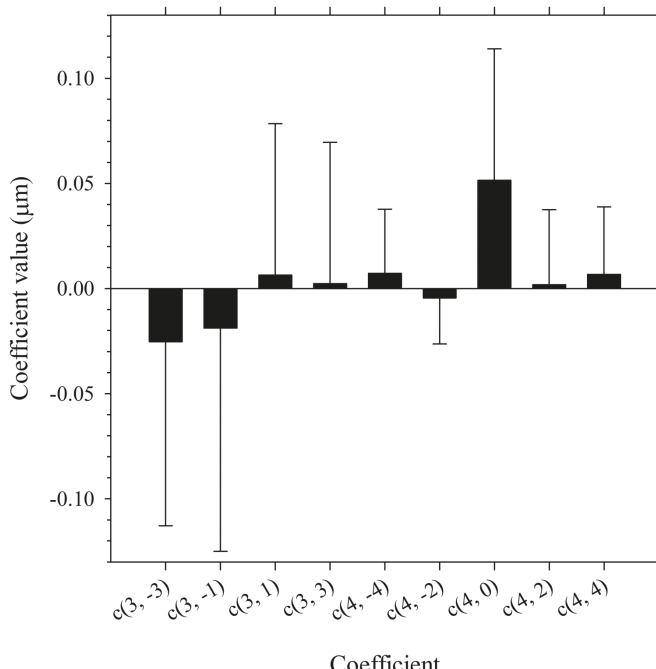


FIGURE 15.8 Third- and fourth-order aberration coefficients from Salmon and van de Pol (2006). Data were assembled from ten previous studies and are shown for right eyes and 5 mm pupils. Error bars are standard deviations. Data were kindly provided by Tom Salmon.

- pupil size, and at a higher rate as the order becomes higher, e.g., Salmon and van de Pol (2006).
3. While more than one coefficient is usually significantly different from zero in various studies, the one that is consistently different in the unaccommodated state is spherical aberration coefficient c_4^0 , with a mean of about $+0.10 \mu\text{m}$ for 6 mm pupils, e.g., Salmon and van de Pol (2006) obtained $+0.10 \pm 0.12 \mu\text{m}$ spherical aberration, with a mean of $+0.10 \pm 0.10 \mu\text{m}$ for 6 mm pupils. Similar results have been obtained by other studies, e.g., Porter et al. (2001); Thibos et al. (2002); Wang and Koch (2003); Plainis et al. (2005).
 4. Probably the most important higher-order terms are the comas. If sign is not considered, combined they contribute more than spherical aberration, e.g., Salmon and van de Pol (2006) obtained $0.17 \pm 0.14 \mu\text{m RMS}$ for the third-order coma coefficients for 6 mm pupils.
 5. Aberrations tend to be symmetric between right and left eyes, e.g., Hartwig and Atchison (2012), and thus is reasonable to combine right and left eyes by appropriate changes in signs of some coefficients of left eyes (section 15.4.2). Marcos and Burns (2000) noted that very different left and right eye aberration patterns are not uncommon.
 6. Higher-order aberrations increase with age, with spherical aberration becoming more positive (McLellan et al. 2001; Artal et al. 2002; Salmon and van de Pol 2006; Hartwig and Atchison 2012; Kingston and Cox 2013). Artal et al. (2002) attributed the increase to a disruption of the balance between corneal and internal aberrations that is present in young eyes, e.g., positive corneal spherical aberration being compensated by negative lenticular spherical aberration. Despite aberrations increasing with age in several studies, it should be remembered that natural compensation is provided by pupil sizes decreasing with age.
 7. Aberrations change with accommodation, but the only systematic change seems to be for spherical aberration coefficient c_4^0 , which becomes negative at about 2–3 D accommodation (Atchison et al. 1995; He et al. 2000; Cheng et al. 2004; Gamba et al. 2009; Hughes et al. 2021).
 8. There are conflicting findings concerning which coefficients are affected by refraction status. In a study of over 24,000 adults, Hartwig and Atchison (2012) found that nearly all third- and fourth-order coefficients changed significantly with refraction, but that the correlations were weak except for spherical aberration for which refractive error explained 8% of the variation. There was a slight increase in positive spherical aberration as refractive error became more positive ($+0.005 \mu\text{m/D}$ for 4.5 mm pupils).

As mentioned above, in most young eyes there is a considerable degree of compensation of the corneal aberrations by the lenticular aberrations (Artal et al. 2006). Within the cornea, there is compensation of the aberrations of the anterior surface by those of the posterior surface, with Atchison et al. (2016) finding compensation of about 30% for most aberration terms, as compared with having about –13% of its power.

Most aberrometers use monochromatic infrared radiation, but usually aberration results are required for visible light. In general, higher-order aberrations are similar

in infrared and visible light (Marcos et al. 1999; Llorente et al. 2003; Fernández et al. 2006; Pérez-Merino et al. 2013; Vinas et al. 2015), and correction is required only for the defocus term (see sections 15.4.8 and 17.8).

Higher-order aberrations are affected by refractive surgery and some pathological conditions. Corneal refractive surgeries, such as photorefractive keratectomy (PRK) and laser assisted *in situ* keratomileusis (LASIK), work by redistributing or differentially removing corneal tissue. For example, in LASIK for myopia most of the tissue is removed near the center rather than in the periphery. Spherical aberration becomes more positive after myopic LASIK and it shifts in the negative direction after hyperopic LASIK (Llorente et al. 2004). This can be attributed to anterior corneas changing from being prolate (flattening away from center) to being much less prolate and even oblate (steepening away from center) in treated myopic eyes, and to anterior corneas becoming more prolate in treated hyperopic eyes. Considerable effort has gone into the design of algorithms to minimize surgically induced aberrations; this is sometimes referred to a wave-guided surgery as the pre-surgical aberrations are taken in account.

Keratoconus (“conical cornea”) is a progressive, often bilateral condition that affects the cornea by causing progressive thinning particularly slightly inferior to its center. This produces high levels of astigmatism, and also large higher-order aberrations, such as vertical coma (coefficient c_3^{-1}), which has been reported to increase the corneal aberration contribution by up to 3.7 times that of normal eyes (Barbero et al. 2002; Kumar et al. 2016). Changes to the anterior surface are partially compensated by those occurring on the posterior surface.

Many optical instruments are used in combination with the eye, including telescopes and microscopes and clinical instruments, such as optometers, keratometers, and ophthalmoscopes. There are ergonomic issues relating to the way in which instruments must be used, e.g., the most appropriate alignment of the two tubes of binocular instruments so that the two eyes are not placed under undue accommodative and convergence stress when looking at close objects. The aberrations of the eye and instrument must be combined. When instruments are aberration-free or have large exit pupils relative to that of the eye, the eye limits image quality. If alignment with the eye is poor, additional aberrations will occur. These matters are covered by Smith and Atchison (1997).

The most common correcting ophthalmic devices are spectacle lenses. Spectacle lenses have minimal aberrations along their axes and make negligible contribution to on-axis aberrations provided that central vision is approximately directed through lens centers with small lens tilt. However, when the eye rotates to look at objects well away from the lens optical axis, tangential and sagittal power errors are introduced, which can become important. Investigation of these aberrations can proceed without taking the central aberrations of the eye into account. These aberrations are discussed in section 10.7.

Design issues of contact lenses are very different from those of spectacle lenses. A contact lens rotates with the eye so that the off-axis aberrations of the lens are not of considerable concern. The surfaces are very curved so that they fit well to the eye, which means that spherical aberration becomes of considerable importance. The aberrations introduced by the contact lens must be combined with those of the

eye. Because the back surface of the contact lens must closely match the cornea, the degree of freedom provided by altering lens bending is no longer available. The major design variable is aspherizing. The large difference between the refractive indices of the cornea and air (≈ 0.376) is replaced by a much larger difference between the refractive indices of the contact lens and air ($\approx 0.45\text{--}0.49$). This has a considerable effect on the combined aberrations. For rigid contact lenses, aberrations change to different extents in different eyes for two reasons: (1) approximately 90 per cent of the departure of the anterior corneal surface away from a sphere is neutralized by the tear film between the lens and eye, and (2) different eyes have different anterior corneal shapes (Atchison 1995). Performance of soft contact lenses is difficult to predict because of effects such as lens flexure, dehydration, and decentration.

Rigid contact lenses have been very effective in reducing aberrations of highly distorted corneas, e.g., Gemoules and Morris (2007); Kumar et al. (2019); Kumar et al. (2021). Attempts have been made to design contact lenses to correct ocular aberrations, with some degree of success. The main challenge is accurate alignment on the eye so that potential improvements in vision are not negated by lens decentration and rotation (see review by Marsack and Applegate (2017)).

The replacing of a cataractous lens by an intraocular lens (IOL) can have considerable effects on higher-order aberrations. Like contact lenses, IOLs move with the eye and their aberrations must be considered as part of the eye's aberrations. Degrees of freedom are lens bending, surface aspherizing, and refractive index. Spherical aberration is an important aberration, but considerable sagittal and tangential power errors may result if the lenses are tilted or decentered (Atchison 1990, 1991a, b). IOLs with spherical surfaces contribute positive spherical aberration, and Marcos et al. (2005) showed that appropriately designed IOLs with negatively aspheric surfaces reduce aberrations (Figure 15.9).

The use of multifocal contact lenses and IOLs provides a challenge for the measurement of aberrations as different parts of the pupil align with different zones of lenses. Diffraction lenses are not suited to aberration measurement.

For further information on magnitudes of central field aberrations, see Marcos, Pérez-Merino et al. (2017).

15.6.2 PERIPHERAL FIELD

Measurement of ocular peripheral aberration has a considerable history. Over 200 years ago, Thomas Young estimated astigmatic image shells in a model based on measurements of his own eye (Young 1801; Atchison and Charman 2010). There were several studies of peripheral refraction in the late 19th and early 20th centuries using various techniques (Ames and Proctor 1921). Ferree et al. (Ferree et al. 1931, 1932; Ferree and Rand 1933) determined different patterns of refraction along the horizontal visual field, and other pattern schemes were later derived (Rempt et al. 1971; Mathur and Atchison 2013a). Hoogerheide et al. (1971) suggested that a pattern in which peripheral refraction is more positive (or hyperopic) than the central refraction predisposes an eye to the development of myopia; this was brought to wide attention through a review by Wallman and Winawer (2004). This pattern is referred to as *relative peripheral hyperopic refraction*, as opposed to *relative peripheral myopic*

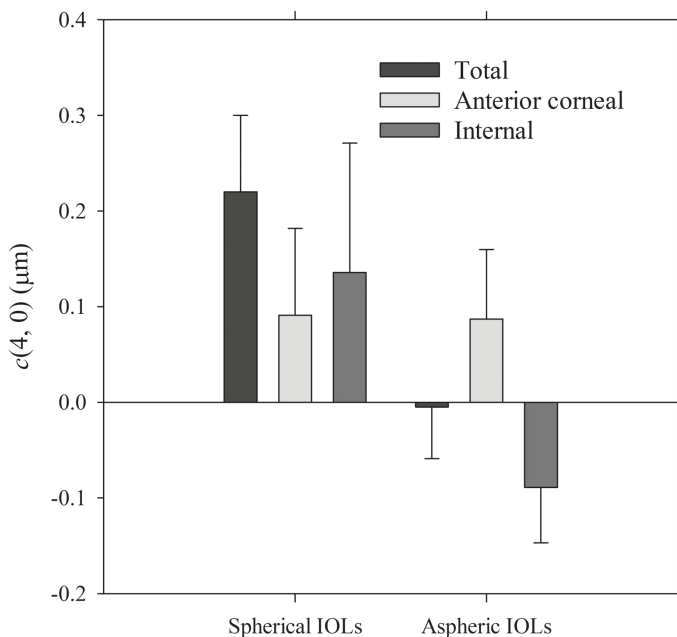


FIGURE 15.9 Average ocular (total), corneal, and internal spherical aberration coefficients in patients implanted with spherical IOLs and aspheric IOLs. Pupil size 4.5 mm. Error bars are standard deviations. Data based on Figure 5 of Marcos et al. (2005).

refraction in which the peripheral refraction is more negative (or myopic) than the central refraction.

Recent studies have shown peripheral refraction differences between different refraction groups, with myopic eyes having more hyperopic/less myopic relative peripheral refraction than emmetropic and hyperopic eyes, but with large variation between individuals (Lundström and Rosén 2017). There are differences between visual field meridians; in the horizontal visual field myopic eyes tend to have relative peripheral hyperopia while emmetropic and hyperopic eyes tend to have relative peripheral myopia, but in the vertical visual field both refractive groups tend to have relative peripheral myopia (Atchison, Pritchard et al. 2006; Berntsen et al. 2010). For relative myopic refraction the sagittal focus is closer than the tangential focus to the retina, and for relative hyperopic refraction the tangential focus is closer to the retina.

Figure 15.10 shows peripheral refraction results for one representative study (Atchison, Pritchard et al. 2006). The 43 participants have been divided into groups according to central refraction; note that some data are noisy because of the small numbers in some groups. Results are shown for horizontal and visual fields. The mean sphere M results are as described above. Both M and J_{180} astigmatism are approximately quadratic functions of visual field angle, but with offsets into the temporal and inferior fields, which can be attributed to the best fit optical axis being a few degrees offset from the line of sight in object space (angle alpha, section 4.4.1). Note that there is a change of sign for J_{180} from the horizontal to the vertical field. J_{45} changes

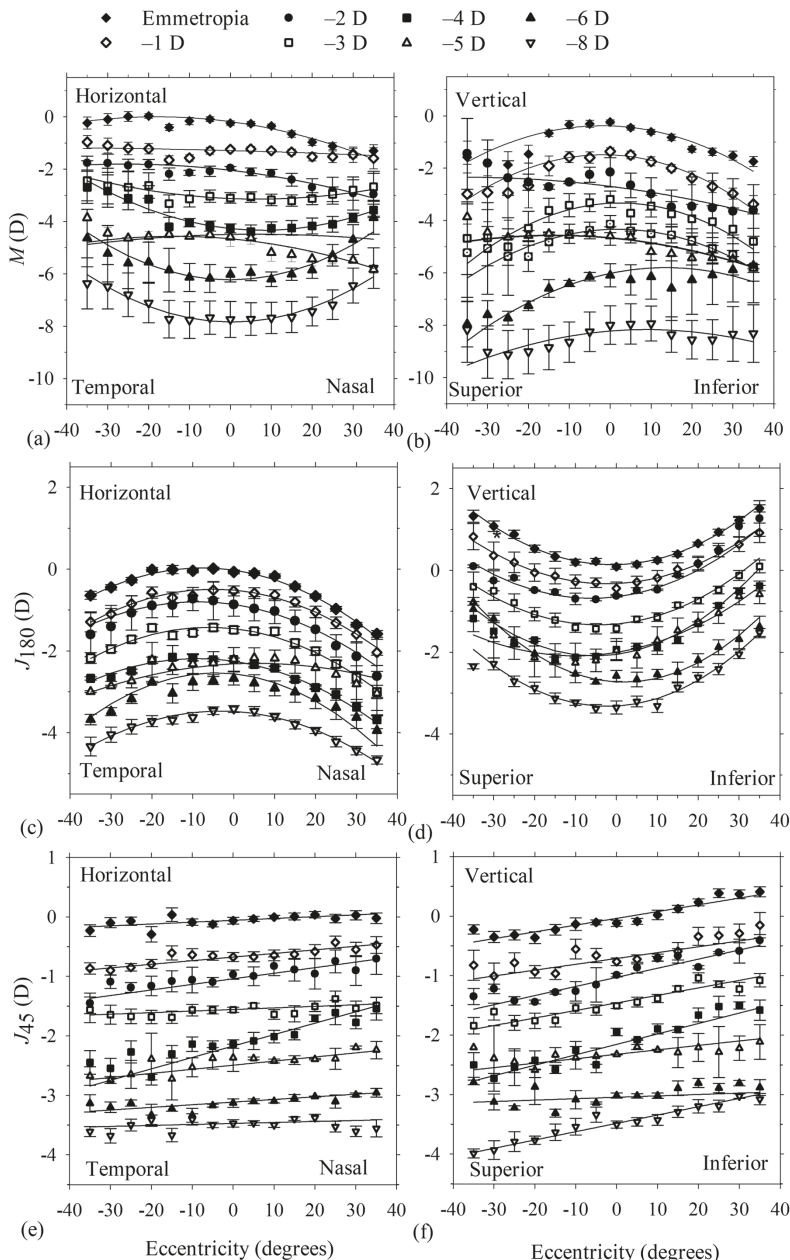


FIGURE 15.10 Refraction components as a function of visual field angle for horizontal (a), (b), (c), and vertical (b), (d), (f) fields. (a) and (b) show spherical equivalent refraction M , (c) and (d) show astigmatism J_{180} , and (e) and (f) show oblique astigmatism J_{45} . The 43 subjects have been subdivided into refraction groups. For (c)–(f), results for each myopic group (and the corresponding fitted curves) have been offset vertically for clarity by increments of 0.5 D such that the -8 D group is offset by 3.5 D. Based on Figures 1, 2, and 3 of Atchison et al. (2006), with permission from Elsevier.

linearly with visual field angle, with the rate being approximately three times greater for the vertical than for the horizontal field (this can be explained by the larger horizontal than vertical component of angle alpha).

The hypothesis that peripheral refraction of the uncorrected eye may be used to predict which people might develop myopia has not been supported in clinical studies (Sng et al. 2011; Lee and Cho 2013; Atchison et al. 2015; Rotolo et al. 2017). A related issue is how far from fixation that peripheral refraction would be considered relevant to development and progression of myopia; in this regard, Mathur and Atchison (Mathur and Atchison 2013b) suggested an outer horizontal meridian limit of 40° from fixation as beyond that angle many adult emmetropes had a pattern of relative peripheral hyperopia.

Despite the results with the clinical studies mentioned above, the different refraction patterns in different meridians, and that Hoogerheide et al. (1971) probably measured peripheral refraction after, rather than before, their participants became myopic (Rosén et al. 2012), the hypothesis has become the basis for treatments to prevent and slow myopia progression. These treatments involve the addition of positive power to the peripheral field to render it myopic or at least myopic relative to the central field. The treatments include the wear of multifocal contact and spectacle lenses, and the use of orthokeratology in which rigid contact lenses are worn overnight to flatten the central anterior cornea. Contact lens and orthokeratology treatments also affect the central aberrations, and in particular increase spherical aberration similar to corneal refractive surgery (Joslin et al. 2003; Berntsen et al. 2005; Hiraoka et al. 2007; Mathur and Atchison 2009). More detail about these treatments was given by Wolffsohn et al. (2019).

Atchison et al. (2005) investigated the effect of age on peripheral refraction and found that this did not change at similar central refractions.

Several studies have assessed the influence of accommodation on peripheral refraction, but with mixed results. Some have found a myopic shift in relative peripheral refraction with increased accommodation (Smith et al. 1988; Whatham et al. 2009; Lundstrom et al. 2009), but others have found little or no change (Calver et al. 2007; Davies and Mallen 2009; Tabernero and Schaeffel 2009; Lundstrom et al. 2009; Mathur et al. 2009a; Liu et al. 2016).

As for central vision, peripheral vision is dominated by the second-order terms, and in particular the astigmatisms. There are, however, important higher-order aberration terms. Spherical aberration changes little across the visual field according to the majority of studies, but the third-order order coma terms become the dominant higher-order aberration terms and change approximately linearly as a function of visual field angle (Lundström et al. 2009; Atchison 2006; Baskaran et al. 2011; Jaeken and Artal 2012) (Figures 15.11 and 15.12). These are susceptible to different situations: they change more quickly for myopia than for emmetropia (Mathur et al. 2009b) (Figure 15.12) and as age increases (Mathur et al. 2010; Baskaran et al. 2011), the sign of the rate of change alters with myopic LASIK surgery (Mathur and Atchison 2010), and there are very high levels in keratoconus (Atchison et al. 2010). As for on-axis aberrations, there is high left eye–right eye mirror symmetry between fellow eyes (Lundström et al. 2011; Osuagwu et al. 2016), confirming that the coefficients with negative correlations require sign changes for left eye data in a pooled data set

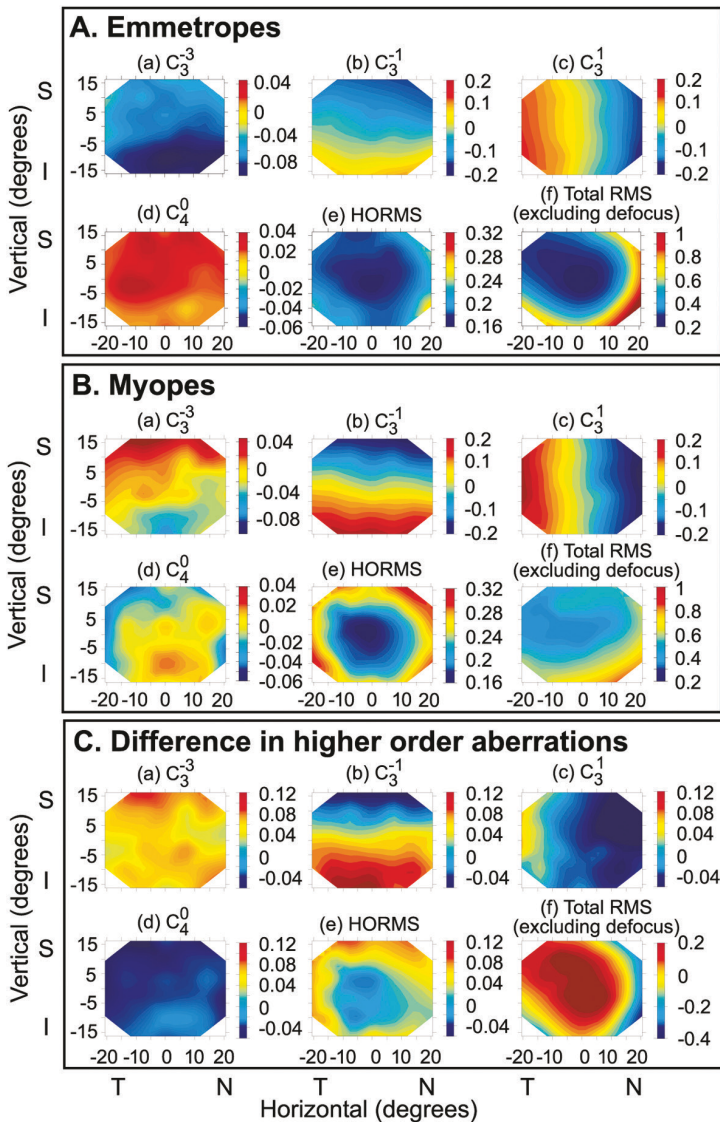


FIGURE 15.11 Individual higher-order aberration coefficients across the visual field for (A) young emmetropes, (B) young myopes, and (C) difference (B – A): (a) oblique trefoil coefficient c_3^{-3} , (b) vertical coma coefficient c_3^{-1} , (c) horizontal coma coefficient c_3^1 , (d) spherical aberration coefficient c_4^0 , (e) higher-order root-mean-squared aberration (HORMS), and (f) total root-mean-squared aberration (total RMS). The color scales represent the magnitude of each aberration in μm and are same for a given aberration in panels A and B. Note that the color scales in panel C are the same for all the aberrations except for total RMS. N, T, S, and I represent nasal, temporal, superior, and inferior visual fields, respectively. Pupil size is 5 mm. The stretched pupil method is used to determine coefficients (section 15.3.8). Reproduced from Figure 4 of Mathur et al. 2009b, copyright 2009 Association for Research in Vision and Ophthalmology.

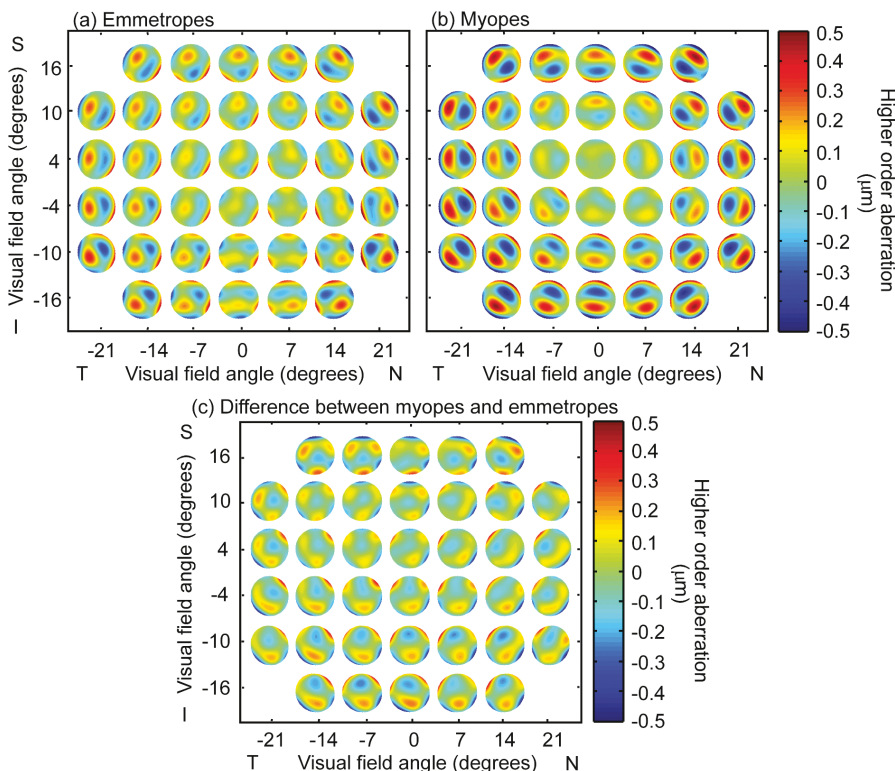


FIGURE 15.12 Higher-order aberration elliptical wavefront maps at each visual field location for (a) young emmetropes, (b) young myopes, and (c) the difference ($B - A$). The minor axis of the elliptical wavefront maps is cosine of visual field angle times the major axis. I, N, S, and T represent inferior, nasal, superior, and temporal visual fields, respectively. The main aberration contributing to the maps is coma. Reproduced from Figure 3 of Mathur et al. 2009b, copyright 2009 Association for Research in Vision and Ophthalmology.

(section 15.4.10). Again as for on-axis aberrations, the internal coma compensation for anterior corneal aberrations is poorer for older than for young adults (Mathur et al. 2012).

As mentioned in section 10.8, spectacle lenses can be designed to correct or modify peripheral vision in which the eye is assumed to be stationary and fixating along the lens optical axis. Peripheral refractive errors of the uncorrected eye should be considered in such designs. The wearing of contact lenses and IOLs affects peripheral as well as central aberrations, with the addition of positive spherical aberration being accompanied by negative shifts in relative peripheral refraction. Some lenses induce negative relative peripheral refraction for the purpose of preventing myopic progression, e.g., Jaisankar et al. (2019).

Detailed reviews of ocular peripheral aberrations were provided by Lundström and Rosén (2017) and by Romashchenko et al. (2020).

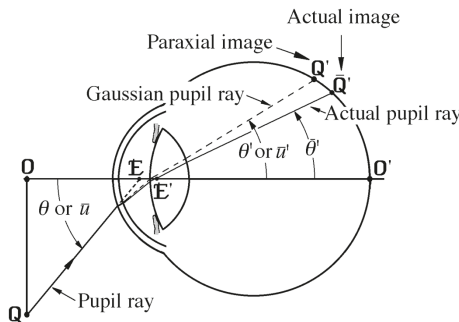


FIGURE 15.13 Pupil ray angles and distortion. The actual image position is at \bar{Q}' and the position Q' is that expected from Gaussian optics.

15.6.2.1 Distortion

Distortion in peripheral vision refers to how far the retinal image is displaced from its (expected) paraxial position. This is shown in Figure 15.13. There are few studies of this type in real eyes. Ames and Proctor (1921) referenced work of Donders (1877), with a subject with exophthalmia (protruding eyeballs), and of Druault (1898) who examined extracted eyes and two eyes of people with exophthalmia. These studies gave the peripheral angle external to the eye and the position of the retinal image position from the corneal margin. Ames and Proctor converted these retinal positions to internal angles without giving any details. Figure 15.14 shows the results.

We can compare such image point positions with those expected from Gaussian optics. If the eye was free of distortion, then the paraxial pupil ray angles \bar{u} and \bar{u}' , shown in Figure 15.13, would be related by equation (5.7), i.e.,

$$\bar{u}' = \bar{m}\bar{u} \quad (15.38)$$

where these paraxial angles are related to real angles θ and θ' by the equations

$$\bar{u} = \tan(\theta) \quad \text{and} \quad \bar{u}' = \tan(\theta') \quad (15.39)$$

and \bar{m} depends upon the actual construction of the particular eye (0.823085 for the Gullstrand exact relaxed eye). These equations have been used to plot θ' against θ as shown in Figure 15.13 and show that the actual image is closer to the axis than that predicted by Gaussian optics, indicating that there is negative distortion in the eye.

15.7 INFLUENCE OF MONOCHROMATIC ABERRATIONS ON VISUAL PERFORMANCE AND CONSEQUENCES OF CORRECTING THEM

Two important issues regarding higher-order aberrations are how they affect vision and what the consequences are of correcting them. These can be investigated in three ways.

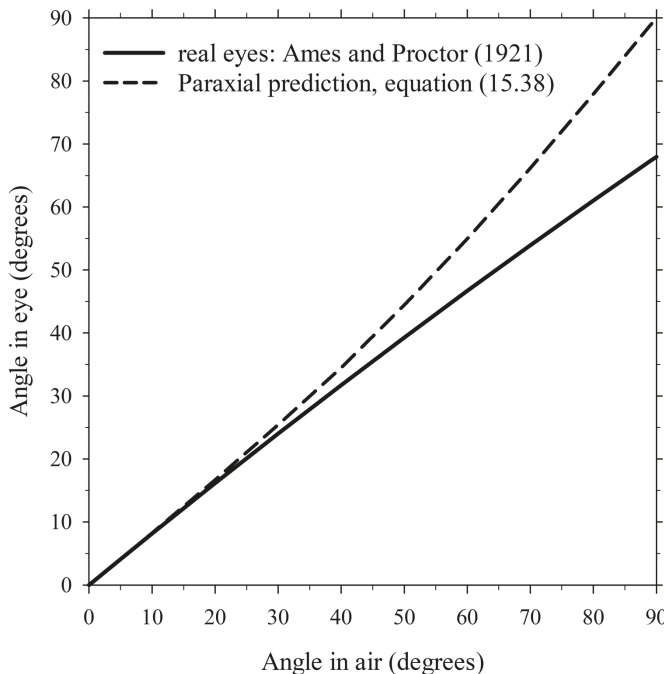


FIGURE 15.14 The measured values of internal and external angles from Ames and Proctor (1921), and predicted paraxial angles determined from equation (15.38). The Ames and Proctor data were well fitted by the equation $\theta' = 0.83209\theta - 0.0007533\theta^2$. The coefficient of the θ term in this equation was fixed at the value expected from the Gullstrand eye, which was used to predict the distortion-free values.

One way is to present displays on a monitor so that they appear as if viewed through aberrated optics and then perform visual performance tasks when people with well-corrected optics view the “aberrated” displays.

Applegate and colleagues have made considerable use of this approach, e.g., Applegate (2004). Aberrated charts were convolved with the point spread function corresponding to particular aberrations at a large pupil size (e.g., 6 mm pupil). Letter charts were “aberrated” by a convolution operation with the aberrated PSF. Well-corrected subjects viewed the charts through 3 mm pupils. Applegate’s work found that different aberrations have different effects on vision and that *RMS* wavefront error is not a good predictor of visual acuity. Aberrations near the center vertical line of the Zernike pyramid (Figure 15.3), such as spherical aberration, affect visual acuity more than aberrations away from the center line (Applegate et al. 2003; Applegate 2004). Polynomials two radial orders apart of the same sign and angular frequency tended to combine to decrease visual acuity. This technique does not fully quantify the effects that aberrations have on vision because of the “uncoupled nature” of the optics from display to subjects’ retinas, e.g., the aberrations of the eye are assumed to be negligible and diffraction of the eye is disregarded.

A second way is to produce sinusoidal gratings on the retina from the interference created by two points at the pupil plane, effectively bypassing the ocular optics by projecting sinusoidal grating targets directly onto the retina, as in the classic study of Campbell and Green (1965). Comparing the contrast sensitivity and high spatial frequency cut-off with those obtained by a conventional presentation on a screen measures how the optics affect vision. This is discussed further in Chapter 18.

A third way to investigate the influence of aberrations on vision is to perform visual tasks by viewing through an optical system containing adaptive optics that can correct or manipulate the ocular aberrations. Liang and colleagues (Liang and Williams 1997; Liang et al. 1997) showed the considerable improvements that can be made to visual performance and retinal imaging by correcting the ocular optics. Following this, in white light Yoon and Williams (2002) obtained 0.3 log (two times) improvement in contrast sensitivity for two subjects at 16-24 cycles/degree and about 0.08 ± 0.03 mean logMAR improvement in visual acuity for seven subjects. When chromatic aberration was also avoided by using monochromatic light, the improvement became 0.6 log (four times) improvement in contrast sensitivity and 0.19 ± 0.04 mean logMAR improvement in visual acuity. Figure 15.15 shows an example of improvement in on-axis visual acuity with adaptive optics.

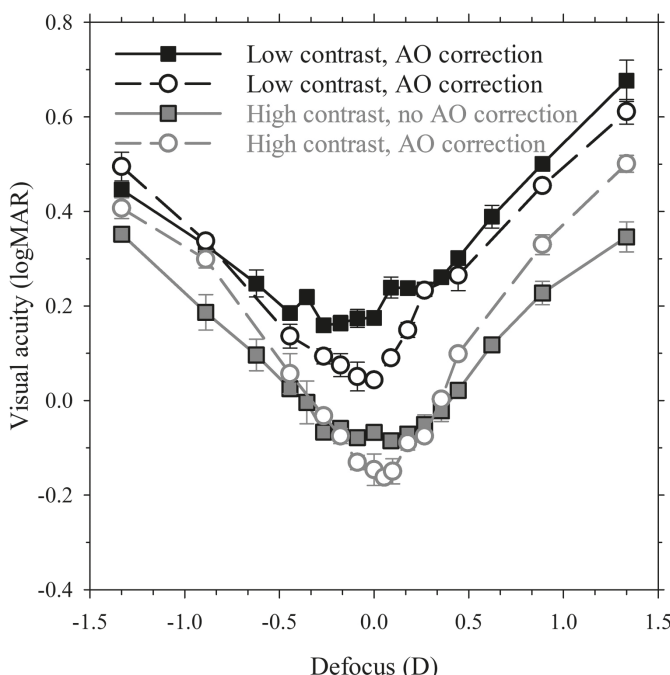


FIGURE 15.15 Effect of correction of higher-order aberrations on through-focus visual acuity for low-contrast and high-contrast letter E targets. Data of Figure 4 of Guo et al. (2008), with permission from Elsevier.

Marcos, Werner et al.'s (2017) review covered the scope of work on the influence of aberration in vision, including the following:

1. The effect of correcting aberrations on the contrast sensitivity function and visual acuity, both centrally and peripherally (see above paragraph).
2. The effect of correcting aberrations on facial recognition.
3. The effect of aberrations on accommodative lag and accommodation.
4. The effect on depth-of-field (see Chapter 19).
5. Investigating the effect of a person's own aberrations compared with those of other people. This work shows a "neural adaptation" in which visual function is better with the subject's native optics than with another subject's optics. People with increased aberrations, such as people with keratoconus, perform better than normal subjects presented with these. Visual performance with one's own "natural" aberrations is better than with rotated forms of these aberrations.
6. Investigating the ability to adapt to different aberration patterns; this is related to the previous point.
7. Simulating the effects of corrections on vision before being given to a patient or prior to manufacture, such as for multifocal types of IOLs.

Manipulating aberrations is of considerable interest for refractive surgery. Despite good levels of visual acuity often following refractive surgery, patients can be dissatisfied because of considerable levels of the higher-order aberrations under low luminance conditions. Following the work of Liang et al. mentioned in the previous section, there were rapid developments in corneal refractive surgery and commercial aberrometers, which were chronicled by MacRae and colleagues (MacRae et al. 2001; Krueger et al. 2004). There was high enthusiasm for the possibility of removing aberrations following refractive surgery, particularly in the case of anterior corneal surgery, and providing "super vision". However, there are many surgical and post-surgical issues with correcting the optics, such as variable rates of healing after surgery, changes to the posterior cornea as a result of surgery, pupil centration changing with age and accommodation (Chapter 3), aberrations changing with accommodation, aberrations changing over time (accommodative microfluctuations, varying thickness of the tear film during the blink cycle, diurnal changes in the cornea, ageing changes), and chromatic aberrations (see Chapter 17). The enthusiasm for "super vision" has been tempered in recent years, and the goal is now one of restricting aberrations to be like those existing pre-surgically.

The visual performance of an eye free of higher-order aberrations is more susceptible to focus errors, i.e., the depth-of-focus is reduced. Accommodation is not always accurate, with characteristic "leads" at low stimulus levels and "lags" at high stimulus levels, respectively (Ciuffreda 1991). It is ironic that whereas in the early 2000s there was attention to providing an aberration-free environment, for correction of presbyopia there is now emphasis on extended depth-of-focus corrections in which optical quality is never good, but is hoped to be acceptable to patients and does not vary much over a range of viewing distances (Chapter 19).

To consider what the likely improvements are in vision by correcting the aberrations of the eye requires an understanding of the optical and the neural (or retinal-brain) limits to vision. This is pursued in Chapter 18.

SUMMARY OF MAIN SYMBOLS

$W(X, Y)$	wave aberration for a ray passing through a point (X, Y) in the pupil
W_1 etc.	general wave aberration coefficients in Taylor series
$W_{4,0}$	primary spherical aberration wave aberration coefficient
$W_{4,0}$	spherical aberration wave aberration coefficient, which includes all field varying terms
$W_{3,1}$	primary coma wave aberration coefficient
$W_{3,1}$	coma wave aberration coefficient, which includes all field varying terms
$W_{2,0}$	wave aberration polynomial coefficient for defocus
ρ, θ	polar coordinates in pupil
$W(\rho, \theta)$	polar representation of wave aberration
$Z_n^m(\rho, \theta)$	Zernike polynomial function
c_n^m	coefficient of $Z_n^m(\rho, \theta)$
$R_n^{[m]}(\rho)$	radial polynomial
N_n^m	normalization term
n	index giving the highest power (or order) of a radial polynomial
m	index describing the meridional frequency of the sinusoidal component of a Zernike polynomial function
RMS	Root-mean square of wave aberration
Z_j	j th Zernike polynomial function in a single index numbering scheme
c_j	coefficient of Z_j
x, y	(relative) cartesian coordinates in the pupil
ΔF_r	radial refraction at a point in the pupil
$\frac{dW}{dr}$	radial slope of the wave aberration function at distance r from pupil center
M, J_{180}, J_{45}	representation of refraction as three components: mean sphere M , astigmatism J_{180} and oblique astigmatism J_{45}
R	pupil semi-diameter
$Z_{mn}(\rho, \theta, \alpha_{nm})$	polynomial functions in which polynomial functions of the same order but opposite angular dependences are combined
c_{nm}	coefficient corresponding to $Z_{mn}(\rho, \theta, \alpha_{nm})$
α_{nm}	angular parameter of $Z_{mn}(\rho, \theta, \alpha_{nm})$
ΔM	mean sphere correction from infrared to visible
Δc_2^0	change in defocus wave aberration coefficient
λ_{IR}, λ_v	infrared and visible wavelengths
S, C, α	representation of refraction as three components: sphere S , cylinder C and axis α
H, V	horizontal and vertical components of refraction

T, S	tangential and sagittal components of refraction in peripheral field
ϕ, β	visual field angle and visual field meridian
IOL	intraocular lens
θ, θ'	pupil ray angles outside and inside eye
\bar{u}, \bar{u}'	paraxial pupil ray angles in object and image spaces
\bar{m}	ratio of paraxial pupil ray angles

REFERENCES

- Ames, A., and C.A. Proctor. 1921. "Dioptrics of the eye." *J Opt Soc Am* 5 (1):22–84.
- Applegate, R. A. 2004. "Glenn Fry award lecture 2002: wavefront sensing, ideal corrections, and visual performance." *Optom Vis Sci* 81 (3):167–77. doi: 10.1097/00006324-200403000-00008.
- Applegate, R. A., J. D. Marsack, R. Ramos, and E. J. Sarver. 2003. "Interaction between aberrations to improve or reduce visual performance." *J Cataract Refract Surg* 29 (8):1487–95. doi: 10.1016/s0886-3350(03)00334-1.
- Applegate, R. A., L. N. Thibos, A. Bradley, S. Marcos, et al. 2000. "Reference axis selection: subcommittee report of the OSA Working Group to establish standards for measurement and reporting of optical aberrations of the eye." *J Refract Surg* 16 (5):S656–8. doi: 10.3928/1081-597X-20000901-35.
- Artal, P., A. Benito, and J. Tabernero. 2006. "The human eye is an example of robust optical design." *J Vis* 6 (1):1–7. doi: 10.1167/6.1.1.
- Artal, P., E. Berrio, A. Guirao, and P. Piers. 2002. "Contribution of the cornea and internal surfaces to the change of ocular aberrations with age." *J Opt Soc Am A* 19 (1):137–43. doi: 10.1364/josaa.19.000137.
- Atchison, D. A. 1990. "Optical design of poly(methyl methacrylate) intraocular lenses." *J Cataract Refract Surg* 16 (2):178–87. doi: 10.1016/s0886-3350(13)80727-4.
- Atchison, D. A. 1991a. "Design of aspheric intraocular lenses." *Ophthalmic Physiol Opt* 11 (2):137–46. doi: 10.1111/j.1475-1313.1991.tb00213.x.
- Atchison, D. A. 1991b. "Optical design of low index intraocular lenses." *J Cataract Refract Surg* 17 (3):292–300. doi: 10.1016/s0886-3350(13)80825-5.
- Atchison, D. A. 1995. "Aberrations associated with rigid contact lenses." *J Opt Soc Am A* 12 (10):2267–73. doi: 10.1364/josaa.12.002267.
- Atchison, D. A. 2004. "Recent advances in representation of monochromatic aberrations of human eyes." *Clin Exp Optom* 87 (3):138–48. doi: 10.1111/j.1444-0938.2004.tb03166.x.
- Atchison, D. A. 2006. "Higher order aberrations across the horizontal visual field." *J Biomed Opt* 11 (3):34026. doi: 10.1117/1.2209566.
- Atchison, D. A., and W. N. Charman. 2010. "Thomas Young's contribution to visual optics: The Bakerian Lecture "On the mechanism of the eye"." *J Vis* 10 (12):16, 1–. doi: 10.1167/10.12.16.
- Atchison, D. A., M. J. Collins, C. F. Wildsoet, J. Christensen, and M. D. Waterworth. 1995. "Measurement of monochromatic ocular aberrations of human eyes as a function of accommodation by the Howland aberrometer technique." *Vision Res* 35 (3):313–23. doi: 10.1016/0042-6989(94)00139-d.
- Atchison, D. A., S. M. Li, H. Li, S. Y. Li, et al. 2015. "Relative hyperopia does not predict development and progression of myopia in children." *Invest Ophthalmol Vis Sci* 56 (10):6162–70. doi: 10.1167/iovs.15-17200.
- Atchison, D. A., A. Mathur, S. A. Read, M. I. Walker, et al. 2010. "Peripheral ocular aberrations in mild and moderate keratoconus." *Invest Ophthalmol Vis Sci* 51 (12):6850–7. doi: 10.1167/iovs.10-5188.

- Atchison, D. A., N. Pritchard, and K. L. Schmid. 2006. "Peripheral refraction along the horizontal and vertical visual fields in myopia." *Vision Res* 46 (8-9):1450–8. doi: 10.1016/j.visres.2005.10.023.
- Atchison, D. A., N. Pritchard, S. D. White, and A. M. Griffiths. 2005. "Influence of age on peripheral refraction." *Vision Res* 45 (6):715–20. doi: 10.1016/j.visres.2004.09.028.
- Atchison, D. A., K. L. Schmid, and N. Pritchard. 2006. "Neural and optical limits to visual performance in myopia." *Vision Res* 46 (21):3707–22. doi: 10.1016/j.visres.2006.05.005.
- Atchison, D. A., D. H. Scott, and M. J. Cox. 2000. "Mathematical treatment of ocular aberrations: a user's guide." In *TOPS 35*, edited by V. Lakshminarayanan, 110–30. Washington DC: Optical Society of America.
- Atchison, D. A., M. Suheimat, A. Mathur, L. J. Lister, and J. Rozema. 2016. "Anterior corneal, posterior corneal, and lenticular contributions to ocular aberrations." *Invest Ophthalmol Vis Sci* 57 (13):5263–70. doi: 10.1167/iovs.16-20067.
- Atchison, D. A., and G. Smith. 2000. "Chapter 15. Monochromatic aberrations." In *Optics of the Human Eye, 1st ed.* Oxford: Butterworth-Heinemann.
- Bará, S., J. Arines, J. Ares, and P. Prado. 2006. "Direct transformation of Zernike eye aberration coefficients between scaled, rotated and/or displaced pupils." *J Opt Soc Am A* 23 (9):2061–6. doi: 10.1364/josaa.23.002061.
- Barbero, S., S. Marcos, J. Merayo-Lloves, and E. Moreno-Barriuso. 2002. "Validation of the estimation of corneal aberrations from videokeratography in keratoconus." *J Refract Surg* 18 (3):263–70. doi: 10.3928/1081-597X-20020501-09.
- Baskaran, K., P. Unsbo, and J. Gustafsson. 2011. "Influence of age on peripheral ocular aberrations." *Optom Vis Sci* 88 (9):1088–98. doi: 10.1097/OPX.0b013e3182234630.
- Berntsen, D. A., J. T. Barr, and G. L. Mitchell. 2005. "The effect of overnight contact lens corneal reshaping on higher-order aberrations and best-corrected visual acuity." *Optom Vis Sci* 82 (6):490–7. doi: 10.1097/01.opx.0000168586.36165.bb.
- Berntsen, D. A., D. O. Mutti, and K. Zadnik. 2010. "Study of Theories about Myopia Progression (STAMP) design and baseline data." *Optom Vis Sci* 87 (11):823–32. doi: 10.1097/OPX.0b013e3181f6f776.
- Calver, R., H. Radhakrishnan, E. Osuobeni, and D. O'Leary. 2007. "Peripheral refraction for distance and near vision in emmetropes and myopes." *Ophthalmic Physiol Opt* 27 (6):584–93. doi: 10.1111/j.1475-1313.2007.00518.x.
- Campbell, C. E. 2003a. "Matrix method to find a new set of Zernike coefficients from an original set when the aperture radius is changed." *J Opt Soc Am A* 20 (2):209–17. doi: 10.1364/josaa.20.000209.
- Campbell, C. E. 2003b. "A new method for describing the aberrations of the eye using Zernike polynomials." *Optom Vis Sci* 80 (1):79–83. doi: 10.1097/00006324-200301000-00011.
- Campbell, F. W., and D. G. Green. 1965. "Optical and retinal factors affecting visual resolution." *J Physiol* 181 (3):576–93. doi: 10.1113/jphysiol.1965.sp007784.
- Castejón, J. F., N. López-Gil, A. Benito, and P. Artal. 2002. "Ocular wave-front aberration statistics in a normal young population." *Vision Res* 42 (13):1611–7. doi: 10.1016/s0042-6989(02)00085-8.
- Charman, W. N., A. Mathur, D. H. Scott, A. Hartwig, and D. A. Atchison. 2012. "Specifying peripheral aberrations in visual science." *J Biomed Opt* 17 (2):025004. doi: 10.1117/1.JBO.17.2.025004.
- Cheng, H., J. K. Barnett, A. S. Vilupuru, J. D. Marsack, et al. 2004. "A population study on changes in wave aberrations with accommodation." *J Vis* 4 (4):272–80. doi: 10.1167/4.4.3.
- Ciuffreda, K. J. 1991. "Accommodation and its anomalies." In *Visual Optics and Instrumentation, Vol. 1 in Cronly-Dillon, J. R. (series ed), Vision and Visual Dysfunction*, edited by W. N. Charman, 231–79. Basingstoke, UK: MacMillan.

- Dai, G.-M. 2006. "Scaling Zernike expansion coefficients to smaller pupil sizes: a simpler formula." *J Opt Soc Am A* 23:539–43.
- Davies, L. N., and E. A. Mallen. 2009. "Influence of accommodation and refractive status on the peripheral refractive profile." *Br J Ophthalmol* 93 (9):1186–90. doi: 10.1136/bjo.2009.159053.
- Díaz, J. A., J. Pizarro Fernández-Dorado, C., and J. Arasa. 2009. "Zernike coefficients for concentric, circular scaled pupils: an equivalent expansion." *J Mod Opt* 56 (1):149–55. doi: 10.1080/09500340802531224.
- Donders, F. C. 1877. "Die Grenzen des Gesichtfeldes in Beziehung zu denen der Netzhaut." *von Graefes Arch Ophthalmol* 23:255–80. Cited by Ames and Proctor (1921).
- Druault, A. 1898. "Note sur la situation des images rétinnes formées par les rayons très obliques sur l'axe optique (1)." *Arch D'Ophthalmol* 18:685–92. Cited by Ames and Proctor (1921).
- Fedtke, C., K. Ehrmann, D. Falk, R. C. Bakaraju, and B. A. Holden. 2014. "The BHVI-EyeMapper: peripheral refraction and aberration profiles." *Optom Vis Sci* 91 (10):1199–207. doi: 10.1097/OPX.0000000000000364.
- Fernández, E. J., A. Unterhuber, B. Povazay, B. Hermann, et al. 2006. "Chromatic aberration correction of the human eye for retinal imaging in the near infrared." *Opt Express* 14 (13):6213–25. doi: 10.1364/oe.14.006213.
- Ferree, C. E., and G. Rand. 1933. "Interpretation of refractive conditions in the peripheral field of vision." *Arch Ophthalmol* 9 (5):925–38. doi: 10.1001/archophth.1933.00830010949006.
- Ferree, C. E., G. Rand, and C. Hardy. 1931. "Refraction for the peripheral field of vision." *Arch Ophthalmol* 5 (6):717–31. doi: 10.1001/archophth.1933.00830010949006.
- Ferree, C. E., G. Rand, and C. Hardy. 1932. "Refractive asymmetry in the temporal and nasal halves of the visual field." *Am J Ophthalmol* 15 (6):513–22.
- Gambra, E., L. Sawides, C. Dorronsoro, and S. Marcos. 2009. "Accommodative lag and fluctuations when optical aberrations are manipulated." *J Vis* 9 (6):4 1–15. doi: 10.1167/9.6.4.
- Gemoules, G., and K. M. Morris. 2007. "Rigid gas-permeable contact lenses and severe higher-order aberrations in postsurgical corneas." *Eye Contact Lens* 33 (6 Pt 1):304–7. doi: 10.1097/ICL.0b013e318033edde.
- Guo, H., D. A. Atchison, and B. J. Birt. 2008. "Changes in through-focus spatial visual performance with adaptive optics correction of monochromatic aberrations." *Vision Res* 48 (17):1804–11. doi: 10.1016/j.visres.2008.04.033.
- Hartwig, A., and D. A. Atchison. 2012. "Analysis of higher-order aberrations in a large clinical population." *Invest Ophthalmol Vis Sci* 53 (12):7862–70. doi: 10.1167/iovs.12-10610.
- He, J. C., S. A. Burns, and S. Marcos. 2000. "Monochromatic aberrations in the accommodated human eye." *Vision Res* 40 (1):41–8. doi: 10.1016/s0042-6989(99)00156-x.
- Hiraoka, T., C. Okamoto, Y. Ishii, T. Kakita, and T. Oshika. 2007. "Contrast sensitivity function and ocular higher-order aberrations following overnight orthokeratology." *Invest Ophthalmol Vis Sci* 48 (2):550–6. doi: 10.1167/iovs.06-0914.
- Hoogerheide, J., F. Rempt, and W. P. Hoogenboom. 1971. "Acquired myopia in young pilots." *Ophthalmologica* 163 (4):209–15. doi: 10.1159/000306646.
- Hughes, R. P. J., S. A. Read, M. J. Collins, and S. J. Vincent. 2021. "Higher order aberrations and retinal image quality during short-term accommodation in children." *Vision Res* 188:74–84. doi: 10.1016/j.visres.2021.07.004.
- International Organization for Standardization. 2008. Ophthalmic optics and instruments: reporting aberrations of the human eye. ISO 24157. 2008. Geneva.

- Iskander, D. R., M. R. Morelande, M. J. Collins, and B. A. Davis. 2002. "Modeling of corneal surfaces with radial polynomials." *IEEE Trans Biomed Imaging* 49 (4):320–8. doi: 10.1109/10.991159.
- Jaeken, B., and P. Artal. 2012. "Optical quality of emmetropic and myopic eyes in the periphery measured with high-angular resolution." *Invest Ophthalmol Vis Sci* 53 (7):3405–13. doi: 10.1167/iovs.11-8993.
- Jaisankar, D., A. Leube, K. L. Gifford, K. L. Schmid, and D. A. Atchison. 2019. "Effects of eye rotation and contact lens decentration on horizontal peripheral refraction." *Ophthalmic Physiol Opt* 39 (5):370–7. doi: 10.1111/opo.12641.
- Jaisankar, D., Y. Liu, P. Kollbaum, M. Jaskulski, et al. 2020. "Nasal-temporal asymmetry in peripheral refraction with an aspheric myopia control contact lens." *Biomed Opt Express* 11 (12):7376–94. doi: 10.1364/BOE.406101.
- Jaskulski, M., N. K. Singh, A. Bradley, and P. S. Kollbaum. 2020. "Optical and imaging properties of a novel multi-segment spectacle lens designed to slow myopia progression." *Ophthalmic Physiol Opt* 40 (5):549–56. doi: 10.1111/opo.12725.
- Joslin, C. E., S. M. Wu, T. T. McMahon, and M. Shahidi. 2003. "Higher-order wavefront aberrations in corneal refractive therapy." *Optom Vis Sci* 80 (12):805–11. doi: 10.1097/00006324-200312000-00010.
- Kingston, A. C., and I. G. Cox. 2013. "Population spherical aberration: associations with ametropia, age, corneal curvature, and image quality." *Clin Ophthalmol* 7:933–8. doi: 10.2147/OPTH.S44056.
- Krueger, R. R., R. A. Applegate, and S. M. (eds.) MacRae. 2004. *Wavefront Customized Visual Correction: The Quest for Super Vision II*. Thorofare: Slack Incorporated.
- Kumar, M., R. Shetty, D. Dutta, H. L. Rao, et al. 2019. "Effects of a semi-scleral contact lens on refraction and higher order aberrations." *Cont Lens Ant Eye* 42 (6):670–4. doi: 10.1016/j.clae.2019.06.002.
- Kumar, M., R. Shetty, R. S. Kumar, S. Nagaraj, and B. Shetty. 2016. "Use of wavefront imaging technology to demonstrate improvement in corneal aberrations using piggyback contact lens in a keratoconus eye with intrastromal corneal ring segment implantation: a case report." *Eye Contact Lens* 42 (3):e12–6. doi: 10.1097/ICL.0000000000000159.
- Kumar, M., R. Shetty, V. G. Lalgudi, P. Khamar, et al. 2021. "The effect of scleral lenses on vision, refraction and aberrations in post-LASIK ectasia, keratoconus and pellucid marginal degeneration." *Ophthalmic Physiol Opt* 41 (4):664–72. doi: 10.1111/opo.12802.
- Lakshminarayanan, V., and A. Fleck. 2011. "Tutorial review. Zernike polynomials: a guide." *J Mod Opt* 58 (7):545–61. doi: 10.1080/09500340.2011.554896.
- Lee, T-T., and P. Cho. 2013. "Relative peripheral refraction in children: twelve month changes in eyes with different ametropias." *Ophthalmic Physiol Opt* 33 (3):283–93. doi: 10.1111/opo.12057.
- Liang, J., and D. R. Williams. 1997. "Aberrations and retinal image quality of the normal human eye." *J Opt Soc Am A* 14 (11):2873–83. doi: 10.1364/josaa.14.002873.
- Liang, J., D. R. Williams, and D. T. Miller. 1997. "Supernormal vision and high-resolution retinal imaging through adaptive optics." *J Opt Soc Am A* 14 (11):2884–92. doi: 10.1364/josaa.14.002884.
- Liu, T., V. Sreenivasan, and L. N. Thibos. 2016. "Uniformity of accommodation across the visual field." *J Vis* 16 (3):1. doi: 10.1167/16.3.6.
- Llorente, L., S. Barbero, J. Merayo, and S. Marcos. 2004. "Total and corneal optical aberrations induced by laser in situ keratomileusis for hyperopia." *J Refract Surg* 20 (3):203–16. doi: 10.3928/1081-597X-20040501-03.

- Llorente, L., L. Diaz-Santana, D. Lara-Saucedo, and S. Marcos. 2003. "Aberrations of the human eye in visible and near infrared illumination." *Optom Vis Sci* 80 (1):26–35. doi: 10.1097/00006324-200301000-00005.
- Lundström, L., J. Gustafsson, and P. Unsbo. 2009. "Population distribution of wavefront aberrations in the peripheral human eye." *J Opt Soc Am A* 26 (10):2192–8. doi: 10.1364/JOSAA.26.002192.
- Lundstrom, L., A. Mira-Agudelo, and P. Artal. 2009. "Peripheral optical errors and their change with accommodation differ between emmetropic and myopic eyes." *J Vis* 9 (6):17 1–1. doi: 10.1167/9.6.17.
- Lundström, L., and R. Rosén. 2017. "Chapter 21. Peripheral aberrations." In *Handbook of Visual Optics: Fundamentals and Eye Optics, Volume I* edited by P. Artal, 313–35. London: CRC Press.
- Lundström, L., R. Rosén, K. Baskaran, B. Jaeken, et al. 2011. "Symmetries in peripheral ocular aberrations." *J Mod Opt* 58 (19–20):1690–5.
- Lundström, L., and P. Unsbo. 2007. "Transformation of Zernike coefficients: scaled, translated, and rotated wavefronts with circular and elliptical pupils." *J Opt Soc Am A* 24 (3):569–77. doi: 10.1364/josaa.24.000569.
- MacRae, S. M., R. R. Krueger, and R. A. (eds.) Applegate. 2001. *Customized Corneal Ablation: The Quest for Super Vision*. Thorofare: Slack Incorporated.
- Marcos, S., S. Barbero, and I. Jimenez-Alfaro. 2005. "Optical quality and depth-of-field of eyes implanted with spherical and aspheric intraocular lenses." *J Refract Surg* 21 (3):223–35. doi: 10.3928/1081-597X-20050501-05.
- Marcos, S., and S. A. Burns. 2000. "On the symmetry between eyes of wavefront aberration and cone directionality." *Vision Res* 40 (18):2437–47. doi: 10.1016/s0042-6989(00)00103-6.
- Marcos, S., S. A. Burns, E. Moreno-Barriuso, and R. Navarro. 1999. "A new approach to the study of ocular chromatic aberrations." *Vision Res* 39 (26):4309–23. doi: 10.1016/s0042-6989(99)00145-5.
- Marcos, S., P. Pérez-Merino, and C. Dorronsoro. 2017. "Chapter 20. Monochromatic aberrations." In *Handbook of Visual Optics: Fundamentals and Eye Optics, Volume I*, edited by P. Artal, 293–311. London: CRC Press.
- Marcos, S., J. S. Werner, S. A. Burns, W. H. Merigan, et al. 2017. "Vision science and adaptive optics, the state of the field." *Vision Res* 132:3–33. doi: 10.1016/j.visres.2017.01.006.
- Marsack, J. D., and R. A. Applegate. 2017. "Chapter 12. Corrections in highly aberrated eyes." In *Handbook of Visual Optics: Instrumentation and Vision Correction, Volume II* edited by P. Artal, 203–10. London: CRC Press.
- Mathur, A., and D. A. Atchison. 2009. "Effect of orthokeratology on peripheral aberrations of the eye." *Optom Vis Sci* 86 (5):E476–84. doi: 10.1097/OPX.0b013e31819fa5aa.
- Mathur, A., and D. A. Atchison. 2010. "Influence of spherical intraocular lens implantation and conventional laser in situ keratomileusis on peripheral ocular aberrations." *J Cataract Refract Surg* 36 (7):1127–34. doi: 10.1016/j.jcrs.2010.01.018.
- Mathur, A., and D. A. Atchison. 2013a. "Peripheral refraction patterns out to large field angles." *Optom Vis Sci* 90 (2):140–7. doi: 10.1097/OPX.0b013e31827f1583.
- Mathur, A., D. A. Atchison, and W. N. Charman. 2009a. "Effect of accommodation on peripheral ocular aberrations." *J Vis* 9 (12):20 1–11. doi: 10.1167/9.12.20.
- Mathur, A., D. A. Atchison, and W. N. Charman. 2009b. "Myopia and peripheral ocular aberrations." *J Vis* 9 (10):15 1–1. doi: 10.1167/9.10.15.
- Mathur, A., D. A. Atchison, and W. N. Charman. 2010. "Effects of age on peripheral ocular aberrations." *Opt Express* 18 (6):5840–53. doi: 10.1364/OE.18.005840.
- Mathur, A., D. A. Atchison, and J. Tabernero. 2012. "Effect of age on components of peripheral ocular aberrations." *Optom Vis Sci* 89 (7):E967–76. doi: 10.1097/OPX.0b013e31825da172.

- Mathur, A., and D. A. Atchison. 2013b. "Peripheral refraction patterns out to large field angles." *Optom Vis Sci* 90:140–7.
- McLellan, J. S., S. Marcos, and S. A. Burns. 2001. "Age-related changes in monochromatic wave aberrations of the human eye." *Invest Ophthalmol Vis Sci* 42 (6):1390–5.
- Nam, J., L. N. Thibos, and D. R. Iskander. 2009. "Describing ocular aberrations with wavefront vergence maps." *Clin Exp Optom* 92 (3):194–205. doi: 10.1111/j.1444-0938.2009.00358.x.
- Osuagwu, U. L., M. Suheimat, and D. A. Atchison. 2016. "Mirror symmetry of peripheral monochromatic aberrations in fellow eyes of isomyopes and anisomyopes." *Invest Ophthalmol Vis Sci* 57 (7):3422–8. doi: 10.1167/iovs.16-19267.
- Pérez-Merino, P., C. Dorronsoro, L. Llorente, S. Duran, et al. 2013. "In vivo chromatic aberration in eyes implanted with intraocular lenses." *Invest Ophthalmol Vis Sci* 54 (4):2654–61. doi: 10.1167/iovs.13-11912.
- Plainis, S., H. S. Ginis, and A. Pallikaris. 2005. "The effect of ocular aberrations on steady-state errors of accommodative response." *J Vis* 5 (5):466–77. doi: 10.1167/5.5.7.
- Porter, J., A. Guirao, I. G. Cox, and D. R. Williams. 2001. "Monochromatic aberrations of the human eye in a large population." *J Opt Soc Am A* 18 (8):1793–803. doi: 10.1364/josaa.18.001793.
- Rempt, F., J. Hoogerheide, and W. P. Hoogenboom. 1971. "Peripheral retinoscopy and the skiamogram." *Ophthalmologica* 162 (1):1–10. doi: 10.1159/000306229.
- Romashchenko, D., R. Rosen, and L. Lundström. 2020. "Peripheral refraction and higher order aberrations." *Clin Exp Optom* 103 (1):86–94. doi: 10.1111/cxo.12943.
- Rosén, R., B. Jaeken, A. Lindskoog Petterson, P. Artal, et al. 2012. "Evaluating the peripheral optical effect of multifocal contact lenses." *Ophthalmic Physiol Opt* 32 (6):527–34. doi: 10.1111/j.1475-1313.2012.00937.x.
- Rotolo, M., G. Montani, and R. Martin. 2017. "Myopia onset and role of peripheral refraction." *Clin Optom* 9:105–11. doi: 10.2147/OPTO.S134985.
- Salmon, T. O., and C. van de Pol. 2006. "Normal-eye Zernike coefficients and root-mean-square wavefront errors." *J Cataract Refract Surg* 32 (12):2064–74. doi: 10.1016/j.jcrs.2006.07.022.
- Schwiegerling, J. 2002. "Scaling Zernike expansion coefficients to different pupil sizes." *J Opt Soc Am A* 19 (10):1937–45. doi: 10.1364/josaa.19.001937.
- Schwiegerling, J., J. E. Greivenkamp, J. M. Miller, R. W. Snyder, and M. L. Palmer. 1996. "Optical modeling of radial keratotomy incision patterns." *Am J Ophthalmol* 122 (6):808–17. doi: 10.1016/s0002-9394(14)70377-0.
- Shu, H., L. Luo, G. Han, and J. L. Coatrieux. 2006. "General method to derive the relationship between two sets of Zernike coefficients corresponding to different aperture sizes." *J Opt Soc Am A* 23 (9):1960–8. doi: 10.1364/josaa.23.001960.
- Smith, G., and D. A. Atchison. 1997. "Aberration theory." In *Chapter 33. The eye and visual optical instruments*, 601–46. Oxford University Press.
- Smith, G., M. Millodot, and N. McBrien. 1988. "The effect of accommodation on oblique astigmatism and field curvature in the human eye." *Clin exp Optom* 71 (4):119–25.
- Sng, C. C., X. Y. Lin, G. Gazzard, B. Chang, et al. 2011. "Change in peripheral refraction over time in Singapore Chinese children." *Invest Ophthalmol Vis Sci* 52:7880–7. doi: 10.1167/iovs.11-7290.
- Tabernero, J., and F. Schaeffel. 2009. "Fast scanning photoretinoscope for measuring peripheral refraction as a function of accommodation." *J Opt Soc Am A* 26 (10):2206–10. doi: 10.1364/JOSAA.26.002206.
- Thibos, L. N., A. Bradley, and X. Hong. 2002. "A statistical model of the aberration structure of normal, well-corrected eyes." *Ophthalmic Physiol Opt* 22 (5):427–33. doi: 10.1046/j.1475-1313.2002.00059.x.

- Thibos, L. N., X. Hong, A. Bradley, and X. Cheng. 2002. "Statistical variation of aberration structure and image quality in a normal population of healthy eyes." *J Opt Soc Am A* 19 (12):2329–48. doi: 10.1364/josaa.19.002329.
- Vinas, M., C. Dorronsoro, D. Cortes, D. Pascual, and S. Marcos. 2015. "Longitudinal chromatic aberration of the human eye in the visible and near infrared from wavefront sensing, double-pass and psychophysics." *Biomed Opt Express* 6 (3):948–62. doi: 10.1364/BOE.6.000948.
- Wallman, J., and J. Winawer. 2004. "Homeostasis of eye growth and the question of myopia." *Neuron* 43 (4):447–68. doi: 10.1016/j.neuron.2004.08.008.
- Wang, L., and D. D. Koch. 2003. "Ocular higher-order aberrations in individuals screened for refractive surgery." *J Cataract Refract Surg* 29 (10):1896–903. doi: 10.1016/s0886-3350(03)00643-6.
- Whatham, A., F. Zimmermann, A. Martinez, S. Delgado, et al. 2009. "Influence of accommodation on off-axis refractive errors in myopic eyes." *J Vis* 9 (3):14 1–3. doi: 10.1167/9.3.14.
- Wolffsohn, J. S., P. S. Kollbaum, D. A. Berntsen, D. A. Atchison, et al. 2019. "IMI - Clinical myopia control trials and instrumentation report." *Invest Ophthalmol Vis Sci* 60 (3):M132–M60. doi: 10.1167/iovs.18-25955.
- Yoon, G. Y., and D. R. Williams. 2002. "Visual performance after correcting the monochromatic and chromatic aberrations of the eye." *J Opt Soc Am A* 19 (2):266–75. doi: 10.1364/josaa.19.000266.
- Young, T. 1801. "On the mechanism of the eye." *Phil Trans Roy Soc Lond* 91:23–88 + plates.

16 Monochromatic Aberrations of Optical Model Eyes

16.1 INTRODUCTION

The monochromatic aberrations of optical model eyes are considered in this chapter. We begin with paraxial schematic eyes, which were introduced in Chapter 5, and show that these models predict ocular aberrations poorly. The construction of more accurate schematic eyes, known as *finite* or *wide angle* schematic eyes, will then be considered. These models have useful applications, such as predicting retinal image sizes, predicting light levels on the retina, and predicting the effects of changes in any ocular structure on ocular aberrations and hence image quality. The last of these is particularly relevant considering that corneal shapes are modified to reduce refractive errors in procedures, such as LASIK and orthokeratology, and the finite schematic eyes can be developed into customized, or personalized, forms.

16.2 ABERRATIONS OF PARAXIAL SCHEMATIC EYES

To determine aberrations of schematic eyes, raytracing was performed backwards through the eyes into object space, with the stops set at the positions of entrance pupils. For comparison between the external and internal paths of pupil rays, the stop was that formed by the iris at the front of the lens. Many rays were traced across the stop to determine coefficients of Zernike aberrations accurately. The horizontal meridian was used for peripheral field raytracing and eyes were taken to be right eyes. Because all the schematic eyes to be considered are rotationally symmetrical, the only higher-order aberration term occurring on-axis is spherical aberration, but a 5° off-axis field angle was used as appropriate for the separation of the line of sight and optical axis. The circular pupil approach was used (section 15.4.10). For the determination of refractions, a stop diameter of 1 mm was used, and wave aberrations were converted using equations (15.20)–(15.22) and (15.32a, b). Refractions were referenced to the anterior cornea. The peripheral aberrations, particularly the second-order terms, depend upon the shape of the retina. Where the model eyes have no specified curved retina, a radius of curvature of –12 mm was used.

16.2.1 ON-AXIS

Table 16.1 shows the Zernike spherical aberration coefficient c_4^0 and the *RMS* of the coma coefficients, i.e., $\sqrt{(c_3^{-1})^2 + (c_3^1)^2}$, for the Gullstrand exact schematic eye and

TABLE 16.1

Zernike Spherical Aberration Coefficient c_4^0 of Two Paraxial Schematic Eyes and from One Study as a Function of Entrance Pupil Size

Schematic Eye/Study	4 mm	5 mm	6 mm
Spherical aberration coefficient			
Gullstrand exact	+0.115	+0.296	+0.654
Emsley reduced	+0.183	+0.478	+1.074
Salmon and van de Pol (2006) ^a	+0.021 (0.029)	+0.051 (0.062)	+0.104 (0.122)
<i>RMS</i> third-order coma			
Gullstrand exact	0.056	0.111	0.195
Emsley reduced	0.262	0.525	0.928
Salmon and van de Pol (2006) ^a	0.056 (0.047)	0.099 (0.083)	0.169 (0.140)

Note: Values in brackets are standard deviations. Unit μm . a Combined data of ten studies involving 2560 eyes for 1433 participants. We thank Tom Salmon for providing data.

the Emsley reduced eye, together with experimental results from Salmon and van de Pol (2006). To determine coma for the schematic eyes, we assumed a 5° angle alpha. Other paraxial schematic eyes have similar spherical aberration as this Gullstrand eye. The coefficient for this eye has three–five times the means of the experimental values, while the coefficient of the Emsley reduced eye is four–nine times higher.

The coma of the Gullstrand eye is similar to the mean coma of the experimental values, while that of the Emsley eye is about ten times higher.

The accommodated version of the Gullstrand eye has about three times the spherical aberration of that of the relaxed eye, with the increase being due mainly to the lens. Other accommodated versions (Le Grand, Gullstrand-Emsley) also show increases in positive spherical aberration. This contrasts with real eyes, for which spherical aberration reduces with accommodation and becomes zero at some value of accommodation (section 15.6.1).

16.2.2 PERIPHERAL FIELD

Figure 16.1 shows Zernike spherical aberration coefficients c_4^0 for the Gullstrand exact schematic eye for a 4 mm pupil, together with experimental results from two experimental studies. This is a clear example of the schematic eye grossly overestimating the aberration of real eyes.

Figure 16.2 shows the Zernike coma aberration coefficients c_3^1 for the Gullstrand exact schematic eye and two experimental studies. The coefficients for the schematic eye are approximately twice those for real eyes.

Figure 16.3 shows the tangential and sagittal refraction components T and S for the Gullstrand exact eye, together with refractions for emmetropic eyes from three experimental studies. Other data for emmetropic eyes would fall within the range of these studies. The tangential refractions are negative while the sagittal refractions are positive (section 15.6.2). The difference between the tangential and sagittal results

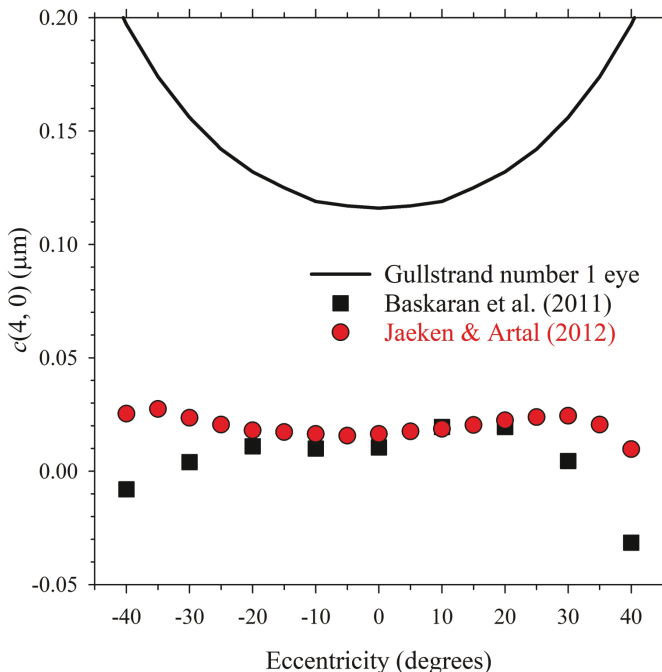


FIGURE 16.1 Zernike coefficient c_4^0 as a function of horizontal visual field angle. These are given for the Gullstrand exact schematic eye and mean results of two studies (Baskaran et al. 2011; Jaeken and Artal 2012). These results are as applied to right eyes and 4 mm pupils, with positive angles corresponding to the nasal visual field. We thank Linda Lundström for providing the experimental data.

(i.e., the astigmatism) is approximately twice as great for the Gullstrand eye as for the experimental studies.

Distortion was discussed for real eyes in section 15.6.2.1. Of importance is the relationship between the angles of the pupil ray θ' inside the eye and that θ outside the eye. We can calculate the exact relationship by tracing exact rays. The results for the Gullstrand number 1 schematic eye are shown in Figure 16.4, together with the data of Ames and Proctor (1921), which have been replotted from Figure 15.14. The internal eye angles are similar at 30° external angle, but the schematic eye angles rise more quickly to be 11% greater than real eyes at 90° external angle.

16.2.3 SUMMARY

The reader is reminded that there are considerable inter-individual and inter-study variations in aberrations of real eyes. Paraxial schematic eyes do not predict accurately the spherical aberration of real eyes, with the predictions being several times that occurring in real eyes. The paraxial schematic eyes do better at predicting the main peripheral aberrations of coma and the tangential and sagittal

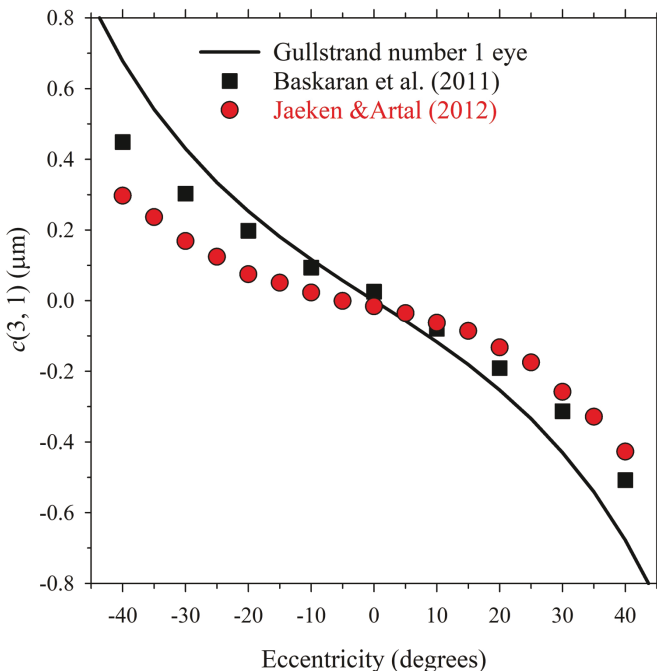


FIGURE 16.2 Zernike coefficient c_3^1 as a function of horizontal visual field angle. Other details are for Figure 16.1.

refractions, but the coma and astigmatism are still approximately twice that of real eyes. Based on some indirect experimental data, the paraxial eyes would seem to be accurate in predicting the position of the off-axis retinal image, which is related to the distortion aberration.

16.3 MODELING SURFACE SHAPES

Having shown that paraxial schematic eyes predict some of the aberrations of real eyes poorly, particularly spherical aberration, we will investigate the ways in which the paraxial models can be improved to represent real eyes more accurately. All paraxial schematic eyes have spherical surfaces, but surfaces of real eyes are non-spherical. The properties of aspheric surfaces, the ways of representing the gradient refractive index of the lens, and how these affect the aberrations will now be considered. As the word “aspheric” simply means “non-spherical”, there is an infinite range of aspheric surfaces. However, we will restrict this range to rotationally symmetric aspheric smooth surfaces. In conventional optics, the aspherical surface most frequently found to be useful is the conicoid.

16.3.1 CONICOID SURFACES

Equation (2.4) gives the form of a conicoid surface as

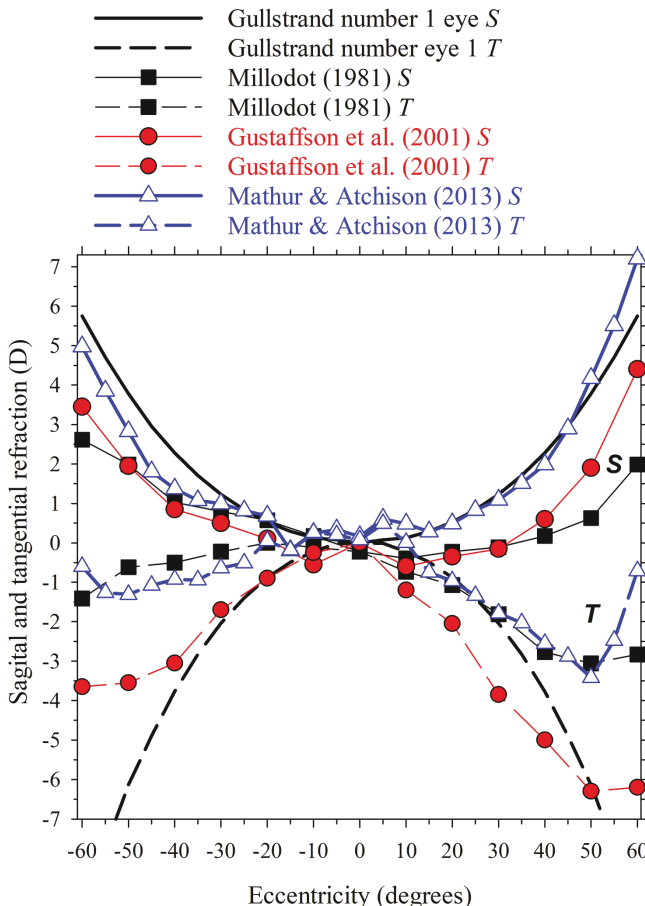


FIGURE 16.3 Tangential and sagittal refraction components as a function of horizontal visual field angle. These are given for the Gullstrand exact schematic eye, emmetropic people in two studies (Gustafsson et al. 2001; Millodot 1981), and unpublished data of emmetropic eyes from Mathur and Atchison's (2013) study.

$$h^2 + (1 + Q)Z^2 - 2ZR = 0 \quad (16.1)$$

where

the Z-axis is the optical axis

$$h^2 = X^2 + Y^2$$

R is the vertex radius of curvature and

Q is the surface asphericity, where

$Q < 0$ means the surface flattens away from its vertex

$Q = 0$ specifies a sphere

$Q > 0$ means the surface steepens away from its vertex.

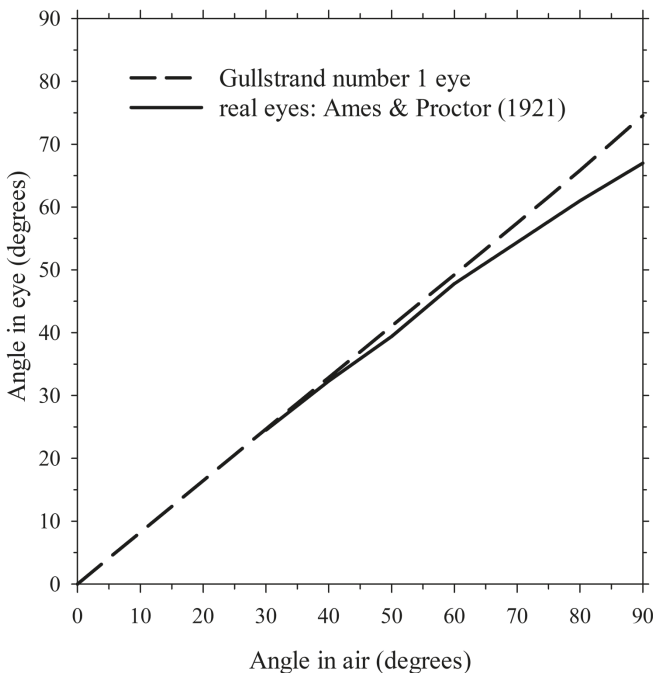


FIGURE 16.4 Internal and external angles for the pupil ray of the Gullstrand exact eye and of the “real eye” results of Ames and Proctor (1921).

The effects of the value and sign of Q on surface shape are shown in Figure 2.3. Other asphericity terms are mentioned in section 2.2.4 and their relationships to Q are described.

16.3.2 FIGURED CONICOID SURFACES

Another type of aspheric surface is given by the polynomial

$$Z = v_1 h^2 + v_2 h^4 + v_3 h^6 + \dots \quad (16.2)$$

A conicoid can always be expressed in this form, but not all polynomials of this form are conicoids. A conicoid can be expressed in this form by firstly solving equation (16.1) as a quadratic equation in Z to give

$$Z = \frac{R - \sqrt{R^2 - (1+Q)h^2}}{1+Q} \quad (16.3a)$$

and then using the binomial theorem to expand the square root term to express this equation for Z in polynomial form. However, equation (16.3a) is not useful for a flat surface (i.e., $R = \infty$) or paraboloids ($Q = -1$), and an alternative form is

$$Z = \frac{h^2}{R + \sqrt{R^2 - (1+Q)h^2}} \quad (16.3b)$$

which is solvable for all values of the parameters. Using vertex curvature rather than vertex radius of curvature, this equation becomes

$$Z = \frac{ch^2}{1 + \sqrt{1 - c^2(1+Q)h^2}} \quad (16.3c)$$

Some non-conicoid surfaces can be approximated by a conicoid and a small surface adjustment. These surfaces are called figured conicoids, and can be described by the equation

$$Z = Z_{\text{conicoid}} + f_4 h^4 + f_6 h^6 + f_8 h^8 + \text{etc.} \quad (16.4)$$

where Z_{conicoid} is the value of Z given by equation (16.3a or b) and the coefficients f_4 , f_6 , etc. are called figuring coefficients. The values of the figuring coefficients depend upon the aspheric surface being modeled. If the surface curvature is not zero, the term f_4 can be omitted provided that the values of Q and figuring coefficients are changed appropriately.

Usually, an exact representation of a non-conicoid aspheric in equation (16.4) requires an infinite number of figuring terms. In practice, the figuring power series is terminated at a finite number of terms, leaving a residual error. The required number of figuring coefficients depends upon the permissible error.

16.3.3 MORE SOPHISTICATED SURFACES

A more sophisticated model can take into account toricity and misalignment (Navarro et al. 2013)

$$z = \frac{c_x x^2 + c_y xy^2}{1 + \sqrt{1 - (1+Q_x)c_x^2 x^2 + (1+Q_{xy})c_{xy}^2 y^2}} + \sum_{j=0}^j a_j Z_j(x, y) \quad (16.5)$$

where there are separate curvatures and asphericities in the x and y directions and the second term is a Zernike polynomial expansion. Furthermore, the surface can be rotated about three meridians.

16.3.4 SURFACE TYPES USED IN STUDIES

Many investigators have fitted corneal shape data to either a conic in certain sections or to conicoids using three-dimensional data. They expressed the results in terms of the asphericity Q , shape factor p , or the eccentricity e (see section 2.2.4.2). Some results, all in terms of Q , are given in Table 2.3. The mean values for the anterior cornea obtained by the larger scale studies are similar, being in the approximate range

–0.2 to –0.3. The effect of the value of Q on corneal shape is shown in Figure 2.4 for corneas with a vertex radius of curvature of 7.8 mm. Negative values of Q will reduce spherical aberration for the anterior corneal surface but increase it for the posterior surface.

Navarro and colleagues have used a more sophisticated approach using equation (16.5) in a number of studies, e.g., Navarro et al. (2019).

In a few studies, lens surface asphericities have been expressed in terms of conicoids (section 2.3.1).

16.4 MODELING THE LENTICULAR REFRACTIVE INDEX DISTRIBUTION

The refractive index of all ocular media except the lens can be regarded as uniform (although see section 2.2.2), and thus only the lens needs special treatment. It has been known for well over a hundred years that the lens has a varying refractive index, and Gullstrand's (1909) representation of the refractive index is given in equation (2.12).

In modeling the internal structure of the lens, two types of lens models have been used. These are a multiple layered shell structure (e.g., Gullstrand 1909; Pomerantzeff et al. 1984; Raasch and Lakshminarayanan 1989; Mutti et al. 1995) and a continuously varying index (e.g., Gullstrand 1909; Blaker 1980; Smith et al. 1991; Navarro et al. 2007a; Bahrami and Goncharov 2014). The advantage of the shell model is that it allows conventional paraxial raytracing procedures to be used to examine powers, but has the disadvantage that it is more difficult to analyze its aberrations because conventional Seidel theory and finite raytracing routines cannot be used with such shell structures. By contrast, while raytracing through a gradient refractive index and aberration analysis is much more complex, routines for performing these calculations are well established. Only the continuous refractive index model will be considered in the rest of this section.

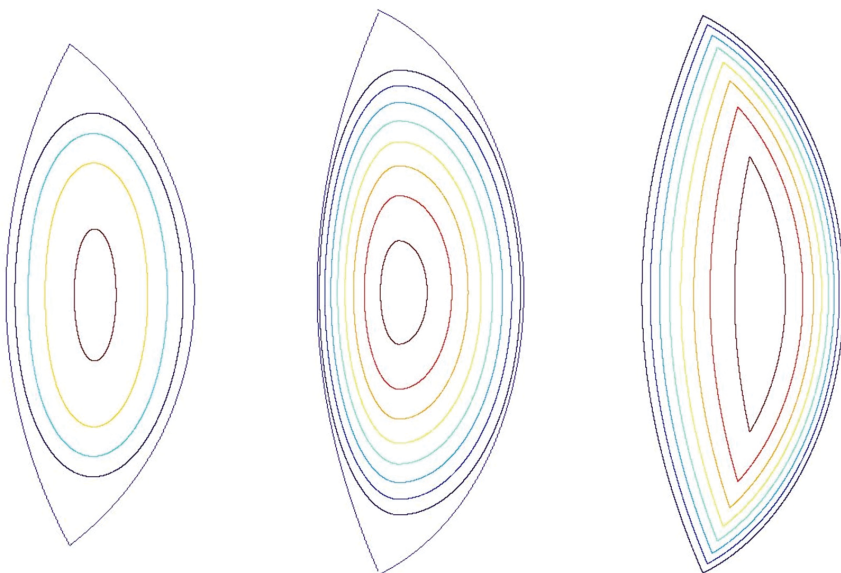
A general mathematical form for representing the refractive index distribution $N(Y,Z)$ in the Y - Z section, assuming rotational symmetry about the optical (Z) axis, is

$$N(Y,Z) = N_0(Z) + N_1(Z)Y^2 + N_2(Z)Y^4 + \dots \quad (16.6)$$

where

$$\begin{aligned} N_0(Z) &= N_{0,0} + N_{0,1}Z + N_{0,2}Z^2 + N_{0,3}Z^3 + N_{0,4}Z^4 \dots \\ N_1(Z) &= N_{1,0} + N_{1,1}Z + N_{1,2}Z^2 + N_{1,3}Z^3 + N_{1,4}Z^4 \dots \\ N_2(Z) &= N_{2,0} + N_{2,1}Z + N_{2,2}Z^2 + N_{2,3}Z^3 + N_{2,4}Z^4 \dots \\ &\text{etc. ...} \end{aligned} \quad (16.6a)$$

The values of the N_{ij} coefficients set the refractive index distribution within the lens. The refractive index distribution, upon which the relaxed form of Gullstrand's number 1 eye lens is based, is shown in Figure 16.5.



(a) Gullstrand (b) Liou & Brennan (c) Navarro

FIGURE 16.5 Lens shapes and iso-incidial contours of (a) the model on which the unaccommodated version of the Gullstrand number 1 eye is based, (b) the Liou and Brennan eye, and (c) the Navarro et al. (2007a) distribution with Liou and Brennan's lens except $p = 2$ rather than 1 in equation (16.9) and the highest axial index occurs at 60% of the lens thickness from the anterior surface. Index contours are shown in 0.05 steps from 1.39 for the Gullstrand lens and 1.37 for the other lenses near the lens edges.

Smith et al. (1991) presented a gradient index model of the lens in which the index along any line from the center of the lens to the edge and at a relative distance r from the lens center can be described by

$$N(r) = c_0 + c_1 r^2 + c_2 r^4 + c_3 r^6 \quad (16.7)$$

They divided the refractive index distribution into two half ellipses (Figure 16.6). The anterior ellipse has a semi-axis a_1 along the optical axis and a semi-axis b along the equatorial meridian. The posterior ellipse has a semi-axis a_2 along the optical axis and semi-axis b along the equatorial meridian. For the anterior half of the ellipse, some of the N_{ij} coefficients are given by

$$\begin{aligned} N_{0,0} &= c_0 + c_1 + c_2 + c_3 \\ N_{0,1} &= (-2c_1 - 4c_2 - 6c_3)/a_1 \\ N_{0,2} &= (c_1 + 6c_2 + 15c_3)/a_1^2 \\ N_{1,0} &= (c_1 + 2c_2 + 3c_3)/b^2 \end{aligned} \quad (16.8a)$$

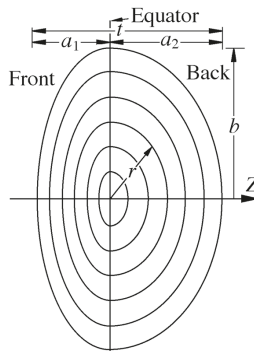


FIGURE 16.6 The gradient index of the lens modelled as two half ellipses joined at the equator. Some iso-incidal lines are shown.

For the posterior half of the ellipse, some of the N_{ij} coefficients are given by

$$N_{0,0} = c_0$$

$$N_{0,1} = 0$$

$$N_{0,2} = c_1 a_2^2$$

$$N_{1,0} = c_1 b^2 \quad (16.8b)$$

A full set of coefficients was given by Smith et al. (1991).

Another equation to describe the gradient index is

$$n(r) = n_0 + (n_s - n_c)r^{2p} \quad (16.9)$$

where $n(r)$ is the index at a relative distance r in any direction between the lens center and edge, from the point of highest refractive index n_0 on the optical axis to the lowest refractive index n_s at the surface, and the coefficient p determines the steepness of the gradient. This has been discussed in section 2.3.3, with Figure 2.8 showing the effect of varying p on the refractive index profile. This has been used in several eye models, e.g., Smith et al. (1991); Navarro et al. (2007a); Navarro et al. (2007b); Bahrami and Goncharov (2012).

The distributions provided by the preceding equations mean that the iso-incidal contours do not mold to the external shape of the lens (Figure 16.5a and b). Navarro et al. (2007a) developed a model that allowed this to happen, with an equatorial plane becoming curved away from the highest index position on the optical axis; however, the anterior and posterior iso-incidal contours meet at sharp angles (Figure 16.5c). In their “geometric-invariant” model, Bahrami and Goncharov (2014) allowed smoothing to occur.

Some authors have modeled changes in the gradient index with age and/or accommodation, e.g., Smith et al. (1992); Goncharov and Dainty (2007); Navarro et al. (2007b); Diaz et al. (2008); Navarro (2014).

There continue to be developments in lens refractive index distribution modeling, e.g., Sheil and Goncharov (2016); Navarro et al. (2021).

16.4.1 THE POWER OF THE LENS

The power of the lens can be divided into two components: (a) one arising from the anterior and posterior surfaces, and (b) one arising from the gradient index alone.

16.4.1.1 Surface Powers

Surface power is

$$F = (n' - n)/R \quad (16.9)$$

where R is the radius of curvature of a surface and n and n' are refractive indices on either side of the surface.

16.4.1.2 The Gradient Index Power

We can study the gradient index contribution to the total refractive power of the lens by regarding the lens bulk as a slab as shown in Figure 16.7. The slab of gradient index material has thickness t and is immersed in a medium of refractive index μ . We can find an approximate equation for the power of this slab by tracing the ray AA' , assuming it is a paraxial ray and that the change of height of this ray in the lens is negligible, and finding where this ray crosses the optical axis at F' . This lens will then have a back vertex focal length f'_v and a corresponding back vertex power F'_v , which are related by the equation

$$F'_v = \mu/f'_v \quad (16.10)$$

The paraxial ray must pass through the point F' for all ray heights Y . According to Fermat's principle, this will be so providing the optical path lengths for the two ray paths $VV'F'$ and $AA'F'$ are equal. Denoting the optical path length by square brackets, we must have

$$[VV'] + \mu f'_v = [AA'] + \mu\sqrt{(Y^2 + f'_v)^2}$$

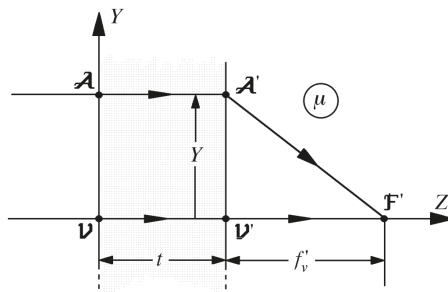


FIGURE 16.7 The power of the gradient index of the lens modeled as a “slab” lens.

Atchison and Smith (1995) showed that this equation reduces to

$$F'_v \approx -2(N_{10}t + N_{11}t^2/2 + N_{12}t^3/3 + N_{13}t^4/4 + N_{14}t^5/5 + \dots) \quad (16.11)$$

Within the approximation, this equation shows that this power is dependent only upon the coefficients $\{N_{ij}, j = 0, 1 \dots\}$, which are the coefficients of Y^2 in the refractive index function $N(Y, Z)$ given by equations (16.6). Therefore, the power does not depend on terms of higher order than Y^2 in the $N(Y, Z)$ function. These higher-order terms are, in effect, aberration terms.

16.4.1.3 Total Lens Power and Positions of the Cardinal Points

Equation (16.11) does not give the equivalent power or any information that allows us to calculate the positions of the cardinal points. If the equivalent power and cardinal point positions are needed, a paraxial raytracing scheme suitable for gradient index media can be used, such as those of Moore (1971) and Doric (1984), or a finite raytraced, which simulates a paraxial ray by being close to the axis, e.g., Sharma et al. (1982). Smith and Atchison (1997) extended the method used to derive equation (16.11), and showed that the equivalent power and cardinal point positions can be predicted from a knowledge of the N_{ij} coefficients.

16.5 MODELING THE RETINA

Compared with many other ocular parameters, the shape of the retina has not been extensively studied because of its inaccessibility. Measurements with magnetic resonance imaging and optical coherence tomography have been used to determine non-rotationally symmetrical ellipsoids, as given by the first right hand term in equation (16.5). Retinas of emmetropic adult eyes are oblate ($0 < Q < 1$), with a longer semi-diameter along (or near) the optical axis than in horizontal and vertical directions. With increase in myopia, the retinas become less oblate but remain this way for most people to high degrees of myopia (Atchison et al. 2005; Pope et al. 2017). Table 16.2 shows conicoid fitting for horizontal and vertical meridians and some schematic eye values.

16.6 SURVEY OF FINITE SCHEMATIC EYES

Comprehensive details of some of the more anatomically accurate schematic eyes are given in Appendix 3. Most of the finite model eyes are based upon established paraxial schematic eyes, improved by aspherizing one or more of the refracting surfaces, but some include a lens gradient index, e.g., Liou and Brennan (1997). Many finite eye models have been developed for a restricted set of conditions. For example, the eye of Liou and Brennan was designed to give realistic spherical aberration, and off-axis monochromatic aberrations were not considered. It is unfair to be critical of any model if it does not predict quantities accurately that are outside the scope of its purpose.

16.6.1 LOTMAR (1971)

Lotmar (1971) modified the Le Grand full theoretical eye by aspherizing anterior corneal and posterior lens surfaces. Lotmar represented the anterior surface of the cornea

TABLE 16.2
Schematic Eye Values and Experimental Values of Retinal Shape

Source	Shape of Retina
Stine (1934)	$R = -11.06 \text{ mm}$
Drasdo and Fowler schematic eye	$R = -12 \text{ mm}$
Lotmar schematic eye	$R = -12.3 \text{ mm}$
Kooijman schematic eye (1983)	$R = -10.08 \text{ mm}$
Kooijman schematic eye (1983)	$R = -14.1 \text{ mm}, Q = 0.346$
Escudero-Sanz and Navarro (1999)	$R = -12 \text{ mm}$
Atchison (2006)	horizontal meridian: $R = -12.91 - 0.094 SR$, $Q = 0.27 + 0.026SR$ vertical meridian: $R = -12.72 + 0.004 SR, Q = 0.25$ $+ 0.017SR$

Note: R = vertex radius of curvature, Q = conicoid asphericity, SR = mean spectacle refraction.

by equation (16.2) up to the sixth power. This function can be interpreted as a figured paraboloid, that is with $Q = -1$, and figuring coefficients of f_4 and f_6 . The f_4 term can be eliminated, provided that the Q and all the other figuring coefficients are adjusted suitably (Smith and Atchison 1983). If this transformation is done for the Lotmar cornea, we have $Q = -0.286$ and new figuring coefficients as given in Appendix 3. This ellipsoid gives a better fit than the paraboloid to Lotmar's full polynomial form and allows a comparison with the data of investigators who fitted ellipsoids or ellipses to the cornea (Table 2.3). Lotmar modified the lens by replacing the posterior spherical surface by a paraboloid.

16.6.2 DRASDO AND FOWLER (1974)

The Drasdo and Fowler (1974) eye is a modified form of a schematic eye attributed by Stine (1934) to Cowan (1927), which is the same as the Gullstrand-Emsley simplified eye except that it uses 1.336 for the refractive index of the aqueous and vitreous and 1.43 for the refractive index of the lens. Stine added a retinal radius of curvature of -11.06 mm . The corneal surface has a radius of curvature of 7.8 mm and an asphericity of $Q = -0.25$, obtained from published data of Prechtel and Wesley (1970) and Mandell and St Helen (1971). The eye length of 23.01 mm is less than the 23.15 mm required for emmetropia. The emmetropic length is used in this chapter.

The purpose of this model was to determine retinal projection from the visual field. While Drasdo and Fowler acknowledged that real crystalline lenses have aspherical surfaces, they argued that the level of asphericity would make little difference to the path of principal rays, and therefore used a simplified lens with spherical surfaces.

16.6.3 KOOIJMAN (1983)

Kooijman (1983) modified the Le Grand full theoretical eye model for the purpose of predicting retinal illumination. Both corneal surfaces have a Q value of -0.25 , with

the value of the anterior corneal surface taken from Mandell and St Helen (1971). The anterior lens surface is hyperbolic with a Q value of -3.06 , taken from Howcroft and Parker (1977). The posterior lens surface is parabolic ($Q = -1$), again taken from Howcroft and Parker. Two forms of the retinal shape were obtained from Krause (Helmholtz 1909). One is spherical with a radius of curvature of -10.8 mm, and the other has a vertex radius of curvature of -14.1 mm with a conic asphericity of $Q = +0.346$. The aberration results presented in the next section and in Appendix 3 were obtained with the spherical retina.

16.6.4 NAVARRO ET AL. (1985)

Navarro et al. (1985) developed a variable accommodating model, in which the crystalline lens parameters and the distance between the cornea and lens are expressed as functions of the level of accommodation. Paraxial variable accommodating eyes are discussed in section 5.7.

The base paraxial model is the Le Grand schematic eye, except for a slightly different anterior corneal radius of curvature and a slightly different refractive index. The anterior corneal surface and the lenticular surfaces are conicoids. The lens surface curvatures and asphericities, the lens thickness, the anterior chamber depth, and the lens refractive index vary as functions of accommodation, most in a logarithmic manner. The combination of parameters leads to spherical aberration decreasing with accommodation, as in real eyes, and it is approximately zero at an accommodation level of 5 D out to approximately 2 mm pupil height. Later, Escudero-Sanz and Navarro (1999) added a retina with a -12 mm radius of curvature.

16.6.5 LIOU AND BRENNAN (1997)

This model includes conicoid corneal and lenticular surfaces and a gradient index lens. Liou and Brennan (1997) selected, where possible, anatomical values based on 45-year-old eyes. The primary purpose of this schematic eye was to model the spherical aberration of real eyes, and it has a level of 1.0 D longitudinal spherical aberration at a ray height of 4 mm. It was also intended that the model should have normal levels of chromatic aberration, but all the chromatic aberration of the model occurs at the anterior corneal surface and its range of chromatic difference of refraction is only 1.1 D (400–700 nm), which is about half the normal level (see Chapter 17). The lenticular gradient index was based on the model of Smith et al. (1991) as described by equations (16.7), (16.8a), and (16.8b). Liou and Brennan used a parabolic gradient in which $c_0 = 1.407$, $c_1 = -0.039$, and c_2 and c_3 are set to zero in equation (16.7). To obtain the N_{ij} coefficients of the anterior and posterior halves of the lens, the values of a_1 , a_2 and b are 1.59 mm, 2.43 mm, and 4.4404 mm, respectively, in equations (16.8a) and (16.8b).

The aperture stop is displaced 0.5 mm from the optical axis to the nasal side and the angle between the line of sight and the optical axis in object space is 5° (also the angle between visual axis and optical axis).

The model does not specify a retinal shape. The aberration results presented in the next section and in Appendix 3 were obtained with a spherical retina of -12 mm radius of curvature.

16.6.6 REDUCED EYE MODELS OF THIBOS AND COLLEAGUES

Unlike the above eye models, there is no intention of anatomical accuracy in these models. However, they are included because they demonstrate features of real eyes such as axes and aberration levels.

Thibos et al. (1992) developed their “Chromatic” eye based on Emsley’s reduced eye, with an aspheric surface of $Q = -0.56$ to correct spherical aberration. This eye contains an aperture stop 1.91 mm from the cornea so that the entrance pupil is a similar distance from the nodal point as that in more sophisticated models. It has longitudinal chromatic aberration similar to that of real eyes (see Chapter 17). The Chromatic eye is not a rotationally symmetrical eye, but has a number of axes with no fixed relationship between them.

Thibos et al. (1997) developed a second schematic eye called the “Indiana” eye. The asymmetries of the Chromatic eye were removed. The asphericity of the eye is variable, but they selected $Q = -0.4$ as giving the best fit to experimental results of longitudinal spherical aberration. This asphericity gives $\approx +1.2$ D longitudinal spherical aberration at a ray height of 2.5 mm.

16.7 PERFORMANCE OF FINITE SCHEMATIC EYES

Some results are shown for the four-refracting surface schematic eyes covered in the previous section.

16.7.1 ON-AXIS

Table 16.3 shows the Zernike spherical aberration coefficient c_4^0 for the four schematic eyes, together with some experimental results from Salmon and van de Pol

TABLE 16.3

Zernike Spherical Aberration Coefficient c_4^0 of Finite Schematic Eyes and from One Study (Salmon and van de Pol, 2006) as a Function of Entrance Pupil Size

Schematic Eye/Study	4 mm	5 mm	6 mm
Lotmar (1971)	0.052	0.122	0.243
Kooijman (1983)	0.048	0.122	0.270
Navarro (1985)	0.042	0.109	0.240
Liou and Brennan (1997)	0.020	0.048	0.098
Salmon and van de Pol (2006)	0.021 (0.029)	0.051 (0.062)	0.104 (0.122)

Note: Values in brackets are standard deviations. Unit μm .

(2006). Comparing this table with Table 16.1 shows that the finite schematic eyes perform much better than the Gullstrand schematic eye. The Liou and Brennan schematic eye has the lowest level of spherical aberration, which is closest to mean real eye values. The Kooijman, Lotmar, and Navarro *et al.* schematic eyes have similar levels of aberration.

16.7.2 PERIPHERAL FIELD

Figure 16.8 shows the Zernike spherical aberration coefficient c_4^0 for the finite schematic eyes, together with those of the experimental studies shown in Figure 16.1. The coefficients for all the schematic eyes increase into the periphery, while those for the real eyes change little or decrease towards the edge of the field (Baskaran *et al.* 2011; Jaeken and Artal 2012).

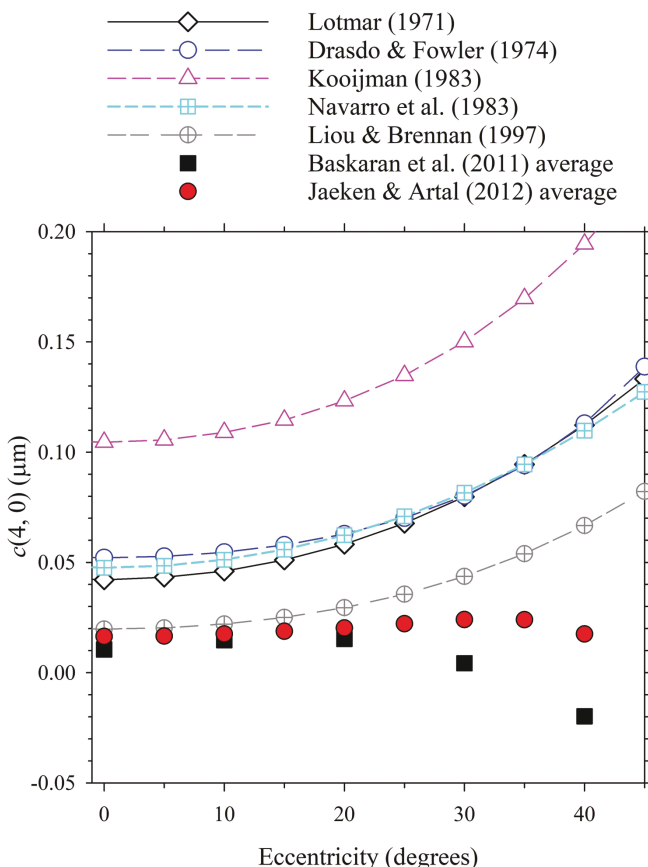


FIGURE 16.8 Zernike spherical aberration coefficients c_4^0 as a function of horizontal visual field angle. These are given for five finite schematic eyes and two studies (Baskaran *et al.* 2011; Jaeken and Artal 2012). The study results are as applied to right eyes and 4 mm pupils and are the averages of temporal and nasal visual field data.

Figure 16.9 shows the Zernike coma aberration coefficient c_3^1 for the finite schematic eyes, together with those of the experimental studies shown in Figure 16.2. The coefficients for three of the schematic eyes are approximately twice those for the real eyes, but the Liou and Brennan schematic eye gives smaller estimates.

Figures 16.10 and 16.11 show peripheral refraction for the finite schematic eyes and one experimental study. Figure 16.10 shows tangential and sagittal refraction components T and S . The spread of the plots is partly because of the different retinal radii of curvature specified for the eyes. Comparing Figure 16.10 with Figure 16.3 shows that most of the finite models are not better than the Gullstrand number 1 eye for estimating errors. The Liou and Brennan eye has reasonable estimations of both components. The Kooijman eye values for both components are much too positive, but improve to be similar to those of the Liou and Brennan eye if the aspheric retina proposed by Kooijman is used.

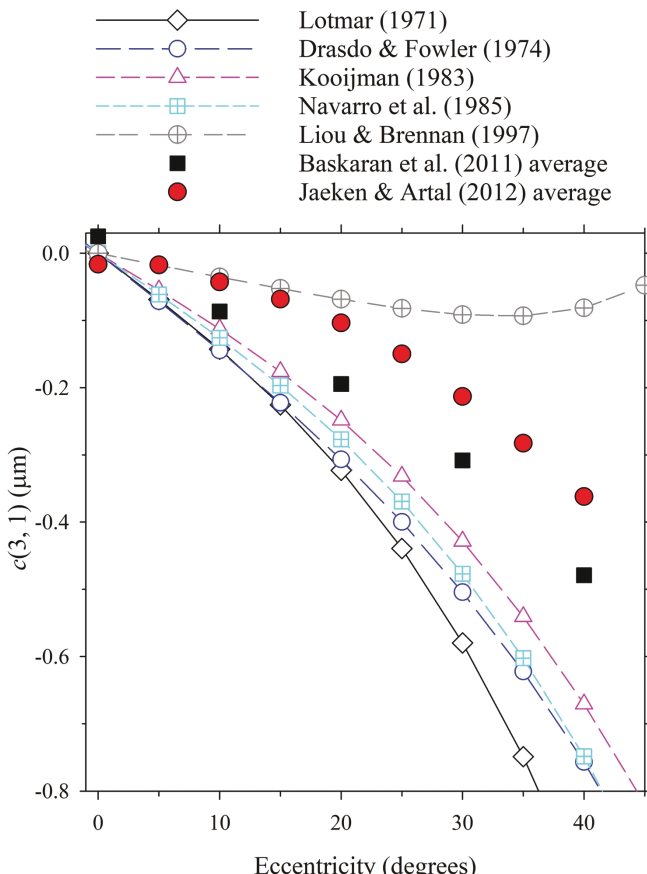


FIGURE 16.9 Zernike coma coefficients c_3^1 as a function of horizontal visual field angle. Other details are as for Figure 16.8., except that positive signs in the temporal field have been converted to negative signs.

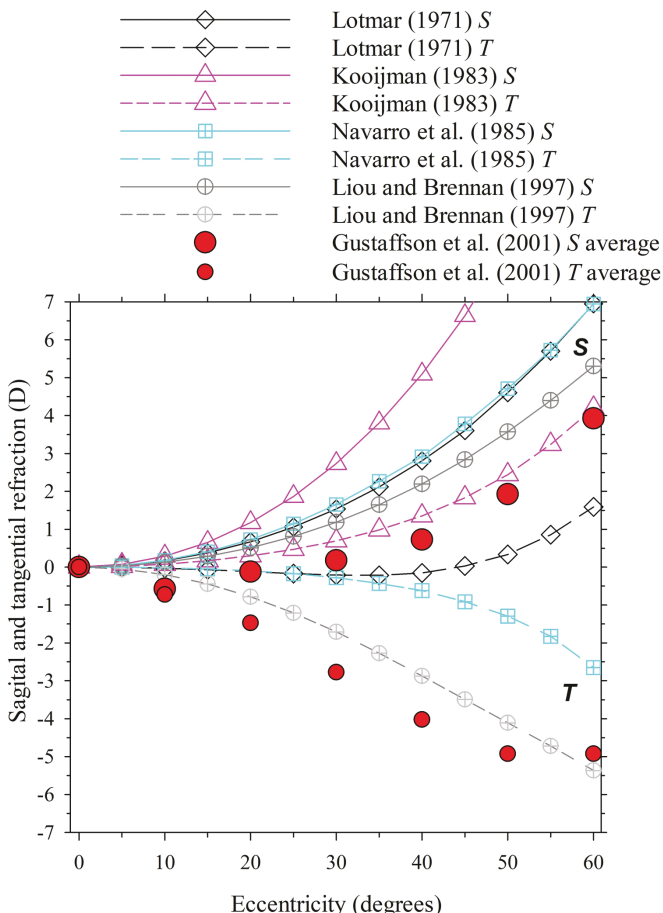


FIGURE 16.10 Tangential and sagittal refraction components as a function of horizontal visual field angle. These are given for four finite schematic eyes and for emmetropic people in one study (Gustafsson et al. 2001). The study results are the averages of temporal and nasal visual field data.

Figure 16.11 shows mean sphere and astigmatism refractive components M and J_{180° . Mean sphere estimation is good for the Liou and Brennan eyes (note that Millodot's (1981) and Mathur and Atchison's (2013) studies give less negative mean sphere than the Gustafsson et al. (2001) study). Mean sphere estimation is poor for the Lotmar and Navarro et al. eyes – their plots are better fits to results of myopes. The Kooijman eye estimates the mean sphere poorly, but if the flatter retina proposed by Kooijman is used, the estimations improve considerably to be similar to those of the Liou and Brennan eye.

The astigmatism, at least for small angles, is not dependent upon the retinal shape and therefore the astigmatism shows less spread than the sagittal and tangential power errors shown in Figure 16.10. The Kooijman, Navarro et al., and Liou and

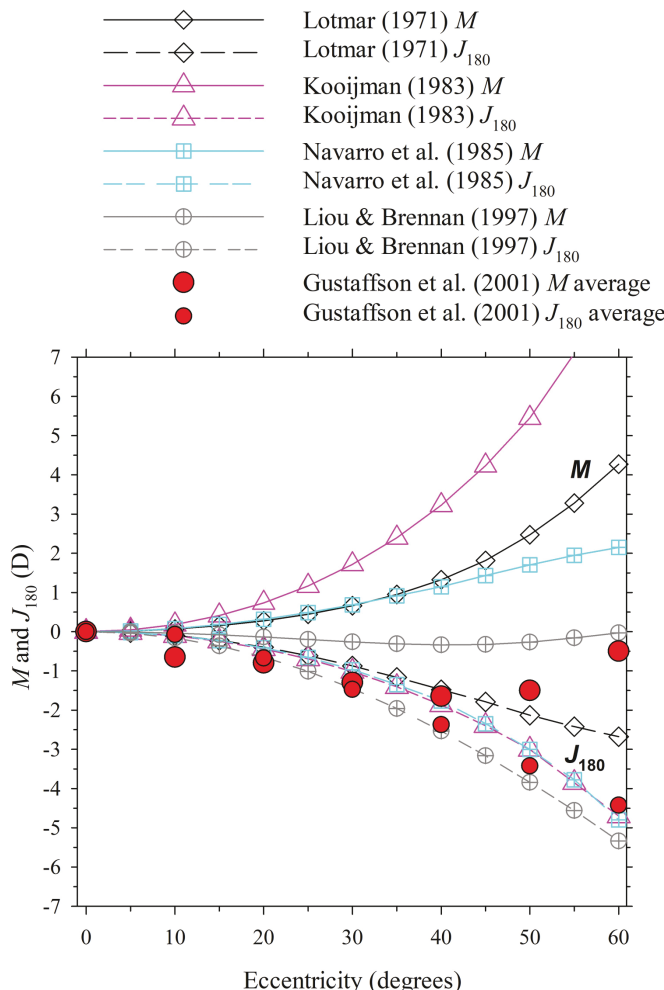


FIGURE 16.11 Mean sphere and astigmatism refraction components as a function of horizontal visual field angle. These are given for four finite schematic eyes and for emmetropic people in one study (Gustafsson et al. 2001). The study results are the averages of temporal and nasal visual field data.

Brennan eyes give reasonable estimate of astigmatism. If the aspheric retina proposed by Kooijman is used rather than his spherical retina, the estimations are worse beyond 40° object angle.

16.7.3 RETINAL IMAGE POSITION

Figure 16.12 shows the relationship between internal and external angles of the pupil ray for four finite schematic eyes and “real” eyes. This relationship is similar for all these eyes.

16.7.4 RETINAL ILLUMINANCE

Close to the optical axis and for small pupils, paraxial schematic eyes give accurate estimates of retinal illuminance. For large pupils and point sources, the effect of aberrations must be included.

For off-axis points, we must consider the influences of distortion, retinal shape, and the size of the oblique pupil. In section 13.2, we estimated the relative retinal illuminance as a function of off-axis angle using paraxial data, a spherical retina and equation (13.12). The estimations were smaller than measurements with excised eyes (Figure 13.2). More accurate estimates require accurate estimates of the apparent pupil area $A(\theta)_p$ and the quantity $\delta\theta'/\delta\theta$ used in equation (13.12).

An estimate of the apparent pupil area was given by equation (3.5b):

$$A(\theta)_p = A(0)_p \cos[(\theta + 5.3)/1.121] \quad (16.12)$$

where $A(\theta)_p$ is the on-axis pupil area. Accurate estimates of $\delta\theta'/\delta\theta$ can be found by exact raytracing through finite schematic eyes (Figure 16.12). For the Liou and Brennan (1997) eye, raytrace results were fitted to a second-order polynomial giving

$$\theta' = 0.82219\theta - 2.8689 \times 10^{-4}\theta^2 \quad (16.13)$$

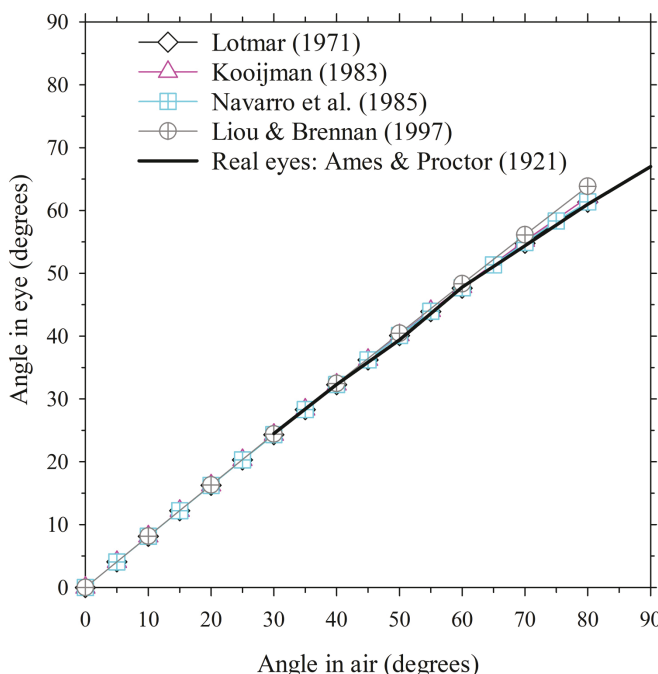


FIGURE 16.12 External and internal angles of the pupil ray for the Gullstrand exact eye, four finite schematic eyes and real eyes according to Ames and Proctor (1921).

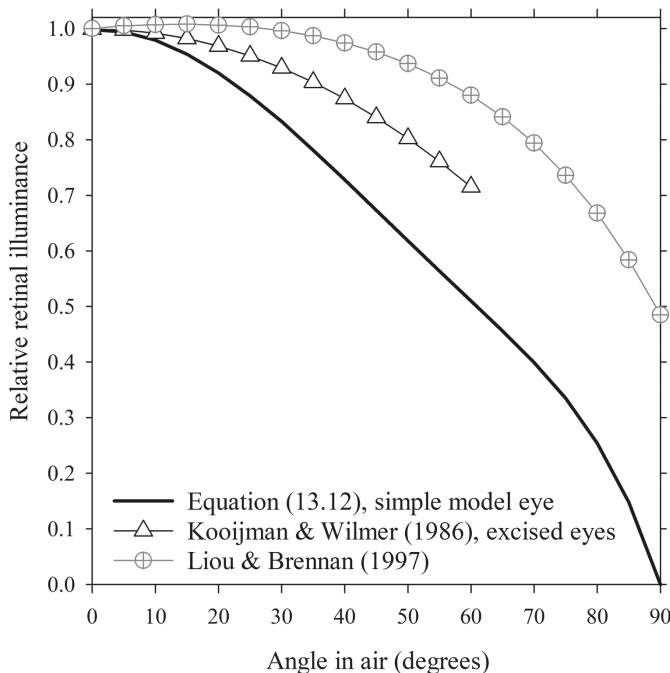


FIGURE 16.13 Retinal illuminance obtained from paraxial calculations with a simple model eye (shown also in Figure 13.2), exact raytracing calculations with the Liou and Brennan eye, and the experiments results of Kooijman and Witmer (1986). For the Liou and Brennan eye, pupil area has been determined using equation (16.12) but ignoring the offset.

Estimates of retinal illuminance for this model eye are shown in Figure 16.13, using the derivative of equation (16.13) together with results using the approximate model in Chapter 13 and measurements of Kooijman and Witmer (1986). The model eye shows higher values of retinal illuminance than given by both the approximate model and the experimental data.

The quantity $\delta\theta/\delta\theta'$ is sensitive to small changes in the relationship between θ and θ' (see Figure 16.12), and will vary between the different eye models. Kooijman (1983) showed that retinal illuminance depends upon the retinal shape, i.e., its radius of curvature and asphericity. The effect of retinal asphericity has not been included in the equations that affect some of the parameters in equation (13.12), but a more sophisticated analysis should take this into account.

16.7.5 SUMMARY

The reader is reminded again to consider the purpose of a schematic eye before criticizing it for failure for accurate estimation in other areas. The finite schematic eyes that were surveyed give better estimations than a representative paraxial schematic eye of mean levels of spherical aberration and retinal illuminance. The retinal shapes of these eyes could be modified to make some improvement in estimations of the

sagittal and tangential power errors, astigmatism, and field curvature. Despite being intended only for the estimation of spherical aberration, Liou and Brennan's (1997) schematic eye, with a retina having a -12 mm radius of curvature, appears to give the best overall estimations of average monochromatic aberrations of the better known finite schematic eyes.

16.8 OTHER OPTICAL MODEL EYES, INCLUDING CUSTOMIZED MODELS

The survey of finite schematic eyes has taken us to the end of the 20th century, if the addition of a curved retina to the Navarro eye is included. Since then, several other models have been developed, most of which are more complicated than those discussed in section 16.6. The gradient index distributions mentioned in section 16.4 were incorporated in some of the models, e.g., Goncharov and Dainty (2007); Navarro et al. (2007a); Navarro et al. (2007b). Two other models are good fits to the data on which they are based (Polans et al. 2015; Nadeem Akram et al. 2018).

Most optical model eyes have been generic, representing population averages. These are usually developed for clinically normal or abnormal situations and in some cases can be stratified by age, gender, ethnicity, refractive error, and/or accommodation.

Customized, or personalized, eye models have been developed for individual predictions of refractions, aberrations, or optical quality. These can be applied to determine the best IOL power, the effects of different designs of intraocular lens or different corneal ablation profiles on optical quality, and depth-of-focus. They can be applied to determining corneal and lenticular components of aberrations (section 15.4.8).

To develop such models, all the information that has been obtained from biometric measurements is often used, e.g., anterior corneal topography. Where information is not available, such as for the posterior cornea, a generic model may be used or an optimization procedure might be used so that the model's ocular aberrations match those that have been measured. Tabernero (2017) described approaches to designing customized eye models.

16.9 WHICH EYE MODEL TO USE

For optical design, it might be considered that the most anatomically correct model that is available is the best to use. However, "it is possible that this model is too complex and unwieldy to be useful for other applications and the increasing complexity of models may make it harder to use them as useful thinking tools" (Atchison and Thibos 2016). It is better to use the simplest model that is adequate for the application, which could even be anatomically inaccurate provided that it is functionally accurate. Customized eye models may need more detail than is often used in the basic schematic eyes, but even here it is possibly to make simplifications without losing functionality (Tabernero 2017).

SUMMARY OF MAIN SYMBOLS

c_4^0	Zernike spherical aberration coefficient
c_3^{-1}, c_3^1	Zernike vertical coma and horizontal coma coefficients
T, S	tangential and sagittal refraction components
M, J_{180}	mean sphere and horizontal astigmatism refraction components
θ, θ'	pupil ray angles outside and inside eye
R	surface radius of curvature
Q	surface asphericity
f_4, f_6 , etc.	surface figuring coefficients
$N(Y, Z)$	refractive index distribution in the Y-Z section
$N_0(Z), N_1(Z)Y^2$, etc.	components of $N(Y, Z)$
$N(r)$	refractive index distribution as a function of relative distance r from center to edge
$c_0, c_1 r^2, c_2 r^4$, etc.	components of $N(r)$
a_1, a_2	semi-axis of anterior and posterior sections of refractive index distribution elliptical parameters
b	semi-axis along equatorial meridian
p	coefficient determining the steepness of refractive index gradient

REFERENCES

- Ames, A., and C. A. Proctor. 1921. "Dioptrics of the eye." *J Opt Soc Am* 5 (1):22–84.
- Atchison, D. A., N. Pritchard, K. L. Schmid, D. H. Scott, et al. 2005. "Shape of the retinal surface in emmetropia and myopia." *Invest Ophthalmol Vis Sci* 46 (8):2698–707. doi: 10.1167/iovs.04-1506.
- Atchison, D. A., and G. Smith. 1995. "Continuous gradient index and shell models of the human lens." *Vision Res* 35 (18):2529–38. doi: 10.1016/0042-6989(95)00019-v.
- Atchison, D. A., and L. N. Thibos. 2016. "Optical models of the human eye." *Clin Exp Optom* 99 (2):99–106. doi: 10.1111/cxo.12352.
- Bahrami, M., and A. V. Goncharov. 2012. "Geometry-invariant gradient refractive index lens: analytical ray tracing." *J Biomed Opt* 17 (5):055001. doi: 10.1117/1.JBO.17.5.055001.
- Bahrami, M., and A. V. Goncharov. 2014. "Geometry-invariant GRIN lens: finite ray tracing." *Opt Express* 22 (23):27797–810. doi: 10.1364/OE.22.027797.
- Baskaran, K., P. Unsbo, and J. Gustafsson. 2011. "Influence of age on peripheral ocular aberrations." *Optom Vis Sci* 88 (9):1088–98. doi: 10.1097/OPX.0b013e3182234630.
- Blaker, J. W. 1980. "Toward an adaptive model of the human eye." *J Opt Soc Am* 70 (2):220–3. doi: 10.1364/josa.70.000220.
- Cowan, A. 1927. *An Introductory Course in Ophthalmic Optics*: F. A. Davis Co. Cited by Stine (1934).
- Diaz, J. A., C. Pizarro, and J. Arasa. 2008. "Single dispersive gradient-index profile for the aging human lens." *J Opt Soc Am A* 25 (1):250–61. doi: 10.1364/josaa.25.000250.
- Doric, S. 1984. "Paraxial ray trace for rotationally symmetric homogeneous and inhomogeneous media." *J Opt Soc Am A* 1 (8):818–21. doi: 10.1364/JOSAA.1.000818.
- Drasdo, N., and C. W. Fowler. 1974. "Non-linear projection of the retinal image in a wide-angle schematic eye." *Br J Ophthalmol* 58 (8):709–14. doi: 10.1136/bjo.58.8.709.
- Escudero-Sanz, I., and R. Navarro. 1999. "Off-axis aberrations of a wide-angle schematic eye model." *J Opt Soc Am A* 16 (8):1881–91. doi: 10.1364/josaa.16.001881.

- Goncharov, A. V., and C. Dainty. 2007. "Wide-field schematic eye models with gradient-index lens." *J Opt Soc Am A* 24 (8):2157–74. doi: 10.1364/josaa.24.002157.
- Gullstrand, A. 1909. "Appendix II: Procedure of rays in the eye. Imagery - laws of the first order." In *Helmholtz's Handbuch der Physiologischen Optik*, vol. 1, 3rd edn (English translation edited by J. P. Southall, Optical Society of America, 1924), 301–58.
- Gustafsson, J., E. Terenius, J. Buchheister, and P. Unsbo. 2001. "Peripheral astigmatism in emmetropic eyes." *Ophthalmic Physiol Opt* 21 (5):393–400. doi: 10.1046/j.1475-1313.2001.00606.x.
- Helmholtz, H. 1909. *Handbuch der Physiologischen Optik*, vol. 1, 3rd ed (English translation edited by J. P. Southall, Optical Society of America, 1924), pp. 143–172.
- Howcroft, M. J., and J. A. Parker. 1977. "Aspheric curvatures for the human lens." *Vision Res* 17 (10):1217–23. doi: 10.1016/0042-6989(77)90157-2.
- Jaeken, B., and P. Artal. 2012. "Optical quality of emmetropic and myopic eyes in the periphery measured with high-angular resolution." *Invest Ophthalmol Vis Sci* 53 (7):3405–13. doi: 10.1167/iovs.11-8993.
- Kooijman, A. C. 1983. "Light distribution on the retina of a wide-angle theoretical eye." *J Opt Soc Am* 73 (11):1544–50. doi: 10.1364/josa.73.001544.
- Kooijman, A. C., and F. K. Witmer. 1986. "Ganzfeld light distribution on the retina of human and rabbit eyes: calculations and in vitro measurements." *J Opt Soc Am A* 3 (12):2116–20. doi: 10.1364/josaa.3.002116.
- Liou, H.-L., and N. A. Brennan. 1997. "Anatomically accurate, finite model eye for optical modeling." *J. Opt. Soc. Am. A* 14 (8):1684–95. doi: 10.1364/josaa.14.001684.
- Lotmar, W. 1971. "Theoretical eye model with aspheric surfaces." *J Opt Soc Am* 61 (11):1522–9. doi: 10.1364/JOSA.61.001522.
- Mandell, R. B., and R. St Helen. 1971. "Mathematical model of the human contour." *Br J Physiol Opt* 26:183–97.
- Mathur, A., and D. A. Atchison. 2013. "Peripheral refraction patterns out to large field angles." *Optom Vis Sci* 90 (2):140–7. doi: 10.1097/OPX.0b013e31827f1583.
- Millodot, M. 1981. "Effect of ametropia on peripheral refraction." *Am J Optom Physiol Opt* 58 (9):691–5. doi: 10.1097/00006324-198109000-00001.
- Moore, D. T. 1971. "Designs of singlets with continuously varying indices of refraction." *J Opt Soc Am* 61 (7):886–94. doi: 10.1364/JOSA.61.000886.
- Mutti, D. O., K. Zadnik, and A. J. Adams. 1995. "The equivalent refractive index of the crystalline lens in childhood." *Vision Res* 35 (11):1565–73. doi: 10.1016/0042-6989(94)00262-k.
- Nadeem Akram, M., R. C. Baraas, and K. Baskaran. 2018. "Improved wide-field emmetropic human eye model based on ocular wavefront measurements and geometry-independent gradient index lens." *J Opt Soc Am A* 35 (11):1954–67. doi: 10.1364/JOSAA.35.001954.
- Navarro, R. 2014. "Adaptive model of the aging emmetropic eye and its changes with accommodation." *J Vis* 14 (13):21. doi: 10.1167/14.13.21.
- Navarro, R., S. Baquedano, and A. I. Sanchez-Cano. 2021. "GRINCU lens with conicoid iso-indicial surfaces: application for modeling the crystalline lens." *Opt Express* 29 (20):30998–1009. doi: 10.1364/OE.435266.
- Navarro, R., F. Palos, and L. Gonzalez. 2007a. "Adaptive model of the gradient index of the human lens. I. Formulation and model of aging ex vivo lenses." *J Opt Soc Am A* 24 (8):2175–85. doi: 10.1364/josaa.24.002175.
- Navarro, R., F. Palos, and L. M. Gonzalez. 2007b. "Adaptive model of the gradient index of the human lens. II. Optics of the accommodating aging lens." *J Opt Soc Am A* 24 (9):2911–20. doi: 10.1364/josaa.24.002911.

- Navarro, R., J. J. Rozema, M. H. Emamian, H. Hashemi, and A. Fotouhi. 2019. "Average biometry of the cornea in a large population of Iranian school children." *J Opt Soc Am A* 36 (4):B85–B92. doi: 10.1364/JOSAA.36.000B85.
- Navarro, R., J. J. Rozema, and M. J. Tassignon. 2013. "Optical changes of the human cornea as a function of age." *Optom Vis Sci* 90 (6):587–98. doi: 10.1097/OPX.0b013e3182928bc6.
- Navarro, R., J. Santamaría, and R. Bescós. 1985. "Accommodation dependent model of the human eye with aspherics." *J Opt Soc Am A* 2 (8):1273–81. doi: 10.1364/josaa.2.001273.
- Polans, J., B. Jaeken, R. B. McNabb, P. Artal, and J. A. Izaat. 2015. "Wide-field optical model of the human eye with asymmetrically tilted and decentered lens that reproduces measured optical aberrations." *Optica* 2 (2):124–34. doi: 10.1364/OPTICA.2.000124.
- Pomerantzoff, O., M. Pankratov, G. J. Wang, and P. Dufault. 1984. "Wide-angle optical model of the eye." *Am J Optom Physiol Opt* 61 (3):166–76. doi: 10.1097/00006324-198403000-00004.
- Pope, J. M., P. K. Verkiculara, F. Sepehrband, M. Suheimat, et al. 2017. "Three-dimensional MRI study of the relationship between eye dimensions, retinal shape and myopia." *Biomed Opt Express* 8 (5):2386–95. doi: 10.1364/BOE.8.002386.
- Prechtel, L. A., and N. K. Wesley. 1970. "Corneal topography and its application to contact lenses." *Br J Physiol Opt* 25 (2):117–26.
- Raasch, T., and V. Lakshminarayanan. 1989. "Optical matrices of lenticular polyindicial schematic eyes." *Ophthalmic Physiol Opt* 9 (1):61–5. doi: 10.1111/j.1475-1313.1989.tb00807.x.
- Salmon, T. O., and C. van de Pol. 2006. "Normal-eye Zernike coefficients and root-mean-square wavefront errors." *J Cataract Refract Surg* 32 (12):2064–74. doi: 10.1016/j.jcrs.2006.07.022.
- Sharma, A., D. V. Kumar, and A. K. Ghatak. 1982. "Tracing rays through graded-index media: a new method." *Appl Opt* 21 (6):984–7. doi: 10.1364/AO.21.000984.
- Sheil, C. J., and A. V. Goncharov. 2016. "Accommodating volume-constant age-dependent optical (AVOCADO) model of the crystalline GRIN lens." *Biomed Opt Express* 7 (5):1985–99. doi: 10.1364/BOE.7.001985.
- Smith, G., and D. A. Atchison. 1983. "Effect of conicoid asphericity on the Tscherning ellipses of ophthalmic spectacle lenses." *J Opt Soc Am* 73 (4):441–5. doi: 10.1364/josa.73.000441.
- Smith, G., and D. A. Atchison. 1997. "Equivalent power of the crystalline lens of the human eye: comparison of methods of calculation." *J Opt Soc Am A* 14 (10):2537–46. doi: 10.1364/josaa.14.002537.
- Smith, G., D. A. Atchison, and B. K. Pierscionek. 1992. "Modeling the power of the aging human eye." *J Opt Soc Am A* 9 (12):2111–7. doi: 10.1364/josaa.9.002111.
- Smith, G., B. K. Pierscionek, and D. A. Atchison. 1991. "The optical modelling of the human lens." *Ophthalmic Physiol Opt* 11 (4):359–69. doi: 10.1016/0275-5408(91)90053-L.
- Stine, G. H. 1934. "Tables for accurate retinal location." *Am J Ophthalmol* 17 (4):314–24.
- Tabernero, J. 2017. "Chapter 22. Customized eye models." In *Handbook of Visual Optics: Fundamentals and Eye Optics, Volume I* edited by P. Artal, 337–47. London: CRC Press.
- Thibos, L. N., M. Ye, X. Zhang, and A. Bradley. 1992. "The chromatic eye: a new reduced-eye model of ocular chromatic aberration in humans." *Appl Opt* 31 (19):3594–600. doi: 10.1364/AO.31.003594.
- Thibos, L. N., M. Ye, X. Zhang, and A. Bradley. 1997. "Spherical aberration of the reduced schematic eye with elliptical refracting surface." *Optom Vis Sci* 74 (7):548–56. doi: 10.1097/00006324-199707000-00024.



Taylor & Francis
Taylor & Francis Group
<http://taylorandfrancis.com>

17 Chromatic Aberrations

17.1 INTRODUCTION

Like other optical systems, the eye suffers from chromatic aberration as well as from monochromatic aberrations. There are two types of chromatic aberration, *longitudinal* and *transverse*, both of which are manifestations of the dispersion (variation of refractive index with wavelength) of the refracting media of an optical system.

The next two sections of this chapter describe longitudinal and transverse chromatic aberration, respectively, and the following two sections discuss their measurement. The effects of these aberrations on visual performance are then discussed, followed by a section on compensation for these effects. Finally, the inclusion of chromatic aberrations in eye modeling is discussed, and this should be considered in conjunction with Chapter 16 on modeling the monochromatic aberrations.

17.2 LONGITUDINAL CHROMATIC ABERRATION

Longitudinal chromatic aberration can be explained as follows. Figure 17.1a shows a beam of light from an axial point **O** entering the eye. Because the refractive indices inside the eye vary with wavelength, the path followed by a ray inside the eye depends upon wavelength. As a rule, refractive indices decrease with increase in wavelength, so the eye has lower power as wavelength increases. Regarding the eye as focused on the point **O** for a yellow wavelength, rays of longer wavelength (e.g., red) are focused behind the retina and shorter wavelength rays (e.g., blue) are focused in front of the retina.

The longitudinal chromatic aberration of the eye can be quantified as the variation in power with wavelength. Thibos, Bradley, and Zhang (1991) referred to this as *chromatic difference of power*. The aberration can also be quantified as the vergences of the source for which the source is focused at the retina for a range of wavelengths (Figure 17.1b). Thibos et al. referred to this as *chromatic difference of refraction*. As for other aberrations of the eye, such as spherical aberration and astigmatism, the second method is how longitudinal chromatic aberration is measured experimentally (see section 17.4).

A formal definition of chromatic difference of refraction is:

For any level of ametropia and accommodation, chromatic difference of refraction is the difference between the vergences of the retinal conjugates for a wavelength λ and a reference wavelength $\bar{\lambda}$.

Figure 17.1b shows a general schematic eye and the retinal conjugates for wavelengths λ and $\bar{\lambda}$. These conjugates are at distances $l(\lambda)$ and $(\bar{\lambda})$ from the eye. Replacing these

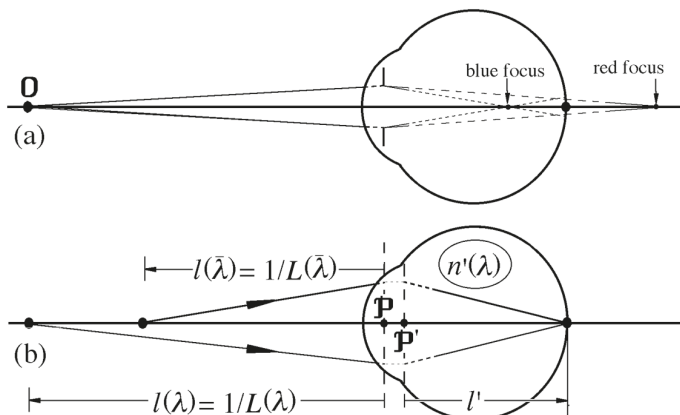


FIGURE 17.1 Longitudinal chromatic aberration. (a) General effect of longitudinal chromatic aberration. (b) Measuring longitudinal chromatic aberration as a chromatic difference of refraction.

distances by their corresponding vergences $L(\lambda)$ and $L(\bar{\lambda})$, the chromatic difference of refraction $R_E(\lambda)$ is

$$R_E(\lambda) = L(\lambda) - L(\bar{\lambda}) \quad (17.1)$$

In measurements of chromatic difference of refraction, rather than comparing the results at a wavelength with those of the reference wavelength, it is common to compare measurements between a short and a long wavelength. When doing so, we shall refer to the range of chromatic difference of refraction. It is important to be careful when comparing the ranges obtained in different studies, as these may have used different wavelength ranges.

Longitudinal chromatic aberration has been explained by considering an axial object point, but it should be realized that it is still present as the object moves off-axis.

17.3 TRANSVERSE CHROMATIC ABERRATION

Transverse chromatic aberration is demonstrated in Figure 17.2a for the case of an eye that is a centered optical system (including pupils), and for an off-axis object point at **Q**. Because of longitudinal chromatic aberration, the different wavelength images of the point are defocused by different amounts relative to the retina. Also, because the power of the eye is less for long wavelengths than for short wavelengths, longer wavelength rays are deviated less than shorter wavelength rays and meet the retina further from the optical axis.

Transverse chromatic aberration is also demonstrated in Figure 17.2b for the case of an eye that is a centered optical system, except that the pupil is decentered. The object point is on the optical axis. The small pupil in this figure has been decentered so that its position coincides with the top of the pupil in Figure 17.1a. The intersection points of the corresponding rays in the two figures at the retina are the same.

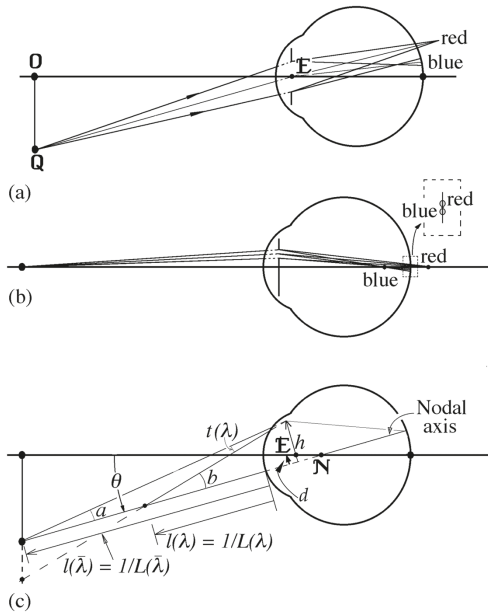


FIGURE 17.2 Transverse chromatic aberration (greatly exaggerated). (a) Centered pupil and an off-axis object point. (b) Decentered pupil and an on-axis object. (c) Measuring transverse chromatic aberration in object space.

As happens for longitudinal chromatic aberration, transverse chromatic aberration must be measured outside the eye. This is shown in Figure 17.2c. Two rays, one of wavelength λ and the other of the reference wavelength $\bar{\lambda}$, originate from different positions in object space but pass through the same point in the pupil and intersect at the retina. The transverse chromatic aberration associated with a height h of the rays relative to the nodal ray is given by

$$t(\lambda) = b - a$$

where a and b are the angles subtended by the two rays with the nodal ray in object space. If angles a and b are small, then

$$a \approx hL(\bar{\lambda}) \quad \text{and} \quad b \approx hL(\lambda)$$

and we have

$$t(\lambda) \approx h[L(\lambda) - L(\bar{\lambda})]$$

Using equation (17.1), it can easily be seen that

$$t(\lambda) \approx hR_E(\lambda) \tag{17.2}$$

which establishes a linear relationship between the transverse chromatic aberration as given by $t(\lambda)$ and longitudinal chromatic aberration as given by $R_E(\lambda)$. In addition,

transverse chromatic aberration increases linearly with ray height in the pupil away from the nodal ray.

Thibos et al. (1991) referred to the angular measure of transverse chromatic aberration $t(\lambda)$ as a *chromatic difference of position (CDP)*.

The transverse chromatic aberration that is of most interest is that associated with foveal vision. In this case, the nodal ray becomes the visual axis, and the pupil location of interest is that representative of the light beam; that is, the center of the pupil. An approximate formula for *CDP* associated with foveal vision (Thibos, Bradley, and Zhang 1991) is

$$\text{CDP} = dR_{\text{E}}(\lambda) \quad (17.2a)$$

where d is the displacement of the pupil center from the visual axis (Figure 17.2c). This is also referred to as *optical transverse chromatic aberration*, as compared with *perceived transverse chromatic aberration* which is a measure of transverse chromatic aberration taking the whole pupil into account. A method for measuring transverse chromatic aberration associated with foveal vision is described in section 17.5.

Transverse chromatic aberration in the eye can be demonstrated by viewing a black–white edge through a small artificial pupil that is decentered at right angles to the edge; a colored fringe is seen. Another way to observe it is to look at a black cross on a pattern consisting of a central red area surrounded by a blue region, as in Figure 17.3a. If a small artificial pupil is decentered vertically, the horizontal black line appears deviated as it crosses the boundary between red and blue (Figure 17.3b). A similar effect occurs for the vertical black line when the artificial pupil is decentered horizontally.

17.3.1 CHROMATIC MAGNIFICATION

As well as an angle, transverse chromatic aberration can be measured as a wavelength-dependent variation in image size of extended objects. Thibos et al. (1991) referred to this as the *chromatic difference of magnification (CDM)*. In practice, this must be measured in object space.

The chromatic difference of magnification is the transverse chromatic aberration in angular terms $t(\lambda)$, divided by the angular size of the object, that is

$$\text{CDM} = t(\lambda)/\theta \quad (17.3)$$

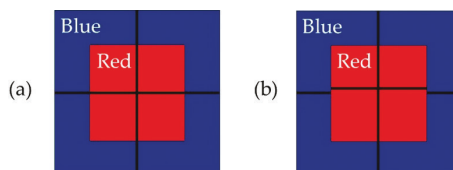


FIGURE 17.3 Demonstration of transverse chromatic aberration. (a) A black cross is placed on a central red area and a blue surround. (b) Appearance of the target when a small pupil is decentered downwards in front of an observer's eye.

where θ is the angular size of the object subtended at the eye's nodal point. For example, if an object has 10° angular size and the angular transverse chromatic aberration for the edge of the object is 0.1° (0.0017 rad), the chromatic difference of magnification is 1 per cent.

The chromatic difference of magnification can be related directly to the chromatic difference of refraction. In Figure 17.2c

$$\theta \approx d/\mathbf{EN} \quad (17.4)$$

where \mathbf{EN} is the distance between the entrance pupil at \mathbf{E} and the front nodal point at \mathbf{N} , and d is the displacement of the pupil center from the visual axis. We can substitute the right-hand side of equation (17.4), together with $hR_{\mathbf{E}}(\lambda)$ for $t(\lambda)$ from equation (17.2), into equation (17.3) to give

$$CDM = R_{\mathbf{E}}(\lambda)\mathbf{EN} \quad (17.5)$$

Based on a range of chromatic difference of refraction of 2.1 D across the visible spectrum (see section 17.4) and a distance \mathbf{EN} of 0.004 m (Gullstrand number 1 eye), the range of CDM across the visible spectrum is less than 0.01 (1 per cent). This may rise considerably if artificial pupils are used in visual experiments. Zhang et al. (1993) described a method for measuring CDM .

17.4 MEASUREMENT OF LONGITUDINAL CHROMATIC ABERRATION

17.4.1 SOME TECHNIQUES

17.4.1.1 Best Focus Method

A target with fine detail, back-illuminated by light of various wavelengths, is moved forwards and backwards in front of an observer until it is judged to be in best focus (Figure 17.4a). This can be done using an achromatic Badal lens, e.g., Howarth and Bradley (1986), which means that the image always subtends the same angle at the eye and that the chromatic difference of refraction is linearly related to the position of the target (section 8.2.1). A clinically related variant of this method is to use trial lenses of different powers in the spectacle plane rather than altering target position (the small chromatic aberration of the lenses should be taken into account).

17.4.1.2 Vernier Method

Two narrow test targets of different wavelengths are imaged on the fovea, but light from them is restricted to pass only through a small aperture in front of the eye (Figure 17.4b). The small aperture can be displaced across the pupil perpendicularly to the length of the target. There is one position in the pupil for which the targets are both aligned and appear aligned – this locates the “foveal achromatic axis”, which is usually taken to be the visual axis (section 4.2.3). One of the targets can then be displaced perpendicularly to its length. For chosen aperture positions relative to the visual axis, this is done so that the targets appear again to be aligned. If the aperture

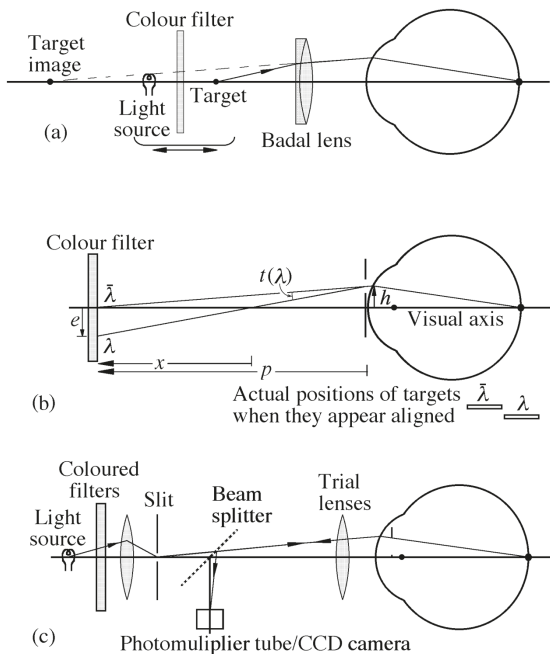


FIGURE 17.4 Some techniques for measuring chromatic difference of refraction. (a) Best focus. (b) Vernier alignment. (c) Double-pass technique to minimize line spread function.

displacement is h , the target displacement is e , the target distance from the eye is p , and the target distance from where the test wavelength ray intersects the axis is x , from similar triangles

$$\frac{e}{h} = \frac{x}{x - p} \quad (17.6)$$

We can replace p by its vergence P where

$$P = 1/p \quad (17.7)$$

The chromatic difference of refraction $R_E(\lambda)$ is given by

$$R_E(\lambda) = 1/(p - x) - 1/p = x/[(p - x)p] \quad (17.8)$$

Using the previous two equations (17.7) and (17.8)

$$-R_E(\lambda)/P = x/(x - p) \quad (17.9)$$

The left-hand side of this equation (17.9) can be substituted for the right-hand side of equation (17.6) to obtain

$$-e/h = R_E(\lambda)/P \quad (17.10)$$

A plot of e as a function of h is only linear in its central region because of the influence of monochromatic aberrations. $R_E(\lambda)$ can be obtained from the slope of this linear section (Thibos et al. 1990). This seems a complicated way to measure the longitudinal chromatic aberration of the eye, but has the advantage that it can be used to determine the transverse chromatic aberration at the same time (section 17.5).

17.4.1.3 Double-Pass Techniques

The image of a narrow illuminated slit (Charman and Jennings 1976) or a spot (López-Gil and Artal 1997; Rynders et al. 1998; Vinas et al. 2015) is formed on the fundus, which reflects a portion of the radiation (Figure 17.4c). An aerial image forms outside the eye (external line spread function or point spread function). Correcting trial lenses or another focusing method can be used to minimize the size of this image for different wavelengths. Charman and Jennings found good agreement with their subjective measurements.

17.4.1.4 Chromo-Retinoscopy

Bobier and Sivak (1978, 1980) used retinoscopy and narrow wave-band filters placed in front of the tested eye to measure the chromatic difference in a number of subjects.

17.4.1.5 Aberrometry

Laser raytracing and Hartmann–Shack techniques (see section 8.4) have been used with lasers of different wavelengths to determine refraction (Llorente et al. 2003; Fernández et al. 2005; Fernández and Artal 2008; Vinas et al. 2015). Care must be taken with such techniques to account for any chromatic aberration of the optical system.

17.4.2 MAGNITUDE

Figure 17.5a shows experimental subjective results of chromatic difference of refraction from some studies (Wald and Griffin 1947; Bedford and Wyszecki 1957; Thibos et al. 1992). These results are for a low level of accommodation stimulus, or under cycloplegia. The data have been adjusted for a common reference wavelength of 589 nm. The figure shows results also for a reduced eye filled with water (Thibos et al. 1992) and a Cauchy equation fit to results of the studies.

For subjective studies, there is a 2.1 D chromatic difference of refraction between 400 and 700 nm, with little variation between most studies despite the different techniques used. The inter-subject differences in the studies were also small. This small variation contrasts with the large variation in monochromatic aberrations (see section 15.6).

The small variation in chromatic aberration is because the main constituent of the ocular media is water, whose dispersion cannot vary between subjects. Nevertheless, eyes modeled on water have insufficient dispersion to fit experimental results well (Figure 17.5a).

Additional data are shown in Figure 17.5b for the near infrared. While it has been suggested that most of the radiation contributing to objective refraction could be due

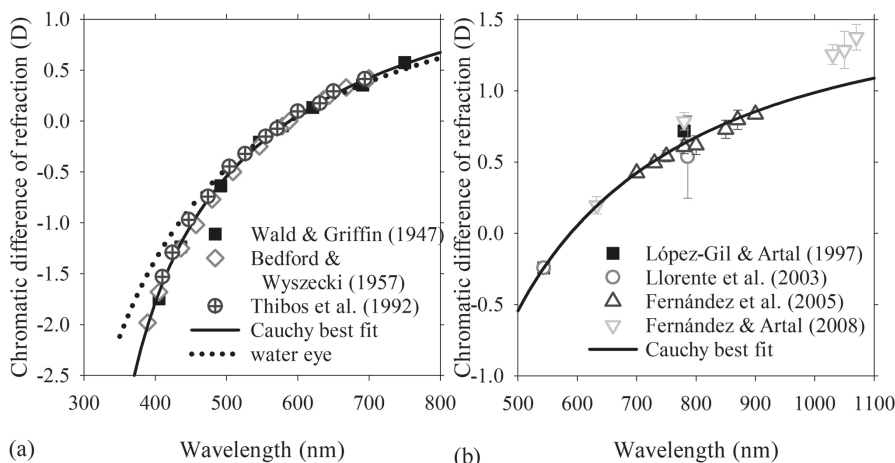


FIGURE 17.5 Chromatic difference of refraction from experimental studies and best-fitting Cauchy equation (Atchison and Smith 2005) to the three studies in the visible: $n(\lambda) = 1.60911 - 6.70941 \times 10^5/\lambda^2 + 5.55334 \times 10^{10}/\lambda^4 - 5.59998 \times 10^{15}/\lambda^6$ (wavelength λ in nm). (a) Subjective studies for visible wavelengths, including data of Wald and Griffin (1947), Bedford and Wyszecki (1957) and Thibos et al. (1992); all data were set to be zero at 589 nm. This includes results for a reduced eye filled with water (Thibos et al. 1992); (b) Objective studies involving infrared wavelengths. Data were moved so that they coincided with the Cauchy equation at the lowest wavelength (543 nm for López-Gil and Artal (1997) and Llorente et al. (2003), 633 nm for Fernández and Artal (2008) and 700 nm for Fernández et al. (2005)). Where shown, error bars indicate standard deviations.

to that captured and guided back from photoreceptors, other radiation that contributes to the objective refraction will penetrate further into the retina and choroid before it is reflected. This tends to reduce the chromatic difference of refraction. Even if chromatic dispersion equations are accurate into the infrared, this should be considered for the purpose of estimating refractions for visible light based on objective infrared measurements.

Two studies found small increases in chromatic difference of refraction with increase in visual field angle out to 30° – 40° (Rynders et al. 1998; Jaeken et al. 2011).

17.4.3 WAVELENGTH IN FOCUS

An issue related to longitudinal chromatic aberration is the wavelength at which a white target is in focus at various levels of accommodation. The accommodation response is usually in excess (“lead”) for low stimulus levels, while the response is insufficient (“lag”) for higher levels of accommodation, e.g., Charman and Tucker (1978). Corresponding to this, a long wavelength is usually in focus for low accommodation stimuli and short wavelengths are in focus for higher accommodation stimuli.

17.4.4 EFFECT OF ACCOMMODATION AND REFRACTIVE ERROR

For optical systems of the same chromatic dispersion, longitudinal chromatic aberration is related linearly to power. Modeling predicts ≈ 2.5 per cent increase in longitudinal chromatic aberration of eyes for each 1 D of accommodation or for each 1 D of refractive error when this is caused by an increase in ocular power (see section 17.8.2).

Jenkins (1963) claimed an early study by Nutting (1914) showed an increase in chromatic aberration with accommodation, but Nutting provided insufficient detail to support this claim. Some studies investigating this relationship were flawed in that wavelength-dependent accommodation may have affected measurements (Jenkins 1963; Millodot and Sivak 1973; Sivak and Millodot 1974). Charman and Tucker (1978) found an increase in chromatic aberration of ≈ 0.2 D for a 4 D increase in accommodation for one subject (≈ 3 per cent per diopter accommodation) between 442 and 633 nm. Wildsoet et al. (1993) measured chromatic difference of refraction in right eyes of 34 young subjects consisting of 12 myopes (-3.4 ± 2.6 D), 10 emmetropes (-0.0 ± 0.2 D), and 10 hyperopes ($+2.3 \pm 1.4$ D), but did not find significant differences between groups.

17.5 MEASUREMENT OF TRANSVERSE CHROMATIC ABERRATION

Compared with longitudinal chromatic aberration, there have been relatively few studies of transverse chromatic aberration associated with foveal vision (Kishto 1966; Ogboso and Bedell 1987; Simonet and Campbell 1990; Thibos et al. 1990; Rynders et al. 1995; Marcos et al. 1999).

17.5.1 TECHNIQUE

The vernier method used by Thibos et al. (1990) can be used as described above (Figures 17.3c and 17.4b). The line of sight may be located by some suitable method, such as determining the edges of the pupil by scanning across the pupil with the aperture until the target disappears and obtaining the mid-point of these limits. This position is compared with the visual axis, and then the distance h in the figures becomes d . The angular transverse chromatic aberration $t(\lambda)$ associated with the line of sight is

$$t(\lambda) = -eP \quad (17.11)$$

Combining equation (17.11) with equation (17.10), but using d instead of h in the latter equation, gives

$$t(\lambda) \approx dR_E(\lambda) \text{ radians} \quad (17.12)$$

which is the same as equation (17.2a).

More sophisticated variations of the vernier method have been used by Simonet and Campbell (1990). Other studies have applied vernier alignment to the whole pupil rather than isolating the line of sight (Hartridge 1947; Ogboso and Bedell 1987; Rynders et al. 1995). Such measurements may be influenced by the Stiles–Crawford effect if its peak is decentered from the line of sight (Rynders et al. 1995).

Marcos et al. (1999) used a *spatially resolved refractometer*, in which light from a source passes through a central pupil position and light from a different source passes through another pupil position. The latter source position is varied to give apparent alignment of the sources. This is done for a range of pupil positions to build up a two-dimensional map of transverse aberrations across the pupil – this is the subjective equivalent to the Hartmann–Shack technique (section 8.4). Maps can be compared for different wavelengths to determine chromatic difference of position by comparing the angular positions for the central pupil location (optical TCA) or determining the pupil position at which chromatic deviation is least.

Winter et al. (2016) used an objective, double-pass measure of transverse chromatic aberration. Spatial structure was recorded in high resolution images using different wavelengths with an adaptive optics scanning laser ophthalmoscope. The first pass into the eye gave a deviation of the two images, but there was no deviation for the second pass out of the eye.

17.5.2 MAGNITUDE

Table 17.1 shows results of experimental studies of foveal transverse chromatic aberration. Although the wavelength range of measurement must be considered, it is reasonable to say that the mean results are less than half the 1.4 min. arc predicted for schematic eyes (486–656 nm) with centered pupils and the fovea 5° to the optical axis. The probable reasons for this discrepancy are that 5° may be larger than that occurring in many people, and that the pupil is usually decentered nasally,

TABLE 17.1
Studies of Transverse Chromatic Aberration Associated with the Fovea

Authors	Mean and Range (min. arc)	No. Participants	Wavelength Range (nm)
Hartridge (1947)	+0.6 ^a	1	486–656
Kishto (1965)	+0.3	1	not given
Ogboso and Bedell (1987)	+0.9, +0.6 to +1.2	3	435–572
Thibos et al. (1990)	+0.61, –0.36 to +1.67		486–656
Simonet and Campbell (1990)	+0.43, –0.20 to +1.28	5	486–656
Rynders et al. (1995)	0.8, up to 2.7	85	497–605
Gullstrand number 1 eye (relaxed)	+1.4 ^b		486–656

Note: When signs are given, a positive sign indicates that the line of sight is nasal to the optical axis in object space. ^a Hartridge gave his results in “cone units” (1 cone unit ≈ 0.69 min. arc). He obtained a vertical component also of 0.8 min. arc. ^b Using angle α of 5°.

and its center is therefore closer to the visual axis. The main concern with transverse chromatic aberration is for severely decentered natural or artificial pupils. The effect of transverse chromatic aberration on visual performance is discussed in section 17.6.

Ogboso and Bedel (1987) made measurements of transverse chromatic aberration in the horizontal peripheral visual field. The results were very different among their four subjects. Out to 40° object eccentricity, all values were less than 7 min. arc and considerably less than the 11 min. arc predicted from their model eye calculations at 40° eccentricity (wavelength range 435–572 nm). Winter et al. (2016) made measurements out to 15° eccentricity in four directions. The mean rate of change was 0.21 min. arc per degree (543–842 nm), which through modeling the authors equated to 0.41 min. arc per degree (430–770 nm).

17.6 EFFECTS OF CHROMATIC ABERRATIONS ON VISION

17.6.1 ACCOMMODATION

Fincham (1951) introduced step changes in accommodative stimulus to his subjects. Most of them made appropriate accommodation responses in white light, but 60 per cent of them were unable to do so in monochromatic light. There is now considerable evidence that the longitudinal chromatic aberration provides a directional cue to guide accommodation. Accommodation responses to steady and moving targets are more accurate in white or broad wavelength light than in monochromatic light, and doubling the eye's normal chromatic aberration has little effect on accommodative accuracy, whereas correcting or reversing the chromatic aberration leads to poor accommodative response (Aggarwala, Nowbotsing and Kruger 1995; Kruger and Pola 1986, 1987; Kruger et al. 1993; Stone et al. 1993; Kruger et al. 1995; Aggarwala, Kruger, et al. 1995; Kruger et al. 1997).

17.6.2 SPATIAL VISION

The effects of chromatic aberration are attenuated by the spectral sensitivity of the eye. For centered pupils, switching from white light to monochromatic light gives a maximum improvement to the contrast sensitivity function of about 0.2 log units (Campbell and Gubisch 1967; Yoon and Williams 2002) and a small effect on visual acuity that has been measured as zero to 0.1 log units (Harridge 1947; Campbell and Gubisch 1967; Yoon and Williams 2002; Schwarz et al. 2014). The use of achromatizing lenses in white light makes negligible improvement to visual acuity and contrast sensitivity in white light (Campbell and Gubisch 1967) because some of these lenses have transverse chromatic aberration when centered, and that additional transverse chromatic aberration is introduced for any of these lenses if they are not carefully centered (Zhang et al. 1991).

Decentering natural or artificial pupils can have devastating effects on foveal spatial vision in white light because large amounts of transverse chromatic aberration are induced. Experimental studies showing up to two-thirds reduction in resolution for ≈ 3 mm displacement of artificial pupils (Green 1967) or Maxwellian-view

instruments (Bradley et al. 1990; Thibos, Bradley, and Still 1991) were supported theoretically (Thibos, Bradley, and Zhang 1991).

Some Maxwellian-view projection systems have been used clinically to evaluate potential visual acuity in patients with cataract by positioning them so that the light passes through a relatively clear part of the cataractous lens. The experimental and theoretical results just mentioned indicate that those instruments using white light are likely to underestimate potential visual acuity if the light beam enters the pupil well away from its center.

Winter et al. (2015) used prisms to induce transverse chromatic aberration, with monochromatic aberrations corrected, for the central vision and 20° nasal visual field. Reduction in detection grating acuity was approximately twice that in the periphery as for central vision, with respective mean effects of 0.057 and 0.032 logMAR per arc min of transverse chromatic aberration.

Effects of chromatic aberration on retinal image quality are discussed further in section 18.4.1.2.

17.6.3 CHROMOSTEREOPSIS

In section 6.4.1 we described stereopsis, in which the two eyes provide the potential for seeing depth in a scene. *Chromostereopsis* is a related binocular phenomenon in which objects at the same distance, but of different colors, are seen in depth. Typically reddish objects appear to be closer than bluish objects, but this order can be reversed according to choice of background colors (Winn et al. 1995). Chromostereopsis is a consequence of transverse chromatic aberration combined with binocular vision.

Figure 17.6a shows the pupil ray paths from red and blue targets at position **O**. The pupil of the eye is decentered temporally relative to the visual axis. The red pupil ray is refracted less than the blue pupil ray, and therefore the red pupil ray intersects the retina to the temporal side of the blue pupil ray. This retinal disparity is equivalent to the red and blue rays coming from different distances, as shown by the dashed lines in the figure. The retinal disparity leads to an apparent longitudinal displacement when the target is viewed binocularly. The red target appears to be closer than the blue target.

The magnitude of chromostereopsis is predicted by the geometry in Figure 17.6b (Ye et al. 1991). Here Δd is the amount of chromostereopsis as a distance measurement, $2B$ is the distance between the position of small pupils in front of the two eyes, d is the viewing distance, and $t(\lambda)_R$ and $t(\lambda)_L$ are the right eye and left eye transverse chromatic aberrations. The relationship between these quantities is

$$t(\lambda)_R - t(\lambda)_L = \frac{2B\Delta d}{d^2 + d\Delta d} \quad (17.13)$$

By making measurements of transverse chromatic aberration induced by displacement of pinholes from the visual axes (section 17.3) and comparing these with measurements of chromostereopsis at these displacements, Ye et al. provided experimental support for this equation and for the theory that chromostereopsis with

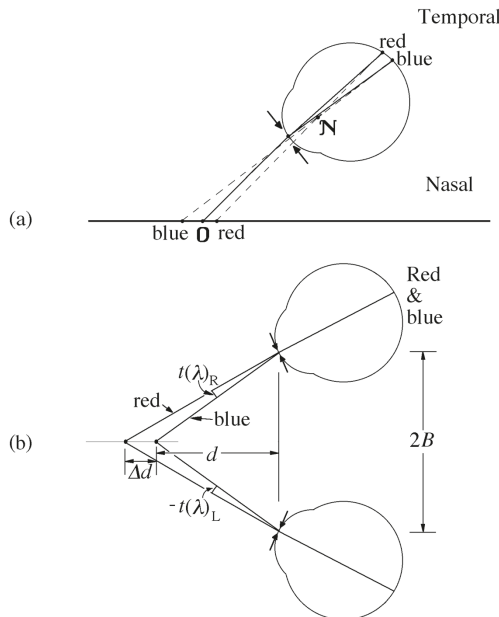


FIGURE 17.6 Chromostereopsis. (a) An explanation of the source of chromostereopsis. (b) The expected relationship estimating chromostereopsis and transverse chromatic aberration induced with small artificial pupils.

small pupils can be explained by the interocular difference in monocular transverse aberration.

Chromostereopsis often diminishes as pupil size increases and may even reverse in direction. For natural pupils, this may be attributed at least partly to change in pupil center as pupil size changes (section 3.3). Ye et al. (1992) attributed the decrease in chromostereopsis, with increase in pupil size, to the Stiles–Crawford effect (see section 14.5) acting as an anchor to shift the effective center of pupils closer to the visual axis, but it may be that the Stiles–Crawford effect is unimportant and transverse chromatic aberration effects reduce as pupil size increases by some other manner (Atchison and Scott 2002).

17.6.4 ABERRATIONS OF OPHTHALMIC DEVICES

Longitudinal chromatic aberration of most correcting ophthalmic devices is not important. In the cases of spectacle lenses and contact lenses, this is because of the low power of the devices relative to that of the eye. In the case of intraocular lenses, this is because the device is merely replacing the lens of the eye, although high dispersion materials will increase the aberration to some extent (Pérez-Merino et al. 2013; Siedlecki et al. 2014). Transverse chromatic aberration is not important in contact lenses or intraocular lenses, because these move with the eye. However, as occurs with sagittal and tangential power errors, it blurs foveal vision when an eye looks

through peripheral parts of a spectacle lens. This is important with high lens powers, particularly when high index materials with low V -values are used.

Longitudinal chromatic aberration becomes important when diffractive optics is used in bifocal, trifocal, and extended depth-of-focus corrections. Atchison et al. (1992) and Atchison and Thibos (1993) described the effect in two bifocal contact lens types produced in the 1990s, in which the addition was produced by the first diffraction order. For a nominal 2.00 D addition, the effective addition varied from approximately +1.0 D at 420 nm to +2.50 D at 694 nm, which means that the chromatic difference of refraction reduced by about 1.5 D across the wavelength range. Diffractive optics is no longer used in contact lenses, but it is used for intraocular lenses for which care must be taken so that the image quality in broadband light is not unduly influenced by wavelength at a range of viewing distances.

17.7 ABERRATION COMPENSATION AND CORRECTION

17.7.1 NATURAL COMPENSATION MECHANISM

The effects of chromatic aberration are attenuated by the non-uniform spectral sensitivity of the eye, which is described by the photopic and scotopic relative luminous efficiency functions (section 11.3). Thibos et al. (1991) estimated that, when the wavelength with peak sensitivity is in focus, most of the luminance in a white light target is less than 0.25 D out of focus. The yellow macular pigment absorbs maximally at 460 nm and then up to about 520 nm (section 14.3). The lack of macular pigment beyond about 4° eccentricity can be expected to remove some of the attenuation.

17.7.2 ACHROMATIZING CORRECTING LENSES

The longitudinal chromatic aberration of the eye can be corrected by a nominally zero power lens, with longitudinal chromatic aberration equal and opposite to that of the eye. Such lenses have been described by several authors (van Heel 1946; Thomson and Wright 1947; Bedford and Wyszecki 1957; Fry 1972; Powell 1981; Lewis et al. 1982). These lenses are designed to cover the visible range of wavelengths. The Powell design is given in Table 17.2 and Figure 17.7. It is a modification of the triplet design described by Bedford and Wyszecki, but incorporates a doublet at the front. This reduces the residual longitudinal chromatic aberration and the transverse chromatic aberration present in the Bedford and Wyszecki lens. In the Powell lens, the doublet

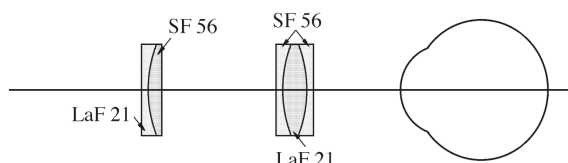


FIGURE 17.7 Achromatizing lens of Powell (1981).

TABLE 17.2
Achromatizing Lens of Powell (1981)

Glass	<i>n</i>	<i>V</i>	<i>d</i>	<i>r</i>	Surface Number
Air	1			0.0	1
LaF21	1.788310	47.39	1.0	15.5	2
SF56	1.784700	26.08	3.0	0.0	3
Air	1.0	—	14.5	0.0	4
SF56	1.784700	26.08	1.0	15.5	5
LaF21	1.788310	47.39	5.0	-15.5	6
SF56	1.784700	26.08	1.0	0.0	7
Air	1.0		17.0	0.0	8 pupil
Air	1.0		—		

Note: The aperture diameter of both components is 15 mm. Units: millimeters.

is designed to have the same longitudinal chromatic aberration as that of the eye, and the triplet is designed to have twice the opposite longitudinal chromatic aberration as that of the eye; these components can be used to investigate effects of doubling and reversing the longitudinal chromatic aberration of the eye (Gupta et al. 2010).

These lenses may be assessed by the level of residual power at the reference wavelength, and by the residual chromatic aberration when used with the eye. The Bedford and Wyszecki, Fry, Powell, and Lewis et al. designs have less than 0.25 D residual equivalent power at 587.6 nm. The residual chromatic aberration of one lens–eye system is shown in Figure 17.8. The lenses introduce transverse chromatic aberration, with that of the sophisticated Powell lens being much less than those of the other lenses. For a 5° field-of-view and between wavelengths from 486 to 656 nm, design values are 2.88 min. arc (Powell), 5.23 min. arc (Bedford and Wyszecki), 7.33 min. arc (Fry) and 9.34 min. arc (Lewis et al.). Alignment of such lenses is critical, as otherwise an additional transverse chromatic aberration is induced, which is proportional to the decentration. Zhang et al. (1991) determined that 0.4 mm of misalignment of an achromatizing lens relative to the eye would cancel any benefit the lens would give to spatial vision.

Optical coherence tomography uses broad bandwidth sources to increase axial resolution, but the full benefit can be realized only if ocular chromatic aberrations are corrected. Achromatizing lenses have been made for the approximately 700–900 nm range used in OCT (Fernández et al. 2006; Zawadzki et al. 2008).

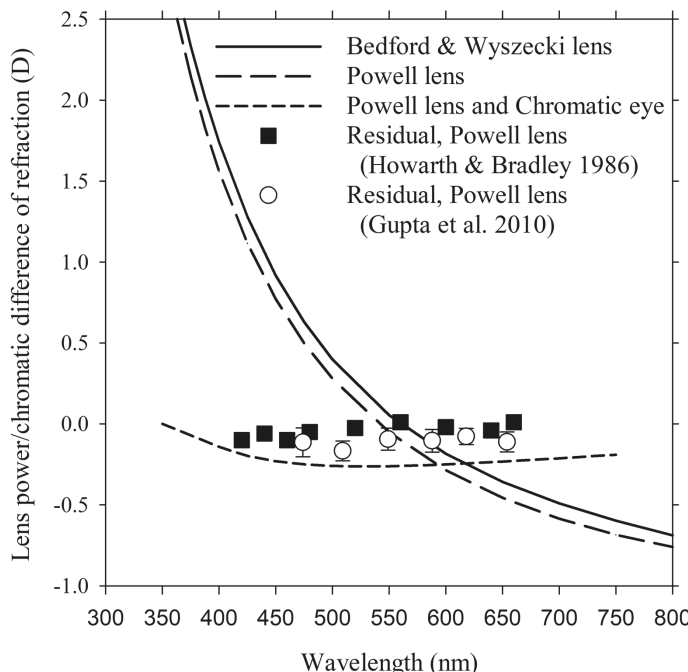


FIGURE 17.8 The power of the Bedford and Wyszecki (1957) and of the Powell (1981) achromatizing lenses, together with residual chromatic difference of focus for the Powell lens. The latter was obtained by combining the Powell lens with the Chromatic eye of Thibos and from mean experimental results (Howarth and Bradley, 1986; Gupta et al. 2010). The theoretical and experimental residuals differ by 0.1–0.3 D at any wavelength, but none vary by more than 0.1 D between 400 nm and 700 nm.

17.7.3 OTHER COMPENSATION METHODS

Other than the simple expedient of using monochromatic illumination, there are other ways to compensate for the chromatic aberration of the eye: sources of different wavelengths at different distances to be combined by beam splitters, partially transmitting mirrors as part of a trombone system so that the optical pathlength of different wavelengths through it is different (Jiang et al. 2019), and the use of spatial light modulators (Martinez et al. 2017; Suchkov et al. 2019).

17.8 MODELING CHROMATIC ABERRATIONS

17.8.1 CHROMATIC DISPERSION

To model the chromatic aberrations of the eye, a knowledge of its dispersive properties is necessary. The most common equations used to describe variation of refractive index $n(\lambda)$ with wavelength are as follows:

1. Cauchy's equation:

$$n(\lambda) = a_1 + a_2/\lambda^2 + a_3/\lambda^4 + a_4/\lambda^6 + \dots \quad (17.14a)$$

2. The Hartmann equation:

$$n(\lambda) = n_0 + A/(\lambda - \lambda_0)^{1.2} \quad (17.14b)$$

3. The Cornu dispersion equation, which is like the Hartman equation:

$$n(\lambda) = n_\infty + K/(\lambda - \lambda_0) \quad (17.14c)$$

4. The Herzberger equation:

$$n(\lambda) = A + B\lambda^2 + \frac{C}{\lambda^2 - \lambda_0^2} + \frac{D}{(\lambda^2 - \lambda_0^2)^2} + \dots \quad (17.14d)$$

In practice, this is determined as

$$n(\lambda) = a_i(\lambda)n_i + a_2(\lambda)n_F + a_3(\lambda)n_C + a_4(\lambda)n_t \quad (17.14e)$$

where $a_i(\lambda)$ through $a_4(\lambda)$ are found from equations of the form

$$a_i(\lambda) = A_0 + A_1\lambda^2 + \frac{P}{\lambda^2 - \lambda_0^2} + \frac{R}{(\lambda^2 - \lambda_0^2)^2} \quad (17.14f)$$

and n_i , n_F , n_C , and n_t are specified refractive indices at wavelengths 365 nm, 486.1 nm, 656.3 nm, and 1014 nm, respectively. A_0 , A_1 , P , and R form a set of constants for each $a_i(\lambda)$, and $\lambda_0 = 167.3$.

5. The Conrady equation:

$$n(\lambda) = n_0 + A/\lambda + B/\lambda^{3.5} \quad (17.14g)$$

6. Sellmeier's equation

$$n^2(\lambda) = 1 + \frac{B_1\lambda^2}{\lambda^2 - C_1} + \frac{B_2\lambda^2}{\lambda^2 - C_2} + \frac{B_3\lambda^2}{\lambda^2 - C_3} \dots \quad (17.14h)$$

7. An un-named equation:

$$n^2(\lambda) = a_1 + a_2\lambda^2 + a_3/\lambda^2 + a_4/\lambda^4 \quad (17.14i)$$

Atchison and Smith (2005) provided information on the origins of these equations. Of these, Sellmeier's has some theoretical basis. Cauchy's equation is an approximate form of Sellmeier's equation and has the advantage of being linear in its coefficients.

The dispersion of any optical material is fully described by such equations, provided they are accurate. For some purposes, the dispersion can be reduced to a single number, such as the Abbe V -value, which is defined as

$$V_d = \frac{n_d - 1}{n_E - n_C} \quad (17.15)$$

where n_d , n_E , and n_C are the refractive indices at the wavelengths 589.3 nm (λ_d), 486.1 nm (λ_E), and 656.3 nm (λ_C), respectively. V -values are useful for comparing the amount of dispersion in different optical media and for calculating the Seidel chromatic aberrations.

Le Grand (1967) quantified the dispersion of the ocular media for his full theoretical eye using the Cornu dispersion equation (17.14c). His reference wavelength was 589 nm, and his values of n_∞ , K , and λ_o for each ocular medium and corresponding V -values are given in Table 17.3.

Navarro et al. (1985) used the Herzberger approach of equations (7.14d–f) for the ocular media, with two errors corrected by Atchison and Smith (2005).

Bennett and Tucker (1975) used the form of equation (17.14i) to give the refractive index of water as

$$n^2(\lambda) = 1.7642 - 1.38 \times 10^{-8}\lambda^2 + 6.12 \times 10^{-3}/\lambda^2 + 1.41 \times 10^{-8}/\lambda^4 \quad (17.16)$$

where the wavelength is in nanometers. Substituting appropriate values obtained from equation (17.16) into equation (17.15) gives $V_d = 55.15$. As shown in Figure 17.5a, the dispersion of water is insufficient to account for the longitudinal chromatic aberration of the eye.

Thibos et al. (1992) used their experimental results and the Cornu dispersion equation (17.15b) to describe the refractive index distribution of their Chromatic version of Emsley's reduced eye as

$$n(\lambda) = 1.320535 + \frac{4.685}{\lambda - 214.102} \quad (17.17)$$

where λ has the unit of nanometers. The corresponding V -value is 50.23.

TABLE 17.3
The Values of the Parameters in Equation (17.14c) for Le Grand's (1967) Dispersion of the Ocular Media

Medium	n_∞	K	λ_o	V
Cornea	1.3610	7.4147	130.0	56.01
Aqueous	1.3221	7.0096	130.0	53.00
Lens	1.3999	9.2492	130.0	50.01
Vitreous	1.3208	6.9806	130.0	53.00

Using fittings derived from Le Grand (1967) and Navarro et al. (1985), Atchison and Smith (2005) used the Cauchy chromatic dispersion equation (17.14a) in conjunction with the Gullstrand number 1 eye. They gave two sets of coefficients for the lens, one set each for the high and low index (1.406 and 1.386, respectively, at reference wavelength 555 nm). Scaling was used to convert the refractive indices for the Gullstrand lens to match the average index 1.3994

$$n(\lambda)_{1.3994} = n(\lambda)_{1.406} \frac{1.3994}{1.406} \quad (17.18)$$

where $n(\lambda)_{1.3994}$ is the refractive index when refractive index at the reference wavelength is 1.3994 and $n(\lambda)_{1.406}$ is the refractive index when refractive index at the reference wavelength is 1.406. Suheimat et al. (2015) applied scaling to convert the refractive indices of the Gullstrand eye to those for the Le Grand eye, with

$$n(\lambda)_L = n(\lambda)_G \frac{n(\bar{\lambda})_L}{n(\bar{\lambda})_G} \quad (17.19)$$

where $n(\lambda)_L$ is the refractive index to be obtained for the Le Grand eye, $n(\lambda)_G$ is the corresponding index for the Gullstrand eye, and $n(\bar{\lambda})_G$ and $n(\bar{\lambda})_L$ are the refractive indices at the reference wavelength of the Gullstrand and Le Grand eyes, respectively.

Suheimat et al. (2015) developed “water-scaling” variants of schematic eyes. Refractive index of water $n(\lambda)_w$ at wavelength λ was obtained as a four-term Sellmeier chromatic dispersion formula

$$n(\lambda)_w = \sqrt{1 + \sum_{i=1}^4 \frac{A_i \lambda^2}{\lambda^2 - 10^6 \lambda_i^2}} \quad (17.20)$$

where A_1-A_4 and $\lambda_1^2-\lambda_4^2$ are constants (Daimon and Masumura 2007). The refractive indices were scaled according to refractive indices of the different media specified in schematic eyes at a reference wavelength $\bar{\lambda}$:

$$n(\lambda) = n(\lambda)_w \frac{n(\bar{\lambda})}{n(\bar{\lambda})_w} \quad (17.21)$$

where $n(\lambda)$ is the scaled refractive index of the media, $n(\bar{\lambda})$ is the refractive index of the media at the reference wavelength and $n(\bar{\lambda})_w$ is the refractive index of water at the reference wavelength. These methods are based on a particular wavelength, usually 555 nm or 589 nm, being chosen to represent the refractive indices of model eyes. Suheimat et al. applied them to the Gullstrand exact and Le Grand full theoretical eyes.

The high dispersion of the eye has been attributed to a high dispersion of the lens. For example, Sivak and Mandelman (1974) measured V -values of the lens as 29 ± 4

for the periphery and 35 ± 6 for the core. These are much less than the values of Le Grand (1967) given in Table 17.3.

17.8.2 SCHEMATIC EYES

17.8.2.1 Gaussian Properties

There are small, wavelength-dependent changes in the principal and nodal points of schematic eyes. For the Gullstrand number 1 eye, over the wavelength range of 400–700 nm, the front principal point moves just less than 0.0007 mm and the back principal point moves by 0.013 mm.

17.8.2.2 Chromatic Difference of Power and Chromatic Difference of Refraction

Figure 17.1b shows a general schematic eye and the retinal conjugates for wavelengths λ and $\bar{\lambda}$. We have

$$n'(\lambda)/l' - L(\lambda) = F(\lambda) \quad \text{and} \quad n'(\bar{\lambda})/l' - L(\bar{\lambda}) = F(\bar{\lambda}) \quad (17.22a, b)$$

For both situations, the distance l' is the distance from the back principal point to the retina and is here assumed to be independent of wavelength. The chromatic difference of refraction $R_E(\lambda)$ is given by equation (17.1), that is

$$R_E(\lambda) = L(\lambda) - L(\bar{\lambda}) \quad (17.1)$$

The chromatic difference of power $\Delta F(\lambda)$, the difference between the equivalent power $F(\lambda)$ at wavelength λ and the equivalent power $F(\bar{\lambda})$ at the reference wavelength $\bar{\lambda}$, is given by

$$\Delta F(\lambda) = F(\lambda) - F(\bar{\lambda}) \quad (17.23)$$

Subtracting equation (17.22b) from (17.22a), and after a small amount of manipulation involving equations (17.1) and (17.23), we have

$$R_E(\lambda) = \frac{n'(\bar{\lambda}) - n'(\lambda)}{l'} - \Delta F(\lambda) \quad (17.24)$$

If we replace the length l' using equation (17.22b), equation (17.24) can be written in the form

$$R_E(\lambda) = \frac{[n'(\lambda) - n'(\bar{\lambda})][L(\bar{\lambda}) + F(\bar{\lambda})]}{n'(\bar{\lambda})} - \Delta F(\lambda) \quad (17.25)$$

For an emmetropic eye focused on infinity, $L(\bar{\lambda}) = 0$ and equation (17.25) reduces to

$$R_E(\lambda) = \frac{[n'(\lambda) - n'(\bar{\lambda})]F(\bar{\lambda})}{n'(\bar{\lambda})} - \Delta F(\lambda) \quad (17.26)$$

This equation shows that there is a difference between the chromatic difference of refraction $R_E(\lambda)$ and the chromatic difference of power $\Delta F(\lambda)$ apart from a change in sign.

Using appropriate chromatic dispersions of the media, paraxial schematic eyes are excellent at estimating the chromatic difference of refraction of real eyes. As an example, Atchison et al. (1993) used the Gullstrand number 1 eye with its refractive indices, but scaled the variations in refractive index so that the chromatic dispersion was the same as for equation (17.17). This gave a range of chromatic difference of refraction of 1.94 D between 400 and 700 nm. This is probably a slight underestimation of chromatic difference of focus in most eyes.

Atchison et al. (1993) determined the effect of refractive error on the range of chromatic difference of refraction for schematic eyes, modified to have axial ametropia and refractive ametropia. The latter was modeled by altering corneal curvature. For the Gullstrand number 1 eye, changes across the 400–700 nm range of wavelengths were 0.012 D (0.56 per cent) per diopter of axial ametropia and 0.047 D (2.4 per cent) per diopter of refractive ametropia. Similar results were obtained for reduced eyes. The accommodated version of the Gullstrand eye gave a range of chromatic difference of refraction 0.55 D greater than the relaxed, emmetropia eye, which corresponds to 0.050 D (2.6 per cent) increase per diopter of accommodation.

17.8.2.3 Chromatic Difference of Refraction of Reduced Schematic Eyes

If the corneal radius of curvature of the reduced eye is r , the equivalent power $F(\lambda)$ as a function of wavelength is simply

$$F(\lambda) = [n'(\lambda) - 1]/r \quad (17.27)$$

where $n'(\lambda)$ is given by equations such as equation (17.17). The radius can be given in terms of the reference power $F(\bar{\lambda})$ as

$$r = [n'(\bar{\lambda}) - 1]/F(\bar{\lambda}) \quad (17.28)$$

The equivalent power of the eye $F(\lambda)$ as a function of wavelength is then

$$F(\lambda) = \frac{[n'(\lambda) - 1]F(\bar{\lambda})}{n'(\bar{\lambda}) - 1} \quad (17.29)$$

and the chromatic difference of power $\Delta F(\lambda)$ is

$$\Delta F(\lambda) = \frac{[n'(\lambda) - n'(\bar{\lambda})]F(\bar{\lambda})}{n'(\bar{\lambda}) - 1} \quad (17.30)$$

Equation (17.30) can be rearranged to give

$$F(\bar{\lambda}) = \frac{[n'(\lambda) - 1]\Delta F(\lambda)}{n'(\lambda) - n'(\bar{\lambda})} \quad (17.31)$$

Substituting the right-hand side of equation (17.31) for $F(\bar{\lambda})$ into equation (17.25) gives

$$R_E(\lambda) = \frac{[n'(\lambda) - n'(\bar{\lambda})]L(\bar{\lambda}) - \Delta F(\lambda)}{n'(\bar{\lambda})} \quad (17.32)$$

For an emmetropic eye focused on infinity, $L(\bar{\lambda}) = 0$ and equation (17.32) reduces to

$$R_E(\lambda) = -\Delta F(\lambda) / n'(\bar{\lambda}) \quad (17.33)$$

Using a value of 1.333 for $n'(\bar{\lambda})$ shows that the chromatic difference of refraction is three-quarters of the chromatic difference of power.

17.8.2.4 Chromatic and Indiana Reduced Eyes of Thibos et al. (1992, 1997)

Some of the details of these reduced eyes are provided in section 16.6.6. The refractive index distribution is given by equation (17.17), and the chromatic difference of refraction is given in diopters by

$$R_E(\lambda) = 1.68524 - \frac{633.46}{\lambda - 214.102} \quad (17.34)$$

where the reference wavelength is 589 nm and the wavelength λ is in nanometers. To obtain good predictions of transverse chromatic aberration of their eyes according to equations (17.2) and (17.5), Thibos et al. placed the stop 1.91 mm inside the eye so that the distance EN of 3.98 mm between the entrance pupil and the nodal point was like that of more sophisticated schematic eyes.

To allow for variations in transverse chromatic aberration, the pupils of the Chromatic eye do not need to be on the optical axis. Thibos et al. (1992) included a number of additional axes: line of sight, visual axis, and achromatic axis (see Chapter 4). The cornea has asphericity Q of -0.56 to correct spherical aberration at the reference wavelength of 589 nm.

The Indiana eye varies from the chromatic eye in that the optical axis, visual axis, and line of sight are now coincident and the cornea has a variable asphericity (Thibos et al. 1997).

17.9 ESTIMATING LENGTHS IN EYES

The chromatic dispersion equations and schematic models selected with them are important for estimating lengths within eyes using partial coherence interferometry instruments. Estimates of refractive index at the infra-red wavelengths of instruments

have to be determined from approaches, such as those described in section 17.8.1 (Cooke et al. 2020). The usual refractive indices, termed “phase” refractive indices n_p , have to be converted to “group” refractive indices n_g , which are applicable to wave packets. For a wavelength λ , the two indices are related by

$$n_g = n_p - \frac{\partial n_p}{\partial \lambda} \cdot \lambda \quad (17.35)$$

Optical path lengths OPL within the eye are converting to geometrical lengths GL using

$$GL = OPL/n_g \quad (17.36)$$

SUMMARY OF MAIN SYMBOLS

$t(\lambda)$	(angular) transverse chromatic aberration
CDM	chromatic difference of magnification
EN	distance between entrance pupil at E and front nodal point at N
λ	wavelength, usually expressed in nanometers
$\bar{\lambda}$	reference wavelength at which the reference power $F(\bar{\lambda})$ of the eye is defined
$F(\lambda)$	equivalent power of a schematic eye as a function of wavelength
$\Delta F(\lambda)$	chromatic difference of power; the difference in equivalent power between the wavelength and that at the reference wavelength $\bar{\lambda}$
$R_E(\lambda)$	chromatic difference of refraction
$t(\lambda)$	transverse chromatic aberration
CDP	chromatic difference of position - same as $t(\lambda)$
CDM	chromatic difference of magnification
h	height of a ray, at the entrance pupil, relative to the nodal ray
d	displacement of the pupil center from the visual axis
θ	angular size of an object subtended at the eye’s front nodal point
V_d	Abbe V -value
n_d, n_F, n_C	refractive indices at 589.3 nm, 486.1 nm, and 656.3 nm, respectively
n_p, n_g	phase and group refractive indices
OPL	optical path length
GL	geometric length

REFERENCES

- Aggarwala, K. R., P. B. Kruger, S. Mathews, and E. S Kruger. 1995. “Spectral bandwidth and accommodative function.” *J Opt Soc Am A* 12 (3):450–5. doi: 10.1364/josaa.12.000450.
- Aggarwala, K. R., S. Nowbotsing, and P. B. Kruger. 1995. “Accommodation to monochromatic and white-light targets.” *Invest Ophthalmol Vis Sci* 36 (13):2695–705.
- Atchison, D. A., and D. H. Scott. 2002. “The Stiles-Crawford effect and subjective measurement of aberrations.” *Vision Res* 42 (9):1089–102. doi: 10.1016/s0042-6989(02)00028-7.

- Atchison, D. A., and G. Smith. 2005. "Chromatic dispersions of the ocular media of human eyes." *J Opt Soc Am A* 22 (1):29–37. doi: 10.1364/josaa.22.000029.
- Atchison, D. A., G. Smith, and M. D. Waterworth. 1993. "Theoretical effect of refractive error and accommodation on longitudinal chromatic aberration of the eye." *Optom Vis Sci* 70 (9):716–22. doi: 10.1097/00006324-199309000-00006.
- Atchison, D. A., and L. N. Thibos. 1993. "Diffractive properties of the Diffralex bifocal contact lens." *Ophthalmic Physiol Opt* 13 (2):186–8. doi: 10.1111/j.1475-1313.1993.tb00451.x.
- Atchison, D. A., M. Ye, A. Bradley, M. J. Collins, et al. 1992. "Chromatic aberration and optical power of a diffractive bifocal contact lens." *Optom Vis Sci* 69 (10):797–804. doi: 10.1097/00006324-199210000-00009.
- Bedford, R. E., and G. Wyszecki. 1957. "Axial chromatic aberration of the human eye." *J Opt Soc Am A* 47 (6):564–5. doi: 10.1364/josa.47.0564_1.
- Bennett, A. G., and J. Tucker. 1975. "Correspondence: chromatic aberration of the eye between 200 and 2000 nm." *Br J Physiol Opt* 30 (2–4):132–5.
- Bobier, C. W., and J. G. Sivak. 1978. "Chromoretinoscopy." *Vision Res* 18 (3):247–50. doi: 10.1016/0042-6989(78)90158-x.
- Bobier, C. W., and J. G. Sivak. 1980. "Chromoretinoscopy and its instrumentation." *Am J Optom Physiol Opt* 57 (2):106–8. doi: 10.1097/00006324-198002000-00005.
- Bradley, A., L. N. Thibos, and D. Still. 1990. "Visual acuity measured with clinical Maxwellian-view system: effects of beam entry location." *Optom Vis Sci* 67 (11):811–7. doi: 10.1097/00006324-199011000-00004.
- Campbell, F. W., and R. W. Gubisch. 1967. "The effect of chromatic aberration on visual acuity." *J Physiol (Lond)* 192 (2):345–58. doi: 10.1113/jphysiol.1967.sp008304.
- Charman, W. N., and J. A. M. Jennings. 1976. "The optical quality of the monochromatic retinal image as a function of focus." *Br J Physiol Opt* 31 (3):119–34.
- Charman, W. N., and J. Tucker. 1978. "Accommodation and color." *J Opt Soc Am* 68 (4):459–71. doi: 10.1364/josa.68.000459.
- Cooke, D. L., T. L. Cooke, M. Suheimat, and D. A. Atchison. 2020. "Standardizing sum-of-segments axial length methods." *Biomed Opt Express* 11 (10):5860–70. doi: 10.1364/BOE.400471.
- Daimon, M., and A. Masumura. 2007. "Measurement of the refractive index of distilled water from the near-infrared region to the ultraviolet region." *Appl Opt* 46 (18):3811–20. doi: 10.1364/ao.46.003811.
- Fernández, E. J., and P. Artal. 2008. "Ocular aberrations up to the infrared range: from 632.8 to 1070 nm." *Opt Express* 16 (26):21199–208. doi: 10.1364/oe.16.021199.
- Fernández, E. J., A. Unterhuber, B. Považay, B. Hermann, et al. 2006. "Chromatic aberration correction of the human eye for retinal imaging in the near infrared." *Opt Express* 14 (13):6213–25. doi: 10.1364/oe.14.006213.
- Fernández, E., A. Unterhuber, P. Prieto, B. Hermann, et al. 2005. "Ocular aberrations as a function of wavelength in the near infrared measured with a femtosecond laser." *Opt Express* 13 (2):400–9. doi: 10.1364/opex.13.000400.
- Fincham, E. F. 1951. "The accommodation reflex and its stimulus." *Br J Ophthalmol* 35 (7):381–93. doi: 10.1136/bjo.35.7.381.
- Fry, G. A. 1972. "Visibility of color contrast borders." *Am J Optom Arch Acad Optom* 49 (5):401–6. doi: 10.1097/00006324-197205000-00002.
- Green, D. G. 1967. "Visual resolution when light enters the eye through different parts of the pupil." *J Physiol (Lond)* 190 (3):583–93. doi: 10.1113/jphysiol.1967.sp008229.
- Gupta, P., H. Guo, A. J. Zele, and D. A. Atchison. 2010. "Effect of optical aberrations on the colour appearance of small defocused lights." *J Opt Soc Am A* 27 (5):960–7. doi: 10.1364/JOSAA.27.000960.

- Hartridge, H. 1947. "The visual perception of fine detail." *Phil Trans R Soc Lond B* 232 (592):519–671. doi: 10.1098/rstb.1947.0004.
- Howarth, P. A., and A. Bradley. 1986. "The longitudinal chromatic aberration of the human eye, and its correction." *Vision Res* 26 (2):361–6. doi: 10.1016/0042-6989(86)90034-9.
- Jaeken, B., L. Lundström, and P. Artal. 2011. "Peripheral aberrations in the human eye for different wavelengths: off-axis chromatic aberration." *J Opt Soc Am A* 28 (9):1871–9. doi: 10.1364/JOSAA.28.001871.
- Jenkins, T. C. A. 1963. "Aberrations of the eye and their effects on vision: Part 2." *Br J Physiol Opt* 20 (3):161–201.
- Jiang, X., J. A. Kuchenberger, P. Touch, and R. Sabesan. 2019. "Measuring and compensating for ocular longitudinal chromatic aberration." *Optica* 6:981–90. doi: 10.1364/optica.6.000981.
- Kishto, B. N. 1966. "The colour stereoscopic effect." *Vision Res* 5 (5):313–29. doi: 10.1016/0042-6989(65)90007-6.
- Kruger, P. B., K. R. Aggarwala, S. Bean, and S. Mathews. 1997. "Accommodation to stationary and moving targets." *Optom Vis Sci* 74 (7):505–10.
- Kruger, P. B., S. Mathews, K. R. Aggarwala, and N. Sanchez. 1993. "Chromatic aberration and ocular focus: Fincham revisited." *Vision Res* 33 (10):1397–411. doi: 10.1016/0042-6989(93)90046-y.
- Kruger, P. B., S. Nowbotsing, K. R. Aggarwala, and S. Mathews. 1995. "Small amounts of chromatic aberration influence dynamic accommodation." *Optom Vis Sci* 72 (9):656–66. doi: 10.1097/00006324-199509000-00009.
- Kruger, P. B., and J. Pola. 1986. "Stimuli for accommodation: blur, chromatic aberration and size." *Vision Res* 26 (6):957–71. doi: 10.1016/0042-6989(86)90153-7.
- Kruger, P. B., and J. Pola. 1987. "Dioptic and non-dioptic stimuli for accommodation: target size alone and with blur and chromatic aberration." *Vision Res* 27 (4):556–67. doi: 10.1016/0042-6989(87)90042-3.
- Le Grand, Y. 1967. *Form and Space Vision*. Translated by M. Millodot, Heath, G. G. Revised ed. Bloomington: Indiana University Press.
- Lewis, A. L., M. Katz, and C. Oehrlein. 1982. "A modified achromatizing lens." *Am J Optom Physiol Opt* 59 (11):909–11. doi: 10.1097/00006324-198211000-00011.
- Llorente, L., L. Diaz-Santana, D. Lara-Saucedo, and S. Marcos. 2003. "Aberrations of the human eye in visible and near infrared illumination." *Optom Vis Sci* 80 (1):26–35. doi: 10.1097/00006324-200301000-00005.
- López-Gil, N., and P. Artal. 1997. "Comparison of double-pass estimates of the retinal-image quality obtained with green and near-infrared light." *J Opt Soc Am A* 14 (5):961–71. doi: 10.1364/josaa.14.000961.
- Marcos, S., S. A. Burns, E. Moreno-Barriuso, and R. Navarro. 1999. "A new approach to the study of ocular chromatic aberrations." *Vision Res* 39 (26):4309–23. doi: 10.1016/s0042-6989(99)00145-5.
- Martinez, J. L., E. J. Fernandez, P. M. Prieto, and P. Artal. 2017. "Chromatic aberration control with liquid crystal spatial phase modulators." *Opt Express* 25 (9):9793–801. doi: 10.1364/OE.25.009793.
- Millodot, M., and J. Sivak. 1973. "Influence of accommodation on the chromatic aberration of the eye." *Br J Physiol Opt* 28 (3):169–74.
- Navarro, R., J. Santamaría, and R. Bescós. 1985. "Accommodation dependent model of the human eye with aspherics." *J Opt Soc Am A* 2 (8):1273–81. doi: 10.1364/josaa.2.001273.
- Nutting, P. G. 1914. "The axial chromatic aberration of the human eye." *Proc R Soc Lond A* 90 (620):440–9. doi: 10.1098/rspa.1914.0070.

- Ogboso, Y. U., and H. E. Bedell. 1987. "Magnitude of lateral chromatic aberration across the retina of the human eye." *J Opt Soc Am A* 4 (8):1666–72. doi: 10.1364/josaa.4.001666.
- Pérez-Merino, P., C. Dorronsoro, L. Llorente, S. Duran, et al. 2013. "In vivo chromatic aberration in eyes implanted with intraocular lenses." *Invest Ophthalmol Vis Sci* 54 (4):2654–61. doi: 10.1167/iovs.13-11912.
- Powell, I. 1981. "Lenses for correcting chromatic aberration of the eye." *Appl Opt* 20 (24):4152–5. doi: 10.1364/AO.20.004152.
- Rynders, M. C., R. Navarro, and M. A. Losada. 1998. "Objective measurement of the off-axis longitudinal chromatic aberration in the human eye." *Vision Res* 38 (4):513–22. doi: 10.1016/s0042-6989(97)00216-2.
- Rynders, M., B. Lidkea, W. Chisholm, and L. N. Thibos. 1995. "Statistical distribution of foveal transverse chromatic aberration, pupil centration, and angle ψ in a population of young adult eyes." *J Opt Soc Am A* 12 (10):2348–57. doi: 10.1364/josaa.12.002348.
- Schwarz, C., C. Canovas, S. Manzanera, H. Weeber, et al. 2014. "Binocular visual acuity for the correction of spherical aberration in polychromatic and monochromatic light." *J Vis* 14 (2). doi: 10.1167/14.2.8.
- Siedlecki, D., A. Józwik, M. Zajac, A. Hill-Bator, and A. Turno-Krećicka. 2014. "In vivo longitudinal chromatic aberration of pseudophakic eyes." *Optom Vis Sci* 91 (2):240–6. doi: 10.1097/OPX.0000000000000137.
- Simonet, P., and M. C. W. Campbell. 1990. "The optical transverse chromatic aberration on the fovea of the human eye." *Vision Res* 30 (2):187–206. doi: 10.1016/0042-6989(90)90035-j.
- Sivak, J. G., and M. Millodot. 1974. "Axial chromatic aberration of the eye with achromatizing lens." *J Opt Soc Am* 64 (12):1724–5. doi: 10.1364/josa.64.001724.
- Stone, D., S. Mathews, and P. B. Kruger. 1993. "Accommodation and chromatic aberration: effect of spatial frequency." *Ophthalmic Physiol Opt* 13 (3):244–52. doi: 10.1111/j.1475-1313.1993.tb00466.x.
- Suchkov, N., E. J. Fernandez, and P. Artal. 2019. "Impact of longitudinal chromatic aberration on through-focus visual acuity." *Opt Express* 27 (24):35935–47. doi: 10.1364/OE.27.035935.
- Suheimat, M., P. K. Verkiculara, E. A. H. Mallen, J. J. Rozema, and D. A. Atchison. 2015. "Refractive indices used by the Haag-Streit Lenstar to calculate axial biometric dimensions." *Ophthalmic Physiol Opt* 35 (1):90–6. doi: 10.1111/opo.12182.
- Thibos, L. N., A. Bradley, and D. L. Still. 1991. "Interferometric measurement of visual acuity and the effect of ocular chromatic aberration." *Appl Opt* 30 (16):2079–87. doi: 10.1364/AO.30.002079.
- Thibos, L. N., A. Bradley, D. L. Still, X. Zhang, and P. A. Howarth. 1990. "Theory and measurement of ocular chromatic aberration." *Vision Res* 30 (1):33–49. doi: 10.1016/0042-6989(90)90126-6.
- Thibos, L. N., A. Bradley, and X. Zhang. 1991. "Effect of ocular chromatic aberration on monocular visual performance." *Optom Vis Sci* 68 (8):599–607. doi: 10.1097/00006324-199108000-00005.
- Thibos, L. N., M. Ye, X. Zhang, and A. Bradley. 1992. "The chromatic eye: a new reduced-eye model of ocular chromatic aberration in humans." *Appl Opt* 31 (19):3594–600. doi: 10.1364/AO.31.003594.
- Thibos, L. N., M. Ye, X. Zhang, and A. Bradley. 1997. "Spherical aberration of the reduced schematic eye with elliptical refracting surfaces." *Optom Vis Sci* 74 (7):548–56. doi: 10.1097/00006324-199707000-00024.
- Thomson, L. C., and W. D. Wright. 1947. "The colour sensitivity of the retina within the central fovea of man." *J Physiol (Lond)* 105 (4):316–31. doi: 10.1113/jphysiol.1947.sp004173.
- van Heel, A. C. 1946. "Correcting the spherical and chromatic aberrations of the eye." *J Opt Soc Am* 36 (4):237–9. doi: 10.1364/josa.36.000237.

- Vinas, M., C. Dorronsoro, D. Cortes, D. Pascual, and S. Marcos. 2015. "Longitudinal chromatic aberration of the human eye in the visible and near infrared from wavefront sensing, double-pass and psychophysics." *Biomed Opt Express* 6 (3):948–62. doi: 10.1364/BOE.6.000948.
- Wald, G., and D. R. Griffin. 1947. "The change in refractive power of the human eye in dim and bright light." *J Opt Soc Am* 37 (5):321–36. doi: 10.1364/josa.37.000321.
- Wildsoet, C. F., D. A. Atchison, and M. J Collins. 1993. "Longitudinal chromatic aberration as a function of refractive error." *Clin Exp Optom* 76 (4):119–22.
- Winn, B., A. Bradley, N. C. Strang, P. V. McGraw, and L. N. Thibos. 1995. "Reversals of the colour-depth illusion explained by ocular chromatic aberration." *Vision Res* 35 (19):2675–84. doi: 10.1016/0042-6989(95)00035-x.
- Winter, S., M. T. Fathi, A. P. Venkataraman, R. Rosen, et al. 2015. "Effect of induced transverse chromatic aberration on peripheral vision." *J Opt Soc Am A* 32 (10):1764–71. doi: 10.1364/JOSAA.32.001764.
- Winter, S., R. Sabesan, P. Tiruveedhula, C. Privitera, et al. 2016. "Transverse chromatic aberration across the visual field of the human eye." *J Vis* 16 (14):9. doi: 10.1167/16.14.9.
- Ye, M., A. Bradley, L. N. Thibos, and X. Zhang. 1991. "Interocular differences in transverse chromatic aberration determine chromostereopsis for small pupils." *Vision Res* 31 (10):1787–96. doi: 10.1016/0042-6989(91)90026-2.
- Ye, M., A. Bradley, L. N. Thibos, and X. Zhang. 1992. "The effect of pupil size on chromostereopsis and chromatic diplopia: interaction between the Stiles-Crawford effect and chromatic aberrations." *Vision Res* 32 (11):2121–8. doi: 10.1016/0042-6989(92)90073-r.
- Yoon, G. Y., and D. R. Williams. 2002. "Visual performance after correcting the monochromatic and chromatic aberrations of the eye." *J Opt Soc Am A* 19 (2):266–75. doi: 10.1364/josaa.19.000266.
- Zawadzki, R. J., B. Cense, Y. Zhang, S. S. Choi, et al. 2008. "Ultrahigh-resolution optical coherence tomography with monochromatic and chromatic aberration correction." *Opt Express* 16 (11):8126–43. doi: 10.1364/oe.16.008126.
- Zhang, X., A. Bradley, and L. N. Thibos. 1991. "Achromatizing the human eye: the problem of chromatic parallax." *J Opt Soc Am A* 8 (4):686–91. doi: 10.1364/josaa.8.000686.
- Zhang, X., A. Bradley, and L. N. Thibos. 1993. "Experimental determination of the chromatic difference of magnification of the human eye and the location of the anterior nodal point." *J Opt Soc Am A* 10 (2):213–20. doi: 10.1364/josaa.10.000213.



Taylor & Francis
Taylor & Francis Group
<http://taylorandfrancis.com>

18 Retinal Image Quality

18.1 INTRODUCTION

The quality of the visual system depends upon a combination of optical and neural factors, with subjective measures depending also upon psychological factors.

The optical factors that determine the retinal image quality and affect visual system quality are aberrations (including the refractive errors), diffraction, and scatter. The levels of the first two depend upon wavelength and pupil size and can be easily quantified. Scatter is complex and depends upon the level and nature of the turbidity of the ocular media, and in particular on the size and spatial distribution of the scattering centers.

The neural factors affecting visual system quality include size and spacing of retinal cells, the degree of spatial summation at the various levels of processing from the retina to the visual cortex, and higher-level processing.

The relative influences of optical and neural factors upon visual system quality vary with retinal position and the criterion used for assessing quality. In the foveal region, the in-focus retinal image quality appears well matched to the neural network's resolution at optimum pupil sizes of 2–3 mm (Campbell and Green 1965), but resolution in the peripheral visual field is limited much more by neural factors than by optical factors. For example, Green (1970) found that “bypassing” the optics did not improve the resolution of sinusoidal gratings beyond about 5° degrees from the fovea. By comparison, the quality of the optics has a large influence on detection in the periphery, e.g., Wang et al. (1997); Jaisankar et al. (2022).

Direct measurement of retinal image quality is not possible because of the inaccessibility of the retina. The retinal image quality can be estimated from aberrations. The aerial image of the retinal image can be analyzed; techniques using this approach are referred to as *double-pass* techniques, and as ophthalmoscopic techniques. Another possibility is psychophysical measurement of visual performance in which two similar methods are used, one of which bypasses the optics of the eye; comparison of the results from the two methods yields the retinal image quality.

The retinal light distribution is not the same as the perceived light distribution, partly because of the Stiles–Crawford effect, which describes the luminous efficiency of rays entering the eye through different positions in the pupil (section 4.5). The Stiles–Crawford effect is a retinal phenomenon, but for some purposes it can be considered as a pupil apodization, that is, as a filter of variable transmittance placed over the pupil (Westheimer 1959). As such, it is often included in calculations of retinal image quality.

In this chapter we examine retinal image quality criteria. The ones that are common in the analysis of general optical systems are the point spread function and the optical transfer function and their derivatives. Equations for calculating the point spread function and the optical transfer function from the aberrations of an optical

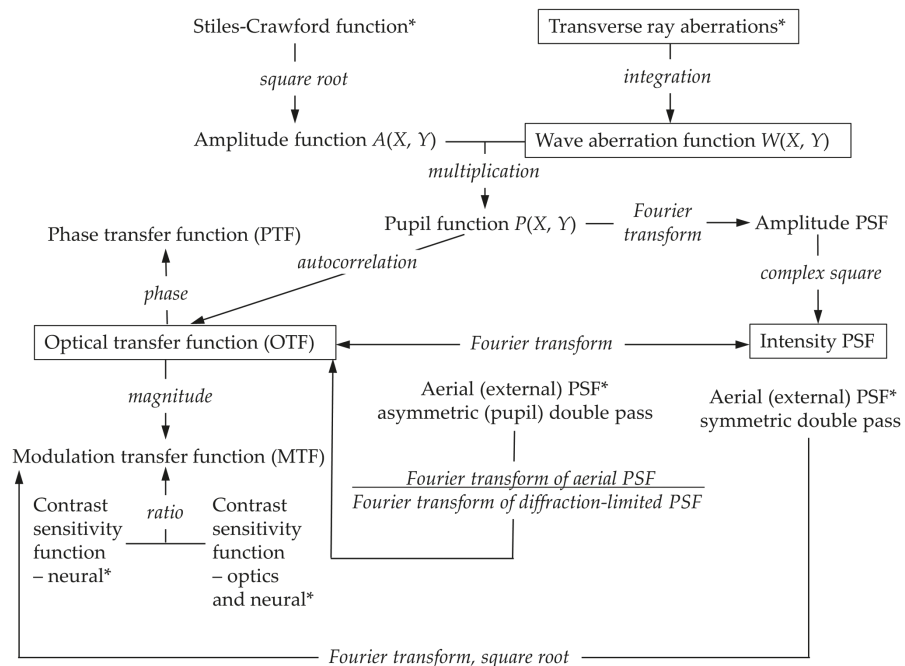


FIGURE 18.1 Relationships between image quality criteria. Main image quality criteria are in boxes, operations are in italics, and the quantities obtained by measurement are marked by *.

system are given in Appendix 5. Relationships between these image quality criteria and measurements are shown in Figure 18.1. Other image quality criteria have been developed for the purpose of refraction of the eye: the combination of added lenses that optimizes a criterion is the refraction.

18.2 THE POINT AND LINE SPREAD FUNCTIONS

The point spread function is the illuminance or luminance distribution in the image of a point source of light, while the line spread function is the distribution in the image of a line (of zero width) source of light. The abbreviations PSF and LSF are often used for the point spread function and line spread function, respectively.

The form of the PSF depends upon diffraction, defocus, aberrations, and scattered light. In the absence of defocus, aberrations, and scatter, the PSF is called the *diffraction-limited PSF*. Defocus, aberrations, and scattered light broaden the PSF. The form of the PSF also depends upon the shape and diameter of the aperture stop. In the following discussion, it is assumed that the pupil is circular.

18.2.1 THE DIFFRACTION-LIMITED PSF (MONOCHROMATIC LIGHT)

For a circular aperture or pupil, the diffraction-limited PSF is a radially symmetric function. For a monochromatic source, the relative light level $L(\zeta)$ at a distance ζ from the center of the PSF is given by the equation

$$L(\zeta) = [2J_1(\zeta)]^2/\zeta^2 \quad (18.1)$$

where $J_1(\zeta)$ is a Bessel function.

In object space with the object at infinity,

$$\zeta = \frac{2\pi\theta\bar{\rho}}{\lambda} = \frac{\pi\theta D}{\lambda} \quad (18.2a)$$

where

$$\theta = \text{angular distance (radian)} = \frac{\zeta\lambda}{2\pi\bar{\rho}} = \frac{\zeta\lambda}{\pi D} \quad (18.2b)$$

and $\bar{\rho}$ is the radius of the entrance pupil of eye, D is the diameter of the entrance pupil ($=2\bar{\rho}$), and λ is the wavelength in a vacuum. If we wish to convert the angular distance θ in object space to a distance on the retina, we can use the conversion equation

$$\text{retinal distance} = \theta F \quad (18.3)$$

where F is the equivalent power of the eye.

This diffraction-limited PSF is plotted in Figure 18.2. The figure shows that the light distribution consists of a central peak and central disc of light, known as the *Airy disc*. This is surrounded by a number of rings of light of ever-decreasing light level.

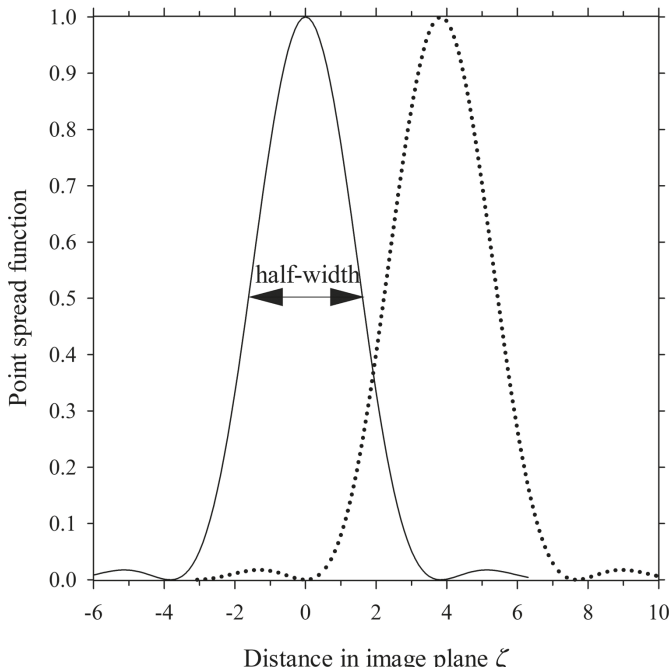


FIGURE 18.2 The monochromatic diffraction-limited PSFs for two light sources. The sources are separated so that the first zero for one source falls on the peak value of the other source (Rayleigh diffraction criterion). The half-width is also shown.

The outer limit of the Airy disc occurs when the above function (that is, the light level) first goes to zero, which occurs at

$$\zeta = 3.8317 \quad (18.4)$$

From equation (18.2a), the corresponding value of θ at which this zero occurs is given by the equation

$$\theta = 1.22\lambda/D \text{ rad} \quad (18.5)$$

This is the angular radius of the Airy disc. Considering only the effect of diffraction, equation (18.5) shows that the PSF decreases in width as the aperture stop diameter increases in size.

The diffraction-limited PSF can be observed by looking at a bright monochromatic point source against a dark background through a small artificial pupil. To be able to resolve the Airy disc and the surrounding rings, the disc must be several times larger than the smallest resolvable detail, which is often taken as 1 min. arc. Assuming that the disc is 2 min. arc in diameter, equation (18.5) predicts that the pupil diameter should be about 2.3 mm diameter at a wavelength of 550 nm.

18.2.2 THE ABERRATED PSF

For pupil diameters greater than about 2 mm, or in polychromatic light, aberrations cannot be neglected, and the point spread function is not accurately described by the above diffraction-limited equation. The effect of any aberration is to spread light out more than predicted by diffraction. Therefore, the aberrated PSF is broader, and the peak is lowered, relative to the diffraction-limited case.

18.2.3 THE PSF AND ITS USE IN QUANTIFYING IMAGE QUALITY

The PSF of the eye is affected by defocus, aberrations, and scatter, and is usually formed by polychromatic light. Thus, it is not generally well described by the diffraction-limited PSF. Furthermore, because of asymmetries in the function, it is difficult often to compare PSFs under different conditions. Comparisons are much easier if the PSFs can be reduced to a single number that specifies the image quality on some meaningful scale. Three of these are the *Rayleigh criterion*, *half-width*, and the *Strehl intensity ratio*.

18.2.3.1 The Rayleigh Criterion (Diffraction-Limited and Monochromatic Sources)

The Rayleigh resolution criterion applies only to monochromatic point sources and states that, for a diffraction-limited system, two point sources can just be resolved if the peak of one of the PSFs lies on the first minimum of the other. The situation is shown in Figure 18.2. Since the radius of the first dark ring of the diffraction-limited PSF is given by equation (18.5), it follows that this is the minimum angular resolution according to the Rayleigh criterion.

18.2.3.2 The Half-Width

Once the influence of aberrations, scatter, and polychromatic light are included, the Airy disc ceases to exist because the PSF has, in general, no well-defined zeros. The width of the PSF is then often taken as the half-width, which is the width at half the peak height, and is also known as the *full width at half maximum*. If the diffraction-limited PSF is analyzed, we find that the half-width $\Delta\zeta$ is

$$\Delta\zeta = 3.2327 \quad (18.6)$$

which is less than the diameter of the Airy disc in equation (18.4). With this value, the diffraction-limited angular half-width $\Delta\theta$ is given by the equation

$$\Delta\theta = \frac{1.029\lambda}{D} \text{ rad or } = \frac{3537\lambda}{D} \text{ min.arc} \quad (18.7)$$

The half-width of the diffraction-limited PSF is shown in Figure 18.2. If aberrations are introduced, the half-width increases.

When astigmatism and coma are present, the half-width should be considered in two mutually perpendicular directions for which the widths are the minimum and the maximum. These can be reduced to a single number by taking the arithmetic or geometric mean of the two widths.

18.2.3.3 The Strehl Intensity Ratio

The Strehl intensity ratio is a measure of the effect of aberrations on reducing the maximum or peak value of the PSF. It is defined as follows:

$$\text{Strehl intensity ratio} = \frac{\text{maximum light level value of aberrated PSF}}{\text{minimum light level value of unaberrated PSF}} \quad (18.8)$$

The Strehl intensity ratio has an advantage over the half-width by always being a single number, even if the PSF is not rotationally symmetric.

Since the effect of aberrations is to spread out the PSF and decrease the peak height, the Strehl intensity ratio is always less than or equal to one. The greater the aberrations, the lower the value of the Strehl intensity ratio and the poorer the image quality. A criterion for a good, near to diffraction-limited system is that the Strehl intensity ratio has a value ≥ 0.8 .

18.2.4 THE PSF AND LSF OF EYES

The light distribution of a point source at the retina cannot be measured directly, but the light passing back out of the eye (the aerial or external image) is measurable. Because the light has passed twice through the eye's optical system, this method is known as a double-pass method. The light is doubly aberrated, and the aerial PSF is wider than the retinal PSF. It was long thought that the retinal PSF is given by the inverse Fourier transform (FT^{-1}) of the square root of the Fourier transform (FT) of the aerial PSF, which is expressed mathematically as

$$\text{PSF} = FT^{-1}\sqrt{[FT(\text{aerial PSF})]} \quad (18.9a)$$

This is not correct, because the aerial image loses the information of asymmetric aberrations, such as coma, which results in loss of phase information (Artal et al. 1995). This does not affect the determination of the modulation transfer function, but it does affect the phase transfer function so that earlier determinations of this are incorrect, e.g., Artal et al. (1988). To overcome this problem, researchers used different diameters of the aperture stops for light entering and leaving the eye, one of which was small enough to be considered diffraction-limited (e.g., 1 mm diameter). This is referred to as a “one-and-a-half” method (Artal, Iglesias et al. 1995; Navarro and Losada 1995) or “asymmetric (pupil) double-pass method”. The retinal PSF with the larger aperture stop is obtained by dividing the Fourier transform of the aerial PSF by the Fourier transform of the diffraction-limited PSF, and then obtaining the inverse Fourier transform of this result. This is expressed mathematically as

$$\text{PSF} = FT^{-1}[FT(\text{aerial PSF})/FT(\text{diffraction-limited PSF})] \quad (18.9b)$$

LSF measurements preceded measurements of the PSF by about 30 years (Santamaría et al. 1987) because of the problem of low light levels before the use of lasers and sensitive detectors.

Techniques have been developed to derive the aberrations of the eye from the PSF (Iglesias, Berrio, et al. 1998; Iglesias, López-Gil, et al. 1998), but with the advent of aberration measuring techniques such as Hartmann–Shack sensing and laser raytracing, these techniques are no longer needed. In fact, it is the PSF that is derived from the aberration measurements.

18.3 THE OPTICAL TRANSFER FUNCTION

Figure 18.3 shows a one-dimensional grating pattern with a light level that varies sinusoidally. The variation of this light level with distance x can be described by the equation

$$\text{Light level } (x) = A_0 + A \sin(2\pi x/p + \delta) \quad (18.10a)$$

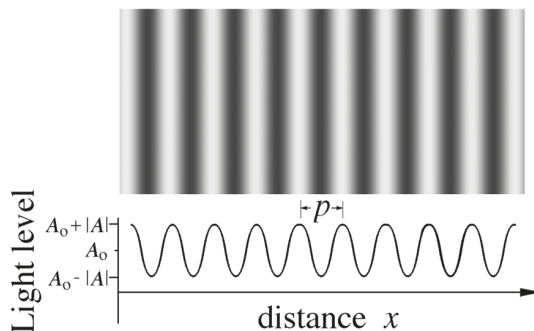


FIGURE 18.3 A one-dimensional pattern with a sinusoidally varying light level.

where A is the amplitude of the variation and its value may be negative, δ is a phase factor, and p is the period of this pattern whose reciprocal is the spatial frequency σ , that is

$$\sigma = 1/p \quad (18.10b)$$

In object space, the period is in units of angle (e.g., radians, degrees, minutes of arc), and thus the units of spatial frequency are cycles/units of angle (e.g., c/rad, c/deg, and c/min. arc).

If this pattern is imaged by an optical system, and providing the aberrations do not change too rapidly over the field of the sinusoidal pattern, the image is also sinusoidal but now has amplitude A' , phase factor δ' , and period p' , and can be represented by the equation

$$\text{Light level } (x') = A'_o + A' \sin(2\pi x'/p' + \delta') \quad (18.11)$$

The *modulation transfer function* is defined as the amplitude A' of the image divided by the amplitude A of the object, and it is a function of spatial frequency. In one dimension, we denote the modulation transfer function by the symbol $G(\sigma)$ and so

$$G(\sigma) = A'/A \quad (18.12)$$

Because this will depend upon light attenuation in the system, the modulation transfer function is normalized so that $G(0) = 1$.

Different aberrations have different effects on the image. Spherical aberration and defocus cause a decrease in the amplitude, but coma causes both a decrease in the amplitude and a transverse shift from the Gaussian (or aberration-free) image position. Astigmatism effects depend upon meridian in the pupil. Distortion (or tilt) causes a transverse shift only. Those aberrations that produce a transverse shift produce an effective phase shift in the image – i.e., δ and δ' have different values. The phase shift across a range of spatial frequencies is the *phase transfer function*.

The *optical transfer function* (OTF) is a complex quantity that includes both the modulation transfer function (MTF) and the phase transfer function (PTF). In some situations, for example on-axis in a rotationally symmetric optical system, there is no change in phase with spatial frequency. In these situations, the OTF is identical to the MTF and we can use the terms interchangeably.

The MTF is closely associated with the *contrast threshold function*, which is the visual threshold contrast of sinusoidal patterns as a function of spatial frequency. Contrast here is given by

$$C = (L_{\max} - L_{\min})/(L_{\max} + L_{\min}) \quad (18.13)$$

where L_{\max} and L_{\min} are the maximum and minimum luminances of a sinusoidal grating. The function depends upon neural factors as well as optical effects. The reciprocal of the contrast threshold function is called the *contrast sensitivity function* (CSF).

18.3.1 THE DIFFRACTION-LIMITED OTF WITH NO STILES–CRAWFORD EFFECT

Using the theory presented in Appendix 5, one can easily show that the monochromatic diffraction-limited optical transfer function, without any Stiles–Crawford effect, is given by the equation

$$G(\sigma) = [\Gamma - \sin(\Gamma)]/\pi \quad (18.14a)$$

where

$$\Gamma = 2 \cos^{-1} [\sigma\lambda / (2\rho)] \quad (18.14b)$$

It is common practice to express the diffraction-limited OTF in terms of a “reduced spatial frequency” s , which is defined in terms of the actual spatial frequency σ , by the equation

$$s = \sigma\lambda / \rho \quad (18.15a)$$

Equation (18.14a) can still be used, but with $G(\sigma)$ replaced by $G(s)$ to calculate the OTF in terms of s so that Γ becomes

$$\Gamma = 2 \cos^{-1}(s/2) \quad (18.15b)$$

The function $G(s)$ giving the diffraction-limited modulation transfer function is plotted in Figure 18.4, and it follows from this figure that the upper limit of s is 2.0, which corresponds to the resolution limit of the optical system. The corresponding actual spatial frequency or resolution limit σ_{\max} is thus

$$\sigma_{\max} = \frac{2\rho}{\lambda} \text{ or } \frac{D}{\lambda} \text{ c / rad or } \frac{180}{\pi} \frac{D}{\lambda} \text{ c / deg} \quad (18.16)$$

and this equation can be used to predict the theoretical OTF resolution limit of the eye for any pupil size and wavelength.

18.3.2 DETERMINATION OF THE OTF

The OTF can be determined in three ways (Figure 18.1).

18.3.2.1 Determining the OTF from the Measured Wave Aberrations

The OTF can be calculated theoretically from the aberrations, and the mathematical basis of this is described briefly in Appendix 5.

18.3.2.2 Determining the OTF from the Aerial PSF

The OTF is the Fourier transform of the PSF. However, as described in section 18.2.4, with a single aperture stop for both ingoing and outgoing light, phase information is lost. The full retinal OTF cannot be determined, but the MTF is the square root of

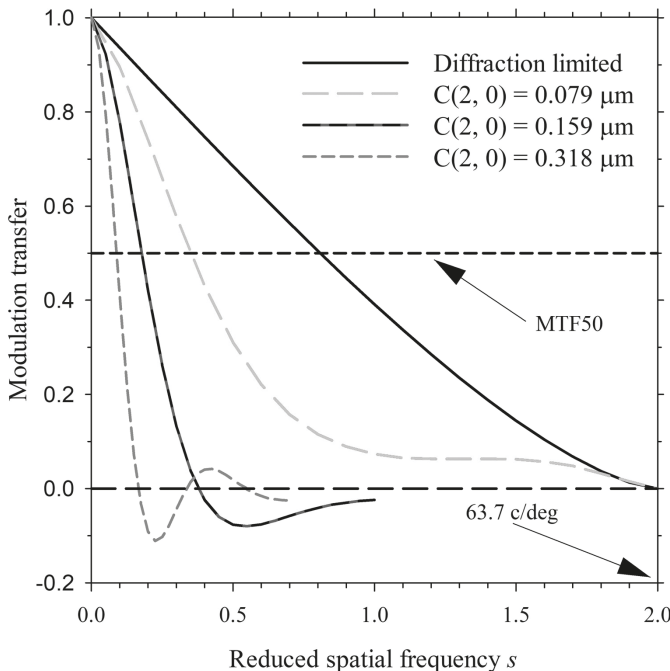


FIGURE 18.4 The diffraction limited and three defocused modulation transfer functions. For a 2 mm diameter pupil and wavelength 550 nm, from equation (18.15a) the diffraction limit is 63.7 cycles/deg. MTF50, the spatial frequency by which the MTF drops to 0.5, is also shown.

the Fourier transform of the aerial PSF. Using the asymmetric double-pass method in which either the ingoing or outgoing light beam is diffraction-limited, the OTF is the ratio of the Fourier transforms of the aerial and diffraction-limited PSFs.

18.3.2.3 Determining the OTF from Psychophysical Comparison

The CSF is measured for sinusoids viewed naturally (e.g., created on a computer monitor), and by using an interferometer with Maxwellian view, which bypasses the optics and projects sinusoidal fringes directly on the retina. The first function includes both the optics and neural factors, and the second function involves only the neural factors.

For the second function, two mutually coherent point sources are produced near the nodal points, and the two resulting beams overlap on the retina to produce a series of parallel fringes with angular separation $\gamma = \lambda/a$, where λ is the source wavelength and a is the source separation in air (Smith and Atchison 1997). Assuming the two sources have equal intensity, the fringes have a contrast of 1. The fringe contrast is reduced by adding light from an incoherent source of the same wavelength.

Denoting the CSF determined with both optics and neural factors as CSF_{opt+n} and the CSF determined with only the neural factors as CSF_n , the modulation transfer function is simply the ratio of these two functions, that is,

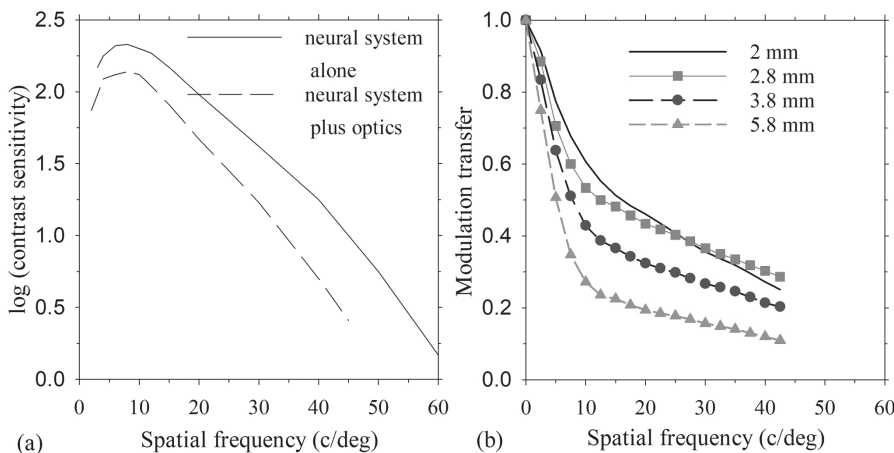


FIGURE 18.5 (a) Results of Campbell and Green (1965) showing the contrast threshold functions for the whole eye; that is, the combined neural and optical systems, and the neural system alone. For the former the subject viewed sinusoidal gratings on a television monitor with a green phosphor through a 2 mm artificial pupil, while for the latter the fringes were generated by interferometry using monochromatic light (wavelength 633 nm). (b) Modulation transfer functions from a range of pupil sizes derived from the ratio of the two types of curves shown in Figure 18.5a.

$$\text{MTF} = \text{CSF}_{\text{o+o}} / \text{CSF}_n \quad (18.17)$$

$\text{CSF}_{\text{o+o}}$ must be measured for each pupil size of interest. Campbell and Green's (1965) CSF results for one subject are shown in Figure 18.5a, with the derived MTFs for a range of pupil sizes appearing in Figure 18.5b.

A variation of the technique is contrast sensitivity function measurements when aberrations are manipulated using adaptive optics. The contrast sensitivity function of an eye with aberrations, or of an eye in which the aberrations are manipulated such as by adding defocus, is compared with that of the eye whose aberrations are corrected with adaptive optics (Jaisankar et al. 2022).

18.3.3 OTF IN THE PRESENCE OF DEFOCUS

To examine the optical transfer function with some defocus, we must add a $W_{2,0}$ term (or c_2^0 term) to the wave aberration function (Appendix 2), and this is related to the defocus expressed as a power ΔF by equation (A2.5). This is another example where the MTF and OTF are identical.

Results are shown in Figure 18.4 for different levels of defocus. For higher levels of defocus, the MTF eventually becomes negative, and then has an oscillatory nature with a decreasing amplitude. When the MTF is negative, the image pattern has reversed contrast compared with that of the object. This means that the brighter parts of the object become the darker parts of the image, and the darker parts of the object become the brighter parts of the image. The spatial frequency at which the

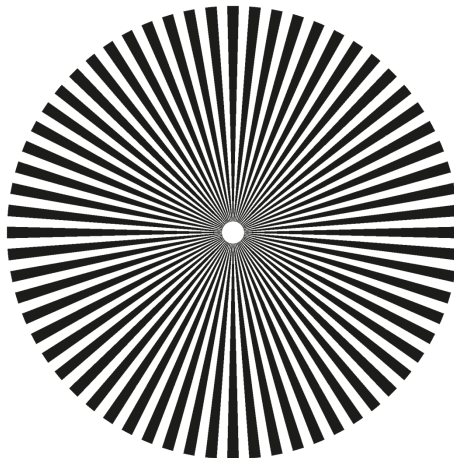


FIGURE 18.6 Siemen's star, which can be used for observing spurious resolution.

modulation transfer function first goes to zero is the resolution limit. Any resolution of higher frequency patterns is called *spurious resolution*.

Spurious resolution can be seen with Siemen's star pattern in Figure 18.6 when this is defocused severely by using lenses or by viewing from a close distance within the accommodation limit. Some regions in the pattern show contrast reversal. If eyes were rotationally symmetric, the regions of contrast reversal would form concentric annuli. However, because real eyes are asymmetric, particularly the aberrations, these annuli have irregularities. The presence of the asymmetries means that the phase transfer function is not zero.

18.3.3.1 The Geometrical Optical Approximation for Defocus

The phenomenon of spurious resolution can be investigated by a much simpler but approximate process if it is assumed that the defocus is large. In this case, the PSF is a uniformly illuminated disc. In section 9.3.1, we showed that the angular diameter Φ of the defocus blur disc was related to the level of refractive error ΔL and pupil diameter D , by equation (9.17), that is

$$\Phi = \Delta L D \quad (18.18)$$

In the simple aberration and diffraction-free defocused system, the PSF is the defocus blur disc of radius Φ . The OTF is the Fourier transform of this PSF. For a circular uniform function with a diameter Φ , the OTF $G(\sigma)$ is given by the equation

$$G(\sigma) = \frac{J_1(\pi\Phi\sigma)}{\pi\Phi\sigma} \quad (18.19)$$

where J_1 is the same Bessel function as in equation (18.1). For distance viewing, i.e., Φ is in radians, the spatial frequency σ is in cycles/radian. The first zero of this equation occurs at $\pi\Phi\sigma = 3.83$, and thus

$$\sigma = \frac{3.83}{\pi\Phi} = \frac{1.22}{\Phi} \quad (18.20)$$

Replacing the blur disc diameter Φ by the right-hand side expression in equation (18.18), we have

$$\sigma = \frac{1.22}{\Delta L \cdot D} \quad (18.21)$$

This value of σ is the resolution limit.

As an example, let us calculate the resolution limit of an eye with a pupil diameter of 4 mm and 1 D of defocus. In equation (18.21), we put $\Delta L = 1$ D and $D = 0.004$ m, and thus the resulting resolution limit is

$$\sigma = 305 \text{ c/rad} = 5.32 \text{ c/deg}$$

Figure 18.7 shows the expected region of spurious resolution in an aberration-free eye according to physical and geometric optics predictions (Smith 1982). Geometric

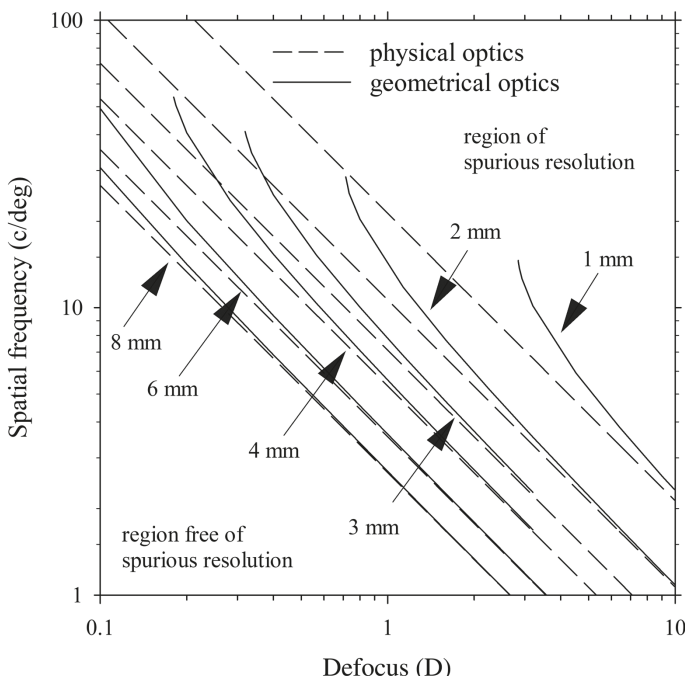


FIGURE 18.7 Physical and geometrical optical predictions of the boundaries of spurious resolution for an aberration-free system and for different pupil diameters as marked (mm). Spurious resolution occurs above the boundaries. The physical optical predictions are given by the curves. The geometrical optics approximations given by the straight lines are increasingly accurate as pupil size increases, defocus increases, and spatial frequency decreases. Wavelength is 550 nm (based on Smith 1982).

optics approximations become more accurate for higher levels of defocus and lower spatial frequencies.

18.4 RETINAL IMAGE QUALITY

To appreciate the limits that the optics of the eye place on vision, we also need some understanding of the limits provided by the retina. To be able to resolve the detail provided by a pattern of light imaged upon the retina, the adjacent “receptor units” must be sufficiently close together to correctly interpret the pattern. In Figure 18.8, oblique square wave light patterns imaged on a square array of receptor units are shown. In Figure 18.8a, the pattern repeats every four units in the vertical meridian. Another way of putting this is that the receptor units are a quarter of a cycle apart. The visual system interprets the spatial frequency and orientation of the pattern correctly (the term *veridical* is sometimes used). In Figure 18.8b, the pattern repeats every two units in the vertical direction. For every two receptor units in the vertical direction struck by adjacent light bars, there is a receptor unit between them, which is struck by a dark bar (and *vice versa*). The visual system is just able to resolve the pattern; that is, vision is again veridical. In Figure 18.8c, the sinusoidal pattern is yet finer, repeating every receptor unit in the vertical meridian, and now the sampling rate of the receptor units is inadequate to correctly interpret the pattern. The visual

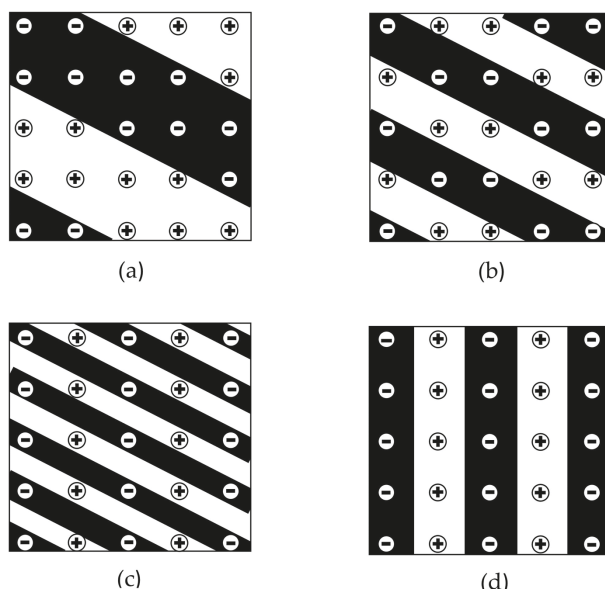


FIGURE 18.8 Oblique square wave patterns are imaged on a square array of receptor units. The receptor units are excited by the bright bars and inhibited by dark bars. (a) The pattern repeats itself every four units in the vertical direction. (b) The pattern repeats itself every two units in the vertical direction. (c) The pattern repeats itself every one unit in the vertical direction. (d) An aliased perception of the pattern in (c).

system “undersamples” the pattern, which may be perceived to have a much lower spatial frequency and a different orientation such as that in Figure 18.8d. This incorrect interpretation of the pattern is referred to as *aliasing*. Another way of considering this is that the visual system cannot distinguish between the light patterns shown in Figures 18.8c and d.

Figure 18.8b shows the finest light pattern that can be correctly resolved by the retina. Its spatial frequency is called the *Nyquist limit (NL)*, and is given by

$$NL = 1/(2c_s) \quad (18.22a)$$

where c_s is the center-to-center spacing of the receptor units.

The “receptor unit” that correlates best with resolution is the spacing between ganglion cells (Thibos et al. 1987). At the fovea there is a one-to-one correspondence between cones and ganglion cells, so the cone spacing can be used to determine resolution limits. Because of the tight hexagonal packing of cones, the previous equation needs to be modified to

$$NL = 1/(\sqrt{3}c_s) \quad (18.22b)$$

Williams (1985) calculated the Nyquist limit to be 56 c/deg in object space (or subtense at back nodal point), by assuming that the closest spacing of human foveal cones is 3 mm and that 0.29 mm on the retina corresponds to 1°. The resolution limit drops quickly away from the fovea because of the rapid decrease in ganglion cell density (Curcio and Allen 1990).

There are two major types of spatial tasks that are performed by the visual system. Resolution has already been referred to; the other type is detection. Perimetry is an example of a detection task in which a patient must detect that a spot of light is present; details such as the shape of the spot are usually unimportant. Although in Figure 18d the pattern is not seen veridically, it is still seen, provided that the contrast is sufficiently high. It is likely that the highest spatial frequency that can be detected by the retina is limited by the size of photoreceptors (Thibos, Bradley, and Still 1991; Thibos et al. 1996). Visual acuity involves resolution, as a patient must be able to resolve detail of a target. It can be argued that visual acuity is more than a resolution task, as identifying the arrangement of resolved elements is important for identification of a letter.

The relative importance of optical and neural limitations to visual performance can be determined by using the CSF both as a resolution task and as a detection task. In the detection task, the subject is asked which of two presentations contains a grating. In the resolution task, the subject is asked to determine the orientation of a sinusoidal grating, such as whether it is horizontal or vertical. For normal presentation of the gratings on a monitor, when the two CSFs are essentially the same, the optics act as a filter to provide the main limitation to both detection and resolution (see central curves in Figure 18.9). However, if the detection CSF is superior to the resolution CSF, then resolution, although not necessarily detection, is limited by the sampling rate of the receptor elements (see peripheral curves in Figure 18.9).

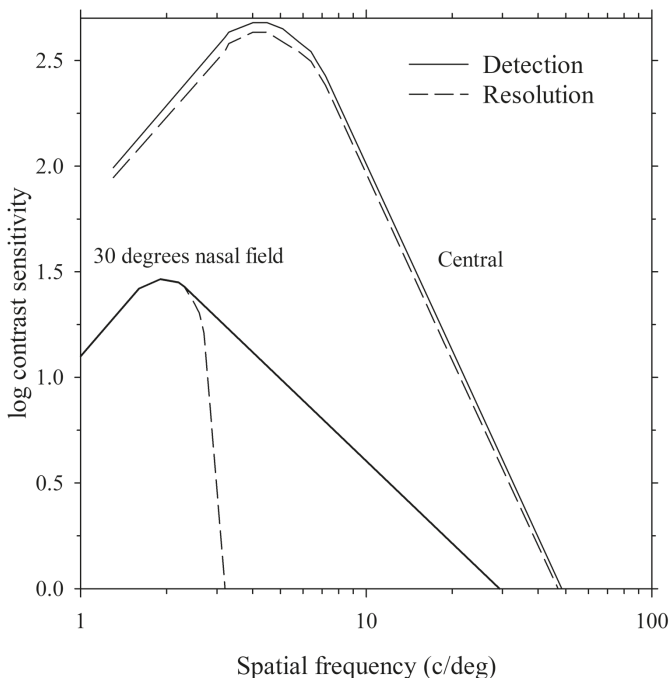


FIGURE 18.9 Normal contrast sensitivity functions for resolution and detection tasks for the center and periphery (30° nasal in object space) of the visual field. The region between the two peripheral vision curves indicates the spatial frequencies for which aliasing occurs. Representation is based on results of Thibos et al. (1996) in which measurements in the periphery were done after careful refraction.

This issue was discussed in detail by Thibos and Bradley (1993), who recommended using the distinction between resolution and detection to design clinical tests to determine at which stage (detection, resolution, or identification) an abnormal visual system is breaking down.

18.4.1 CENTRAL VISION

Despite being carried out in the mid-1960s, the classic work of Campbell and colleagues is still considered to provide good data on the quality of the optics of the eye. Figure 18.5b shows the psychophysically determined modulation transfer functions of Campbell and Green (1965) for one subject. Optical performance is near diffraction-limited for 2 mm diameter pupils. As pupil size increases, aberrations cause performance to decrease relative to diffraction-limited performance, with optimum quality occurring for 2.0–2.8 mm pupil diameters. The maximum spatial frequency at which resolution of the pattern is possible is approximately 60 c/deg. Using an improved technique with reduced spatial noise masking effects, which can affect the CSF measured by bypassing the optics, Williams (1985) showed that the

neural ability is better than that given by Campbell and Green (1965) beyond 40 c/deg. This indicates that the retinal image quality beyond 40 c/deg is worse than calculated by Campbell and Green. Although both the optics and neural factors contribute to the normal CSF, the optics are the major limitation to central vision because both detection and resolution CSFs give similar results – that is, there is no aliasing (Thibos et al. 1996).

The aberration methods of determining image quality might be expected to overestimate image quality because media scattering effects are ignored. The psycho-physical comparison method has several considerations. Again, the scattering effects may be ignored, if they affect the two CSFs equally. There is also the problem of making the two contrast sensitivity measurements equivalent for subjects to perform. The ophthalmoscopic techniques involve assumptions, including that the retina acts as a diffuse reflector and that scatter is similar for both directions of light. They may be affected by a retinal effect similar to the Stiles–Crawford function (Artal 1989). They also involve imaging manipulations to remove influences of forward- and back-scattered light.

Although considerable emphasis has been given to the modulation transfer function, the phase transfer function is an aspect of image quality that should not be neglected. Phase transfer functions of eyes are very different from zero, corresponding to the presence of coma-like aberrations (Charman and Walsh 1985; Walsh and Charman 1985). This is very important in recognition of complex objects, which do not look like the originals because of different phases at different spatial frequencies (Piotrowski and Campbell 1982). While phase shifts have been calculated often from aberration functions, there are few experimental studies (Zhang et al. 1993; Atchison et al. 2003). Figure 18.10 shows some results from one study.

As mentioned in section 15.7, Liang and colleagues (Liang and Williams 1997; Liang et al. 1997) used adaptive optics in conjunction with the wave-front sensor technique to correct ocular aberrations. They were able substantially to correct the aberrations of the eyes, obtaining near diffraction-limited performance with 6 mm diameter pupils. Contrast sensitivity and resolution limits were improved markedly with the adaptive optics, and retinal cones could be seen easily for the first time with a fundus camera through the adaptive optics. Marcos et al. (2017, 2022) have provided “state of the art” accounts of the application of adaptive optics in visual science.

18.4.1.1 Defocus and Refraction

The most important optical defect affecting retinal image quality is defocus, and it lowers the contrast sensitivity function. Fluctuations in the modulation transfer function, e.g., Figure 18.4, produced by defocus should be accompanied by fluctuations in the CSF. With fine spatial frequency sampling, notches (local depressions or local minimums) have been found in the CSF and when through-focus contrast sensitivity is determined at specific spatial frequencies (Atchison, Woods, et al. 1998; Atchison and Scott 2002; Guo et al. 2008). For through-focus contrast sensitivity, application of adaptive optics correction increases the maximum contrast sensitivity, provides a

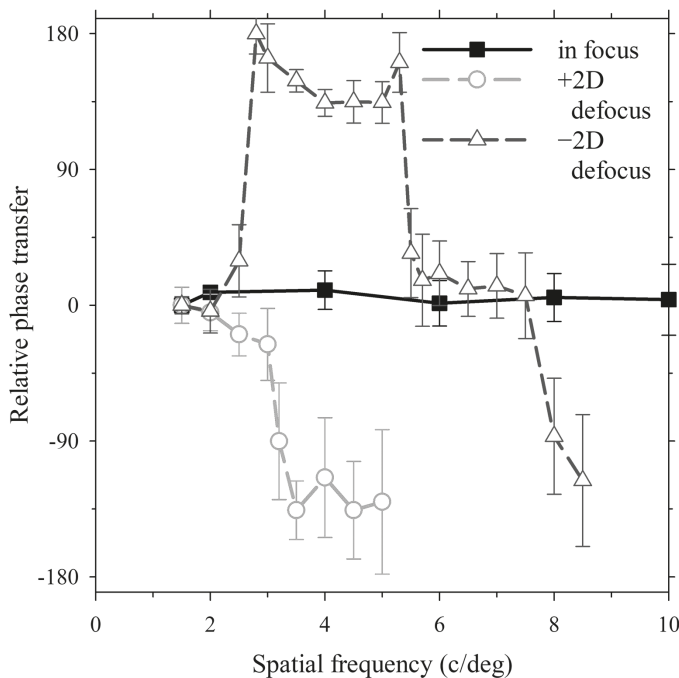


FIGURE 18.10 Relative phase transfer functions for vertical gratings measurements for a participant and a 6 mm pupil: in-focus, -2D focus, and +2D defocus. Data are relative to those for 1.5 c/deg gratings. Positive defocus means that defocus is produced as if a positive lens were placed in front of an emmetropic eye. Rapid changes in the functions correspond to rapid changes in the contrast sensitivity function. Data are from Figure 6 of Atchison et al. (2003).

more rapid deterioration in contrast sensitivity away from the peak, makes the plots more symmetric, and increases depth of notches (Figure 18.11). Even small levels of defocus (0.5 D) can produce marked losses to the CSF (Woods et al. 2000), so it is important to correct even small refractive errors to prevent incorrect attribution of losses to retinal or neural pathological causes.

Refraction is dealt with elsewhere in relation to higher-order aberrations (section 15.4.3) and metrics (section 18.5), but some observations are included here. Under photopic conditions, refraction using letter targets alters little with changes in pupil size (Charman et al. 1978; Koomen et al. 1949; Atchison et al. 1979). This small variation in refraction with pupil size can be explained by the use of small letters containing a relatively high proportion of high spatial frequency information. When luminance is lowered, there is often a substantial negative (myopic) shift in refraction (Koomen et al. 1951). A large amount of this is due to the combination of decrease in visual acuity, which means that high spatial frequencies are not available for determining refraction, and the natural increase in pupil size and hence increase in aberrations such as spherical aberration. Optimal focus depends upon spatial frequency for large pupils (Green and Campbell 1965; Charman et al. 1978). In Figure 18.11 top left,

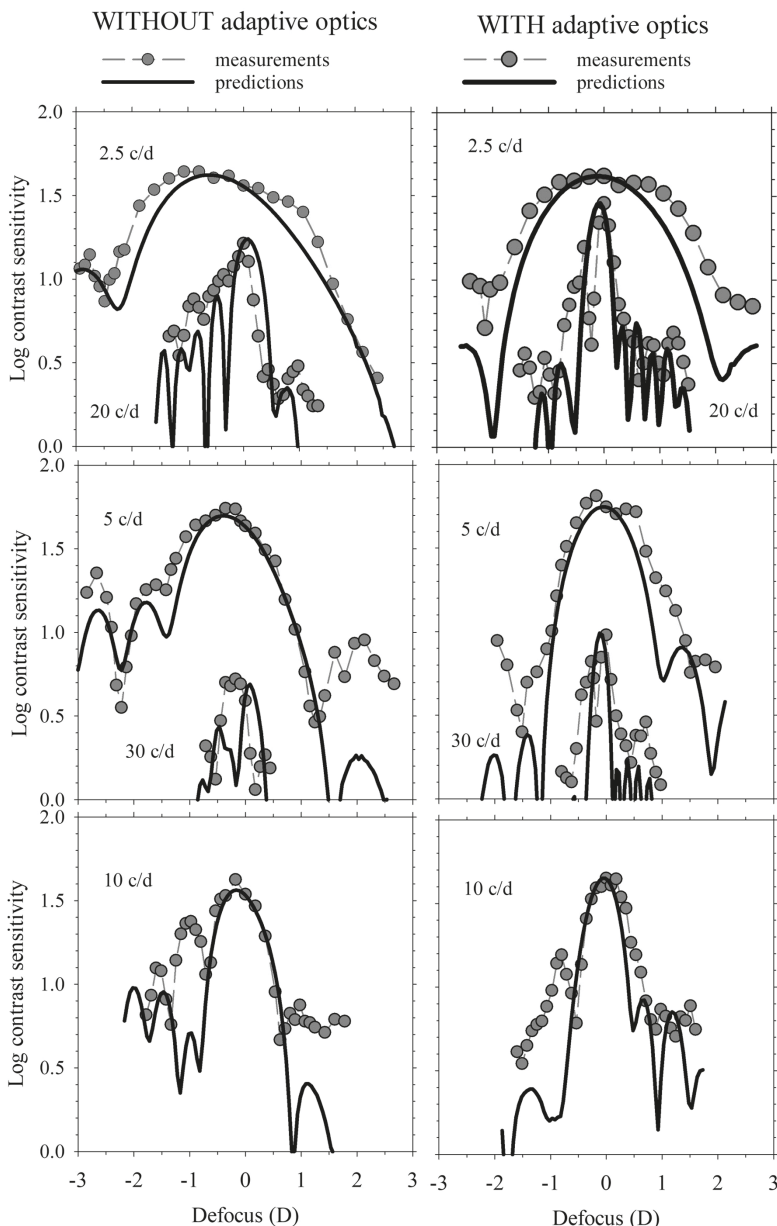


FIGURE 18.11 Through-focus contrast sensitivities for one participant at five spatial frequencies without (left) and with (right) adaptive optics correction. Positive defocus means that defocus is produced as if a positive lens were placed in front of an emmetropic eye. Spatial frequencies are indicated. Pupil size 5.5 mm. Also shown are predicted contrast sensitivities, which were obtained by multiplying the in-focus contrast sensitivity for the in-focus condition by the ratio of MTFs for the defocused and in-focus conditions. MTFs were calculated from aberration measurements). Reproduced from Figure 5 of Guo et al. (2008), with permission from Elsevier.

without adaptive optics correction the optimum refraction shifted 1.0 D between 2.5 and 20 cycles/deg for this participant with large spherical aberration (c_4^0 0.17 μm , 5.5 mm pupil).

18.4.1.2 Polychromatic Light

Thibos, Bradley, and Zhang (1991) showed theoretically that, with 2.5 mm centered pupils, the longitudinal chromatic aberration would have similar effects in white light to only 0.2 D defocus in monochromatic light (Figure 18.12). They obtained a maximum contrast sensitivity loss of 0.2 log unit and a visual acuity loss of ~10 per cent (< 0.05 log unit) relative to those in monochromatic light, similar to the experimental findings of Campbell and Gubisch (1967).

As mentioned in section 17.8, decentration of natural or artificial pupils in white light can have devastating effects on retinal image quality. Large levels of transverse

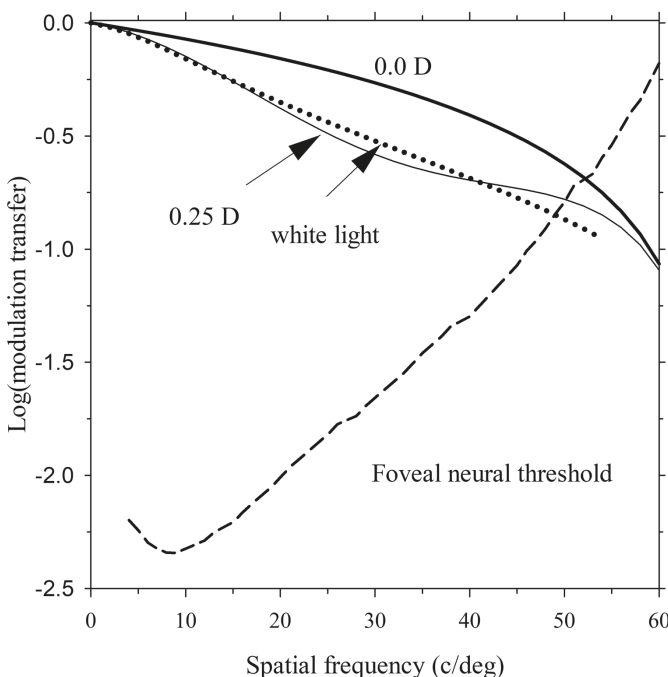


FIGURE 18.12 Comparison of in-focus white-light MTF with defocused monochromatic MTFs for the “Chromatic” eye, which is free of monochromatic aberrations (pupil diameter 2.5 mm, white light provided by a P4 phosphor, reference wavelength 589 nm). Also shown is the neural contrast threshold of one subject from Campbell and Green (1965). Intersection of the MTF curves with the neural contrast threshold predicts the cut-off spatial frequency of 48 c/deg. Within this limit, the extent to which the MTF exceeds the neural contrast threshold indicates how much the contrast of the sinusoidal grating may be reduced from a value of 1 for it still to be resolved. Based on Figure 4 of Thibos, Bradley and Zhang (1991), with data kindly provided by Larry Thibos.

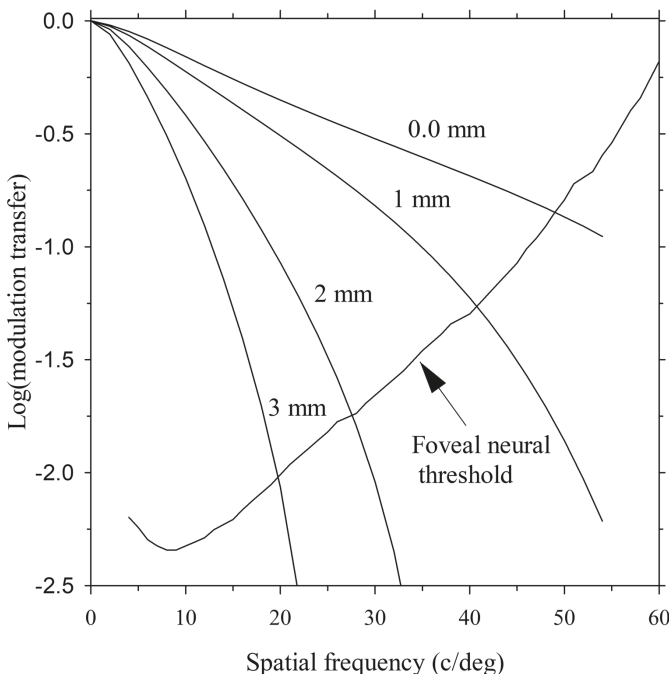


FIGURE 18.13 White-light MTFs for the “Chromatic” eye, which is free of monochromatic aberrations, for various displacements of a 2.5 mm diameter pupil perpendicular to the grating orientation (white light provided by a P4 phosphor, reference wavelength 589 nm). Also shown is the neural contrast threshold of one subject from Campbell and Green (1965). Intersection of the MTF curves with the neural contrast threshold predicts the cut-off spatial frequency. Based on Figure 9 of Thibos, Bradley and Zhang (1991), with data kindly provided by Larry Thibos.

chromatic aberration produce wavelength-dependent spatial phase shifts of the image of a sinusoidal target, leading to loss of image contrast. This has its greatest effects for target orientation at right angles to the decentration direction, with up to three times loss of resolution for 3 mm displacements of small artificial pupils (Figure 18.13) (Green 1967; Thibos, Bradley, and Zhang 1991).

18.4.1.3 The Stiles–Crawford Effect

The Stiles–Crawford effect (SCE) has often been implicated by vision researchers to explain the difference between expected and actual findings – for example, the failure of depth-of-field to decrease with increase in pupil size as quickly as expected (Campbell 1957; Tucker and Charman 1975; Charman and Whitefoot 1977; Legge et al. 1987). However, the results of theoretical investigations using the apodization model (section 18.1) suggest that the SCE is not important for spatial resolution for in-focus imagery, even in the presence of considerable aberrations (Metcalf 1965; Krakau 1974; van Meeteren 1974; Carroll 1980). Even in the presence of defocus, the influence of the SCE should be small, e.g., van Meeteren (1974); Atchison, Joblin,

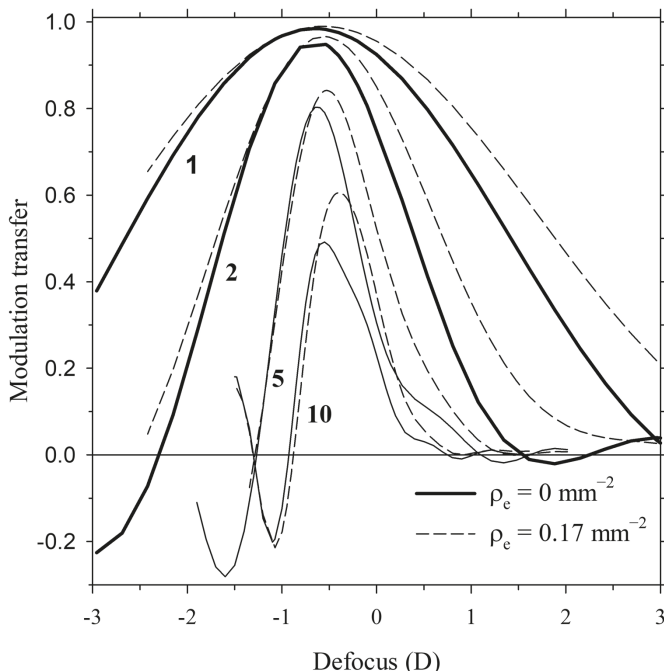


FIGURE 18.14 Modulation transfer as a function of defocus at various object spatial frequencies (cycles/degree) when there is +1.0 D of primary longitudinal spherical aberration at the edge of a 6 mm diameter pupil in 605 nm wavelength light (Zernike aberration coefficients are $c_2^0 = +0.6495 \mu\text{m}$ and $c_4^0 = +0.1677 \mu\text{m}$). Results are shown with and without Stiles–Crawford apodization of $\rho_e = 0.17 \text{ mm}^{-2}$, which is near the 97.5 per cent upper limit of Table 14.1). The Stiles–Crawford effect has only a small influence on image quality, which is greater when the defocus and spherical aberration are in the same direction than when they are opposed. Data are from Figure 6 of Atchison et al. (1998), with permission from The Optical Society.

et al. (1998). The SCE is expected to influence optimal refraction in the presence of aberrations, but the magnitude is likely to be small – e.g., approximately 0.2 D at 10 c/deg in Figure 18.14.

Atchison and colleagues manipulated the SCE with optical filters, conjugate with the eye's pupil, that neutralized the SCE, doubled the SCE, or shifted its peak across the pupil (Atchison et al. 2003; Atchison and Scott 2002; Atchison et al. 2002). The influence of the SCE was more noticeable for myopic defocus than for hyperopic defocus, generally more noticeable for high contrast than for low contrast, and increased as pupil size increased, with a maximum effect of 0.29 log unit for a 7.6 mm pupil. The magnitudes of SCE-neutralized and SCE-doubled conditions on the CSF was usually small at about 0.2 to 0.3 log units, and manipulating the peak had small effects on the CSF. In summary, the SCE appears to play only a minor role in improving visual performance.

18.4.1.4 Pupil Decentration

Decentration of the eye's pupil induces additional optical aberrations, such as transverse chromatic aberration and coma, which decrease spatial visual performance (Green 1967; van Meeteren and Dunnewold 1983; Artal et al. 1996). The Stiles–Crawford effect may be of minor assistance to spatial vision by reducing the influence of the aberrations of the parts of the pupil furthest from the peak of the Stiles–Crawford effect.

18.4.2 PERIPHERAL VISION

The optics associated with the peripheral retina are poor, mainly because of focusing errors in the form of defocus and astigmatism (see section 15.6.2). Retinal image quality declines steadily with increasing object angle (Navarro et al. 1993; Navarro et al. 1998; Jaeken and Artal 2012) (Figure 18.15). However, when the periphery is

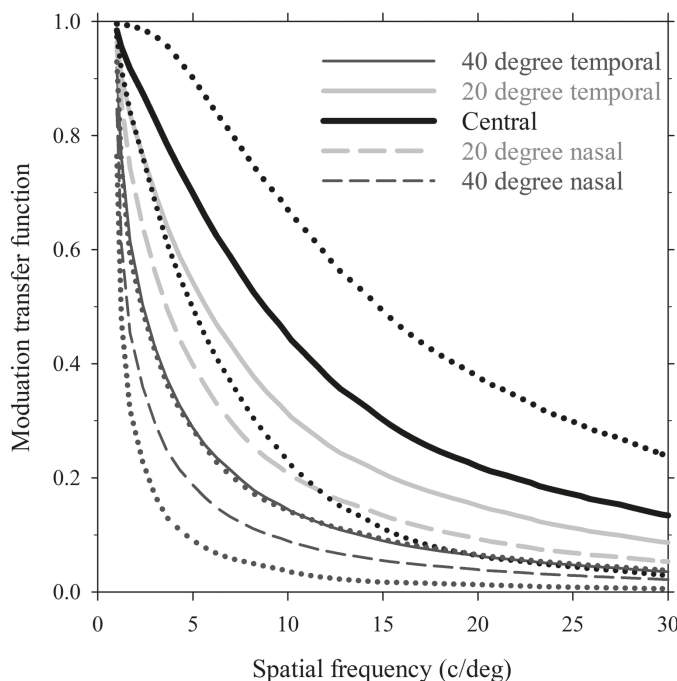


FIGURE 18.15 Mean modulation transfer functions, averaged across all sinusoidal orientations, for 4 mm elliptical pupils for different horizontal visual field positions. The dashed lines are for temporal field and the solid lines are for the nasal field. The dotted lines are one standard deviation from the mean central values (top pair) and from the mean nasal values (bottom pair). Note that image quality is better in the temporal visual field than in the nasal visual field for angles of the same magnitude. Data were determined from aberration measurements of all right eyes of participants in the Jaeken and Artal (2012) study, the central defocus coefficient was subtracted from all aberration measurements, and modulation transfer functions were derived. These results appear in Figure 21.12 of Lundström and Rosén (2017) and were kindly provided by Linda Lundström.

carefully refracted, the image quality improves considerably (Still 1989; Williams et al. 1996). The importance of the peripheral optics has often been discounted because improving them has given little improvement in resolution of high contrast targets, e.g., Green (1970). However, it has been shown that improving the peripheral optics will improve low contrast resolution (Rosén et al. 2011), while marked improvement in detection occurs (Thibos et al. 1996; Wang et al. 1997; Williams et al. 1996; Atchison et al. 2013). With adaptive optics correction of higher-order aberrations, it is possible to identify defocus-induced notches in the detection contrast sensitivity function (Jaisankar et al. 2022), such as those reported under “Defocus and Refraction” in section 18.4.1.

18.5 MORE IMAGE QUALITY CRITERIA – METRICS

The range of image quality criteria has been extended in recent years for application to the eye. These image criteria are often referred to as metrics. Guirao (2017) divided metrics into five groups and gave an extensive coverage; what follows is based in part on this work.

The first group of metrics, optical quality (aberration based), are defined in the pupil plane. The metrics include the aberration coefficients (usually specified in the Zernike polynomial system), the root-mean-squared aberration described in section 15.4, and peak-to-valley, which is the range of aberration across the pupil.

The second group, image quality of the PSF, includes the Strehl intensity ratio and the other measures described in section 18.2.3.

The third group, image quality in the Fourier domain, involves metrics based on the OTF or MTF. As these functions depend on spatial frequency and orientation, single value metrics have been derived. These include the spatial frequency by which the MTF reduces to a certain value such as 0.50 (Figure 18.4), the cutoff beyond which the MTF is effectively zero, the area under the MTF, which usually excludes low spatial frequencies (for which image quality is little affected by high aberrations) and high spatial frequencies that do not contribute to vision.

The fourth group, visual metrics, has many members. Some of these are tests used by ophthalmic professionals, such as visual acuity, letter contrast, contrast sensitivity function, and grating acuity. Others may be variations of those in the image quality in the Fourier domain group, in which the image quality is weighted by some aspects of visual function, such as the neural CSF. Two of these are the area under the MTF weighted by the neural CSF, and the visual Strehl ratio (VSR or VSOTF), which is the ratio of the volumes under the aberrated OTF and the diffraction-limited OTF (OTF_{DL}) in which the OTFs are weighted by the neural CSF. Formally, the VSR is

$$VSR = \frac{\int_{-\infty}^{\infty} \int_{-\infty}^{\infty} OTF(u, v) \cdot NCSF(u, v) dudv}{\int_{-\infty}^{\infty} \int_{-\infty}^{\infty} OTF_{DL}(u, v) \cdot NCSF(u, v) dudv} \quad (18.23)$$

The neural CSF in this calculation is based on a single subject (Campbell and Green 1965). In practice, the calculation is made over a restricted range of visually relevant spatial frequencies such as 0 to 60 cycles/degree. The visual Strehl ratio is one of the

best predictors of subjective refraction (Cheng et al. 2004) as well as the best predictor of visual acuity (Marsack et al. 2004).

The fifth group involves determining similarity of the object and retinal image, so that the higher the similarity the better the optical performance. Full-reference metrics compare each pair of corresponding pixels in the object and image – variants involve mean square error between object and image, peak signal-to-noise ratio, and correlation coefficient. Other metrics are “mutual information”, “receiver operator”, and “structural similarity”.

Guirao (2017) provided applications and references for several metrics. Optimizing such criteria by manipulating the second-order aberration coefficients gives estimates of refractions. Thibos et al. (2004) evaluated 33 objective metrics and obtained accuracies and precisions of these compared with subjective refractions on 200 participants.

SUMMARY OF MAIN SYMBOLS

PSF	point spread function
LSF	line spread function
CSF	contrast sensitivity function
CSF_{o+n}	CSF involving optics and neural factors
CSF_n	CSF involving neural factors only
MTF	modulation transfer function
OTF	optical transfer function
PTF	phase transfer function
C	grating contrast
L_{\min}, L_{\max}	minimum and maximum luminances of a sinusoidal grating
$G(\sigma)$	optical transfer function
σ	spatial frequency (c/radian)
s	modified spatial frequency, called “reduced spatial frequency” related to σ by equation (18.15a)
Φ	angular diameter of defocus blur disc
NL	Nyquist limit
c_s	center to center spacing of receptor units
VSR (VSOTF)	visual Strehl ratio

REFERENCES

- Artal, P. 1989. “Incorporation of directional effects of the retina into computations of optical transfer functions of human eyes.” *J Opt Soc Am A* 6 (12):1941–4. doi: 10.1364/josaa.6.001941.
- Artal, P., I. Iglesias, N. López-Gil, and D. G. Green. 1995. “Double-pass measurements of the retinal-image quality with unequal entrance and exit pupil sizes and the reversibility of the eye’s optical system.” *J Opt Soc Am A* 12 (10):2358–66. doi: 10.1364/josaa.12.002358.
- Artal, P., S. Marcos, I. Iglesias, and D. G. Green. 1996. “Optical modulation transfer and contrast sensitivity with decentered small pupils in the human eye.” *Vision Res* 36 (22):3575–86. doi: 10.1016/0042-6989(96)00107-1.

- Artal, P., S. Marcos, R. Navarro, and D. R. Williams. 1995. "Odd aberrations and double-pass measurements of retinal image quality." *J Opt Soc Am A* 12 (2):195–201. doi: 10.1364/josaa.12.000195.
- Artal, P., J. Santamaría, and J. Bescós. 1988. "Phase-transfer function of the human eye and its influence on point-spread function and wave aberration." *J Opt Soc Am A* 5 (10):1791–5. doi: 10.1364/josaa.5.001791.
- Atchison, D. A., A. Joblin, and G. Smith. 1998. "Influence of Stiles-Crawford effect apodization on spatial visual performance." *J Opt Soc Am A Opt Image Sci Vis* 15 (9):2545–51. doi: 10.1364/josaa.15.002545.
- Atchison, D. A., S. Marcos, and D. H. Scott. 2003. "The influence of the Stiles-Crawford peak location on visual performance." *Vision Res* 43 (6):659–68. doi: 10.1016/s0042-6989(02)00681-8.
- Atchison, D. A., A. Mathur, and S. R. Varnas. 2013. "Visual performance with lenses correcting peripheral refractive errors." *Optom Vis Sci* 90 (11):1304–11. doi: 10.1097/OPX.0000000000000033.
- Atchison, D. A., and D. H. Scott. 2002. "Contrast sensitivity and the Stiles-Crawford effect." *Vision Res* 42 (12):1559–69. doi: 10.1016/s0042-6989(02)00084-6.
- Atchison, D. A., D. H. Scott, N. C. Strang, and P. Artal. 2002. "Influence of Stiles-Crawford apodization on visual acuity." *J Opt Soc Am A* 19 (6):1073–83. doi: 10.1364/josaa.19.001073.
- Atchison, D. A., G. Smith, and N. Efron. 1979. "The effect of pupil size on visual acuity in uncorrected and corrected myopia." *Am J Optom Physiol Opt* 56 (5):315–23. doi: 10.1097/00006324-197905000-00006.
- Atchison, D. A., R. L. Woods, and A. Bradley. 1998. "Predicting the effects of optical defocus on human contrast sensitivity." *J Opt Soc Am A* 15 (9):2536–44. doi: 10.1364/josaa.15.002536.
- Campbell, F. W. 1957. "The depth of field of the human eye." *Optica Acta* 4 (4):157–66.
- Campbell, F. W., and D. G. Green. 1965. "Optical and retinal factors affecting visual resolution." *J Physiol* 181 (3):576–93. doi: 10.1113/jphysiol.1965.sp007784.
- Campbell, F.W., and R.W. Gubisch. 1967. "The effect of chromatic aberration on visual acuity." *J Physiol (Lond)* 192 (2):345–58. doi: 10.1113/jphysiol.1967.sp008304.
- Carroll, J. P. 1980. "Apodization model of the Stiles-Crawford effect." *J Opt Soc Am* 70 (9):1155–6. doi: 10.1364/josa.70.001155.
- Charman, W. N., J. A. Jennings, and H. Whitefoot. 1978. "The refraction of the eye in the relation to spherical aberration and pupil size." *Br J Physiol Opt* 32:78–93.
- Charman, W. N., and G. Walsh. 1985. "The optical phase transfer function of the eye and the perception of spatial phase." *Vision Res* 25 (4):619–23. doi: 10.1016/0042-6989(85)90169-5.
- Charman, W. N., and H. Whitefoot. 1977. "Pupil diameter and the depth-of-focus of the human eye for Snellen letters." *Optica Acta* 24 (12):1211–6.
- Cheng, X., A. Bradley, and L. N. Thibos. 2004. "Predicting subjective judgment of best focus with objective image quality metrics." *J Vis* 4 (4):310–21. doi: 10.1167/4.4.7.
- Curcio, C. A., and K. A. Allen. 1990. "Topography of ganglion cells in human retina." *J Comp Neurol* 300 (1):5–25. doi: 10.1002/cne.903000103.
- Green, D. G. 1970. "Regional variations in the visual acuity for interference fringes on the retina." *J Physiol* 207 (2):351–6. doi: 10.1113/jphysiol.1970.sp009065.
- Green, D. G. 1967. "Visual resolution when light enters the eye through different parts of the pupil." *J Physiol (Lond)* 190 (3):583–93. doi: 10.1113/jphysiol.1967.sp008229.
- Green, D. G., and F. W. Campbell. 1965. "Effect of focus on the visual response to a sinusoidally modulated spatial stimulus." *J Opt Soc Am* 55 (9):1154–7. doi: 10.1364/JOSA.55.001154.

- Guirao, A. 2017. "Chapter 18. Optical and visual metrics." In *Handbook of Visual Optics: Instrumentation and Vision Correction, Volume II* edited by P. Artal, 276–97. London: CRC Press.
- Guo, H., D. A. Atchison, and B. J. Birt. 2008. "Changes in through-focus spatial visual performance with adaptive optics correction of monochromatic aberrations." *Vision Res* 48 (17):1804–11. doi: 10.1016/j.visres.2008.04.033.
- Iglesias, I., E. Berrio, and P. Artal. 1998. "Estimates of the ocular wave aberration from pairs of double-pass retinal images." *J Opt Soc Am A* 15 (9):2466–76. doi: 10.1364/josaa.15.002466.
- Iglesias, I., N. López-Gil, and P. Artal. 1998. "Reconstruction of the point-spread function of the human eye from two double-pass retinal images by phase-retrieval algorithms." *J Opt Soc Am A* 15 (2):326–39. doi: 10.1364/josaa.15.000326.
- Jaeken, B., and P. Artal. 2012. "Optical quality of emmetropic and myopic eyes in the periphery measured with high-angular resolution." *Invest Ophthalmol Vis Sci* 53 (7):3405–13. doi: 10.1167/iovs.11-8993.
- Jaisankar, D., M. Suheimat, R. Rosen, and D. A. Atchison. 2022. "Defocused contrast sensitivity function in peripheral vision." *Ophthalmic Physiol Opt* 42 (2):384–92. doi: 10.1111/opo.12932.
- Koomen, M., R. Scolnik, and R. Tousey. 1951. "A study of night myopia." *J Opt Soc Am* 41 (2):80–90. doi: 10.1364/JOSA.41.000080.
- Koomen, M., R. Tousey, and R. Scolnik. 1949. "The spherical aberration of the eye." *J Opt Soc Am* 39 (5):370–6. doi: 10.1364/josa.39.000370.
- Krakau, C. E. 1974. "Letter: On the Stiles-Crawford phenomenon and resolution power." *Acta Ophthalmol (Copenh)* 52 (4):581–3. doi: 10.1111/j.1755-3768.1974.tb01768.x.
- Legge, G. E., K. T. Mullen, G. C. Woo, and F. W. Campbell. 1987. "Tolerance to visual defocus." *J Opt Soc Am A* 4 (5):851–63. doi: 10.1364/josaa.4.000851.
- Liang, J., and D. R. Williams. 1997. "Aberrations and retinal image quality of the normal human eye." *J Opt Soc Am A* 14 (11):2873–83. doi: 10.1364/josaa.14.002873.
- Liang, J., D. R. Williams, and D. T. Miller. 1997. "Supernormal vision and high-resolution retinal imaging through adaptive optics." *J Opt Soc Am A* 14 (11):2884–92. doi: 10.1364/josaa.14.002884.
- Lundström, L., and R. Rosén. 2017. "Chapter 21. Peripheral aberrations." In *Handbook of Visual Optics: Fundamentals and Eye Optics, Volume I* edited by P. Artal, 313–35. London: CRC Press.
- Marcos, S., J. S. Werner, S. A. Burns, W. H. Merigan, et al. 2017. "Vision science and adaptive optics, the state of the field." *Vision Res* 132:3–33. doi: 10.1016/j.visres.2017.01.006.
- Marcos, S., P. Artal, D. A. Atchison, K. M. Hampson, et al. 2022. "Adaptive optics visual simulators: a review of recent optical designs and applications. [Invited]" *Biomed Opt Express* 13(12):6508–32. doi: 10.1364/BOE.473458.
- Marsack, J. D., L. N. Thibos, and R. A. Applegate. 2004. "Metrics of optical quality derived from wave aberrations predict visual performance." *J Vis* 4 (4):322–8. doi: 10.1167/4.4.8.
- Metcalf, H. 1965. "Stiles-Crawford apodization." *J Opt Soc Am* 55 (1):72–4. doi: 10.1364/JOSA.55.000072.
- Navarro, R., P. Artal, and D. R. Williams. 1993. "Modulation transfer of the human eye as a function of retinal eccentricity." *J Opt Soc Am A* 10 (2):201–12. doi: 10.1364/josaa.10.000201.
- Navarro, R., and M. A. Losada. 1995. "Phase transfer and point-spread function of the human eye determined by a new asymmetric double-pass method." *J Opt Soc Am A Opt Image Sci Vis* 12 (11):2385–92. doi: 10.1364/josaa.12.002385.

- Navarro, R., E. Moreno, and C. Dorronsoro. 1998. "Monochromatic aberrations and point-spread functions of the human eye across the visual field." *J Opt Soc Am A Opt Image Sci Vis* 15 (9):2522–9. doi: 10.1364/josaa.15.002522.
- Piotrowski, L. N., and F. W. Campbell. 1982. "A demonstration of the visual importance and flexibility of spatial-frequency amplitude and phase." *Perception* 11 (3):337–46. doi: 10.1080/p110337.
- Rosén, R., L. Lundström, and P. Unsbo. 2011. "Influence of optical defocus on peripheral vision." *Invest Ophthalmol Vis Sci* 52 (1):318–23. doi: 10.1167/iovs.10-5623.
- Santamaría, J., P. Artal, and J. Bescos. 1987. "Determination of the point-spread function of human eyes using a hybrid optical-digital method." *J Opt Soc Am A* 4 (6):1109–14. doi: 10.1364/josaa.4.001109.
- Smith, G. 1982. "Ocular defocus, spurious resolution and contrast reversal." *Ophthalmic Physiol Opt* 2 (1):5–23.
- Smith, G., and D. A. Atchison. 1997. "Chapter 25. Interferometry and interferometers." In *The Eye and Visual Optical Instruments*, 505–25. London: Cambridge University Press.
- Still, D. L. 1989. "Optical limits to contrast sensitivity in human peripheral vision." PhD, Optometry, Indiana University.
- Thibos, L. N., and A. Bradley. 1993. "New methods for discriminating neural and optical losses of vision." *Optom Vis Sci* 70 (4):279–87. doi: 10.1097/00006324-199304000-00006.
- Thibos, L. N., F. E. Cheney, and D. J. Walsh. 1987. "Retinal limits to the detection and resolution of gratings." *J Opt Soc Am A* 4 (8):1524–9. doi: 10.1364/josaa.4.001524.
- Thibos, L. N., X. Hong, A. Bradley, and R. A. Applegate. 2004. "Accuracy and precision of objective refraction from wavefront aberrations." *J Vis* 4 (4):329–51. doi: 10.1167/4.4.9.
- Thibos, L. N., D. L. Still, and A. Bradley. 1996. "Characterization of spatial aliasing and contrast sensitivity in peripheral vision." *Vision Res* 36 (2):249–58. doi: 10.1016/0042-6989(95)00109-d.
- Thibos, L. N., A. Bradley, and D. L. Still. 1991. "Interferometric measurement of visual acuity and the effect of ocular chromatic aberration." *Appl Opt* 30 (16):2079–87. doi: 10.1364/AO.30.002079.
- Thibos, L. N., A. Bradley, and X. Zhang. 1991. "Effect of ocular chromatic aberration on monocular visual performance." *Optom Vis Sci* 68 (8):599–607. doi: 10.1097/00006324-199108000-00005.
- Tucker, J., and W. N. Charman. 1975. "The depth-of-focus of the human eye for Snellen letters." *Am J Optom Physiol Opt* 52 (1):3–21. doi: 10.1097/00006324-197501000-00002.
- van Meeteren, A. 1974. "Calculations on the optical modulation transfer function of the human eye for white light." *Optica Acta* 21 (5):395–412.
- van Meeteren, A., and C. J. Dunnewold. 1983. "Image quality of the human eye for eccentric entrance pupils." *Vision Res* 23 (5):573–9. doi: 10.1016/0042-6989(83)90133-5.
- Walsh, G., and W. N. Charman. 1985. "Measurement of the axial wavefront aberration of the human eye." *Ophthalmic Physiol Opt* 5 (1):23–31.
- Wang, Y. Z., L. N. Thibos, and A. Bradley. 1997. "Effects of refractive error on detection acuity and resolution acuity in peripheral vision." *Invest Ophthalmol Vis Sci* 38 (10):2134–43.
- Westheimer, G. 1959. "Retinal light distribution for circular apertures in Maxwellian view." *J Opt Soc Am* 49 (1):41–4. doi: 10.1364/josa.49.000041.
- Williams, D. R. 1985. "Visibility of interference fringes near the resolution limit." *J Opt Soc Am A* 2 (7):1087–93. doi: 10.1364/josaa.2.001087.

- Williams, D. R., P. Artal, R. Navarro, M. J. McMahon, and D. H. Brainard. 1996. "Off-axis optical quality and retinal sampling in the human eye." *Vision Res* 36 (8):1103–14. doi: 10.1016/0042-6989(95)00182-4.
- Woods, R. L., N. C. Strang, and D. A. Atchison. 2000. "Measuring contrast sensitivity with inappropriate optical correction." *Ophthalmic Physiol Opt* 20 (6):442–51. doi: 10.1016/S0275-5408(99)00089-7.
- Zhang, X., A. Bradley, and L. N. Thibos. 1993. "Experimental determination of the chromatic difference of magnification of the human eye and the location of the anterior nodal point." *J Opt Soc Am A* 10 (2):213–20. doi: 10.1364/josaa.10.000213.

Section V

Miscellaneous



Taylor & Francis
Taylor & Francis Group
<http://taylorandfrancis.com>

19 Depth-of-Field

19.1 INTRODUCTION

In any optical system, the ultimate precision in focusing is set by the ability to detect errors in focus. The range of distances over which the system's detector cannot detect any change in focus is called the depth-of-field, and this range may be specified by a movement of the object plane or by the corresponding movement of the image plane. Because these two distances are usually different, some textbooks differentiate between depth-of-field, a movement of the object plane, and depth-of-focus, a movement of the image plane. In vision science, depth-of-field is usually expressed as a change in reduced vergence, which has the same value in both object and image space. Hence, generally we will use the term depth-of-field to cover both object and image situations. Distinctions can be made between object and image space quantities where this is necessary, such as when using visual optical instruments.

The general definition adopted here for depth-of-field is the vergence range of focusing error $\Delta L'$ (in diopters), which does not result in objectionable deterioration in retinal image quality. This is sometimes referred to as the *total* depth-of-field. This can be determined according to a few criteria. Some studies mentioned in this chapter used half the total depth-of-field and expressed values as $\pm \Delta L'$, e.g., Campbell (1957). When referring to such studies in this chapter, their numbers have been doubled. This is satisfactory where depth-of-field is measured in just one direction from a focus position, or where simple theory is used in which the depth-of-field is symmetrical about the position of focus.

While we have used the word "objectionable" in the above definition of depth-of-field, distinction can be made between what may be regarded as merely noticeable, what is troublesome and what is objectionable (Atchison et al. 2009). An example of where this is useful is the design of progressive addition spectacle lenses where it is useful to know the blur levels that wearers are likely to tolerate. Furthermore, as it is possible to manipulate aberrations other than defocus, such that objectionable deterioration in these may be determined (Atchison and Guo 2010), a more general term than depth-of-field, such as blur limits, is sometimes appropriate.

The depth-of-field sets the precision to which refractive state, including the amplitude of accommodation, can be measured by subjective methods. It also determines the distance range for which a target can be seen clearly when using visual optical instruments, such as simple magnifiers, microscopes, and telescopes. For example, the depth-of-field of a simple magnifier or microscope of magnification M can be given as a total distance Δl_m in object space. This distance is related to the depth-of-field of the eye $\Delta L'$ by the approximate equation (Smith and Atchison 1997)

$$\Delta l_m = \Delta L' / (16M^2) \quad (19.1a)$$

As another example, the depth-of-field of a two-lens afocal telescope of magnification M can be given as a total vergence in object space ΔL_t , and this is related to the depth-of-field of the eye $\Delta L'$ by

$$\Delta L_t = \Delta L/M^2 \quad (19.1b)$$

Increasing the depth-of-field is advantageous in some circumstances. For example, the loss of accommodation can be ameliorated by increasing depth-of-field. One way to do this is to introduce additional aberrations, but there is a trade-off as peak optical and visual performance will be reduced (Cheng et al. 2004; Guo et al. 2008).

Depth-of-field depends upon several factors, including

1. *Optical properties of the eye*
 - pupil diameter (interacts with the other optical properties and whether one eye or two eyes are being used)
 - accommodation level
 - monochromatic and chromatic aberrations
 - diffraction.
2. *Retinal and visual processing properties*
 - photoreceptor size and ganglion cell density
 - Stiles–Crawford factor
 - Binocular factors such as binocular summation
 - visual acuity and contrast thresholds
 - disease in ocular pathway.
3. *Target properties*
 - luminance
 - spatial detail
 - contrast
 - spectral profile, e.g., color.

One complication in determining depth-of-field, except in complete presbyopia, is accommodation. Attempting to induce hyperopic blur, such as by putting negative lenses in front of the eye, can be overcome by accommodation and thus depth-of-field is over-estimated. This complication can be removed by paralyzing accommodation with cycloplegic drugs or by determining depth-of-field in only the myopic direction, but the problem with the latter is the accurate determination of a reference position.

Depth-of-field in the eye can be explained at a simple level using the defocus blur disc model of defocused systems (Chapter 9) and the size of the detector elements in the image plane. In an aberration and diffraction-free system, the image of a defocused point is a defocus blur disc. If this disc is smaller than a detector element, the system will not be able to detect defocus. Defocus will be detectable only once the defocus blur disc overlaps at least two detectors. Because this model neglects aberrations, diffraction, and how the visual system processes retinal images, e.g., interactions between adjacent receptors, it is a crude model and cannot be expected to predict accurately the depth-of-field of the eye.

In the following sections we look at experimentally determined values, and consider models, such as the above defocus blur disc model, that can be used to predict depth-of-field.

19.2 CRITERIA FOR DETERMINING DEPTH-OF-FIELD

There are several criteria for measuring depth-of-field according to a focusing error range that causes an “objectionable deterioration in retinal image quality”. Five of these are considered here. Because these criteria may depend upon different optical, neural, and psychological factors, it is not always meaningful to compare depth-of-field results based on different criteria. The common feature of experimental results according to most criteria is that depth-of-field decreases as pupil size increases, at least out to 5–6 mm pupil diameters.

19.2.1 CRITERION 1: THE RANGE OF FOCUSING ERRORS FOR WHICH NO PERCEPTEBLE BLUR OF A TARGET IS NOTICEABLE

This criterion is relevant to subjective refraction and determining the amplitude of accommodation. The vergence of the target is varied, and the extremes at which the target first appears to be blurred are measured. The details of presentation can vary. The target can be moved backwards and forwards to locate the range within which it appears to be in focus (Campbell 1957; Atchison et al. 1997). Two targets may be presented, either in succession or simultaneously side-by-side, one in focus and the other with various levels of defocus, and the subject is asked to decide which is not in focus (Jacobs et al. 1989).

In section 19.1, a distinction was made between noticeable, troublesome, and objectionable blurs. The former is used to describe criterion 1, but the criterion could be altered to include, as appropriate, troublesome, and objectionable blur, e.g., the range of focusing errors for which no troublesome blur occurs.

Instead of altering the optics, the source may be blurred when it is an image on the screen by image-processing methods, such as convolving an in-focus image with the defocused point-spread function. This *source method* approach has been used in several studies in which blur is simulated for large pupils and viewed with well-corrected eyes and small pupils, e.g., Cheng et al. (2010). Blur limits for aberrations other than defocus can also be determined.

Studies using this criterion show that the depth-of-field decreases with increase in pupil diameter (Campbell 1957; Atchison et al. 1997) (Figure 19.1), increasing target luminance, and correction of longitudinal chromatic aberration of the eye (Campbell 1957) As an example of the dependence on pupil size, in Campbell’s study the depth-of-field decreased from 1.7 D to 0.3 D between the pupil diameters of 1 mm and 7 mm (Figure 19.1). Depth-of-field is smallest for target sizes near the visual acuity limit, and increases slowly with increase in target size (Jacobs et al. 1989; Atchison et al. 1997; Atchison et al. 2009) (Figure 19.2). Jacobs et al. (1989) measured the threshold of just detectable change in defocus of an already defocused target and found that the threshold was slightly less than the depth-of-field.

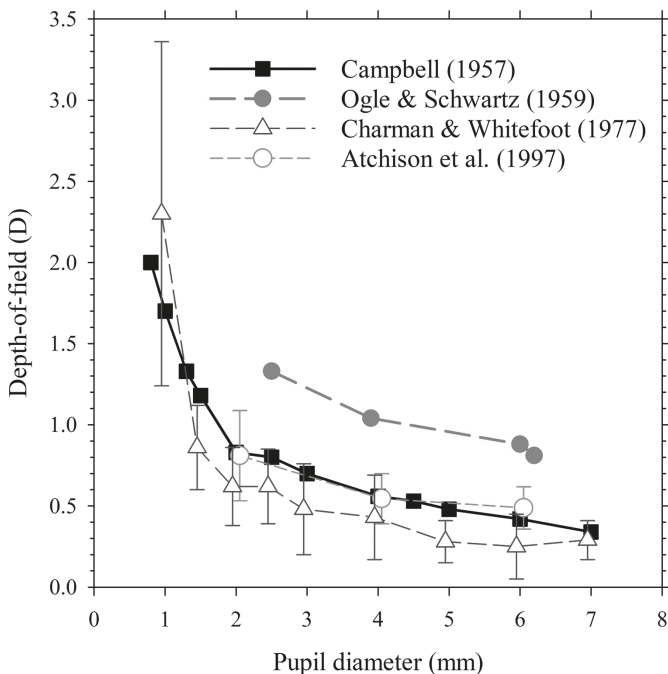


FIGURE 19.1 Depth-of-field as a function of pupil size from different studies. Campbell (1957): threshold blur, retinal illuminance constant (corresponding to 318 cd/m² at 1 mm pupil diameter), one participant. Ogle and Schwartz (1959): 50 per cent probability limits of correctly resolving checkerboard with equivalent letter size 6/7.5, one participant. Charman and Whitefoot (1977): limits of depth-of-field give 95% correct identification of the direction of movement of laser speckle, mean of six participants, error bars indicate ± 1 standard deviation of subjects. Atchison et al. (1997): threshold blur, 6/7.5 letter E, mean of five participants, error bars indicate ± 1 standard deviation of subjects.

19.2.2 CRITERION 2: THE RANGE OF FOCUSING ERRORS FOR WHICH THE VISUAL ACUITY OR CONTRAST SENSITIVITY DOES NOT DECREASE BELOW A PARTICULAR LEVEL OR BY MORE THAN A CERTAIN AMOUNT

Figure 19.3 shows an example of criterion 2 for visual acuity. Here higher-order aberrations are either uncorrected or are corrected with a deformable mirror (Guo et al. 2008). At best focus, the visual acuity for the no adaptive optics correction is poorer than for the adaptive optics condition by 0.07 log unit. Setting the visual acuity threshold to 0.07 logMAR, the depth-of-field is 1.1 D for the no adaptive optics condition and is 0.9 D with the adaptive optics correction. If the depth-of-field is determined by a loss in visual acuity of 0.15 logMAR, the limits for the no adaptive optics condition are unchanged but reduce to 0.6 D with adaptive optics correction. To highlight the dependency of depth-of-field on the criterion level, if a stringent visual acuity threshold of -0.1 logMAR had been adopted, the depth-of-field for the no adaptive optics condition would be zero and hence less, rather than greater, than with the adaptive optics correction (0.3 D).

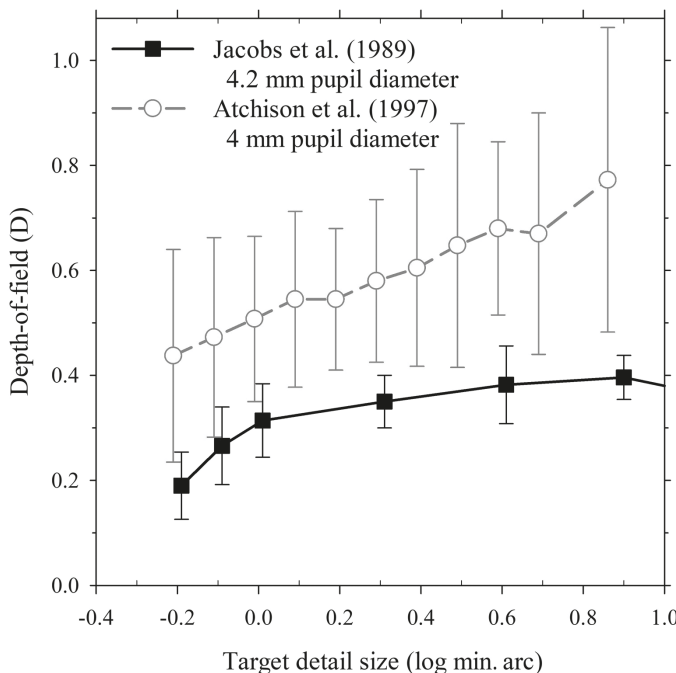


FIGURE 19.2 Depth-of-field as a function of target size. Jacobs et al. (1989) measured the depth-of-field in only one direction from the optimum focus, and their results have been doubled so that they are comparable with those of Atchison et al. (1997).

Applying criterion 2 to contrast sensitivity, depth-of-field depends on spatial frequency. Using the data in Figure 19.4 with a criterion of 0.3 log units of contrast sensitivity loss, depth-of-field reduces from 0.9 D at 10 c/deg to 0.5 D at 30 c/deg.

Criterion 2 is used in an intraocular lens standard (International Standardization Organization 2022), for which the criterion is 0.2 logMAR. For *extended depth-of-focus* lenses, the range of added negative lenses for which this shall occur is -1.5 D to less than -2.5 D.

19.2.3 CRITERION 3: THE RANGE OF FOCUSING ERRORS FOR WHICH CHANGES IN CONTRAST ARE NOT DETECTED FOR A TARGET IN LONGITUDINAL SINUSOIDAL MOTION

The subject views a target through a Badal optical system. The target is usually periodic, i.e., the luminance profile is generally that of a sine wave or square wave. As measured as a vergence at the eye, the target is moved forwards and backwards in sinusoidal motion. The peak-to-peak amplitude of the movement is varied until the subject can detect apparent variation in the target's contrast (for non-periodic targets some other criterion can be used, such as the appearance of blur or changes in target shape).

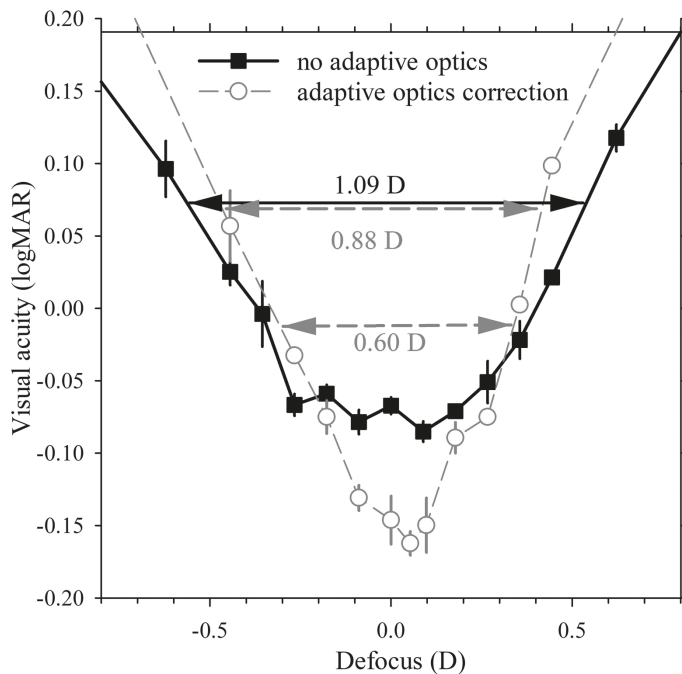


FIGURE 19.3 Visual acuity as a function of defocus. Square symbols are for the no adaptive optics correction and open circle symbols are for the adaptive optics correction. The top two straight lines indicate depth-of-field for 0.07 logMAR visual acuity and the top and bottom straight lines indicate 0.15 logMAR loss of visual acuity (top line for no adaptive optics and bottom line for adaptive optics correction). Monochromatic light (550 nm), pupil diameter 5.5 mm, luminance 8 cd/m². Error bars are standard deviations. These results are included in Figure 15.15. Data are from Figure 4 of Guo et al. (2008), with permission from Elsevier.

The depth-of-field is a minimum when the center of the range is slightly off-set to one side of the optimal focus (Campbell and Westheimer 1958; Walsh and Charman 1988) (Figure 19.5). Typically, the depth-of-field at optimal focus is 0.6 D, while the minimum depth-of-field is approximately 0.2 D (Walsh and Charman 1988). The effect of increasing pupil size is to decrease the difference between the optimum focus and the center of the range at which the minimum depth-of-field occurs. Walsh and Charman investigated a range of variables, including target color, luminance, and temporal frequency.

19.2.4 CRITERION 4: THE RANGE OF FOCUSING ERRORS FOR WHICH THE ACCOMMODATION RESPONSE DOES NOT CHANGE

This criterion has been used little. Change in accommodative response is measured objectively. Mordi and Ciuffreda (1998) found objective depth-of-field to be smaller at 0.76 D than subjectively at 1.24 D, but Vasudevan et al. (2007) did not find any difference.

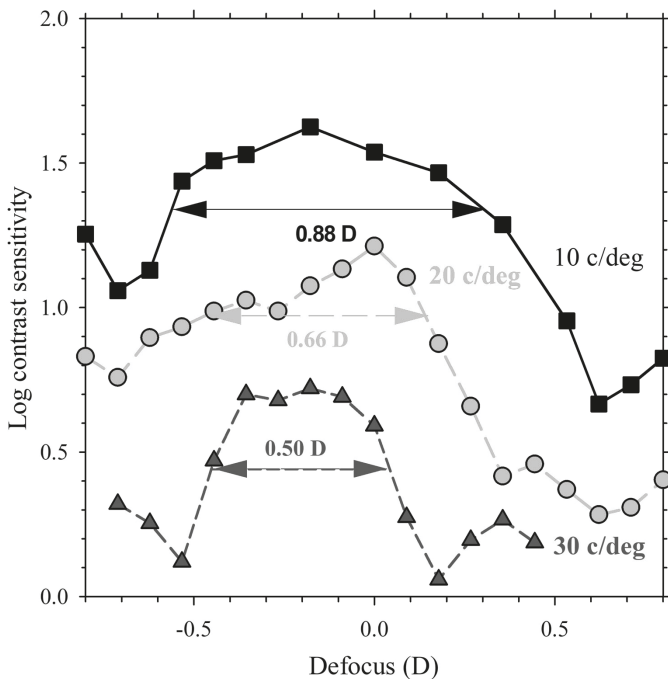


FIGURE 19.4 Contrast sensitivity of sinusoidal gratings as a function of defocus at three spatial frequencies: monochromatic light (550 nm), pupil diameter 5.5 mm, luminance 35 cd/m². The numbers show the depth-of-field for a criterion of 0.3 log unit loss of contrast sensitivity relative to peak contrast sensitivity. Data are from Guo et al. (2008), with permission from Elsevier Press.

19.2.5 CRITERION 5: THE RANGE OF FOCUSING ERRORS WHICH DEGRADES RETINAL IMAGE QUALITY BELOW A PARTICULAR LEVEL OR BY MORE THAN A CERTAIN AMOUNT

This is the objective equivalent to criterion 2. Many of the image quality metrics described in Chapter 18 can be used, e.g., the point-spread function and modulation transfer functions and their derivatives. The depth-of-field is the computationally determined range of focus for which a metric exceeds a particular value or exceeds a particular proportion of the peak value. The attraction of image quality metrics for estimating DOF is that the only required clinical/experimental measurement is an eye's aberrations. Yi et al. (2010) compared depth-of-field estimates obtained with the visual Strehl ratio, described in section 18.5, with the subjective "just noticeable" blur criterion using a 0.6 logMAR letter. The subjective limits corresponded to the range in which the visual Strehl ratio was above 66±10% and 37±18% of its maximum values for 5 mm and 3.5 mm pupils, respectively. Their results indicated that under some circumstances an individual's subjective depth-of-field may be determined from a single measurement of the aberrations.

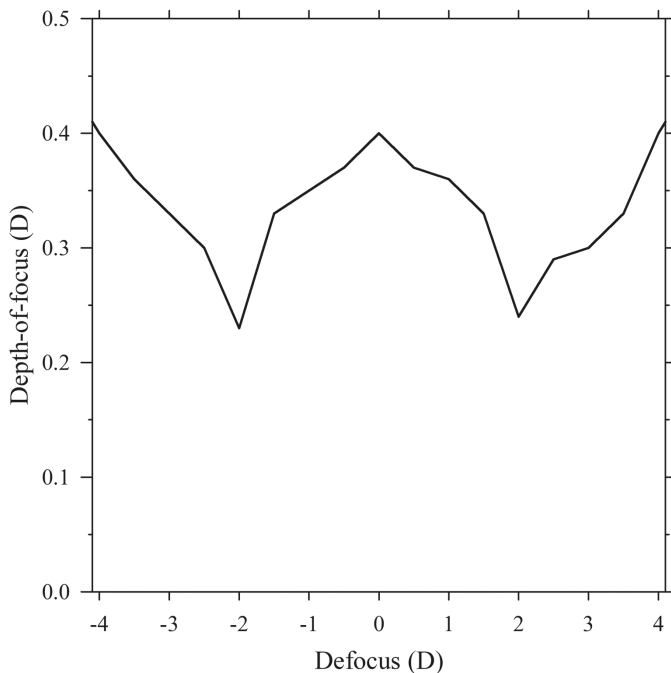


FIGURE 19.5 Depth-of-field as a function of central focus setting relative to the in-focus setting. Depth-of-field without an offset is approximately 0.4 D but reduces to a minimum of approximately 0.2 D at ± 2 D offset. Based on data of Walsh and Charman (1988), with green color, 3 mm pupil diameter, 2.55 c/deg spatial frequency and 2 Hz oscillation.

19.3 MODELING DEPTH-OF-FIELD

Various models will be discussed here that can be used in understanding the factors that affect depth-of-field, by examining the optics of defocused images using two image quality criteria at various levels of complexity.

19.3.1 CRITERION 1: THE RANGE OF FOCUSING ERRORS FOR WHICH NO PERCEPTEBLE BLUR OF A TARGET IS NOTICEABLE

The threshold of blur can be modeled by examining the image of a defocused point source of light and making assumptions about the threshold of defocus. We will begin by considering the simplest of models, assuming that the system is aberration- and diffraction-free and, therefore, a point is imaged as a point. When this point is defocused, its image is a uniformly illuminated blur disc as already referred to in the previous section.

Equation (9.17) gave the angular diameter Φ of the defocus blur disc as

$$\Phi = D \Delta L \quad (19.2a)$$

where D is pupil diameter and ΔL is refractive error. Using (total) depth-of-field to replace the refractive error, this equation becomes

$$\Phi = D \Delta L / 2 \quad (19.2b)$$

We will now assume that the depth-of-field is set by the range over which this defocus blur disc is smaller than a certain threshold diameter. If this diameter is Φ_{th} , the depth-of-field is

$$\Delta L = 2\Phi_{\text{th}} / D \quad (19.3a)$$

This equation predicts that the depth-of-field is inversely proportional to the pupil diameter.

The smallest meaningful estimate of Φ_{th} is obtained using the diameter of a central foveal cone, which is approximately 0.0023 mm (Curcio et al. 1990). At the back nodal point, a 0.0023 mm distance subtends an angular diameter of

$$\approx 0.0023/17 \approx 0.00013 \text{ rad} (\approx 0.44 \text{ min. arc})$$

where 17 mm is the approximate distance from the back nodal point to the retina. Substituting this value for Φ_{th} in equation (19.3a) gives the threshold of defocus as

$$\Delta L = 0.00026 / D \quad (19.3b)$$

If we use a pupil diameter of 3 mm, i.e., $D = 0.003 \text{ m}$, this equation gives a depth-of-field of 0.09 D, which is much less than the experimental values given in the preceding section. Therefore, there are serious flaws in this model.

19.3.1.1 Effects of Diffraction and Aberrations

Because of diffraction and aberrations, the focused image of a point is not a point but a patch of light – the point spread function as discussed in section 18.2. The size of this patch depends upon the pupil diameter since both diffraction and aberrations depend upon the size of the pupil.

In the presence of diffraction and aberrations, the point spread function is much more complex than a uniform disc, and this complexity presents problems in measuring its diameter. In such cases, the diameter or width is often represented by its half-width, which is the width at which the light level drops to half the central or maximum value. In-focus point spread functions have half-widths of about 2–3 minutes of arc.

We will now adopt the defocus, which would produce a blur disc equal to the half-width of the in-focus point spread function, for our blur detection model. Any defocus with a blur disc less than this size can be expected to have little chance of being detected. Taking the threshold of blur disc size Φ_{th} as 2 min. arc (i.e., 0.000582 rad), we put $\Phi_{\text{th}} = 0.000582$ in equation (19.3a) to obtain

$$\Delta L = 0.00116 / D \quad (19.3c)$$

For a pupil diameter of 3 mm this equation gives a depth-of-field value of 0.38 D, which is much closer to experimental values (Figure 19.1).

19.3.1.2 Influence of Diffraction Alone at Small Pupil Diameters

At small pupil diameters, e.g., 2 mm, the threshold value Φ_{th} is governed by diffraction and not by aberrations. Diffraction theory predicts that the width of the point spread function is proportional to wavelength and inversely proportional to pupil diameter (equation (18.5)). Thus, and assuming Φ_{th} follows the same trend, equation (19.3a) becomes

$$\Delta L \propto \mu\lambda/D^2 \quad (19.4)$$

This equation predicts that, for small pupil sizes, the depth-of-field is inversely proportional to the square of pupil diameter.

19.3.1.3 Influence of Aberrations Alone at Large Pupil Diameters

As pupil diameter increases, the effects of diffraction become less, and the influence of aberrations increases. For larger pupil diameters, the point spread function can be regarded as being affected by aberrations alone.

As aberrations usually increase with pupil diameter, the size of the focused point spread function is expected to increase with pupil diameter, and the threshold diameter Φ_{th} of the defocus blur disc is expected to increase. In the presence of primary spherical aberration, the transverse aberration at the edge of the pupil is proportional to the cube of the pupil diameter. Therefore, we could expect that Φ_{th} would show some higher-order dependence on pupil diameter. For large pupil sizes, from equation (19.3a) it is expected that depth-of-field increases with increase in pupil diameter. However, from the results of Figure 19.1 this does not happen out to at least 5–6 mm in diameter. This may be because the aberrations of the eye are too low to have a large effect, or because the aberrations are too irregular. The Stiles–Crawford effect (section 14.5) may play a small role here by reducing the effect of aberrations and defocus at larger pupil sizes.

19.3.1.4 More Complex Objects

We have so far examined the effect of defocus only on the image of a point object. This is not realistic since few scenes are composed of point sources. On the other hand, edges are very common, and we will consider a sharp luminous edge of high contrast. Using the defocus blur disc model, a luminance profile slope forms at the image, and the width of this edge is equal to the width of the corresponding defocus blur disc. The threshold for defocus will depend in some complex manner on the width of the image edge and on the image's contrast.

Now suppose that the edge is the edge of a bar of a finite width (e.g., in a letter). The defocus now has two phases. In the first phase (low levels of defocus), only the edge of the image is affected. The second phase begins once the defocus reaches the level when the two sloping edges (on either side of the bar) of the image meet in the center. Once this occurs, the contrast of the bar is reduced. The narrower the bar, the sooner this second phase occurs. Depending upon how the visual system detects defocus, it may be more sensitive to this reduction in image contrast than on the profile of the image's edge.

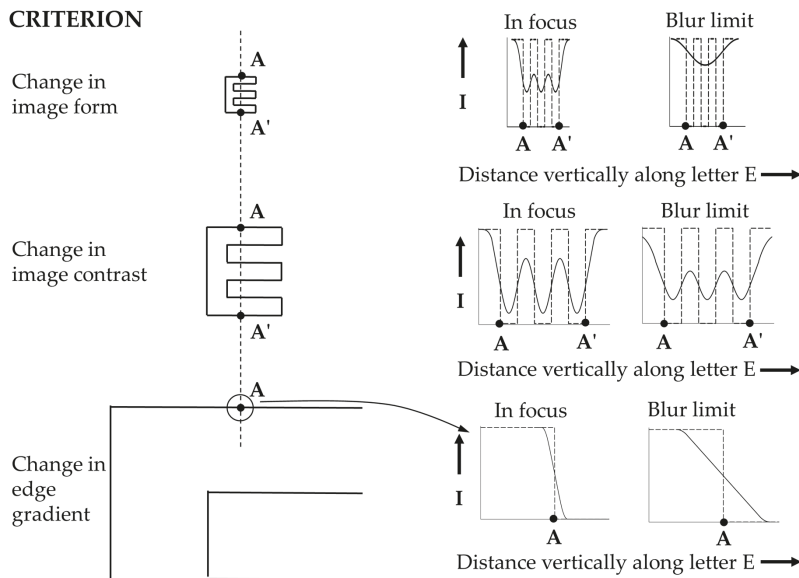


FIGURE 19.6 A model for determining of what is perceptible blur of a letter. For a small letter (top), the low spatial frequency information in the letter is used; for an intermediate-sized letter (middle), the contrast between light and dark bars in the image is used; for a large letter (bottom), the luminance slope at the image edge is used.

These considerations suggest that depth-of-field depends on target size. Atchison et al. (1997) developed a model to describe how the visual system might change its criterion of what is perceptible blur, according to the size of letter targets (Figure 19.6). According to this model, for very small letter sizes (e.g., < 0.0 log min. arc of target detail), the perception of blur is based on low spatial frequency information in the letters. This low spatial frequency information affects mainly the overall contrast of the retinal image of the letter against its background. As letter size increases, the fundamental spatial frequency of the pattern moves into the spatial frequency range at which modulation transfer is very sensitive to defocus, and thus the contrast between dark and light bars of an image is important. For even larger letter sizes (e.g., > 1.0 log min. arc of target detail), the spatial frequency of the fundamental is so low that its modulation transfer is relatively unaffected by defocus. However, higher-order harmonics in the letter will be at spatial frequencies whose modulation transfer is affected by defocus. These are important to the detection of edges, so the perception of blur may be now based on edge sharpness rather than bar contrast.

19.3.2 CRITERION 5: THE RANGE OF FOCUSING ERRORS, WHICH DEGRADES RETINAL IMAGE QUALITY BELOW A PARTICULAR LEVEL OR BY MORE THAN A CERTAIN AMOUNT

Image quality metrics such as the visual Strehl ratio mentioned in section 18.5 can be considered to be modeling approaches, e.g., Dhallu et al. (2019). By correlating

them with changes in visual acuity or contrast sensitivity as defocus varies, they can be used to predict subjective depth-of-field. Watson and Ahumada (2008) used a sophisticated decision process to predict visual acuity from wavefront aberrations, and this approach could be modified to predict depth-of-field based on visual acuity thresholds.

19.4 METHODS FOR INCREASING DEPTH-OF-FIELD

There are two conflicting principles in ophthalmic correction. The first principle is the minimization of aberrations, including where possible the higher-order aberrations, to improve in-focus vision. The second principle is the deliberate increase in aberrations so that the rate of deterioration of the quality of vision away from best focus is reduced. The balance applied to these principles depend upon accommodative ability and pupil size, with high accommodation and larger pupils favoring the former and with poor (or non-existent) accommodation and small pupils favoring the latter. Essentially, the balance depends on age. The benefits of the second approach, in which depth-of-field is deliberately increased, for presbyopia are obvious, but are obtained at the expense of lowered optimum visual acuity and contrast sensitivity.

19.4.1 ARTIFICIAL PUPILS

One simple way to increase DOF is to include a small artificial pupil (2 mm diameter or smaller) near the position of the actual pupil; this can be referred to as *pinhole optics* or *small aperture optics*. This reduces the diameter of the retinal blur circles at any level of defocus and hence increases depth-of-field. It can be applied as corneal inlays, as intraocular lenses, or as miotic eye drops (Charman 2019; Charman et al. 2019; Montes-Mico and Charman 2019). This approach can be applied to one eye only, with the potential disadvantage of creating a retinal illuminance difference between the two eyes that may be disturbing: perceptual latency in the eye with the lower retinal illuminance may result in incorrect perception of the paths of moving objects or of the positions of static objects when a person is moving (the *Pulfrich effect*) (Plainis et al. 2013).

19.4.2 ASPHERIC SURFACES

Ophthalmic correcting devices for which there is simultaneous correction of distance and near vision are referred to as “simultaneous vision” devices. One type uses aspheric surfaces to give variable surface power

The asphericity of a surface of a cornea, contact lens, or intraocular lens may be manipulated to alter aberrations, in particular spherical aberration. In IOLs, spherically surfaced intraocular lenses contribute positive spherical aberration to the eye that adds to the normally positive spherical aberration of the cornea. Negative asphericity can be added to one surface to optimize in-focus performance (Atchison 1989). Alternatively, applying positive asphericity increases spherical aberration for both contact lenses and intraocular lenses that can aid presbyopes by the effective add supplied.

The asphericity Q of a conicoid surface is related to the sagitta Z of the surface by equations given in sections 2.2.4 and 16.3. Equation (16.3c) is

$$Z = \frac{ch^2}{1 + \sqrt{1 - c^2(1+Q)}h^2} \quad (19.5)$$

where c is vertex curvature of the surface and h is height at the surface. Q is negative if the surface flattens away from the vertex. The change LSA in power from the center to height h , or the longitudinal spherical aberration associated with h , produced by a change in surface asphericity ΔQ is given approximately by (Atchison 1989)

$$LSA = c^3 h^2 \Delta Q (n' - n) / 2 \quad (19.6)$$

where n and n' are the refractive indices on either side of the surface. The change in longitudinal spherical aberration can be related to the change in wave aberration spherical aberration over the same height. If the spherical aberration change is given as a change in Zernike aberration coefficient Δc_4^0 , then equation (15.27c) applies:

$$LSA = 24\sqrt{5}\Delta c_4^0 / h^2 \quad (19.7)$$

Combining the equations (19.6) and (19.7) gives

$$\Delta Q = 48\sqrt{5}\Delta c_4^0 / [h^4 c^3 (n' - n)] \quad (19.8)$$

This equation shows that the required change in asphericity is proportional to the change in spherical aberration coefficient and inversely proportional to the fourth-order of the height over which the coefficient change is applicable. The addition can be expressed as the longitudinal spherical aberration at some specified height.

The success of aspherizing a surface of a contact lens or of an intraocular lens to provide presbyopic correction will depend upon how the change in aberration interacts with the existing aberrations of the eye. Too large a pupil size may give more addition that is required, while a small pupil will not allow the full addition to be expressed. As pupil diameter reduces with age (section 20.4), a design that works well with a younger presbyope (e.g., 45-year-old) may not be successful with a 60-year-old.

19.4.3 OTHER METHODS

Other ophthalmic correcting devices for which there is simultaneous correction of distance and near vision are concentric/annular and diffractive. The first type has two or more discrete zones of different power, and the third type has two or more different powers, which all operate over a large part of a lens. Through-focus plots show modulations in visual performance (e.g., visual acuity), and lenses which smooth these out to increase depth-of-field are referred to as extended depth-of-focus lenses. These can involve either or both concentric/annular and diffractive approaches. Diffractive lenses can have considerable chromatic aberration, and this

must be considered in design. Richdale et al. (2021) gave an account of contact lens types for the correction of presbyopia.

SUMMARY OF MAIN SYMBOLS

D	pupil diameter
ΔL	(total) depth-of-field
Φ	angular diameter of defocus blur disc
Φ_{th}	detection threshold value of Φ
Z	surface sagitta
Q	asphericity of conicoid
c	vertex curvature of a surface
h	surface height
LSA	longitudinal spherical aberration
n, n'	refractive indices on object and image sides of a surface

REFERENCES

- Atchison, D. A. 1989. "Optical design of intraocular lenses. I. On-axis performance." *Optom Vis Sci* 66 (8):492–506. doi: 10.1097/00006324-198908000-00002.
- Atchison, D. A., W. N. Charman, and R. L. Woods. 1997. "Subjective depth-of-focus of the eye." *Optom Vis Sci* 74 (7):511–20. doi: 10.1097/00006324-199707000-00019.
- Atchison, D. A., and H. Guo. 2010. "Subjective blur limits for higher order aberrations." *Optom Vis Sci* 87 (11):E890–8. doi: 10.1097/OPX.0b013e3181f6fb99.
- Atchison, D. A., H. Guo, and S. W. Fisher. 2009. "Limits of spherical blur determined with an adaptive optics mirror." *Ophthalmic Physiol Opt* 29 (3):300–11. doi: 10.1111/j.1475-1313.2009.00637.x.
- Campbell, F. W. 1957. "The depth of field of the human eye." *Optica Acta* 4 (4):157–64.
- Campbell, F. W., and G. Westheimer. 1958. "Sensitivity of the eye to differences in focus." *J Physiol* 143:18P.
- Charman, W. N. 2019. "Pinholes and presbyopia: solution or sideshow?" *Ophthalmic Physiol Opt* 39 (1):1–10. doi: 10.1111/opo.12594.
- Charman, W. N., Y. Liu, and D. A. Atchison. 2019. "Small-aperture optics for the presbyope: do comparable designs of corneal inlays and intraocular lenses provide similar transmittances to the retina?" *J Opt Soc Am A Opt Image Sci Vis* 36 (4):B7–B14. doi: 10.1364/JOSAA.36.0000B7.
- Charman, W. N., and H. Whitefoot. 1977. "Pupil diameter and the depth-of-focus of the human eye as measured by laser speckle." *Optica Acta* 24 (2):1211–6. doi: 10.1080/713819479.
- Cheng, X., A. Bradley, S. Ravikumar, and L. N. Thibos. 2010. "Visual impact of Zernike and Seidel forms of monochromatic aberrations." *Optom Vis Sci* 87 (5):300–12. doi: 10.1097/OPX.0b013e3181d95217.
- Cheng, X., A. Bradley, and L. N. Thibos. 2004. "Predicting subjective judgment of best focus with objective image quality metrics." *J Vis* 4 (4):310–21. doi: 10.1167/4.4.7.
- Curcio, C. A., K. R. Sloan, R. E. Kalina, and A. E. Hendrickson. 1990. "Human photoreceptor topography." *J Comp Neurol* 292 (4):497–523. doi: 10.1002/cne.902920402.
- Dhallu, S. K., A. L. Sheppard, T. Drew, T. Mihashi, et al. 2019. "Factors influencing pseudo-accommodation-the difference between subjectively reported range of clear focus

- and objectively measured accommodation range.” *Vision (Basel)* 3 (3). doi: 10.3390/vision3030034.
- Guo, H., D. A. Atchison, and B. J. Birt. 2008. “Changes in through-focus spatial visual performance with adaptive optics correction of monochromatic aberrations.” *Vision Res* 48 (17):1804–11. doi: 10.1016/j.visres.2008.04.033.
- International Standardization Organization. 2022. ISO 11979-7:2022 Ophthalmic implants - Intraocular lenses - Part 7: Clinical investigations of intraocular lens for the correction of aphakia. Geneva, Switzerland.
- Jacobs, R. J., G. Smith, and C. D. Chan. 1989. “Effect of defocus on blur thresholds and on thresholds of perceived change in blur: comparison of source and observer methods.” *Optom Vis Sci* 66 (8):545–53. doi: 10.1097/00006324-198908000-00010.
- Montes-Mico, R., and W. N. Charman. 2019. “Pharmacological strategies for presbyopia correction.” *J Refract Surg* 35 (12):803–14. doi: 10.3928/1081597X-20191010-04.
- Mordi, J. A., and K. J. Ciuffreda. 1998. “Static aspects of accommodation: age and presbyopia.” *Vision Res* 38 (11):1643–53. doi: 10.1016/s0042-6989(97)00336-2.
- Ogle, K. N., and J. T. Schwartz. 1959. “Depth of focus of the human eye.” *J Opt Soc Am* 49 (3):273–80. doi: 10.1364/josa.49.000273.
- Plainis, S., D. Petratou, T. Giannakopoulou, H. Radhakrishnan, et al. 2013. “Interocular differences in visual latency induced by reduced-aperture monovision.” *Ophthalmic Physiol Opt* 33 (2):123–9. doi: 10.1111/opo.12018.
- Richdale, K., I. Cox, P. Kollbaum, M. A. Bullimore, et al. 2021. “CLEAR - Contact lens optics.” *Cont Lens Ant Eye* 44 (2):220–39. doi: 10.1016/j.clae.2021.02.005.
- Smith, G., and D. A. Atchison. 1997. “Chapter 36. Visual ergonomics of monocular systems.” In *The Eye and Visual Optical Instruments*, 697–725. New York: Cambridge University Press.
- Vasudevan, B., K. J. Ciuffreda, and B. Wang. 2007. “Subjective and objective depth-of-focus.” *J Mod Opt* 54 (9):1307–16.
- Walsh, G., and W. N. Charman. 1988. “Visual sensitivity to temporal change in focus and its relevance to the accommodation response.” *Vision Res* 28 (11):1207–21. doi: 10.1016/0042-6989(88)90037-5.
- Watson, A. B., and A. J. Ahumada, Jr. 2008. “Predicting visual acuity from wavefront aberrations.” *J Vis* 8 (4):17 1–9. doi: 10.1167/8.4.17.
- Yi, F., D. R. Iskander, and M. J. Collins. 2010. “Estimation of the depth of focus from wavefront measurements.” *J Vis* 10 (4):3 1–9. doi: 10.1167/10.4.3.



Taylor & Francis
Taylor & Francis Group
<http://taylorandfrancis.com>

20 The Aging Eye

20.1 INTRODUCTION

Age-related optical changes in the eye have been mentioned in earlier chapters, but here we give a fuller account, with emphasis on changes occurring in the adult eye. Changes in the eye are most rapid early in life, with axial length increasing from 17 mm to 24 mm and with flattening of the cornea and lens with corresponding reductions in power. Many of the changes in adult life produce progressive reduction in visual performance. Several changes in the optical properties may be regarded as pathological, e.g., cataract, but these will not be considered here. Neural properties also change with age, but these are beyond the scope of this book.

20.2 CORNEA

Chapter 2 contained considerable coverage of the biometry of the cornea, including how this can be described.

With increasing age, there is decreased spacing between collagen fibrils of the stroma, some fiber degeneration, and increases in the cross-sectional area of collagen fibers (Kanai and Kaufman 1973; Malik et al. 1992). Descemet's membrane increases in thickness with age (Cogan and Kuwabara 1971). Possibly the most important age-related change is endothelial degeneration. The size of endothelial cells becomes more variable (*polymegathism*), because some cells either increase in size or fuse (Daus and Völcker 1987). Eventually endothelial function may be impaired, and then aqueous humor may seep into the cornea, disrupting the structural order and increasing light scatter (Pierscionek 1996).

20.2.1 CORNEAL SHAPE

In young eyes the curvature of the anterior surface is usually greater in the vertical meridian than that in the horizontal meridian, referred to as "with-the-rule" astigmatism, but this reverses with increase in age to an "against-the-rule" astigmatism (Lyle 1971; Anstice 1971; Baldwin and Mills 1981; Fledelius and Stubgaard 1986; Goh and Lam 1994; Lam et al. 1994; Rozema et al. 2019). Some studies have found the anterior curvature increases along the horizontal meridian than along the vertical meridian (Kiely et al. 1984; Hayashi et al. 1995; Topuz et al. 2004) and others have found increases only along the horizontal meridian (Lam et al. 1999; Lam and Douthwaite 2000; Goto et al. 2001).

Either the anterior corneal asphericity does not change (Kiely et al. 1984; Atchison et al. 2008) or it becomes less negative with increase in age (Pardhan and Beesley 1999; Guirao et al. 2000; Dubbelman et al. 2006); Dubbelman et al. and Pardhan

and Beesley reported changes of +0.002 and +0.003/year, respectively. For the posterior cornea, Dubbelman et al. reported an increase in negative corneal asphericity of 0.006/year.

20.2.2 CORNEAL THICKNESS

Doughty and Zaman's (2000) review of the literature to 2000 indicated that age does not appear to influence central thickness across studies of Caucasian groups, but that age-related changes occur in non-Caucasian groups. Some recent studies have reported age effects (Lekskul et al. 2005; Suzuki et al. 2005; Landers et al. 2007; Rüfer et al. 2007), while others have not (Sanchis-Gimeno et al. 2004; Eysteinsson et al. 2005; Altinok et al. 2007; Khoramnia et al. 2007).

20.2.3 TRANSMITTANCE

Some studies of corneal transmittance have not found significant variation with age (Boettner and Wolter 1962; Beems and van Best 1990; van den Berg and Tan 1994), although Boettner and Woltner found a decrease in the direct (non-scattered) light with increased age. Ní Dhubhghaill et al. (2014) found increase in back scatter with age in the corneal periphery.

20.3 ANTERIOR CHAMBER

The anterior chamber depth increases with age until the age of 10–12 years (Iribarren 2015). The estimates of the subsequent decrease vary from approximately half (Dubbelman et al. 2006; Atchison and Markwell 2008) to nearly all (Wojciechowski et al. 2003; Koretz et al. 2004; Shufelt et al. 2005) of the increase in lens thickness with age. Estimates of the rate of change of the depth vary between –0.010 and –0.022 mm/year.

20.4 PUPIL DIAMETER

Pupil size decreases with increased age (Birren et al. 1950; Kunnick 1954; Kadlecova et al. 1958; Leinhos 1959; Said and Sawires 1972; Winn et al. 1994) (Figure 20.1). This is referred to as *senile miosis*. In addition, the speed and extent of pupillary reactions decrease with increase in age, e.g., Kunnick (1954). The maximum pupil size in dark-adapted eyes is reached in the teenage years, after which it declines (Kadlecova et al. 1958; Said and Sawires 1972). For example, Kadlecova et al. found maximum diameters ranging from about 7.5 mm at 10 years of age to about 5 mm at 80 years of age. As age increases, the variation in pupil diameter with change in luminance decreases (Figure 20.4). Although reducing retinal illuminance, a smaller pupil has the helpful features of reducing higher-order aberrations, reducing scatter, and compensating for loss of accommodation with age by increasing depth-of-field. Watson and Yellott (2012) included age in their modeling of pupil size.

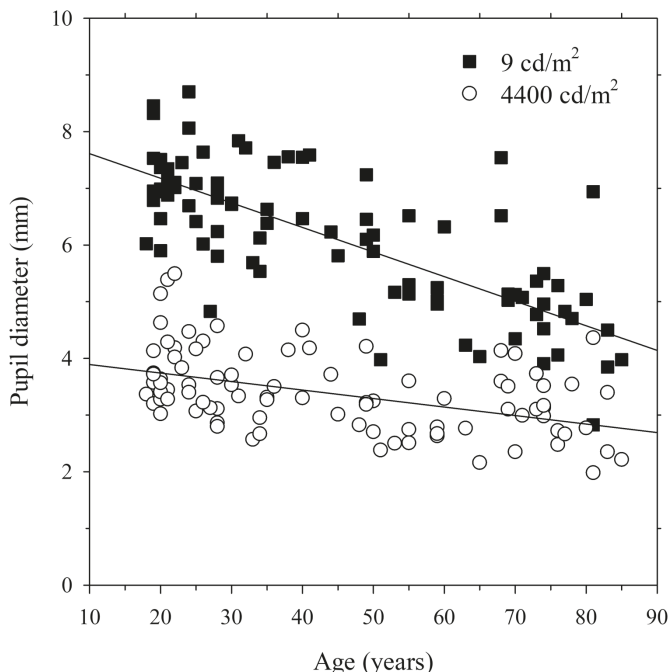


FIGURE 20.1 Effect of age on pupil size. Ninety-one participants viewed a 10° field monocularly in Maxwellian view. Results, including regression equations, are shown for luminance levels of 9 cd/m^2 and 4400 cd/m^2 . Data from Figures 2a and 2e of Winn et al. (1994), kindly provided by Barry Winn.

20.5 LENS

The most dramatic age-related optical changes in the eye occur in the lens. Its shape, size, and mass alter markedly, its ability to vary its shape (i.e., accommodation) diminishes, and its light transmission reduces considerably, particularly at short wavelengths. Sections 2.3 and 2.4 contain considerable coverage of the biometry of the lens. Table 20.1 gives the results of several studies investigating age-related changes in lens biometry during adulthood.

20.5.1 SHAPE

Studies have found approximately linear reduction in the anterior surface radius of curvature of unaccommodated eyes with increase in age of between 0.03 and 0.11 mm/year (Table 20.1). A few, but not the majority, found small reductions in the posterior surface radius of curvature (Brown 1974; Dubbelman et al. 2001; Chang et al. 2019). There have been few studies of lens surface asphericity. Dubbelman and Van der Heijde (2001) did not find change with age, but Kasturirangan et al. (2011) found an increase in positive asphericity.

TABLE 20.1
Changes in Lens Parameters (Unit/Year) with Age from *In Vivo* Studies of Adult Eyes

Ocular Parameter	Study	Method, Comment	Change Unit /Year
Anterior radius of curvature (mm)	Brown 1974	Scheimpflug photography,	-0.106
	Dubbelman and Van der Heijde 2001	Scheimpflug photography	-0.057
	Koretz et al. 2004	MRI, Scheimpflug photography	-0.08
	Atchison et al. 2008	Purkinje imaging	-0.044
	Richdale et al. 2013	Purkinje imaging	-0.11
	Richdale et al. 2016	Purkinje imaging	-0.11
	Chang et al. 2019	Extended-depth OCT	-0.072
	Li et al. 2022	Swept-source OCT, uncyclopleged	-0.032
	Brown 1974	Scheimpflug photography, peripheral chord	-0.02
	Dubbelman and Van der Heijde 2001	Scheimpflug photography	-0.012
Posterior radius of curvature (mm)	Koretz et al. 2004	MRI, Scheimpflug photography	ns
	Atchison et al. 2008	Purkinje imaging	ns
	Kasthurirangan et al. 2011	MRI, based on 19-29 and 60-70 yr groups	ns
	Richdale et al. 2013	Purkinje imaging	ns
	Richdale et al. 2016	Purkinje imaging	ns
	Chang et al. 2019	Extended-depth OCT	-0.020
	Li et al. 2022	Swept-source OCT, uncyclopleged	ns
Anterior surface asphericity (Q)	Dubbelman and Van der Heijde 2001	Scheimpflug photography	ns
Posterior surface asphericity (Q)	Dubbelman and Van der Heijde 2001	Scheimpflug photography	ns
Axial thickness (mm)	Kasthurirangan et al. 2011	MRI, based on 19-29 and 60-70 yr groups	-0.025
	Brown 1973	Scheimpflug	+0.026
	Dubbelman et al. 2001	Scheimpflug photography	+0.024
	Koretz et al. 2004	MRI	+0.019
	Shufelt et al. 2005	ultrasonography	+0.010
	Richdale et al. 2008	OCT	+0.021
	Richdale et al. 2013	Ultrasound, OCT	+0.031
		MRI	+0.027
	Atchison et al. 2008	ultrasound	+0.024
	Li et al. 2022	Swept-source OCT, uncyclopleged	+0.024

TABLE 20.1 (Continued)
Changes in Lens Parameters (Unit/Year) with Age from *In Vivo* Studies of Adult Eyes

Ocular Parameter	Study	Method, Comment	Change Unit /Year
Equivalent refractive index	Chang et al. 2018	Extended source OCT	+0.029
	Dubbelman et al. 2001	Scheimpflug photography	-0.0004
	Atchison et al. 2008	Purkinje imaging	-0.0004
	Richdale et al. 2013	Purkinje imaging	-0.0008
	Richdale et.al. 2016	Purkinje imaging	-0.0006
Lens diameter (mm)	Chang et al. 2018	Extended source OCT	-0.0007
	Atchison et al. 2008	MRI, based on 19–29 and 60–70 yr groups	+0.008
	Strenk et al. 1999	MRI	ns
	Fea et al. 2005	MRI	ns
	Richdale et al. 2013	MRI	ns
Lens power (D)	Richdale et al. 2016	MRI	ns
	Atchison et al. 2008	Purkinje imaging	-0.033
	Chang et al. 2019	Extended source OCT	-0.07
	Jongenelen et al. 2015	Calculations based on ocular biometry	-0.08

Note: Both anterior and posterior surfaces have been assigned positive radii of curvature, and steepening results in negative changes for both. ns = no significant change.

20.5.2 THICKNESS

The lens increases in volume and mass throughout life, with most of this being due to increase in axial thickness of the cortex (Brown 1973; Niesel 1982; Cook et al. 1994; Dubbelman et al. 2003). There have been many studies of age-related thickness in adulthood, with only as few included in Table 20.1. Reported rates vary from 0.01 to 0.03 mm/year.

20.5.3 REFRACTIVE INDEX DISTRIBUTION

Models for the refractive index distribution of the lens were discussed in sections 2.3.3 and 16.4. Based on the increasing thickness and surface curvatures of the lens with age, it would be expected that eyes should become more myopic. However, the general shift is in the other direction, with Saunders (1986) finding a mean hyperopic shift of 2 D between the ages of 30 and 60 years (Figure 20.2); the failure of change in refraction to match changes in lens shape is referred to as the *lens paradox*. In young eyes, the lens refractive index decreases away from its center and provides a considerable component of the lens power. Aging changes were modeled by Smith et al. (1992) such that the gradient index profile became flatter near the middle of

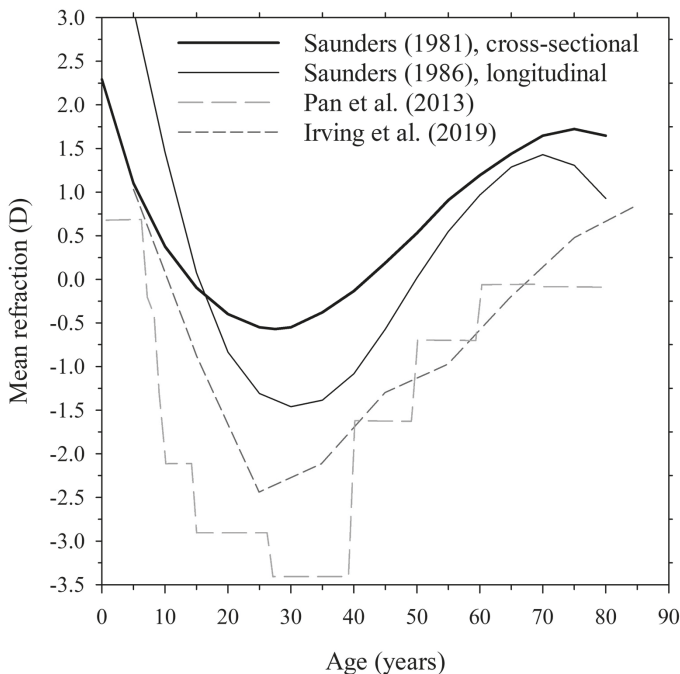


FIGURE 20.2 Changes in mean refraction with age. Cross-sectional data of Saunders (1981), longitudinal data of Saunders (1986), cross-sectional data of Pan (2013), and cross-sectional data of Irving et al. (2019).

the lens and steeper towards the edge, which had the effect of reducing the contribution that the gradient index makes to the overall lens power. This modeling has received support from *in vitro* studies and from an *in vivo* MRI study (Kasthurirangan et al. 2008).

20.5.4 EQUIVALENT REFRACTIVE INDEX

As mentioned in section 2.3.4, the gradient index power can be modeled in homogeneous lenses by using an equivalent refractive index higher than the refractive index in the lens center. Loss in the refractive index power with age can be modeled by the refractive index reducing with age. The studies in Table 20.1 gives age rates of loss of 0.0004 to 0.0008/year.

The zones in the lens seen with the slit-lamp, which become more obvious and greater in number with increasing age, are of considerable interest. Although several reasons for their appearance have been suggested, including refractive index discontinuities, the nature and origin of these is not yet known.

20.5.5 DIAMETER

Most of the studies do not find an age trend, but Atchison et al. (2008) found a + 0.3 mm larger diameter in a 61–69 year group than in an 19–28 year group.

20.5.6 LENS POWER

There is decrease in lens power with age, with estimates of -0.03 to -0.08 D/year.

20.5.7 LENTICULAR TRANSMITTANCE, SCATTER, AND FLUORESCENCE

The transmittances of both ultraviolet and visible wavelengths decrease with increase in age, with the lens becoming more yellow, particularly in the nucleus (Said and Weale 1959; Boettner and Wolter 1962; Mellerio 1971, 1987; Pokorny et al. 1987; Sample et al. 1988). There is an increase in both forward and backward scattered light with age, particularly after the age of 40 years (Ben-Sira et al. 1980; IJsspeert et al. 1990; Fujisawa and Sasaki 1995). There is increased fluorescence with increase in age (Hockwin et al. 1984).

20.6 VITREOUS CHAMBER

With increase in age, the vitreous gel is gradually replaced by water. The overall transmittance changes little, but people become more aware of “floaters”, which are the shadows formed on the retina by fiber clusters and other material in the vitreous chamber.

20.7 REFRACTIVE ERRORS AND AXIAL LENGTH

Refractive errors are relatively stable between the ages of 20 and 40 years (Grosvenor and Scott 1991), after which there is a shift in the hyperopic direction (Saunders 1986) (Figure 20.2). After the approximate age of 70 years, there is some shift of the mean refractive error in the myopic direction associated with the development of nuclear cataract (Brown and Hill 1987). Studies of Asian populations suggest higher myopia than Western populations at any age, but with similar age trends, e.g., Pan et al. (2013). The distribution of refractive errors of a young adult population is more sharply peaked than a normal distribution (**leptokurtosis**). The distribution of refractive errors becomes more normal with increasing age, with increases in the proportions of both myopes and hyperopes (Grosvenor and Scott 1991).

Several studies have found a decline in axial length with age. Rozema and Ní Dhubhghaill (2020) explained this as a cohort effect, in which there has been a change in the basic biometry over time that is related to increases in body size and educational levels. Another way of putting this is that axial length depends more upon date of birth than of age. No doubt this cohort effect influences at least some of the other optical parameters described in this chapter. In this regard, the cross-sectional study of emmetropic eyes by Atchison et al. (2008) is interesting; they found increase in axial length of 0.011 mm/year, which they attributed to the younger subjects likely to become hyperopic as they age and some of the older subjects being myopic when younger.

Age-related changes in the corneal shape, discussed earlier in this chapter, are reflected in the astigmatism of the eye, e.g., Hirsch (1959); Anstice (1971); Saunders (1981); Rozema et al. (2019). The prevalence of with-the-rule astigmatism increases

up to about 40 years of age, after which it decreases and the prevalence of against-the-rule astigmatism increases.

20.8 ACCOMMODATION AND PRESBYOPIA

Accommodation was introduced in section 2.4 as the ability of the eye to change its power to bring objects of interest at different distances into focus. The anterior and posterior surfaces become more rounded, the center thickness increases, and the diameter reduces. As age increases, the maximum possible changes in lens movements decline (Koretz et al. 1997). Uncertainty exists about the exact interaction between the zonules and the ciliary body (Atchison 1995).

The range, or amplitude, of accommodation reaches a peak early in life, then gradually declines. The decline in accommodation becomes a problem for most people in their forties when they can no longer see clearly to perform near tasks. This condition is called *presbyopia*. It was introduced in section 7.2. The age at which this occurs for any person depends on the refractive error, nature of close work, stature, and, probably, on genetic and environmental factors. Accommodation is completely lost in the fifties, well before most other physiological functions are appreciably affected. However, as discussed below, most clinically based studies do not show this complete loss.

There have been many studies of the reduction in the amplitude of accommodation with age. Figure 20.3 shows Anderson and Stuebing's (2014) results for participants between the ages of 3 and 64 years using a conventional clinical push-up method and an autorefractor for which object distance was varied to provide the stimulus. The subjective amplitude is considerably higher than the "true" amplitude of accommodation given by the autorefractor. The main reasons are likely to be cognitive factors, particularly in young children, instruction, and depth-of-field effects. Adnan et al. (2014) obtained a more consistent difference between subjective and objective methods of 1.4 ± 1.2 D for an adult population. Studies such as these indicate that accommodation probably does not occur beyond the early fifties.

Cross-sectional studies mask the age-related decline in amplitude of individual subjects. They show a non-linear trend in the mean amplitude with age, but with the rate of decline decreasing as presbyopia is approached (Figure 20.3). Two small-scale longitudinal studies (Hofstetter 1965; Ramsdale and Charman 1989) found that individual subjects have a linear decrease of accommodation with age. The second study followed a participant between the ages of 41 and 51 years, with a fit of

$$\text{Amplitude (D)} = 17.3 - 0.0325\text{age} \quad (20.1)$$

as the average of right and left eyes. This equation estimates that accommodation will be zero by 54 years. The non-linear trend in cross-sectional studies is probably due to artefacts introduced by the averaging process (Charman 1989). At any age beyond that at which some individuals no longer accommodate, the distribution of amplitudes is truncated, because these individuals cannot contribute negative values to it.

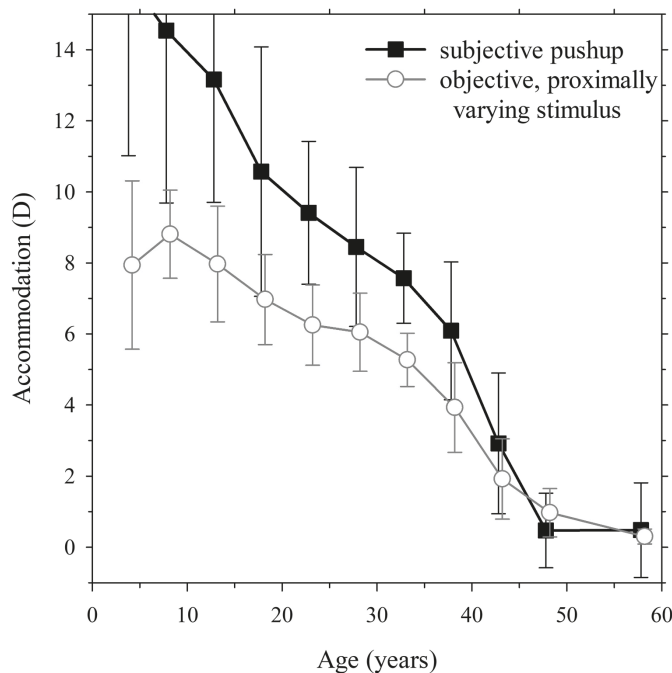


FIGURE 20.3 Accommodative amplitude as a function of age for a subjective push-up method and an objective “proximal” method. There were approximately 230 participants, who were grouped into age ranges. Errors bars show standard deviations. Data of Anderson et al. (2014).

The rate of amplitude decline varies considerably between studies, and may be affected by several factors. The rate of progression of presbyopia is faster the closer people live to the equator, and faster for people living at low altitudes than at higher altitudes. These findings indicate that ambient temperature may affect the progression of presbyopia (Miranda 1979; Weale 1981).

See Glasser (2011) for coverage of age-related changes occurring in the lens, capsule, ciliary body, and zonules.

20.8.1 PRESBYOPIA THEORIES

Theories of the development of presbyopia can be categorized as follows (Atchison 1995):

1. Lenticular theories
 - a. Mechanical changes in lens and capsule
 - i. Hess–Gullstrand theory
 - ii. Fincham theory
 - b. Geometric theories

2. Extra-lenticular theories
 - a. Duane's theory and changes in ciliary muscle
 - b. Changes in elastic components of zonule and/or ciliary body.

The development of presbyopia is generally regarded as originating in the “plant” of the accommodative system, either within the lens and its capsule or within their support structures, rather than being neural. Because the optical parameters of the eye are involved in several of these theories, they are discussed briefly below.

20.8.1.1 Lenticular Theories – Mechanical Changes in Lens and Capsule

The lens is purported to become more rigid with age and to be increasingly resistant to the elastic forces of the capsule upon it. Fisher's ref *in vitro* measurements of the mechanics of the various parts of the accommodative “plant”, e.g., Fisher (1969b, a, 1971, 1973; Fisher and Pettet 1973; Fisher 1977, 1986) provides evidence for this group of theories: the ciliary muscle does not lose its power with age; the lens behaves as a simple elastic body, which requires more energy to deform it with increasing age; and the capsule's elasticity declines so that it is less able to provide this deforming energy.

In the *Hess–Gullstrand theory*, the amount of muscle contraction required for a given change in accommodation is purported to remain constant throughout life (Hess 1901; Gullstrand 1909; Alpern 1962). This theory predicts that an increasing proportion of ciliary muscle contraction will be “latent”, i.e., it does not affect accommodative status. This theory is distinct from all other theories of presbyopia, which predict that the maximum possible amount of ciliary muscle contraction is required to produce maximum accommodation at any age.

The Hess–Gullstrand theory would be supported by evidence that the ciliary muscle increases its contraction at accommodation stimulus levels beyond those which produce the maximal accommodation response, but this evidence is limited. Some studies have found electrical changes in the region of the equator of the eyeball for stimuli beyond those producing the maximal response, but whether this indicates ciliary muscle activity has been disputed.

The Hess–Gullstrand theory predicts that zonule slackness should be more apparent in older subjects trying to accommodate beyond the amplitude limit, but the reverse has been noted in monkeys without irises. Similarly, the predicted increased zonule slackness upon accommodation in older subjects should allow the lens to be more influenced by gravity for older rather than younger participants. Lister et al. (2016) found small effects of gravity on lens position, i.e., on anterior chamber depth, but maximal effects were small at 0.12 mm and were not greater for older rather than for younger participants.

According to the mechanical changes in lens and capsule theories, the lens becomes more resistant to change in shape with age. *Fincham's theory* (Fincham 1937) is that greater pressure from the capsule, necessary with increase in age to achieve a given level of accommodation, can only be achieved by further releasing the zonular tension on the capsule. This means that the changes responsible for the

decline in accommodation reside in the lens and capsule, but ciliary muscle contraction required for a given change in accommodation increases throughout life. Another way of putting this is that maximum contraction of the ciliary muscle coincides with the amplitude of accommodation. In the latter sense, the theory is sometimes referred to as the Duane–Fincham theory, although Duane proposed loss of accommodation was due to weakening of the ciliary muscle (see below).

Fincham's theory is not supported by the effects of gravity on lens position as mentioned above. However, it is supported by studies of the effects of age and drugs on the accommodation–convergence synkinesis. For example, the response AC/A ratio (amount of convergence induced by 1 D change in accommodation response) increases with age, as predicted if increasing innervation to the ciliary muscle is required to produce a unit change in accommodation response as age increases (Bruce et al. 1995). By contrast, the Hess–Gullstrand theory predicts that this ratio should be unaffected by age. The evidence supporting the Fincham theory, at the expense of the Hess–Gullstrand theory, also supports the following theories.

20.8.1.2 Lenticular Theories – Geometric Theories

These attribute the decline in amplitude with age mainly to the increased size and curvature of the lens (see section 20.3) produced by the addition of lens fibers to the cortex throughout life. Koretz and Handelmann (1986, 1988) suggested that the increasing curvature and the likely change in orientation of the zonules due to shifting zonule insertions means that zonules apply tension less radially to the capsule's surface. This means that, upon ciliary muscle contraction, the zonule relaxation may have smaller effects on the lens shape. This theory was modified by Strenk et al. (2005) to include effects of the growing lens on the iris and ciliary body.

Schachar (1992) developed a variation of the geometric theory. He rejected the Helmholtzian explanation for accommodation, believing instead that the ciliary body moves away from the lens upon increased accommodation, so that tension of the equatorial zonules increases and the lens becomes spindle-shaped with minimal changes in central thickness. As part of his theory of presbyopia, he claimed that increasing lens diameter with age will restrict the ability of the zonules to provide this tension, thus providing the mechanism for presbyopia. Only one of the five studies shown in Table 20.1 supports increasing diameter with age. Schachar has published several experimental and theoretical papers, letters to the editor, and a book claiming to support his theories of accommodation and presbyopia, e.g., Schachar (2012); Schachar et al. (2017). The experiments of Fisher (1977) and Glasser and Campbell (1998, 1999), which showed that stretching human lenses decreases the power rather than increasing it, would seem to provide overwhelming evidence against Schachar's accommodation theory. Other studies giving changes in anterior chamber depth and lens thickness with accommodation and aging and in equatorial diameter with accommodation, and the effects of gravity (Lister et al. 2016), provide evidence against Schachar's theories. Many of these changes are reported in this chapter and in section 2.4.

20.8.1.3 Extra-Lenticular Theories – Duane's Theory and Changes in Ciliary Muscle

The extra-lenticular theories attribute accommodation amplitude decline either to weakening of the ciliary muscle or to loss of elasticity of zonules or ciliary body components. Workers using the rhesus monkey as an animal model for human accommodation found that electrically stimulating the mid-brain region that influences accommodation produced axial thickening of the lens, narrowing of the ciliary ring, and zonule slackening at high amplitudes. As the monkeys' age increased, these findings were less noticeable.

Duane (1922, 1925) believed that the ciliary muscle weakens with increased age. However, Fisher (1977) found that the strength of muscle contraction should decline only slightly before 45–50 years of age, and anatomical studies of the ciliary muscle and surrounding tissue suggest that its possible movement should not decrease markedly with increase in age.

The muscle form does change with age (Tamm et al. 1992; Pardue and Sivak 2000) to affect the geometry between the ciliary ring and the equator of the lens, such that the ring diameter slowly decreases in diameter with increasing age (Strenk et al. 1999). This has been incorporated in Strenk et al.'s modified geometric theory (see above). Charman (2012) pointed out that, while a decrease in ciliary ring diameter does not fit with Schachar's theories, it would support a decrease in lenticular tension with increase in age that is the basis of his geometric presbyopia theory.

20.8.1.4 Extra-Lenticular Theories – Changes in Elastic Components of Zonules and/or Ciliary Body

Bito and Miranda (1989) claimed that presbyopia is a loss of the ability to relax accommodation, rather than loss of the ability to increase accommodation, which is opposite to the usual way in which presbyopia is considered. This occurs through deterioration of elastic components in the ciliary body and choroid. As age increases, the lens takes up a more curved shape under its elastic forces, even when ciliary muscle contraction does not occur, because the elastic antagonists of the ciliary muscle in the ciliary body and choroid are not doing their work. As discussed in section 20.5.1, the lens certainly does become more curved with increasing age. The theory ignores changes in lens and capsule elasticity. Some anatomical studies have found age-related changes in the attachments to the ciliary muscle.

20.8.1.5 Summary

Presbyopia probably has a few causes, and at the least these are changes in capsule and lenticular elasticity combined with changes in lens geometry. As mentioned in section 10.8, there has been considerable work in developing “accommodating” intraocular lenses, most of which assumes that the accommodative apparatus remains largely functional during most of life.

20.9 ABERRATIONS

The central, monochromatic *RMS* higher-order aberrations increase with age throughout adulthood for fixed pupil sizes (Calver et al. 1999; McLellan et al. 2001; Artal et al. 2002; Kuroda et al. 2002; Fujikado et al. 2004; Applegate et al. 2007). Spherical aberration increases towards more positive values (Calver et al. 1999; McLellan et al. 2001; Smith et al. 2001; Artal et al. 2002; Amano et al. 2004; Kingston and Cox 2013). As mentioned in section 15.6.1, this has been attributed to a loss of balance between the cornea and lens. Two studies limited to emmetropes have reported smaller changes than in other studies and without significant increases in spherical aberration (Atchison and Markwell 2008; Plainis and Pallikaris 2008), with the main changes occurring for the third-order terms.

Some studies have found a decrease in longitudinal chromatic aberration with age (Millodot and Sivak 1973; Millodot 1976; Mordi and Adrian 1985), but others have found no change (Lau et al. 1955; Ware 1982; Howarth et al. 1988; Morrell et al. 1991).

Peripheral refraction changes little with age along the horizontal visual field provided that central refraction is taken into account (Atchison et al. 2005), although Atchison and Markwell (2008) noted a small shift in the turning point of astigmatism J_{180} towards less temporal field values.

Concerning higher-order aberrations in peripheral vision, Mathur et al. (2010) found that the rate of change of coma across the visual field increased with age by approximately three times between the ages of 25 and 63 years. They found also that the internal coma and spherical aberration of the older subjects were considerably smaller in magnitude than those of the young subjects such that the compensation for anterior corneal aberrations was poorer, similar to that reported by Artal et al. (Artal et al. 2002; Berrio et al. 2010) for central vision.

20.10 PHOTOMETRY

Retinal illumination decreases with age due to two factors. One is the reduction of pupil diameter with age, particularly at low light levels, and the other is the decrease in ocular transmittance with age.

The data of Winn et al. (1994), shown in Figure 20.1, can be used to predict the effect of changing pupil size. At 9 cd/m² background luminance, the pupil diameter decreased approximately linearly with age from 20 years to 60 years by about 25 per cent. This corresponds to a light loss at the retina of more than 43 per cent at low light levels.

The decrease in ocular transmittance with age is due mainly to the lens, particularly for the shorter wavelengths. Figure 20.4 shows the curve fits of van de Kraats and van Nooren (2007), for which the ocular transmittance decreases by about 12% between the ages of 20 and 60 years at 550 nm. Combining the pupil size and ocular transmittance changes with age given above indicates a reduction in light level reaching the retina, between the ages of 20 and 60 years, of approximately 67 per cent at lower light levels.

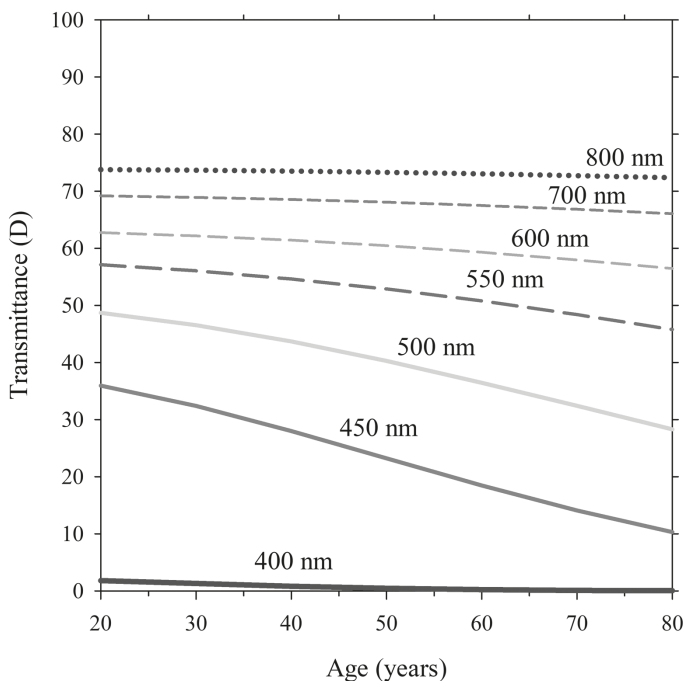


FIGURE 20.4 Variation in lens transmittance with age at different wavelengths. Equation (8) of van de Kraats et al. (2007), with densities converted to transmittances. The equation was derived from results of several studies.

20.10.1 EFFECT OF LIGHT LOSS ON VISUAL PERFORMANCE

Spatial visual performance decreases with increase in age, due to both optical and neural causes (Wood and Black 2017). Loss in performance is much more marked at low than at higher luminances, so that transmittance decreases at lower light levels can be compensated to a large extent by increasing the light level. The greater loss in transmittance at the shorter wavelengths affects color perception, reducing the ability to discriminate shades of greens and blues (Knoblauch et al. 1987).

The decrease in transmittance has two contributions: absorption and backward scatter. Unlike these, increasing the light level cannot compensate for the forward scatter. Forward scatter produces a veiling glare over the retina, which reduces the contrast of the retinal image. Low-contrast objects may become invisible. This becomes worse at low ambient light levels when bright lights are in the field-of-view, e.g., on dark streets with streetlamps.

With increase in age, there is an increase in the amount of forward light scatter from the lens, so that K increases in the equivalent veiling luminance equation (13.15)

$$L_v(\theta) = KE/\theta^n \quad (20.2)$$

although the angular dependency remains similar (Fisher and Christie 1965; IJsspeert et al. 1990). For example, Fisher and Christie found that K increased linearly with

age, but that n was essentially independent of age. K increased by a factor of 1.9 to 3.3 in their experiments between the ages of 20 and 70 years.

Rozema et al. (2010) found that the straylight parameter s defined in equation (13.16e) changed with age in non-cataractous people as

$$\log(s) = 0.931 + \log [1 + (\text{age}/65)^4] \quad (20.3)$$

so that s increases 2.3 times between 20 and 70 years.

20.10.2 STILES–CRAWFORD EFFECT

Two longitudinal studies have shown that the ρ_e coefficient in equation (14.1) is relatively unaffected by age for healthy eyes (Rynders et al. 1995; DeLint et al. 1997).

20.11 SCHEMATIC EYES

Structures of paraxial and finite schematic eyes were discussed in Chapters 5 and 16, respectively, and the dimensions of some of these eyes are listed in Appendix 3. We found in the preceding sections that many dimensions of the eye depend upon age, but designers of most schematic eyes gave no indication that a particular age was modeled. An exception is the finite eye of Liou and Brennan (1997), which contains ocular parameters for an eye near the age of 45 years. Also, Blaker (1991), Smith et al. (1992), and Smith and Pierscionek (1998) designed model eyes adapted for age, and Rabbatts (2007) presented an “elderly” version of the Bennett and Rabbatts’ simplified eye. Any selection of parameters is complicated by other factors, such as sex and race. As examples, female eyes are shorter and hence have a higher power than male eyes (Atchison et al. 2008) and there are many racial variations including pupil size (Said and Sawires 1972) and refractive error distributions. A sophisticated schematic eye would be adaptable for these effects.

We include a brief description of an age-dependent, relaxed, emmetropic, paraxial schematic eyes (Atchison 2009). This is the successor to the schematic eye presented in the first edition. It is based on the Atchison et al. (2008) study of approximately 106 emmetropic eyes of mainly Caucasian participants aged 18 to 69 years. Parameters of the models are based on linear regression equations. Vitreous and hence axial lengths were manipulated so that the eyes were within ± 0.1 D of emmetropia over the range of ages and of genders. The models have non-gender and gender forms. Atchison (2009) listed surface, component and ocular powers, and cardinal point positions. Table 20.2 shows the parameters of the models.

With increase in age, changes are decreased anterior chamber depth (0.0105 mm/yr), increased lens thickness (0.0235 mm/yr), decreased anterior lens radius of curvature (0.0438 mm/yr), increased axial length (0.0102 mm/yr) decreased lens equivalent refractive index (0.00035/yr), and lower lens power (0.045 D/yr). Relative to the male model, the female model has the following changes: smaller anterior corneal radii of curvature (0.07 mm), smaller vitreous lengths and axial lengths (0.72 mm), and higher lens equivalent refractive indices (0.007); the

TABLE 20.2
Parameters of the Atchison (2009) Schematic Eye as a Function of Age A in Years

Surface	Medium	Refractive Index	Radius of Curvature (mm)	Distance to Next Surface (mm)
1	Air	1.000	7.75 M: 7.83 F: 7.66	
2	Cornea	1.376	6.50	0.54
3	Aqueous	1.336		3.369 – 0.0105A
4	Lens	1.4506 – 0.00035A M: 1.4471 – 0.00035A F: 1.4541 – 0.00035A	12.283 – 0.0438A	3.1267 + 0.0235A
	Vitreous	1.336	-6.86	16.146 – 0.0028A M: 16.506 – 0.0028A F: 15.786 – 0.0028A

Note: M, F: male and female eyes where their parameters are different.

female model also has higher ocular powers (2.3 D), corneal powers (1.1 D), and lens powers (1.6 D).

SUMMARY OF MAIN SYMBOLS

- $L_v(\theta)$ equivalent veiling luminance
- θ off-axis angle
- E illuminance
- s straylight parameter

REFERENCES

- Adnan, N., Efron, A., Mathur, K., Edwards, et al. 2014. “Amplitude of accommodation in type 1 diabetes.” *Invest Ophthalmol Vis Sci* 55 (10):7014–8. doi: 10.1167/iovs.14-15376.
- Alpern, M. 1962. “Chapter 8. Accommodation.” In *The Eye: Muscular Mechanisms, Volume 3* edited by H. Davson, 191–229. Academic Press.
- Altinok, A., E. Sen, A. Yazici, F. N. Aksakal, et al. 2007. “Factors influencing central corneal thickness in a Turkish population.” *Curr Eye Res* 32 (5):413–9. doi: 10.1080/02713680701344361.
- Amano, S., Y. Amano, S. Yamagami, T. Miyai, et al. 2004. “Age-related changes in corneal and ocular higher-order wavefront aberrations.” *Am J Ophthalmol* 137 (6):988–92. doi: 10.1016/j.ajo.2004.01.005.

- Anderson, H. A., and K. K. Stuebing. 2014. "Subjective versus objective accommodative amplitude: preschool to presbyopia." *Optom Vis Sci* 91 (11):1290–301. doi: 10.1097/OPX.0000000000000402.
- Anstice, J. 1971. "Astigmatism - its components and their changes with age." *Am J Optom Arch Am Acad Optom* 48 (12):1001–6. doi: 10.1097/00006324-197112000-00002.
- Applegate, R. A., W. J. Donnelly, J. D. Marsack, D. E. Koenig, and K. Pesudovs. 2007. "Three-dimensional relationship between high-order root-mean-square wavefront error, pupil diameter, and aging." *J Opt Soc Am A* 24 (3):578–87.
- Artal, P., E. Berrio, A. Guirao, and P. Piers. 2002. "Contribution of the cornea and internal surfaces to the change of ocular aberrations with age." *J Opt Soc Am A* 19 (1):137–43. doi: 10.1364/josaa.19.000137.
- Atchison, D. A. 1995. "Review of accommodation and presbyopia." *Ophthalmic Physiol Opt* 15 (4):255–72. doi: 10.1016/0275-5408(95)00020-E.
- Atchison, D. A. 2009. "Age-related paraxial schematic emmetropic eyes." *Ophthalmic Physiol Opt* 29 (1):58–64. doi: 10.1111/j.1475-1313.2008.00598.x.
- Atchison, D. A., and E. L. Markwell. 2008. "Aberrations of emmetropic subjects at different ages." *Vision Res* 48 (21):2224–31. doi: 10.1016/j.visres.2008.06.023.
- Atchison, D. A., E. L. Markwell, S. Kasthurirangan, J. M. Pope, et al. 2008. "Age-related changes in optical and biometric characteristics of emmetropic eyes." *J Vis* 8 (4):29 1–0. doi: 10.1167/8.4.29.
- Atchison, D. A., N. Pritchard, S. D. White, and A. M. Griffiths. 2005. "Influence of age on peripheral refraction." *Vision Res* 45 (6):715–20. doi: 10.1016/j.visres.2004.09.028.
- Baldwin, W. R., and D. Mills. 1981. "A longitudinal study of corneal astigmatism and total astigmatism." *Am J Physiol Opt* 58:206–11. doi: 10.1097/00006324-198103000-00004.
- Beems, E. M., and J. A. van Best. 1990. "Light transmission of the cornea in whole human eyes." *Exp Eye Res* 50 (4):393–5. doi: 10.1016/0014-4835(90)90140-p.
- Ben-Sira, I., D. Weinberger, J. Bodenheimer, and Y. Yassur. 1980. "Clinical method for measurement of light backscattering from the in vivo human lens." *Invest Ophthalmol Vis Sci* 19 (4):435–7.
- Berrio, E., J. Tabernero, and P. Artal. 2010. "Optical aberrations and alignment of the eye with age." *J Vis* 10 (14). doi: 10.1167/10.14.34.
- Birren, J. E., R. C. Casperson, and J. Botwinick. 1950. "Age changes in pupil size." *J Gerontol* 5 (3):216–21. doi: 10.1093/geronj/5.3.216.
- Bito, L. Z., and O. C. Miranda. 1989. "Accommodation and presbyopia." In *Ophthalmology Annual*, edited by R. D. Reinecke, 103–28. Raven Press.
- Blaker, J. W. 1991. "A comprehensive optical model of the aging, accommodating adult eye." In *Technical Digest on Ophthalmic and Visual Optics*, 28–31. Optical Society of America.
- Boettner, E. A., and J. R. Wolter. 1962. "Transmission of the ocular media." *Invest Ophthalmol* 1 (6):776–83.
- Brown, N. A., and A. R. Hill. 1987. "Cataract: the relation between myopia and cataract morphology." *Br J Ophthalmol* 71 (6):405–14. doi: 10.1136/bjo.71.6.405.
- Brown, N. P. 1973. "Lens changes with age and cataract; slit-image photography." In *The human lens in relation to cataract*, edited by CIBA Symposium Foundation, 65–78. Amsterdam: Elsevier.
- Brown, N. P. 1974. "The change in lens curvature with age." *Exp Eye Res* 19 (2):175–83. doi: 10.1016/0014-4835(74)90034-7.
- Bruce, A. S., D. A. Atchison, and H. Bhoola. 1995. "Accommodation-convergence relationships and age." *Invest Ophthalmol Vis Sci* 36 (2):406–13.

- Calver, R. I., M. J. Cox, and D. B. Elliott. 1999. "Effect of aging on the monochromatic aberrations of the human eye." *J Opt Soc Am A* 16 (9):2069–78. doi: 10.1364/josaa.16.002069.
- Chang, Y. C., K. Liu, F. Cabot, S. H. Yoo, et al. 2018. "Variability of manual ciliary muscle segmentation in optical coherence tomography images." *Biomed Opt Express* 9 (2):791–800. doi: 10.1364/BOE.9.000791.
- Chang, Y. C., G. M. Mesquita, S. Williams, G. Gregori, et al. 2019. "In vivo measurement of the human crystalline lens equivalent refractive index using extended-depth OCT." *Biomed Opt Express* 10 (2):411–22. doi: 10.1364/BOE.10.000411.
- Charman, W. N. 1989. "The path to presbyopia: straight or crooked?" *Ophthalmic Physiol Opt* 9 (4):424–30. doi: 10.1016/0275-5408(89)90261-5.
- Charman, W. N. 2012. "Theories of presbyopia." In *Presbyopia: Origins, Effects and Treatments*, edited by I. G. Pallikaris, S. Plainis and W. N. Charman, 95–101. Thorofare, New Jersey, USA: Slack Incorporated.
- Cogan, D. G., and T. Kuwabara. 1971. "Growth and regenerative potential of Descemet's membrane." *Trans Ophthalmol Soc UK* 91:875–94.
- Cook, C. A., J. F. Koretz, A. Pfahnl, J. Hyun, and P. L. Kaufman. 1994. "Aging of the human crystalline lens and anterior segment." *Vision Res* 34 (22):2945–54. doi: 10.1016/0042-6989(94)90266-6.
- Daus, W., and H. E. Völcker. 1987. "Entstehung der ZellPolymorphie im menschschlichen Hornhautendothel" *Klin Mbl Augenheilk* 191 (3):216–21. doi: 10.1055/s-2008-1050496.
- DeLint, P. J., J. J. Vos, T. T. Berendschot, and D. van Norren. 1997. "On the Stiles-Crawford effect with age." *Invest Ophthalmol Vis Sci* 38 (6):1271–4.
- Doughty, M. J., and M. L. Zaman. 2000. "Human corneal thickness and its impact on intraocular pressure measures: a review and meta-analysis approach." *Surv Ophthalmol* 44 (5):368–408. doi: 10.1016/s0039-6257(00)00110-7.
- Duane, A. 1922. "Studies in monocular and binocular accommodation, with their clinical application." *Trans Am Ophthalmol Soc* 20:132–57.
- Duane, A. 1925. "Are the current theories of accommodation correct?" *Am J Ophthalmol* 8 (3):196–202.
- Dubbelman, M., V. A. D. P. Sicam, and G. L. Van der Heijde. 2006. "The shape of the anterior and posterior surface of the aging human cornea." *Vision Res* 26 (6-7):993–1001. doi: 10.1016/j.visres.2005.09.021.
- Dubbelman, M., and G. L. Van der Heijde. 2001. "The shape of the aging human lens: curvature, equivalent refractive index and the lens paradox." *Vision Res* 41 (14):1867–77. doi: 10.1016/s0042-6989(01)00057-8.
- Dubbelman, M., G. L. Van der Heijde, and H. A. Weeber. 2001. "The thickness of the aging human lens obtained from corrected Scheimpflug images." *Optom Vis Sci* 78 (6):411–6. doi: 10.1097/00006324-200106000-00013.
- Dubbelman, M., G. L. Van der Heijde, H. A. Weeber, and G. F. Vrensen. 2003. "Changes in the internal structure of the human crystalline lens with age and accommodation." *Vision Res* 43 (22):2363–75. doi: 10.1016/s0042-6989(03)00428-0.
- Eysteinsson, T., F. Jonasson, A. Arnarsson, H. Sasaki, and K. Sasaki. 2005. "Relationships between ocular dimensions and adult stature among participants in the Reykjavik Eye Study." *Acta Ophthalmol* 83 (6):734–8. doi: 10.1111/j.1600-0420.2005.00540.x.
- Fea, A. M., F. Annetta, S. Cirillo, D. Campanella, et al. 2005. "Magnetic resonance imaging and Orbscan assessment of the anterior chamber." *J Cat Refract Surg* 31 (9):1713–8. doi: 10.1016/j.jcrs.2005.02.040.
- Fincham, E. F. 1937. "The mechanism of accommodation." *Br J Ophthalmol Suppl* 8 (5–80).

- Fisher, A. J., and A. W. Christie. 1965. "A note on disability glare." *Vision Res* 5 (9):565–71. doi: 10.1016/0042-6989(65)90089-1.
- Fisher, R. F. 1969a. "Elastic constants of the human lens capsule." *J Physiol* 201 (1):1–19. doi: 10.1113/jphysiol.1969.sp008739.
- Fisher, R. F. 1969b. "The significance of the shape of the lens and capsular energy changes in accommodation." *J Physiol* 201 (1):21–47. doi: 10.1113/jphysiol.1969.sp008740.
- Fisher, R. F. 1971. "The elastic constants of the human lens." *J Physiol* 212 (1):147–80. doi: 10.1113/jphysiol.1971.sp009315.
- Fisher, R. F. 1973. "Presbyopia and the changes with age in the human crystalline lens." *J Physiol* 228 (3):765–79. doi: 10.1113/jphysiol.1973.sp010111.
- Fisher, R. F. 1977. "The force of contraction of the human ciliary muscle during accommodation." *J Physiol* 270 (1):51–74. doi: 10.1113/jphysiol.1977.sp011938.
- Fisher, R. F. 1986. "The ciliary body in accommodation." *Trans Ophthalmol Soc U K* 105 (Pt 2):208–19.
- Fisher, R. F., and B. E. Pettet. 1973. "Presbyopia and the water content of the human crystalline lens." *J Physiol* 234 (2):443–7. doi: 10.1113/jphysiol.1973.sp010353.
- Fledelius, H. C., and M. Stubgaard. 1986. "Changes in refraction and corneal curvature during growth and adult life. A cross-sectional study." *Acta Ophthalmol* 64 (5):487–91. doi: 10.1111/j.1755-3768.1986.tb06959.x.
- Fujikado, T., T. Kuroda, S. Ninomiya, N. Maeda, et al. 2004. "Age-related changes in ocular and corneal aberrations." *Am J Ophthalmol* 138 (1):143–6. doi: 10.1016/j.ajo.2004.01.051.
- Fujisawa, K., and K. Sasaki. 1995. "Changes in light scattering intensity of the transparent lenses of subjects selected from population-based surveys depending on age: analysis through Scheimpflug images." *Ophthalmic Res* 27 (2):89–101. doi: 10.1159/000267604.
- Glasser, A. 2011. "Chapter 3. Accommodation." In *Adler's Physiology of the Eye*, edited by P. L. Kaufman and A. Alm, 41–70. Elsevier.
- Glasser, A., and M. C. Campbell. 1998. "Presbyopia and the optical changes in the human crystalline lens with age." *Vision Res* 38 (2):209–29. doi: 10.1016/s0042-6989(97)00102-8.
- Glasser, A., and M. C. Campbell. 1999. "Biometric, optical and physical changes in the isolated human crystalline lens with age in relation to presbyopia." *Vision Res* 39 (11):1991–2015. doi: 10.1016/s0042-6989(98)00283-1.
- Goh, W. S., and C. S. Lam. 1994. "Changes in refractive trends and optical components of Hong Kong Chinese aged 19–39 years." *Ophthalmic Physiol Opt* 14 (4):378–82. doi: 10.1111/j.1475-1313.1994.tb00129.x.
- Goto, T., S. D. Klyce, X. Zheng, N. Maeda, et al. 2001. "Gender- and age-related differences in corneal topography." *Cornea* 20 (3):270–6. doi: 10.1097/00003226-200104000-00007.
- Grosvenor, T., and R. Scott. 1991. "Comparison of refractive components in youth-onset and early adult-onset myopia." *Optom Vis Sci* 68 (3):204–9. doi: 10.1097/0006324-199103000-00008.
- Guirao, A., M. Redondo, and P. Artal. 2000. "Optical aberrations of the human cornea as a function of age." *J Opt Soc Am A* 17 (10):1697–702. doi: 10.1364/josaa.17.001697.
- Gullstrand, A. 1909. "Appendix IV: The mechanism of accommodation." In *Helmholtz's Handbuch der Physiologischen Optik*, vol. 1, 3rd edn (English translation edited by J. P. Southall, Optical Society of America, 1924), pp. 382–415.
- Hayashi, K., H. Hayashi, and F. Hayashi. 1995. "Topographic analysis of the changes in corneal shape due to aging." *Cornea* 14 (5):527–32.
- Hess, C. 1901. "Arbeiten aus dem Gebiete der Accommodationslehre. VI. Die relative Accommodation." *Graefe's Arch Klin Exp Ophthalmol* 52:143–74 [cited by M. Alpern, 1962].

- Hirsch, M. J. 1959. "Changes in astigmatism after the age of forty." *Am J Optom Arch Am Acad Optom* 36:395–405. doi: 10.1097/00006324-195908000-00001.
- Hockwin, O., S. Lerman, and C. Ohrloff. 1984. "Investigations on lens transparency and its disturbances by microdensitometric analyses of Scheimpflug photographs." *Curr Eye Res* 3 (1):15–22. doi: 10.3109/02713688408997183.
- Hofstetter, H. W. 1965. "A longitudinal study of amplitude changes in presbyopia." *Am J Optom Arch Am Acad Optom* 42 (1):3–8. doi: 10.1097/00006324-196501000-00002.
- Howarth, P. A., X. X. Zhang, A. Bradley, D. L. Still, and L. N. Thibos. 1988. "Does the chromatic aberration of the eye vary with age?" *J Opt Soc Am A* 5 (12):2087–92. doi: 10.1364/josaa.5.002087.
- IJspeert, J. K., P. W. de Waard, T. J. van den Berg, and P. T. de Jong. 1990. "The intraocular straylight function in 129 healthy volunteers; dependence on angle, age and pigmentation." *Vision Res* 30 (5):699–707. doi: 10.1016/0042-6989(90)90096-4.
- Iribarren, R. 2015. "Crystalline lens and refractive development." *Prog Retin Eye Res* 47:86–106. doi: 10.1016/j.preteyeres.2015.02.002.
- Irving, E. L., C. M. Machan, S. Lam, P. K. Hryncak, and L. Lillakas. 2019. "Refractive error magnitude and variability: Relation to age." *J Optom* 12 (1):55–63. doi: 10.1016/j.optom.2018.02.002.
- Jongenelen, S., J. J. Rozema, M. J. Tassignon, Evicr.net, and Group Project Gullstrand Study. 2015. "Distribution of the crystalline lens power in vivo as a function of age." *Invest Ophthalmol Vis Sci* 56 (12):7029–35. doi: 10.1167/iovs.15-18047.
- Kadlecova, V., M. Peleska, and A. Vasko. 1958. "Dependence on age of the diameter of the pupil in the dark." *Nature* 182 (4648):1520–1. doi: 10.1038/1821520a0.
- Kanai, A., and H. E. Kaufman. 1973. "Electron microscopic studies of corneal stroma: aging changes of collagen fibers." *Ann Ophthalmol* 5 (3):285–7 passim.
- Kasturirangan, S., E. L. Markwell, D. A. Atchison, and J. M. Pope. 2008. "In vivo study of changes in refractive index distribution in the human crystalline lens with age and accommodation." *Invest Ophthalmol Vis Sci* 49 (6):2531–40. doi: 10.1167/iovs.07-1443.
- Kasturirangan, S., E. L. Markwell, D. A. Atchison, and J. M. Pope. 2011. "MRI study of the changes in crystalline lens shape with accommodation and aging in humans." *J Vis* 11 (3):19, 1–6. doi: 10.1167/11.3.19.
- Khoramnia, R., T. M. Rabsilber, and G. U. Auffarth. 2007. "Central and peripheral pachymetry measurements according to age using the Pentacam rotating Scheimpflug camera." *J Cat Ref Surg* 33 (5):830–6. doi: 10.1016/j.jcrs.2006.12.025.
- Kiely, P. M., G. Smith, and L. G. Carney. 1984. "Meridional variations of corneal shape." *Am J Optom Physiol Optom* 61 (10):619–26. doi: 10.1097/00006324-198410000-00001.
- Kingston, A. C., and I. G. Cox. 2013. "Population spherical aberration: associations with ametropia, age, corneal curvature, and image quality." *Clin Ophthalmol* 7:933–8. doi: 10.2147/OPTH.S44056.
- Knoblauch, K., F. Saunders, M. Kusuda, R. Hynes, et al. 1987. "Age and illuminance effects in the Farnsworth-Munsell 100-hue test." *Appl Opt* 26 (8):1441–8. doi: 10.1364/AO.26.001441.
- Koretz, J. F., C. A. Cook, and P. L. Kaufman. 1997. "Accommodation and presbyopia in the human eye. Changes in the anterior segment and crystalline lens with focus." *Invest Ophthalmol Vis Sci* 38 (3):569–78.
- Koretz, J. F., and G. H. Handelman. 1986. "Modeling age-related accommodative loss in the human eye." *Math Modelling* 7 (5–8):1003–14. doi: 10.1016/0270-0255(86)90146-6.
- Koretz, J. F., and G. H. Handelman. 1988. "How the human eye focuses." *Sci Am* 259 (1):92–9. doi: 10.1038/scientificamerican0788-92.

- Koretz, J. F., S. A. Strenk, L. M. Strenk, and J. L. Semmlow. 2004. "Scheimpflug and high-resolution magnetic resonance imaging of the anterior segment: a comparative study." *J Opt Soc Am A* 21 (3):346–54. doi: 10.1364/josaa.21.000346.
- Kumnick, L. S. 1954. "Pupillary psychosensory restitution and aging." *J Opt Soc Am* 44 (9):735–41. doi: 10.1364/josa.44.000735.
- Kuroda, T., T. Fujikado, S. Ninomiya, N. Maeda, et al. 2002. "Effect of aging on ocular light scatter and higher order aberrations." *J Refract Surg* 18 (5):S598–S602. doi: 10.3928/1081-597X-20020901-20.
- Lam, A. K. C., C. C. Y. Chan, M. H. Lee, and K. M. Wong. 1999. "The aging effect on corneal curvature and the validity of Javal's rule in Hong Kong Chinese." *Cur Eye Res* 18 (2):83–90.
- Lam, A. K. C., and W. A. Douthwaite. 2000. "The ageing effect on the central posterior corneal radius." *Ophthalmic Physiol Opt* 20 (1):63–9. doi: 10.1046/j.1475-1313.2000.00469.x.
- Lam, C. S. Y., W. S. H. Goh, Y. K. Tang, K. K. Tsui, et al. 1994. "Changes in refractive trends and optical components of Hong Kong Chinese aged over 40 years." *Ophthalmic Physiol Opt* 14 (4):383–8. doi: 10.1111/j.1475-1313.1994.tb00129.x.
- Landers, J. A., K. R. Billing, R. A. Mills, T. R. Henderson, and J. E. Craig. 2007. "Central corneal thickness of indigenous Australians within central Australia." *Am J Ophthalmol* 143 (2):360–2. doi: 10.1016/j.ajo.2006.09.047.
- Lau, E., K. Mütze, and K. Weber. 1955. "Die chromatische Aberration des menschlichen Auges." *Graefe's Arch Klin Exp Ophthalmol* 157:39–41.
- Leinhos, R. 1959. "Die Altersabhängigkeit des Augenpupillendurchmessers." *Optik* 16:669–71.
- Lekskul, M., P. Aimpun, B. Nawanopparatskul, S. Bumrungsawat, et al. 2005. "The correlations between central corneal thickness and age, gender, intraocular pressure and refractive error of aged 12–60 years old in rural Thai community [abstract]." *J Med Assoc Thailand* 88 Suppl 3:S175–S9.
- Li, Z., W. Qu, J. Huang, Z. Meng, et al. 2022. "Effect of age and cycloplegia on the morphology of the human crystalline lens: swept-source OCT study." *J Cataract Refract Surg* 48 (1):8–15. doi: 10.1097/j.jcrs.0000000000000693.
- Liou, H.-L., and N. A. Brennan. 1997. "Anatomically accurate, finite model eye for optical modeling." *J Opt Soc Am A* 14 (8):1684–95. doi: 10.1364/josaa.14.001684.
- Lister, L. J., M. Suheimat, P. K. Verkicular, E. A. Mallen, and D. A. Atchison. 2016. "Influence of gravity on ocular lens position." *Invest Ophthalmol Vis Sci* 57 (4):1885–91. doi: 10.1167/ios.15-18533.
- Lyle, W. M. 1971. "Changes in corneal astigmatism with age." *Am J Optom Arch Am Acad Optom* 48 (6):467–78. doi: 10.1097/00006324-197106000-00002.
- Malik, N. S., S. J. Moss, N. Ahmed, A. J. Furth, et al. 1992. "Ageing of the human corneal stroma: structural and biochemical changes." *Biochim Biophys Acta* 1138 (3):222–8. doi: 10.1016/0925-4439(92)90041-k.
- Mathur, A., D. A. Atchison, and W. N. Charman. 2010. "Effects of age on peripheral ocular aberrations." *Opt Express* 18 (6):5840–53. doi: 10.1364/OE.18.005840.
- McLellan, J. S., S. Marcos, and S. A. Burns. 2001. "Age-related changes in monochromatic wave aberrations of the human eye." *Invest Ophthalmol Vis Sci* 42 (6):1390–5.
- Mellerio, J. 1971. "Light absorption and scatter in the human lens." *Vision Res* 11 (2):129–41. doi: 10.1016/0042-6989(71)90229-x.
- Mellerio, J. 1987. "Yellowing of the human lens: nuclear and cortical contributions." *Vision Res* 27 (9):1581–7. doi: 10.1016/0042-6989(87)90166-0.
- Millodot, M. 1976. "The influence of age on the chromatic aberration of the eye." *Albrecht Von Graefes Arch Klin Exp Ophthalmol* 198 (3):235–43. doi: 10.1007/BF00410716.

- Millodot, M., and J. Sivak. 1973. "Influence of accommodation on the chromatic aberration of the eye." *Br J Physiol Opt* 28 (3):169–74.
- Miranda, M. N. 1979. "The geographic factor in the onset of presbyopia." *Trans Am Ophthalmol Soc* 77:603–21.
- Mordi, J. A., and W. K. Adrian. 1985. "Influence of age on chromatic aberration of the human eye." *Am J Optom Physiol Opt* 62 (12):864–9. doi: 10.1097/00006324-198512000-00007.
- Morrell, A., H. D. Whitefoot, and W. N. Charman. 1991. "Ocular chromatic aberration and age." *Ophthalmic Physiol Opt* 11 (4):385–90.
- Ní Dhubhghaill, S., J. J. Rozema, S. Jongenelen, I. Ruiz Hidalgo, et al. 2014. "Normative values for corneal densitometry analysis by Scheimpflug optical assessment." *Invest Ophthalmol Vis Sci* 55 (1):162–8. doi: 10.1167/iovs.13-13236.
- Niesel, P. 1982. "Visible changes of the lens with age." *Trans Ophthalmol Soc UK* 102 (3):327–30.
- Pan, C. W., Y. F. Zheng, A. R. Anuar, M. Chew, et al. 2013. "Prevalence of refractive errors in a multiethnic Asian population: the Singapore epidemiology of eye disease study." *Invest Ophthalmol Vis Sci* 54 (4):2590–8. doi: 10.1167/iovs.13-11725.
- Pardhan, S., and J. Beesley. 1999. "Measurement of corneal curvature in young and older normal subjects." *J Refract Surg* 15 (4):469–74.
- Pardue, M. T., and J. G. Sivak. 2000. "Age-related changes in human ciliary muscle." *Optom Vis Sci* 77 (4):204–10. doi: 10.1097/00006324-200004000-00013.
- Pierscionek, B. K. 1996. "Aging changes in the optical elements of the eye." *J Biomed Opt* 1 (2):147–56. doi: 10.1117/12.230729.
- Plainis, S., and I. G. Pallikaris. 2008. "Ocular monochromatic aberrations statistics in a large emmetropic population." *J Mod Opt* 55 (4–5):759–72. doi: 10.1080/09500340701469831.
- Pokorny, J., V. C. Smith, and M. Lutze. 1987. "Aging of the human lens." *Appl Opt* 26 (8):1437–40. doi: 10.1364/AO.26.001437.
- Rabbetts, R. B. 2007. "Chapter 12. Schematic eyes." In *Bennett and Rabbetts' Clinical Visual Optics*, 221–43. Butterworth-Heinemann.
- Ramsdale, C., and W. N. Charman. 1989. "A longitudinal study of the changes in the static accommodation response." *Ophthalmic Physiol Opt* 9 (3):255–63. doi: 10.1111/j.1475-1313.1989.tb00903.x.
- Richdale, K., M. A. Bullimore, L. T. Sinnott, and K. Zadnik. 2016. "The effect of age, accommodation, and refractive error on the adult human eye." *Optom Vis Sci* 93 (1):3–11. doi: 10.1097/OPX.0000000000000757.
- Richdale, K., M. A. Bullimore, and K. Zadnik. 2008. "Lens thickness with age and accommodation by optical coherence tomography." *Ophthalmic Physiol Opt* 28 (5):441–7. doi: 10.1111/j.1475-1313.2008.00594.x.
- Richdale, K., L. T. Sinnott, M. A. Bullimore, P. A. Wassenaar, et al. 2013. "Quantification of age-related and per diopter accommodative changes of the lens and ciliary muscle in the emmetropic human eye." *Invest Ophthalmol Vis Sci* 54 (2):1095–105.
- Rozema, J. J., S. Hershko, M. J. Tassignon, and Project Gullstrand Study Group for Evicr.net. 2019. "The components of adult astigmatism and their age-related changes." *Ophthalmic Physiol Opt* 39 (3):183–93. doi: 10.1111/opo.12616.
- Rozema, J. J., and S. Ní Dhubhghaill. 2020. "Age-related axial length changes in adults: a review." *Ophthalmic Physiol Opt* 40 (6):710–7. doi: 10.1111/opo.12728.
- Rozema, J. J., T. J. van den Berg, and M. J. Tassignon. 2010. "Retinal straylight as a function of age and ocular biometry in healthy eyes." *Invest Ophthalmol Vis Sci* 51 (5):2795–9. doi: 10.1167/iovs.09-4056.
- Rüfer, F., A. Schroder, C. Bader, and C. Erb. 2007. "Age-related changes in central and peripheral corneal thickness - Determination of normal values with the Orbscan II topography system." *Cornea* 26 (1):1–5. doi: 10.1097/01.ico.0000240095.95067.3f.

- Rynders, M. C., T. Grosvenor, and J. M. Enoch. 1995. "Stability of the Stiles-Crawford function in a unilateral amblyopic subject over a 38-year period: a case study." *Optom Vis Sci* 72 (3):177–85. doi: 10.1097/00006324-199503000-00005.
- Said, F. S., and W. S. Sawires. 1972. "Age dependence of change in pupil diameter in the dark." *Optica Acta* 19 (5):359–61. doi: 10.1080/713818582.
- Said, F. S., and R. A. Weale. 1959. "The variation with age of the spectral transmissivity of the living human crystalline lens." *Gerontol* 3 (4):213–31. doi: 10.1159/000210900.
- Sample, P. A., F. D. Esterson, R. N. Weinreb, and R. M. Boynton. 1988. "The aging lens: in vivo assessment of light absorption in 84 human eyes." *Invest Ophthalmol Vis Sci* 29 (8):1306–11.
- Sanchis-Gimeno, J. A., A. Lleo-Perez, L. Alonso, and M. S. Rahhal. 2004. "Caucasian emmetropic aged subjects have reduced corneal thickness values: emmetropia, CCT and age." *Int Ophthalmol* 25 (4):243–6. doi: 10.1007/s10792-005-5017-1.
- Saunders, H. 1981. "Age-dependence of human refractive errors." *Ophthalmic Physiol Opt* 1 (3):159–74.
- Saunders, H. 1986. "A longitudinal study of the age-dependence of human ocular refraction. 1. Age-dependent changes in the equivalent sphere." *Ophthalmic Physiol Opt* 6 (1):39–46.
- Schachar, R. A. 1992. "Cause and treatment of presbyopia with a method for increasing the amplitude of accommodation." *Ann Ophthalmol* 24 (12):445–7, 52.
- Schachar, R. A. 2012. *The Mechanism of Accommodation and Presbyopia*. Amsterdam: Kugler Publications.
- Schachar, R. A., M. Mani, and I. H. Schachar. 2017. "Image registration reveals central lens thickness minimally increases during accommodation." *Clin Ophthalmol* 11:1625–36. doi: 10.2147/OPTH.S144238.
- Shufelt, C., S. Fraser-Bell, M. Ying-Lai, M. Torres, and R. Varma. 2005. "Refractive error, ocular biometry, and lens opalescence in an adult population: the Los Angeles Latino Eye Study." *Invest Ophthalmol Vis Sci* 46 (12):4450–60. doi: 10.1167/iovs.05-0435.
- Smith, G., D. A. Atchison, and B. K. Pierscionek. 1992. "Modeling the power of the aging human eye." *J Opt Soc Am A* 9 (12):2111–7. doi: 10.1364/josaa.9.002111.
- Smith, G., M. J. Cox, R. Calver, and L. F. Garner. 2001. "The spherical aberration of the crystalline lens of the human eye." *Vision Res* 41 (2):235–43. doi: 10.1016/s0042-6989(00)00206-6.
- Smith, G., and B. K. Pierscionek. 1998. "The optical structure of the lens and its contribution to the refractive status of the eye." *Ophthalmic Physiol Opt* 18 (1):21–9. doi: 10.1046/j.1475-1313.1998.97000586.x.
- Strenk, S. A., L. M. Strenk, and J. F. Koretz. 2005. "The mechanism of presbyopia." *Prog Retin Eye Res* 24 (3):379–93. doi: 10.1016/j.preteyes.2004.11.001.
- Strenk, S. A., J. L. Semmlow, L. M. Strenk, P. Munoz, et al. 1999. "Age-related changes in human ciliary muscle and lens: a magnetic resonance imaging study." *Invest Ophthalmol Vis Sci* 40 (6):1162–9.
- Suzuki, S., Y. Suzuki, A. Iwase, and M. Araie. 2005. "Corneal thickness in an ophthalmologically normal Japanese population." *Ophthalmol* 112 (8):1327–36. doi: 10.1016/j.ophtha.2005.03.022.
- Tamm, S., E. Tamm, and J. W. Rohen. 1992. "Age-related changes of the human ciliary muscle. A quantitative morphometric study." *Mech Ageing Dev* 62 (2):209–21. doi: 10.1016/0047-6374(92)90057-k.
- Topuz, H., M. Ozdemir, A. Cinal, and Y. Gumusalan. 2004. "Age-related differences in normal corneal topography." *Ophthal Surg Lasers Imaging* 35 (4):298–303. doi: 10.3928/1542-8877-20040701-06.

- van de Kraats, J., and D. van Nooren. 2007. "Optical density of the aging human ocular media in the visible and the UV." *J Opt Soc Am A* 24 (7):1842–56. doi: 10.1364/josaa.24.001842.
- van den Berg, T. J. T. P., and K. E. W. P. Tan. 1994. "Light transmittance of the human cornea from 320 to 700 nm for different ages." *Vision Res* 34 (11):1453–6. doi: 10.1016/0042-6989(94)90146-5.
- Ware, C. 1982. "Human axial chromatic aberration found not to decline with age." *Graefes Arch Clin Exp Ophthalmol* 218 (1):39–41. doi: 10.1007/BF02134100.
- Watson, A. B., and J. I. Yellott. 2012. "A unified formula for light-adapted pupil size." *J Vis* 12 (10):12.
- Weale, R. A. 1981. "Human ocular aging and ambient temperature." *Br J Ophthalmol* 65 (12):869–70. doi: 10.1136/bjo.65.12.869.
- Winn, B., D. Whitaker, D. B. Elliott, and N. J. Phillips. 1994. "Factors affecting light-adapted pupil size in normal human subjects." *Invest Ophthalmol Vis Sci* 35 (3):1132–7.
- Wojciechowski, R., N. Congdon, W. Annineri, and A. Teo Broman. 2003. "Age, gender, biometry, refractive error, and the anterior chamber angle among Alaskan Eskimos." *Ophthalmol* 110 (2):365–75. doi: 10.1016/S0161-6420(02)01748-7.
- Wood, J. M., and A. A. Black. 2017. "Chapter 27. Aging and the eye's optics." In *Handbook of Visual Optics: Instrumentation and Vision Correction*, Volume II, edited by P. Artal, 361–75. London: CRC Press.

Appendices



Taylor & Francis
Taylor & Francis Group
<http://taylorandfrancis.com>

Appendix 1: Paraxial Optics

A1.1 INTRODUCTION

The study of the image formation by optical systems can be reduced to the imagery of selected points in the object space or field. The study of the image formation of an object point can be reduced to tracing a number of rays from this point, through the system, and examining their paths in image space. Such a situation is shown in Figure A1.1, which shows an object point **Q** and a set of three image-forming rays. Ideally, these rays should be concurrent at some point – say **Q'** – in the image space, as shown in the figure. However, they are not usually concurrent, and this is due to what are known as **aberrations**. The greater the spread of the rays in the image plane, the greater the aberrations. Usually, the aberrations increase as the light beam widens and the object point **Q** moves further away from the optical axis. If rays are traced very close to the axis, aberrations are reduced and the raytrace equations can be simplified by making some simple approximations called paraxial approximations.

In this book, exact or actual rays are referred to as **finite** or real rays, and rays traced using the paraxial approximations are referred to as **paraxial** rays.

A1.1.1 FINITE RAYTRACING

The tracing of a finite ray through an optical system involves a few steps:

1. Choosing an origin or starting point and a direction for the ray, such as the point **O** and angle u , shown in Figure A1.2 (sometimes the starting point may be off-axis).
2. Locating the point of intersection **B** of the ray with the surface, using trigonometry, algebra, and a knowledge of the surface position and shape.
3. Determining the angle of incidence i at this surface.
4. Refraction at **B** by the application of Snell's law, which connects the angles of incidence i and refraction i' with the refractive indices, n and n' , by

$$n' \sin(i') = n \sin(i) \quad (\text{A1.1})$$

to find the angle of refraction i' and angle u' the ray makes with the optical axis (Figure A1.2). These angles specify the direction of the refracted ray. This is called the “refraction” step. If there is more than one surface in the system, the above steps 2–4 are repeated until the last surface is reached. Each return to step 2 requires the point of intersection with the next surface to be

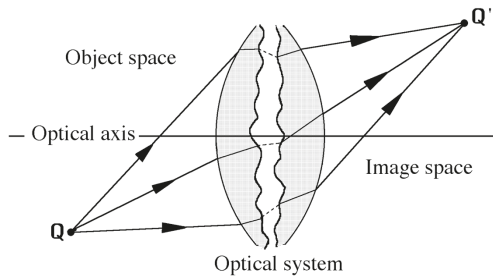


FIGURE A1.1 Ideal imagery.

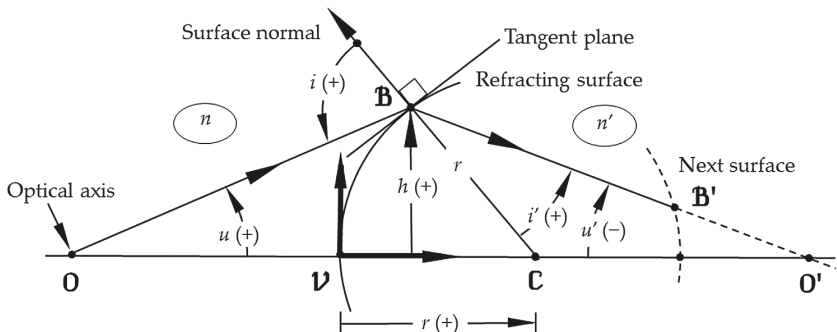


FIGURE A1.2 Refraction by a surface, showing important variables and the sign convention.

found. Figure A1.1 shows a raytrace to the point \mathbf{B}' on the next surface. The process of tracing to the next surface is called the “transfer” step.

- Locating the point of intersection with the optical axis or the expected image surface.

The sign convention used for tracing rays is that shown in Figure A1.2. Distances to the left of a surface or below the optical axis are negative and those to the right or above are positive. Angles due to an anticlockwise rotation of the ray from the optical axis are positive, and those due to a clockwise rotation are negative. The origin for axes at each surface is the vertex \mathbf{V} . The signs enclosed in brackets indicate the signs of the quantities shown in the figure.

A1.2 THE PARAXIAL APPROXIMATIONS AND PARAXIAL RAYS

If rays are traced very close to the optical axis, then all the angles shown in Figure A1.2 are small. For small angles x expressed in radians,

$$\tan(x) \approx \sin(x) \approx x \quad (\text{A1.2})$$

This approximation improves as the size of the angle decreases. When we apply this paraxial approximation to raytracing equations, Snell's law reduces to

$$n'i' = ni \quad (\text{A1.3})$$

The useful outcome of this paraxial approximation is that, if all the rays within the beam shown in Figure A1.1 are traced as paraxial rays, they are all concurrent at some point in image space. In this sense, paraxial rays are aberration-free rays.

A1.2.1 DEFINITION OF A PARAXIAL RAY

A paraxial ray is a finite ray traced close to the optical axis, in which the angles involved are sufficiently small that replacing the sines and tangents of the angles by the angles themselves (in radians) in raytrace equations produces a negligible error.

A1.2.2 PARAXIAL RAYTRACE EQUATIONS

There are two paraxial raytrace equations that are used for steps 2–4 in the previous section.

A1.2.2.1 Paraxial Refraction Equation

This equation is used to determine the new direction of the ray after refraction:

$$n'u' - nu = -hF \quad (\text{A1.4})$$

where

$$F = C(n' - n) \quad (\text{A1.5})$$

is the refractive power of the surface, C is the surface curvature ($= 1/r$), and the other variables are shown in Figure A1.2.

A1.2.2.2 Paraxial Transfer Equation

This equation is used to locate the intersection point or height at the next surface:

$$h' = h + u'd \quad (\text{A1.6})$$

This equation can be derived with the quantities shown in Figure A1.3.

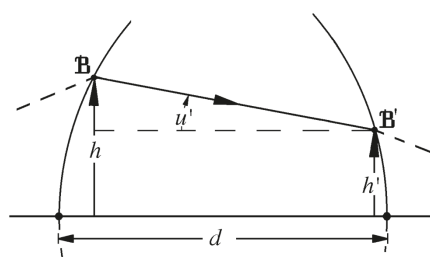


FIGURE A1.3 Raytracing: the transfer step.

A1.3 A PARAXIAL RAYTRACING SCHEME

Since most optical systems consist of more than one surface, equations (A1.4) to (A1.6) are used repeatedly. The following scheme shows how this is done, with a small change in notation. The variables given in the following equations are defined in Figure A1.4.

A1.3.1 STEP 1: CHOOSING A RAY

We assume that the position of the axial point \mathbf{O} , which is the origin of the ray or where an off-axis ray crosses the axis, is known. Let the distance of this point from the first surface vertex be l_v . We now choose a direction of the ray by selecting a pair of values u_1 and h_1 , which satisfy the equation

$$l_v = -h_1/u_1 \quad (\text{A1.7})$$

A1.3.2 STEP 2: REFRACTION AT THE j TH SURFACE

Starting at the first surface (i.e., $j = 1$), we use equation (A1.4), i.e.,

$$n'_j u'_j - n_j u_j = -h_j F_j \quad (\text{A1.8})$$

where

$$F_j = C_j(n'_j - n_j) \quad (\text{A1.9})$$

is the power of the j th surface.

A1.3.3 STEP 3: TRANSFER TO THE NEXT ($j + 1$)TH SURFACE

Here we use equation (A1.6), i.e.,

$$h_{j+1} = h_j + u'_j d_j \quad (\text{A1.10})$$

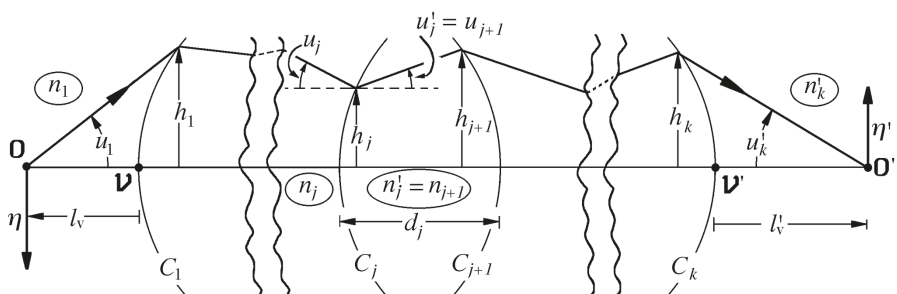


FIGURE A1.4 The tracing of a paraxial ray through a general system consisting of k surfaces.

Steps 2 and 3 are repeated at each surface, using the following equivalences:

$$n'_j = n_{j+1} \text{ and } u'_j = u_{j+1} \quad (\text{A1.11})$$

until the last (k th) surface is reached. At this point, the axial distance of the point where this ray crosses the axis is given by the equation

$$l'_v = -h_k / u'_k \quad (\text{A1.12})$$

A1.3.4 IMAGE SIZE AND MAGNIFICATION

Usually, we need to know the transverse magnification M of the image, which is defined as

$$M = \frac{\text{image size}(\eta')}{\text{object size}(\eta)} \quad (\text{A1.13})$$

where the object size (η) and image size (η') are shown in Figure A1.4. The magnification can be found from the above raytrace and is given by the equation

$$M = \frac{n_1 u_1}{n'_k u_k} \quad (\text{A1.14})$$

A1.3.5 SPECIAL CASE OF THE OBJECT AT INFINITY

If the object is at infinity, equation (A1.7) cannot be used to generate a ray because the value of l_v is infinite. In this case, $u_1 = 0$, and we can choose any suitable value of h_1 .

A1.3.6 CHOICE OF RAY

Since paraxial rays are aberration-free rays, all paraxial rays in a beam arising from an object point are concurrent at the image point. To locate the image point, we need in principle to trace only two rays in the beam to find the point of concurrency. However, for an axial object point, one of these rays may be taken as the optical axis. Therefore, for axial objects we need to trace only one ray, and where this ray intersects the optical axis is the image point and the location of the paraxial image plane.

A1.4 THE OPTICAL INVARIANT

If two distinct paraxial rays, denoted by A and B, are traced through any optical system, the quantity

$$n_A(u_A h_B - u_B h_A)$$

at any surface and on either side of the surface has the same value throughout the system, and thus its value is invariant. Using the symbol H to denote its value,

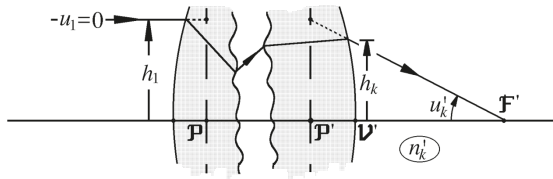


FIGURE A1.5 Particular raytraces for determining the positions of the back cardinal points.

$$H = n_A(u_A h_B - u_B h_A) \quad (\text{A1.15})$$

This quantity is useful in aberration theory, which we discuss in Appendix 2.

A1.5 CARDINAL POINTS AND EQUIVALENT POWER

The location of the back cardinal points \mathbf{P}' and \mathbf{F}' can be found from the results of a paraxial ray trace from object space to image space, initially parallel to the axis (i.e., $u_1 = 0$), as shown in Figure A1.5. Given the initial ray height h_1 , final ray height h_k , and final angle u'_k , the positions of these points can be found from the equations

$$\mathbf{P}'\mathbf{F}' = -h_1/u'_k \quad (\text{A1.16})$$

$$\mathbf{V}'\mathbf{F}' = -h_k/u'_k \quad (\text{A1.17})$$

The equivalent power F is given by the equation

$$F = n'_k/\mathbf{P}'\mathbf{F}' \quad (\text{A1.18a})$$

The position of the back nodal point \mathbf{N}' is given by the equation

$$\mathbf{P}'\mathbf{N}' = (n'_k - n_1)/F \quad (\text{A1.19})$$

The positions of the front cardinal points \mathbf{P} , \mathbf{F} , and \mathbf{N} can be found by tracing a similar paraxial ray from the image space (i.e., $u'_k = 0$) back through the system into object space. The equivalent power can also be calculated from this raytrace with

$$F = -n_1/\mathbf{P}\mathbf{F} \quad (\text{A1.18b})$$

giving the same numerical value as equation (A1.18a). It can also be found that

$$\mathbf{P}\mathbf{N} = \mathbf{F}'\mathbf{N}' \quad (\text{A1.20})$$

A1.6 THE LENS EQUATION

If the positions of the cardinal points and the equivalent power of an optical system are known, the position of an image can be found without the above detailed raytracing. Instead, it can be found by the direct application of the lens equation

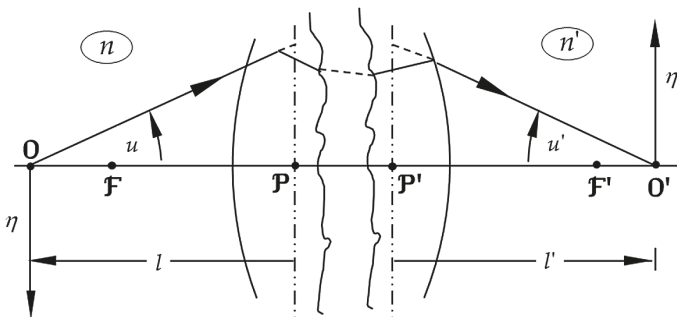


FIGURE A1.6 The general system and the lens equation.

$$n'l' - n'l = L' - L = F \quad (\text{A1.21})$$

where n' and n are the object and image space refractive indices, L is the object reduced vergence ($= n/l$) and L' is the image vergence ($= n'/l'$), the distance l is measured from the front principal plane \mathbf{P} and the distance l' is measured from the back principal plane at \mathbf{P}' . F is the equivalent power of the system, defined by equations (A1.18a) or (A1.18b), and is the power of an equivalent thin lens placed at the principal planes (Figure A1.6).

In this situation, equation (A1.14) for the transverse magnification is still applicable and, using the symbols shown in Figure A1.6, this equation can be written as

$$M = nu/(n'u') \quad (\text{A1.22})$$

It can also be expressed in terms of the distances l and l' of the object and images from the respective principal planes by the equation

$$M = nl'/(n'l) \quad (\text{A1.23})$$

For air, where the refractive index is 1, the corresponding reduced vergence (L or L') is also referred to as the vergence. The latter term is used throughout this book when air is on the object side of the eye.

A1.7 GAUSSIAN OPTICS

Sometimes it is useful to assume that rays that are beyond the paraxial region, according to the approximation in equation (A1.2), nevertheless behave as if they are paraxial rays (i.e., are aberration-free). The application of paraxial approximations beyond the paraxial region is called Gaussian optics.

SUMMARY OF MAIN SYMBOLS

i	angle of incidence
u	paraxial ray angle

<i>h</i>	paraxial ray height
<i>n</i>	refractive index
<i>F</i>	(equivalent) power of a surface or lens
<i>C</i>	surface curvature (reciprocal of radius of curvature)
<i>d</i>	separation between adjacent refracting surfaces
<i>l</i>	for thin components, this is the distance from the vertex V of the component to the axial object point O . For thick components, the distance is measured from the front principal plane P to the axial object point O .
<i>L</i>	corresponding reduced vergence ($= n/l$) of /
<i>M</i>	transverse magnification
<i>H</i>	optical invariant
η	object size
F	focal point
N	nodal point
P	principal point
Q	off-axis object point
O	on-axis object point
V	vertex point

A prime ('') superscript following the above symbols (except *F*, *C*, *d*, *M*, and *H*) means that a quantity occurs after refraction or in image space.

Appendix 2: Seidel Aberration Theory

A2.1 QUANTIFICATION OF ABERRATIONS

In the absence of aberrations, diffraction, and scatter, all rays from any point in object space, that are refracted by an optical system, are focused to one point in the image plane – that is, they are concurrent. The position of this point can be predicted by using the paraxial equations described in Appendix 1. In the presence of aberrations, the rays are not concurrent at the expected image point, but intersect the paraxial image plane in a spread-out pattern.

There are three common ways of quantifying the aberrations of an optical system, namely *wave*, *transverse*, and *longitudinal*. Aberrations of a system are often determined by calculating the aberrations of representative rays. For each ray, there is always a wave and a transverse aberration, and sometimes a longitudinal aberration. Figure A2.1 shows a schematic system and typical rays traversing the system. The wave, transverse, and longitudinal aberrations of this ray are described as follows.

A2.1.1 RAYS FROM AN AXIAL POINT

Figure A2.1a shows a particular real, or finite, ray **OBB'H** in a beam from the point **O**. This ray should cross the optical axis and the paraxial image plane at the point **O'** but, because of aberrations, it intersects the axis at the point **G** and the paraxial image plane at the point **H**. The path **OBO'** indicates the route of the corresponding paraxial ray. The aberration of the real ray may be specified in terms of any of the following quantities:

$$\text{Longitudinal aberration } \mathbf{O}'\mathbf{G} = \delta l'$$

$$\text{Transverse aberration } \mathbf{O}'\mathbf{H}$$

$$\text{Wave (path length) aberration } [\mathbf{OEE}'\mathbf{O}'] - [\mathbf{OBO}'] \quad (\text{A2.1a})$$

where the square brackets refer to optical path lengths, which are products of physical path lengths and refractive indices. The wave aberration is the difference in optical path length between that of the pupil ray (the central ray of the beam) and that of any other ray of the beam. In this case, it is assumed that the pupil ray of the beam travels along the optical axis.

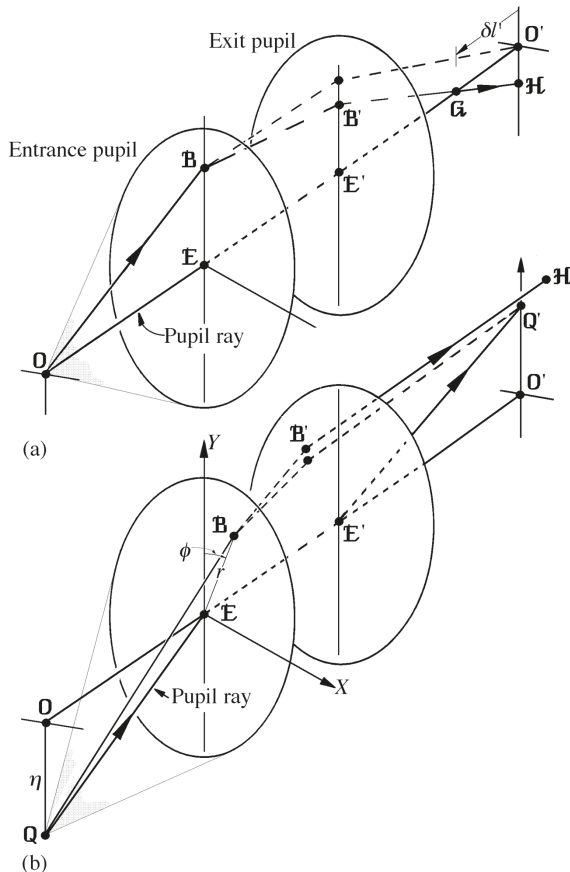


FIGURE A2.1 Three forms for quantifying the aberrations of a ray: wave, transverse, and longitudinal.

A2.1.2 RAYS FROM AN OFF-AXIS POINT

Figure A2.1b shows a general ray from an off-axis point Q . If such a ray does not intersect the optical axis or the pupil ray of the beam, longitudinal aberration is not applicable to the ray. The transverse aberration is $Q'H$. The wave aberration is similar to that given by equation (A2.1a), but now the pupil ray follows the path $QEE'Q'$ instead of the optical axis. In summary,

$$\text{Transverse aberration } Q'H$$

$$\text{Wave (path length) aberration } [QEE'Q'] - [QBQ'] \quad (\text{A2.1b})$$

There are other methods of quantifying the level of aberrations of rays and beams that depend upon the particular aberration. For example, the spherical aberration of the eye is often expressed as an equivalent power error.

A2.2 THE WAVE ABERRATION FUNCTION

The aberration of a particular ray depends upon the co-ordinates of the point **B**, where the ray passes through the entrance pupil. If we set up a (X, Y) co-ordinate system in the entrance pupil, as shown in Figure A2.1b, we can express the wave aberration as a function of X and Y . The wave aberration for the ray through **B** is also a function of the position η of the object point **Q** in the field. The wave aberration W is thus a function of X, Y , and η and can be expressed as a power series in these variables. For a rotationally symmetric system, it has the form

$$W(\eta; X, Y) = {}_0W_{4,0}(X^2 + Y^2)^2 + {}_1W_{3,1}\eta(X^2 + Y^2)Y + {}_2W_{2,0}\eta^2(X^2 + Y^2) + {}_2W_{2,2}\eta^2Y^2 + {}_3W_{1,1}\eta^3Y + \text{higher-order aberrations} \quad (\text{A2.2})$$

The first five terms in this expansion are the *primary aberrations* or *third-order aberrations*, and are known as

$$\begin{aligned} {}_0W_{4,0}(X^2 + Y^2)^2 &\text{ spherical aberration} \\ {}_1W_{3,1}\eta(X^2 + Y^2)Y &\text{ coma} \\ {}_2W_{2,0}\eta^2(X^2 + Y^2) &\text{ field curvature} \\ {}_2W_{2,2}\eta^2Y^2 &\text{ astigmatism} \\ {}_3W_{1,1}\eta^3Y &\text{ distortion} \end{aligned}$$

It is often more convenient to express this function in terms of polar coordinates (r, ϕ) where

$$X = r \sin(\phi) \text{ and } Y = r \cos(\phi) \quad (\text{A2.3})$$

and ϕ is the angle between the line **EB** and the Y -axis, as shown in Figure A2.1b. The above polynomial can then be expressed in the form

$$W(\eta; r, \phi) = {}_0W_{4,0}r^4 + {}_1W_{3,1}\eta r^3 \cos(\phi) + {}_2W_{2,0}\eta^2 r^2 + {}_2W_{2,2}\eta^2 r^2 \cos^2(\phi) + {}_3W_{1,1}\eta^3 r \cos(\phi) + \text{higher-order aberrations} \quad (\text{A2.4})$$

The level of the wave aberration need only be as large as a wavelength to have a significant effect on image quality.

A2.2.1 UNITS OF ABERRATIONS

All the aberrations defined above are distances or differences in distances, and therefore have units of length. Because even very small values can be significant, it is common practice to express wave aberrations in units of the wavelength. For example, a distance of 0.001 mm is equivalent to two wavelengths if the wavelength is 500 nm.

A2.2.2 DEFOCUS AND WAVE ABERRATION

The wave aberration polynomial is very useful in studying the effects of a defocus as well as aberrations on an image. If a defocus is present, we can add the following term:

$$_0 W_{2,0} r^2$$

to the wave aberration polynomial given by equation (A2.4), and the value of $_0 W_{2,0}$ is related to the defocus ΔF by the equation

$$\Delta F = 2_0 W_{2,0} \quad (\text{A2.5})$$

where ΔF is the change in power required to produce that level of defocus.

A2.2.3 CALCULATION OF THE WAVE ABERRATION FUNCTION

The definitions of wave aberration given by equations (A2.1a and b) is ideal for the theoretical analysis of, and deriving explicit equations for, the wave aberration, but only for relatively simple systems. For complex systems, it is easier in practice to determine the wave aberration by numerically raytracing specific rays. Such raytraces do not give the path \mathbf{QBQ}' but the path $\mathbf{QBB}'\mathbf{H}$, so we cannot determine the wave aberration using equations (A2.1a) or (A2.1b). Therefore, in practice, we need a different and more practical definition of wave aberration.

In the ideal optical system, a point source can be thought of as emitting light with spherical wavefronts as shown in Figure A2.2. These wavefronts enter the system

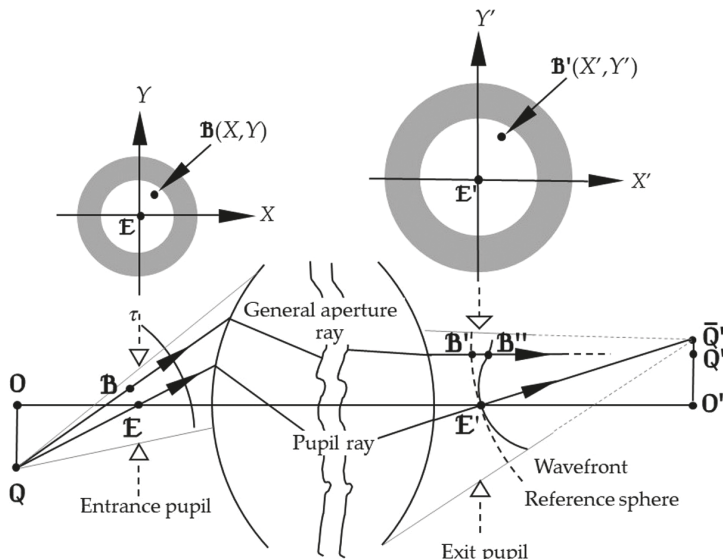


FIGURE A2.2 The distortion of a wavefront passing through an optical system and the wave aberration $[\mathbf{B}'\mathbf{B}'']$.

through the entrance pupil. If the imagery is perfect, these wavefronts exit the system also with a spherical shape. However, if aberrations are present, the wavefronts are distorted. The wave aberration is a measure of the distortion.

Figure A2.2 shows a distorted or aberrated wavefront leaving the exit pupil, and also shows an undistorted wavefront (the reference sphere). The wave aberration of any ray is the optical distance along the ray between the distorted wavefront and the reference sphere. Arbitrarily, the two wavefronts are defined to coincide at the center of the exit pupil.

$$W = [\mathbf{QEE}'] - [\mathbf{QBB}'] \quad (\text{A2.6})$$

As

$$[\mathbf{QEE}'] = [\mathbf{QBB}'\mathbf{B}''],$$

equation (A2.6) reduces to

$$W = [\mathbf{B}'\mathbf{B}''] \quad (\text{A2.7})$$

Since for any specific optical system the position and shapes of all the surfaces are known, the ray intersection points with each surface can be found by conventional geometrical and trigonometrical rules and the above path differences can be calculated for any specific ray.

The two definitions of wave aberration used (equations (A2.1) and (A2.7)) are slightly different, but at low levels of aberration they lead to similar results. They will give different results for large levels of aberration.

A2.3 SEIDEL ABERRATIONS

There are seven Seidel aberrations, and these are listed in Table A2.1 along with some of their properties. The five monochromatic aberrations are related to the primary wave aberrations given in equation (A2.2). The Seidel aberrations can be calculated from the paths of the paraxial marginal and paraxial pupil rays.

Seidel aberrations are usually calculated as wave aberrations, although they are occasionally calculated in the transverse or longitudinal aberration forms. Equations for their calculations can be found in texts by Hopkins (1950) and Smith and Atchison (1997). They are calculated from the system constructional parameters (refractive indices, surface curvatures and shapes, and surface separations), and depend upon the beam width and the size of the field-of-view, which in turn are defined by the paraxial marginal and paraxial pupil rays. Values are given in Appendix 3 for selected schematic eyes, and are calculated for a beam width limited by the paraxial marginal ray passing through the edge of an 8 mm diameter entrance pupil (that is, through the edge of pupil of radius $\bar{p} = 4$ mm), and for a field width specified by the paraxial pupil ray inclined at angle of 5° to the optical axis. Figure A2.3 shows a beam arising from the point **Q**, which is at the edge of the nominal field-of-view and subtends an angle θ_1 at the entrance pupil at **E**. The pupil ray subtends a paraxial angle \bar{u}_1 to the axis, and this paraxial angle is the tangent of the real angle according to

TABLE A2.1
The Seven Seidel Aberrations

Aberration	Symbol	Imagery Point to Point	Dependence on*	
			Aperture (p)	Field (q)
<i>Monochromatic</i>				
spherical	S_1	no	4	0
Coma	S_2	no	3	1
astigmatism	S_3	no	2	2
field curvature	S_4	yes	2	2
distortion	S_5	yes	1	3
% distortion			0	2
<i>Chromatic</i>				
longitudinal	C_L	no	2	0
transverse	C_T	no	1	1

Note: * These values are for wave aberrations, except for distortion expressed as a percentage. For transverse aberrations the p power dependence reduces by 1, and for longitudinal aberrations the p power dependence reduces by 2.

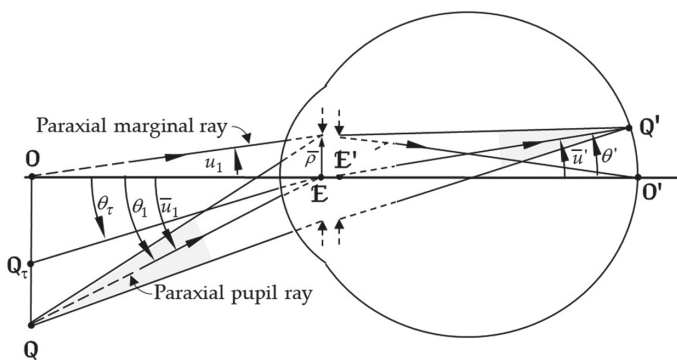


FIGURE A2.3 Field points and field angles.

$$\bar{u}_1 = \tan(\theta_1) \quad (\text{A2.8})$$

Thus, in this case, $\theta_1 = 5^\circ$ and so

$$\bar{u}_1 = \tan(5^\circ) = 0.087488663 \quad (\text{A2.8a})$$

The combination of beam width and field size is embodied in the optical invariant H , which we introduced in Appendix 1. Using the paraxial marginal and pupil rays, we have

$$H = n(\bar{u}h - u\bar{h}) \quad (\text{A2.9})$$

where u and h are the marginal ray angle and height at any plane in the system, \bar{u} and \bar{h} are the corresponding pupil ray values, and n is the refractive index on the side of the plane where the above paraxial angles are measured. At the entrance pupil plane,

$$H = n\bar{u}_1 \bar{\rho} \quad (\text{A2.9a})$$

Therefore, for the data in Appendix 3,

$$H = 1 \times 0.0874887 \times 4 = 0.349955 \quad (\text{A2.10})$$

For a beam with a different width and from a different field point, the aberrations are different and can be found from

$$\begin{aligned} \text{New aberration value} &= \text{old aberration value} \times (\text{fractional pupil radius})^p \\ &\times (\text{fractional field position } \tau)^q \end{aligned} \quad (\text{A2.11})$$

where the values of p and q are given in Table A2.1.

The fractional value τ can be used to specify the position of some other field point, say the point \mathbf{Q}_τ shown in Figure A2.3, and this point is off-axis by an angle θ_τ , measured at the entrance pupil. The fractional field value τ is defined as

$$\tau = \tan(\theta_\tau)/\tan(\theta_1) \quad (\text{A2.12})$$

where θ_τ is an off-axis angle point inside or outside the 5° field.

A2.3.1 SEIDEL ABERRATIONS AND THE PRIMARY WAVE ABERRATION COEFFICIENTS

The five monochromatic Seidel aberrations are directly related to the wave aberration coefficients of equations (A2.2) and (A2.4) as follows:

$$S_1 = 8_0 W_{4,0} \bar{\rho}^4 \text{ spherical aberration} \quad (\text{A2.13a})$$

$$S_2 = 2_1 W_{3,1} \bar{\rho}^3 \text{ coma} \quad (\text{A2.13b})$$

$$S_3 = 2_2 W_{2,0} \bar{\rho}^2 \text{ astigmatism} \quad (\text{A2.13c})$$

$$S_4 = (4_2 W_{2,0} - 2_2 W_{2,2}) \bar{\rho}^2 \text{ Petzval curvature} \quad (\text{A2.13d})$$

$$S_5 = 2_3 W_{1,1} \bar{\rho} \text{ distortion} \quad (\text{A2.13e})$$

The Seidel aberration values can be found from the wave aberration polynomial coefficients, if the latter are known, as well as from the Seidel formulae given in texts such as Hopkins (1950) and Smith and Atchison (1997). If the Seidel aberrations are known, the wave aberration coefficients can be calculated after re-arranging the above equations as

$$_0 W_{4,0} = S_1/(8\bar{\rho}^4) \text{ spherical} \quad (\text{A2.14a})$$

$$_1 W_{3,1} = S_2 / (2\bar{\rho}^3) \text{ coma} \quad (\text{A2.14b})$$

$$_2 W_{2,0} = (S_3 + S_4) / (4\bar{\rho}^2) \text{ field curvature} \quad (\text{A2.14c})$$

$$_2 W_{2,2} = S_3 / (2\bar{\rho}^2) \text{ astigmatism} \quad (\text{A2.14d})$$

$$_3 W_{1,1} = S_5 / (2\bar{\rho}) \text{ distortion} \quad (\text{A2.14e})$$

The chromatic wave aberration coefficients are related to their Seidel equivalents by

$$_0 W_{2,0} = C_L / (2\bar{\rho}^2) \text{ longitudinal chromatic aberration} \quad (\text{A2.14f})$$

$$_1 W_{1,1} = C_t / \bar{\rho} \text{ transverse chromatic aberration} \quad (\text{A2.14g})$$

A2.3.2 SAGITTAL, TANGENTIAL, AND PETZVAL SURFACES

In the Seidel approximation, the sagittal and tangential surfaces are spherical with radii of curvatures given by the following equations (Smith and Atchison 1997)

$$r_s = -\frac{H^2}{n'(S_3 + S_4)} \text{ sagittal surface} \quad (\text{A2.15a})$$

$$r_t = -\frac{H^2}{n'(3S_3 + S_4)} \text{ tangential surface} \quad (\text{A2.15b})$$

In the absence of astigmatism, i.e., $S_3 = 0$, we can see from the above equations that the two radii of curvatures are the same. The corresponding surface is known as the Petzval surface, and it follows that its radius of curvature, denoted as r_p , is

$$r_p = -\frac{H^2}{n'S_4} \text{ Petzval surface} \quad (\text{A2.15c})$$

The sagittal and tangential image surfaces can be represented by the corresponding reduced vergences L_s and L_t . This is particularly useful if the image plane is at infinity, because then the image surfaces cease to have any meaning. Using equations in Smith and Atchison (1997), for raytracing out of the eye and for the object (instead of the image) at infinity, we can show that the reduced vergences are related to the off-axis angle θ by the equations

$$L_s(\theta) = \frac{\theta^2}{2n_{\text{vit}} r_s} \quad (\text{A2.16a})$$

$$L_t(\theta) = \frac{\theta^2}{2n_{\text{vit}} r_t} \quad (\text{A2.16b})$$

where θ is the off-axis angle in radians.

A2.3.3 WAVE ABBERRATION COEFFICIENTS $W_{2,0}$ AND $W_{2,2}$

In visual optics, the peripheral power errors $L_s(\theta)$ and $L_t(\theta)$ are more meaningful than the Seidel or wave aberration values. However, if we wish to calculate the point spread or optical transfer functions, we need to know the corresponding wave aberration coefficients $W_{2,0}$ and $W_{2,2}$. We have

$$W_{2,0} = -L_s(\theta)/2 \quad (\text{A2.17a})$$

$$W_{2,2} = [L_s(\theta) - L_t(\theta)]/2 \quad (\text{A2.17b})$$

or

$$L_s(\theta) = -2W_{2,0} \quad (\text{A2.18a})$$

$$L_t(\theta) = -2(W_{2,0} + W_{2,2}) \quad (\text{A2.18b})$$

A2.3.4 MODIFICATIONS FOR A CURVED RETINA

The use of Seidel aberrations assumes usually that the image surface is flat. Some of the above equations can be modified by considering the radius of curvature of the retina. The equivalents of equations (A2.16a) and (A2.16b), for the sagittal and tangential surface reduced vergences, now become

$$L_s(\theta) \approx \frac{\theta^2}{2n_{\text{vit}}} \left(\frac{1}{r_s} - \frac{1}{r_R} \right) \quad (\text{A2.19a})$$

$$L_t(\theta) \approx \frac{\theta^2}{2n_{\text{vit}}} \left(\frac{1}{r_t} - \frac{1}{r_R} \right) \quad (\text{A2.19b})$$

where r_R is the radius of curvature of the retina.

In the Seidel approximation, the wave aberration $W_{2,2}$ is independent of the retinal radius of curvature, but the coefficient $W_{2,0}$ changes by an amount $\Delta W_{2,0}$ where

$$\Delta W_{2,0} = \frac{\theta^2}{4n_{\text{vit}} r_R} \quad (\text{A2.20})$$

A2.3.5 SEIDEL ABBERRATIONS OF A GRADIENT INDEX MEDIUM

Sands (1970) presented a set of equations for determining the Seidel aberrations of gradient index media. To make these equations consistent with the Seidel aberrations of Hopkins (1950) and Welford (1986), Sands' aberration values must be multiplied by a factor of two and the signs changed. The aberrations are broken up into two types: the refractive contribution arising at the surfaces, and the transfer contribution arising from the passage of the rays through the lens from the anterior to the posterior surface.

A2.3.5.1 Refractive Contribution

$$\kappa = +2C_1 \{2N_1(0) + 0.5C_1 \partial N_0 / \partial Z\} - 2C_2 \{2N_1(d) + 0.5C_2 \partial N_0 / \partial Z\} \quad (\text{A2.21})$$

Spherical aberration (S_1)	κh^4
Coma (S_2)	$\kappa h^3 \bar{h}$
Astigmatism (S_3)	$\kappa h^2 \bar{h}^2$
Field curvature (S_4)	0
Distortion (S_5)	$\kappa h \bar{h}^3$

where C_1 and C_2 are the front and back surface curvatures of the lens, d is its thickness, $\partial N_0 / \partial Z$ is the differential of $N_0(Z)$ with respect to Z , h is the paraxial marginal ray height at the surface, and \bar{h} is the paraxial pupil ray height at the surface.

A2.3.5.2 Transfer Contribution

Spherical aberration (S_1)

$$\begin{aligned} & -[N_0(d)h(d)u^3(d) - N_0(0)h(0)u^3(0)] \\ & - \left\{ 2 \int_0^d [4N_2(Z)h^4(Z) + 2N_1(Z)h^2(Z)u^2(Z) \right. \\ & \quad \left. - 0.5N_0(Z)u^4(Z)] \partial Z \right\} \end{aligned}$$

Coma (S_2)

$$\begin{aligned} & -[N_0(d)h(d)u^2(d)\bar{u}(d) - N_0(0)h(0)u^2(0)\bar{u}(0)] \\ & - \left\{ 2 \int_0^d [4N_2(Z)h^3(Z)\bar{h}(Z) + N_1(Z)h(Z)u(Z)[h(Z)\bar{u}(Z) + \bar{h}(Z)u(Z)] \right. \\ & \quad \left. - 0.5N_0(Z)u^3(Z)\bar{u}(Z)] \partial Z \right\} \end{aligned}$$

Astigmatism (S_3)

$$\begin{aligned} & -[N_0(d)h(d)u(d)\bar{u}^2(d) - N_0(0)h(0)u(0)\bar{u}^2(0)] \\ & - \left\{ 2 \int_0^d [4N_2(Z)h^2(Z)\bar{h}^2(Z) + 2N_1(Z)h(Z)\bar{h}(Z)u(Z)\bar{u}(Z)] \right. \\ & \quad \left. - 0.5N_0(Z)u^2(Z)\bar{u}^2(Z)] \partial Z \right\} \end{aligned}$$

Distortion (S_5)

$$\begin{aligned} & -[N_0(d)h(d)\bar{u}^3(d) - N_0(0)h(0)\bar{u}^3(0)] \\ & - \left\{ 2 \int_0^d [4N_2(Z)h(Z)\bar{h}^3(Z) + N_1(Z)\bar{h}(Z)\bar{u}(Z)[h(Z)\bar{u}(Z) + \bar{h}(Z)u(Z)]] \right. \\ & \quad \left. - 0.5N_0(Z)u(Z)\bar{u}^3(Z)] \partial Z \right\} \end{aligned}$$

A2.3.5.3 Relevance of Gradient Index Expressions to the Eye

If a ray passing through the lens of the eye has a shallow trajectory, the angle $u(Z)$ is small. In the expressions above, the effects of the $N_0(Z)$ and $N_1(Z)$ coefficients are attenuated by the value of u , and so their contributions are also likely to be small. The $N_2(Z)$ coefficients are likely to be the main gradient index contributors to Seidel aberration of the lens. The equations show that the spherical aberration has the opposite sign to that of the $N_2(Z)$ coefficients. Thus, if the gradient index medium is to reduce the spherical aberration of the eye, the sign of these coefficients must be positive.

SUMMARY OF MAIN SYMBOLS

λ	vacuum wavelength
n'	refractive index of the vitreous humor
\bar{p}	radius of entrance pupil
r	ray height in pupil (say in millimeters)
τ	relative field position defined by equation (A2.12)
H	optical invariant defined by equation (A2.9)
θ	direction of a point in the object field
η	distance of object from axis

Seidel Aberrations

S_1	spherical aberration
S_2	coma
S_3	astigmatism
S_4	Petzval curvature
S_5	distortion
C_L	longitudinal chromatic aberration
C_T	transverse chromatic aberration
$W(r)$	wave aberration for ray passing through the pupil at a height r
${}_0 W_{4,0}$ etc.	wave aberration coefficients

REFERENCES

- Hopkins, H. H. 1950. *Wave Theory of Aberrations*. London: Oxford University Press.
 Sands, P. J. 1970. “Third-order aberrations of inhomogeneous lenses.” *J Opt Soc Am* 60 (11):1436–43. doi: 10.1364/AO.9.000828.
 Smith, G., and D. A. Atchison. 1997. “Chapter 33. Aberration theory.” In *The Eye and Visual Optical Instruments*, 641–6. New York: Cambridge University Press.
 Welford, W. T. 1986. *Aberrations of Optical Systems*: Adam Hilger.



Taylor & Francis
Taylor & Francis Group
<http://taylorandfrancis.com>

Appendix 3: Schematic Eyes

A3.1 INTRODUCTION

This appendix lists constructional data, Gaussian constants, such as the pupil positions and sizes, the positions of the cardinal points, and the Seidel aberrations of several paraxial and finite schematic eyes. The constructional data were taken from references, but Gaussian and aberration values were determined by the authors.

Seidel aberrations were evaluated for the schematic eyes using an 8 mm entrance pupil diameter, a semi-field angle of 5°, and a reference wavelength of 589 nm. They are given as primary wave aberration coefficients (equations (A2.14)). The optical invariant H has the value 0.349955. The V -value of all ocular media is taken as 50.23, based on equations (17.15) and (17.17).

A3.1.1 UNITS

Distances are in millimeters and are generally measured from the front surface vertex of the cornea.

Powers are expressed in units of diopters (D or m⁻¹).

Accommodation levels are measured at the anterior corneal surface vertex.

The Seidel aberrations and the primary wave aberration coefficients are given in units of wavelengths ($\lambda = 589$ nm), except for S_s and C_T , which are given as percentages.

A3.2 PARAXIAL SCHEMATIC EYES

A3.2.1 LIST OF EYES

Gullstrand exact (Gullstrand 1909a, b)

 relaxed

 accommodated 10.870 D

Le Grand theoretical (Le Grand and El Hage 1980)

 relaxed

 accommodated 7.053 D

Gullstrand–Emsley simplified (Emsley 1952)

 relaxed

 accommodated 8.599 D

Bennett–Rabbets simplified (Rabbets 2007)

 relaxed

Emsley reduced (Emsley 1952)

A3.2.2 RELAXED “EXACT” SCHEMATIC EYES

TABLE A3.1
Gullstrand Exact or Number 1

Medium	<i>n</i>	<i>R</i>	<i>d</i>	Equivalent Powers		
				Surface	Component	Whole Eye
Air	1.000		7.700	48.831		
Cornea	1.376		0.500		43.053	
			6.800	-5.882		
Aqueous	1.336		3.100			58.636
			10.000	5.000		
Lens Cortex	1.386		0.546			
			7.911	2.528		
Lens Core	1.406		2.419		19.111	
			-5.760	3.472		
Lens Cortex	1.386		0.635			
			-6.000	8.333		
Vitreous	1.336		17.185			

TABLE A3.2
Le Grand Full Theoretical Eye

Medium	<i>n</i>	<i>R</i>	<i>d</i>	Equivalent Powers		
				Surface	Component	Whole Eye
Air	1.000		7.800	48.346		
Cornea	1.3771		0.550		42.356	
			6.500	-6.108		
Aqueous	1.3374		3.050			59.940
			10.200	8.098		
Lens	1.4200		4.000		21.779	
			-6.000	14.000		
Vitreous	1.3360		16.600			

A3.2.3 RELAXED SIMPLIFIED SCHEMATIC EYES

TABLE A3.3
Gullstrand–Emsley

Medium	<i>n</i>	<i>R</i>	<i>d</i>	Equivalent Powers		
				Surface	Component	Whole Eye
Air	1.000					
Cornea	4/3	7.800		42.735	42.735	
			3.6			60.483
Lens	1.416	10.000		8.267		
			3.6		21.755	
Vitreous	4/3	−6.00		13.778		
			16.696			

TABLE A3.4
Bennett–Rabbets

Medium	<i>n</i>	<i>R</i>	<i>d</i>	Equivalent Powers		
				Surface	Component	Whole Eye
Air	1.000					
Cornea	1.336	7.800		43.077	43.077	
			3.6			60.000
Lens	1.422	11.000		7.818		
			3.6		20.828	
Vitreous	1.336	−6.47515		13.280		
			16.786			

A3.2.4 REDUCED EYES

TABLE A3.5
Emsley

Medium	<i>n</i>	<i>R</i>	<i>d</i>	Equivalent Powers		
				Surface	Component	Whole Eye
Air	1.000					
Vitreous	4/3	5.555*				60.00
			22.222			

A3.2.5 ACCOMMODATED 'EXACT' SCHEMATIC EYES

TABLE A3.6
Gullstrand (Accommodation Distance –92.00 mm (10.870 D))

Medium	<i>n</i>	<i>R</i>	<i>d</i>	Equivalent Powers		
				Surface	Component	Whole Eye
Air	1.000		7.700	48.831		
Cornea	1.376		0.500		43.053	
		6.800		–5.882		
Aqueous	1.336		2.700		70.576	
		5.333*		9.376		
Lens Cortex	1.386		0.6725		33.057	
		2.655		7.533		
Lens Core	1.406		2.6550		7.533	
		–2.655		7.533		
Lens Cortex	1.386		0.6725		9.376	
		–5.333*		9.376		
Vitreous	1.336		17.185			

TABLE A3.7
Le Grand Full Theoretical Eye (Accommodation Distance =–141.793 mm (7.053 D))

Medium	<i>n</i>	<i>R</i>	<i>d</i>	Equivalent Powers		
				Surface	Component	Whole Eye
Air	1.000		7.800	48.346		
Cornea	1.3771		0.550		42.356	
		6.500		–6.108		
Aqueous	1.3374		2.650		67.677	
		6.000		14.933		
Lens	1.4270		4.500		30.700	
		–5.500		16.545		
Vitreous	1.3360		16.49655			

A3.2.6 ACCOMMODATED SIMPLIFIED SCHEMATIC EYES

TABLE A3.8
Gullstrand-Emsley (Accommodation Distance = -116.298 mm (8.599 D))

Medium	<i>n</i>	<i>R</i>	<i>d</i>	Equivalent Powers		
				Surface	Component	Whole Eye
Air	1.000		7.800	42.735	42.735	
Cornea	4/3		3.2			69.721
		5.00		16.533		
Lens	1.416		4.0		32.295	
		-5.00		16.533		
Vitreous	4/3		16.696			

A3.2.7 GAUSSIAN PROPERTIES

TABLE A3.9
Gaussian Properties

	<i>Relaxed eyes</i>				<i>Reduced</i> Emsley	<i>Accommodated eyes</i>			
	'Exact'		<i>Simplified</i>			<i>Reduced</i> Emsley	'Exact'		
	Gull. 1	Le Grand	Gull-Ems	B-R		Gull. 1	Le Grand	Gull-Ems	
power (D)	58.636	59.940	60.483	60	60	70.576	67.677	69.721	
eye length $\mathbf{VR'}$	24.385	24.197	23.896	24.086	22.222	24.385	24.197	23.896	
$\mathbf{VV'}$	7.2	7.6	7.2	7.3	0.000	7.2	7.7	7.2	
\mathbf{OV}	∞	∞	∞	∞	∞	92.000	141.792	116.298	
acccom. (D)	0	0	0	0	0	10.870	7.053	8.599	
<i>Cardinal point positions</i>									
\mathbf{VF}	-15.706	-15.089	-14.983	-15.156	-16.667	-12.397	-12.957	-12.561	
$\mathbf{VF'}$	24.385	24.197	23.896	24.086	22.222	21.016	21.932	21.252	
\mathbf{VP}	1.348	1.595	1.550	1.511	0.000	1.772	1.819	1.782	
$\mathbf{VP'}$	1.601	1.908	1.851	1.819	0.000	2.086	2.192	2.128	
\mathbf{VN}	7.078	7.200	7.062	7.111	5.556	6.533	6.784	6.562	
$\mathbf{VN'}$	7.331	7.513	7.363	7.419	5.556	6.847	7.156	6.909	
$\mathbf{PN} = \mathbf{P'N'}$	5.730	5.606	5.511	5.600	5.556	4.761	4.965	4.781	
$\mathbf{FP} = \mathbf{N'F'}$	17.054	16.683	16.534	16.667	16.667	14.169	14.776	14.343	
$\mathbf{PF'} = \mathbf{FN}$	22.785	22.289	22.045	22.267	22.222	18.930	19.741	19.124	
$\mathbf{N'R'}$	17.054	16.683	16.534	16.667	16.667	17.539	17.041	16.987	
$\mathbf{F'R'}$	0	0	0	0	0	3.370	2.265	2.644	

Pupils (NA for 8 mm diameter entrance pupil)

VE	3.047	3.038	3.052	3.048	0.000	2.668	2.660	2.674
VE'	3.665	3.682	3.687	3.699	0.000	3.212	3.255	3.249
\bar{M}_{EA}	1.133	1.131	1.130	1.131	1.000	1.117	1.115	1.114
$\bar{M}_{EA'}$	1.031	1.041	1.036	1.036	1.000	1.051	1.055	1.049
<i>NA</i>	0	0	0	0	0	0.0423	0.0277	0.0375
<i>NA'</i>	0.235	0.240	0.242	0.240	0.240	0.237	0.241	0.271
\bar{m}	0.823	0.813	0.818	0.818	0.750	0.796	0.791	0.797
E'R'	20.720	20.515	20.209	20.387	22.222	21.173	20.942	20.647

A3.2.8 SEIDEL ABERRATIONS

TABLE A3.10
Seidel Aberrations

	${}_0W_{4,0}$	${}_1W_{3,1}$	${}_2W_{2,2}$	${}_2W_{2,0}$	${}%_3W_{1,1}$	${}_0W_{2,0}$	${}%_1W_{1,1}$
<i>Relaxed eyes</i>							
Gullstrand exact eye (by surface contribution)							
1	23.6327	9.6202	0.979	1.8447	-0.0800	9.5960	-0.3287
2	-2.0030	-0.7207	-0.0648	-0.1663	0.0060	-0.8665	0.0262
3	0.1577	0.2090	0.0692	0.1404	-0.0195	0.4821	-0.0538
4	0.2057	0.2100	0.0536	0.0675	-0.0081	0.2489	-0.0214
5	5.1871	-1.0374	0.0518	0.0926	0.0020	0.5175	0.0087
6	11.7803	-2.0552	0.0898	0.2340	0.0041	1.2479	0.0183
Total	38.9605	6.2258	1.1786	2.2127	-0.0955	11.2259	-0.3506
Le Grand	39.1445	6.2642	1.1238	2.2578	-0.1012	11.3592	-0.3694
Gullstrand–Emsley	41.2324	5.8719	1.1802	2.2731	-0.0990	11.5061	-0.3603
Bennett–Rabbatts Emsley	38.5293	5.8075	1.1638	2.2534	-0.0997	11.4031	-0.3622
Le Grand	59.4091	28.8757	3.5086	2.3392	-0.1674	12.1682	-0.4977
<i>Accommodated eyes</i>							
Gullstrand exact eye (by surface contribution)							
1	29.6779	12.4057	1.2964	1.8447	-0.0877	9.8212	-0.3455
2	-2.5355	-0.9513	-0.0892	-0.1663	0.0067	-0.8856	0.0280
3	5.6696	2.8705	0.3634	0.2632	-0.0190	1.2617	-0.0538
4	22.8734	6.7077	0.4916	0.2009	-0.0110	1.0154	-0.0251
5	34.7899	1.8831	0.0254	0.2009	-0.0010	1.0154	-0.0046
6	15.8359	-1.4826	0.0346	0.2632	0.0021	1.3966	0.0110
Total	106.311	21.4332	2.1226	2.6066	-0.1098	13.6247	-0.3900
Le Grand	53.5239	12.0929	1.6878	2.5104	-0.1126	12.9305	-0.4044
Gullstrand–Emsley	65.9357	14.0976	1.8432	2.5765	-0.1092	13.4028	-0.3921

A3.3 FINITE SCHEMATIC EYES

A3.3.1 LIST OF EYES

- Lotmar (1971)
- Kooijman (1983)
- Navarro et al. (1985)
- Liou and Brennan (1997)

Further information about these model eyes is given in Chapter 16.

TABLE A3.11
Lotmar (1971) – Same as Le Grand Eye Except for Surface Asphericities

Medium	<i>n</i>	<i>R</i>	<i>Q</i>	<i>d</i>	Equivalent Powers		
					Surface	Component	Whole Eye
Air	1.000				48.346		
		7.8	-0.286*				
Cornea	1.3771			0.550		42.356	
		6.5	0		-6.108		
Aqueous	1.3374			3.050			59.940
		10.2	0		8.098		
Lens	1.4200			4.000		21.779	
		-6.0	-1.0		14.000		
Vitreous	1.3360			16.5966			
Retina		-12.3					

Note: * Lotmar represented the front surface of the cornea by equation (16.2), and the above value of *Q* is the value for a figured conicoid fitted to equation (16.4). The conicoid asphericity and figuring coefficients are $Q = -0.2857143$, $f_4 = 0.0$, $f_6 = -2.547626 \times 10^{-6}$, $f_8 = -8.104263 \times 10^{-9}$, $f_{10} = -6.660308 \times 10^{-11}$, $f_{12} = -5.864599 \times 10^{-13}$. The termination of the figuring coefficient at the f_{12} term gives an error of less than 2×10^{-6} mm at a ray height of $h = 4$ mm.

TABLE A3.12
Kooijman (1983) – Same as Le Grand Eye Except for Surface Asphericities

Medium	<i>n</i>	<i>R</i>	<i>Q</i>	<i>D</i>	Equivalent Powers		
					Surface	Component	Whole Eye
Air	1.000				48.346		
		7.8	-0.25				
Cornea	1.3771			0.55		42.356	
		6.5	-0.25		-6.108		
Aqueous	1.3374			3.05			59.940
		10.2	-3.06		8.098		
Lens	1.4200			4.00		21.779	
		-6.0	-1.0		14.000		
Vitreous	1.3360			16.597			
Retina*							

Note: * Two models of retina were offered; one with a radius of curvature of -10.8 mm and a *Q* value of 0, and the other with a radius of curvature of -14.1 mm and a *Q* value of +0.346.

TABLE A3.13
Navarro et al. (1985)

Medium	<i>n</i>	<i>R</i>	<i>Q</i>	<i>d</i>	Equivalent Powers		
					Surface	Component	Whole Eye
Air	1.000				48.705		
		7.72	-0.26				
Cornea	1.376			0.55		42.882	
		6.50	0		-5.938		
Aqueous	1.3374			$(3.05)d_2$			60.416
		$(10.2)R_3$	$(-3.1316)Q_3$		8.098		
Lens	$(1.42)n_3$			$(4.000)d_3$		21.779	
		$(-6.0)R_4$	$(-1.0)Q_4$		14.000		
Vitreous	1.3360			$(16.4040)d_4$			
Retina*		-12.0					

Note: The bracketed values are for the relaxed condition. The model is set any level of accommodation *A* (diopters) by the following equations:

$$n_3 = 1.42 + 0.00009 (10A + A^2)$$

$$R_3 = 10.2 - 1.75 \ln(A + 1)$$

$$R_4 = -6.0 + 0.2294 \ln(A + 1)$$

$$Q_3 = -3.1316 - 0.34 \ln(A + 1)$$

$$Q_4 = -1.0 - 0.125 \ln(A + 1)$$

$$d_2 = 3.05 - 0.05 \ln(A + 1)$$

$$d_3 = 4.0 + 0.1 \ln(A + 1)$$

$$d_4 = 16.40398 - 0.05 \ln(A + 1)$$

TABLE A3.14
Navarro et al. (1985) Example at 10 D of Accommodation

Medium	<i>n</i>	<i>R</i>	<i>Q</i>	<i>d</i>	Equivalent Powers		
					Surface	Component	Whole Eye
Air	1.000				48.705		
		7.72	-0.26				
Cornea	1.376			0.55		42.882	
		6.50	0		-5.938		
Aqueous	1.3374			2.930110			71.145
		6.00368	-3.94688		16.756		
Lens	1.4380			4.23979		34.548	
		-5.44992	-1.29974		18.716		
Vitreous	1.3360			16.28415			
Retina		-12.0					

TABLE A3.15
Liou and Brennan (1997)

Medium	<i>n</i>	<i>R</i>	<i>Q</i>	<i>d</i>	Equivalent Powers		
					Surface	Component	Whole Eye
Air	1.000				48.391		
		7.77	-0.18				
Cornea	1.376			0.50		42.25115	
		6.40	-0.60		-6.250		
Aqueous	1.336			3.16			60.349
		12.40	-0.94		2.581		
Lens	Grad A			1.59	6.283	22.134	
		∞	-				
Lens	Grad B			2.43	9.586		
		-8.10	+0.96		3.950		
Vitreous*	1.3360			16.2700			

Note: * No retinal radius of curvature was provided. The stop is displaced 0.5 mm from the optical axis to the nasal side.

TABLE A3.16
Gradient Index Details of Lens of Liou and Brennan Eye

Refractive Index Coefficient	Grad A	Grad P
$N_{0,0}$	1.368	1.407
$N_{0,1}$	0.049057	
$N_{0,2}$	-0.015427	-0.006605
$N_{1,0}$	-0.001978	-0.001978

A3.3.2 GAUSSIAN PROPERTIES

TABLE A3.17
Gaussian Properties

	Lotmar, Kooijman*	Navarro		Liou and
		Relaxed	Accomm	Brennan
power (D)	59.940	60.416	70.145	60.349
eye length VR'	24.197	24.004	24.004	23.950
VV'	7.6	7.6	7.2	7.68
OV	∞	∞	100	∞
<i>Cardinal point positions</i>				
VF	-15.089	-14.969	-12.051	-15.040
VF'	24.197	24.004	21.172	23.950

(continued)

TABLE A3.17 (Continued)
Gaussian Properties

	Lotmar, Kooijman*	Navarro		Liou and Brennan
		Relaxed	Accomm 10 D	
VP	1.595	1.583	2.005	1.532
VP'	1.908	1.890	2.393	1.810
VN	7.200	7.145	6.727	7.100
VN'	7.513	7.452	7.116	7.378
PN = P'N'	5.606	5.561	4.723	5.568
FP = N'F'	16.683	16.552	14.056	16.572
P'F' = FN	22.289	22.114	18.779	22.140
N'R'	16.683	16.552	16.888	16.572
F'R'	0	0	2.832	0
<i>Pupils</i>				
VE	3.038	3.042	2.928	3.098
VE'	3.682	3.682	3.551	3.721
\bar{M}_{EA}	1.131	1.133	1.128	1.133
$\bar{M}_{E'A}$	1.041	1.041	1.058	1.035
\bar{m}	0.813	0.814	0.798	0.837
E'R'	20.515	20.322	20.453	20.229

Note: * Same as Le Grand full theoretical eye.

A3.3.2 SEIDEL ABERRATIONS

TABLE A3.18
Seidel Aberrations

	${}_0W_{4,0}$	${}_1W_{3,1}$	${}_2W_{2,2}$	${}_2W_{2,0}$	$\% {}_3W_{1,1}$
<i>Relaxed eyes</i>					
Lotmar	20.3144	7.1107	0.6784	2.2578	-0.1001
Kooijman	15.7668	6.2829	0.7296	2.2578	-0.0995
Navarro	13.8628	7.0582	0.6842	2.2775	-0.0991
Liou and Brennan*	7.7345	1.6754	1.0848	1.8371	-0.2064
<i>Accommodated eyes</i>					
Navarro (10 D)	-26.1827	9.0316	0.9752	2.6315	-0.1019

Note: * The stop is displaced 0.5 mm from the optical axis to the nasal side, but this has been ignored for the analysis.

SUMMARY OF MAIN SYMBOLS

n	refractive indices
r	radius of curvature
d	surface separations
\mathbf{E}, \mathbf{E}'	entrance and exit pupils
\mathbf{F}, \mathbf{F}'	front and back focal points
\mathbf{P}, \mathbf{P}'	front and back principal points
\mathbf{N}, \mathbf{N}'	front and back nodal points
\mathbf{O}, \mathbf{O}'	object and image points
\mathbf{V}, \mathbf{V}'	front and back vertex points
\mathbf{R}'	position of retina (at axial pole)
$\bar{M}_{EA}, \bar{M}_{E'A}$	magnifications of entrance and exit pupils
NA, NA'	numerical apertures in object and image spaces
\bar{m}	ratio of the paraxial pupil ray angles in image and object space

REFERENCES

- Emsley, H. H. 1952. *Visual Optics*. 5th ed. Vol. 1: Butterworths.
- Gullstrand, A. 1909a. “Appendix II: Procedure of rays in the eye. Imagery - laws of the first order.” In *Helmholtz’s Handbuch der Physiologischen Optik*, vol. 1, 3rd edn (English translation edited by J. P. Southall, Optical Society of America, 1924), 301–58.
- Gullstrand, A. 1909b. “Appendix IV: The mechanism of accommodation.” In *Helmholtz’s Handbuch der Physiologischen Optik*, vol. 1, 3rd edn (English translation edited by J. P. Southall, Optical Society of America, 1924), 382–415.
- Kooijman, A. C. 1983. “Light distribution on the retina of a wide-angle theoretical eye.” *J Opt Soc Am* 73 (11):1544–50. doi: 10.1364/josa.73.001544.
- Le Grand, Y., and S. G. El Hage. 1980. *Physiological Optics. Translation and update of Le Grand, Y. (1968). La dioptrique de l’œil et sa correction*, vol. 1 of Optique physiologique, pp. 65–7: Springer-Verlag.
- Liou, H.-L., and N. A. Brennan. 1997. “Anatomically accurate, finite model eye for optical modeling.” *J Opt Soc Am A* 14 (8):1684–95. doi: 10.1364/josaa.14.001684.
- Lotmar, W. 1971. “Theoretical eye model with aspheric surfaces.” *J Opt Soc Am* 61 (11):1522–9. doi: 10.1364/JOSA.61.001522.
- Navarro, R., J. Santamaría, and J. Bescós. 1985. “Accommodation-dependent model of the human eye.” *J. Opt. Soc. Am. A* 2 (8):1273–81. doi: 10.1364/josaa.2.001273.
- Rabbets, R. B. 2007. “Chapter 12. Schematic eyes.” In *Bennett and Rabbets’ Clinical Visual Optics*, 221–43. Butterworth-Heinemann.



Taylor & Francis
Taylor & Francis Group
<http://taylorandfrancis.com>

Appendix 4: Refraction Powers across the Pupil

The Cartesian geometry inherent in square lenslet arrays commonly used in Hartmann–Shack aberrometers yields a matrix of horizontal and vertical values of wavefront slope from which radial and tangential slopes may be inferred. The combination of measurements at many places in the pupil from a single data image allows us to make pupil maps of slopes and power along any direction in which we are interested.

Wave aberration slopes (in radians) at pupil location **O** are indicated in Figure A4.1 using a local coordinate system centered on **o** with axes showing horizontal and vertical slopes $\frac{dW}{dX}$ and $\frac{dW}{dY}$. Measured values of horizontal slope h and vertical slope v are shown graphically by the thick arrow labeled $P(h, v)$. If $W(x, y)$ is a wave aberration, the solid arrow shows the ray aberration for that ray perpendicular to the wavefront error surface at **o**.

Another local coordinate system centered on **o** is aligned with the radial line joining the pupil center with measurement point **o**. The tangential direction is perpendicular to the radial direction. The radial component of the wavefront slope $\frac{dW}{dr}$ is obtained by projecting the solid arrow onto the radial axis as shown by the lower dashed arrow. Similarly, the tangential component of the wavefront slope $\frac{dW}{dt}$ is obtained by projecting the solid arrow onto the tangential axis as shown by the upper dashed arrow. The length of the radial component is the sum of two parts, such that

$$\frac{dW}{dr} = \mathbf{oa} + \mathbf{aq} = h \times \cos(\theta) + v \times \sin(\theta)$$

which is equation (15.28)

$$\frac{dW}{dr} = \frac{dW}{dX} \cos(\theta) + \frac{dW}{dY} \sin(\theta) \quad (\text{A4.1})$$

The length of the tangential component is the difference of two parts:

$$\frac{dW}{dt} = \mathbf{ob} - \mathbf{bt} = v \times \cos(\theta) - h \times \sin(\theta)$$

or

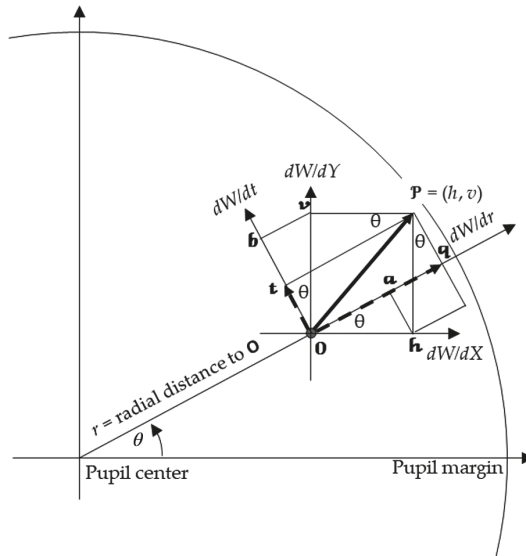


FIGURE A4.1 Geometry to determine horizontal, vertical, radial, and tangential wavefront slopes.

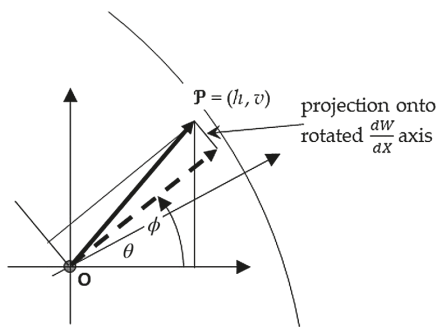


FIGURE A4.2 Additional geometry for general angle ϕ .

$$\frac{dW}{dt} = \frac{dW}{dY} \cos(\theta) - \frac{dW}{dX} \sin(\theta) \quad (\text{A4.2})$$

Dividing any of the four components of wavefront slope by r (the distance of the measurement location from the pupil center) yields the corresponding power. Power for a correcting lens has the opposite sign, such as given by equation (15.17):

$$\Delta F_r = -\frac{dW}{dr} / r \quad (\text{A4.3})$$

In Figure A4.1 the local coordinate axes have been rotated by θ , the polar angle of the pupil position. This is a special case of the more general geometry in Figure A4.2

TABLE A4.1
Radial, Horizontal, and Vertical Wave Aberration Slopes for Different Zernike Coefficients up to the Sixth-Order

Zernike Polynomial	dW/dr (mrad)	dW/dX (mrad)	dW/dY (mrad)
Z_2^{-2}	$2\sqrt{6}c_2^{-2}\rho\sin(2\theta)/R$	$2\sqrt{6}c_2^{-2}y/R$	$2\sqrt{6}c_2^{-2}x/R$
Z_2^0	$4\sqrt{3}c_2^0\rho/R$	$4\sqrt{3}c_2^0y/R$	$4\sqrt{3}c_2^0y/R$
Z_2^2	$2\sqrt{6}c_2^2\rho\cos(2\theta)/R$	$2\sqrt{6}c_2^2x/R$	$-2\sqrt{6}c_2^2y/R$
Z_3^{-3}	$3\sqrt{8}c_3^{-3}\rho^2\sin(3\theta)$	$6\sqrt{8}c_3^{-3}xy/R$	$\sqrt{8}c_3^{-3}(3x^2 - 3y^2)/R$
Z_3^{-1}	$9\sqrt{8}c_3^{-1}\rho^2\sin(\theta)$	$6\sqrt{8}c_3^{-1}xy/R$	$\sqrt{8}c_3^{-1}(3x^2 + 9y^2)/R$
Z_3^1	$9\sqrt{8}c_3^1\rho^2\cos(\theta)$	$\sqrt{8}c_3^1(9x^2 + 3xy^2 - 2)/R$	$6\sqrt{8}c_3^1xy/R$
Z_3^3	$3\sqrt{8}c_3^3\rho^2\cos(3\theta)/R$	$\sqrt{8}c_3^{-3}(3x^2 - 3y^2)/R$	$-6\sqrt{8}c_3^{-3}xy/R$
Z_4^{-4}	$4\sqrt{10}c_4^{-4}r^3\sin(4\theta)/R$	$\sqrt{10}c_4^{-4}(12x^2y - 4y^3)/R$	$\sqrt{10}c_4^{-4}(4x^3 - 12xy^2)/R$
Z_4^{-2}	$\sqrt{10}c_4^{-2}(16r^3 - 6r)\sin(2\theta)/R$	$\sqrt{10}c_4^{-2}(24x^2y + 8y^3 - 6y)/R$	$\sqrt{10}c_4^{-2}(8x^3 + 24xy^2 - 6x)/R$
Z_4^0	$\sqrt{5}c_4^0(24r^3 - 12r)/R$	$\sqrt{5}c_4^0(24x^3 + 24xy^2 - 12x)/R$	$\sqrt{5}c_4^0(24x^2y + 24y^3 - 12y)/R$
Z_4^2	$\sqrt{10}c_4^2(16r^3 - 6r)\cos(2\theta)/R$	$\sqrt{10}c_4^2(16x^3 - 6x)/R$	$\sqrt{10}c_4^2(-16y^3 + 6xy)/R$
Z_4^4	$4\sqrt{10}c_4^4r^3\cos(4\theta)/R$	$\sqrt{10}c_4^4(4x^3 - 12xy^2)/R$	$\sqrt{10}c_4^4(-12x^2y + 4y^3)/R$
Z_5^{-5}	$5\sqrt{12}c_5^{-5}\rho^4\sin(5\theta)/R$	$\sqrt{12}c_5^{-5}(20x^3y - 20xy^3)/R$	$\sqrt{12}c_5^{-5}(5x^4 - 30x^2y^2 + 5y^4)/R$
Z_5^{-3}	$\sqrt{12}c_5^{-3}(25\rho^4 - 12\rho^2)\sin(3\theta)/R$	$\sqrt{12}c_5^{-3}(60x^3y + 20xy^3 - 24xy)/R$	$\sqrt{12}c_5^{-3}(15x^4 + 30x^2y^2 - 12x^2 - 25y^4 + 12y^2)/R$
Z_5^{-1}	$\sqrt{12}c_5^{-1}(50\rho^4 - 36\rho^2)\sin(\theta)/R$	$\sqrt{12}c_5^{-1}(40x^3y + 40xy^3 - 24xy)/R$	$\sqrt{12}c_5^{-1}(10x^4 + 60x^2y^2 + 50y^4 - 12x^2 - 36y^2 + 3)/R$
Z_5^1	$\sqrt{12}c_5^1(50\rho^4 - 36\rho^2)\cos(\theta)/R$	$\sqrt{12}c_5^1(50x^4 + 60x^2y^2 + 10y^4 - 36x^2 - 12y^2 + 3)/R$	$\sqrt{12}c_5^1(40x^3y + 40xy^3 - 24xy)/R$
Z_5^3	$\sqrt{12}c_5^3(25\rho^4 - 12\rho^2)\cos(3\theta)/R$	$\sqrt{12}c_5^3(25x^4 - 12x^2 - 30x^2y^2 - 15y^4 + 12y^2)/R$	$\sqrt{12}c_5^3(-20x^3y - 60xy^3 + 24xy)/R$
Z_5^5	$5\sqrt{12}c_5^5\rho^4\cos(5\theta)/R$	$\sqrt{12}c_5^5(5x^4 - 30x^2y^2 + 5y^4)/R$	$\sqrt{12}c_5^5(-20x^3y + 20xy^3)/R$
Z_6^{-6}	$6\sqrt{14}c_6^{-6}\rho^5\sin(6\theta)/R$	$\sqrt{14}c_6^{-6}(30x^4y - 60x^2y^3 + 6y^5)/R$	$\sqrt{14}c_6^{-6}(6x^5 - 60x^3y^2 + 30xy^4)/R$
Z_6^{-4}	$\sqrt{14}c_6^{-4}(36\rho^5 - 20\rho^3)\sin(4\theta)/R$	$\sqrt{14}c_6^{-4}(120x^4y - 60x^2y - 24y^5 + 20y^3)/R$	$\sqrt{14}c_6^{-4}(24x^5 - 20x^3 - 120xy^4 + 60xy^2)/R$

(continued)

TABLE A4.1 (Continued)
Radial, Horizontal, and Vertical Wave Aberration Slopes for Different Zernike Coefficients up to the Sixth-Order

Zernike Polynomial	dW/dr (mrad)	dW/dX (mrad)	dW/dY (mrad)
Z_6^{-2}	$\sqrt{14}c_6^{-2}(90\rho^5 - 80\rho^3 + 12\rho)\sin(2\theta)/R$	$\sqrt{14}c_6^{-2}(150x^4y + 180x^2y^3 + 30y^5 - 120x^2y - 40y^3 + 12y)/R$	$\sqrt{14}c_6^{-2}(30x^5 + 180x^3y^2 + 150xy^4 - 40x^3 - 120xy^2 + 12x)/R$
Z_6^0	$\sqrt{7}c_6^0(120\rho^5 - 120\rho^3 + 24\rho)/R$	$\sqrt{7}c_6^0(120x^5 + 240x^3y^2 + 120xy^4 - 120x^3 - 120xy^2 + 24x)/R$	$\sqrt{7}c_6^0(120x^4y + 240x^2y^3 + 120y^5 - 120x^2y - 120y^3 + 24y)/R$
Z_6^2	$\sqrt{14}c_6^2(90\rho^5 - 80\rho^3 + 12\rho)\cos(2\theta)/R$	$\sqrt{14}c_6^2(90x^5 + 60x^3y^2 - 80x^3 + 12x - 30xy^4)/R$	$\sqrt{14}c_6^2(30x^4y - 60x^2y^3 - 90y^5 + 80y^3 - 12y)/R$
Z_6^4	$\sqrt{14}c_6^4(36\rho^5 - 20\rho^3)\cos(4\theta)/R$	$\sqrt{14}c_6^4(36x^5 - 20x^3 - 120x^3y^2 - 60xy^4 + 60xy^2)/R$	$\sqrt{14}c_6^4(-60x^4y - 120x^2y^3 + 60x^2y + 36y^5 - 20y^3)/R$
Z_6^6	$6\sqrt{14}c_6^6\rho^5 \cos(6\theta)/R$	$\sqrt{14}c_6^6(6x^5 - 60x^3y^2 + 30xy^4)/R$	$\sqrt{14}c_6^6(-30x^4y + 60x^2y^3 - 6y^5)/R$

wherein the angle of rotation ϕ of the local coordinate system can be any value between 0° and 180° . Figure A.4.1 for computing radial slopes is thus the special case of $\theta = \phi$. In the general case, if we project the thick arrow onto the rotated $\frac{dW}{dX}$ axis that makes angle ϕ with the horizontal, the length of the projection varies sinusoidally with rotation angle ϕ . This occurs because, as Gauss proved long ago, all smooth surfaces are spherocylindrical locally, and spherocylindrical surfaces have sinusoidal power profiles obtained by projecting the slope vector $P(h, v)$ onto the rotated dW/dx axis as a function of rotation angle ϕ .

Table A4.1 lists wave aberration slopes for different Zernike coefficients. To determine the slopes, the relative pupil co-ordinates shown in Table 5.1 were converted to absolute co-ordinates, i.e., $r = \rho R$, $X = xR$, $Y = yR$, but were converted back to the relative coordinates after differentiation. The form of these is simpler than given in equation (15.19). The tilt components of the coma terms in the third- and fifth-orders have been omitted.

Figure A4.3 shows some examples of wavefront aberration, wavefront slopes, and radial power.

SUMMARY OF MAIN SYMBOLS

$\frac{dW}{dX}, \frac{dW}{dY}, \frac{dW}{dr}, \frac{dW}{dt}$ horizontal, vertical, radial, and tangential wavefront slopes across the pupil.

REFERENCE

Nilagiri, V. K., S. Metlapally, C. M. Schor, and S. R. Bharadwaj. 2020. "A computational analysis of retinal image quality in eyes with keratoconus." *Sci Rep* 10 (1):1321. doi: 10.1038/s41598-020-57993-w.

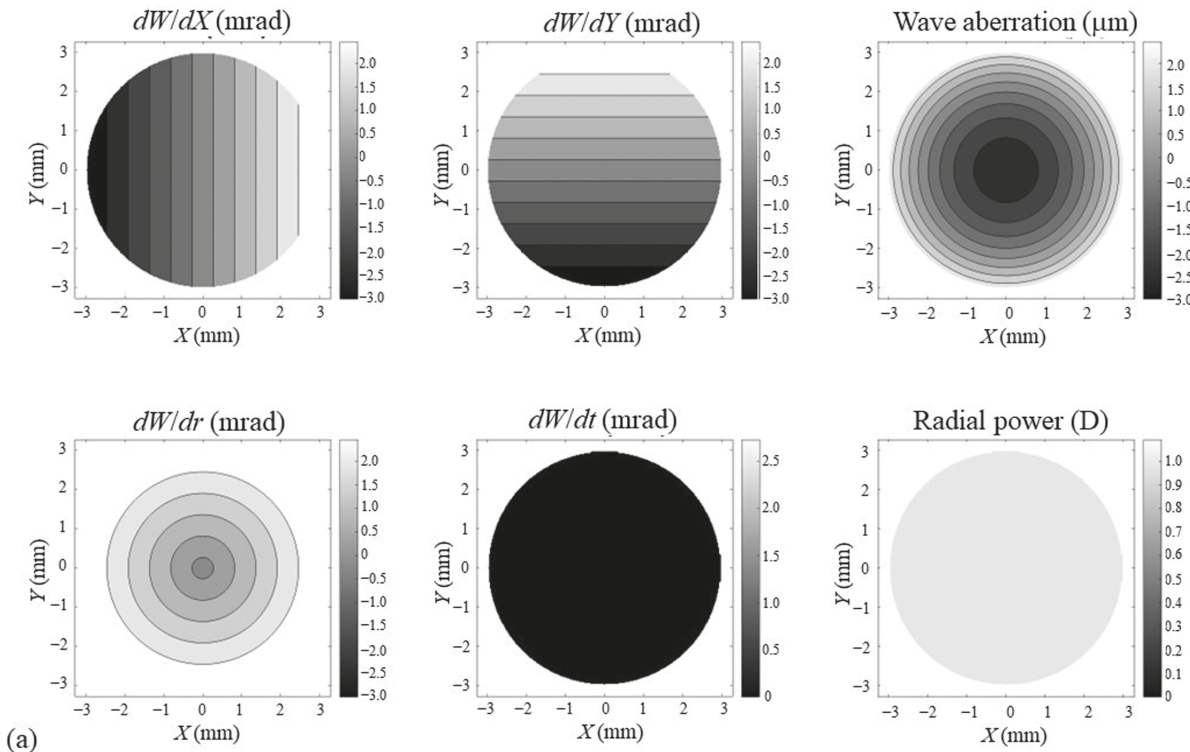


FIGURE A4.3 Wavefront aberration across the pupil, horizontal, vertical, radial and tangential wavefront slopes across the pupil, and radial power across the pupil for (a) defocus with coefficient $c_2^0 = +1.3 \mu\text{m}$ (+1.0 DS), (b) combination of defocus with coefficient $c_2^0 = +1.3 \mu\text{m}$ and horizontal astigmatism with coefficient $c_2^2 = -0.92 \mu\text{m}$ to give a +1.00 D cylinder with axis 180 degrees (Plano/+1.00 DC \times 180), (c) horizontal coma with $c_3^1 = +0.5 \mu\text{m}$, (d) spherical aberration with coefficient $c_4^0 = +0.3 \mu\text{m}$, and (e) aberrations of an eye with keratoconus from Nilagiri et al. (2020). Pupil diameter is 6 mm in (a)–(d) and 5 mm in (e). The figures were modified from those kindly provided by Larry Thibos. We thank Shrikant Bharadwaj for kindly providing data for (e).

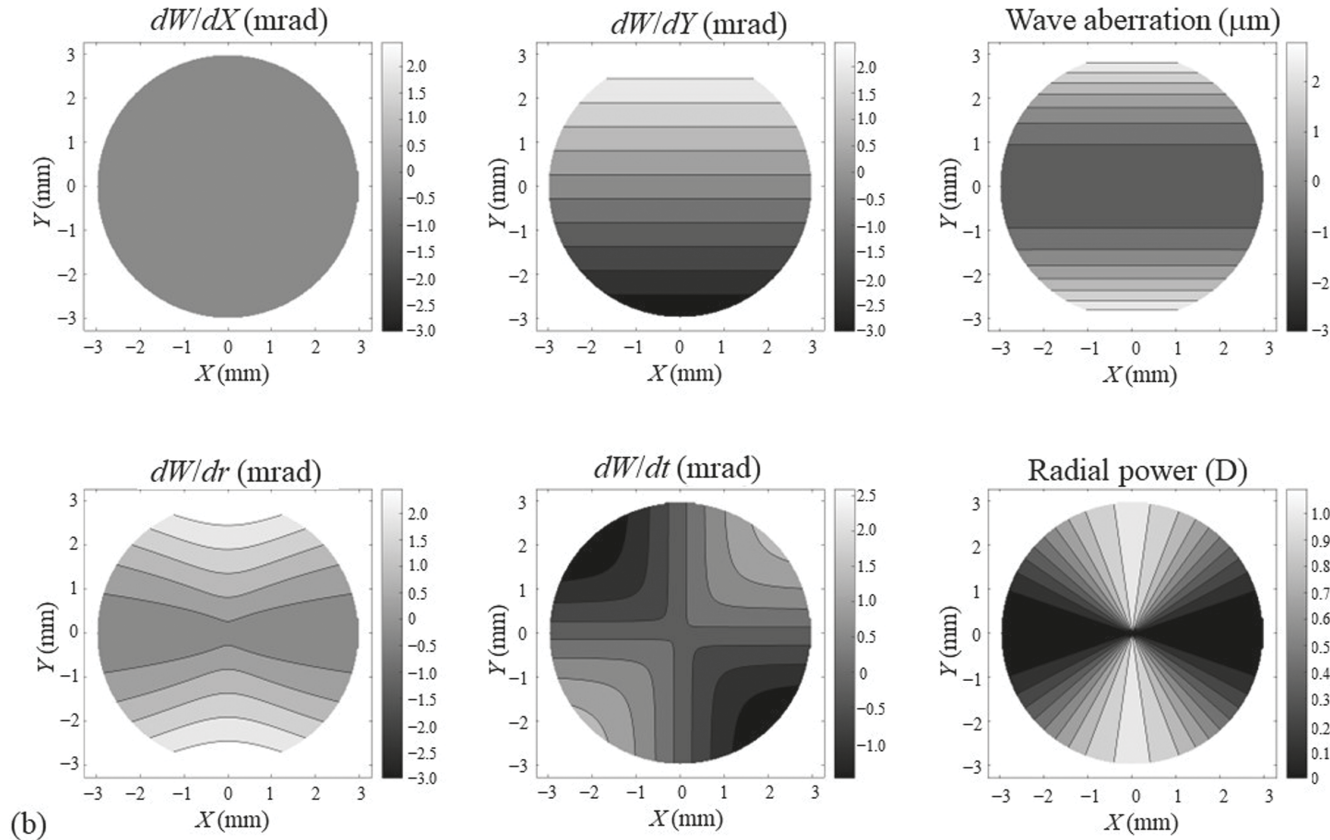


FIGURE A4.3 (Continued)

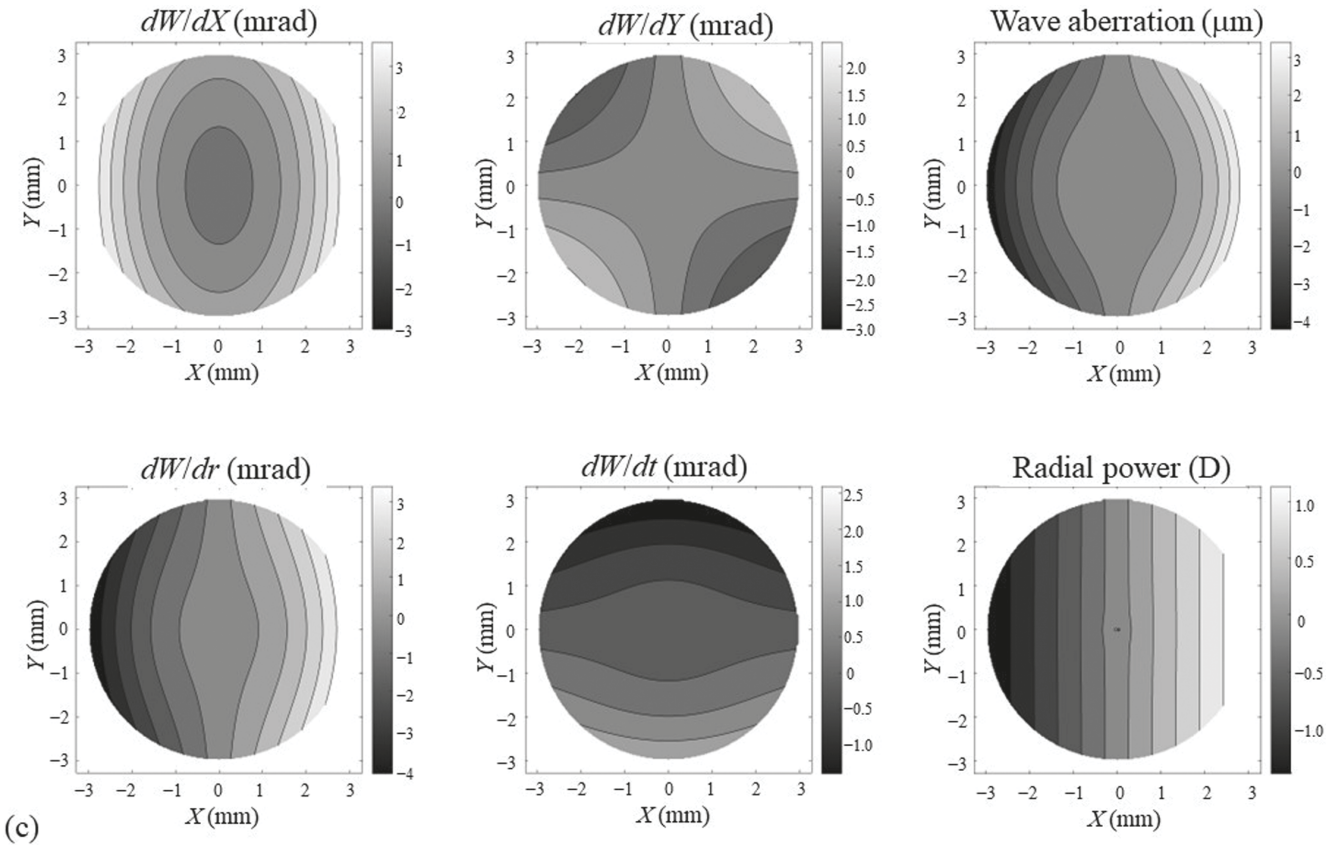


FIGURE A4.3 (Continued)

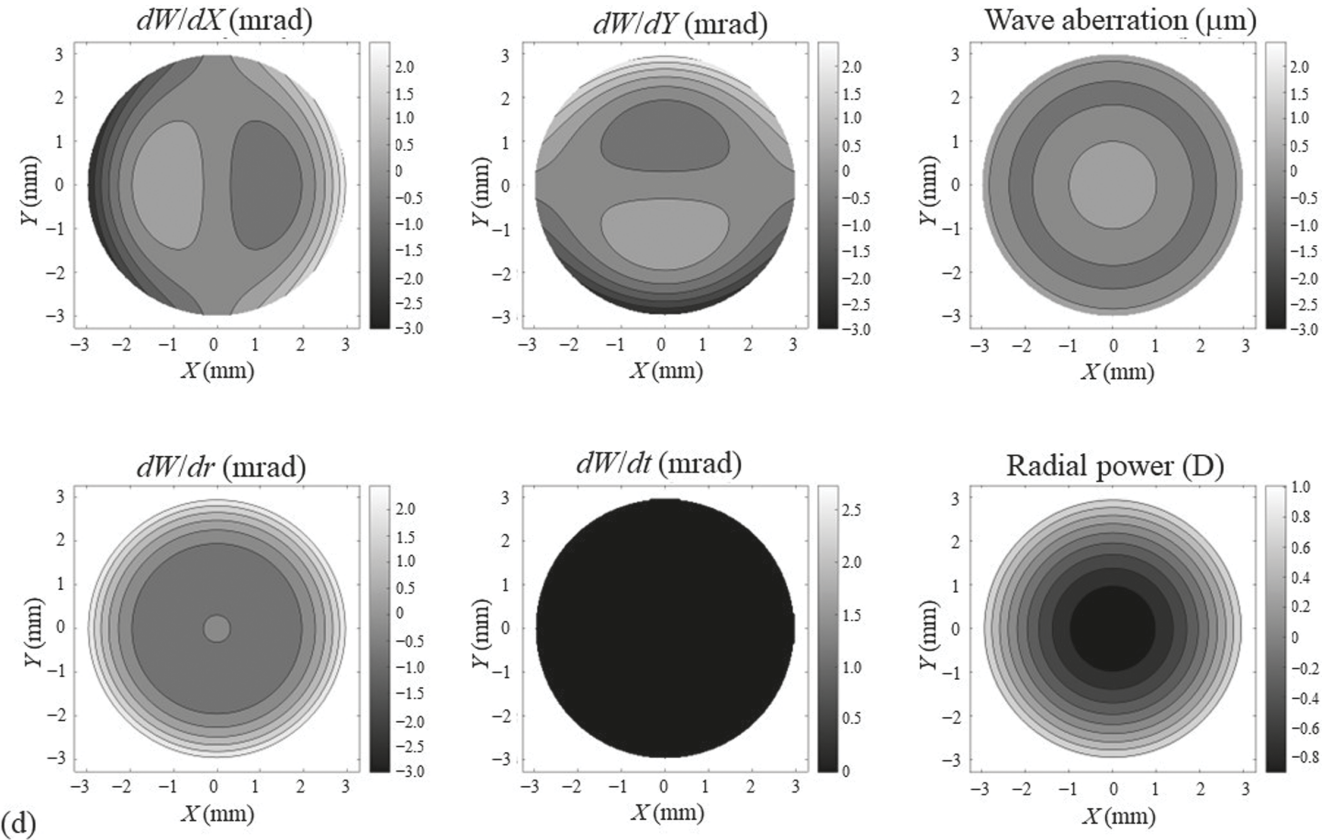


FIGURE A4.3 (Continued)

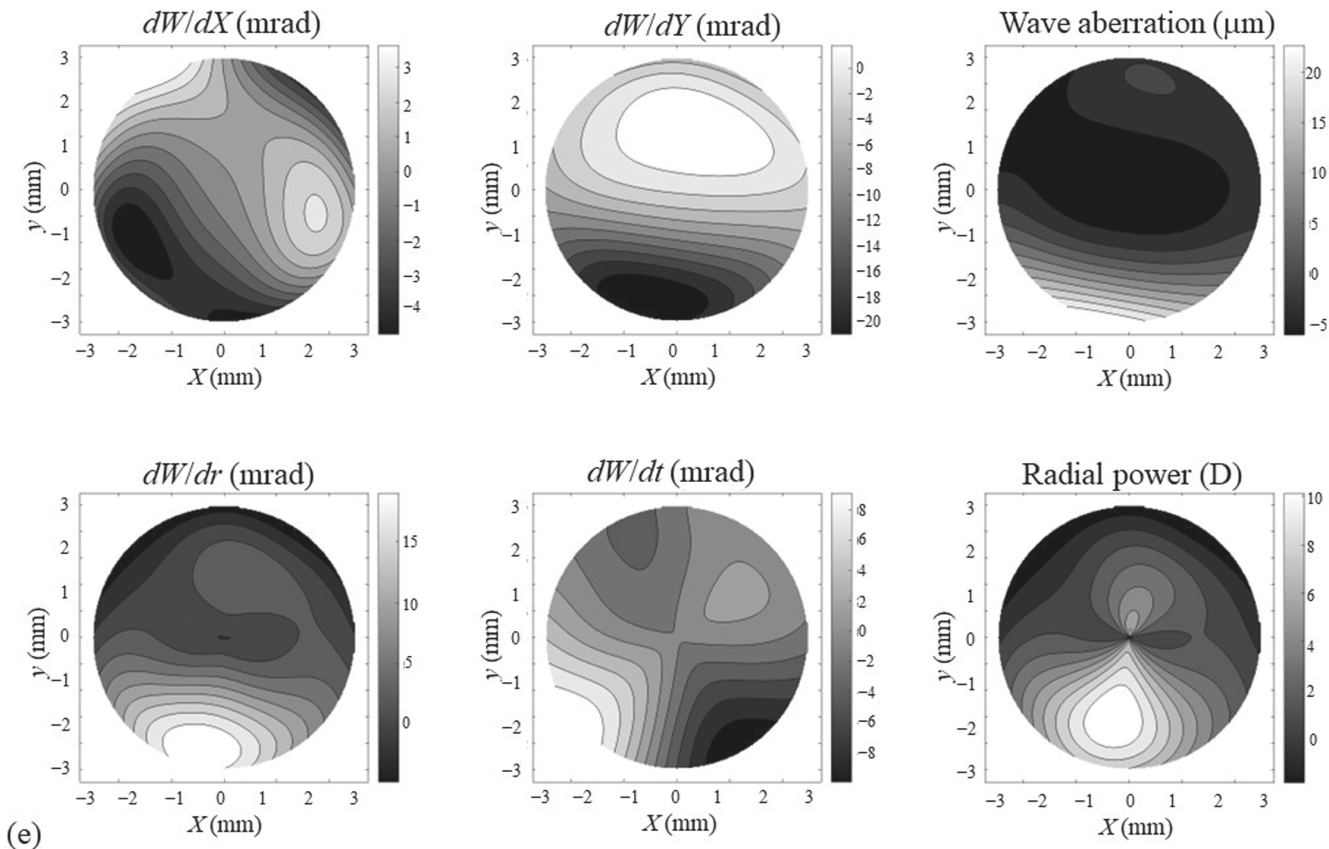


FIGURE A4.3 (Continued)

Appendix 5: Calculation of PSF and OTF from Aberrations of an Optical System

A5.1 THE POINT SPREAD FUNCTION (PSF)

We show how to calculate the PSF, considering diffraction, defocus, aberrations, polychromatic light, the photopic luminous efficiency function $V(\lambda)$ and the Stiles–Crawford effect. Scatter is more difficult to include in these calculations, so we will neglect it.

The PSF can be calculated if the wave aberration in the pupil of the eye is known. From optical image formation theory, the PSF is related to the wave aberration via a Fourier transform (Goodman 2017; Thibos 2000). The background for the following equations is taken from Smith and Atchison (1997).

Rather than express the PSF as a light distribution at the retina, we will express it as the equivalent distribution projected back into object space. The major difference will be that, in the first case spatial co-ordinates will be in linear quantities such as millimeters, and in the second case they will be in angular units. Calculating the point spread function back in object space, taken as air, also avoids the need to use the image space refractive index in the diffraction integral.

Before we present equations for calculating the PSF from the wave aberration in the pupil, we must first distinguish the amplitude PSF from the intensity PSF. The amplitude PSF is the complex amplitude of the light distribution, whereas the intensity PSF is the actual light distribution that we measure with a light meter. When we refer to the PSF, we mean the intensity PSF unless otherwise indicated.

If we denote the amplitude PSF as $g_a(u,v)$, where u and v are the directions in object space, and the PSF as $g(u,v)$, these two quantities are related by the equation

$$g(u,v) = g_a(u,v)g_a^*(u,v) \quad (\text{A5.1})$$

where * refers to the complex conjugate. The amplitude PSF is related to the wave aberration $W(X,Y)$ by the equation

$$g_a(u,v) = C \iint_{\text{E}} P(X,Y) e^{-i2\pi(uX + vX)} dXdY \quad (\text{A5.2})$$

where

$$C \text{ is a constant} = (1/\lambda) \quad (\text{A5.3})$$

E implies integration over the pupil of radius \bar{p} , (u, v) are related to the actual angles (in radians) θ_x and θ_y in the X and Y directions, respectively, by the equations

$$\theta_x = \lambda u \text{ and } \theta_y = \lambda v \quad (\text{A5.4})$$

(X, Y) are the cartesian coordinates in the pupil, and $P(X, Y)$ is the complex amplitude in the pupil known as the *pupil function*, which is mathematically defined as

$$P(X, Y) = A(X, Y)e^{[-ikW(X, Y)]} \quad (\text{A5.5})$$

The constant $k = 2\pi/\lambda$, $A(X, Y)$ is the amplitude transmittance at the point (X, Y) in the pupil, and is included to allow for the Stiles–Crawford effect. $W(X, Y)$ is the wave aberration as an optical path difference and is expressed in normal units of distance and not wavelength.

Equation (A5.2) is a Fourier transform of the pupil function $P(X, Y)$, and is zero outside the pupil. However, it would not be a Fourier transform if the object space variables were the real angles θ_x and θ_y , instead of u and v . In other words, the use of u and v and not θ_x and θ_y allows the amplitude point spread function to be expressed as a Fourier transform.

We will regard the Stiles–Crawford effect as rotationally symmetric and centered in the pupil, and we can write it as

$$A(X, Y) = e^{-[\rho_e(X^2 + Y^2)/2]} \quad (\text{A5.6})$$

where ρ_e is the Stiles–Crawford attenuation factor to base e and the “/2” factor is included because we must use an “amplitude” Stiles–Crawford effect and not the normal “intensity” effect (Krakau 1974). Typical values for ρ_e are given in section 14.5.

A5.1.1 THE WAVE ABERRATION FUNCTION $W(X, Y)$

The wave aberration function $W(X, Y)$ is described in detail in Appendix 2. It is one way of quantifying the level of aberrations. The function is a polynomial in X and Y , and the different terms represent the different aberrations, e.g., spherical aberration and coma. It can also incorporate defocus and chromatic aberrations.

A5.1.1.1 Defocus

If the eye is defocused by an amount ΔF , a defocus term $W_{2,0}(X^2 + Y^2)$ can be added to the wave aberration polynomial, where ΔF and the coefficient $W_{2,0}$ are related by equation (A2.5), i.e.,

$$W_{2,0} = \Delta F/2 \quad (\text{A5.7})$$

For example, a defocus of +0.5 D gives $W_{2,0} = +0.00025 \text{ mm}^{-1}$.

A5.1.1.2 Chromatic Aberration

As discussed in Chapter 17, longitudinal and transverse chromatic aberration arise because of the dispersion of the ocular media. The dispersion leads to a chromatic change in power $\Delta F(\lambda)$ given by the equation

$$\Delta F(\lambda) = F(\lambda) - F(\bar{\lambda}) \quad (\text{A5.8})$$

where $F(\lambda)$ is the power at the wavelength λ and $\bar{\lambda}$ is the reference wavelength for zero chromatic aberration. Equations for $F(\lambda)$ are given in Chapter 17.

For on-axis and off-axis point spread functions, longitudinal chromatic aberration is considered with a wave aberration term $W_{2,0}(\lambda)(X^2 + Y^2)$. The coefficient is related to the chromatic change in power $\Delta F(\lambda)$ by the equation

$$W_{2,0}(\lambda) = \Delta F(\lambda)/2 \quad (\text{A5.9})$$

For off-axis point spread functions, transverse chromatic aberration is considered with a wave aberration term $W_{1,1}(\lambda)Y$ or $W_{1,1}(\lambda)X$. The coefficient is related to the chromatic change in power $\Delta F(\lambda)$ by the equation

$$W_{1,1}(\lambda) = \bar{\theta} \mathbf{EN} \Delta F(\lambda) / n(\lambda) \quad (\text{A5.10})$$

where $\bar{\theta}$ is the angular distance off-axis, \mathbf{EN} is the distance from the entrance pupil to the front nodal point, and $n(\lambda)$ is the refractive index of the vitreous medium. Transverse chromatic aberration leads to a PSF having a transverse shift that is wavelength dependent.

A5.1.1.3 Polychromatic Sources

For polychromatic light sources, the PSF is calculated at several wavelengths. The chromatic aberrations are included in the wave aberration function. Each point spread function is weighted by both the relative sensitivity of the eye $V(\lambda)$ (section 11.3) and the relative radiance of the source $S(\lambda)$. The polychromatic point spread function is formed by adding the weighted individual point spread functions, but only after these have been expressed in terms of the real angles θ_x and θ_y , instead of u and v . That is,

$$g(\theta_x, \theta_y) = \sum_{\lambda} V(\lambda) S(\lambda) g(\theta_x, \theta_y)_{\lambda} \quad (\text{A5.11})$$

A5.1.1.4 Computation Checks

For any computation of the point spread function via equation (A5.2), it is good practice to have independent checks of the result. The following three conditions can be used:

1. If the system is free of aberration:

$$\begin{aligned} g(0,0) &= |g_a(0,0)|^2 = \left| C \int \int_E P(X,Y) dXdY \right|^2 \\ &= \left\{ (\pi/\lambda) \left\{ 1 - \exp \left[-(\rho_e/2) \bar{\rho}^2 \right] \right\} / (\rho_e/2) \right\}^2 \end{aligned} \quad (\text{A5.12a})$$

If no Stiles–Crawford apodization is present, i.e., $\rho_e = 0$,

$$g(0,0) = \left[(\pi/\lambda) \bar{\rho}^2 \right]^2 \quad (\text{A5.12b})$$

2. Volume under PSF = effective flux passing through pupil

$$= \pi \left(1 - \exp(-\rho_e \bar{\rho}^2) \right) / \rho_e \quad (\text{A5.13a})$$

If no Stiles–Crawford apodization is present, i.e., $\rho_e = 0$,

$$\text{Volume} = \pi \bar{\rho}^2 \quad (\text{A5.13b})$$

3. For an off-axis calculation and a single wavelength, the peak of the point spread function should occur at the angle in equation (A5.10), i.e.,

$$\theta_{\text{peak}} = \bar{\theta} \quad (\text{A5.14})$$

A5.2 THE OPTICAL TRANSFER FUNCTION (OTF)

A sinusoidal pattern with a real spatial frequency σ and an orientation ψ is shown in Figure A5.1. The spatial frequency components in the X and Y directions are

$$\sigma_x = \sigma \cos(\psi) \text{ and } \sigma_y = \sigma \sin(\psi) \quad (\text{A5.15})$$

The two-dimensional OTF, which we write as $G(\sigma_x, \sigma_y)$, is the Fourier transform of the PSF $g(\theta_x, \theta_y)$, that is

$$G(\sigma_x, \sigma_y) \int_{-\infty}^{+\infty} \int_{-\infty}^{+\infty} g(\theta_x, \theta_y) e^{-i2\pi(\theta_x \sigma_x + \theta_y \sigma_y)} d\theta_x d\theta_y \quad (\text{A5.16})$$

However, calculation of the OTF by this direct relationship is not necessarily the best approach, because the PSF has no bounds and the integral should therefore be carried out over an infinite range. In practice we must use finite bounds but, depending upon

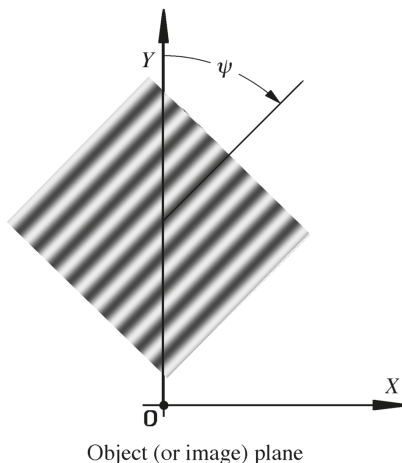


FIGURE A5.1 Sinusoidal pattern of grating inclined at an angle ψ .

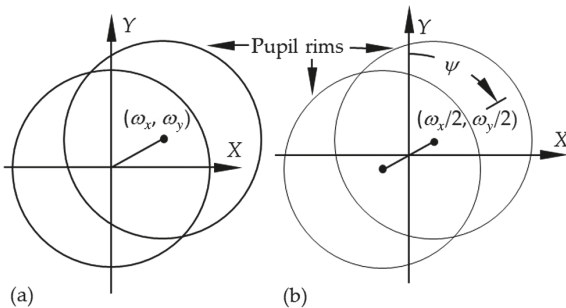


FIGURE A5.2 The sheared pupils used to calculate the OTF from equations (A5.17) and (A5.18).

how much of the PSF is outside these bounds, there will be errors in the results. A better alternative is to use a Fourier transform identity (Bracewell 1986), that states that the Fourier transform of the product of the transforms of two functions is the convolution of two functions. In this case, equation (A5.16) reduces to a convolution of the pupil function $P(X, Y)$ with its complex conjugate, as follows:

$$G(\omega_x, \omega_y) = \iint_c P(X, Y) P^*(X - \omega_x, Y - \omega_y) dXdY \quad (\text{A5.17a})$$

where

$$\omega_x = \sigma_x \lambda \text{ and } \omega_y = \sigma_y \lambda \quad (\text{A5.17b})$$

replace σ_x and σ_y in G and in the integrand.

Since the pupil function $P(X, Y)$ is zero outside the pupil, the limits of integration reduce to the region ‘c’ common to the two sheared pupils shown shaded in Figure A5.2a, and we do not have to write the integral limits from $-\infty$ to $+\infty$. A useful alternative and equivalent form of this integral is

$$G(\omega_x, \omega_y) = \iint_c P\left(X + \omega_x/2, Y + \omega_y/2\right) P^*\left(X - \omega_x/2, Y - \omega_y/2\right) dXdY \quad (\text{A5.18})$$

with the region of integration now being that shown in Figure A5.2b.

Macdonald (1971) has described such a method for the routine calculation of the OTF based upon the above auto-correlation integral, but with the amplitude function $A(X, Y) = 1$.

It is common practice to normalize the OTF so that $G(0, 0) = 1$.

SUMMARY OF MAIN SYMBOLS

$g(\theta_x, \theta_y)$	point spread function (PSF)
θ_x, θ_y	angles in X and Y directions

X, Y	cartesian co-ordinates in the actual pupil
ρ_e	Stiles–Crawford parameter to base e
$G(\sigma_x, \sigma_y)$	optical transfer function (OTF)
σ	spatial frequency (c/rad)
σ_x, σ_y	components of σ in the X and Y directions
ω_x, ω_y	corresponding modified spatial frequencies, related to (σ_x, σ_y) by equation (A5.17b).

REFERENCES

- Bracewell, R. 1986. *The Fourier Transform and its Applications*. Revised ed: McGraw-Hill.
- Goodman, J. W. 2017. *Introduction to Fourier Optics*. 4th ed. New York: W. H. Freeman and Company.
- Krakau, C. E. T. 1974. “Letter to the editor: On the Stiles-Crawford phenomenon and resolution power.” *Acta Ophthalmol* 52 (4):581–3. doi: 10.1111/j.1755-3768.1974.tb01768.x.
- Macdonald, J. 1971. “The calculation of the optical transfer function.” *Optica Acta* 18 (4):269–90.
- Smith, G., and D. A. Atchison. 1997. “Chapter 34. Image quality criteria.” In *The Eye and Visual Optical Instruments*, 647–72. New York: Cambridge University Press.
- Thibos, L. N. 2000. “Formation and sampling of the retinal image.” In *Seeing*, edited by K. K. De Valois, 1–54. San Diego, CA: Academic Press.

Index

A

- Abbe V-value, 338, 441
Aberrations, 251–343
 and depth-of-field, 380, 388–91
 higher-order, 254–9
 longitudinal, 252, 268–70, 455–64
 model eyes, 295–317
Aberrations, chromatic
 longitudinal, 120, 331–2
 compensation, 334–6
 effect of accommodation, 329, 331
 effect on accommodation, 331
 effect of age, 407
 effect of refractive error, 329, 392
 effect on spatial vision, 331–2, 367–8
 magnitude, 327–8
 measurement techniques, 325–7
modelling, 336–42
 and refraction, 120, 135
Seidel, 433–4, 436
 and wavelength in focus, 328
transverse, 322–4, 330–1
magnitude, 330–1
measurement techniques, 329–30
optical and perceived, 324
Aberrations, monochromatic
 and accommodation, 275, 280
 and age, 275, 280–2, 407
 astigmatism, 253, 257–8, 266–7, 272–3,
 277–80, 296–9, 311–13
 coma, 254, 258, 267, 275, 280–2, 295–8, 311
 distortion, 49–50, 254, 283, 297
 higher-order, 254, 258, 274–6, 280–3
 measurement techniques, 273–4
 ocular component contributions, 270–1, 275
 other aberration systems, 270
 peripheral aberrations, 271–3, 277–83, 296–9,
 310–13
 primary (also Seidel and third order), 254,
 433–9
 and pupil size, 256, 260, 274–5
 reference axis, 270
 representation, 251–2
 right and left eyes, 264, 275, 280
 tangential and sagittal refraction components,
 271–2, 278, 296–9, 311–12
 schematic eyes, 295–9, 309–16, 448, 452
 spherical aberration, 258, 259–63, 268, 274–7,
 280–2
 Taylor series, 253, 259–64
 and wavelength, 271
 Zernike system, 254–73
Absorption
 fundus, 229–30, 232–3
Accommodation, 3, 31–5
 accommodating IOLs, 176
 amplitude, 32, 402–3
 and cardinal points, 76, 80
 demand,
 ocular and spectacle, 160–2
 and depth-of-field, 380
effect of longitudinal chromatic aberration, 331
effect on longitudinal chromatic aberration,
 329, 341
effect on monochromatic aberrations, 275, 280
effect on ocular parameters, 32–5
and gradient index of lens, 35, 380
and hyperopia, 96
mechanism, 31
and presbyopia, 96–7
and pupils, 45, 46, 48–9
and refraction, 134
and schematic eyes, 76–80, 308, 444–5, 450
and Stiles-Crawford effect, 242
stimulus and response, 35
Achromatizing correcting lenses, 334–5
Adaptive optics, 358, 364, 365, 371
Age, 395–410
 and aberrations, 407
 and amplitude of accommodation, 402–3
 and anterior chamber, 396
 and axial length, 401
 and cornea, 395–6
 and lens, 397–401
 and paraxial schematic eyes, 409–10
 and photometry, 407–9
 and pupil diameter, 396
 and refractive errors, 98, 401–2
 and Stiles-Crawford effect, 409
 and theories of presbyopia, 403–6
 and vitreous chamber, 401
Airy disc, 351
Aliasing, 361–2
Ametropia (*see* Refractive errors)
Amplitude of accommodation, 32, 402–3
Angles, 63–7
 alpha (α), 64
 gamma (γ), 66–7
 kappa (κ), 66
 lambda (λ), 65–6
 psi (Ψ), 66

- Aniseikonia, 90–1, 160
 Anisometropia, 90, 95, 153, 160, 176
 Anisotropy, 207
 Anterior chamber, 3
 and age, 396
 Apodization, 238, 349
 Aqueous, transmittance, 199–200
 Artificial pupils, 54
 defocus, 143
 depth-of-field, 390
 Asphericity
 conicoid, 19–23, 298–300
 of cornea, 22–4, 39
 figured conicoid, 301
 of lens, 28–9
 Zernike terms, 301
 Astigmatism (refractive error), 97–8
 and age, 102, 401–2
 Axes
 definitions and significance, 57–68
 fixation, 60
 foveal achromatic, 58–9
 keratometric, 61, 63
 line of sight, 58, 62
 optical, 10, 57–8
 pupillary, 59–60
 pupillary circular, 61–2
 visual, 10, 58–9, 62–3
 Axial length
 influence of chromatic dispersion on
 measurement, 342–3
 and refraction error, 101
- B**
- Badal optometer, 117–19
 Best form/corrected curve lenses, 167
 Binocular overlap, 12
 Binocular vision, 11, 89–91
 aniseikonia, 290–1
 stereopsis, 89–90
 Birefringence, 207–8
 cornea, 208
 form, 208
 intrinsic, 208
 lens, 209
 nerve fiber layer, 234
 Black body, 192, 223
 Blind spot, 8
 Blur disc, *see* Defocus blur disc
 Bowman's membrane of cornea, 16
- C**
- Capsule of lens, 25
 Cardinal points, 8–9, 426
 and accommodation, 76, 80
 of finite schematic eyes, 451–2
 of paraxial schematic eyes, 71–3, 446–7
 Center-of-rotation of eye, 10, 57, 60, 66–7, 165
 Chambers of the eye, 3
 Choroid, 3
 Chromatic aberrations, *see* Aberration, chromatic
 Chromatic difference of magnification, 324–5
 Chromatic difference of power, 321–2, 340–1
 Chromatic difference of position, 324
 Chromatic difference of refraction, 321, 327–8,
 340–2
 Chromatic dispersion, 321, 336–40
 Chromo-retinoscopy, 327
 Chromostereopsis, 332–3
 Ciliary body, 3, 402
 Coddington refraction equations, 165–6
 Colorimetry, 191–3
 chromaticity co-ordinates, 191–2
 color matching functions, 191
 color temperature, 192
 correlated color temperature, 192
 tristimulus values, 191
 Component ametropia, 100
 Cones, 6–7, 243
 Conicoid, 19–23, 298–300
 ellipsoid, 19–21
 hyperboloid, 19–21
 paraboloid, 19–21
 Contact lens optics, 168–73
 aberrations, 277
 fluid lens, 168–9, 171–2
 hard (rigid), 169
 over-refraction, 171
 soft (flexible), 169
 spectacle magnification, 173
 Contrast sensitivity function, 355, 357–8, 364–7
 Cornea, 3, 15–19
 and age, 395–6
 asphericity, 22–4, 29
 astigmatism, 19, 24, 395
 birefringence, 208
 power, 17–19
 principal points, 25
 radii of curvature, 17–18
 refractive index, 17
 sagittal (axial) radius of curvature, 23–4
 scatter, 205–6
 short term changes, 25
 tangential (instantaneous) radius of curvature,
 23–4
 thickness, 24, 396
 toricity, 19, 24
 transmittance, 199–200, 396
 vertex powers, 17–19

Corneal sighting center (visual center of the cornea), 58, 63
Correlation ametropia, 100
 Cos^4 law, 216
Crystal,
 biaxial and uniaxial, 208
Cyclotorsional eye movements, 25, 60
Cylindrical lens and axis, 104

D

Defocus, 139–49
 and alignment of objects at different distances, 148
 and change of wavelength, 271
 effect on image quality, 364–8
 effect on visual acuity, 148–9
 and optical transfer function, 358–61
 in peripheral refraction, 271–2
 and phase transfer function, 364
 and wave aberration, 432, 466
Defocus blur disc, 140–7
Defocus ratio, 149
 Depth-of-field, 370–92
 and aberrations, 380, 388–91
 and accommodation, 380
 criteria, 381–90
 effect of luminance, 380
 geometrical approximation, 386–7
 modeling, 386–90
 and pupil size, 380–3, 386–8
 and target size, 380, 389
Depth-of-focus *see* Depth-of-field
Descemet's membrane, 16–17
 and age, 395
detectiontask, 362
Diffraction
 and depth-of-field, 387
 diffraction-limited, 350–2, 356
Dimensions of eye, 12
Diopter, 10
Diplopia with ophthalmic lenses, 164
Distance notation and sign, xv, 422
Double-pass techniques, 330, 349, 353–4
Dua's layer, 16
Duochrome test, 120

E

Eccentric fixation, 60, 65
Eccentricity e , 21–2
Eikonometer, 91
Emmetropia, 94
Emmetropization, 98
Endothelium of cornea, 17
Entrance and exit pupils, 43–4

and accommodation, 45
of paraxial schematic eyes, 72–4
Epithelium of cornea, 15–16
Equivalent power, 9–10
Equivalent refractive index 30, 400
Equivalent sphere (mean sphere), 98
Equivalent veiling luminance, 219
 and age, 408–9
 conventional threshold method, 221
 flicker compensation comparison method, 221–2
Hartmann-Shack aberrometer, 222

F

Far point, 32, 93–7, 160
Far point sphere, 165
Field-of-view of ophthalmic lenses, 163–4
Field-of-vision, 10–11
 of ophthalmic lenses, 164
Figured conicoids, 301
Finite (real) ray, 421
Fluid lens, 168–9, 171–2
Fluorescence, 206–7
Fluorogens, 206–7
Focal length, 9
Focal points, 8–9, 426
Fovea, 7
Foveola, 7
Fundus, 3, 115, 229
 absorption, 229, 232–3
 reflectance, 230–1

G

Gaussian optics, 427
Gender (male/female) differences, 409–10
corneal radius of curvature, 17–18
Glare, veiling, 232
Gradient refractive index of the ocular lens, 29, 71, 302–5, 308, 451
 and accommodation, 35
 and age, 253–4
 and lens power, 305–6
Grating focus, 125
Greek symbols, xv

H

Halation, 232
Half-width of point spread function, 353
Hartmann-Shack aberrometer, 128–30
Heterotropia (tropia), 60, 65–6
Hippus, 47
Hirschberg test, 65–6
Hyperopia (hypermetropia), 65–6, 96, 164

I

- Illuminance, 189
 retinal, 213–22, 314–15
 Image quality criteria
 line spread function, 350, 353–4
 metrics, 371–2
 modulation transfer function (MTF), 355–8
 optical transfer function (OTF), 350, 354–9,
 468–9
 phase transfer function (PTF), 355, 359, 364
 point spread function (PSF), 350–3, 465–8
 wave aberration function, 253–6, 431–3, 466

Image-size principle, 125–7

Inter-pupillary distance (PD), 11

Intraocular lenses (IOLs), 173–8
 aberrations, 277–8, 282
 accommodating, 176
 power, 175
 relative magnification, 176–8

Inverse square law, 189

Iris, 3, 43

Iseikonic lenses, 91

Isogonal lenses, 91

Isotropic, 207

J

Jackson crossed-cylinders, 106

K

Knapp's law, 159, 160

Knife-edge techniques, 124

L

Lambertian sources, 188

Laser raytracing, 129

Lens equation, 426–7

Lens of the eye, 25–31

- and accommodation, 31–5
- and age, 379–401
- asphericity, 28–9
- birefringence, 209
- diameter, 30, 35, 400
- equivalent refractive index, 30, 400, 401
- fluorescence, 206–7, 401
- power, 30–1
- principal points, 31
- radii of curvature, 28–9, 307
- refractive index distribution, 29, 35, 302–5,
 399–400
- scatter, 206, 401
- thickness, 29, 35, 399
- transmittance, 199, 401

Lenses, Ophthalmic

contact, 168–73, 276–7, 333–4

intraocular, 173–8, 277, 333–4

iseikonic, 91

isogonal, 91

spectacle, 153–67, 273–4, 333

thick, 107–8

Light, definition, 183–4

Line spread function (LSF), 350, 353–4

Luminance, 188–9

Luminous flux, 187

Luminous intensity, 187

Luminous transmittance, 203

M

Macula, 8

Magnification

chromatic, 324–5

pupil, 49–50, 73–4, 76, 156–7

relative spectacle, 158–60

spectacle, 153–6

transverse (lateral), 425, 427

Maximum spectral luminous efficacies of radiation

 for photopic vision, 185

 for scotopic vision, 186

Maxwellian view, 224–5

 adapting pupil size, 225

equivalent luminance of a Lambertian source, 224–5

Mean oblique error of spectacle lenses, 167

Mean sphere (equivalent sphere), 98, 106

Mesopic vision, 186

Mie theory, 205

Mirror symmetry of right and left eyes

 astigmatism of cornea, 19

 higher-order aberrations, 280–2

Model eyes, *see* Schematic eyes

 customized, 316

Modulation transfer function (MTF), 355–8

Monochromatic aberrations, *see* Aberrations,

 monochromatic

Monovision, 175

Myopia, 94–5, 101, 164

 and peripheral coma, 280

 and peripheral refraction, 278–80

N

Near point, 32, 96, 160–1

Nerve fiber layer (retinal), 5, 234

Nodal points, 9, 71, 86–8, 143, 426

 of schematic eyes, 72, 76, 80, 446–7, 451–2

Nyquist limit, 362

O

Oblique astigmatism of spectacle lenses, 166

Ophthalmic lenses *see* Lenses, ophthalmic

- Ophthalmometric pole, 59, 62
Ophthalmophakometer, 64
Optic disc, 8
Optical invariant, 425–6, 434–5
Optical path length, 429
Optical radiation, 183
Optical transfer function (OTF), 350, 354–9, 468–9
 diffraction limited, 356
 effect of defocus, 358–61
Optometers, 115–35
 Badal, 117–19
 Hartmann-Shack sensor, 128–9
 laser raytracing, 129
 polarizing, 122
 telescopic, 119–20
Orthokeratology, 280
- P**
- Pantoscopic tilt, 167
Parallax movement between object and image, 124–5
Paraxial image, defocused, 139–51
 Defocus blur disc, 143–7
Paraxial marginal ray, 45, 434–5
Paraxial optics, 421–8
Paraxial pupil ray, 45, 434–5
Paraxial pupil ray angle ratio, 75–6, 87
Paraxial ray, 422–3
Paraxial ray-tracing scheme, 424–5
Paraxial refraction equation, 423
Paraxial transfer equation, 423
PD (inter-pupillary distance), 11
Phase transfer function, 355, 359, 64
Photography (photorefraction), 128–31
Photometric efficiency and Stiles–Crawford effect, 237
Photometry
 and age, 407–9
 equivalent veiling luminance, 219
 illuminance, 189
 inverse square law, 189
 luminance, 188–9
 luminous flux, 187
 luminous intensity, 187
 measurement of ambient light level, 191
 photon density levels at retina, 222–3
 point brilliance, 189
 relation between photometric quantities, 189–90
 scatter, 203–6
 specular reflectance, 196–9
 supra-threshold visibility, 190–1
 threshold detection, 190
 transmittance, 198–203
Troland, 214
units, 187–9
- Photon density levels at retina, 223–4
Photopic vision, 185–6
Photoretinoscopy, 130
Piper's law, 190
Point brilliance, 189
Point spread function (PSF), 350–3, 465–8
 aberrated, 352
 diffraction limited, 350–2
 in eyes, 353–4
 half-width, 353
 polychromatic sources, 467
 and Rayleigh criterion, 352
and Strehl intensity ratio, 353
Planckian locus, 192
Polarization
 retina, 231, 232
Polymegathism, 395
Power
 equivalent, 426
 of a surface, 17, 423
 thick lens, 107–8, 153
 thick lens equation, 18
 thin lens, 108, 153
 vertex, 155
Presbyopia, 96–7, 402–6
 theories, 403–6
Principal points, 8–9
 of cornea, 25
 of lens, 31
Pupil, 43–56
 aberration, 49–50
 and accommodation, 45
 artificial, 54, 143, 390
 centration, 46
 decentration effects, 335, 368, 370
 entrance, 43–4
 exit, 43–4
 magnification, 49–50, 73–4, 76, 156–7
 position, 156–7
 senile miosis, 396
 size, 46–54, 215–26, 358, 379–83, 396
Pupil function, 466
Pupillary light response purpose, 53
Pupillometry, 54
Purkinje images, 196–7
Purkinje shift, 186
- R**
- Radiant flux, 183
Radiometry, 183
Ray
 extra-ordinary, 200
 finite (real), 429
 ordinary, 200
 paraxial, 422–3

- paraxial marginal, 45, 74, 433
 paraxial pupil, 45, 74, 433
 pupil (chief), 251
 pupil nodal, 59
 Rayleigh criterion, 352
 Rayleigh–Gans (Rayleigh–Debye) theory, 205
 Rayleigh scattering, 204
 Ray-tracing
 finite, 422–3
 paraxial, 425
 Real (finite) ray, 421
 Reduced vergence, 427
 Reference sphere, 433
 Reflectance, fundus, 230–2
 Reflection, specular, 196–7
 Refraction
 components in $F_{sp}/F_{cy} \times \alpha$ system, 104
 components in $M, J_{180^\circ}, J_{45^\circ}$ system, 104–7
 factors influencing, 133–5
 ocular, 103
 paraxial (Seidel), 266
 power variation across the pupil, 268–70, 455–9
 spectacle, 102
 Zernike, 266
 Refraction techniques, objective, 123–31
 subjective–objective, 121–3
 subjective only, 115–20
 Refractive errors
 and age, 98, 401
 anisometropia, 98
 astigmatism, 97–8
 and axial length, 101
 component ametropia, 100
 correlation ametropia, 100
 distribution, 98–100
 effect of ocular parameter changes, 108–11
 emmetropia, 93–4
 factors affecting, 133–5
 hyperopia (hypermetropia), 96
 and longitudinal chromatic aberration, 341, 392
 myopia, 94–5
 Refractive index
 of cornea, 17
 of lens, 29–30, 35, 302–5, 399–400
 Relative peripheral hyperopic refraction, 277–8
 Relative peripheral myopic refraction, 277–8
 Relative spectacle magnification, 158–60
 and axial ametropia, 159
 and Knapp's law, 159
 and refractive ametropia, 159–60
 Remote refraction and relay systems, 121
 Resolution limit, 356, 359–60
 Resolution task, 362
 Retina, 5–8
 birefringence, 234
 fovea, 7
 foveola, 7
 macula, 8
 modelling (shape), 306–7
 Retinal directionality, *see* Stiles-Crawford effect
 Retinal illuminance, 213–25
 direct light, 213–19, 314–15
 scattered light, 219–22
 Retinal image quality, 349–72
 central, 363–70
 peripheral, 370–1
 Retinal image size
 defocus blur disc, 143–7
 defocus ratio, 147, 149
 defocused image, 139–51
 focused image, 85–91
 Retinoscopy, 124
 Ricco's law, 190
 Rods, 6–7
- ## S
- Scatter, 203–6
 cornea, 205–6
 fundus, 232
 iris and sclera, 206
 lens, 206
 Mie theory, 205
 Rayleigh, 204
 and Stiles-Crawford effect, 196, 243–6
 Scheiner principle, 122–3
 Schematic eyes, finite (wide angle)
 aberrations, 309–15, 448–52
 Chromatic eye, 309, 342
 Drasdo and Fowler, 307
 Indiana eye, 309, 342
 Kooijman, 307–8, 449
 Liou-Brennan, 308–9, 451
 Lotmar, 306–7, 499
 Navarro et al., 308, 450
 performance, 309–15
 retinal illuminance, 314–15
 Schematic eyes, paraxial, 69–82, 441–8
 aberrations, 295–300, 330, 48
 and age, 409–10
 Bennett-Rabbatts reduced, 78
 Bennett-Rabbatts simplified, 78, 443
 Emsley reduced, 78, 443
 entrance and exit pupils, 73–4
 Exact schematic eyes, 76–7, 442, 444
 Gaussian properties and cardinal points, 71–3
 Gullstrand number 1 (exact), 76–7, 442, 444

- Gullstrand–Emsley (simplified), 78, 443, 445
history, 70–1
Le Grand full theoretical, 77, 442, 444
Le Grand simplified, 78
reduced, 78, 443
simplified, 77–8, 443, 445
variable accommodating, 79–80
- Sclera, 3
- Scotoma with ophthalmic lenses, 164
- Scotopic vision, 186
- Seidel aberrations, 429–39
of finite schematic eyes, 452
influence of gradient index, 437–9
influence of retinal curvature, 437
- of paraxial schematic eyes, 446–7
- Senile miosis, 396
- Sign convention and symbols, xv, 422
- Simple perception of blur, 115–20
- Snell's law, 421
- Spectacle lens design, 164–8
best form/corrected curve, 167
center-of-rotation of eye, 165
Coddington refraction equations, 165–6
mean oblique error, 167
oblique astigmatism, 166
tangential and sagittal power errors, 166
Tscherning ellipse, 167–8
- Spectacle lenses, 153–68
aberrations, 165–7, 276, 333–4
- Spectacle magnification, 153–6
contact lenses, 173
rotational magnification, 163
- Spectral luminous efficiency function
for photopic vision, 185–6
for scotopic vision, 186
- Spherical aberration, 254, 259–63
and accommodation, 275
and age, 407
and cornea, 23
effect on depth-of-field, 391
in real eyes, 275, 276, 281, 295–7, 309–10
in schematic eyes, 295–9, 309–16
- Split image and vernier acuity (coincidence method), 121–2
- Spurious resolution, 359–60
- Stereopsis, 11, 89–90
- Stiles–Crawford effect (retinal directionality), 234–44
and accommodation, 242
and age, 409
and eccentricity, 239
and eye disease, 242
and field size, 241
- Gaussian and super-Gaussian fits, 235
- Geometric optics absorption model, 243
influence on effective image quality, 368–9
integration across the pupil, 237
and luminance, 240
measurement, 243
and photometric efficiency, 237–8
photometric equivalent pupil (diameter), 237
and phototropism, 242, 368–9
and pupil function, 466
and refractive errors and aberrations, 241
role, 196, 243–4
and scatter, 243–4
theory, 243
waveguide theory, 243
and wavelength, 238–9
- Straylight parameter s , 220–1, 409
- Strehl intensity ratio, 353, 371
- Stroma of cornea, 16
- T**
- Tangential and sagittal refraction, 271–3, 296–9, 311–12
- Tear film, 15
- Thick lenses, 107–8
- Transmittance, 198–203
absorption bands, 201–3
aqueous, 199–200
cornea, 199–200
direct, 198–9
lens, 199, 201
loss throughout eye, 199, 202
luminous, 203
vitreous, 199, 201
whole eye, 198–9
- Transverse aberrations, 252, 429–30
- Troland, 214
- Tropia (heterotropia), 60, 65–6
- Tryptophan, 206–7
- U**
- Units, xv
- V**
- V -value (or Abbe V -value), 338, 441
- Veiling glare 232
- Vergence, 427
Vernier alignment and chromatic aberration, 325–6, 329–30
and refraction, 121–2
- Vertex distance, 102–3, 107–8

Vertex normal of cornea, 61
Visual acuity, 148–9
Visual center of the cornea (corneal sighting center), 58
Visual evoked response (VER), 131
Visual performance, 283–6, 331–2, 361–3, 408
Visual Strehl ratio, 371
Vitreous
 transmittance, 191, 201

W

Wave aberration
 function (polynomial), 253–9, 431–3, 466
Wave-front sensing, 128

Z

Zonules, 26, 406